Creative students, what would be the best cover for this fusion technology textbook?

Join the contest and maybe your design will be selected for the hard cover

FUNDAMENTALS OF MAGNETIC FUSION TECHNOLOGY

Edited by: Guido van Oost
Sehila M. Gonzalez de Vicente

IAEA
International Atomic Energy Agency

FUNDAMENTALS OF MAGNETIC FUSION TECHNOLOGY

COPYRIGHT NOTICE

Marketing and Sales Unit
Publishing Section
International Atomic Energy Agency
Vienna International Centre
PO Box 100
1400 Vienna, Austria
fax: +43 1 2600 29302
tel.: +43 1 2600 22417
email: sales.publications@iaea.org http://www.iaea.org/books

For further information on this publication, please contact:

Nuclear Fuel Cycle and Materials Section
International Atomic Energy Agency
Vienna International Centre
PO Box 100
1400 Vienna, Austria
Email: Official.Mail@iaea.org

EDITORIAL NOTE

PREFACE

Reliable and sustainable sources of energy will remain an essential ingredient for human development. Since carbon-based energies have an enormous impact on our climate, alternative energy sources must be developed. The solution to the energy and climate problems can only come in the form of a portfolio of options that includes improvements in energy efficiency and (to varying degrees in different countries) renewable energy, nuclear fission, carbon capture and storage and nuclear fusion. Controlled thermonuclear fusion is one of the very few options to provide us with a long-term, environmentally friendly and inherently safe contribution to solve the energy problem we are facing. Fusion has advantages that ensure sustainability and security of supply, safety and sustainability: fuels are geographically widely available (energy independence) and virtually unlimited; it is inherently safe and does not provide long-term radioactive waste. A fusion power plant provides a centralized source of base load electricity.

Making fusion energy a reality depends crucially on the success of ITER (the Latin word for "The Way"), currently under construction in the south of France. ITER is a large-scale scientific experiment intended to prove the viability of fusion as an energy source. In an unprecedented international effort, seven partners—China, the European Union, India, Japan, Korea, Russia and the United States—have pooled their financial and scientific resources to build the biggest fusion reactor in history. When finished, it will be the first fusion device to produce net energy, and will allow to demonstrate the scientific and technological basis for large-scale fusion energy. It will lead the way to the subsequent implementation of the DEMO fusion reactors, followed by commercial fusion power plants. The first plasma in ITER is scheduled for the end of 2025.

The continued education of scientists and engineers in fusion science and technology is essential both to the success of the ITER Project and to the application of the scientific and engineering insights gained through ITER to the goal of realizing fusion as an energy source. A large number of scientists and engineers will be required in two main categories: “Plasma physics” and “Fusion technology and engineering”. Their training and education takes typically 10 years, requiring a structured master level education.

The need for an integrated and international fusion education programme is further motivated by the increasingly important role of industry in fusion R&D. Indeed, over the coming decades the Fusion R&D Programme will shift from being science-driven and laboratory-based towards a technology-driven, industry-based venture. ITER will test or validate most technological solutions for DEMO, and significant innovation is and will be required in some areas such as breeding blanket technology, plasma-facing and structural materials, superconducting magnets, microwave sources, high power beam sources, remote handling, control technology and fuelling and pumping systems. Furthermore, the transition will focus on technologies and standards associated with the “nuclearization of fusion” which has consequences for the competences of the workforce. Fusion research further shows an increasing and very important spin-off in many fields of science and engineering, such as new materials, nanotechnologies, superconducting coils, robotics, electronic components, high power RF sources and space propulsion.

The role of industrial partners will evolve from that of a provider of high-tech components to that of driver of the fusion development. This will be a stepwise, long and gradual process, through consortia that will bring together industry, research laboratories and universities, in connection with DEMO R&D. Indeed, although at this moment innovation is already being jointly pursued in fusion by industry, research laboratories and universities, their synergies can only be fully exploited by facing the challenge of the realization of large projects like ITER and DEMO and focusing on them. This necessitates a close interaction between industry, research centers and universities through consortia.

The main objective of this textbook is to contribute to the consolidation and better exploitation of the achievements already reached in the past and to tackle the present challenges in preparing the workforce in the different areas, with special attention to continuous professional development and life-long learning. This textbook is primarily intended for a course “Fundamentals of Magnetic Fusion Technology” at master level. It has been prepared in the framework of the FuseNet Association (the European Fusion Education

Network). Given the fast evolution in the broad field of magnetic fusion technology in view of ITER, DEMO and fusion power plants, the fusion education community needs such a textbook that will be suitable as lecture material. The book will also be useful for specialists from academia, research institutions and companies who want to acquire knowledge of other areas in magnetic fusion technology, as well as for a wider range of readers interested in the establishment of magnetic fusion as an energy source.

Twenty-five experts have contributed to the book which contains 12 chapters covering a wide range of topics (*magnetic fusion and fusion reactors, plasma heating and current drive, plasma diagnostics, plasma control and data analysis, magnetic confinement, plasma facing components, fusion neutronics, materials for fusion reactors, vacuum pumping and fueling, tritium handling and tritium plant, remote handling and maintenance, stellarators*). The book is edited by Professor Guido Van Oost and Dr Sehila M. Gonzalez de Vicente.

Acknowledgements

The editors want to thank for the qualified contributions of all the authors who, through their work, are helping to advance fusion technology worldwide. Professor Thomas J. Dolan (University of Illinois, USA), editor of the book Magnetic Fusion Technology (Springer, 2013) deserves special thanks for kindly reviewing the chapters and making very useful suggestions.

The editors would like to acknowledge the contribution of the European Fusion Education Network (FuseNET) to the publication of this book, and in particular of Mr Guido Lange.

The authors are most grateful to Alexis Devitre (Ghent University, Belgium and MIT, USA) and Lukas Kripner (Charles University in Prague & Institute of Plasma Physics of the Czech Academy of Sciences, Prague, Czech Republic) who very carefully made the extensive preliminary editing work, and provided valuable feedback. Also to Matteo Barbarino (IAEA) who contributed to the publication of this book.

Guido Van Oost
Sehila M. Gonzalez de Vicente

TABLE OF CONTENTS

Chapter 1

INTRODUCTION TO MAGNETIC FUSION AND FUSION REACTORS

Guido Van Oost
Ghent University, Department of Applied Physics
Belgium
National Research Nuclear University "MEPHI"
Moscow, Russia
National Research University "MPEI"
Moscow, Russia

1.1. PROSPECTS FOR FUSION AS AN ENERGY SOURCE

In a most profound sense, humankind's quality of life depends on an acceptable response to a continually rising demand for energy. To satisfy the world's future energy needs investment is needed in all viable energy options compatible with our environment. *Carbon-based energies are* non-sustainable and dangerous for several reasons:

- Burning fossil fuels is having a measurable impact on the Earth's atmosphere and could trigger serious changes in climate.
- A much more interesting use could be made of these resources such as in the chemical and pharmaceutical industry.
- Fossil fuels will run out.

The solution to the energy and climate problems can only come in the form of a portfolio of options that includes improvements in energy efficiency and (to varying degrees in different countries) renewable energy, nuclear fission, carbon capture and storage and nuclear fusion.

Non-fossil candidates which could substantially contribute to sustainable energy production in the long-term are limited to renewable energies, nuclear fission and nuclear fusion. Although renewable energy resources are inexhaustible, low energy densities and fluctuations in time imply a need for storage. This reduces the efficiency of renewables and leads to extra costs [1.1].

In the case of fission, rising concerns are directed towards waste management, operational safety and nuclear proliferation. However, it seems unwise to plan a complete shutdown if no good alternative is ready to take over the nuclear share. Likewise, it would serve no good to import nuclear power from other countries or end up with an increased dependency on fossil fuels. In this respect, ill-advised decisions could result in the loss of a highly-valuable know-how associated to a technology that can serve good purposes in the coming decades [1.1].

Fusion is the least developed alternative, yet offers particularly valuable advantages that ensure sustainability and security of supply, safety and sustainability: fuels are geographically widely available (energy independence) and virtually unlimited; it is inherently safe and does not provide long term radioactive waste. A fusion power plant provides a centralized source of large-scale base load electricity.

Energy-quality criteria are becoming more and more important: energy production needs to be economically, but also environmentally and societally acceptable [1.1]. If R&D in fusion energy delivers the advances predicted, then in the second half of the twenty-first century it could be on the way to achieve these goals.

Fusion features exclusive properties, some of which present distinct advantages over the other major energy sources. These can be grouped into 3 aspects [1.1]:

- Fuel: abundant supply of cheap non-radioactive fuels (deuterium and lithium), the extraction of which does not cause any significant ecological problem.
- Safety: fusion reactors offer inherent passive safety. They are not based on a neutron multiplication reaction nor do they contain a large supply of fuel in their core. An uncontrolled burn of the Chernobyl type is excluded.
- Environment: fusion reactions produce energy and no direct radioactive waste. However, in current fusion reactor concepts, there is radioactivity from two sources. First from tritium, which is locally bred from lithium and directly consumed. Second, by the activation of reactor structures by neutrons. Future reactor concepts might strongly limit this radioactivity. Anyhow, by carefully choosing structural materials (see Chapter 8), the radioactive waste will not constitute a burden for future generations. In addition, there is no production of combustion gases, hence no contribution to the greenhouse effect, acid rains or the destruction of the ozone layer.

The first breakthrough into the peaceful use of fusion as an energy source came from Russia in 1968 when a magnetic confinement device was invented with an excellent capacity for containing high temperature plasmas. The device is called a tokamak and has been the focus of the mainstream of fusion R&D ever since. The success of the tokamak prompted the construction of large devices that started operation in the first half the 1980s, such as the Joint European Torus (JET) in Europe at Culham, UK and the Tokamak Test Fusion Reactor (TFTR) at the Princeton Plasma Physics Laboratory, USA. Many complementary devices and facilities around the world were also built to investigate the broad range of science, technology and engineering challenges. The second big breakthrough came in the 1990s when JET and TFTR confirmed the physics of generating fusion energy using a mixture of tritium and deuterium. On this basis, Europe developed a coherent, success oriented and comprehensive programme for addressing all the challenges of a fusion power plant based on the tokamak concept. Plans were thus drawn up for a next step device approaching the power plant scale.

Great progress has been made in magnetic fusion during the past decades through succesive generations of tokamaks with doubling characteristic dimensions at each step, leading to a 10000-fold increase in the fusion triple product (density times temperature times confinement time). [1.1,1.2].

A proposal for an international project was tabled by General Secretary Gorbachev of the Soviet Union to US President Reagan at the Geneva Superpower Summit in November 1985. One year later, an agreement was reached: the European Union (European Atomic Energy Community, Euratom), Japan, the Soviet Union and the USA would jointly pursue the design of a large international fusion facility. Subsequently with another three parties joining (China, India and South Korea), the decision to construct ITER (International Thermonuclear Experimental Reactor) was taken in 2006. The ITER Members are engaged in a 35-years collaboration to build and operate the ITER experimental device, and to bring fusion to the point where a demonstration fusion reactor can be built. The ITER project is expected to start operation mid-2020s and to progress to full power, 500MW, mid to late-2030s. In addition to demonstrating magnetic confinement fusion at near power plant size, ITER will test technologies vital for the next step, DEMO (DEMOnstration power plant prototype).

Making fusion energy a reality depends crucially on the success of ITER. When finished, it will allow us to demonstrate the scientific and technological basis for large scale fusion energy. It will lead the way to the subsequent implementation of the different DEMOs (producing net electricity for the grid at the level of a few hundred Megawatts is foreseen to start operation around 2050), followed by commercial fusion power plants (FPP) by the decade 2060–2070 (see Section 1.3.5).

Still, the realisation of fusion energy has to face a number of technical challenges. For all of them candidate solutions have been developed and the goal of the programme is now to demonstrate that they will also work at the scale of a reactor. DEMO requires the direct involvement of industry in the fusion programme that in the coming decades will move from being science-driven, laboratory-based towards an industry-driven and technology-driven undertaking with an increasingly important role of industry in fusion R&D. ITER will test or validate most technological solutions for DEMO, and significant innovation is and will be required in some areas such as breeding blanket technology, plasma-facing and structural materials, superconducting magnets, microwave sources, high power beam sources, remote handling, control technology and fuelling and pumping systems. The role of industrial partners will evolve from that of a provider of high-tech components to that of driver of the fusion development. This will be a stepwise, long and gradual process, through consortia that will bring together industry, research laboratories and universities, in connection with DEMO R&D. Indeed, although at this moment innovation is already being jointly pursued in fusion by industry, research laboratories and universities, their synergies can only be fully exploited by facing the challenge of the realization of large projects like ITER and DEMO and focusing on them. This necessitates a close interaction between industry, research centers and universities through consortia and a transition of fusion to a programme that fully includes nuclear aspects (nuclearization of fusion). To facilitate this transition to the nuclear level, coordinated education and training actions will be undertaken with the fission community where most of the relevant nuclear expertise is available.

The EU has developed a long-term perspective for the development of controlled magnetic confinement fusion (MCF) in which it has presently a leading position. Europe can only keep pace if it focuses its effort and pursues a pragmatic approach to fusion energy. With this objective in mind, the EUROfusion consortium has created a "European Roadmap to the Realisation of Fusion Energy" (September 2018) which is an evolutionary revision of the Fusion Roadmap that was published in 2012 by EFDA (European Fusion Development Agency, the predecessor of EUROfusion) that guides research and development on Fusion in Europe (see Section 1.3.5). F4E (Fusion for Energy in Barcelona) is the European Union organisation responsible for Europe's contribution to ITER.

The Broader Approach agreement, concluded between the European Atomic Energy Community (Euratom) and Japan, consists of activities which aim to complement the ITER project and to accelerate the realisation of fusion energy through R&D and advanced technologies for future demonstration fusion power reactors (DEMO). Both

parties contribute equally financially. The Broader Approach agreement entered into force on 1 June 2007 and the second phase started in March 2020. To develop synergy with its activities related to ITER, it was decided that F4E should also be the Implementing Agency of Euratom for the Broader Approach. The resources for the implementation of the Broader Approach are largely (88%) volunteered by several participating European countries (Belgium, France, Germany, Italy, Spain and Switzerland).

The development of nuclear fusion as an energy source is one of the most complex scientific and technical tasks ever undertaken for non-military purposes and will still span several human generations. The European fusion effort, and hence this textbook, is concentrated on magnetic fusion. Magnetic fusion uses magnetic fields to confine the fuel. Inertial fusion is another approach to realise nuclear fusion on earth and is based on micro-explosions of small fuel pellets ignited by powerful lasers or particle beams. Confinement of the fuel is based on the inertia of the pellet fuel mass, which resists the natural expansion when it is heated to thermonuclear fusion temperatures.

1.2. CHARACTERISTICS OF MAGNETIC FUSION REACTORS

1.2.1. Fuel

The first generation of fusion power plants will be based on the least difficult fusion reaction to put to work in a reactor, namely the D-T reaction between deuterium (the stable isotope of hydrogen with a nucleus consisting of one proton and one neutron) and T for tritium (the radioactive hydrogen isotope with a nucleus of 2 neutrons and 1 proton). The fusion fuels have to be heated to about 200 million °C.

$$\mathrm{D} + \mathrm{T} \rightarrow {}^{4}\mathrm{He}\ (3.5\ \mathrm{MeV}) + \mathrm{n}\ (14.1\ \mathrm{MeV})$$

The reaction products are an α particle (helium nucleus) and a very energetic neutron. Twenty percent of the energy is taken by the α particles that remain confined (owing to their charge) and delivered back to the background plasma. ln this way, α-particles can compensate for losses and make the reaction self-sustaining. The ash from the D-T reaction is atomic helium, after recombination of the α-particles with electrons. The kinetic energy of the fast neutrons will be converted into heat in a blanket and then into electricity using conventional technology (steam) [1.1,1.2].

Fusion is the virtually unlimited energy source. The fuels are deuterium and lithium, tritium being an intermediate product burned in the fusion reaction. Deuterium and lithium are widely available. Deuterium can be distilled from all forms of water and is is routinely produced for scientific and industrial applications. The deuterium content of the oceans is estimated at 4.6×10^{13} tons, equivalent to ~5×10^{11} TWyr (terawatt year) [1.1]. Tritium is the radioactive isotope of hydrogen and decays to ^{3}He by emission of an electron

$$\mathrm{T} \rightarrow {}^{3}\mathrm{He} + \mathrm{e}^{-} + 18.7\ \mathrm{keV}$$

with the rather short half-life of 12.3 years. It exists only in tiny quantities. The neutrons produced in the fusion reactions will be used to breed it by bombarding a blanket around the burn chamber containing a lithium compound, according to:

$$^{6}\mathrm{Li} + \mathrm{n} \rightarrow {}^{4}\mathrm{He}\ (2.05\ \mathrm{MeV}) + \mathrm{T}\ (2.73\ \mathrm{MeV})$$

$$^{7}\mathrm{Li} + \mathrm{n} \rightarrow {}^{4}\mathrm{He} + \mathrm{T} + \mathrm{n} - 2.47\ \mathrm{MeV}$$

^{6}Li is the most useful isotope as it reacts with neutrons in the lower energy range (below 1 MeV). Naturally it occurs at 7.5%. For each ^{6}Li atom, one tritium atom is formed, with an extra energy of 4.78 MeV. Including the energy released in D-T fusion reactions, 22.38 MeV are released per ^{6}Li atom. The energy content of natural Li is therefore ~27×10^{15} J.ton^{-1}. Estimated reserves of natural Li are somewhat less than 29 million tons in known ore deposits and brines and ~200 billion tons dissolved in sea water (0.1 to 0.2 ppm), equivalent to ~2.4×10^{4} and 1.7×10^{8} TW·yr, respectively [1.1].

Since only one neutron is produced in each fusion reaction and since each tritium nucleus to be bred from lihium requires one neutron, it is necessary to provide a small additional neutron source (Be, Pb) to balance the losses in the breeding blanket. With a view to sustainability, tritium self-suffiency is to be ensured for DEMO and commercial power plants (see also Chapters 6, 7 and 10).

1.2.2. Safety and Environment

In many countries today, the discussion on nuclear energy safety is crucial for public acceptance. The inherent safety properties of a fusion power plant should therefore play a central role in the design and R&D of a DEMO reactor. The claim — reinforced by all major European safety studies — that it is possible to design a fusion power plant for which the worst possible accident will constitute no major hazard to populations outside the plant perimeter

that might result in an evacuation should be the main overall-design target. Indeed, compromising this objective could not be understood in the public discussion and would severely hinder the image of fusion; likewise, for the second safety claim made by the same studies: radioactive waste resulting from the operation of a fusion power plant should not require isolation from the environment for a geological time span and therefore should not constitute a burden for future generations. The development of low activation materials will therefore be crucial to the licensing of the first fusion power plants.

The primary fuels (deuterium and lithium) and the direct end product (helium) are not radioactive. However, the radioactive isotope of hydrogen, tritium is an indispensable intermediate fuel in the present mainstream fusion development, and D-T reactions produce very energetic neutrons. Therefore, the presence of T and waste contaminated by tritium, besides neutron-activated reactor materials, will require radiation shielding. The radioactive isotopes produced by irradiation strongly depend on the exposed materials, their purity and the types of radioactive species they can generate. An adequate choice of materials can minimize the induced radioactivity; such that recycling should become possible after a few decades up to a century.

An important advantage of fusion is the absence of direct radioactive reaction products, in contrast to fission where the reaction itself leads to long-lived radioactive products and where thuis radioactive waste is unavoidable. *In short, radioactivity is not inherent to nuclear fusion* [1.1].

The management of the materials and waste (for replacement or dismantling) can be optimized to avoid generating radioactive waste difficult to handle and dispose. A smart management of the materials and components, from the design phase until the end-of-life of the components can limit the footprint of fusion on the environment to short-lived waste.

The safety aspects approach of a fusion plant is like the approach carried out in nuclear fission power plants, aiming to avoid any impact on the public or the environment in all operational scenarios, i. e. from normal operation processes to unexpected events and accidents. Another important aspect is the global impact of a fusion plant on the environment considering the operational gaseous and liquid releases, but mainly the management of radioactive waste and materials. All possible efforts are currently made to reduce these impacts and control the back end of the fusion cycle to minimize its environmental footprint.

The hazard (Sec. 1.2.2.1), safety (Sec. 1.2.2.2) and environmental (Sec. 1.2.2.3) aspects outlined below are of prime importance to the implementation of magnetic fusion as an industrial energy source. In addition, sustainability will be a touchstone for fusion. To ensure sustainability, all aspects of tritium self-sufficiency and low activation of power plant components will be major pre-requisites.

1.2.2.1. Hazards in a fusion plant

The fundamental differences in the physics and technology used in fusion reactors make fission-type nuclear meltdowns or a runaway reaction impossible. The fusion process is inherently safe. In a magnetic-confinement fusion power plant, the amount of fuel available at each instant is sufficient for only a few tens of seconds, in contrast with a fission power plant. Moreover, the fusion process is not based on a neutron multiplication reaction. With any malfunction or incorrect handling, the reactions will stop. An uncontrolled burn (nuclear runaway) of the fusion fuel is therefore excluded on physical grounds. Even in the event of the total loss of the cooling function, the confinement barriers would not be affected. The temperatures of the vacuum vessel that provides the first confinement barrier would under no circumstances reach the melting temperatures of the materials. However, different types of hazards exist in a D-T fusion plant: tritium, neutron activation, activated corrosion products, erosion dust, radiactive inventory, and non-nuclear hazards. Those are briefly described below.

(a) Tritium

Tritium is a radioactive species (with a rather large mobility) and one of the sources of hazards in fusion reactors. Given the importance of tritium, a detailed description of its properties and their consequences, the concepts of a closed tritium cycle, tritium handling rules and tritium analytics are given in Chapter 10 of this textbook.

(b) Neutron activation

Neutrons born in D-T reactions are chargeless particles thus they escape from the magnetic fields that confine the plasma and permeate the surrounding structures. Unlike photons, which are readily attenuated and absorbed (as surface heat), neutrons are largely transparent and can penetrate deep into matter. D-T neutrons are born with energies close to 14.1 MeV. The mean free path (mfp) of such energetic neutrons in iron is ~8cm; for comparison, the mfp of 100 keV photons in the same material is ~3mm.

The interaction between neutrons and the nuclei of the elements of the reactor materials is outlined in Chapters 7 and 8. In nuclear reactions, the neutron can induce a change (transmutation) in the target nucleus and the emission

of reaction products. A special case of nuclear reaction is absorption, in which the neutron is absorbed by the target nucleus, which thus transmutes into a different kind of nucleus, which can be unstable and thus radioactive[1].

Natural elements in structural materials as well as a large part of the reaction products and transmuted nuclei are stable, i.e. they have the minimum binding energy to hold their protons and neutrons together. Some of the products and transmuted nuclei, however, are radioactive nuclides, which decay at a later stage into stable nuclei. This is known as "activation", and occurs when a stable nucleus is transmuted and acquires excessive binding energy, moving away from stability. These nuclides have a natural tendency to decay to expel the excess energy and return to stability. Radioactive decay is a statistical process. A population of radioactive nuclides decays at an exponential rate and the half-life, which is a measure of the nuclide's decay rate, depends on the excess energy. With some exceptions, the typical half-life of fusion activation products is well below 100 years. Typical radioactive products from neutron irradiation of steel are Mn-56 and Mn-54 (from Mn, Fe), Ni-57 (from Ni) and Co-58 and Co-60 (from Co, Ni). Other important hazardous activation products include W-187 (from W), C-14 (from C, N, O), Cu-64 and Cu-66 (from Cu) and N-16 (from O). The above examples correspond to main constituents; however, any real material contains traces of impurities from the fabrication process, in some cases spanning a large number of elements. This means that neutron irradiation can generate a very large variety of radioactive products, with serious implications for safety. As a general rule for radioprotection purposes, high-energy gamma emitters (above 0.5 MeV) like Co-60 are serious sources of direct radiation while volatile or mobile elements with beta and mostly alpha radioactivity (e.g. tritium) represent internal contamination hazards.

(c) Activated corrosion products

Activated corrosion products (ACPs) are responsible for ~90% of occupational radiation exposure (ORE) in nuclear fission power plants. The presence of a significant quantity (a few kg distributed or deposited on cooling circuits) of ACPs, makes the evaluation of the ACP inventory an important task from the safety point of view in fission light water reactors (LWRs) [1.3]. Many efforts have been made to reduce this hazard with technical and operational measures like the proper selection of materials in the new plants, by component replacements in the old ones, or by operating the primary coolant chemistry in a more controlled manner, etc. In case of a severe accident in a fission LWR, the ACPs are negligible in terms of radioactive inventory, mobilized inventory and the environmental source term (EST), as compared to the inventory releasable from the reactor core (gas and fission products). For fusion on the contrary, the ACPs could be a concern in terms of occupational dose, but also in case of accidents (e.g. loss-of-coolant accidents) since they are not negligible compared to the whole mobilized inventory. Many studies have been carried out about activated corrosion products both for LWRs and fusion devices projects. Two types of radioactive corrosion product formation processes coexist. On the one hand, the activation of corrosion products occurs when they are deposited on surfaces under neutron flux. On the other hand, the corrosion of structural materials under neutron flux is accompanied by a release of radioactive corrosion products) [1.3].

For LWRs and water cooled fusion plants, corrosion control is compulsory for an optimum performance of the plants. Without it, system integrity may be jeopardised, activity transport may give rise to high doses of radiation to plant staff and corrosion-product build-up may create barriers to heat transfer and interfere with the smooth operation of the mechanical components. In fact, the build-up of radioactive crud on the surfaces of steam generators and associated piping starts as soon as a reactor begins operating. Furthermore, if no decontamination is applied, radiation levels in spaces containing this hardware will increase in time, thereby adding to the radiation dose received by the staff during inspection and maintenance operations. These radiation levels make maintenance operations time consuming, increase the reactor downtime, and ultimately increase the cost of generating electricity. The activated corrosion products are present in the primary coolant both as dissolved materials (solutes) and as particulate materials (cruds). The solutes follow liquid leakage pathways and contribute to the offsite radioactive source terms (liquid and airborne). A significant fraction of the corrosion/erosion products is removed from the coolant by deposition in the steam generator and piping surfaces outside the core. The limitation of radioactive material in the primary coolant loop is attained by a continuous transfer of a portion of the primary coolant flow rate to the chemical and volume control system (CVCS). Ion exchangers and solution filters in the CVCS will remove most of the ACP from the primary coolant that enters the treatment system. The CVCS helps maintaining the purity of the primary coolant, to minimize the problems listed above, and ultimately to maintain releases of radioactive materials to the environment as low as reasonable achievable (ALARA).

Like in a LWR, the formation process of ACPs in the primary heat transfer system (PHTS) of a fusion power plant (FPP) is very complex [1.4]. It involves many different mechanisms acting among each other. The first mechanism is the uniform and generalized corrosion of metallic alloys. For stainless steel materials, this leads to the

[1] In such case no reaction products are emitted other than gamma rays.

generation of a dual oxide layer, i.e. an inner compact layer (chromite) and an outer porous layer (ferrite). The inner layer is a passive oxide layer, which limits ion exchanges between metallic alloys and primary coolant but does not eliminate them. However, the quantities of released materials are small (several $mg \cdot dm^{-2}$ per month) and do not alter the structural soundness of the component. The primary coolant transports ions generated by the corrosion-release phenomenon or by oxide dissolution. When the coolant becomes supersaturated in corrosion products, ions can precipitate on the walls or in the bulk of the fluid to form particles. Particles are also generated by erosion processes. Transported by the primary coolant, particles are deposited inside the circuits or they can agglomerate. Dissolution and precipitation depend on the corrosion product equilibrium concentrations, which depend on coolant chemical treatment. ACPs will be present in FPPs in the various in-vessel and vacuum vessel water coolant loops as well as in any coolant loop related to test blanket modules, auxiliary heating or diagnostics equipment. These products have an impact on occupational exposure, routine effluents to the environment, and potential releases during accidents. Therefore, the ACP inventory evaluation is important for FPP public and occupational safety. ACPs could be important in terms of the total mobilized inventory in case of accidents compared to other major source terms, tritium and dust. The enveloping ACP inventory adopted for ITER accident analyseswas assumed to be 10 kg per loop as deposit and 0.6% of deposit mass in the suspended forms (soluble ions or crud particulates), irrespective of the cooling loop type (first wall, shielding blanket, divertor or vacuum vessel) [1.4].

(d) Erosion dust

Plasma created inside FPPs will inevitably interact with plasma-facing materials (PFM); see Section 6.2.4. Current experience shows that such interaction, depending on conditions, may lead to numerous effects such as trapping of fuel species, erosion and co-deposition of PFM. Experiments in present thermonuclear devices show that the main fraction of the sputtered away and redeposited PFM finally transforms into dust. On top of that, the high fluxes of fusion neutrons produced in FPPs will lead to a high activation of all materials near the plasma. Plasma facing materials will be exposed to all plasma-surface interactions and may contain fusion species, that are the result of fusion products interactions with PFM (e.g. fusion alpha particles interacting with beryllium will produce carbon) and will be highly activated (especially if there is tungsten dust). This will affect the composition of the dust particles. The collection and investigation of dust properties in ITER will elucidate plasma-surface interactions. In addition, monitoring the dust level in ITER is essential for safety reasons (activated materials). ITER licensing requires that the quantity of dust in the vacuum vessel remain below given limits. The maximum allowed amount of mobilizable dust in the vessel is 1000 kg.

(e) Radioactive inventory

In a D-T fusion facility there are various sources of ionising radiation: plasma, tritium and activated material. Exposure to ionising radiation can be external (direct radiations) or internal (ingestion, inhalation). Radiation sources can be fixed (in-house problem) or mobile (may become a public hazard). The main sources of radiation in a D-T magnetic fusion facility are the plasma itself, tritium and neutrons. Those are briefly described below.

During plasma operation, the main source of radiation is the plasma itself. The plasma mainly emits neutron radiation, but also photons from Bremsstrahlung, synchrotron and line radiation. D-T neutrons have a Gaussian energy distribution centred at 14.1 MeV and with a spread according to the plasma temperature. Neutron emission is proportional to fusion power, with $\sim 3.5 \times 10^{21}$ neutrons per second being emitted by a 1 GW fusion plasma. Photons from plasma radiation are in the range of 1 to 100 keV (weak gammas). Photon emission depends on plasma physics in a complex manner; $\sim 10^{22}$ photons are emitted every second by a 1 GW fusion plasma (corresponding to hundreds of MW). The plasma is a fixed source and is non-existent during abnormal events due to immediate plasma termination; therefore, there is no risk of criticality or runaway reactions.

Tritium is a weak beta emitter (13.8 keV) radionuclide with no gammas. It produces negligible external exposure, but the main risk is related to internal exposure. As tritium is chemically equivalent to hydrogen, it can replace normal hydrogen in water and all kinds of hydrocarbons. Importantly, being a radioactive nuclide, it is a decaying source: its 12.3 years' half-life means it will have decayed to 90% after 1 year, 55% after 10 years, and 0.0001% after 100 years. For details see Chapter 10 and [1.5].

Neutrons escape from the plasma and cause the activation (transmutation) of constituent nuclides in structural materials. Some activation products are radioactive, mostly beta emitters with associated gammas. Both external and internal exposure is possible. Activation builds up from nil during operation, and decays after shutdown. Decay patterns and radiological hazards depend on the half-lives and line emission features of the radioactive products. Activation products appear in structures, tokamak dust and coolant (corrosion products). The clear majority is fixed, but some may become mobile during accidents. In addition to human exposure, activation decay also produces decay heat which is of concern in loss-of-coolant scenarios.

For a facility with radiation sources, regulatory bodies impose the control of safety (occupational and public) and environmental (waste and effluents) impact at all times — i.e. during design, operation and decommissioning — and for both normal operation and abnormal events (accidents). Both nuclear and "conventional" safety (e.g. fire safety, work accident prevention, industrial waste, cryogenics) need to be addressed. In terms of nuclear safety, regulators impose limitations (e.g. dose to workers, radionuclide releases) and optimisation principles (ALARA, defence in depth, etc. see Section 1.2.2.2) during the design, operation and decommissioning of radiation facilities. ITER is the first magnetic fusion facility with routine D-T operation undergoing a regulatory licensing process [1.6]. It has been classified as a basic nuclear installation (installation nucléaire de base) by the French nuclear regulatory body, Autorité de Sûreté Nucléaire (ASN).

(f) Non-nuclear hazards

Non-nuclear "internal" hazards concern the various industrial aspects present in the plant. Some of them are classical in power plants of this size (like electric hazards, fire, fluid leakages, presence of chemicals, etc.), others are more specific and typical of fusion plants such as the presence of strong magnetic fields, the presence and potential dispersion of toxic materials (e.g. beryllium which is considered toxic and carcinogenic) or the use of hot fluids (primary cooling system) and gases, and cryogenics lines and components with potential leakages and insulation losses. All these hazards and the consequences of failure of the systems are considered in the safety analysis of the plant and the mitigation methods deployed to limit the impact on the operators, the public and the environment.

1.2.2.2. Safety aspects of fusion [1.5] [1.6] [1.7] [1.8][1.9]

The safety principles that will be applied in nuclear fusion facilities follow the well-established approach to nuclear safety applied to existing nuclear fission reactors and other installations with radiological hazards. Some adaptation of those principles is necessary to allow for the specific favourable characteristics of fusion. The top-level safety and environmental objectives for fusion are:

- To protect workers, the public and the environment from harm.
- To ensure that exposure below prescribed limits and minimized to be as low as reasonably achievable (ALARA) in case of hazards within the premises and release of hazardous material from the premises is controlled,
- To ensure that the likelihood of accidents is minimized and that their consequences are bounded.
- To ensure that the consequences of the most frequent incidents, if any, are minor.
- To limit the hazards from accidents such that in any event there is no need for public evacuation on technical grounds.
- To minimize radioactive waste hazards and volumes and ensure that they are as low as reasonably achievable.

These objectives are an adaptation of internationally recognized objectives for nuclear facilities, for example those in reference [1.7]. The fifth bullet point is an additional target commonly adopted for safety studies of fusion facilities, often referred to as the no-evacuation criterion. It effectively places a limit on the maximum public dose impact of accidents, assuming there is a radiological criterion for the evacuation of the public from the area around a site. The level of this trigger for evacuation varies among countries and is usually defined in national regulations. However, the IAEA recommendation is that evacuation should be initiated if the projected dose exceeds 100 mSv in 7 days [1.8].

Safety principles are implemented to satisfy the above-stated objectives. Again, these are not new but adapted from commonly-applied principles in existing nuclear facilities. The main safety principles are defence in depth, ALARA, and passive safety. Those are briefly described below.

Defence in depth is a fundamental nuclear safety strategy. It provides multiple levels of protection to assure that a safe state is maintained even if failures occur. Defence in depth as a principle was defined by the International nuclear safety advisory group (INSAG), who describes it as follows [1.7]: "To compensate for potential human and mechanical failures, a defence in depth concept is implemented, centred on several levels of protection including successive barriers preventing the release of radioactive material to the environment. The concept includes protection of the barriers by averting damage to the plant and to the barriers themselves. It includes further measures to protect the public and the environment from harm in case these barriers are not fully effective."

The principle of maintaining radiation doses as low as reasonably achievable is also described by INSAG [1.7]: "To ensure in normal operation that radiation exposure within the plant and due to any release of radioactive material from the plant is as low as reasonably achievable, economic and social factors being taken into account, and below prescribed limits, and to ensure mitigation of the extent of radiation exposure due to accidents."

The safety functions required to mitigate hazards and satisfy the safety objectives are provided by systems, structures and components in the plant. These will thus fulfil their function with a very high level of reliability in all

situations including abnormal and accidental conditions. The principle of passive safety is that wherever possible the safety functions should be provided by components that do not need electrical power, compressed gas or active control systems to fulfil their required action. This usually results in a higher level of reliability than that of active components.

Security of fusion facilities containing and managing radioactive materials will be guaranteed. Particularly, it guarantees that people are protected from radiological, chemical and all the other hazards, that the plant is protected from sabotage, access by unqualified personnel or theft of radioactive material (particularly tritium). Safeguards, technical systems and management procedures should be set to meet the security objectives in all circumstances, i.e. normal operating conditions or plasma operation phases, short maintenance during normal operating conditions, shutdown phases for normal maintenance or long-term maintenance including the transfer of in-vessel components from vacuum vessel to hot cell, incidental and accidental conditions.

Like any other nuclear facility, a fusion plant that contains radiological hazards will be subject to licensing requirements and will require authorisation for its construction, commissioning, operation and decommissioning. The legal requirements and processes to obtain such authorisation vary from country to country, but there are certain common elements. Many devices using deuterium to obtain D-D plasmas generate some neutron activation of materials from the small fluence arising from the plasma. However, such levels of radioactivity have been too small to require full nuclear licensing. Only two tokamaks have so far used tritium fuel to generate a significant fluence of neutrons from the D-T fusion reaction: the Tokamak Fusion Test Reactor (TFTR, Princeton, New Jersey, USA) and the Joint European Torus (JET, Culham, United Kingdom). In both cases the quantities of tritium involved were not sufficient to require licensing as a nuclear facility, according to the regulations in force.

Although there have been many experimental fusion devices, only one so far has been subject to nuclear licensing: the International Thermonuclear Experimental Reactor (ITER, Cadarache, France), where the tritium site inventory amounts up to 4 kg. ITER is being licensed by the French nuclear authorities just as any other nuclear facility in France, including fission power reactors. A key part of the licensing documentation submitted to the French nuclear safety authorities in March 2010 was the preliminary safety report (Rapport Préliminaire de Sûreté, RPrS) [1.9]. A detailed technical examination was performed by the ASN and their technical advisors[2], during which many questions were raised and many further documents were provided by ITER to the regulator to justify all aspects of the safety case. In parallel, a public enquiry convened by local government officials and the outcome of the examination was considered by a panel of independent experts appointed by the ASN. This led, in November 2012, to the granting of the authorisation to construct the ITER facility. Further stages in the licensing process will involve the submission of additional, more detailed, safety reports leading to separate authorisations to permit commissioning (including the introduction of tritium into the plant), initial operation with hydrogen and helium plasmas, and "nuclear" operation with D-D and ultimately D-T plasmas.

As shown by the ITER experience, progressive integrated safety design analysis will be needed during all phases of the DEMO design. Because of the interlinks between safety requirements and design choices (e.g. materials, coolants and operating conditions), safety analyses play an important role in the selection of the most promising concepts and are constantly updated to match the progressive evolution of the design. Although there are differences between ITER and DEMO, much of what has been learned on safety from the ITER experience is being extrapolated to DEMO.

1.2.2.3. Environmental aspects of fusion

There are no problems related to lithium mining and fuel transportation; and no ecological, geophysical and land-use problems exist such as those associated with biomass energy, hydropower and solar energy. Helium is in addition chemically inert and very useful in industry [1.1]

The radioactive inventory of a fusion reactor will consist of (i) tritium and waste contaminated by tritium and (ii) reactor materials activated by the neutrons from the D-T fusion reactions. Adequate disposal of radioactive waste is especially difficult if the products are volatile, corrosive or long-lived. The neutron-activated structural materials of a fusion reactor will not pose such problems and, owing to their high melting points and low decay heats, will not necessitate active cooling during decommissioning, transport or disposal. However, over their lifetime, fusion reactors will generate (by component replacement and decommissioning) a similar volume of activated material as fission reactors, however qualitatively different in that the long-term toxicity is considerably lower (no radioactive spent fuel) [1.1].

[2] Mainly the Institut de Radioprotection et de Sûreté Nucléaire (IRSN)

(a) Tritiated waste management

Tritiated waste (solid, liquid and gaseous) requires a specific management strategy considering the physical and chemical properties of tritium, its capability to diffuse through metals and its half-life of 12.3 years (5.6% of the tritium decays annually); see Chapter 10 and [1.5,1.10]. Solid waste will come from the in-vessel material such as plasma-facing components, dust and structural material [1.11]. The co-deposition of tritium with beryllium (Be) is currently seen as the dominant tritium retention mechanism in ITER and it is assumed that most of the retained tritium (more than 90%) will accumulate in beryllium co-deposited layers and beryllium dust. The tritiated and activated components will be transferred to the hot cell facility for refurbishment. Parts that are not re-used are considered as waste and processed. Purely tritium-contaminated material will mainly be generated by the fuel cycle systems and fuel injection systems. Other solid waste will arise from the processes and housekeeping such as gloves, paper, clothes, etc.

Gaseous tritium released into the internal atmosphere during normal operations, maintenance or during accidents is collected by the atmosphere detritiation systems; see Chapter 10 and [1.5][1.11]. After collection, the gases are treated and the systems convert tritium-containing gaseous species into tritiated water that is further processed by the water detritiation system allowing the tritium to be reused in the fuel cycle. Tritium present in liquid effluents, arising from the maintenance of the tokamak cooling systems and from the detritiation processes (atmosphere detritiation, waste detritiation), will be recovered and reused.

The waste produced during the fusion power plant lifetime will be classified depending on the tritium and activated products concentration [1.11]. ITER solid radioactive waste falls into three categories as defined by ANDRA, the French national agency for radioactive waste management. This classification depends on the half-lives and activities of the nuclides in the activated material and includes:

Very low-level waste (VLLW) such as the central solenoid or housekeeping items such as gloves, paper, clothes, etc.

Short-lived low and intermediate-level waste (SL-LILW) such as the vacuum vessel and parts of the magnetic coil structure,

Long-lived intermediate-level waste (LL-ILW) such as the blankets and other in-vessel components.

The purely-tritiated waste, from the tritium plant for example, may not comply with the acceptance criteria of the ANDRA. Solid waste with a tritium content below 10^3 Bq·g^{-1} is considered as low-level waste. If there are other radionuclides, the contribution of these nuclides in the overall activity is considered and this reduces the tritium acceptance level. Waste with tritium content lower than 2×10^5 Bq·g^{-1} and higher than 10^3 Bq·g^{-1} is considered as low- and intermediate-level short-lived waste. Above 2×10^5 Bq·g^{-1} of tritium, waste is considered as intermediate-level long-lived waste. In addition to the tritium content threshold, the current acceptance value for tritium outgassing from waste in shallow land disposal (low- and intermediate-level short-lived waste) is 2×10^6 Bq·ton^{-1} per day.

The waste disposal facilities in the ITER host country (France) have thus stringent acceptance criteria in terms of tritium content and outgassing, imposing a proper waste management strategy. This strategy includes detritiation techniques aiming to minimize tritium discharges and a fifty-year interim storage phase allowing for tritium decay before shipment to the final repository [1.8]. Furthermore, to limit the tritium release in case of a loss of vacuum accident (LOVA), the total quantity of tritium trapped in the ITER in-vessel components has been limited to 630 g during operation. With a beryllium wall and a tungsten divertor, this limit may be reached after 1400 to 4600 discharges ($Q_{D\text{-}T}$ = 10, 0.1 to 0.5 of tritium trapped per shot) [1.12].

Thus, the total tritium in-vessel inventory will be controlled and in-situ detritiation techniques will be available during ITER operation. When evaluating detritiation techniques, one always considers the secondary waste produced (mainly tritiated water) and the consequences in term of storage and cost compared to a simple waste intermediate depository waiting for pure tritium decay.

(b) Detritiation techniques

The control of the ITER in-vessel tritium inventory will be undertaken mainly by baking [1.1][1.12], which gives the best results in terms of efficiency. In the D-T phase, tritium retention is expected to be dominated by co-deposition with beryllium eroded from the main chamber walls, on the main chamber surfaces and on dust. Laboratory experiments show that, unlike the case for carbon co-deposits, desorption of tritium from beryllium layers is 90% complete at 350 °C for pure beryllium deposits. However, if there are other components (e.g. W) in the layer, the outgassing is less efficient for a given baking temperature. Based on these results, baking for a few hours of the divertor cassettes to 350 °C (using high pressure gas, requiring divertor drying and draining) and the vessel walls at 200 to 240°C has recently become part of the ITER project baseline. ITER is designed to accommodate forty baking cycles during D-T operation. This baking frequency is required to maintain the tritium inventory under the prescribed limits of 630 g. A first estimate leads to in vessel wall baking of 2 to 8 times a year. It should be pointed out that all results concerning baking temperature and detritiation efficiency largely depend on the material properties, especially

on the internal defect concentration. In the case of neutron bombardment, the structure of the material constituting the plasma facing components will be substantially modified (creation of vacancies, dislocations, etc.) leading to higher tritium trapping capability. Moreover, the temperature of tritium release will be shifted to a higher value reducing the efficiency of tritium removal by baking.

Usual glow discharge cleaning (GDC) will be used in conjunction with baking to control the in-vessel tritium inventory. However, standard GDC can only be used when the toroidal field is absent, during maintenance. GDC is usually meant to remove part of the tritium trapped in the vessels walls. However, a major open issue is the evolution of the wall during this conditioning and detritiation procedure. For example, helium GDC has been observed, in an all metal environment, to form bubbles, dislocation loops and cracks. Such damage may increase the tritium inventory just by increasing the trapping site concentration in the material. Other promising techniques (described below) are considered or under evaluation to control the in-vessel tritium inventory such as RF wall conditioning, the separatrix scanning technique, controlled disruptions and ablation by light [1.11].

During plasma operations, ITER expects to use RF wall conditioning techniques exploiting the hardware that will be installed for ion cyclotron and electron cyclotron heating. From experimental studies, ion cyclotron wall conditioning (ICWC) is more efficient than electron cyclotron wall conditioning (ECWC) and has been by far the most investigated on tokamaks. Thus, ICWC with deuterium or helium gas might be useful to remove tritium (~0.05 g) from the first few monolayers of the surface. Regular inter-shot cleaning might thus allow small amounts of tritium to be recovered, allowing maintenance of the tritium in-vessel inventory under the safety limit. More research is required, however, to fully understand the results coming from ICWC experimental studies (homogeneity, efficiency, etc.).

To condition the plasma facing component (PFC) surfaces that are in contact with the plasma, it may be useful to slowly scan the separatrix plasma along the PFC surfaces in lower power phases. With an L-mode hydrogen plasma with a plasma current of 7.5 MA and an input power of 60 MW, the peak steady state heat flux density can be in the range of ~3.5 $MW \cdot m^{-2}$ in ITER whereby the tungsten substrate surface temperature can reach ~300°C. Due to the poor thermal conductivity (~$2W \cdot K^{-1}.m^{-1}$), the temperature of deposited layers could be much higher, which would desorb the co-deposited tritium with a rather good efficiency.

However, for the main chamber, the bake-out temperature is lower (only 200°C) and the separatrix scanning technique is not useful. It is thus proposed to heat the surfaces using photonic flash from mitigated disruptions in the lower energy phases of discharge termination. Calculations show that for a radiative termination of an ITER 9-MA discharge with a stored energy of 120 MJ (~0.2 $MJ.m^{-2}$) triggered by injection of neon gas, the surface temperature of a beryllium substrate may reach ~800 °C, way above the temperature expected for tritium release. Nevertheless, mitigated disruptions are to be used with caution since the heat flux density impinging onto fragile W-based material could produce dust, and hence contribute a lot to the increase of the in-vessel dust inventory.

Finally, it has been demonstrated in JET and Tore Supra that carbon deposits can easily be removed by light interaction with deposited material; up to 5 $m^2.h^{-1}$ can be removed by laser ablation [1.13]. However, neither ITER nor other future nuclear fusion facilities will contain carbon material inside the vessel. Deposit removal of beryllium and mixed material (Be/W) is yet to be demonstrated. The thickest main chamber deposits are likely to occur in very specific places (e.g. in the secondary divertor region at the top of the machine). Thus, an ablation tool on a remote handling device could be foreseen and might not actually have to clean a very wide surface area and is faster than treating the whole wall surface. This technique is to be considered in combination with a dust recovery device to avoid contributing to the dust in-vessel inventory and to extract the tritiated dust from the machine.

If periodic detritiation by in-situ baking is not taken into account, the tritium specific activity in the plasma facing materials ranges from 10^6 to 10^{10} $Bq \cdot g^{-1}$. Tritium will be further removed from these intermediate-level long-lived waste (particularly divertor and blanket plasma facing components and in-vessel dust) in the hot cell facility using remote handling tools. This process will involve ~1000 tons of solid waste, three tons of in-vessel dust during operation and ~2500 tons of solid waste during decommissioning. Reducing the tritium inventory in the primary waste has several advantages [1.10]:

- Potential downgrading of the primary waste classification.
- Decrease in the interim storage time.
- Reduction of the radioprotection constraints.
- Reduction of the tritium outgassing from the waste.
- Recovery and reuse of the trapped tritium.

In any case, detritiation processes always produce secondary waste (tritiated water) which will then be recycled, otherwise compromising the economic attractiveness of a detritiation process. In the case of ITER, solid waste includes soft housekeeping (mainly plastics, tissues and clothes) and metallic parts (beryllium, tungsten and copper alloys, stainless steel, etc.). For each type of waste, several processes were studied within the framework of EFDA (European

Fusion Development Agency, the predecessor of EUROfusion) or by institutes or organizations operating with large amounts of tritium, these include: thermal desorption under atmospheric air, thermal desorption with isotopic exchange with gaseous hydrogen, heating with flame, vacuum melting, melting under a static hydrogen atmosphere and argon flow, etc. The fraction of recovered tritium depends a lot on the process. In stainless steel, 99.8% of tritium is recovered in case of isotopic exchange with hydrogen at 700°C giving a detritiation factor of 500. The detritiation factor is the ratio between the initial tritium content and the tritium content after treatment. For melting under a static hydrogen atmosphere, the proportion of tritium recovered can reach to 99.9% (detritiation factor of 1000). Among the readily available techniques, thermal desorption in an oven at 800 to 1000°C in a flow of argon gas (which may contain hydrogen, not exceeding 4% in volume to prevent a hazardous atmosphere) is presently considered to be the most promising in terms of efficiency, ease of process and safety. More specific studies are underway aimed at defining the efficiency and technical feasibility of those detritiation processes expected to meet the disposal acceptance criteria. Present studies focus on: the thermal treatment, incineration and melting for metallic parts, and the thermal treatment and full combustion for soft housekeeping of waste.

Tritium trapping technologies are being developed to reduce outgassing. The CEA recently developed and is currently testing a compound able to trap tritium regardless of its chemical form (tritiated water or hydrogen) under ambient temperature and atmospheric pressure to reduce tritium out-gassing from ITER radwaste in the intermediate depository facility.

(c) Neutron-activated waste management

Even if fusion produces no long-lived radioactive waste, special attention should be paid to reducing the impact of material activation caused by neutron irradiation. Fusion could be made even more attractive using advanced structural materials with low activation as e.g. vanadium alloys or silicon carbides (see Chapter 8). In principle, these materials offer the prospect of recycling ~100 years after the shutdown of the reactor as the radioactivity would fall to levels comparable to those of the ashes from coal-fired plants (which always contain small amounts of thorium and other actinides). It is not yet clear if those materials will meet several technical specifications regarding thermo-mechanical properties and the ability to withstand high neutron fluxes. In any case, even if existing structural materials like stainless steel are used, the induced radioactivity in a fusion reactor is still ~10 times less than in a fission reactor of comparable power [1.1].

The activation of materials within a fusion device is an issue mainly for plasma-surrounding components due to their proximity to the plasma (the neutron source) and consequently represent the main source of radioactive waste. This process is dependent on the careful selection of the irradiated materials, alloying elements and impurities, which could be carefully monitored to effectively reduce the radioactive inventory in any fusion device. It is also crucial to develop an integrated management strategy that avoids the geological disposal option as the amount of low activated materials generated by future fusion power plants during operation and after decommissioning would rapidly fill up the space available in repositories [1.14]. In this matter, clearance and recycling offer a potential solution to reduce the volume of radioactive waste assigned for disposal [1.11]. Clearance is the unconditional release of slightly radioactive materials to the commercial market to fabricate consumer products [1.11]. By definition, the clearance index for any material is the ratio of the specific activity (in $Bq \cdot g^{-1}$) of the individual radioisotope to the allowable clearance limit summed over all radioisotopes. A component qualifies for clearance if the clearance index drops below one at any time during a defined storage period. Recycling is the reuse of radioactive materials within the nuclear industry, provided it is technically and economically feasible [1.11]. In this simplified analysis, the technical feasibility of recycling is based on the dose rate to the remote handling equipment (see Chapter 11). This dose determines the remote handling needs (hands-on, conventional and advanced tools) and the interim storage period necessary to meet the dose limit. Clearance and recycling will be important in order to reduce the radwaste burden for future generations and to maintain a positive perception of fusion in competition with other energy sources.

1.2.3. Economic aspects

1.2.3.1. Economic viability of future fusion plants

It is obviously difficult to estimate with any useful precision the cost of a system that will only be put into service several decades from now and that will highly depend on future developments which are largely unknown, such as the future cost of fuels and other commodities (e.g. for windmills, solar panels and batteries), costs associated with pollution constraints and with carbon emission. The present drive is primarily strategic rather than pure cost of electricity (COE). In most present economic models, only the direct costs such as construction, operation and maintenance are considered without considering externalities or external costs to society (e.g. damages to public health, ecosystems, agriculture, etc.) related to energy production. In comparison with other energy sources,

environmental and safety-related advantages of fusion and its virtual inexhaustibility of the fuel sources should be considered, as well as the evolution of the COE based on (exhaustible) resources. Present studies, embodying many uncertainties, produce cost estimates that are close to those of present power plants. Investment costs (reactor chamber, blanket, magnets, percentage of recirculating power, etc.) might be higher, but the fuel is cheap and abundant [1.1]. Strategies to use the economics of scale (size and number) will be explored.

Fusion is likely to be a centralized energy source for large-scale base-load supply, which can provide a backup for fluctuations of renewable energy sources. Based on present knowledge, technologically sophisticated power plants will probably need an electrical output larger than 1GW to be economic [1.1]. The reactor size is related to the power density which could be enhanced in advanced tokamak concepts with high beta (ratio between plasma pressure and magnetic pressure; see 1.3.2.2) plasma operation. The developments of advanced materials such as SiC/Sif should enhance the thermal conversion efficiency, hence the cost efficiency (see Chapter 8). It is also expected that large-scale production of high temperature superconductors (HTS) will be available for DEMO making fusion reactors much simpler and cheaper. Furthermore, HTS would also widen the parameter space for design and operation scenarios (field strength and geometry and related plasma parameters), which could turn out to be even more important.

The fast neutrons produced in the D-T reaction could be used to produce fissile material in fusion-hybrid breeder reactors. This complementary role for fusion might improve system economics compared with pure fusion systems; however, such hybrid fusion-fission reactors would increase societal concerns related to safety, environment and weaponry [1.1].

Once the other criteria (sustainability, safety) have been met, economic viability will determine the success of fusion. Though not a primary target of DEMO, the reactor is intended to show the potential for economic energy production by incorporating the efficiency technologies that will have matured and shown potential for extrapolation. Those technologies therefore need to be developed and evaluated in time. Cost-efficiency will also depend on the efficiency of the power extraction and conversion process, the fraction of re-circulating power, the availability of the plant and its lifetime in relation to its overall costs. Power extraction and conversion efficiency is basically determined by the temperature level of operation of the blanket and the divertor, and in turn, by the operation temperature window of the materials, coolants, and combinations employed (see Chapter 8). Optimizing these windows is closely related to safety considerations. To minimize the re-circulating power, the best-suited heating, pumping and magnet systems need to be identified and developed. Plant availability requires the optimization of pulse and interpulse duration, maintenance intervals, and overall reliability, as well as the minimization of the consequences of failure beyond safety limits. The lead components and effects limiting plant lifetime are to be identified and optimized. In the area of heating and current drive, emphasis will be given to the improvement of port plug efficiency (i.e. efficiency of sources and transmission lines) and the coupling efficiency to the plasma (see Chapter 2). Power extraction is based upon the blanket system and is described in Chapter 6.

1.2.3.2. The cost of fusion research

For the period of 2007 to 2013, the European Atomic Energy Community (Euratom) and ITER (in France) drew a combined €759 million average annual support from the EU's outgoing research spending scheme the Seventh Framework Programme (FP7) for 2007-2013. Every comparison unavoidably has its disadvantages; however, fusion energy being an important candidate source of electricity for our future, it seems fair to compare this number to (i) the present COE in Europe and (ii) to the investments in other energy systems under development.

Concerning (i): The total electricity bill spent e.g. in 2006 in the European Community by end users can be estimated as the product of the net consumption times an average electricity price, or roughly $3.3\ 10^9$ kWh × 0.1 Euro/kWh = 330 billion Euro. The fusion effort in Europe was thus equivalent to ~0.3% of the yearly European electricity bill. Alternatively, one can calculate the cost of fusion research per European citizen. With over 500 million Europeans, the fusion effort boils down to ~€1.5 per capita per year.

Concerning (ii): The clear majority of funds for fusion research are a fortiori public due to the long period still needed before fusion reactors can become commercially available systems. For the other energy sources (especially wind and solar), it is not so easy to get a complete picture of the money spent on research as private companies are contributing with research investments. In addition, subsidies or tax reductions may be applied to promote these systems, which should be included as part of the public expenditure [1.1].

1.3. A TOKAMAK FUSION REACTOR

A staged development has generally been adopted in view of the realization of commercial fusion reactors, whereby the next stage is based on the successful results obtained on the critical path to the present stage. From the current stage, at least two further steps will be necessary towards commercial fusion reactors, in addition to which a materials test facility like IFMIF/DONES (see Chapter 8) will be needed. The two main reasons are:

- An insufficient knowledge of the behaviour of fusion burning plasma. In the experimental devices built and operated so far, power has been injected through external systems to heat up plasma and simulate generated fusion power. However, such power inputs are somewhat artificial because real fusion plasma will be predominantly heated by alpha-particles, which will in turn influence the time evolution of the plasma (internal structures of plasma profiles are self-organized). Thus, the behaviour of fusion burning plasma is at present unknown, at least experimentally, and therefore the generation and control of such plasmas can only be achieved by building (experimental) plants that burn D-T fuel at a reactor scale.
- The second reason is related to the uncertainties in fusion reactor technology concerning superconducting magnets, heating systems, tritium fueling, the vacuum vessel, in-vessel components and remote handling and maintenance. While the first electricity-producing fusion plant cannot be built without sufficient experience and knowledge of nuclear technology, so-far built experimental devices have not been exposed to a heavy neutron irradiation environment. It is therefore necessary to build an integrated machine, incorporating and able to test most elements of reactor technology in a neutron environment.

1.3.1. ITER and fusion power plants

Figure 1.1 shows a schematic view of a fusion power plant. Fusion energy produced in the core plasma region is mainly released in the blanket by energetic neutrons. A coolant flowing inside the blanket transports the thermal power to the steam generators. Like in a conventional plant, the steam drives a turbine resulting in the generation of electric power. A part of the electric power is recirculated into the core plasma for non-inductive current drive, in addition to ancillary power.

The power amplification factor Q is defined as the ratio of the power P_f produced by fusion reactions to the total externally-supplied heating power P_{in}. To each value of Q corresponds a given value for the fusion triple product $n\,T_i\,\tau_E$ (plasma density times temperature of the reacting species times energy confinement time). The energy confinement time is the average time taken for the energy to escape from the plasma, usually defined as the total amount of energy stored in the plasma divided by the rate at which energy is lost. Two important milestones for the value of Q are customarily used in fusion research. The first, scientific breakeven, is reached when the heating power is equal to the power produced from fusion reactions, corresponding to a Q value of one. The second, ignition, is reached when the additional heating systems can be switched off and the heat of the fusion reactions alone is sufficient to maintain the high temperatures needed for fusion. This corresponds to an infinite value for Q, but in a tokamak fusion power plant a continuous power input might be indispensable for steady-state operations by non-inductive current drive. Typically, a value of Q larger than 30 to 50 is required because the thermal conversion efficiency η_{th} is 30 to 50 % and the conversion efficiency of the current drive facility η_{CD} might be ~50 %.

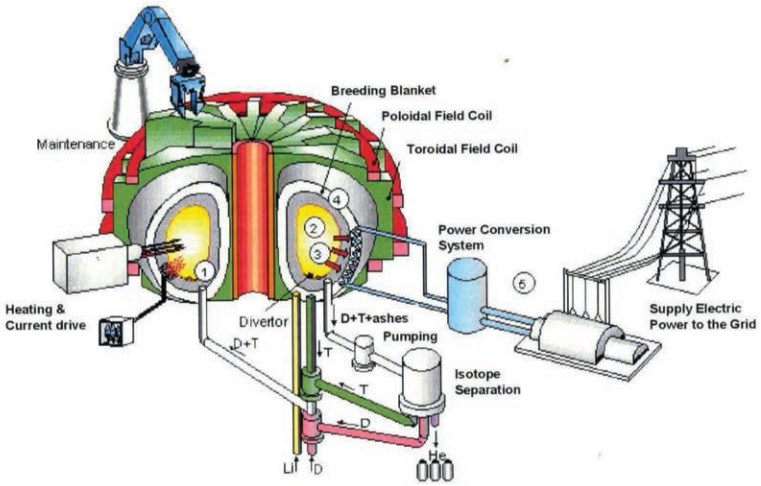

FIG. 1.1. Schematic diagram of a tokamak fusion reactor (Courtesy of KIT).

The realization of fusion as a sustainable energy source requires close interaction between plasma and fusion physics, materials research, plasma-wall interaction, and fusion technologies. The ITER project will be the world's largest experiment in magnetic confinement fusion and will be the first fusion device to produce net energy and to maintain fusion for long periods of time.

ITER is a critical step in the development of the magnetic confinement approach to fusion energy. The overall programmatic objective of ITER is to demonstrate the scientific and technological feasibility of fusion energy for peaceful purposes. The technical goal of the project is to construct and operate a tokamak experiment at a scale which satisfies this objective: ITER is designed to confine a deuterium-tritium plasma in which α-particle heating dominates all other forms of plasma heating. It will therefore provide an integrated demonstration of much of the physics and technological basis required for a fusion power plant and will allow access to the exciting field of burning plasma physics. Figure 1.2 is a diagram of ITER, as it is being built in Cadarache, near Aix-en-Provence, France.

The principal physics goals of ITER

- An extended burn of inductively-driven plasmas with a ten-fold return on energy ($Q \geq 10$). The duration will be sufficient to achieve stationary conditions on the time scales characteristic of plasma processes.
- Steady-state operations using non-inductive current drive with $Q \geq 5$.
- To explore higher Q operation if favourable confinement conditions can be achieved.
- Achieve a D-T plasma in which the reaction is sustained through internal heating (α-particles).

The specific technological goals of ITER

- To demonstrate the integrated operation of technologies essential for a fusion reactor, such as heating, control, diagnostics, cryogenics and remote handling.
- To test components for a future reactor (e.g. for power and particles exhaust).
- To test in-vessel tritium breeding module concepts in view of tritium self-sufficiency and the extraction of heat and electricity production.
- Testing of nuclear and high-heat flux components with an average first wall neutron flux greater than or equal to 0.5 $MW \cdot m^{-2}$ and an average lifetime neutron fluence greater than or equal to 0.3 $MW \cdot yr \cdot m^{-2}$.
- Demonstrate the safety characteristics of a fusion device.

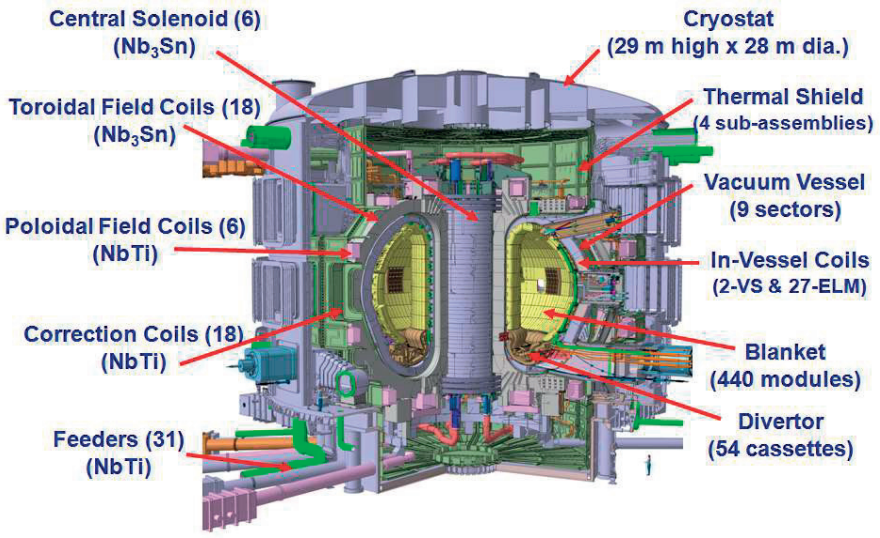

FIG. 1.2. Diagram of ITER and its main components (Courtesy of ITER Organization)

Over the years, several regimes of operation have been developed in tokamaks which are at varying degrees of readiness with respect to their application in a fusion reactor. The Type I ELMy H-mode is the most developed regime. It has been selected for standard operations in ITER. ITER will be capable of three different modes of plasma operation that will encompass an increasing degree of non-inductive current-drive capability and hence achievable burn pulse duration, albeit at different Q. In the inductive mode, which solely relies on the edge transport barrier (e.g. Type I ELMy H-mode of operation) to improve the global plasma confinement properties, the safety factor profile (q-profile) has a standard monotonic ohmic shape with a minimum value located on-axis below or close to unity. The expected performance is an improved confinement factor of ~2 over the standard L-mode. At lower plasma current operation, hybrid and advanced modes of operation are envisaged to extend the pulse duration of the standard inductive H-mode regime from typically 400 s to 1000 s and 3000 s respectively. In this context, it will be possible and necessary to investigate DEMO specific scenario issues as part of the ITER research programme.

1.3.2. Physics of a fusion reactor [1.2] [1.15]

The critical fusion-power-plant design issues related to core plasma physics are summarized in [1.15], a review article on the ITER physics design basis, and in [1.2]. Key issues concern the plasma confinement, the beta value, the density limit, the power and particle exhaust, and the current drive efficiency.

1.3.2.1. Plasma confinement

The energy confinement time in a tokamak is mainly governed by microturbulence rather than by binary collisions leading to so-called neoclassical transport. Plasma microturbulence leads to so-called anomalous transport and can be (partially) controlled in advanced regimes of operation. The theoretical prediction of plasma confinement is unfortunately premature because of the strongly nonlinear characteristics of core plasma. Therefore, an empirical scaling law has been proposed for the global energy confinement time of the core plasma. At first, the Alcator group (MIT, USA) presented the so-called neo-Alcator scaling based on ohmically heated plasma. As strong deterioration of plasma confinement was observed in auxiliary heated plasmas, an empirical scaling law has been proposed for auxiliary heated plasmas encompassing various parameter ranges in plasma size and current, magnetic field, etc.

Unified empirical scaling laws of the plasma confinement have been established based on elaborate joint work among various tokamaks around the world [1.15]. A typical example is the following scaling law for an ELMy H-mode plasma (ELMs are edge localised modes) which is the most developed regime and forms the basis for standard operation in ITER:

$$\tau_{\mathrm{E,th}}^{\mathrm{IPB98(y,2)}}(\mathrm{sec}) = 0.0562 M^{0.19} I_{\mathrm{P}}^{0.93} B_{\mathrm{t}}^{0.15} R^{1.39} a^{0.58} \kappa^{0.78} n_{19}^{0.41} P^{-0.69} \quad ,$$

where R (in m), a (in m) and κ are major and minor radii and the elongation, while M (in kg), I_{p} (in MA), B_{t} (in T), n_{19} (in 10^{19} m^{-3}) and P (in MW) are the ion mass, the plasma current, the toroidal magnetic field, the electron density and

the heating power, respectively. The improvement of the energy confinement compared to the H-mode is represented by a factor of HH, i.e. $\tau^{\text{required}} = HH \times \tau_{\text{E,Th}}^{\text{IPB98(y,2)}}$

$\tau^{\text{required}} = HH \times \tau_{\text{E,th}}^{\text{IPB98(y,2)}}$.

A number of regimes of operation have been developed in tokamaks which are at varying degree of readiness with respect to application in a fusion reactor.

1.3.2.2. Beta value

Since fusion power density is proportional to $\beta^2 B^4$, a higher beta is preferable to make a compact fusion reactor. The beta limit is governed by magnetohydrodynamic (MHD) stability considerations such as kink modes and ballooning modes. An intensive theoretical and computational study has revealed that the maximum achievable beta value [1.15] is given by the following formula;

$$\beta_{\text{t}} = \beta_{\text{N}} \frac{I_{\text{P}}}{aB_{\text{t}}} ,$$

where a (in m), I_p (in MA) and B_t (in T) are the plasma minor radius, the plasma current and the toroidal magnetic field, respectively. The proportionality constant β_N is called as a normalized beta value; and achievable values of β_N are intensively studied both experimentally and theoretically. The normalized beta value depends on plasma pressure and current profiles, and a maximum normalized beta value β_N is predicted to be somewhere in between 3 and 3.5 in the no wall stabilization case and between 5 and 6 in the wall stabilization one. To achieve these high beta plasmas, MHD instabilities need to be overcome.

1.3.2.3. Density limit

In tokamak plasma, an excessive increase of the plasma density results into a degradation of the energy confinement time and eventually induces a plasma disruption. It has been experimentally revealed that the critical density follows from the relation:

$$n_{\text{GW}} = \frac{I_{\text{P}}}{\pi a^2} ,$$

where a (in m) and I_p (in MA) are the minor radius and the plasma current, respectively, and n_{GW} (10^{20} m^{-3}) is called the Greenwald density limit. The underlying physics of this density limit is theoretically unclear, and a core plasma density can sometimes be designed to be larger than the Greenwald limit in view of a future improvement of this density limit experimentally, theoretically or both.

1.3.2.4. Power exhaust

Exhaust is a primary mission, with a substantial R&D programme and several concepts for the plasma, divertor and plasma facing components. Neglecting radiation losses, the alpha heating power P_α (20% of the fusion power) deposited into the core plasma is eventually transported to the divertor region through the scrape-off layer (SOL). Since the SOL plasma flows to the divertor region along the magnetic field with little spread in the perpendicular direction, the heat load at the divertor plate may be extremely high. For example, the heat load is sometimes roughly estimated to be $P_{\text{div}} \approx P_\alpha / (2\pi R \cdot w_{\text{div}} \cdot 2)$, where w_{div} is the width of the SOL, and a factor of two is coming from inner and outer divertor plates resulting in $P_{\text{div}} \approx 80$ MW m^{-2}, for $P_\alpha = 0.6$ GW, $R = 6$ m, and $w_{\text{div}} = 0.1$ m. Since the technically-acceptable heat flux might be in the range of 5 to 10 MW·m^{-2}, a remarkable reduction of the heat flux to the divertor plate is indispensable (see Chapter 8).

The introduction of radiation loss at the core and in the SOL region is an important strategy in reducing the heat load to the divertor plate. Since the Bremsstrahlung and synchrotron radiation losses are not sufficient at the core plasma, an additional form of radiation loss is needed, e.g. an injection of noble gas into the core and SOL regions. Although the introduction of impurity ions would induce the degradation of the core plasma characteristics, the fraction of radiation loss to the total heating power is one of the important operational parameters. Some of these topics and the corresponding technological solutions are presented in more detail in Chapter 6 concerned with the discussion of Plasma Facing Components.

1.3.2.5. Current drive

Non-inductive current drive is indispensable for the steady-state operation of commercial tokamak reactors. Current drive efficiencies defined by $\gamma_{CD} = n_{20} I_{CD} R / P_{CD}$ (see Chapter 2) are theoretically evaluated for the various methods (neutral beam injection, ion cyclotron resonant frequency, lower-hybrid and electron cyclotron resonant frequency). If the total current is driven by non-inductive methods, the current drive power is estimated to become a few hundreds of megawatts, which is an unacceptable level for an electric-power generating plant. Fortunately, radial transport in a plasma torus induces a toroidal current, which is called bootstrap current. A large fraction of the plasma current (e.g. 50 to 80 %) should be driven by this bootstrap current, and the remaining fraction of the plasma current would be externally driven by the non-inductive methods. The fraction of the bootstrap current is therefore an important parameter for tokamak reactor design.

In a fusion power plant, neutral beam injection (NBI) and ion cyclotron range of frequency (ICRF) are primary candidates for heating and current drive while electron cyclotron heating (ECH) might be considered for current profile control, if necessary. Neutral beam energy should be large enough to achieve a high current drive efficiency and penetrate deep into the higher density plasma. This has motivated the development of 1 to 2 MeV NBI systems. In the ICRF case the wave launching system, e.g. an antenna or waveguide, might be a concern in the strong irradiation environment. These topics and the corresponding technological solutions are presented in more detail in Chapter 2.

1.3.2.6. Plasma diagnostics

As stated in Chapter 3, although present knowledge is sufficient to build the next step machine (ITER), many plasma phenomena such as certain anomalous losses of energy and particles from the plasma are still not well understood. This lack of understanding of detailed processes has not hindered plasma physicists from finding operational regimes in which the overall confinement is improved. For proper operation of the tokamak in these regimes, the active and simultaneous control of many plasma parameters is needed. This implies that new robust and failsafe diagnostic techniques should be developed, for instance to control the temperature, density and current density profiles. Roughly speaking, it can be stated that progress in plasma diagnostics is dictated by the desire to understand the detailed physical processes occurring in the plasma, as well as by the wish to actively control many important plasma parameters. An additional driver for diagnostic innovation comes from the requirement for better machine protection systems (see Chapter 4).

1.3.2.7. Fusion neutronics

The subject of fusion neutronics is concerned with the transport of 14 MeV neutrons through matter. This includes the mathematical representation of the propagation process and all nuclear interactions. The nuclear interactions result in the generation of secondary particles including neutrons and photons, which are subject to further transport, and charged particles, which are assumed to be locally absorbed and to contribute to the nuclear heating of the material. The interactions also affect the atomic nuclei which can be transmuted into other nuclei, which may be stable or radioactive. The chemical composition of the considered materials thus changes during irradiation and a radioactive inventory is built-up, which may represent a radiation hazard. These topics are presented in more detail in Chapter 7.

1.3.2.8. Plasma control

DEMO diagnostics and associated control systems are constrained by the extreme environmental conditions inside the reactor, mostly due to the high neutron flux and fluence and the stringent requirements on reliability, availability and maintainability. At the same time, plasma operation will be even more robust than on ITER since e.g. the pulse length is increased and disruptions are to be fully avoided. These topics are presented in more detail in Chapter 4.

1.3.3. Engineering design of a fusion reactor

1.3.3.1. Magnets

Till the beginning of the 1980's, all fusion magnet systems were resistive with silver alloyed copper conductors to improve their mechanical properties and resist the large electromagnetic stresses. This was possible due to the small size of the machines operating in pulses.The largest machine of this type is JET (with a major radius of 2.98 m); the

required power to energise the JET system is more than 1 GW and can only be produced by flywheel generators, a solution which is possible due to the short duration of the JET plasma discharges (10 to 30 s).

ITER will still be a pulsed machine, but the electrical power necessary to energize the whole system in the case of a solution with resistive magnets (2 GW for 500 s) cannot be reasonably obtained from the electrical grid. The high level of electrical power in the case of resistive magnets, as well as the perspective for future steady-state machines, pushed the plasma physics community to develop superconducting magnet systems in their experimental fusion machines. The production of the magnetic field with superconducting magnets in the large vacuum chamber of ITER (835 m^3) is one of the main technological challenges. These topics and the corresponding technological solutions are presented in more detail in Chapter 5.

High temperature superconductors (HTS) offer the opportunity for higher magnetic fields at higher operating temparature and margins. This in turn would lead to a higher overall efficiency of the FPP due to higher fusion power density and lower cryogenic power requirements.

1.3.3.2. Plasma facing components

Fusion power is captured and produced in an integrated first-wall and blanket system that surrounds the plasma. This system will operate at a high temperature to efficiently convert fusion power into electricity. Furthermore, tritium fuel will be bred by capturing fusion neutrons in lithium-bearing materials. Additional systems associated with the power extraction and tritium breeding blanket include additional shielding of various components (e.g. superconducting magnets), heat transport loops, coolant chemistry control, heat exchangers, and systems to recover and process bred tritium from the blanket and tritium and deuterium in the plasma exhaust. These topics and the corresponding technological solutions are presented in more detail in Chapter 6.

1.3.3.3. Materials

Materials constitute a key issue on the path to fusion power reactors. There is a strong need for materials which (1) are resistant to irradiation by a typical fusion neutron spectrum, (2) can operate at the highest possible temperatures to allow for a good plant thermal efficiency, and (3) are as low activation as possible to ease the public acceptance of fusion as a future energy source. These topics and the corresponding technological solutions are presented in more detail in Chapter 8.

1.3.3.4. Vacuum pumping and fueling

A fusion power plant is a very large and complex vacuum system. ITER will become the most complex vacuum system in the world, given the sheer large-volume size of the experiment, the need to have double containment barriers for all tritium-carrying systems and the variety of operational states at which it will be operated. On another note, vacuum pumping is a good example to illustrate fusion-triggered innovative spin-offs for the industry (e.g. new vacuum pump technologies) and opportunities in science (e.g. the rigorous use of advanced vacuum gas dynamic methods in vacuum system design).

The fuelling of a confined plasma is a central operational task and it turns out to be much more complicated than one would think. This comes from the fact that the steady-state gas throughput of a fusion device is not primarily given by the consumption of fuel in the fusion reaction (in fact a negligibly small part) but by control and stability issues that ask for a significantly larger fuel throughput. Furthermore, non-fuel type gases also need to be injected, e.g. for radiative protection of the divertor high heat-flux surfaces (see 1.3.2.4). These topics and the corresponding technological solutions are presented in more detail in Chapter 9.

1.3.3.5. Remote handling and maintenance

The development of the remote maintenance system for DEMO is driven by the need to maximise the overall plant availability (the strongest downward driver of the COE in a fusion power plant), therefore minimising the plant down time for the foreseen maintenance operations. Delivering a reactor-relevant maintenance concept will drive the design towards a lower number of replaceable maintenance modules (e.g. multi-module blanket segments, divertor cassettes, etc.) and the elimination of complex in-vessel operations that are commonly used on experimental fusion devices. The in-vessel environmental conditions (radiation, activation, decay heating, temperature, etc.) will be far more aggressive than those to be experienced in ITER. This will restrict the type of maintenance operations that can be performed in-vessel and the type of equipment that can be deployed, possibly ruling out optical camera systems entirely. In Chapter11 the elements and design principles of a remote maintenance system for a FPP are presented.

1.3.4. Stellarator-based fusion reactors

In a stellarator, the required helical twisting of the magnetic field lines needed for confinement is achieved mainly with external coils. This results in a complex 3-D geometry of the plasma and the magnetic field coils. A stellarator configuration can be achieved with one or several continuous helical coils or several discrete coils. Stellarators have intrinsic advantages relative to the tokamak, mainly an inherent steady-state capability and an absence of current-driven instabilities, both connected to the fact that an internal plasma current is not required to maintain the magnetic geometry, as well as a much higher achievable density than that in stellarators. Stellarator experiments are at least one generation behind tokamaks, since an optimization of the 3-D magnetic field structure was required to mitigate the classical stellarators' shortcomings related to insufficient fast-particles and energy confinement. Therefore, the stellarator configuration is not suitable for DEMO on the time scale considered in the European Roadmap to the Realisation of Fusion Energy [16].

Stellarators can overcome potential difficulties in the tokamak line of development and vice versa. Therefore, the parallel development of both magnetic confinement fusion lines is an important overall risk mitigation measure.

In Chapter 12, the physics of stellarators and several major experimental findings are addressed as well as the question of how the magnetic field topology can be optimized to improve desired plasma properties. Technological aspects proper to stellarators are discussed focussing on the tailoring of magnetic field topology.

1.3.5. From ITER to commercial fusion power plants (FPP))

To minimize the overall resources investment, while minimizing risk of retrace or failure, a staged development is generally adopted for the large-scale long-range development program of commercial fusion reactors; see e.g. [1.16]. The development of the next stage device proceeds based on the successful results obtained on the critical path to the present stage machine.

ITER preparation and operation will be crucial for the further development of the tokamak line. However, power plant operation will necessitate scenarios of significantly longer burn and higher fusion power, with a considerably reduced number of sensors and fewer actuators. Consistent plasma operation scenarios will be determined considering the need for stable operation over sufficiently long times.

According to the current planning the proposed date for first plasma in ITER is at the end of 2025, moving towards 500 MW of fusion power with a power amplification factor $Q = 10$ by 2035, and to long-pulse operation with $Q = 5$ and testing of tritium breeding modules in the following years. High-power D-T operation is planned for the years 2035 to 2040. European conceptual design studies for the following step, a DEMOnstration power plant prototype (DEMO) producing several hundreds of megawatts of net electrical output power, are planned for the years 2020 to 2027, while engineering design activities (EDA) should start by 2030, i.e. well before ITER $Q = 10$. To achieve fusion electricity DEMO construction has to start in the early 2040s, immediately after ITER achieves the milestone of a net energy surplus. The dates are indicative [1.16].

A substantial part of DEMO research is planned at the ITER Satellite tokamak JT-60SA (super advanced), in the framework of the Broader Approach agreement (see Section 1.1), concluded between the European Atomic Energy Community (Euratom) and Japan. The first plasma is scheduled for spring 2021. JT-60SA [1.17] is a fully superconducting tokamak and able to operate for 100 s pulses with 41 MW of external heating. It will be used as a "satellite" facility of ITER to model proposals for optimising plasma operation and to investigate advanced operating modes for DEMO to be tested on ITER. Europe is contributing the Toroidal Field (TF) magnet and all coil current leads, the cryoplant, most of the cryostat, and magnet and heating power supplies.

The planned China Fusion Engineering Test Reactor (CFETR) is the next device in the roadmap for the realization of fusion energy in China, which aims to bridge the gaps between the fusion experimental reactor ITER and the DEMO [1.18].

Design studies of DEMO reactors have been performed by several groups in the fusion output power range of 1500 to 5000 MW [1.19][1.20][1.21]. The key knowledge so far gained from these studies concerns the dense but stable plasma performance, the tritium breeding blanket system including the tritium breeding ratio, the machine size versus performance, and the maintenance scenario of the in-vessel components such as blanket modules and divertors for scheduled replacement within a relatively short time. The common view shared by these studies was that DEMO would be the last integrated R&D device before the first generation of commercial reactors. This implicitly assumes government funding up to the DEMO, but with a strong participation of industry. The following step reactors would then essentially be funded by the utility companies. Exactly where DEMO should be located in between ITER and an FPP depends on the resources, the gaps towards a commercial plant as well as the development risks that can be accepted, and the time scale to fusion deployment[1.20]. Safety will play an important role in the ultimate selection.

Important lessons can be learnt from the fission experience of developing and deploying reactor plants through succesive generations. In contrast to fission where the benchmark design point is represented by operating plants (mostly Gen II) with very high availability, the only broadly representative fusion plant that will exist in the next thirty years is ITER [1.20].

The detailed technical objectives of DEMO depend on the kind of commercial reactors envisaged. DEMO should integrate all necessary components for fusion reactors to demonstrate electricity production with adequate perspectives on maintainability and reliability. Altough it is preferred to provide the qualification of the components required by the first-generation reactors, this approach also allows component level R&D or improvements to be continued in commercial reactors. Since DEMO will be the first integrated reactor incorporating all plasma physics and component technologies, a DEMO should provide flexibility or redundancy (it is not optimized). For each component, there will remain margins to be effectively cut for cost savings and performances to be improved seeking for higher reliability and availability. DEMO-stage activities should thus provide a feasible roadmap towards the first generation of commercial reactors, which will be primarily lead by utility companies considering the socio-economical aspects.

Following the demonstration in DEMO of an electric output to the grid, a significant development or improvement in plasma performance will no longer be necessary. Once an optimized burning plasma steady-state scenario will have been established, a range of operations will provide the information needed to optimise the basic components of a commercial reactor. Exploring DEMO operation with a minimum set of sensors and control knobs will then provide guidance to simplify the operation of commercial reactors. Through the experience of DEMO exploitation, operation and maintenance, improvements and simplifications of the components, reducing the fabrication and operational costs of a reactor system, will be found and incorporated in the design of successive commercial reactors. Three categories of high level requirements of equal priority have been identified by a DEMO technology stakeholder group:

- Safety and environmental sustainability.
- Plant performance.
- Assessment of the economic viability of a fusion power plan (FPP) beyond DEMO.

A successful DEMO reactor will meet a range of high-level requirements in each of these categories. It will entail, inter alia:

- Demonstrating workable solutions for all physics and technology questions associated with capturing the energy released by burning plasma, converting it into a useful power flow in a safe, reliable, and sustainable manner through the successful integration of many systems and physical processes.
- Demonstrating significant net electricity production with a realistic availability target (~several hundreds of megawatts).
- Demonstrating a closed tritium fuel cycle.

Subsequently, experience with the first commercial reactors (by the decade 2060–2070) will enable further improvements in a normal approach to build economic fusion power plants. A significant fusion contribution by 10% to the large growth in electricity demand to the order 10 TW by 2100 implies hundreds of FPPs worldwide.

1.4. REFERENCES

[1.1] ONGENA,J. and VAN OOST, G., Energy for future centuries: Prospects for fusion power as a future energy source, Fusion Science and Technoly **57** (2T) (2012).

[1.2] INTERNATIONAL ATOMIC ENERGY AGENCY, Fusion Physics, IAEA, Vienna (2012).

[1.3] DI PACE,L., CAMBI,G., CEPRAGA,D.G., SOBRERO,E., COSTA,M. Activated corrosion products in ITER first wall and shielding blanket heat transfer system, Fusion Engineering (1995), DOI: 10.1109/FUSION.1995.534235.

[1.4] DI PACE, L.,DACQUAIT,F., SCHINDLER,P., BLET,V., NGUYEN,F., PHILIBERT,Y., LARAT,B.,"Development of the PACTITER code and its application to safety analyses of ITER primary cooling water system", Fusion Eng. Des. **82** (2007) 237.

[1.5] TANABE, T., Tritium: Fuel of Fusion Reactors, Springer (2017).

[1.6] TAYLOR, N., CIATTAGLIA, S., CORTES, P., ISELI, M., ROSANVALLON, S., TOPILSKI, L., ITER Safety and Licensing Update, Fusion Eng. Des. **87** (2012) 476–481.

[1.7] Basic Safety Principles for Nuclear Power Plants 75-INSAG-3 Rev.1, INSAG-12, IAEA Vienna (1999).

[1.8] Radiation Protection and Safety of Radiation Sources: International Basic Safety Standards, Interim Edition, General Safety Requirements part 3, IAEA Vienna (2011).

[1.9] ITER Safety Analysis Data List, Vers. 4.0.1, IDoMS G 81 RI 10 03-08-08 W 0.1 (2003).
[1.10] PAMELA, J., BOTTEREAU, J.M., CANAS, D., DECANIS, C., LIGER, K., GAUNE, F, ITER tritiated waste management by the Host state and first lessons learned for fusion development, Fusion Engineering and Design **89** (2014) 2001–2007.
[1.11] ROSANVALLON, S., BENCHIKHOUNE, M., CIATTAGLIA, S., UZAN, J.E., GASTALDI, O., NA, B.C., TAYLOR, N., Management of tritium in ITER waste, Fusion Science and Technology **60** (2011) 855–860.
[1.12] SHIMADA, M., PITTS, R.A., Wall Conditioning on ITER, Journal of Nuclear Materials **415** (2011) S1013–S1016.
[1.13] MERCADIER, L.,GRISOLIA,C., ROCHE,H., SEMEROK,A., HERMANN,J., POCHEAU,C., THRO,P.-Y., SIRVEN,J.-B., WEULERSSE,J.-M., MAUCHIEN,P., SENTIS,M.,In situ tritium measurements and control by laser techniques, Fusion Science and Technology **60** (2011) 1049–1052
[1.14] DESECURES, M., EL-GUEBALY,L., DRUYTS,F., VAN ISEGHEM,P., MASSAUT,V., VAN OOST,G.,Study of radioactive inventory generated from W-based components in ITER and PPCS fusion designs,Fusion Eng. Des. **88** (2013) 2674–2678.
[1.15] INTERNATIONAL ATOMIC ENERGY AGENCY, Progress in the ITER Physics Basis, Nuclear Fusion **47** (2007), Special Issue
[1.16] EUROfusion,: European Roadmap to the Realisation of Fusion Energy, EUROfusion (September 2018); www.euro-fusion.org/eurofusion/roadmap.
[1.17] ISHIDA,S., BARABASCHI, P., KAMADA, Y., and the JT-60SA team, Team overview of the JT-60SA project, Nuclear Fusion **51** (2011).
[1.18] WAN,Y., LI,J., Yong LIU,Y., WANG,X., Vincent CHAN,V., CHEN, C., DUAN, X., Peng FU,P., Xiang GAO,X.,FENG,K., Overview of the present progress and activities on the CFETR, Nuclear Fusion **57** (2017)
[1.19] Special issue, Fusion Eng. Des. **83**, Issues 7–9 (2008) 858–892, Proc. of the Eight Int. Symp. on Fus.Nucl. Technology (ISFNT-8 SI)
[1.20] FEDERICI, G., BIEL,W., GILBERT,M.R., KEMP,R., TAYLOR, N., European DEMO design strategy and consequences for materials, Nuclear Fusion **57** (2017).
[1.21] FEDERICI, G.et al., Overview of the DEMO staged design approach in Europe, Nuclear Fusion **59** (2019)

Chapter 2

PLASMA HEATING & CURRENT DRIVE TECHNOLOGY

P. Agostinetti, P. Sonato
Consorzio RFX Padova
Italy

J.–M. Noterdaeme
IPP Garching and UGent, Ghent
Belgium

J. Hillairet
CEA, IRFM, Cadarache
France

M. Q. Tran
EPFL, Lausanne
Switzerland

This chapter gives an overview of the main heating and current drive methods. While it concentrates on those heating methods used in magnetically confined plasmas, the general principles are also applicable to other confinement concepts. To achive fusion, ions (whose positive charges repel each other) are heated allowing them to acquire enough energy to overcome the Coulomb potential barrier. As the nuclei come close enough together, the strong nuclear force overcomes the electrostatic repulsion. Fortunately, quantum mechanical effects allow ions to “tunnel” through, such that fusion can already take place at energies lower than the maximum value of the potential energy. The probability that two ions fuse expressed in terms of the cross section is given in **Error! Reference source not found.** as a function of the energy of a deuterium ion impinging on a fixed target.

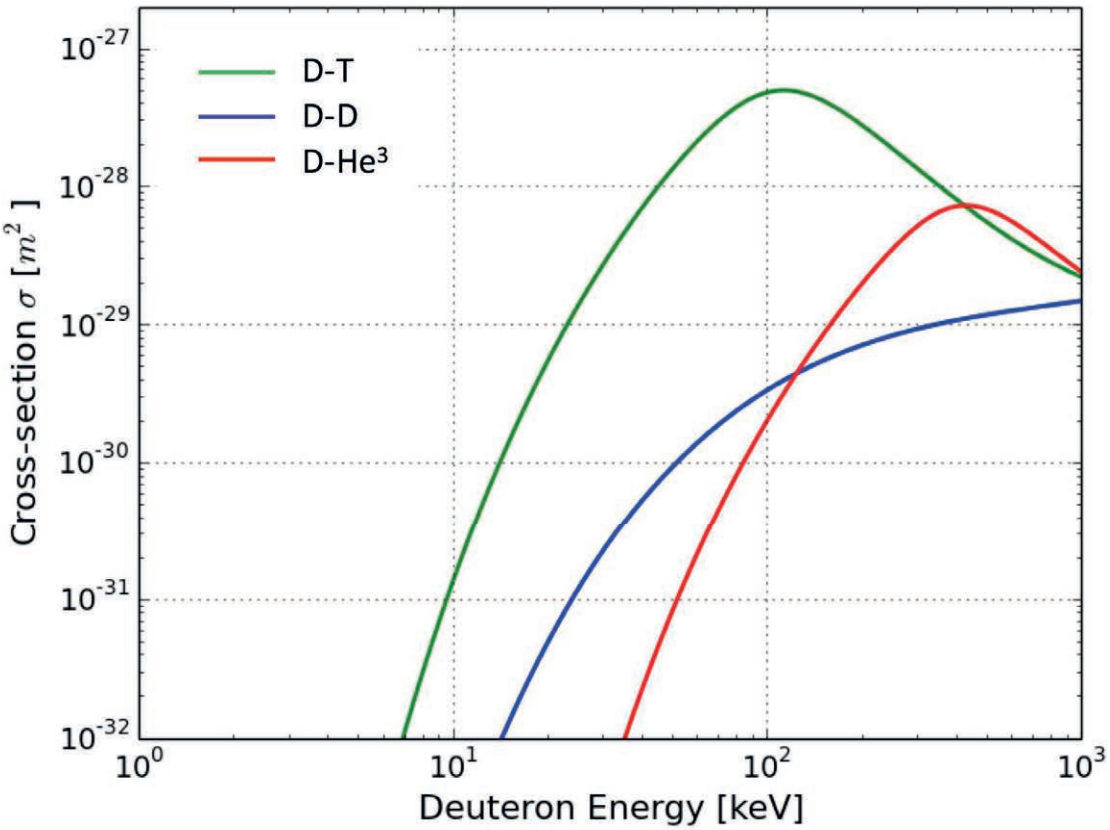

FIG. 2.1. Cross section of reactions involving deuterium (D), tritium (T) or the light isotope of helium (^{3}He) as a function of the energy of a deuterium (D) ion impinging on a fixed target (based on the NRL Formulary 2013).

Since the time between Coulomb collisions is much shorter than either the confinement time[3] or the time to undergo fusion, the ions usually have a Maxwellian distribution with a temperature T_i. The reaction rates as a function of this temperature (in eV) are given in FIG. 2.2. The lower temperature at which the reaction rate peaks in Fig. 2.2, as compared to the energy of the D ion for which the reaction rate peaks in Fig. 2.1, is due to two effects: first, in Fig. 2.2, it is more effective to have the energy in both colliding ions (Fig. 2.2) rather in ions colliding with a fixed target (Fig. 2.1) since in the second case non-useful energy is in the centre of mass; second: ions in the tail of the distribution contribute (thus with an energy higher than the corresponding temperature) significantly to the fusion reaction rates. Non-Maxwellian ion distributions can be created by certain heating methods, which can further enhance the reaction rates at low temperatures.

[3] The confiment time is defined as the time it takes for the ions in this case to lose 1/e of their energy, if the heating was stopped.

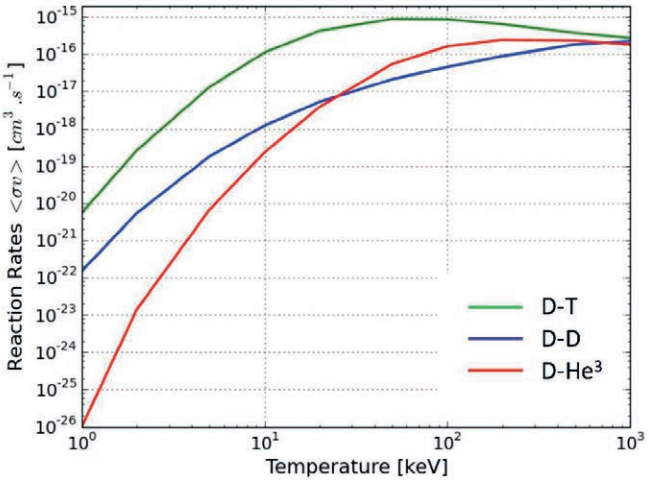

FIG. 2.2. Reaction rates as a function of the temperature of the ions (based on NRL Formulary 2013).

Note that in cases where the Coulomb potential of the ion is shielded by a heavy negative particle (e.g. muonic fusion), significant fusion rates can be achieved at much lower temperatures and heating would thus barely be necessary. Presently, such a scheme is not usable since the energy produced by number of reactions a muon can catalyse is smaller than the energy to produce a muon. In the more standard case of non-muonic fusion, external heating is needed to heat the plasma to the high temperature required to improve the fusion reaction rates.

If the fusion conditions are fulfilled, meaning high enough temperatures to overcome the coulomb potential, high enough density to have enough reactions and high enough confinement time for the power from fusion to compensate for the losses (i.e. high enough $n\tau T$), then heating by fusion products, such as the alpha's, can take over and completely replace the external heating. Since the heating system will represent a significant fraction of the investment needed to construct a power plant and since, in a (quasi-)steady state reactor, its heating role may only be needed for a short time, there is a strong incentive to favour a system which can also be used for other purposes (e.g. driving a current, where needed, or controlling the plasma). These aspects will also be discussed for each heating system. However, the methods under consideration still be referred to as heating systems. This text will not emphasise the physical aspects of heating systems, for which the reader is referred to the corresponding books, e.g. Fusion Physics [2.1].

2.1. GENERAL PRINCIPLES

Which heating methods can be used depends on the confinement concept: magnetically confined plasmas and inertial fusion plasmas use different heating methods yet all of them share some common traits, which will be emphasised. Those common traits are useful to understand why only those methods can be and are being used and to structure the presentation of each heating method. For a method to be considered at all, a necessary condition is that each of the following five steps be possible:

1) Conversion from electrical power to some other type of power: be it electromagnetic power in some frequency range (including light), energetic particles (neutral or charged) or a combination of it.

2) Transport of this power from the location where it is produced to where it will be used: this can be achieved by waveguides or cables for electromagnetic power, mirrors for light or short wavelength radiation, or simple ducts in the case of particles.

3) Coupling of the power to the plasma: for electromagnetic power, this can be done with antennas or mirrors; for particles, no special structure is usually needed, though structures are sometimes needed to protect certain components of the machine.

4) Transport inside the plasma: for electromagnetic radiation, this is typically carried out via some kind of plasma wave, whereas particles usually simply follow their trajectory (straight or bend, depending on their charge and the presence of electrical and magnetic fields).

5) Absorption and thermalisation of the power inside the plasma: by wave–particle interaction in the case of electromagnetic waves, or by particle–particle interaction in the case of particles.

Step 1 is the transformation from electrical power to power that can be transported in steps 2 to 4, which are all related to transport of the power. Step 5 is again the transformation of power to power in plasma. We will use those 5 steps as a framework to discuss each of the heating methods in the following sections. That all 5 steps be possible is a necessary condition. Indeed, it does not help to have a method that can only achieve 4 of those conditions. A "perfect" method (in the sense of the first 4 steps), whose power is not absorbed in the plasma (step 5) is of no use, e.g. lasers in magnetic confinement fusion: the power is not absorbed by the plasma. A method where the power is easily absorbed but cannot be transported inside the plasma (step 4) is not useful either, e.g. electromagnetic power for which no plasma wave is available to transport the power inside the plasma to the absorbtion zone. Note that this is a necessary condition for a heating method to be useful and successful, but it is not sufficient. Additional properties (which will become increasingly important as fusion ventures into the commercial area) are reliability, availability, maintainability and inspectability (RAMI), as well as investment costs and overall efficiency.

2.2. NEUTRAL BEAM INJECTION

2.2.1. General concept

For neutral injection, the five steps are shown schematically in Fig. 2.3, while Fig. 2.4 shows the neutral beam box of JET.

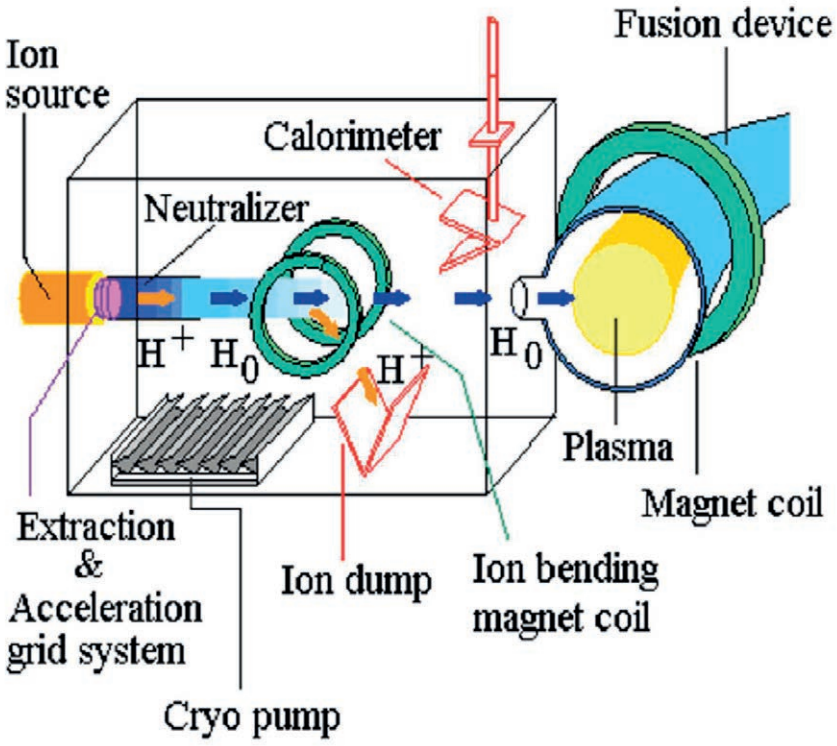

FIG. 2.3. Principle of neutral beam injection (JET Graphics)

2.2.1.1. Generation of fast neutral particles.

Fast particles are generated by producing ions (positive or negative) in a plasma source (called ion source in the figure) and using electric fields to extract and accelerate them to high energy. The particles are then converted into neutral particles (in a neutralizer) so that they can easily cross the strong magnetic field that confines the plasma and can be injected into the toroidal chamber. The first step is thus the transformation of electrical energy to fast neutral particles.

2.2.1.2. Transport of those particles inside a duct.

The duct is evacuated to high vacuum in order to avoid reionisation of the fast neutral particles.

2.2.1.3. Injection into the plasma

The particles simply follow their path as they are exiting the duct until they reach the plasma.

2.2.1.4. Propagation as neutral particles inside the plasma

Inside the plasma, the neutral particles propagate along their (straight) trajectory, until they are ionized by collision with electrons and ions. The propagation inside the plasma is a function of the beam energy, of the plasma density and temperature, and also depends on the plasma composition (i.e. taking into account the impurity content). For low energy beams (<100 to 130 keV) the propagation is characterized by typical characteristic lengths of a few tens of centimetres, whereas for high beam energy this length exceeds the meter. Therefore, energies well above 500 keV need to be considered to deposit the power in the center of a fusion reactor relevant device.

2.2.1.5. Ionisation and thermalisation inside the plasma.

Once the particles are ionized, they are trapped by the magnetic field and transfer their energy to the other particles (ions, electrons) through collisions. The ratio of energy transferred to the electrons and to the ions depends on the beam energy, on the plasma density and on the electron temperature. For low energy beams (<100 to 130 keV) the beam energy is mostly transferred to the ions, whereas for high energy (> 500 keV) the energy is mainly transferred to the electrons.

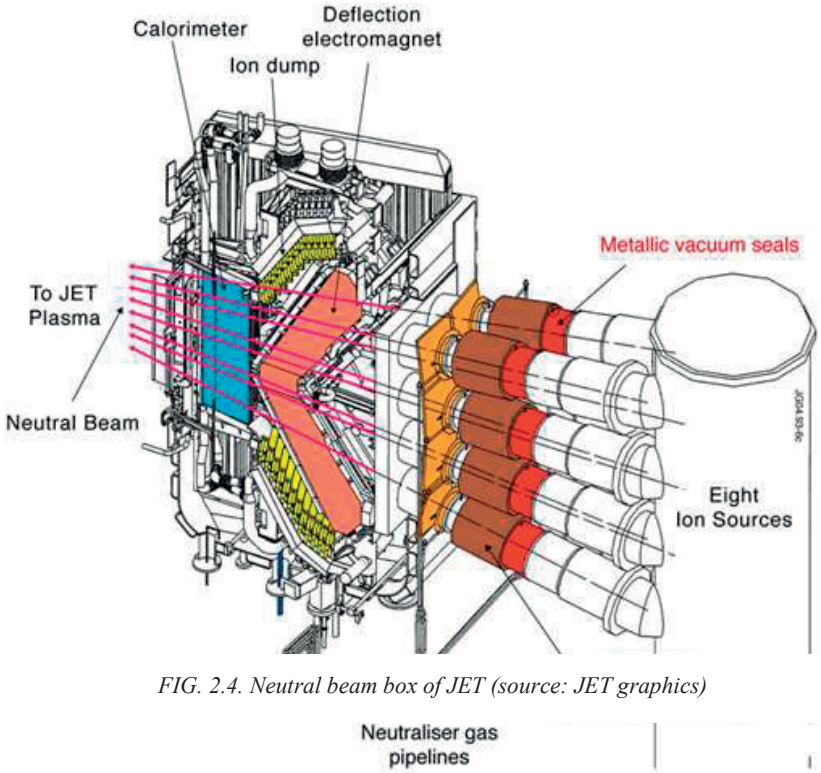

FIG. 2.4. Neutral beam box of JET (source: JET graphics)

Neutral beam injection is a typical example where the five steps are interlinked and the requirements to fulfil one of the steps can make it much more difficult to fulfil another. For example, to penetrate sufficiently far into the centre of a large and dense plasma (step 3), the particles need to be very energetic (step 1), lest they become ionized already far into the plasma edge (step 5, ionization in the plasma but not where intended). The neutralization efficiency of fast positive ions however decreases very drastically at high energy (e.g. ~50% at 100 keV for D^+ ions to ~20% at 200 keV, see also later, Fig. 7). Negative ions are thus needed to efficiently neutralize higher energetic ions (>120 keV). Creating and handling negative ions is, however, more difficult than creating and handling positive ions since the additional electron is loosely bound and is easily lost. This requires special type of sources. Lets now go back to each of the steps in more details.

2.2.2. Generation of fast neutrals

To generate fast neutral particles, ions are first produced then accelerated using electrostatic fields. The fast ions are then neutralized before they get close to the tokamak since the magnetic field would deflect any charged particles, destroying the beam and possibly any material surface they encounter.

2.2.2.1. Generation of ions

There are now essentially two types of sources used to produce ions: arc sources and Radio Frequency (RF) sources. Both kinds of ion sources are shown in FIG. 2.5. Arc sources produce plasma by creating a discharge between a few tens of filaments and the wall of the source [2.2, 2.3]. The plasma is kept away from the walls of the discharge chamber with permanent magnets ordered in such a way as to create cusp–like fields at the boundary. A disadvantage of the arc source is its need for regular maintenance, since the electrode filaments (typically made of tungsten) are being used up and may require a replacement. In RF sources, the plasma is produced by an RF antenna surrounding a vessel made of ceramic or quartz. A Faraday screen inside the vessel protects it from sputtering by the ions. The RF source, mostly developed at IPP Garching (Germany) [2.4, 2.5], has the important advantage of being essentially maintenance-free and has been adopted in ITER NBI.

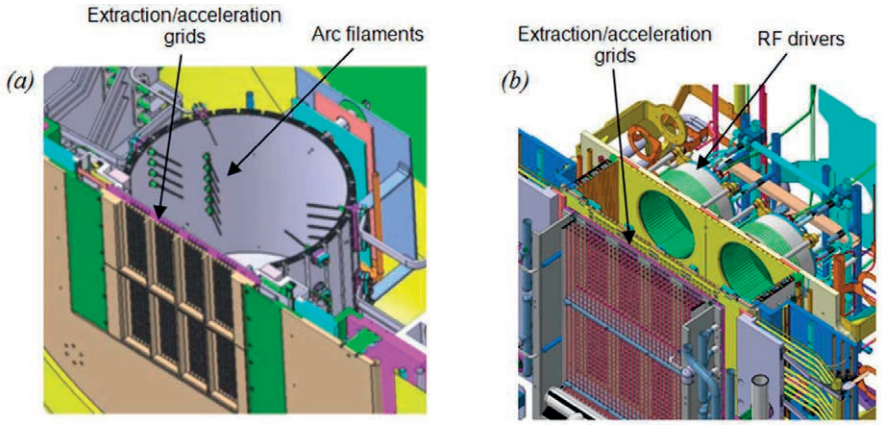

FIG. 2.5. Overview of the two concepts of ion sources: (a) Arc source (b) RF source.

2.2.2.2. Extraction and acceleration of the ions

Once the ions have been produced, they need to be extracted from the source and accelerated to the high energies required to penetrate sufficiently far into the plasma. The extraction and acceleration are done by electrostatic grids. Two concepts, shown in FIG. 2.6, are currently in use: the multi aperture, multi grid (MAMuG) and the single aperture, single gap (SINGAP). The names refer to the acceleration stage only (multi-aperture or single aperture and multi-stage or single-stage). In both cases, the extraction itself is done using grids with multiple apertures since this is the only way to get a sufficiently homogeneous beam over the whole aperture. For example a SINGAP version [2.6] of the 1 MV beams for ITER, would use a plasma grid (at −1 MeV), an extraction grid (at −994 keV) and even a pre-acceleration grid (at −960 keV), all with multiple apertures, but a single final acceleration grid at ground potential with only 16 big apertures (for a total dimension of approximately 1 m × 2 m). In the MAMuG version of the same system [2.7], plasma extraction and electron suppression grids are followed by a multi-stage acceleration. The total voltage drop is achieved over 5 grids, each with 1280 apertures.

In addition to the electrostatic fields generated by the grids, magnetic fields are often superimposed to remove co-extracted electrons before they are accelerated. This is particularly important in the case of negative ions, since the extracting fields also draw electrons. It is usually difficult to extract less than one electron per extracted negative ion. The presence of co-extracted electrons reduces the overall number of extracted ions (the power supplies are rated to a current, mainly composed of ions such that every electron carrying part of the current reduces the amount of ions drawn). Accelerating electrons is a waste of energy since they cannot be “neutralized” and they are useless to neutralize the fast ions (remember that the ions are negative). For this reason, the electrons are locally deflected by magnetic fields immediately after the extraction and further, all along the acceleration stages. The removal of the electrons before the acceleration relies on their much smaller Larmor radius as compared to the ions.

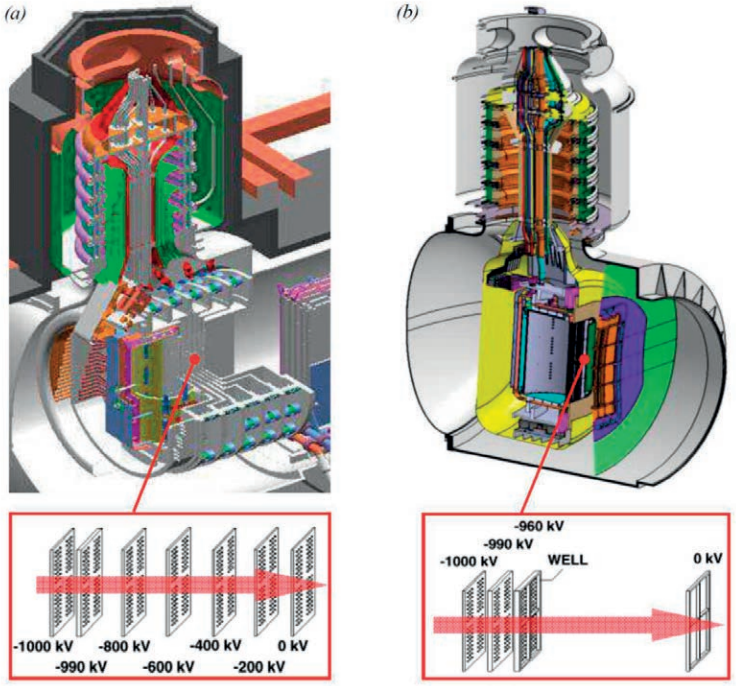

FIG. 2.6. Overview of the two accelerator concepts: (a) MAMuG; (b) SINGAP.

The design of the extraction and acceleration system is a very sophisticated task as the components have to fulfil several demanding but often contrasting requirements while being heavily constrained. For example, grids have to be as open as possible to allow the highest possible extracted current density, but this also implies a higher fraction of neutral molecules diffusing into the accelerator and causing the destruction of the accelerating ions through collisions. On the other hand, the grids are thermally heavily loaded, thus proper cooling channels need to be foreseen. The optimization of the extraction and acceleration stage is supported by powerful numerical tools that calculate the electric field distribution, the particle trajectories and self-consistent electric fields in the presence of magnetic fields [2.8], the interaction of the particles with the background gas and with material boundaries [2.9], the interaction between the beamlets and the resulting beam divergence [2.10]. Finally, the thermo-mechanical behaviour of the accelerator grids also needs to be considered [2.11].

2.2.2.3. Neutralization of the accelerated ions

Once the ions have been accelerated, they need to be neutralized. Both positive and negative ions can be neutralized by passing them through a cell with a low-pressure gas (the gas neutralizer). For positive ions (since electrons need to be added to the ions) the efficiency of neutralisation through collisions drops strongly as a function of energy: starting from ~90% at low energy (10 keV) to 50% at 100 keV and 20% at 200 keV, it rapidly decreases to 0% for higher energies. The efficiency for neutralizing negative ions is also reduced from 90% at low energies to 70% at 50 keV and 60% at 200 keV but then remains approximately constant (~60%) for the highest energies, as shown in FIG. 2.7. Clearly, for energies above 100 keV, only negative ions can be the starting point for the neutralisation process. Since the neutralisation efficiency plays such a major role in the overall efficiency of the neutral beam injection (NBI) system, efforts are under way to achieve even higher efficiencies than 60% (the maximum neutralization efficiency obtained at high energies with the gas neutralisation of the negative ions). Laser dissociation of the attached electrons (photoneutraliser) is a possible route with a neutralisation efficiency of up to 95%. The use of a photoneutraliser, rather than a gas neutraliser would, in addition, reduce the gas load in the NBI vacuum chamber, where the pressure needs to be kept as low as possible to avoid reionisation of the neutralised particles [2.12, 2.13].

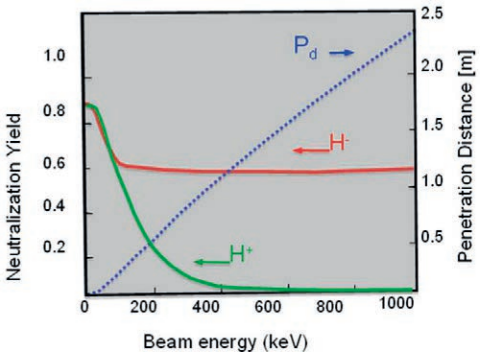

FIG. 2.7. Optimum neutralization efficiency for positive and negative hydrogen ions versus beam energy per nucleon. The penetration distance for D neutrals is also shown as a function of energy per nucleon for a flat density profile of 10^{20} m^{-3}.

After the neutralization cell, ions that are still not neutralised need to be removed from the beam in a controlled way. As they approach the magnetic fields of the machine (which can be varying, like the poloidal fields), the ions could otherwise be directed in an uncontrolled way to material surfaces that are not designed to take the heavy thermal load. Magnetic fields or electrostatic fields in the path of the beam are used to deflect the non-neutralised ions onto a dedicated target, which are designed to take the thermal load. Since the non-neutralised ions can consist of ions with several charge-to-mass ratios (e.g. H^-, H^+, H_2^+) these fields and the corresponding target (beam dump) need to be carefully designed. Within the beam box, other components such as a calorimeter, to measure the beam power and pumps, to keep the neutral pressure low, can be found. The calorimeter is a target that can be moved in the path of the neutral beam to measure the beam power. It is usually made of copper and heavily cooled to sustain the power. It can be sometimes split in several parts, which are individually diagnosed such that information can be obtained on the spatial power distribution of the beam. Very powerful vacuum pumps (able to guarantee a very low pressure) are used to minimise the reionisation of the beam despite the presence of non-negligible gas sources like the plasma source and the gas neutraliser. Ti getter pumps or cryogenic pumps are usually adopted for this purpose. Both require a periodic refresh of the film or the regeneration of the cryogenic panels. Between the beam box and the beam duct (which connects the region where the fast particles are created and the region where they are injected in the plasma), a high vacuum valve is installed to be able to insulate (in a vacuum sense) the box from the torus. This allows regeneration of the pumps as well as maintenance or repairs inside the box without affecting the torus vacuum.

2.2.3. Transport outside the plasma

Step 2, in the case of neutral beam systems, is the transport of the power from the location where it is produced to where it will be used. Formally, this partly happens in the NBI box already, but more specifically, it concerns the duct that connects the neutral beam box to the torus. In the case of NBI, the particles simply follow their path along the duct until they reach the plasma. As was already mentioned, the density of the background gas along the duct is kept as low as possible to reduce the losses generated by re-ionization of the neutral beam. Since the duct is often the narrowest space of the beam through which the beam travels, the power density of the beam is there the highest. Beams of several sources are sometimes combined to pass through the same port. This high power density has several consequences. Despite the optimisation of the beam profiles, the beams have no sharp edge, and to maximise the power per unit area a part of the beam's edge will be scraped off. Proper structures need to be included in the duct to cope with this thermal load. The high power density and the neutral gas load from the torus can sometimes lead to a partial reionisation of the beam in the duct. The ions then hit the walls of the duct where they will desorb gas and lead to an increase in gas pressure and a resulting self-enhancement of the ionisation. This is called beam blocking. Therefore, it is essential that the design of the system requires the minimization of the neutral pressure in the duct through appropriate vacuum pumps.

2.2.4. Coupling

Step 3 in our five steps process is where the particles exit the duct until they reach the plasma. Separating this step is a bit formal in this case since the particles simply follow their path as they are exiting the duct until they reach the plasma.

2.2.5. Transport inside plasma

Step 4 is the propagation of the particles as neutrals inside the plasma. Inside the plasma, the neutral beam ions continue their trajectory until they are ionized. Ionization can happen by electrons, ions, impurities or charge exchange with ions or impurities. Multi-step processes, where the ionization occurs not only from the ground state but also from excited states (in a multi-step ionisation process), start to play a non-negligible role at the high energies used for large plasmas. Cross sections for those processes can be found in the literature, and with those a beam attenuation length can be calculated. The beam energy is usually chosen such that the attenuation length corresponds to a substantial part of the minor radius at the operating densities of the machine, in order to deposit the power close to the plasma center. This justifies the need for 1 MeV beams in the case of ITER. However, if the density is substantially lower than the normal operating density (for which the energy was chosen is this way), as is the case on start-up and shut-down, the attenuation length can be much larger than the plasma cross section. This would lead to power deposition on the opposite wall of the beam injection port (known as "shine-through"). Care must be taken to provide interlocks preventing the beam from being used under such circumstances or shutting it off before damage occurs.

2.2.6. Absorption

In a last step, once the fast particles are ionized, they are trapped by the magnetic field and they transfer their energy to the plasma (ions and electrons) through collisions. The energy transfer cross sections are such that a high energy (above an energy of ~15 T_e, called critical energy), the beam power is transferred to the electrons, while, as the beam energy decreases below this critical energy the power is mostly transferred to the ions (FIG. 2.8).

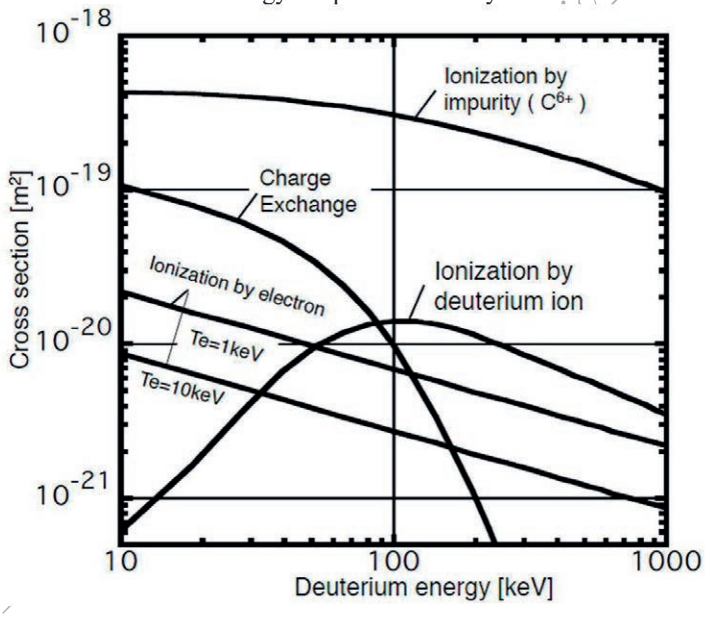

FIG. 2.8. Dependence of charge exchange, ion, impurity and electron ionization cross sections on the energy of the beam [2.1].

The energetic ions have large Larmor radii and large banana orbits. From the location of ionisation, the particle can start its banana orbit with an inward excursion (in the case of injection in the direction of the plasma current) or an outward excursion (in the case of injection in the counter–current direction) leading to particles being lost on the wall. The injection angle is thus chosen not to be purely perpendicular to the torus as particles could become trapped in the magnetic ripple and be lost before they can thermalize.

2.2.7. Discussion on strength and weaknesses

Neutral beam systems based on the acceleration of positive ions, have been a reliable method used in many tokamaks to heat ions and electrons. The present systems are pulsed and work at energies up to 130 keV. When going to higher energies and to long pulse (even steady state) systems, several new challenges appear, which are being addressed for ITER. Higher energy beams require the generation of negative ions as starting ions for the acceleration. The yield of negative ion production and extraction from the plasma source is lower with respect to the positive ions (typically by an order of magnitude).

Long pulses imply finding solutions for the continuous supply of caesium, used in the production of the negative ions, and the periodic caesium vapour deposition on the plasma source. Another issue related to the long pulse operation is the need for continuous working pumps or long–lasting operation of pumps requiring periodic regeneration. The handling and holding of voltage up to 1 MeV DC (or even beyond) is another challenging task requiring dedicated R&D on both theoretical understanding and material development [2.14]. Looking to the future, another aspect that will become important is the neutron load from which the insulators will need to be shielded, and against which the grids will have to be strengthened. Since the beam box is directly connected to the torus, the use of tritium will require to make the box components tritium-compatible and to extend the tritium barrier such that the beam components are included. The need to be economically competitive will require solutions that increase the efficiency. Some of these solutions are already implemented in the conceptual design of the DEMO NBI, described in the next paragraph.

2.2.8. Overview of parameters achieved and planned

Table 2.1 gives the parameters achieved for the major operating positive and negative systems, those planned for ITER and those considered for DEMO.

TABLE 2.1 Parameters of the main NBI systems [2.15]

	Number of Injectors	Type of ions	Energy (keV)	Total Power (MW)	Pulse duration (s)
JET (Culham, UK)	2 × 8	Positive	130	34	10
ASDEX Upgrade (Garching, Germany)	2 × 4	Positive	90	20	10
DIII-D (San Diego, USA)	2	Positive	84	6	3
LHD (Toki, Japan)	4	Negative	180	23	100
JT60-SA (Naka, Japan)	12	Positive	85	20	100
	2	Negative	500	10	100
ITER	2	Negative	1000	33	3600
DEMO	3	Negative	1000	50	7200

In ITER, two heating and current drive neutral beam injectors (H&CD NBIs) will be installed with the possibility for a third one for advanced operating scenarios. Each of these injectors will deliver a power up to 16.5 MW for at least an hour in the steady operation of hydrogen or deuterium plasmas. To fulfil these requirements, the neutral beam injector will provide up to 40 A of negative D ions accelerated at up to 1 MV (slightly different parameters are foreseen for hydrogen operation).

The main components of the ITER NBI, shown in FIG. 2.9, are: a negative ion beam source, that provides the beam of negative hydrogen or D ions (H^- or D^-) accelerated at an energy of 1 MeV; a neutralizer, that transforms the negative ions into neutrals; a residual ion dump, that dumps the remaining negative and positive ions from the beam; and a calorimeter, that measures the power of the neutral beam.

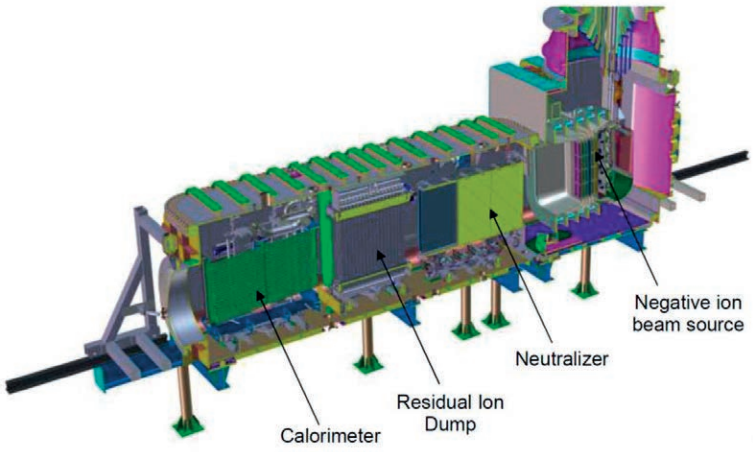

FIG. 2.9. Design of the heating and current drive neutral beam injector for ITER.

High efficiency and low recirculating power are fundamental requirements for the success of DEMO. These have been taken into great consideration for the DEMO neutral beam injectors whose conceptual design, shown in FIG. 2.10, is currently being developed in a collaborative effort involving several European laboratories. Moreover, particular attention has been paid to issues related to RAMI.

To reach these goals, studies on innovative solutions are been carried out [2.16], particularly for the ion source (studies on the modular design and on the racetrack-shaped drivers), neutralizer (studies on the beam driven plasma neutralizer and on the photo-neutralization process, with the gas neutralizer still being the baseline solution) and on the vacuum pumping systems (studies on innovative Non-Evaporable Getter materials). These solutions are currently being developed by means of several R&D programmes throughout Europe under the EUROfusion Consortium umbrella, in parallel with the experiments underway since 2018 at the ITER Neutral Beam Test Facility at Padova (Italy) [2.17] that hosts the SPIDER and MITICA experiments [2.18].

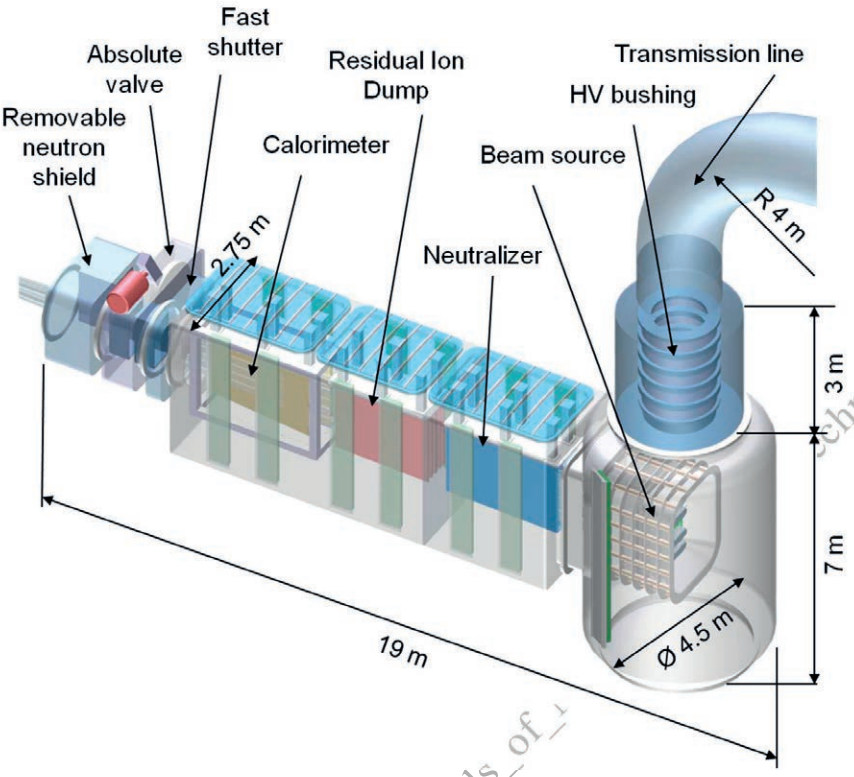

FIG. 2.10. Conceptual design of the DEMO NBI (2020).

2.2.9. Other uses

Neutral beam injection can also be used to fuel the plasma, to inject torque into the plasma (leading to plasma rotation) and to drive current. The role of plasma fueling and torque injection is reduced as beam energies increase since the number of particles is reduced. In ITER, the fueling contribution is well below 10% and therefore does not play a significant role. Neutral beam injection is also an efficient tool to drive current. The injection angle is then chosen to be as tangent as possible to the equatorial mean radius. The overall current drive is proportional to the NBI power and to a figure of merit η_{CD} (expressed in A m^{-2} W^{-1}) that positively scales with the electron temperature and the beam energy, as shown in FIG. 2.11.

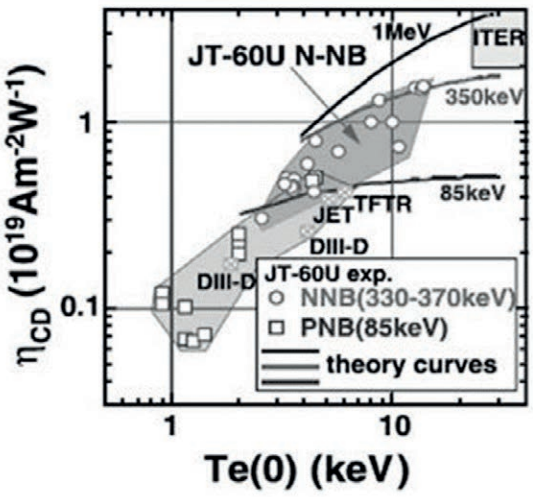

FIG. 2.11. Current drive efficiency as a function of central electron temperature Te(0) [2.19]

2.3. ION CYCLOTRON RANGE OF FREQUENCIES

2.3.1. General principle

For the ion cyclotron range of frequency (ICRF) method, radiofrequency (RF) generators transform electrical power into electromagnetic power in step 1, which is transported to the plasma using coaxial transmission lines in step 2. The power is coupled to the plasma via (usually magnetic) antennas in step 3, transported inside the plasma by plasma waves (typically the fast wave) in step 4, and absorbed on ions or electrons by wave–particle interaction in step 5.

2.3.2. Waves in plasmas

Since this is the first mention of waves in plasma in the context of this textbook, a very simple introduction is provided with just the physics needed to address the technological aspects. The interested reader is referred to other, more physics oriented textbooks or articles for a treatment in depth [2.1]. Waves in plasmas are non-zero solutions of the system comprising Maxwell's equations and those relating currents and electric fields in the plasma. These equations identify the combination of plasma parameters under which the waves exist. It is then necessary to determine which of those are suitable to transport power from the plasma edge to the plasma center. As an example, this relationship is calculated in its simplest form; that is, when there are no externally imposed magnetic and electric fields. The current density is given by $j = -envv$. Now, using the equation of motions for the electrons $\mathrm{d}\boldsymbol{v}/\mathrm{d}t = q_s/m_s(\boldsymbol{E} + \boldsymbol{v} \times \boldsymbol{B})$, with $B = 0$, and assuming harmonic oscillations ($\partial/\partial_t \rightarrow -i\omega t$) one obtains – $i\omega v = -e\boldsymbol{E}/m_e$, from which the velocity can be calculated, yielding the relationship between current density and electric field in the plasma:

$$\boldsymbol{j} = \frac{-ie^2 n_e}{m_e \omega}\boldsymbol{E},$$

Now turning to Maxwell's equations

$$\nabla \times \boldsymbol{E} = -\frac{\partial \boldsymbol{B}}{\partial t},$$

$$\nabla \times \boldsymbol{B} = \mu_0 \varepsilon_0 \frac{\partial \boldsymbol{E}}{\partial t} + \mu_0 \boldsymbol{j},$$

we can take the curl of the first equation and use the second one to eliminate B, finding:

$$\nabla \times (\nabla \times \boldsymbol{E}) = -\frac{\partial(\mu_0 \varepsilon_0 \frac{\partial \boldsymbol{E}}{\partial t} + \mu_0 \boldsymbol{j})}{\partial t}$$

Using plane waves ($\nabla \times \rightarrow ik \times$) and, again, harmonic oscillations, as well as the previously obtained relationship between current and electrical field, one obtains:

$$(\boldsymbol{k} \cdot \boldsymbol{E})\boldsymbol{k} - k^2 \boldsymbol{E} + \frac{\omega^2}{c^2}\left(1 - \frac{\omega_p}{\omega^2}\right)\boldsymbol{E} = 0$$

where ${\omega_{p,e}}^2 = e^2 n_e/\varepsilon_0 m_e$. The only non-zero solutions are the electromagnetic waves and the plasma oscillations (for $\boldsymbol{k}$ perpendicular to $\boldsymbol{E}$):

$$\omega = {\omega_{p,e}}^2 \text{ and } N^2 = \frac{c^2 k^2}{\omega^2} = 1 - \frac{\omega_p^2}{\omega^2}$$

where N is the wave refractive index, and (for $\boldsymbol{k}$ parallel to $\boldsymbol{E}$). The first solution is a wave. For a given frequency, the solution of the equation gives the wave vector of the wave that can propagate (or not) in the plasma. For $\omega > \omega_p$, N^2 is positive and the wave is propagating. For $\omega < \omega_p$, N^2 is negative and the wave is non-propagating. For $\omega = \omega_p$, N goes to zero, the wavelength λ goes to ∞ and the wave is in cutoff; at such location, the wave behavior can change for slightly different parameters: (e.g. toward a region with lower density) the wave can start to propagate if it was non-propagating or (toward a region with higher density) be reflected if it was propagating, whereby part of the energy

can also tunnel through the non-propagating region over a limited length. In cases where N goes to ∞, the wavelength goes to 0 and k goes to ∞. Since the wavelength becomes smaller than the Larmor radius, our assumption of zero temperature breaks down and other approximations are needed. In those cases, wave energy can be dissipated or the wave can convert to another type (e.g. one which does not exist under the zero-temperature assumption). The number and properties of the waves that can be calculated to exist in a plasma will depend on the approximations included in the equation that relates the current in the plasma to the electrical field. In a magnetized plasma and using a two-fluid zero-temperature model, two roots can be found, namely the slow and the fast wave modes[4]. The wave that can be used in the ion cyclotron range of frequencies to transport power from the plasma edge (step 3) – mostly perpendicularly to the (toroidal) magnetic field – is the fast wave. After this short introduction on plasma waves, lets come back to the five-steps of the ICRF method.

2.3.3. RF Generator

FIG. 2.12. One of the final stages (2 MW) of the ASDEX Upgrade generators (total height ~4 m).

In this frequency range, the transformation of electrical power to electromagnetic oscillations is typically carried out by a series of amplifiers. In ASDEX Upgrade for example, the amplification stages consist of 4 amplifiers. Starting with a 20-mW oscillator, the power is amplified to 100 W, 4 kW, 100 kW and finally 2 MW (see FIG. 2.12). The first amplifier is solid state, but the subsequent ones are based on electronic tubes, such as triodes or tetrodes. The highly efficient generators are derived from high-power, steady state broadcast transmitters. The very high frequency (VHF) band (30 to 300 MHz) used for radio and television broadcasting covers the frequency range used for heating the fusion plasmas (30 to 120 MHz). Typical unit sizes for present pulsed systems are 2 MW, while steady state systems already exist at slightly lower powers. The solid-state amplifier (which can be used at low power) offers the advantage of being more reliable, needing little maintenance and operating at lower voltages.

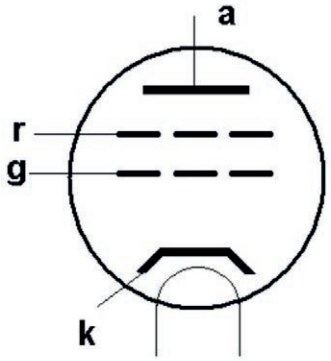

[4] A nomenclature which comes from their associated perpendicular phase velocity $v_{\perp}$.

FIG. 2.13. Schematic of a tetrode with (a) an anode, (k) a cathode, (g) a control grid and (r) a screen grid

At high power, a triode or tetrode remains indispensable as the active element in the amplifier. A triode consists of three electrodes: an anode, a control grid and a cathode. A tetrode has 4 electrodes: an anode, a screen grid, a control grid and a cathode (see FIG. 2.13). In both cases the anode is heated by a filament and emits electrons, which are accelerated towards the cathode by the potential drop between the anode and the cathode. This current can be controlled by a voltage on a control grid between the cathode and the anode. A low-power variation on the control grid can affect the much larger current between the cathode and the anode. With a proper circuit, this can be used for power amplification. In a tetrode, a screen grid is introduced to compensate for some negative effects caused by the position of the control grid close to the anode. With the voltage on the grid set to a constant value, the current in the tube is now much less affected by the variation of the anode voltage. The current can thus be controlled more precisely by the voltage of the control grid.

The operation of RF amplifiers is labelled class A, B or C depending on the fraction of an oscillation period during which the tube is conducting (conduction angle). It affects the maximum gain, the maximum theoretical efficiency and the harmonic content [2.20]. If the tube is conducting over its whole period (conduction angle 360°), the maximum theoretical efficiency is 50%. For class C, where the conduction angle is less than 180°, the maximum theoretical efficiency is 100%. The achievable gain decreases when going from class A to C, while the harmonic content of the power increases. Present generators for fusion are typically operated in class B (conducting angle 180°). Up to ~60 MHz, the components of RF amplifiers can be lumped elements (capacitor, inductance and resistance). Above that frequency, which corresponds to a vacuum wavelength of 5 m, amplifiers are built in a coaxial way, where the tube is part of a resonating coaxial cavity. As the wavelength becomes even shorter, it can become beneficial to use a diacrode, which is essentially a tetrode fed at both ends. While RF generators are sturdy, reliable and efficient systems, they can be very sensitive to reflected power (power coming back from the load — the antenna in this case — to the generators), which would lead to the destruction of the tube. Measures need to be taken for this not to happen or, if the reflected power is unavoidable, to reduce the power of the generator. In present-day systems, generator efficiencies of up to 75% can be achieved, with total efficiencies[5] of typically 45%. With several technical improvements and increased plasma absorption in larger machines, this can be increased to a total efficiency of 75%.

2.3.4. Transport outside the plasma: transmission lines

The second step is the transport of the power to the launching structure. When the geometrical size of the system is of the same order as the wavelength, the voltage and current cannot be considered to be constant along the length of the electrical conductor. Indeed, at typical frequencies (30 MHz to 120 MHz), the wavelength in vacuum is 2.5 to 10 m while the typical dimensions of our network are between 10 and 500 m. This variation thus needs to be considered.

Transmission line theory has long since been developed to deal with this issue (the basic equation is called the telegrapher equation). Some major concepts are the characteristic impedance Z_0, the forward and reflected power, the voltage standing wave ratio (VSWR) and the impedance matching. If one considers a wave propagating from the generator to the load, the voltage along the line due to the wave is given by

$$V(z) = V_1 e^{-\gamma}$$

While the current is given by

$$I(z) = I_1 e^{-\gamma z}$$

where V_1 and I_1 are complex quantities, and

$$\gamma = \sqrt{(R + j\omega L)(G + j\omega C)}$$

with R, the total series resistance of the transmission line per unit length, L, the total series inductance of the transmission line per unit length, G, the shunt conductance per unit length, and C, the shunt capacity per unit length. The characteristic impedance Z_0 is the ratio of the complex voltage and the corresponding complex current of a single wave (when there is no reflection) on the line. It can be shown to be:

$$Z_0 = \sqrt{\frac{R + j\omega L}{G + j\omega C}}$$

For a line where losses can be neglected ($R = G = 0$), the characteristic impedance is real:

[5] Defined as power into the plasma divided by the electrical plug power of the system.

$$Z_0 = \sqrt{\frac{L}{C}}$$

If the line is infinitely long or terminated by the characteristic impedance Z_0, there is no reflected wave. In all other cases, the wave is reflected at the end of the line. The sum of forward and reflected waves on the line leads to a standing wave pattern for voltage and current:

$$V(z) = V_1 e^{-\gamma z} + V_2 e^{+\gamma z}$$
$$I(z) = I_1 e^{-\gamma} + I_2 e^{+\gamma z}$$

Moreover, the reflection coefficient for a line termination of impedance Z_L is given by:

$$\rho_T = \frac{Z_T/Z_0 - 1}{Z_T/Z_0 + 1}$$

The voltage standing wave ratio is given by:

$$\text{VSWR} = \frac{1 + |\rho_T|}{1 - |\rho_T|}$$

The impedance presented by the antenna, which, in our case, terminates the transmission line, is usually different from the characteristic impedance of the transmission line used to transport the power from the generator to the torus. In addition, this impedance depends on the plasma parameters and can thus be varying. To avoid reflected power to the generator, one either "matches" the terminating impedance to the characteristic impedance of the line or directs the reflected power away from the generators, or do both. Matching the antenna impedance (the load) to the characteristic impedance of the line can be done by adding impedances in parallel to the load. This is usually done by adding in parallel several short-circuited transmission lines to the load (typically two, to match the real and imaginary parts of the impedance). Pieces of transmission line, terminated by a short, have an input impedance that varies with their length. To perform the matching for varying load, the position of the short in the transmission line can be varied remotely (varying their length and thus their impedance). However, since the variation of the antenna load is in many cases much faster (typically on the submillisecond scale) than one could change the matching by mechanically moving the position of the short in the transmission line, additional measures are taken to prevent the reflected power from reaching the generators. A very effective method is the use of so called 3-dB couplers. Such a coupler is a 4-ports network with the property that, depending on the phase and the amplitude of the power going into two of the ports (call them 1 and 2), the power is directed to one (port 3) or the other (port 4) remaining ports. The power going into one of those ports (3 or 4) is equally distributed between the two original ports (port 1 and 2) with a phase difference of 90°. Thus, for example, if the generator is connected to port 3 and the lines going to the antennae are connected to port 1 and 2, the power from the generator is equally distributed between the two antennas. On the other hand, if the power coming back from the antennas on line 1 and 2 has the same amplitude and the proper phase, it is not directed to port 3 (the generator) but to port 4, where a matched load can be connected to fully absorb the reflected power.

When matched, the sections of the line between the antenna and the matching systems become resonant. In this situation, the RF energy stored into these transmission line sections leads to locally high voltages and currents, and thus to risks of arcing and higher dissipation losses. To minimize such losses (in long pulses or steady state applications) some antenna concepts use capacitors in the antenna to provide the matching right at the strap input. A disadvantage of such a design is the maintability of the system because it requires diassembling the antenna to access the capacitors. Examples include the Tore Supra load resilient prototype (2007) and the JET ILA (2008–2009). The transmission lines, matching components and possibly other components like the 3-dB coupler are usually filled with dry air at typical pressures of 3 atm, and exceptionally with SF_6 (to increase the maximum voltage). Since the line is connected to the antenna (which is in vacuum) a barrier needs to be present in the line to separate the pressurised part of the line from the vacuum part of the line. This is done with a feedthrough: a ceramic piece that provides the vacuum barrier. The feedthrough provides a sealing barrier function without changing the characteristic impedance of the line at that point, nor reducing its voltage standoff capability. One design that has evolved from many iterations consists of a conical piece of ceramic soldered to the central and outer conductor of the transmission line. The dimensions of those conductors are varied to keep the characteristic impedance of the line constant. Indeed, the ceramic (a dielectric) would modify this characteristic impedance if the dimensions of the line would stay the same.

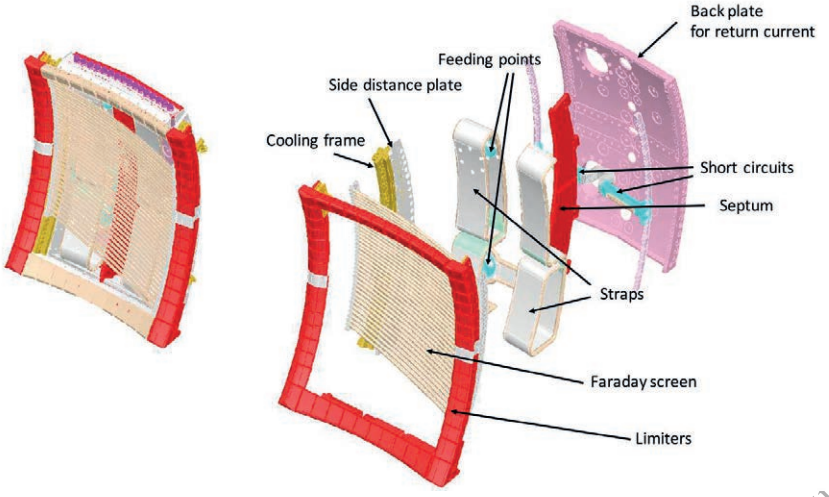

FIG. 2.14. The ICRF antenna of ASDEX Upgrade (left), and an exploded view of the antenna (right) showing the different components.

2.3.5. Coupling

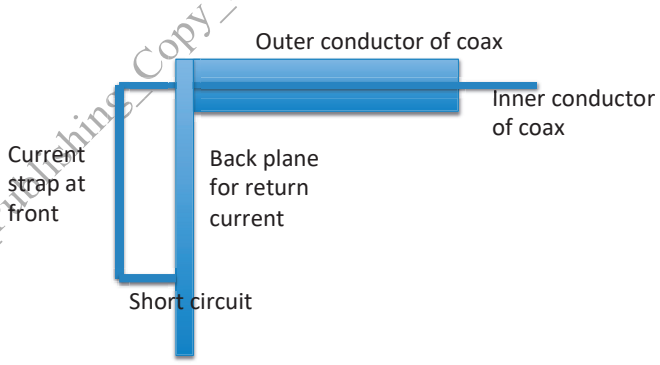

FIG. 2.15. Schematic of an ICRF antenna.

The third step is the coupling of the power, (arriving through the transmission lines) to the plasma. Generally, the antennas used to couple the electromagnetic power to the plasma consist of two (more-or-less flat plate) conductors: one conductor (typically called strap) is attached to the central conductor of the transmission line and short circuited after some length to the second conductor (called back plate) connected to the external conductor of the transmission line. An exploded view is shown in Fig. 2.14 and a schematic of a single strap is shown FIG. 2.15. The current distribution on the strap produces RF electric and magnetic fields, which are evanescent in the vacuum

vessel. Where the plasma density is high enough though, those fields can excite the fast wave, which propagates into the plasma.

From this simple concept, more complicated designs have evolved. For instance, a Faraday screen in front of the simple straps inside the vacuum vessel can be used as a polarizer: an array of conductors is arranged to short circuit the RF electric field along the magnetic field lines. The reason for this is that those are the fields that excite the slow wave, which is undesirable in this context. Additional straps can be used in the toroidal direction to shape the power density radiaded by the antenna (referred to as the 'spectrum' of the antenna). This can be used to enhance the absorption in the plasma (two straps in phase opposition suppress the part of the power near $k_{\parallel} = 0$, which is badly absorbed in the plasma) or to provide a directed spectrum (e.g. in current drive applications); see FIG. 2.14.

The antenna design needs to be optimized to reduce impurity production at or near the antenna. Indeed, as metallic walls and surroundings of the antenna are increasingly being used in experiments[6], the ICRF method has been accompanied by impurity releases. The hypothesis is that parallel RF electric fields, parasitically excited by the antenna, are rectified near material boundaries, accelerating ions to the wall and sputtering impurities from it. The Faraday screen reduces the parallel electrical fields produced by the straps. However, induced currents in the antenna box can lead to parallel electrical fields that are not shielded by the Faraday screen. New antenna concepts try to minimize those induced currents. For ITER, the antenna has been designed to fit into a port, resulting in a high power density and high voltages (45 kV maximum design value) see Fig. 2.14. For DEMO, alternative ideas are being pursued: distributed antennas (which would be integrated into the blanket) could lead to low power density antennas operating at low voltage, and very precise antenna spectra. This will reduce the impurity production and improve the coupling.

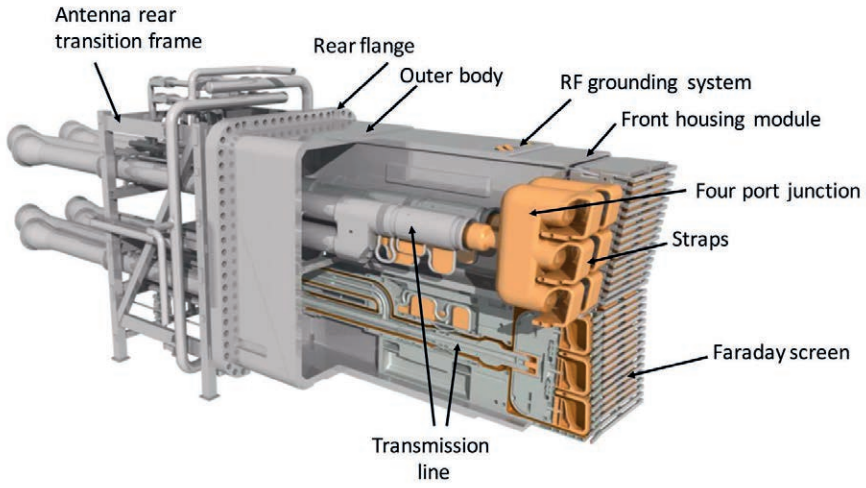

FIG. 2.16. Three-dimensional rendering of the ITER ICRF antenna. The antenna dimensions are 3.5 m (L) × 2.4 m (H) × 1.9 m (W).

2.3.6. Transport inside plasma

From the location where the plasma density is high enough for the (fast) wave to propagate, this wave is used to transport the power towards the plasma centre. At the very edge, where there is no plasma or the plasma density is too low, the fast wave is non-propagative. The minimum density, at which the wave will propagate depends on the frequency and the spectrum of the antenna, and is called the cutoff density. Normally the wave propagates until it is absorbed or reflected from the high field side cutoff. In a plasma with more than one ion species, the wave can encounter a cutoff, also in the plasma center. At a cutoff the wave can be reflected, partially tunnelled through up to the point where it can propagate again or mode converted to some other wave.

2.3.7. Absorption

Absorption of the ICRF wave power in the ion cyclotron range of frequency can happen by three mechanisms: minority heating, harmonic heating or mode conversion. Despite the fact that the method is also sometimes called ion

[6] Where the use of carbon would lead to excessive tritium inventories trapped in the machine.

cyclotron resonant heating, heating at the ion cyclotron resonance is not as evident as the naming seems to imply. The fast wave, which is used to propagate the power from the edge to the plasma interior is elliptically polarized: it has two circularly polarized components of different amplitudes (the ratio can in addition be varying depending on the plasma conditions); one rotating in the direction of the ions and one rotating in the direction of the electrons. It is the former component, which (in the resonance) can accelerate the ions: a rotating ion then sees in its frame of reference a constant electric field that can accelerate (or decelerate) it depending on the phase of the electric field (i.e. its direction) with respect to the instanteneous speed of the ion.

In a single species plasma, the polarisation of the wave at resonance is such that the amplitude of the component whose electrical field is in the direction of the cyclotron rotation of the ions is exactly zero: a system where the power can be generated, transported to the plasma, coupled to the plasma, propagated inside of the plasma, but… cannot be absorbed! Luckily, there exists a way around this dilemma. Inside the plasma, the polarisation of the wave is set by the dominant species, while the absorption depends on the resonant species. By taking the dominant species to be different from the resonant species, the component of the wave with the right polarisation at the resonance (of the resonant species) is different from zero. This method is called minority heating. An example is hydrogen as a minority, in a plasma consisting mostly of D.

An alternative method for absorption of the wave power is absorption at the harmonics. When the wave has a frequency equal to n times ($n \neq 1$) the cyclotron resonance of the absorbing species, then the component with the proper polarization is not zero. However, in this case, in its frame of reference, the ion no longer sees (e.g. for $n = 2$) a stationary electric field but a rotating electric field that will, accelerate and decelerate it in turn. If, however, the Larmor radius of the particle and the wavelength of the wave is such that the amplitude of the electric field the ion sees along its orbit is not constant, then a net acceleration or deceleration can be obtained. This method is called harmonic heating and relies on the fact that the ions have a finite orbit and may thus sample different parts of the wave amplitude. The interaction increases with the Larmor radius as the ions sample parts of the wave with increasingly different amplitude. This goes on until the Larmor radius increase leads to the sampling (along the second part of the ion's orbit) of an electric field which again starts to cancel the effect of the first part of the orbit.

In both cases the (minority or harmonic) interaction can lead to an acceleration or deceleration of the ions. Whether a net transfer of power of the wave to the ions or the opposite occurs depends on the shape of the distribution function of the ions. For a distribution function that is monotonously decreasing, the energy transfer is from the wave to the ions. Indeed, consider ions with a particular velocity v_0, as many ions can be accelerated as can be decelerated. Similarly, at a highter velocity v_1, as many ions are decelerated as accelerated. If the number of ions at velocity v_0 is equal to the number of ions at velocity v_1 then the ions accelerated at v_0 is compensated exactly by the number decelerated at v_1. If, however, there are more ions at the lower velocity v_0 than at the higher velocity v_1, then there are more ions accelerated at v_0 than there are decelerated at v_1 and a net transfer of power from the wave to the ions can take place. The opposite can also occur: tranfer of power from the particles to the wave if there are more ions with velocity v_1 than with velocity v_0 for $v_1 > v_0$ (the case of a distribution function with positive slope).

Power can also be absorbed directly by the electrons near $\omega/k = v_{the}$ (by Landau damping or transit time magnetic pumping). For the spectra (k values) typically launched by the antennas, this occurs in our frequency range when the temperature is high or when the wave has been transformed to another type of wave, with shorter wavelength and larger k. This mode transformation happens, for example, in plasmas with multiple ions, where (between the resonances of the ions) a pair of resonance and cutoff appears, at which the wave can be mode converted to a shorter wavelength wave (Bernstein or cyclotron wave).

A recent development uses a combination of three ions to integrate a minority heating with the mode conversion scenario. A mix of two majority ions leads to a mode conversion layer where the amplitude of the electric field of the wave with the right polarization is increased. Locating this layer at the position of the resonance of a third, minority species can lead to strong absorption by this minority and highly accelerated ions.

2.3.8. Discussion on strength and weaknesses

The main advantage of the ICRF system is that the generators are mature systems due to their long history and development as broadcast transmitters. They exist in unit sizes of the order of 2 MW, operate in steady state and have high plug to power efficiency. Low loss transmission lines allow the generator to be located far from the torus, making them easily accessible for maintenance and repair. A critical component is the feedthrough that needs to include ceramic, thus has to be positioned where the neutron flux is low enough. Transmission lines, however, do not need to be straight and dog-legs can be used to position the feed-through in shielded areas. The influence of the plasma on the coupling has been an issue because of the fast-varying impedance that could not be matched on the same timescale and would thus lead to reflected power reaching the generators. This has been solved with the use of 3-dB couplers.

Such couplers are being developed for the long pulses envisaged for ITER. High power densities and high voltages (leading to arcing and component damage) can be an issue if the coupling is too low. This can be the case when the antenna is limited to a port. If, however, the antenna can be distributed (as proposed for DEMO), this issue would be substantially mitigated. An area of active research is the impurity production due to ICRF power. Solutions are being developed, backed by the parallel development of the theories and numerical codes. It is expected that a distributed antenna would also be much less prone to impurity production.

2.3.9. Overview of parameters achieved

Some examples of recent, existing and planned systems are shown in Table 2.2.

TABLE 2.2. ICRF systems of AUG, Alcator C-mod, Tore-Supra/WEST, EAST, LHD, JET, ITER and DEMO.

	Number of generators	**Total installed power (MW)**	**Frequency range (MHz)**	**Number of antennae and number of straps in toroidal direction**	**Pulse Length capability of the ICRF system (s)**
AUG	4	8	30–120	2 antennae (2 straps) 2 antennae (3 straps)	10
Alcator C-Mod [2.21, 2.22]	4	8	4 MW at 80 MHz 4 MW at 40–80 MHz	2 antennae (2 straps) 1 antenna (4 straps field aligned)	5
Tore-Supra/WEST	6	12	40–70	3 antennae, (2 straps)	30 (9 MW) 1000 (3 MW)
EAST	6	12	25–70	2 antennae (2 straps and 4 straps)	1000
LHD	4	8	38.5	3 antennae (1, 2 both field aligned and 1 strap)	2700
JET [2.23]	16	32	23–57	4 antennae (4 straps) 1 antenna (2 straps)	20
ITER	8 + 1	24	40–55	2 antennae (4 straps)	3600
DEMO	25	50	Depending on the field (e.g. 45–65 MHz)	Distributed (e.g. 72)	3600 or steady state

2.3.10. Other uses

ICRF can also be used for current drive when the power is coupled to the electrons and the antenna has a directed spectrum. Other uses include: plasma breakdown assist, wall conditioning, stabilisation and destabilisation of sawtheeth, influencing plasma rotation and acting on the transport of fast particles.

2.4. LOWER HYBRID

2.4.1. Introduction

Originally, the occurrence of the lower hybrid resonance was anticipated to lead to strong wave–particle interaction through linear and non-linear mode conversion to a hot plasma wave. An appropriate RF launcher would excite cold plasma waves that would propagate into the plasma until they reach the lower hybrid resonant layer. At this layer, the perpendicular group velocity would vanish and the waves could be converted into a hot plasma mode, which would then be absorbed. This heating technique, known as lower hybrid plasma ion heating (LHIH) or lower hybrid resonance heating (LHRH), was the originally investigated method. However, effective ion heating was only obtained in a small number of experiments. Rather than trying to heat ions, it was then theorized and confirmed that high phase velocity waves traveling in the direction parallel to the magnetic field could interact quasi-linearly with the electron population by Landau interaction, and, by using an asymmetric spectrum could drive a large amount of additional toroidal plasma current. This technique is known as lower hybrid[7] current drive (LHCD) [2.24].

In this frequency range, which lies close to the ion plasma frequency in the lower end of the microwave band (1 to 5 GHz), the electromagnetic power is generated by klystrons in step 1. The power is transmitted to the plasma through rectangular waveguides in step 2 and coupled to the plasma via launchers made of rectangular waveguides stacked periodically in the horizontal direction parallel to the toroidal magnetic field in step 3. The launchers are called "grills" because of their characteristic shape. The power is propagated into the plasma by plasma waves, typically the slow wave, also called the LH wave in this frequency range (step 4). The power is finally damped on the electrons by electron Landau damping in step 5.

2.4.2. Klystrons

A klystron is a vacuum tube used as amplifier at narrow band microwave and radio frequencies. In the fusion domain, they are mainly used to produce high power electromagnetic waves at the level of hundreds of kW during many seconds. The first klystrons were intensively used during World War II as RF power generators for RADAR systems. Klystrons sources between 2.45 GHz and 5 GHz are now available at the 0.5 to 0.8 MW and 10 to 1000 s level. The basic idea of the klystron is illustrated in **Error! Reference source not found.** [2.25]: A continuous electron beam is emitted by the klystron's cathode and accelerated to high voltage in a DC gun. The electron beam passes through a resonant cavity (input cavity) which is excited by an external source of RF power (typically in the milliwatt to watt range) at the resonant frequency of the cavity (resonant cavity). While passing through the first cavity, the electron beam velocity is modulated by the weak RF signal: the sinusoidal variation in the cavity voltage causes alternate acceleration and deceleration of electrons in the beam. The beam then passes through a drift tube, in which the accelerated electrons travel faster and the decelerated ones travel slower, resulting in a beam which is bunched at the frequency of the RF drive signal; thus, a significant fraction of the beam's power has been moved from DC to the drive frequency. The beam then passes through a series of cavities in which standing waves are induced at the same frequency as the input signal. The signal induced in the second chamber is much stronger than that in the first, thus leading to amplification of the velocity and density modulation of the beam. A larger number of cavities may be used to increase the gain of the klystron, or to increase the bandwidth. The output cavity is located at a point where the electron bunches are fully formed. The resonant frequency of the output cavity is the same as that of the input cavity and the power is so transferred from the (bunched) electron beam to electromagnetic fields in the output cavity. The RF power extracted from the output cavities travels to one or multiple output waveguide(s) and exits the klystron body. Since the klystron is vacuum pumped, a RF window is necessary. RF feed-through (or "windows") are mounted at the RF outputs to ensure the transition between the vacuum inside the tube and the pressurized waveguides. The residual electron beam energy is dissipated in an actively cooled collector.

[7] The term remained despite the fact that the *lower hybrid* resonance is not anymore involved in the use of this method in tokamaks.

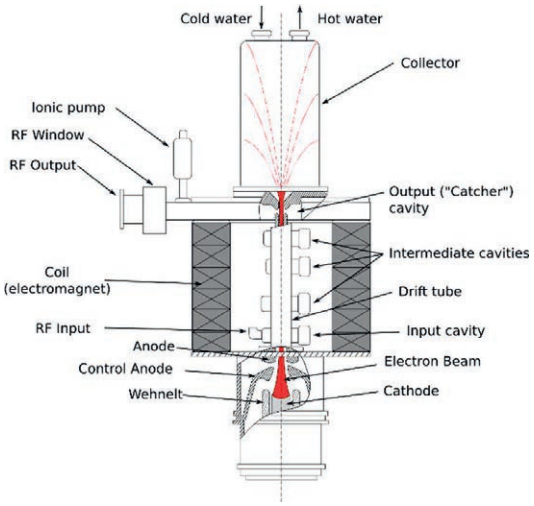

FIG. 2.17. Schematic diagram of a klystron [2.25]

2.4.3. LH Transmission Lines: waveguides

As the RF frequency increases, coaxial line losses become too high for high power applications. In the LH range of frequencies (1 to 5 GHz), hollow rectangular waveguides are preferred for the transport of the RF power from the klystrons to the torus. In addition to their low losses, they also allow a greater breakdown voltage than coaxial lines of the same size. In this frequency range, the wavelength in vacuum is of the order of 6 to 30 cm.

2.4.3.1. Rectangular waveguides

A hollow rectangular waveguide of width *a* and height *b* is illustrated in FIG. 2.18. Solving Maxwell's equations for this geometry leads to multiple possible solutions, or modes, expressing how the electromagnetic waves can propagate. Each mode is characterized by a cutoff frequency, below which the mode cannot propagate in the guide. In a rectangular waveguide, modes can be expressed as tranverse electric (TE) or transverse magnetic (TM) depending on their respective polarization. Since the walls of a rectangular waveguide constrain the electromagnetic field boundary conditions along two dimensions (the walls on the large side and on the small side), two integer indices are used to describe a mode. Thus, modes in rectangular waveguides are labelled TE_{10}, TE_{20}, TM_{11}, etc.

For practical applications, the dimensions of the waveguides are generally chosen to have one and only one mode allowed to propagate for a specified frequency band. This single mode is the first one to appear to be propagating, and is referred to as the fundamental mode (generally the TE_{10} mode). Other modes can eventually be excited by waveguide discontinuities (such as bends or connections), but can't propagate since they are evanescent. They are referred to as high order modes.

For high-power applications, great attention is paid to the inner walls of the waveguide, the bends and connections, since reflected power and arcs may occur due to discontinuities in the conducting walls (e.g. the ones caused by misalignments, bumps, holes etc).

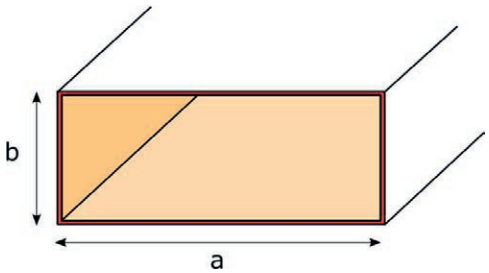

FIG. 2.18. Illustration of a rectangular hollow waveguide.

2.4.3.2. Waveguide plumbery – a practical example

Many waveguide devices have been developed to transmit, measure, combine or split the power from one point to another. These devices are commonly used on LHCD systems to transport the power from a klystron to (a section of) an antenna, but also to protect the klystron from possible reflected RF power by the plasma. As an example of the usage of such devices, the Tore Supra LHCD system is illustrated in FIG. 2.19. The power is generated at the klystron plant and transmitted to the two launchers through rectangular waveguides (8 lines per launcher).

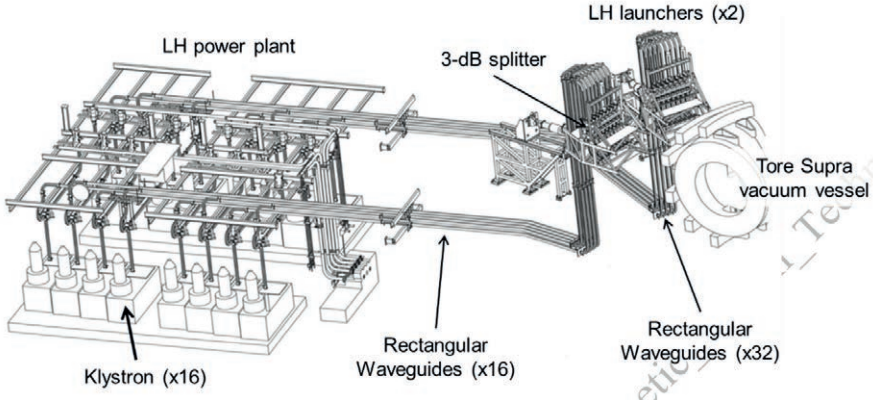

FIG. 2.19. Schematic of the Tore Supra LHCD system, from the klystrons plant to the vacuum vessel.

Once reaching the rear end of the launcher, the power goes trough a 3-dB splitter (also called a hybrid junction). This device splits the incident power into two waveguides, one to feed the upper part and the other for the lower part of the launcher. If reflected power (from the plasma) returns from these two waveguides, the power is recombined and directed to a fourth one. An actively cooled water load is connected to this fourth port to dump the remaining RF power reflected by the plasma thus protecting the klystron. After being split, the RF power goes through various devices up to the plasma (FIG. 2.20):

- A bidirectional coupler, which measures the forward and reflected power amplitude and phase;
- A DC break, which isolates the DC potential of the tokamak from the DC potential of the transmission line (for human protection);
- A vacuum feed-through (or window), which isolates the tokamak vacuum from the pressurized medium existing in the waveguide. These windows (16 by launchers) are illustrated in FIG. 2.20. A window consists in a dielectric medium inserted between two rectangular waveguides. The dimensions of the dielectric medium (a ceramic, such as beryllium oxide BeO or alumina) are calculated not to produce reflected power. Since part of the power is always absorbed in the ceramic, great care is applied to correctly cool the window to avoid heating the ceramic which could make it break.
- A TE_{10}–TE_{30} mode converter, converts the electromagnetic modes and then splits the incoming RF power into three new waveguides leading to a split of the power into three poloidal rows of waveguides. A mode converter is a rectangular waveguide device which large side is modulated to allow higher modes (such as TE_{20}, TE_{30} and TE_{40}) and such that the power is totally transferred from one mode to another with an efficiency close to 100%. Once the power is transferred to the TE_{30} mode, metallic septa located in zero field regions split the power into three independent waveguides. The device is illustrated in FIG. 2.21.
- Finally, a multijunction – a structure which will be described in detail in the next section – splits and phases the power in the toroidal direction, then leads to the plasma.

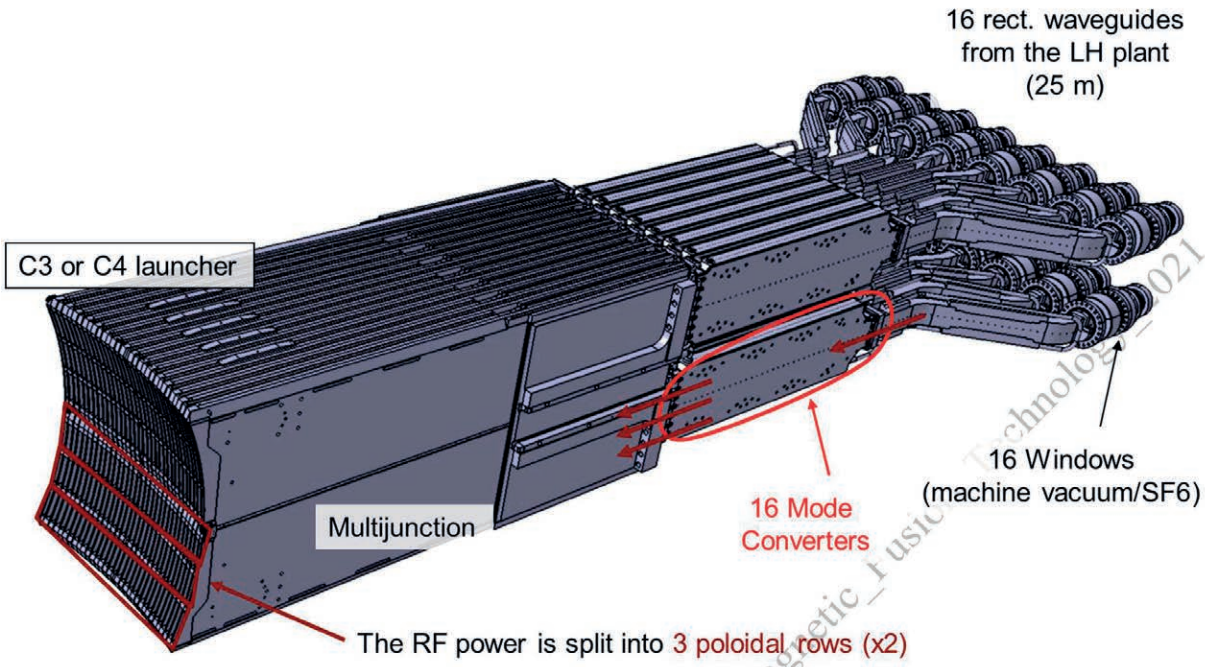

FIG. 2.20. Illustration of the power splitting scheme in the Tore Supra LHCD launcher C3 or C4.

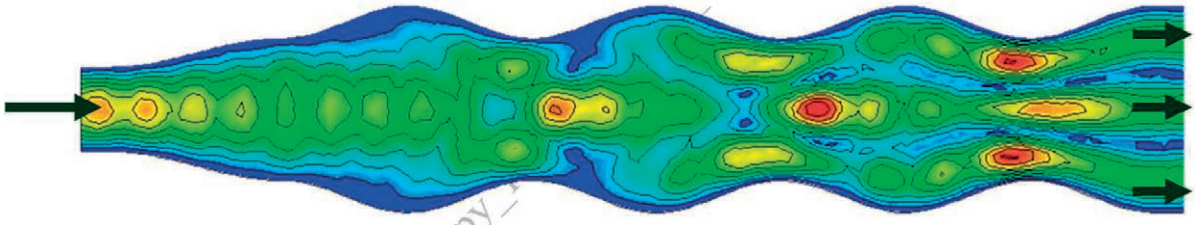

FIG. 2.21. Illustration of the electric field distribution in a TE_{10}–TE_{30} mode converter at 5 GHz. The device is excited from the left.

2.4.4. LHCD launchers

As the plasma cross-section of toroidal devices became sufficiently large to accommodate the free space wavelength at the lower hybrid frequencies, it becomes possible to couple the RF power directly with open-ended waveguides inserted in the vacuum vessel wall, thus avoiding coils or antennas within the vacuum chambre. However, for the wave to access from outside the plasma to inside the plasma, the wave has to be "slowed down" along the static toroidal magnetic field. This means that the parallel phase velocity of the wave $v_{\parallel}$ has to be reduced with respect to the speed of light c_0 to satisfy an accessibility condition (i.e. to be able to penetrate trough the plasma centre). Equivalently, this condition requires the wave to have a sufficiently large refractive parallel index $n_{\parallel} = c_0/v_{\parallel} = k_{\parallel}/k_0$ (parallel to the magnetic field). A phased array is used to form and launch such a wave. A set of properly phased waveguides, where the short side of the waveguides are mounted parallel to the toroidal magnetic field, can effectively couple a slow plasma wave mode into the plasma.

The coupling is the process by which RF power propagates and possibly tunnels from the antenna to the plasma. In the case of the LH wave, the properties of the propagation of cold-plasma waves into the plasma show that the wave is evanescent if the electron density is below a certain cutoff density n_{cutoff}. If such a low-density layer is thin enough, the wave can tunnel through it. Similar to ICRF antennas, either the LH launcher is close enough to the plasma or the local density is to be increased by gas puffing. The closeness to the plasma leads to demanding thermal conditions. As for ICRF antennas, LHCD launchers distributed around the vacuum vessel is a proposed scheme for DEMO, substancially mitigating these issues.

2.4.4.1. LH launcher main figures of merit

There are three important figures of merit to measure the efficiency and performance of a LH launcher: The first one is the *k*-space radiated power spectrum, generally characterized by its parallel power spectrum $p(n_\parallel)$. This quantity represents the amount of power excited by the launcher for each parallel index. The relation between this power spectrum and the array excitation is related to the Fourier transform of the electromagnetic field at the plasma-antenna interface. The second one is the ratio of the reflected power (at the mouth or at the end of the launcher) to the input power, named the reflection coefficient and sometime expressed in percents: $RC = P_r/P_i$. The third one is the directivity of the launcher, which is the fraction of the power spectrum over its total power content. It can be viewed as the fraction of the power that goes toward one toroidal direction over the total coupled power. One can define the directivity as: $D = \int_{n_\parallel>0} p(n_\parallel) \cdot \mathrm{d}n_\parallel \,/\, \int_{n_\parallel} p(n_\parallel) \cdot \mathrm{d}n_\parallel$. Since the wave field at the launcher aperture (and thus the launcher spectrum) depends on both the antenna and the plasma, numerical coupling codes are required to make a self-consistent numerical evaluation of the coupling. Different types of launchers have been developped to balance the sometimes conflicting requirements of experimental flexibility, reduced complexity and thermal constraints. These are the grill launchers, the multijunction launchers and the passive–active multijunction launchers.

2.4.4.2. Grill Launchers

When all waveguides are fed separately by independent RF sources, and thus can be independently phased, the launchers have a wide flexibility in terms of operational space (excited spectrum), which is of great interest for physics studies. However, with each waveguide independently fed with power, the complexity of the launcher grows enormously with the number of output waveguides, leading to cumbersome transmission systems at multi-megawatt power levels. Typical grill launchers have high reflection coefficients (~20 to 40%) but directivities higher than 80%.

2.4.4.3. Multijunction Launchers

In a large tokamak, a conventional LH grill made of independently fed waveguides would require hundreds of waveguides, leading to a very complex power splitting design behind the antenna. A multijunction grill, where the main waveguide is divided into N smaller (secondary waveguides) can overcome this limitation. The division is made by thin metallic walls parallel to the wall of the main waveguide and perpendicular to the electric field: The E-plane N-junctions. Built-in phase shifters made by reducing the waveguide height (to increase the guided wave phase velocity) are added in the structure to obtain the desired output phasing of the grill. The multijunction launcher makes it simpler to create and feed a large number of waveguides as compared to the classic grill launchers. However, since the phase shift is created by the built-in phase shifter inside the launcher, a drawback is that the adjustment of the power density spectrum is limited to a smaller range than for classic grill launchers. A judicious choice of phasing of the output waveguides leads to an important self-matching or recycling effect, as property of the multijunction. Indeed, for specific phase values, the reflected waves from the plasma, which return through the secondary waveguides, can be reflected back to the plasma, thus leading to multiple reflections in the secondary waveguides. This self-matching effect, which takes place between the plasma-antenna discontinuity and the E-plane bi-junctions, leads to an attenuation of the waves at each passage by the plasma, and an ultimate decrease of the reflected power toward the RF sources. Because of the self-matching property, the typical reflection coefficient of multijunction launchers is generally less than 10%. However, the multiple back and forth of the waves creates standing waves and increases the peak electric field in secondary waveguides.

FIG. 2.22. Left: The Tore Supra multijunction "C3" launchers as viewed from inside the vacuum vessel. The system, installed in 1999, features 288 waveguides, total front face dimensions of 60cm × 60cm, and a frequency of 3.7GHz. Right: The Tore Supra PAM (C4) launcher was installed in 2009 and weighs ~7 tons. It features 96 active waveguides, 102 passive waveguides, total front face dimensions of 60 cm x 60 cm, and a frequency of 3.7 GHz.

2.4.4.4. Passive–Active waveguide array launchers

Since the launcher is necessarily close to the plasma, its front face is subject to high-heat fluxes. Because of the frequency, the dimensions of the waveguides (and their walls) are small and thus little space is available for cooling. To improve the cooling of the launcher's front face, one can insert between each active waveguide (a waveguide that is directly fed from the generator) a passive waveguide (a waveguide closed by a short-circuit), behind which a water pipe could efficiently water-cool the structure. To insure a lower reflected power than in a conventional grill, the concept can be combined with the use of a multijunction. This passive-active multijunction (PAM) concept adresses two of the main criticism made to LH launchers, i.e. the coupling efficiency and the heat load resilience. The PAM concept tested in FTU and in the Tore Supra tokamak showed that low reflected power (i.e. high coupling efficiency) and continuous operations could be combined (c.f.FIG. 2.23).

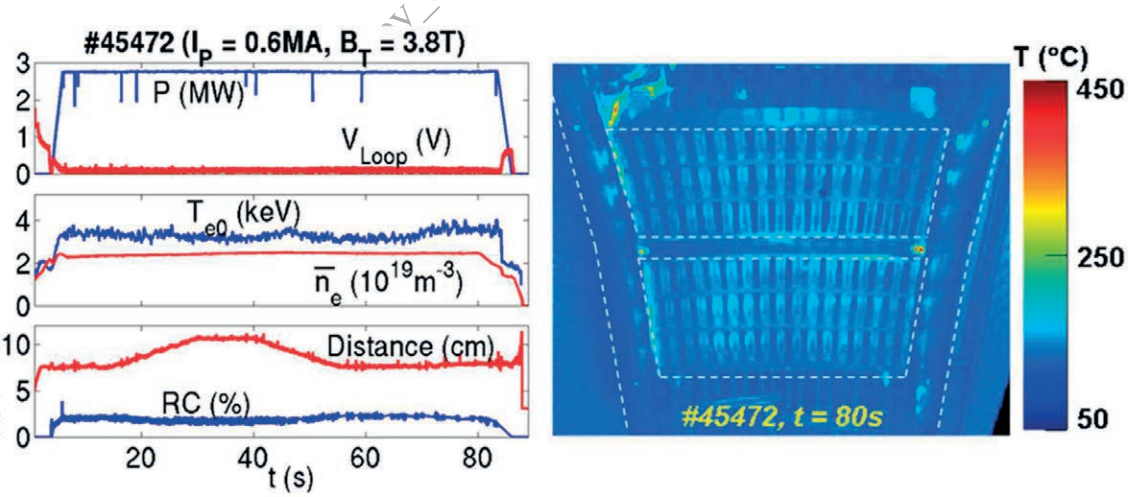

FIG. 2.23. Illustration of a Tore Supra discharge with the PAM launcher (TS discharge #45472, 2010). The design goal power density (25MW.m^{-2}) is achieved during 78 s, with very low reflected power (<2% of the input power), even at large plasma launcher distance (~10 cm). The infra-red monitoring shows that the global temperature of the launcher mouth is lower than 270°C, validating its efficient cooling structure [2.26].

2.4.4.5. Poloidal splitter launchers

To keep the flexibility in the parallel index $n_{\parallel}$ spectrum of the "grill" configuration (sacrificed by the multijunction), while keeping the complexity manageable, one can split the power in the poloidal direction. Since the power splitting is done poloidally (e.g using a four-way splitter), the launched parallel power spectrum can be changed with the same flexibility as with conventional grill antennas. This design simplifies the feeding structure of the antenna — reducing the RF losses due to multiple power splitters and flanges of previous grill configurations — while keeping a simple manufacturing assembly. The RF power is redistributed depending on the plasma load on each of the four rows of the splitter. If the load is the same for each row, the power is evenly split among rows. Such antennas are used in Alcator C-Mod and the KSTAR tokamak (FIG. 2.24).

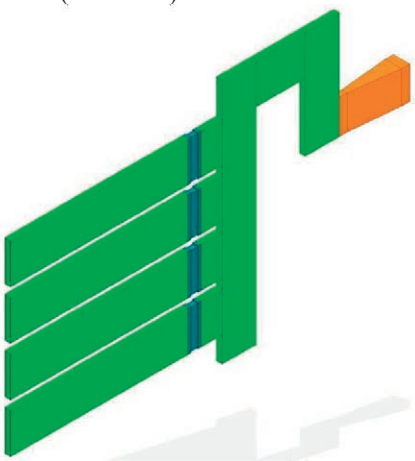

FIG. 2.24. Conceptual schematic of the Alcator C-Mod four-way splitter [2.27].

2.4.5. Wave propagation in the plasma

For the RF power to reach the plasma core, the waves excited by a LHCD launcher need to satisfy several criteria:

- A cutoff condition: the electron density in front of the launcher is close to or higher than the slow-wave cutoff density.
- A propagation condition: for the LH waves to propagate into the magnetized plasma, the absolute value of the parallel index of the excited waves need to be greater than one, i.e. $|n_{\parallel}| > 1$.
- An accessibility condition: for the LH waves to access the core plasma without being mode-converted into fast waves, a minimum value of $n_{\parallel}$ for a given plasma density and magnetic field is required: $|n_{\parallel}| > |n_{\parallel\,\mathrm{access}}| \approx \mathrm{sqrt}\,(1 - \omega_{pi}^2/\omega^2 + \omega_{pe}^2/\omega_{ce}^2) + \omega_{pe}/|\omega_{ce}|$. When the accessibility condition is satisfied, the slow and the fast branch of the dispersion relation are separated and the LH slow waves can reach the core plasma. Inversely, for a given $n_{\parallel}$, the previous condition leads to an upper limit on the density, above which the wave can't propagate.

The RF power is coupled by the launcher to the plasma, which means that the electromagnetic waves in the launcher's waveguides are (mainly) converted to slow waves in the plasma. In the LH range of frequencies (~2 to 8 GHz), the wavelength of the RF waves in the plasma is well below the typical beam size, which itself is smaller than the equilibrium non-uniformity scale. It this situation, the evolution of the waves in the plasma can be described by the ray–tracing formalism. Since the evolution of the electron population can be described by a Fokker–Planck calculation, the combination of both tools is standard for modeling LHCD experiments.

2.4.6. Waves Absorption, Landau damping

Landau damping is the dominant absorption mechanism for current drive with LH waves. Landau damping is a collisionless damping process in which particles exchange energy with waves traveling at nearly same phase velocity parallel to the magnetic field, that is, for particle parallel velocities $v_{\parallel}$ satisfying the resonant condition $\omega - k_{\parallel} v_{\parallel} = 0$. The parallel wavenumber of the wave is $k_{\parallel} = k_0 n_{\parallel}$, whereby $n_{\parallel}$ is the parallel index of refraction and $k_0 = \omega/c$ is the wavenumber in vacuum. From the previous relation, one deduces that the LHCD launcher excites waves satisfying

the resonant condition $v_{\parallel} = c/n_{\parallel}$. As for the slow wave to be able to penetrate the plasma, the parallel index needs to be greater than one and greater than $|n_{\parallel\,\mathrm{access}}|$. Typical LHCD launchers in current tokamaks excite a main parallel index between $n_{\parallel 0}$ =1.5 and 3.0. However, in many past and present LHCD experiments, the resonant velocity $v_{\parallel 0} = c/n_{\parallel 0}$ corresponds to a suprathermal region where the number of electrons is, in principle, too small for any significant wave damping to take place and to account for the observed current drive. This paradox is commonly referred to as the spectral gap problem and is an active area of research. Various explanations have been proposed to explain this spectral gap, among these the toroidal effects on the wave propagation that can cause sufficient upshift (increase of the parallel wavenumber) in the parallel refraction index $n_{\parallel}$ to "fill" the spectral gap, nonlinear interactions such as parametric decay instabilities (PDI), diffraction effects or electron density fluctuations in front of the launcher.

2.4.7. Overall discussion on strength and weaknesses

In present devices, as lower hybrid waves exhibit the highest current drive efficiency, its main usage is for current drive applications, in the development of quasi or fully steady state plasma physics and scenarios. For this reason, LHCD systems are common on superconducting tokamaks and useful for continuous wave operations, using continuous wave RF sources, actively cooled transmission lines and launchers. In ITER or in a tokamak fusion reactor, the high densities prevent the LH waves from propagating to the plasma center and the waves only reach the outer portion of the minor radius. LH waves can then not be used from driving central current. However off-axis current drive is well suited for startup phases, steady state or advanced scenarios. LHCD, in combination with other heating and current drive methods, will be a key tool to sustain advanced tokamak steady state plasmas, to save volts–seconds in the current ramp-up phase, to extend the plasma duration and to provide some control over the current profile.

2.4.8. Overview of parameters achieved and example of some systems

In terms of performances, fully non-inductive discharges of up to 3.6 MA in JT-60U and 3 MA in JET have been achieved with LHCD. Plasma currents of 0.8 MA and 0.27 MA have been sustained for more than 6 minutes in Tore Supra and EAST in L-mode. At densities below 0.1×10^{19} m^{-3}, the tokamak TRIAM-1M sustained a 5 hours plasma discharge with 0.05 MW of LHCD. The EAST team also demonstrated a 30-s pulse H-mode operation (thus setting a record for the longest H-mode duration achieved to date) and an ELM mitigation possibility using LHCD. The measured current drive efficiency of LH waves, which is the figure of merit of the LHCD, is between $\eta = 0.9$ and 1.55×10^{19} A m^{-2} W^{-1} in JET and Tore Supra, which is equal or greater of than for other current drive systems. It is to be noted that the current drive efficiency decreases as $1/\bar{n}_{e,\mathrm{average}}$. In some experiments, the current drive efficiency drops abnormally, in correlation with observations of non-linear effects such as parasitic absorptions and wave spectrum distortions. In ITER, the high central and edge temperatures will lead to a strong single pass Landau damping. In this case, the calculated average current drive efficiency is 2×10^{19} A m^{-2} W^{-1}.

TABLE 2.3. LHCD systems of JET, Tore Supra/WEST, Alcator C-Mod, EAST, HL-2A, KSTAR, TRIAM-1M, SST-1 and ITER.

	Number of sources	Total installed power (MW)	Frequency range (GHz)	Number and type of the antennae	Max. pulse length achieved with LHCD (s)
JET	24	15	3.7	1 Multijunction	13 s (*)
Tore Supra/ WEST	16	9	3.7	1 Multijunction 1 PAM	390 s
Alcator C-Mod	8	2	4.6	1 Grill	5 s (*)
EAST	20 24	4 6	2.45 4.6	1 grill 1 Multijunction	400 s (L-mode) 61 s (H-mode)
HL-2A	4	1.6	3.7	1 PAM	2 s (*)
TRIAM-1M	9	0.45	2.45 8.2	2 Grill	5 h 16 min
SST-1	4	2	3.7	1 Grill	N.A.
KSTAR	1	0.5	5	1 Grill	5 s
ITER	48	24	3.7–5	1 PAM	1000 s

* The maximum pulse duration on non-superconducting tokamaks is limited by other constraints such as high-voltage supply or coil temperature.

2.5. ELECTRON CYCLOTRON RESONANCE FREQUENCY

2.5.1. General principle

The electron cycloton resonance heating (ECRH) method uses electromagnetic radiation at the cyclotron frequency of the electrons (or its harmonics). Such frequencies are of the order of a few hundred GHz, with a corresponding wavelength of the order of a few millimeters. The frequency f is related to the toroidal magnetic field B_T by the relation f [GHz] = 28 n B_T [T], where n is the harmonic number. For the electron cycloton resonance heating (ECRH) method, gyrotrons transform electrical power into electromagnetic power (step 1), which is transported to the plasma using oversized waveguides or optical transmission (step 2). The power is coupled to the plasma with horn antennas or by mirrors (step 3), transported inside the plasma by plasma waves, typically the X or the O mode wave (step 4), and absorbed on electrons by wave–particle interaction at the fundamental frequency or harmonics (step 5).

2.5.2. Gyotron

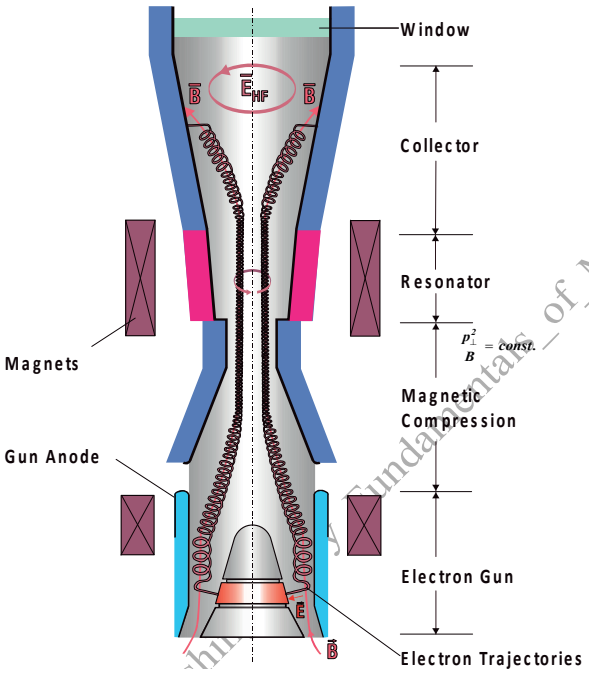

FIG. 2.25. Conceptual drawing of a gyrotron.

A gyrotron in its simplest form (FIG. 2.25) consists of an electron gun (also called a magnetron injection gun, MIG), which produces a mildly relativistic (relativistic factor γ of ~1.18) annular electon beam, and which is at the same time the anode of a set of electrodes that accelerate the electrons in a drift tube,

- a resonant cavity, part of the drift tube, in which the transfer between the energy of the electron beam and the energy of the electromagnetic radiation occurs,
- a collector, which acts as cathode, on which the remaining energy of the electron beam is dumped and
- an exit window, through which the electromagnetic radiation leaves the gyrotron.

A superconducting magnet produces the magnetic field in the resonator. Due to the mildly relativistic nature of the electons, the electron cyclotron frequency $\omega_{ce} = eB/m$ depends on the energy through the energy dependence of the relativistic mass $m = \gamma m_o$. In the cavity, the electromagnetic mode at the cyclotron frequency is made to coincide with a TE resonance, which can have multiple peaks in the radial, azimutal and longitudinal directions. The electrons can be made to interact with a particular $TE_{m.n}$ mode, with m the azimuthal mode number and n the radial mode number. They can be decelerated as well as accelerated assuming their phase is initially random with respect to the phase of the RF electric field. As the electrons l ose energy, their mass decreases and the cyclotron frequency increases

(their phase increases), leading to less deceleration. On the contrary, when their energy increases, their mass increases and the cyclotron frequency decreases (their phase decreases), leading to less accelleration. Since the phase change leading to less acceleration is larger than the phase change leading to more acceleration (because of the energy dependence of the mass), the net effect for electrons, which started with random phases, is a phase bunching, a net deceleration and a transfer of perpendicular energy from the electrons to the wave. In the cavity, up to 75% of the perpendicular energy of the electrons can in this way be transformed into electromagnetic energy. The energy of the electron beam in the direction parallel to the magnetic field is unaffected by the interaction with the RF field since the TE_{mn} mode has no axial field.

A critical aspect of the gyrotrons is the small wavelength at those frequencies, which at first implies small dimensions, in stark contrast to the high power that needs to be handled. From this simple design, more sophisticated gyrorons were developed which incorporate several improvements, mostly with the aim to reduce the high power density. The final section of the tube was originally both a waveguide for the electromagnetic mode (dimension of which were contrained by electromagnetic requirements) and a beam dump. By having the RF power leaving the gyrotron radially rather than axially, it was possible to make the beam dump much larger than its function as a waveguide would allow, thus reducing the power density. The power is coupled radially out of the gyrotron by a mode convertor and a serie of mirrors right at the exit of the resonator, directing the RF power radially out of the gyrotron. To cope with the required high output power, a highly overmoded cavity functioning in $TE_{m,n}$ (m = 32, n = 9 at 170 GHz in the European design of the 1 MW ITER gyrotron) is used to limit the RF ohmic losses on the wall while keeping the cavity RF quality factor at the desired value for an efficient transfer of energy between the electron beam and the fields. However, in a highly overmoded cavity, the frequencies of neighbouring modes which can be excited are close to each other leading to the problem of mode competition. This problem is solved by a careful design of the gyrotron parameters, such as the electron beam radius and the cavity itself. It can be further alleviated by using a coaxial cavity, where the coaxial insert is corrugated, leading to a better separation between the competing modes.

Since only part of the electon beam energy is transferred to the RF wave, the spent beam still carries an appreciable power which is dissipated in the collector. A method to decrease the power density on the collector is to sweep the electron beam at the collector, thus depositing the power on a larger area. Putting a “voltage depression” on the collector allows to recuperate part of the spent beam power, therefore decreasing the power density on the collector while at the same time increasing the efficiency η_{RF} = RF power / electrical power. The exit window is a critical component that needs to separate the high vacuum inside of the gyrotron from the conditions in the waveguide while being able to sustain the transmission of high power without significant losses (which need to be cooled away). This was achieved by the development of diamond windows, which have very low transmission losses (low tg $\delta(\omega)$ = $\mathrm{Im}(\varepsilon)/\mathrm{Re}(\varepsilon)$, $\varepsilon(\omega)$ being the complex dielectric constant), and very high thermal conductivity. The high thermal conductivity allows the window to be cooled only at its edges. Gyrotrons are normally optimised to operate at a single frequency. However, multi-frequency gyrotrons have recently been developed. Different radial and azimutal modes are now used at the different frequencies for the interaction of the beam and the RF field. Care is then taken that the exit window is designed for low losses and to be matched at those different frequencies, or be broadband (i.e. at the Brewster angle).

2.6. TRANSPORT OUTSIDE

Waveguides (typically oversize and corrugated) or quasi-optical transmission is used to transport the power from the gyrotron to the torus. Several components have been developed to allow for this to happen efficiently. Beam shaping will reduce the losses, while bends and switches allow flexibility in the layout and combination of beams.

2.7. COUPLING

The very short wavelength of the radiation of the ECRH power means that it can propagate in vacuum. The launcher can thus be simply an ended waveguide, which can be at some distance from the plasma. As the wave, at the end of the waveguide simply continues to propagate optically with the same velocity, there is little discontinuity and little reflected power. More complicated launcher structures, allowing to direct the beam in toroidal and poloidal direction involve a combination of mirrors. Another way to allow some steering of the beam, without positioning mirrors close to the plasma is to use a mirror at the entrance end of an oversize waveguide of proper length. By injecting the wave at an angle in the waveguide, it will exit the waveguide at the same angle, thereby allowing some steering of the beam without having mirrors near the plasma.

2.8. TRANSPORT INSIDE PLASMA

Two types of waves can be used to propagate the power from the plasma edge into the plasma center, both with a wave vector perpendicular to the externally imposed magnetic field: the ordinary or O mode (where the wave electric field is parallel to the externally imposed magnetic field) and the extraordinary or X mode (where the wave electric field is perpendicular to the externally imposed magnetic field). Near the fundamental electron cyclotron frequency, both wave can encounter a cutoff preventing them to propagate towards the location where they could be absorbed. For the O mode, if the density is above the electron plasma frequency, the wave is in cutoff, and cannot propagate to the electron cyclotron resonance. For the X mode, the X mode cutoff prevents a wave launched from the low-field side to propagate to the upper hybrid resonance where the wave would be absorbed. This upper hybrid resonance however could be reached at all densities from the high-field side. To reach the plasma center without hindrance, also from the low magnetic field side, waves with frequencies corresponding to higher harmonics of the cyclotron frequencies are used. While those can propagate to the center of the plasma without encountering the cutoffs, absorption of the waves becomes more difficult, with the corresponding problem of non-absorbed wave power damaging in-vessel components. An alternative way to reach the center despite the cutoffs is by using mode conversion at cutoffs. The ordinary–extraordinary–Bernstein (OXB) method is a method by which an O mode is launched from the low field side. The O mode travels up to the O mode cutoff, where it is converted into a backward propagating X mode. This mode propagates back towards the low-field side, up to the upper hybrid resonance. At this location, it is in turn mode converted to a Bernstein wave, which propates again towards the high-field side unhindered by the O mode cutoff. It can thus reach the electron cyclotron resonance where it is absorbed.

2.9. ABSORPTION

Formulas for the absorption at the fundamental frequency and harmonics of the O and X mode can be found in the literature. For the X mode, absorption increases with the angle of incidence. At the second harmonic of the X mode — accessibility of which is given by $\omega_{pe}^2 = 2\,\omega_{ce}^2$ — the absorption is comparable to the absorption at the fundamental O mode. The second harmonic O mode, however, — accessibility of which is given by $\omega_{pe} = 2\,\omega_{ce}$ — has a lower absorption (by a factor T_e/mc^2).

2.10. OVERALL DISCUSSION ON STRENGTH AND WEAKNESSES

The high power density in the gyrotron initially represented a significant drawback of this method. However, the recent developments have significantly eased this issue. In small machine with low toroidal field B_T, the difficulty to reach the absorption layers in high density plasma can require the use of cyclotron frequency harmonics, with the related problem of insufficient absorption due to the dependency of the absorption on electron temperature. This is not expected to not be an issue any more in high magnetic field (and sufficiently low beta) machines like ITER and DEMO. The method presently benefits of relatively well-developed sources (1 MW), with potential for efficiency improvements. Higher power gyrotrons (2 MW) are under development. The method can deposit energy very locally on electrons to heat them or drive current.

2.11. OVERVIEW OF PARAMETERS ACHIEVED AND SOME EXAMPLE OF SYSTEMS

TABLE 2.4: Main parameters of the ECRH systems of TCV, AUG, DIII-D, LHD, W7X, ITER, EU DEMO1 2015.

	Installed power (MW)	Frequency (GHz)	Comments (pulse length capability)
TCV	3 MW	82.7 GHz	Including the upgrades, not all the power is usable simultaneously. Pulse length is limited to 2 seconds.
	1.5 MW	118 GHz	
	2 MW	84 GHz, 125 GHz (dual-frequency units)	

AUG	8 dual-frequency units provide 8 MW (at 140 GHz) or 6.4 MW (at 105GHz)	140 105 GHz	GHz,	10 seconds. (Installed power as of 2018)
DIII-D	6 tubes at 1 MW	110 GHz		5 seconds.
	1 tube at 1.5 MW	117.5 GHz		
LHD	3 MW at 77 GHz	77 GHz		77 GHz and 154 GHz tubes are capable of 1 MW for 10 seconds (0.3 MW CW). 2 seconds.
	2 MW	154 GHz		
	0.4 MW	82.7 GHz		
W7X	10 dual-frequency units provide 8 MW (at 140 GHz) or 3 MW (at 105 GHz)	140 105 GHz	GHz,	Simultaneous operation of 10 gyrotrons for 30 minutes. Upgrade to 12 gyrotrons started. The installation is designed for 1.5 MW unit power.
ITER	20 MW	170 GHz		3600 seconds.
EU DEMO1 2015	50 MW	170–204 GHz		2 hours. Since DEMO is still in the pre-conceptual phase, this baseline may still evolve.

2.12. OTHER USES

ECRH can also be used for plasma breakdown and for non-inductive current drive. Its very local power deposition allows the possibility to shape the current profile and get 100% bootstrap current. It has also been used to stabilize magnetohydrodynamic modes by driving current precisely at the island location (e.g. neo-classical tearing modes and sawteeth).

REFERENCES

[2.1] INTERNATIONAL ATOMIC ENERGY AGENCY, Fusion Physics. IAEA, Vienna (2012).
[2.2] ZACCARIA, P., et al., Design integration of SINGAP accelerator and RF Source in the ITER NB injector, 21st IEEE/NPSS Symposium on Fusion Engineering, Knoxville, Tennessee (2005).
[2.3] DE ESCH, H.P.L., Physics Design of the HNB Accelerator for ITER, Nucl. Fusion **55** (2015) 096001.
[2.4] CHITARIN, G., et al., Cancellation of the ion deflection due to electron-suppression magnetic field in a negative-ion accelerator, Rev. Sci. Instrum. **85** (2014) 02B317.
[2.5] AGOSTINETTI, P., et al., Detailed design optimization of the MITICA negative ion accelerator in view of the ITER NBI, Nucl. Fusion **56** (2016), 016015.
[2.6] SIMONIN, A., et al., R&D around a photoneutralizer-based NBI system (Siphore) in view of a DEMO Tokamak steady state fusion reactor, Nucl. Fusion **55** (2015) 123020.
[2.7] LASSINA, A., et al., "Feasibility Study of a NBI Photoneutralizer Based on Nonlinear Gating Laser Recirculation", Rev. Sci. Instrum. **87** (2016) 02B318.
[2.8] SONATO P., International School of Fusion Reactor Technology, 15th Course: “Plasma Heating and Current Drive for ITER Operation and DEMO Needs”, Erice (2015).
[2.9] OIKAWA, T., et al., Heating and non-inductive current drive by negative ion based NBI in JT-60U, Nucl. Fusion **40** (2000) 435.
[2.1] INTERNATIONAL ATOMIC ENERGY AGENCY, Fusion Physics. IAEA, Vienna (2012).
[2.2] KOJIMA, A., et al., Progress in long-pulse production of powerful negative ion beams for JT-60SA and ITER, Nucl. Fusion **55** (2015), 063006.
[2.3] TAKEIRI, Y, et al., High Performance of Neutral Beam Injectors for extension of LHD operational regime, Fusion Science and Technology **58** (2010), 482.

[2.4] HEINEMANN, B., Latest achievements of the negative ion beam test facility ELISE, Fus. Eng. Des. **136** (2018) 569-574.
[2.5] FANTZ, U., et al., Technology developments for a beam source of an NNBI system for DEMO, Fusion Eng. Des. **136** (2018) 340.
[2.6] ZACCARIA, P., et al., Design integration of SINGAP accelerator and RF Source in the ITER NB injector, 21st IEEE/NPSS Symposium on Fusion Engineering, Knoxville, Tennessee (2005).
[2.7] DE ESCH, H.P.L., Physics Design of the HNB Accelerator for ITER, Nucl. Fusion **55** (2015) 096001.
[2.8] CHITARIN, G., et al., Optimization of the electrostatic and magnetic field configuration in the MITICA accelerator, Fusion Eng. Des. **88** (2013) 507-511.
[2.9] SARTORI, E., et al., Comparative study of beam losses and heat loads reduction methods in MITICA beam source, Rev. Sci. Instrum. **85**, 02B308 (2014).
[2.10] VELTRI, P., et al., Compensation of Beamlet Deflections and Focusing Methods in the Electrostatic Accelerator of MITICA Neutral Beam Injector, IEEE Trans. on Plasma Science, **42**/4 (2014) 1047-1052.
[2.11] AGOSTINETTI, P., et al., Detailed design optimization of the MITICA negative ion accelerator in view of the ITER NBI, Nucl. Fusion **56** (2016), 016015.
[2.12] SIMONIN, A., et al., R&D around a photoneutralizer-based NBI system (Siphore) in view of a DEMO Tokamak steady state fusion reactor, Nucl. Fusion **55** (2015) 123020.
[2.13] FASSINA, A., et al., "Feasibility Study of a NBI Photoneutralizer Based on Nonlinear Gating Laser Recirculation", Rev. Sci. Instrum. **87** (2016) 02B318.
[2.14] PILAN, N., et al., Study of high DC voltage breakdown between stainless steel electrodes separated by long vacuum gaps, Nucl. Fusion **60** (2020) 076010.
[2.15] SONATO P., International School of Fusion Reactor Technology, 15th Course: "Plasma Heating and Current Drive for ITER Operation and DEMO Needs", Erice (2015).
[2.16] SONATO, P., et al., Conceptual design of the DEMO neutral beam injectors: main developments and R&D achievements, Nucl. Fusion **57** (2017) 056026.
[2.17] TOIGO, V., et al., The PRIMA Test Facility: SPIDER and MITICA test-beds for ITER neutral beam injectors, New J. Phys. 19 (2017) 085004.
[2.18] SERIANNI, G., et al., First operation in SPIDER and the path to complete MITICA, Rev. Sci. Instrum. **91**, 023510 (2020).
[2.19] OIKAWA, T., et al., Heating and non-inductive current drive by negative ion based NBI in JT-60U, Nucl. Fusion **40** (2000) 435.
[2.20] CARTER, R., Radio-frequency power generation, 2013, https://arxiv.org/pdf/1303.1355
[2.21] BONOLI, P. T., et al. Wave-Particle Studies in the Ion Cyclotron and Lower Hybrid Ranges of Frequencies in Alcator C-Mod. FST **51** (2007) 401–436.
[2.22] WUKITCH, S. J., et al. Characterization and performance of a field aligned ion cyclotron range of frequency antenna in Alcator C-Mod. Physics of Plasmas **20** (2013) 056117-056117- 8.
[2.23] GRAHAM, M., et al. Plasma Phys. Control. Fusion **54** (2012) 074011.
[2.24] BONOLI, P., Phys. Plasmas **21** (2014) 061508.
[2.25] TENENBAUM, P., A brief introduction to RF power sources (2003), www.desy.de/~njwalker/uspas/coursemat/notes/power_sources.pdf
[2.26] EKHEDAHL A., et al., Validation of the ITER-relevant passive-active-multijunction LHCD launcher on long pulses in Tore Supra, Nuclear Fusion **50** 11 (2010).
[2.27] KOERT, P., et al., Waveguide Splitter for Lower Hybrid Current Drive, Fusion Science and Technology **56** 1 (2009) 109–113.

Chapter 3

PLASMA DIAGNOSTICS

A. J. H. Donné
EUROfusion
Germany
Dutch Institute for Fundamental Energy Research
The Netherlands
Eindhoven University of Technology
The Netherlands

Magnetic confinement fusion has evolved from a discipline with many small-scale devices to one in which the main research is done on a limited number of large machines. Although present knowledge is sufficient to build ITER — the next step machine, many plasma phenomena are still not well understood. For instance, a basic understanding of the anomalous losses of energy and particles from the plasma is still lacking. Even relatively simple phenomena like the crash of the sawtooth instability (discovered in 1973) have not been fully explained. This lack of understanding of detailed processes has not hindered plasma physicists from finding operational regimes in which the overall confinement is improved. For proper operation of the tokamak in these regimes, the active and simultaneous control of many plasma parameters is needed. This implies that new robust and failsafe diagnostic techniques need to be developed, for instance to control the temperature, density and current density profiles. Progress in plasma diagnostics is on the one hand dictated by the desire to understand the detailed physical processes occurring in the plasma and on the other hand by the wish to actively control many important plasma parameters. An additional driver for diagnostic innovation comes from the requirement for better machine protection systems.

To obtain a better insight in the processes taking place in the plasma it is a prerequisite that as many plasma parameters as possible be diagnosed simultaneously; preferably with temporal and spatial resolutions smaller than the typical time and length scales of the instabilities. Because many of the instabilities are very localised, there is a need for multi-channel diagnostics in order to view all relevant details. The constraints that are imposed upon the diagnostics are quite severe. Temperatures in magnetic confinement devices may range from several eV in the scrape-off layer and divertor plasma to tens of keV in the plasma core. The density range covers many orders of magnitude from 10^{17} to 10^{22} m^{-3}. Diagnostic systems should therefore preferably have a large dynamic range, especially because access to the plasma is usually strongly limited by a small number of available ports.

To measure basic discharge behaviour, it is sufficient to apply diagnostics with a rather coarse spatial and temporal resolution. However, if one is interested in transport processes and the underlying instabilities, the spatial resolution should be as good as possible, preferably in the order of a few millimetres. Temporal resolution should be in the order of a few μs to be able to follow even the fastest plasma processes. One should be aware though, that an improvement of spatial and/or temporal resolution is often connected to a deterioration of measuring accuracy (e.g. lower counting statistics or smaller signal–to–noise ratio).

Apart from the constraints on resolution, dynamic range and accuracy, there are other complications to consider when developing diagnostics. Because of the high temperatures and densities of present-day fusion plasmas, most diagnostic techniques that can be employed make no physical contact with the plasma (except for probes applied at the very edge of the plasma). Hence, the plasma is diagnosed by analyzing the emitted radiation and particles (passive diagnostics) or by probing the plasma with electromagnetic waves or particle beams (active diagnostics). Of course, none of these techniques should perturb the plasma. Especially in the larger fusion devices, it is important that the diagnostics be resilient to the hostile environment (e.g. high heat loads, neutron and gamma-radiation), which can lead to thermal and mechanical stresses and many radiation–induced effects. Moreover, they should be well screened from the high electromagnetic stray fields around these devices.

A schematic overview of existing diagnostic techniques is shown in Fig. 3.1. A frequency scale is generally used to describe diagnostic systems up to several hundreds of GHz. For frequencies above the few GHz a wavelength scale is more practical. It is used from a few centimeters to ~10 nm. For even shorter wavelengths an energy scale is preferred.

Plasma diagnostics may be categorized in various ways. In this chapter, a sub-division per underlying techniques is used: magnetics, spectroscopy (visible, ultra violet, X ray), mm and sub-mm diagnostics, laser-aided diagnostics, particle diagnostics, fusion product diagnostics, and finally, first wall and operational diagnostics.

Several textbooks and a special issue of Fusion Science and Technology have been published on plasma diagnostics. All of them largely focus on the underlying physical principles of diagnostics. This chapter focuses instead

on diagnostic technology without discussing the underlying principles in too much detail. Different techniques to measure radiation, emission and particles from the plasma and others which actively probe the plasma, will be described.

Because the field of diagnostics is very wide it is virtually impossible to cover all techniques in detail. For this the reader is referred to specific literature.

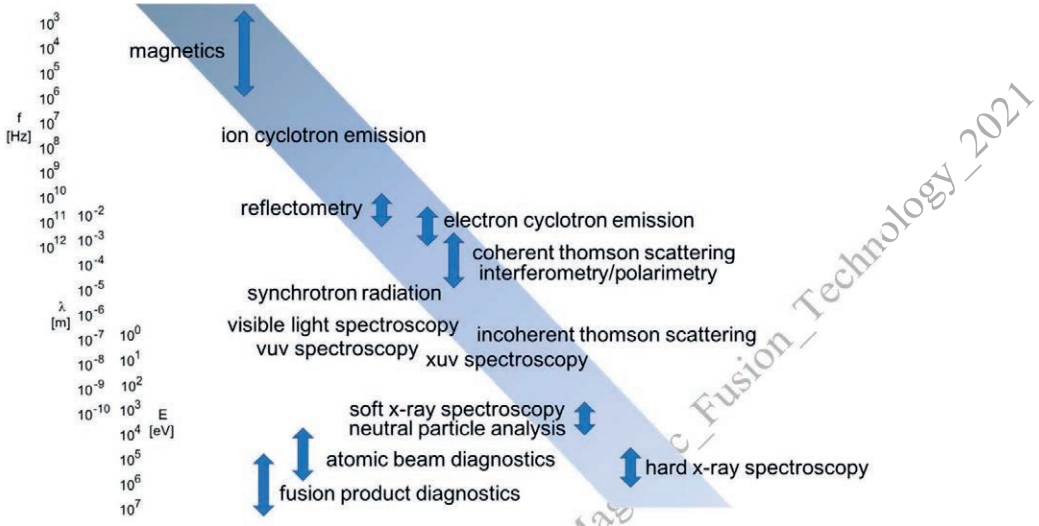

FIG. 3.1. Overview of existing plasma diagnostics on a frequency, wavelength, energy scale.

From Fig. 3.1 it is evident that passive techniques can almost cover the full range of frequency, wavelength and energy. However, many passive techniques only give limited localized information on the plasma. Moreover, the signal levels can often be quite low. Active probing of the plasma yields in most cases higher signal levels and/or more localized information. For active probing one most often uses microwave beams, lasers or (neutral or charged) particle beams. In general, one can deduce plasma parameters from the transmission or scattering characteristics of the beams. Reflection of microwave beams can also be used to diagnose the plasma. In many active diagnostics one observes the same type of particle that was injected into the plasma. In others, one observes a different type of particle (e.g. in some active spectroscopy diagnostics one observes light emitted by the plasma in response to an injected particle beam).

In discussing the various diagnostic implementations, this chapter will follow the order of Fig. 3.1 starting with magnetic diagnostics and moving down to the fusion product diagnostics. The only class of diagnostics that will come out of order is that of operational diagnostics. Operational diagnostics monitor the condition of plasma facing components and the plasma close to the wall. These will be presented near the end of the chapter.

3.1. MAGNETIC DIAGNOSTICS

3.1.1. Passive coils and loops

Magnetic diagnostics operate in the frequency range of 100 Hz up to several MHz. This is the frequency range of very common plasma processes such as magnetohydrodynamic (MHD) instabilities. Magnetic diagnostics are indispensable for the operation of magnetic confinement devices. They are used for measuring basic plasma parameters such as the plasma current, position, shape and pressure, and for detecting plasma instabilities. Magnetic diagnostics are passive diagnostics, making use of the electromagnetic waves emitted by the plasma.

The simplest magnetic diagnostic is the pick-up coil whose integrated voltage output is a measure for the magnetic field strength. Combinations of various pick-up coils are generally used to determine the plasma position and shape. The Rogowski coil is a solenoid wound around a poloidal cross section of the plasma in such a way that its integrated output voltage is proportional to the enclosed plasma current (see Fig. 3.2). Voltage loops are used to measure the loop voltage and yield the ohmic input power if the plasma current is known from a Rogowski coil. Diamagnetic loops are used to obtain the total energy contained in the plasma (i.e. plasma pressure).

Flux loops, saddle loops and diamagnetic loops are in general single-turn loops of a conducting material. The voltage difference between the terminals of the conducting loop is equal to the rate of change of the magnetic flux surrounded by the loop. The voltage of the loop is thus integrated to find the magnetic flux. Pick-up coils and Rogowski coils are in principle a series of many loops. Here again, the signal is integrated to measure quantities such as the plasma position and shape (for pick-up coils) and the plasma current (for a Rogowski coil). A challenge arises from trying to measure the fields in long duration steady state plasmas. In principle, the magnetic field is constant, hence no signal is induced in some of the loops. This can lead to drifts in the integrators. Therefore, much attention is presently devoted to the development of integrators with negligible drift, even in very long plasma discharges. In future fusion devices, which will be operated in a (quasi-) continuous mode, pick-up coils may not be employed anymore because of the limitations on the integrator. Therefore, alternative techniques, like strain gauges, Hall or nuclear magnetic resonance (NMR) probes, should be employed.

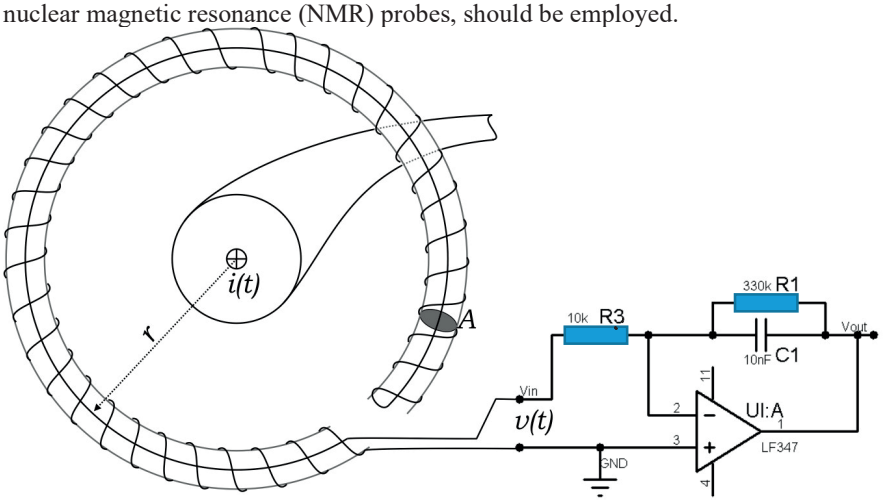

FIG. 3.2. Schematic diagram of a plasma current measurement using a Rogowski coil equipped with an integrator. Note that the return lead is running on the axis of the coil to avoid picking up spurious fluxes. (Source: Creative Commons).

The raw, unintegrated, signal of magnetic pick-up coils is often used to deduce high–frequency fluctuations (from hundreds of kHz to several MHz) in the magnetic field due to plasma instabilities. For this purpose, however, the pick-up coils need to be mounted inside the vacuum vessel and other conducting structures, since otherwise eddy currents in the wall will attenuate the high-frequency signal. The fast coils are often mounted into a ceramic holder, such that on the one hand they are protected from the hostile plasma environment and on the other hand they do not suffer from attenuation of high frequency signals due to eddy current in the surrounding structures.

3.1.2. Other passive methods to measure magnetic fields

To avoid the application of integrators for measuring steady state magnetic fields, research is also being done in the field of other sensors. One of those is the Hall probe (see Fig. 3.3). The Hall probe consists of semi-conductor material. When a current I is run through the material in the presence of a magnetic field $\boldsymbol{B}$, a charge carrier with charge q and drift velocity $\boldsymbol{v}$ will experience a transverse Lorentz force $q\,(\boldsymbol{v} \times \boldsymbol{B})$. This leads to a charge separation until $q\,(\boldsymbol{E} + \boldsymbol{v} \times \boldsymbol{B}) = 0$. The resulting potential difference between the sides of the probe (V) is linearly related to the current through the probe (I) and to the normal component of the magnetic field. Hall probes are thus ideally suited for the measurement of constant or steady state magnetic fields. A drawback is that the semiconductor material is vulnerable to the hostile fusion environment, often requiring active cooling to control its temperature. Moreover, since the measured voltages are rather small, one should be very careful not to pick-up any noise before signal amplification.

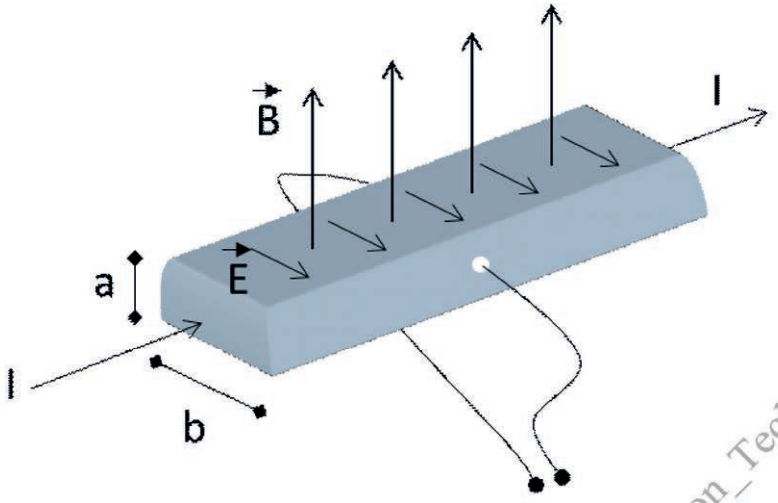

FIG. 3.3. Schematics of a Hall probe. When immersed in a magnetic field, a current injected through the semiconductor material results in a voltage difference between the two sides of the probe due to the charge separation induced by the Lorentz force.

Another method to measure a constant magnetic field is the strain gauge. It is in essence a small coil through which a known current is flowing. When positioned in a magnetic field, a measurable torque is exerted on the coil. Since the torque is proportional to the magnetic field strength, the measurement is basically converted into an electromechanical measurement of the torque. Strain gauges don't have the accuracy of Hall probes or magnetic coils, but may offer certain advantages in measuring magnetic fields in environments with a high level of nuclear radiation (e.g. in the future generation of fusion reactors). Although both Hall probes and strain gauges involve currents being run through the probe, they are still categorized as passive diagnostics since they do not depend on sending in radiation or particles into the plasma.

3.1.3. Active MHD spectroscopy

In general, passive magnetic diagnostics give a wealth of information about the plasma equilibrium and details can be obtained of many types of plasma instabilities. However, it is also possible to perform active measurements with magnetic diagnostics. Saddle coils (and other appropriate antennas) located inside the vacuum vessel can be externally driven by high frequency currents. When the coil current is swept through the frequency spectrum of the Alfvénic eigenmodes, these modes will be excited and can be observed by pick-up coils placed around the plasma. The damping rate of the eigenmodes is deduced from the phase response of the signal after the signal has been swept through the resonant frequencies. In principle, this also gives some information on the fast ions in the plasma.

A similar approach can be used at much lower frequencies to estimate how close the plasma may be of an external kink stability limit. This could form part of an active control system to avoid resistive wall modes that could occur when the plasma device is working close to its operational limits.

3.2. MICROWAVE AND FAR-INFRARED DIAGNOSTICS

3.2.1. Introduction

Microwave diagnostics (also referred to as millimetre and sub-millimetre diagnostics) operate in the frequency range from 1 GHz to 3 THz and includes a number of routinely used diagnostics such as reflectometry, electron cyclotron emission (ECE), electron cyclotron absorption (ECA) and interferometry/polarimetry. All diagnostics in this group are active techniques, apart from ECE that diagnoses the emission from the plasma. Interferometry/polarimetry is sometimes also classified as a laser-aided diagnostic.

Electron cyclotron emission is based on the cyclotron radiation emitted by the electrons during their gyration around the magnetic field lines. The frequency depends on the strength of the magnetic field and hence on the position in the plasma. In optically thick plasmas, the intensity of the radiation is proportional to the local electron temperature. For optically thin plasmas, reflections from the vessel and the presence of suprathermal electrons affect the signal,

which seriously complicates the interpretation of ECE measurements. In this regime, it can be more advantageous to use ECA. The absorption of the radiation is a function of electron temperature and density[8].

Reflectometry is based on the reflection of a wave, launched into the plasma, from a critical density layer where the wave frequency matches the cutoff frequency. The position of that layer can be deduced by measuring the phase shift of the probing wave with respect to a reference wave or, alternatively, by measuring the time–of–flight of a short microwave pulse to the cutoff layer and back.

Interferometry is based on the phase shift that a wave experiences upon passage through the plasma with respect to the vacuum case. By simultaneously measuring changes in the plane of polarization of the wave it is possible to extract information about the internal magnetic field and thus the current density in the plasma.

Collective Thomson scattering is a technique that can be employed to measure fluctuations in either the electron density or the velocity distribution of fast ions. Fig. 3.4 shows the various characteristic frequencies that play an important role in microwave diagnostics.

3.2.2. Electron Cyclotron Emission

In contemporary fusion plasmas, the frequency of ECE is a function of the magnetic field strength, which is typically in the range of 2 to 8 GHz. The corresponding radiation, at the first and higher harmonics of the ECE, is in the range of 50 to 500 GHz. In tokamaks, the ECE frequency is a monotonically decreasing function of the plasma radius. For optically thick plasmas, the radiation intensity is proportional to the electron temperature and one can retrieve the electron temperature profile by simultaneously measuring the intensity of ECE radiation as a function of frequency[9]. The plasma emission is both in the ordinary (O) and extraordinary (X) modes, each with a different emission spectrum. An ECE diagnostic should thus carefully select the proper polarization mode. This can be done by polarization sensitive antennas. There are basically three widely employed techniques to measure the ECE spectrum: Fourier transform spectrometers, grating polychromators and heterodyne radiometers.

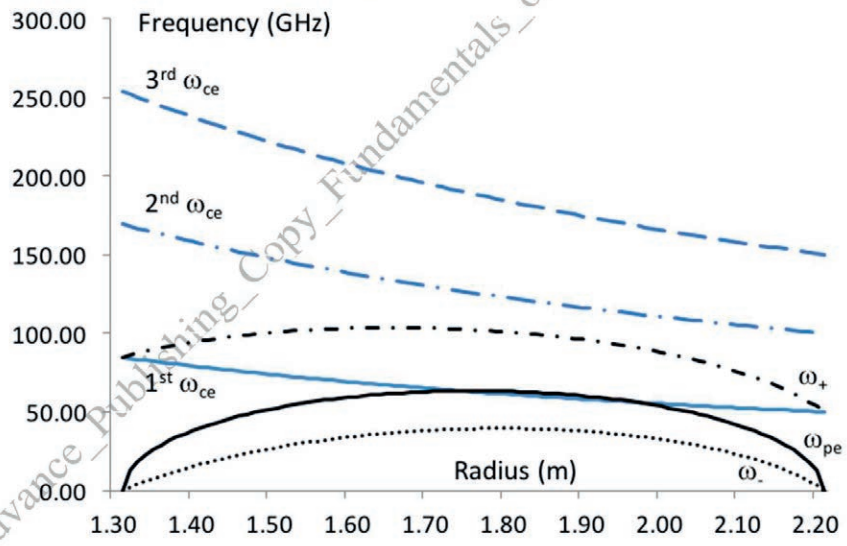

FIG. 3.4. Typical frequencies in a plasma with major radius R_0 = 1.75 m, B_0 = 2,25 T and a parabolic density profile $n_e(r) = 5 \cdot 10^{19}(1 - (r/a)^2)$ m^{-3}. From bottom-up, the monotonically decaying blue lines are the first, second and third cyclotron harmonic, respectively. The three black lines are the lower cut-off, plasma frequency and the upper cut-off, respectively.

3.2.2.1. Fourier transform spectrometer or Michelson interferometer

The Fourier transform spectrometer is a Michelson interferometer with a movable mirror. Light from the plasma is split into two beams by a semi-transparent mesh; one beam is reflected off a fixed mirror, while the other reflects off a movable mirror, which introduces a time delay (see Fig. 3.5). The beams are combined to interfere, such that the temporal coherence of the light can be measured at each different time delay setting. This effectively converts the time domain into a spatial coordinate. The spectrum is reconstructed by a Fourier transform of the temporal coherence of

[8] An independent measurement of the electron density should be used to disentangle the electron temperature.
[9] Depending on the specific plasma conditions this is usually done at the first or second harmonic.

the light. Michelson interferometers have a poor temporal resolution because of the time needed for a full scan of the movable mirror, which is usually in the range of several tens of ms. Their major advantage is that they can measure the full ECE spectrum from the lowest to the highest frequencies. Since all frequencies are measured at all times, the Michelson interferometer can be absolutely calibrated in a straightforward way by measuring the emission from known cold and hot sources (usually ceramic blocks cooled to liquid nitrogen temperature or heated to a few hundreds of degrees). As detector, a liquid-He cooled InSb detector is typically used because it features a low noise equivalent power.

3.2.2.2. Grating polychromator

Improved (μs) temporal resolution is possible with a grating polychromator. In such an instrument, a grating is employed to disperse the ECE radiation into a number of separate wavelength bands, each one associated to its own detector. The frequency band of the grating polychromator is usually limited but it can be tuned by tilting the grating or by selecting an adequate grating.

A grating polychromator is usually cross calibrated against an absolutely calibrated Michelson interferometer. Most grating polychromators are equipped with a set of liquid-He cooled InSb detectors. Grating polychromators are rather bulky because of the space needed for quasi-optical imaging onto the grating. During the last two decades, most of these systems have been replaced by a more compact generation of diagnostics: heterodyne radiometers.

3.2.2.3. Heterodyne radiometer

In a heterodyne radiometer, the signal from the plasma is down converted (in one or two steps) to an intermediate frequency (f_{IF}) that is more suited for subsequent amplification and signal handling. The down conversion is done by a mixer, which is a non-linear electrical circuit with two inputs and one output. One of the inputs is the radiation coming from the plasma *f*. The second input is coming from a local oscillator f_{LO}, which can be any type of microwave source like a Gunn oscillator, backward wave oscillator, etc. The mixer produces two new signals: one of them is the sum frequency of the incoming signals, which is usually filtered out, while the other is the difference frequency, often referred to as intermediate frequency f_{IF}. Most mixers have a specific 6 to 18 GHz wide pass band. A second down conversion step is often used to convert the signal to an even lower frequency (see Fig. 3.6). Heterodyne radiometers feature Schottky diodes as detectors. Advantages of heterodyne radiometers are high frequency and high sensitivity, yielding a high temporal resolution. A limitation of heterodyne systems is that the frequency coverage is usually limited to a waveguide band, which implies that multiple receivers are needed to cover the full spectrum of a specific harmonic. Heterodyne radiometers are usually cross calibrated versus a Michelson interferometer or by comparing them with other techniques such as Thomson scattering.

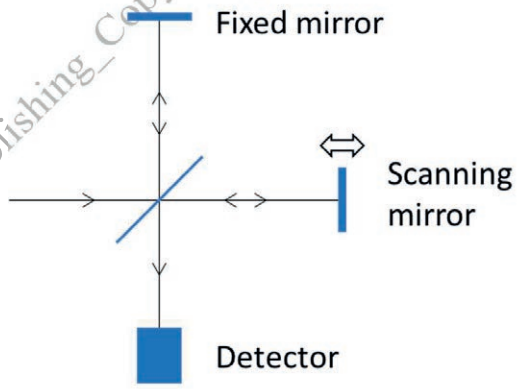

FIG. 3.5. Schematic diagram of a Michelson interferometer used to measure the full ECE spectrum.

3.2.2.4. Electron Cyclotron Emission Imaging

In the last decades, ECE imaging systems have been developed, in which a vertical chord in the plasma is imaged by an optical system on a microwave detection array. Every single element of the array acts as a heterodyne radiometer. ECE imaging systems therefore sample a two-dimensional plasma volume: the different array elements perform measurements at various heights in the plasma with respect to the midplane, while the heterodyne splitting of the signals into different frequency channels, yields different radial positions.

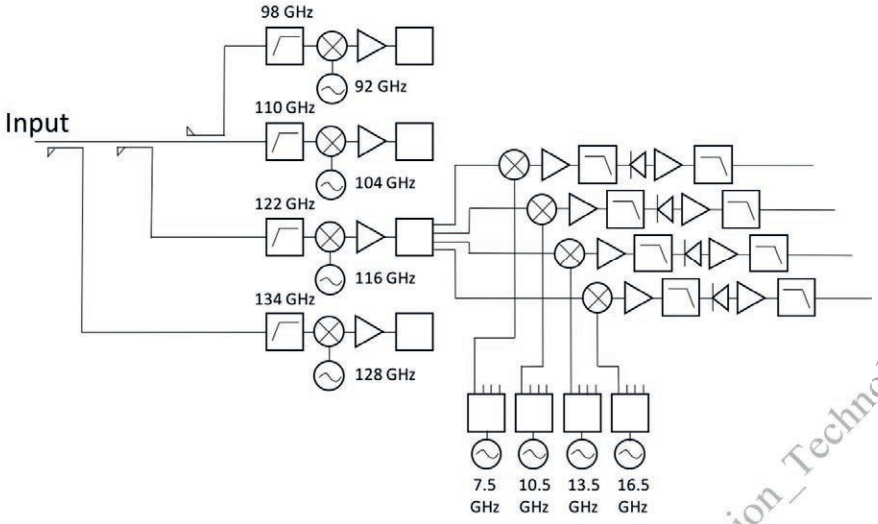

FIG. 3.6. Diagram of a 16-channel heterodyne radiometer (only four of the channels are completely drawn). The signal from the input is split into four wavelength bands, high-pass filtered and then mixed with a signal from a local oscillator (92, 104, 116, 128 GHz). The mixer has a pass-band of 6 to 18 GHz. The signal is subsequently amplified and split by a power divider. The signals are again down-converted by a LO with lower frequency. After a second amplification step and low-pass filtering, the signal is detected by a Schottky diode.

3.2.2.5. Electron Cyclotron Absorption

In optically thin plasmas, it is possible to diagnose the plasma with an active variant of ECE. In this set-up, microwave radiation (e.g. from a backward wave oscillator) is injected into the plasma by an antenna that is opposing the antenna of the ECE system, on the other side of the plasma. The measurement is based on determining the absorption of the microwaves at the various frequencies. From the absorption one can determine the plasma pressure profile. Electron cyclotron absorption can be only done in a rather narrow operational regime (in terms of plasma size and pressure), it is therefore not routinely used at contemporary fusion devices.

3.2.3. Interferometry and polarimetry

3.2.3.1. Interferometry

Interferometry is based on the phase shift that a wave experiences upon passage through the plasma with respect to the vacuum case. The frequency needs to be above the cutoff frequency and it is a trade-off between maximum phase shift and minimum disturbance by vibrations and refraction.

Interferometry is done in a rather wide wavelength range. If the plasma density, hence the refraction, is not too high, it is possible to use microwave sources (e.g. at a 2-mm wavelength). However, most interferometers at contemporary fusion devices are based on laser sources operating in the far-infrared. Popular sources are DCN lasers (at 337 μm), and CO_2-pumped far infrared lasers (at e.g. 432 μm). At these wavelengths, the phase shift experienced by the wave is still rather large and easy to measure. Vibrations have a relatively small effect and refraction is usually not too big a problem provided the local density gradients in the plasma are not too large. Sources of much shorter wavelength can also be employed, such as CO_2 lasers (~10 μm) and HeNe lasers (632.8 nm). In general, these systems only work with adequate vibration compensation, which usually implies two-colour operation.

The very first interferometers were homodyne set-ups (see Fig. 3.7, top). Their drawback is that in case of fast plasma density transients, one is not sure anymore in which direction the density changes (e.g. near the top of an interferometer fringe, a change in the signal could imply either an increase or a decrease of the density).

Nowadays nearly all interferometers are heterodyne. These systems have a second laser beam that is shifted by a frequency $\Delta\omega$ with respect to the probing beam (see Fig. 3.7, bottom). The frequency offset (or beat frequency) can be generated by either reflecting the reference beam of a rotating diffraction grating or by using two separate frequency-locked sources. The time resolution that can be obtained by a heterodyne interferometer is directly related to the beat frequency. Mechanical modulation by a rotating diffraction grating typically limits the beat frequency to

an approximate range of 20 to 100 kHz. By applying a CO_2-pumped far-infrared laser system with two slightly detuned cavities, one can easily generate frequencies in the MHz range.

In principle, various interferometer schemes can be used. Fig. 3.7 shows the Mach-Zehnder interferometer, most often employed for density measurements; alternatively the Michelson interferometer (see Fig. 3.5) can be used. Instead of a moving mirror, one then uses two fixed mirrors. The plasma is positioned in one of the two interferometer arms and is probed twice. A single interferometer chord only yields the density along one chord through the plasma. Many plasma devices are therefore equipped with several interferometer chords, to make it possible to retrieve the density profile by numerical Abel inversion techniques. In some set-ups, the laser beam is converted into a slab-like beam that passes through the plasma. This strongly reduces the required amount of individual optical components. After passage through the plasma, different parts of the beam are detected by different detectors. Typical detectors used for interferometers in the far-infrared range from very slow (but accurate) pyroelectric detectors to more advanced Schottky diodes, mounted in a corner cube geometry to tailor the antenna pattern and match the wavelength of the laser beam. A basic feature of any interferometer system is that the induced phase shift is seen by the detector as several interference fringes. Depending on the probing wavelength and the maximum density in the plasma this can range up to several hundreds of fringes. The drawback of fringe counting techniques is that one can make mistakes in counting the fringes, resulting in fringe jumps. This is often evidenced by the signal not returning to zero after plasma is terminated. To cope with this issue, various techniques have been developed, with varying degrees of success, including ultra-fast electronics and scanning interferometers.

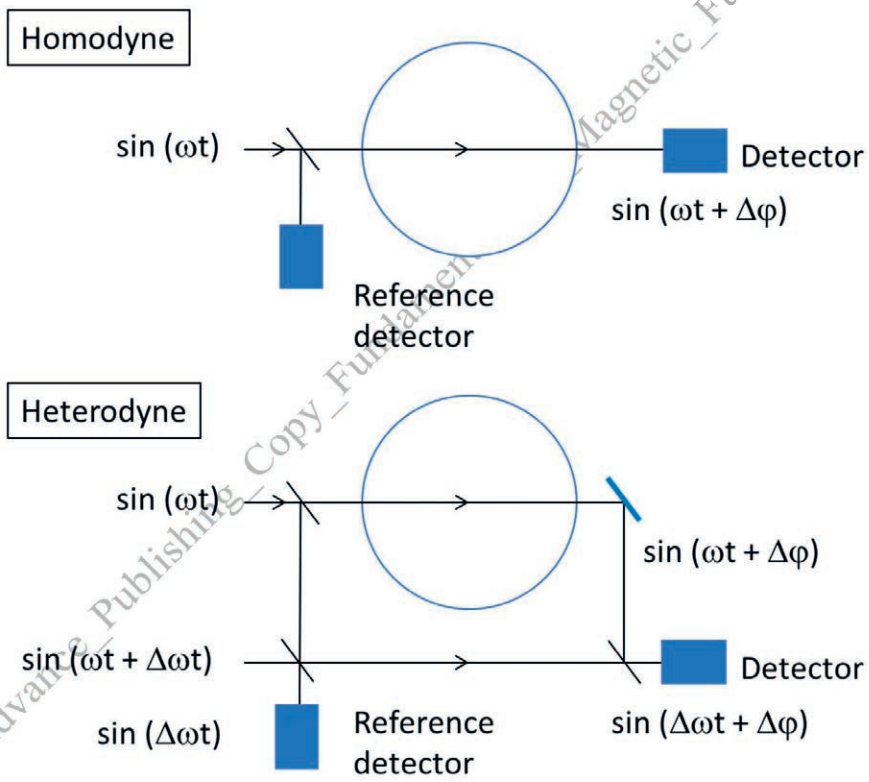

FIG. 3.7. In the homodyne Mach-Zehnder interferometer one measures straightforwardly the phase shift experienced by an electromagnetic wave passing the plasma. The drawback of this scheme is that in general, one doesn't know whether the density is going up or down. This is circumvented in the heterodyne set-up in which a second beam, frequency shifted with respect to the probing beam, is applied.

3.2.3.2. Polarimetry

An interferometry system can also be extended to measure the Faraday effect, which is the rotation of the plane of polarization of a linearly polarized beam due to its interaction with the parallel component (to the beam) of the magnetic field as it passes through the plasma. Since most interferometer set-ups are in the poloidal plane, the

polarimeter is measuring the poloidal magnetic field, which is related to the safety factor. A classical method to combine interferometry and polarimetry is depicted in Fig. 3.8, where a combination of half-wave plates and polarizing grids is used in conjunction with two detectors. The orientation of the grids is such that one detector is mainly sensitive to the part of the beam polarized in the orthogonal direction, whereas the other one measures a signal proportional to the phase shift experienced by the beam. Although the Faraday rotation angle is readily determined from the amplitude of the signal measured by the polarimeter, higher reliability can be achieved by measuring the phase difference between two detectors.

Many combined interferometer/polarimeter systems have been developed based on a modulation of the plane of polarization of the probing beam. Originally, the modulation was done by mechanical modulation of the probing beam (e.g. by a rotating half wave plate). This sets limitation on the maximum time resolution that can be obtained and makes the system sensitive to vibrations and jittering in the modulation system. A method that doesn't suffer from this drawback is depicted in Fig. 3.9. This system is based on a triple-beam far-infrared laser pumped by a single CO_2 laser. Two of the three beams probe the plasma in orthogonal polarization states; the third beam is the reference. Since far-infrared laser systems can be chosen with beat frequencies separated by about a few MHz, it is possible to achieve μs time resolution in both the interferometer as well as in the polarimeter signal.

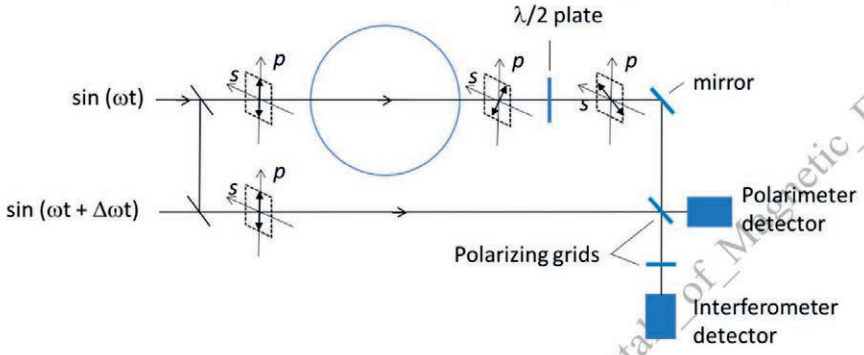

FIG. 3.8. Classical polarimeter set-up. A linear polarized beam not only undergoes a phase shift due to the plasma density, but also a rotation of its plane of polarization due to the Faraday effect. By an appropriate combination of half-wave plates and polarizing grids, the system can be designed such that one detector is sensitive to the polarization in the orthogonal direction, thus measuring the Faraday effect, while the other detector measures the phase shift.

Although the main function of most polarimeter systems is to measure the poloidal magnetic field (hence the safety factor in the plasma), some polarimeter systems are focused on the measurement of the electron density. In such systems, the plasma is probed in the tangential direction. The Faraday effect is determined by the line integral of the density times the component of the toroidal magnetic field parallel to the beam. Since the toroidal magnetic field is known to high precision, the density, in principle, unfolds straightforwardly from the measurement. An additional advantage is that the typical polarization rotation angles are always below 2p, which implies that fringe jumps (a plague of interferometer systems) cannot occur.

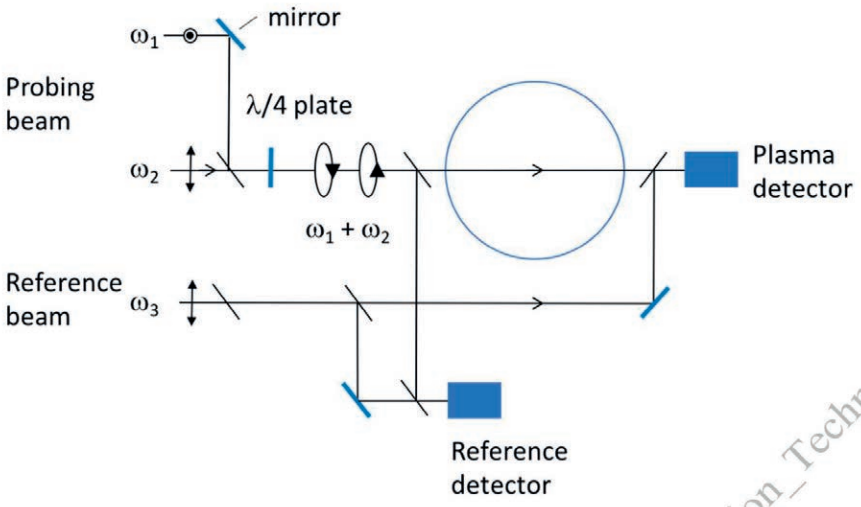

FIG. 3.9. In the triple-beam polarimeter set-up, two laser beams with angular frequencies ω_1 and ω_2 are transmitted through the plasma in orthogonal circular polarization states. Coalignment of the two beams can be achieved using a polarizer/quarter wave plate combination. A third laser beam at ω_3 acts as a local oscillator for heterodyne detection of the interferometric fringe shift.

3.2.4. Reflectometry

In reflectometry, a wave with frequency below the cutoff frequency is launched into the plasma such that the wave will be reflected from the so-called critical density layer. The phase shift of the reflected probing wave with respect to a reference wave yields information on the position of the critical density layer. Alternatively, it is possible to measure the time-of-flight of a short microwave pulse to the reflecting layer and back. Multiple-fixed or swept frequency systems can be employed to measure the electron density profile. Reflectometers can either probe in the ordinary mode (reflecting from the layer where the probing frequency equals ω_{pe}) or in the extra-ordinary mode (reflecting from either the ω_- or the ω_+ layer). The different frequencies are plotted in Fig. 3.4.

3.2.4.1. Profile measurements

A simple heterodyne reflectometer scheme is drawn in Fig. 3.10. The system features two oscillators that are kept at a constant frequency difference by a phase lock loop. The reference mixer yields a signal at the difference frequency $f_1 - f_2$; the plasma mixer gives a signal at frequency $f_1 + f_p - f_2$ which includes the phase information from the plasma. In principle, the scheme is rather similar to that of the heterodyne interferometer (see Fig. 3.7). In the first generation of reflectometers, the density profile was measured by heterodyne reflectometry systems featuring many different fixed frequency sources. To obtain the position of the reflection layer, the time delay Δt is extracted from the measured phase φ of the probing frequency f. Since the propagation speed in vacuum is known, the position of the reflection layer can be estimated.

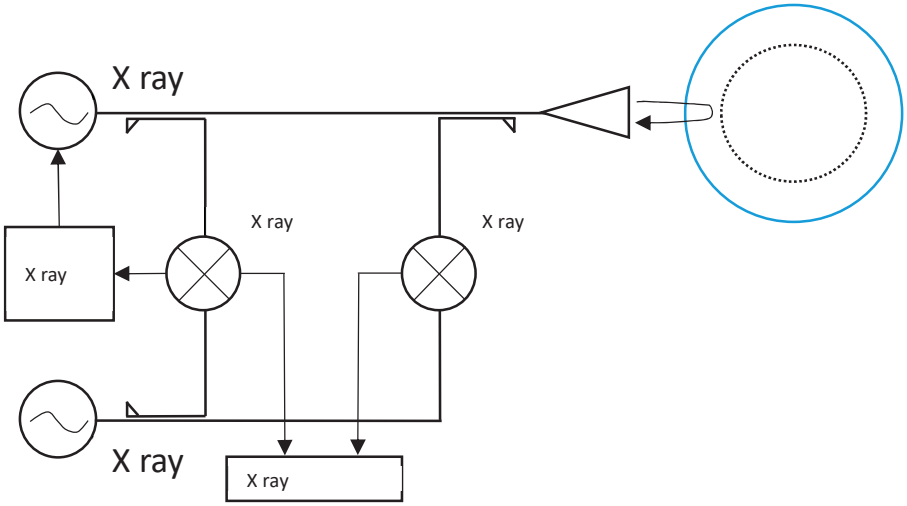

FIG. 3.10. Simplified diagram of a heterodyne reflectometer. Instead of a single monostatic antenna combining both launching and receiving of the waves in/from the plasma, a bistatic system is often used with two independent antennas.

Reflectometer systems measuring the phase change of the carrier frequency have the disadvantage that the absolute phase difference is not well determined. It is therefore imnot possible to measure the absolute position of the reflecting layer unless the phase signal is tracked from the beginning of the discharge. If during some time instant the signal reflected from the plasma is lost, which occurs frequently it is no longer possible to reconstruct the density profile. Many reflectometry schemes have been developed to measure the density profile more reliably.

In frequency modulation (FM) radar systems, the density profile is covered either by multi-frequency narrow-band sweeping or by single–frequency broadband sweeping. For FM reflectometry profile measurements, the sweep time of the generators should be less than the typical lifetime of plasma fluctuations, which is of the order of 10 to 20 μs. Today's techniques allow for sweep times of ~10 μs using hyperabrupt varactor tuned oscillators (HTO). In this case, the fluctuations can be considered as frozen during one sweep of the oscillator. The group delay is estimated either by a sliding fast Fourier transform (FFT) or wavelet analysis. Whereas the use of the sliding FFT washes out fast changes in the profile, it will be conserved by the wavelet method.

The phase ambiguity of reflectometers can be overcome if signals with long wavelengths can be forced to reflect from critical density layers where only short wavelengths would normally reflect. This is done in amplitude modulation (AM) reflectometry, where the amplitude of the probing wave is modulated with a typical frequency of ~100 MHz. By choosing an appropriate modulation frequency one can choose a phase change that never exceeds 2π, thus basically converting the signal into an absolute measurement. In contrast to conventional reflectometry one does not measure the phase delay of the wave, but the group delay. To cover the full density profile many sources of different frequencies are required.

One can also directly measure the time delay of a short (~1 ns) microwave pulse launched into the plasma. Such a pulse radar reflectometer provides a direct time measurement and can easily discriminate parasitic reflections (by selecting the time window of the pulse reflected at the plasma). It also allows for high-power single-frequency sources. One of the drawbacks, however, is that these systems are difficult to sweep, hence spatial sampling of the profile is limited to a few discrete channels.

Ultra-short pulse radars are based on the reflection of extremely short (~1 ps) pulses in the plasma. Because of their short duration, the pulses contain a frequency spectrum with a very wide bandwidth such that all frequencies needed to cover the whole density profile can be excited in a single pulse. Detection can be done with a broadband receiver in combination with a fast digitizer. Although there exist several other systems, like chirped radars and noise radars, which are relevant to present day fusion experiments, these will not be discussed here because of space limitations.

3.2.4.2. Fluctuation measurements

The previously discussed systems are focused on measuring the electron density profile. Reflectometry systems are also extremely sensitive to density fluctuations in the plasma that can modulate both the phase and amplitude of the reflected beam. Since the absolute density information is not of direct interest, the set-up for measuring fluctuations is based on a fixed probing frequency (rather than a swept, modulated, chirped or short-pulse source) with homodyne

detection. With heterodyne or homodyne quadrature techniques, it is possible to disentangle the phase and the amplitude fluctuations in the reflected beam. The interpretation of fluctuation measurements is not at all straightforward and it is tempting to treat density fluctuations around the cut-off layer as a moving corrugated mirror. Although this approach has been successful to interpret some experiments, it failed in others because the reflection is not perfectly localized at the cut-off layer and because density perturbations along the propagation path of the beams through the plasma might lead to additional scattering.

Correlation reflectometers measure the correlation length (and time) of fluctuations by two beams that reflect from nearby position; either different radial positions, by using collinear beams at nearby frequencies, or different poloidal or toroidal positions, by using different lines of sight at the same frequency.

In microwave imaging reflectometry (MIR) large-aperture optics is used to collect as much of the reflected wave front as possible. A two-dimensional part of the cut-off layer is imaged onto a two-dimensional array of detectors. The underlying idea is to restore the integrity of the phase measurement such that unambiguous phase measurements are possible. MIR is a rather novel approach that is still is in the demonstration phase.

3.2.4.3. Doppler reflectometry

A special type of reflectometer explores the fact that rotating corrugated structures at the plasma cut-off surface can lead to a Doppler shift in the reflected signal: the Doppler reflectometer. The cut-off layer is probed at an oblique angle with respect to the normal of the cut-off surface (see Fig. 3.11). The set-up is reminiscent to a moving diffraction grating that is actively probed under an oblique angle. The 0^{th} order reflection of the probing wave does not contain any Doppler shift, but the higher orders that are reflected at nonsymmetric angles are Doppler shifted. In principle, the fluctuation velocity can be determined in a rather straightforward way from the measurements. However, one needs to be careful since several diffraction orders related to different values of k_{perp} could be superimposed. Although this does not necessarily preclude the measurement of the fluctuation velocity, the observation could be severely hampered in case a strong reflection of the 0^{th} order reaches the receiver. Doppler reflectometers have been used to perform detailed measurements of the plasma flows (e.g. due to geodesic acoustic modes).

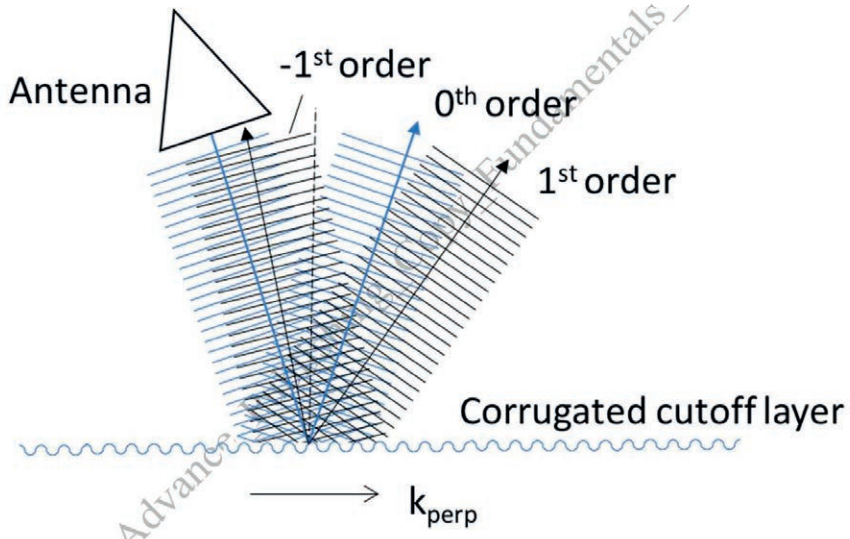

FIG. 3.11. Doppler reflectometry is based on observing the higher order reflections from a moving corrugated cut-off layer.

3.2.5. Microwave scattering

In electromagnetic wave scattering experiments one can distinguish several different regimes. In case the probing wavelength is smaller than the Debye wavelength, individual electrons are scattered off. This is called incoherent Thomson scattering and it is a very powerful technique to measure the local electron temperature and density in the plasma.

In case the probing wavelength is longer than the Debye wavelength the contributions from all individual electrons in the Debye sphere should in principle cancel, resulting in a zero net signal. However, in case the electrons exhibit a collective motion they still lead to a net signal that can be measured. The collective motion can be due to density fluctuations in the plasma where all electrons are driven by fluctuations of the same direction or by electrons

surrounding ions in their Debye sphere. When the ions move in the plasma they drag a wake in the electron population that can be measured. This type of scattering on either density fluctuations or ions is called collective or coherent scattering.

3.2.5.1. Collective scattering on plasma fluctuations

In density fluctuation measurements by collective scattering experiments, one essentially measures the intensity of a probing wave scattered over a certain angle. It is even better to scatter the beam over a set of different angles, since each angle corresponds to different wave vectors of the probed fluctuations. The scattered radiation can be detected either by homodyne or heterodyne methods, like in Fig. 3.7. With heterodyne detection, one can retrieve both the amplitude and the direction of propagation of the fluctuations.

By far, most of the collective scattering diagnostics are developed to measure plasma density fluctuations. However, with special provisions, it is also possible to measure other quantities such as fluctuations in the magnetic field. This is done by cross-polarization scattering, which relies on the fact that when a linearly polarized microwave beam is scattered off magnetic field fluctuations its polarization is changed into the orthogonal direction (O mode is changed into X mode and vice versa). In principle, a cross polarization scattering set-up is like a regular collective scattering set-up to which polarisers are added to analyse the proper polarization direction of the beam. Care should be taken to align the polarization of the beams with respect to the magnetic field at the edge of the plasma. Cross polarization scattering uses the presence of cut-off layers in the plasma to prevent unwanted signals from reaching the detector.

3.2.5.2. Ion Collective Thomson scattering.

Ion collective Thomson scattering is based on scattering off the electrons in the Debye cloud of ions. To reach the conditions in which this scattering would prevail, one can use sources in the millimetre wavelength range (e.g. gyrotrons) at moderate scattering angles or lasers in the far-infrared (e.g. CO_2 lasers) at far forward scattering angles. The most successful applications utilize gyrotrons as a source. The plasma conditions should be well chosen to avoid any of the electron cyclotron harmonics to lie in the plasma, as the injected radiation would be resonantly absorbed. One option is to use the window between the first and second cyclotron harmonic (see Fig. 3.4). For the plasma depicted in Fig. 3.4 this would imply a gyrotron frequency around 90 GHz. Another option would be to utilize a source in the far-infrared, far above the highest cyclotron harmonic (e.g. frequencies from 500 GHz to several THz).

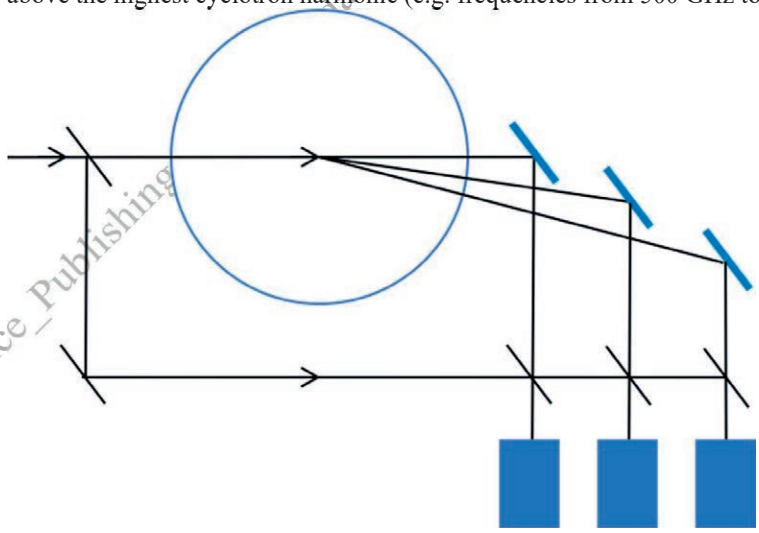

FIG. 3.12. Schematic depiction of a three-channel homodyne collective scattering system.

The scattered radiation is spectrally resolved to retrieve the information about the ions in the plasma. The difficulty is that the information on the ion distribution is not easy to separate from the main gyrotron frequency. The width of the scattering distribution is typically only a few GHz. This implies that care should be taken to optimize the frequency spectrum of the gyrotron source and additionally that very good narrow notch filters need to be employed to prevent any stray radiation (from the gyrotron) to enter the sensitive detectors. Ion collective Thomson scattering is also suited for diagnosing the fast ion population, including confined alpha particles. The fast ion distribution is

typically wider in wavelength than the bulk distribution. On the one hand, it can be better separated in frequency from the main gyrotron line, but on the other hand the scattered intensity is much lower than that for the bulk distribution, making ion collective Thomson scattering a very difficult measurement.

3.3. SPECTROSCOPY

In principle, spectroscopic diagnostics can be employed from very long to very short wavelengths (see Fig. 3.1). The full range runs from approximately 10 m (ion cyclotron emission spectroscopy) down to 10 pm (hard X ray spectroscopy). However, in practice, the working range of a spectroscopist is from approximately 10 nm to 10 μm (i.e. the range in which optical techniques can be employed). Apart from charge exchange recombination (CXRS) and beam emission (BES) spectroscopy, all spectroscopic diagnostics are passive.

Spectroscopy in the visible, vacuum ultraviolet (VUV), extreme ultraviolet (XUV or EUV) and soft X ray spectral regions can give a wealth of information on the atomic (ionic) processes in the plasma. The plasma emission in these spectral regions consists of continuum radiation (eg. Bremsstrahlung and recombination radiation) and line radiation. The intensity of the continuum radiation depends in a complicated way on the electron temperature and density, and on the impurity content. The impurity enhancement factor (related to Z_{eff}) may be obtained from measurements in line-free spectral regions, provided the electron temperature and density are measured by other diagnostics,. Measurements of line intensities, broadening and shifts can yield valuable information on ion densities[10], temperatures and plasma rotation. For many of these measurements a good spectral resolution is of prime importance. Around 10 μm one can observe synchrotron radiation, which is a fingerprint of the runaway electrons in a tokamak[11].

The aim of spectroscopy is to measure the emission from the plasma in a certain wavelength range, where the wavelength resolution needs to be adequate for the measurements. A common part to all spectrometers is the dispersion element, which could be a prism or a grating in the visible range and a crystal or a multilayer mirror in the XUV and soft X ray range. Because the spectrometers usually contain sensitive detectors that are vulnerable to the hostile environment nearby magnetic confinement device, conventional optical systems (made up of lenses and mirrors) and/or optical fibres are used to guide the light from the plasma to the spectrometer, often positioned at a remote location.

3.3.1. Visible and UV spectroscopy

3.3.1.1. Passive spectroscopy

In the visible and UV spectral ranges (*i.e.* $\lambda > 200$ nm), spectrometers (for plasma spectroscopy) usually feature plane gratings in combination with focusing mirrors and lenses. The grating consists of a substrate that is ruled with many grooves. The grooves can be equally spaced, but the more advanced gratings have variably spaced grooves to reduce aberrations and/or to produce a flat focal surface. The light from the plasma is diffracted by the groove structure into one or more spectral orders, according to the well-known grating equation:

$$m\lambda = d(\sin\alpha + \sin\beta), \tag{3.1}$$

where λ is the wavelength of the light, d is the groove spacing, m is the number of the spectral order, α and β the angles of incidence and diffraction with respect to the direction normal to the grating surface.

One of the most commonly used spectrometers is the Czerny-Turner spectrometer (Fig. 3.13) in which the light from the plasma is aimed at the entrance slit, which is placed at the effective focus of a curved mirror. The result is that the light from the entrance slit is collimated (focused at infinity), diffracted by the grating and then refocused by a second curved mirror on the exit slit. At the exit slit the light is dispersed. By rotating the grating one can scan the spectrum over the exit slit. The amount of light available for analysis depends on the width and height of the entrance slit, as well as on the acceptance angle of the optical system.

[10] Albeit after considerable modelling.
[11] Synchrotron radiation spectroscopy is only being applied in a small number of fusion devices.

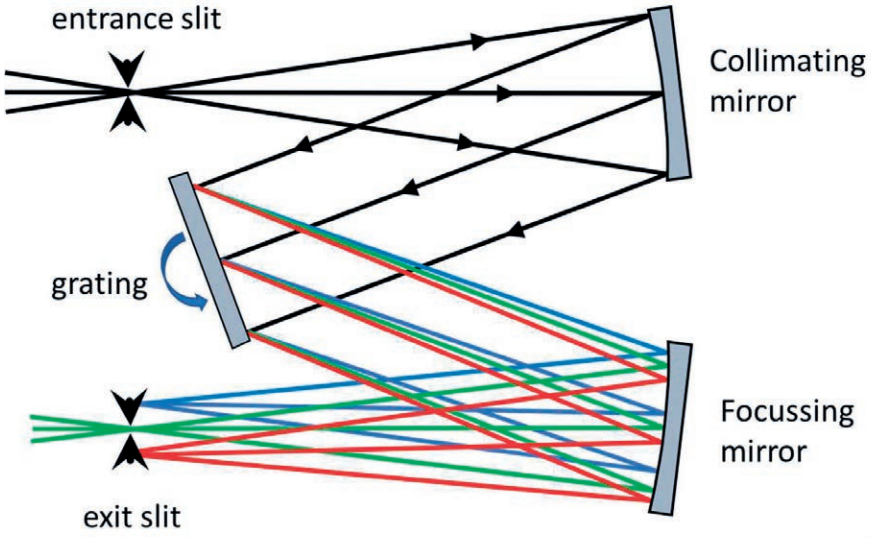

FIG. 3.13. Schematic diagram of a Czerny-Turner spectrometer.

Since scanning of the grating over the exit slit is a slow process, multi-element detectors such as charge-coupled devices (CCD) or photodiode arrays are usually employed. In case one-dimensional detectors are used, their pixels are usually oriented along the dispersion direction such that the detectors can record a part of the wavelength spectrum with high time resolution. Two-dimensional detectors can be employed to view simultaneously different chords through the plasma (i.e. the pixels in the direction perpendicular to the dispersion direction).

In principle, passive spectroscopy yields line–integrated signals through the plasma. However, the signal is strongly weighed towards the locations where most line radiation is emitted. In medium to large-sized plasmas this is typically at the plasma edge where the ions are not fully ionized. In the plasma core, temperatures are so high that most atoms are fully ionized; hence no line radiation is emitted. This is immediately evident by looking at the movies taken in the visible region of a plasma discharge where one can clearly see the H_α emission from the plasma edge but almost no emission from the plasma core.

Nowadays, novel compact visible spectrometers have been developed based on volume phase holographic gratings. These spectrometers have several advantages over Czerny–Turner spectrometers like high throughput, stigmatic imaging, high grating efficiency and compactness. The drawback is that the holographic gratings cover only a limited wavelength range. In case of routine measurements of a few specific spectral lines this is not a problem. However, if a wider spectral coverage is desired one either switches between multiple gratings or operates multiple spectrometers. Various other types of spectrometers have been developed for specific purposes like the electro–optically modulated solid-state (MOSS) spectrometer, a modulated Fourier transform spectrometer around a fixed delay. This system features high throughput and high time resolution. It is particularly suited to make fast 2D measurements of line widths and line shifts.

3.3.1.2. Beam-aided spectroscopy

Various active spectroscopy methods are based on observing the emission of light from the plasma after interaction with a beam of neutral atoms injected into the plasma. The light can originate from either the plasma particle or from the beam particle, which are left in an excited state after the interaction.

Charge exchange recombination spectroscopy is an active diagnostic and in principle a combination of a particle diagnostic and a spectroscopy system. In CXRS a powerful beam of neutral atoms is injected into the plasma; this can be either a neutral heating beam or a dedicated diagnostic neutral beam (see Fig. 3.14). The neutral beam atoms have charge exchange reactions with the fully stripped ions in the plasma, due to which they get partially ionized and may consequently radiate. Spectrometers (like those for passive spectroscopy) are used to observe this radiation from plasma ions. CXRS is a very powerful diagnostic that can yield information on the impurity ion temperature and density, plasma rotation and fast ions; even in the core of hot plasmas.

Beam emission spectroscopy is related to CXRS. The main difference is that BES observes the radiation from the neutral beam particles themselves, while CXRS observes the plasma ions. The neutral beam particles are mainly

excited by electron collisions. The intensity of the BES signal is proportional to the electron density, thus its variations yield detailed information on electron density fluctuations.

In a motional Stark effect (MSE) diagnostic one also observes the radiation from the beam particles. Neutral particles moving in a magnetic field experience an electric field, which is the sum of the Lorentz electric field $\boldsymbol{E}_b = \boldsymbol{v}_b \times \boldsymbol{B}$ and the radial electric field $\boldsymbol{E}_r$. The $(\boldsymbol{E}_r + \boldsymbol{v}_b \times \boldsymbol{B})$-force causes a Stark splitting of the line emission spectra. Since the electric field is generated by particles moving with velocity $\boldsymbol{v}_b$ through a magnetic field, the splitting is referred to as motional Stark effect. For hydrogen and deuterium, the effect is linear with the electric field resulting in a symmetric pattern of π and σ components with polarization parallel and perpendicular to the electric field, respectively. For Balmer-α light, the emission is split into 15 distinct lines with π and σ polarisation. In principle, the measurement of the polarisation of only one line already gives the magnetic field pitch angle, and is hence related to the current density and the safety factor q. Most MSE systems make use of the readily available neutral hydrogen or deuterium heating beams, with typically energies of 25 to 70 keV/amu. The large velocity of the beam atoms ensures that i) that the beam emission is sufficiently well separated from the plasma emission due to the Doppler shift; ii) that the Lorentz field is large enough to be measured and iii) that MSE dominates other effects like Zeeman splitting.

Spectrometers used in MSE systems usually focus on the emission of Stark splitted Balmer-α light. Several MSE systems are based on spectra-polarimetry: a measure of the Balmer-α spectrum from the beams fitted to the full spectrum from which the individual π and σ components can be deduced. Most systems however, are based on passing the beam emission through two crossed photo-elastic modulators (PEMs) that modulate the direction of polarization at two different frequencies. The PEMs are followed by a linear polarizer, transforming the polarization modulation into an intensity modulation. A narrow band interference filter selects the light from only one of the π or σ components, after which it is detected. The ratio of the detector signal at twice the modulating frequencies is then directly proportional to the magnetic pitch angle. Even though the polarization angles are small, accurate measurements are possible by utilizing lock-in techniques that separate the desires signal from the unpolarised background light. Moreover, only relative measurements are required making the diagnostic insensitive to beam fluctuations.

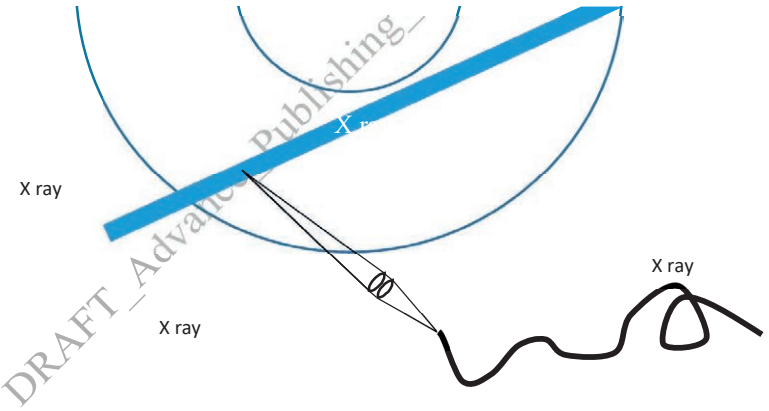

FIG. 3.14. Schematic diagram of an active beam spectroscopy system. The collection optics views the beam in a direction tangent to the plasma to achieve the highest possible spatial resolution.

3.3.1.3. Laser-aided spectroscopy

Very similar to passive spectroscopy, laser-aided diagnostics are applied in a very wide wavelength range. However, for wavelengths exceeding 100 μm the diagnostics are often referred to as far-infrared, microwave or sub-mm diagnostics. The short wavelength limit of laser-aided diagnostics is approximately 100 to 150 nm and is continuously shifting towards smaller values due to progress made in laser technology.

Incoherent Thomson scattering is being applied at nearly every confinement device. It is a powerful method to measure localized values (or profiles) of the electron temperature and density. It is based on measuring the wavelength broadening and intensity of radiation of a laser beam scattered by the plasma. The drawback of this technique is that it only yields snapshots, since its repetition rate is usually limited to a maximum of a few hundred Hz. Most often ruby or Nd:YAG lasers are applied for incoherent Thomson scattering.

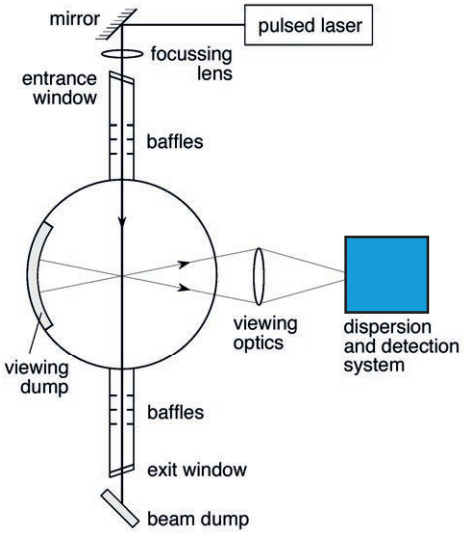

FIG. 3.15. Schematic diagram of a coherent Thomson scattering set-up. Straylight should be reduced as much as possible. Therefore, windows are mounted at the Brewster angle and are positioned far from the plasma, and baffles and a viewing dump are utilised.

In the instrumental set-up, much care needs to be taken to minimize laser light scattered from the windows. This can be done by placing the windows at the Brewster angle, far from the plasma and using a sequence of baffles (or diaphragms) to reduce the straylight cone (see Fig. 3.15).

In principle, the spectrometer set-up could be similar to that used in passive spectroscopy. However, in many cases, one makes use of purposely-made spectrometers often relying on the fact that the spectrum has a maxwellian shape. In principle, this implies that only a limited number of wavelength channels are needed. One of the simplest spectrometers is the filter polychromator (Fig. 3.16), in which a sequence of dichroic filters is used to select several individual wavelength channels. Nowadays most filter polychromators are equipped with avalanche photodiodes as detector. These are highly sensitive semiconductor devices that exploit the photoelectric effect to convert light into electricity. Each filter polychromator can be used to observe only one spatial point in the plasma. To measure profiles of the electron temperature and density along the laser chord one needs to utilize a range of separate filter polychromators (one for every spatial point).

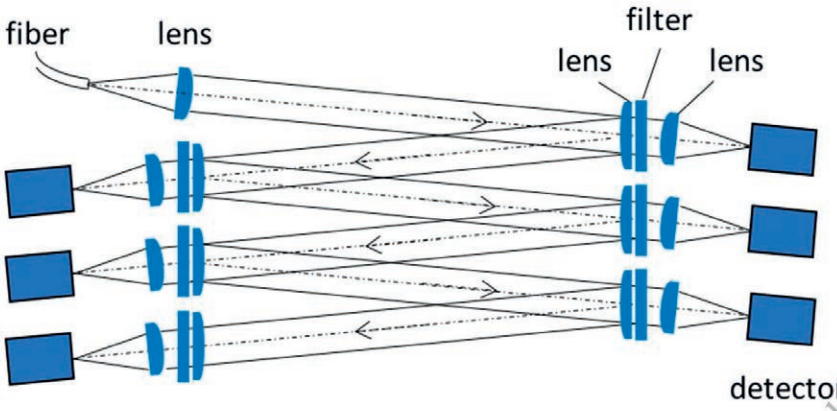

FIG. 3.16. In a filter polychromator a sequence of dichroic filters is used to select several wavelength bands. The light not selected by a specific filter is reflected towards the next filter. The filters are chosen such that the channels cover the wavelength distribution of scattered light. Moreover, light at the laser wavelength can be avoided.

Instead of using many individual filter polychromators one can also image the laser chord with a suitable spectrometer onto a charge coupled device (CCD) or a complementary metal–oxide–semiconductor (CMOS) camera. The advantage of 2D cameras is that they can simultaneously measure the full wavelength distribution along many points of the laser chord. Care should be taken that light at the laser wavelength does not impinge on the detectors. Most coherent or collective Thomson scattering systems used for measuring either the velocity distributions of fast ions or electron density fluctuations in the far-forward direction employ sources in the far-infrared or in the sub-mm wavelength range.

In laser-induced fluorescence (LIF), transitions are induced between excited states of certain ion species. Dye lasers are often employed to tune to the specific wavelength of the transition. The induced radiation yields information on the impurity ion densities in the plasma. In principle one could say that the spectrometer used in a LIF set-up is rather like that in a Thomson scattering system. Namely, one seeks to measure the radiation in a specific wavelength range. Whereas in Thomson scattering the wavelength range is in the direct vicinity of the laser wavelength and great care should be taken to reduce straylight, the presence of the laser is usually a problem of a lesser extent in LIF studies. Because one often wants to observe different excited species, a spectrometer with a relatively wide wavelength range is in many cases preferred. By measuring the fluorescence radiation at different positions (and times) one can determine the transport properties of the ions.

3.3.2. XUV and VUV spectroscopy

At wavelengths below 200 nm the reflectivity of most mirror coatings falls significantly below 90%, such that one needs to minimize the number of reflective elements in the diagnostic. Moreover, the transmission of air is strongly reduced at these wavelengths, which necessitates the use of vacuum spectrometers. Spectrometers with concave gratings are most commonly used in this wavelength region. In those, the gratings functions as both diffracting and focusing element. In the vacuum ultraviolet (VUV) region (30 to 200 nm), grating spectroscopy at near normal incidence can be employed, but in the extreme ultraviolet (EUV) region, grazing incidence spectrometers need to be employed because of the very low coating reflectivities at these wavelengths.

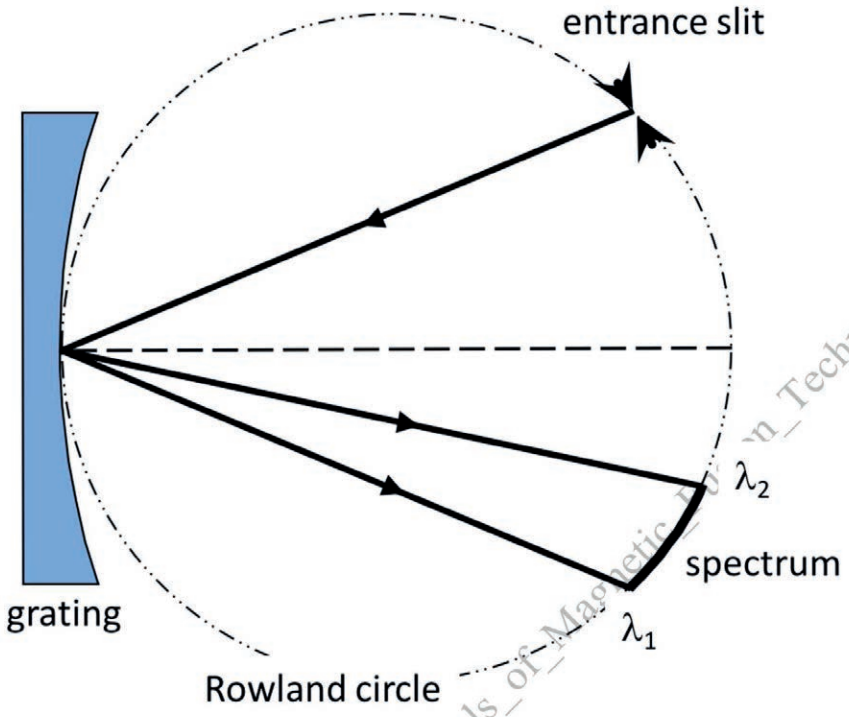

FIG. 3.17. Schematic diagram of a Rowland circle spectrometer. The entrance slit, the grating centre and the diffracted spectrum all lay on the Rowland circle. The diameter of the Rowland circle is equal to the tangential radius of curvature of the grating.

The basic concept of many spherical–concave grating spectrometers is that of the Rowland circle spectrograph (Fig. 3.17). In case the grating is tangent to a circle with diameter equal to the radius of curvature of the grating, light from a point source on the circle (such as the entrance slit) is dispersed and focused onto the circle (Fig. 3.17). For grazing incidence spectrometers, the astigmatism can be large, such that a point on the entrance slit is imaged into a curved line in a direction perpendicular to the dispersion. In the modern, more advanced, spectrometers this problem is tackled using toroidal gratings to compensate for the astigmatism. Non-constant groove spacing can also be used over the grating to correct for aberrations and produce a flat focal surface at the position of planar detectors.

Photodiode arrays and charge–coupled devices can usually not be applied in the VUV and XUV regions because of the bad transmission characteristics of their input windows. Image intensifiers consisting of a microchannel plate coupled to a phosphor screen are therefore often used to convert the input radiation to visible light, which can subsequently be detected by photodiodes or charge coupled devices (CCDs).

The survey, poor resolution, extended domain (SPRED) spectrometer is widely used to observe the EUV and VUV region. A toroidal grating is used to image the light of the entrance slit onto an array detector without astigmatism. By using a grating with curved grooves, a flat image can be produced and matched to the detector plane. Typical SPRED spectrometers observe a wavelength domain in which $l_{min} \cong l_{max}/10$ (e.g. from λ_{min} = 10 nm to λ_{max} = 100 nm; or from 17 to 170 nm). Very often, the spectrum at the smallest wavelengths (10 to 30 nm) is not well resolved because of the high density of $\Delta n = 0$ transitions from transition metals and $\Delta n > 0$ transitions from carbon and oxygen ions. Therefore, separate SPRED spectrometers are often used to specifically observe the EUV region.

Several other types of spectrometers can be used in the EUV/VUV region. Compact polychromators can be designed featuring plane gratings or transmission gratings in combination with input and output grid collimators. These instruments have a high light throughput and therefore a good temporal resolution, albeit at not too high a spectral resolution. For relatively simple spectra this is not a problem. For very simple spectra one can even consider using filtered detectors. In such a spectrometer, each channel is equipped with a filter with a different K absorption edge.[12] The first channel is sensitive to a single line, the second to two lines, and so on. From the combination of all

[12] The K absorption edge relates to the binding of the K shell electron of an atom. There is a sudden increase in the attenuation coefficient of photons occurring at a photon energy just above the binding energy of the K shell electrons of the atoms interacting with the photons. This is due to photoelectric absorption of the photons.

channels one can unfold the intensity of the individual lines with no need for detailed information on the spectral shapes of the lines. Filtered spectrometers can only be applied in relatively cold plasmas ($T_e < 500$ eV) where the high-energy continuum radiation from the plasma is negligible.

For many applications, a high time resolution is more important than a high spectral resolution (e.g. to observe the evolution of a specific, well-isolated, impurity line). A good approach here is to use a multi-layer mirror, which is a periodic structure of alternating layers each consisting of a high-Z reflecting layer and a low-Z spacer layer (see Fig. 3.18). The principle of a multilayer mirror, which can be made up of 50 to 100 layers, is that of Bragg reflection, where d is the thickness of a 2-component layer, m the order of refraction and θ the Bragg angle as measured from the surface:

$$m\lambda = 2d \sin\theta, \tag{3.2}$$

The typical bandpass depends on the flatness, thickness and uniformity of the layers. It is typically in the order of 0.3 to 1 nm, while peak reflectivities in the range of 30 to 70% can be achieved (with higher values for the longer wavelengths). Multilayer mirrors can typically be employed in the wavelength range of 5 to 20 nm.

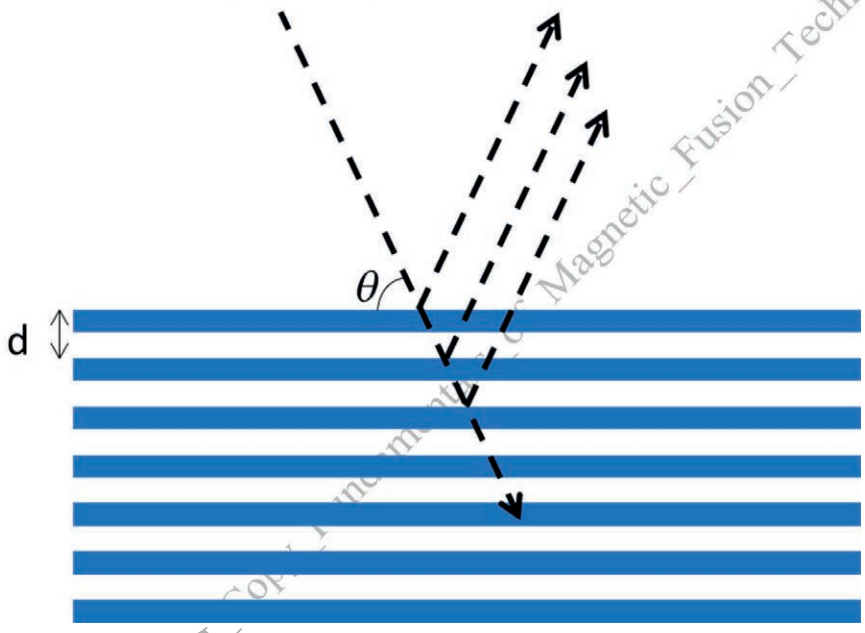

FIG. 3.18. Schematic diagram of a multilayer mirror. The path length difference of two rays reflecting from adjacent layers is $2d \sin\theta$. Constructive interference of the rays occurs when the path length difference equals an integer number of wavelengths.

3.3.3. Soft X ray spectroscopy

The soft X ray (SXR) region of the spectrum starts at energies of 1 keV (see Fig. 3.1). Basically, three types of SXR diagnostics can be distinguished: pulse-height analysis spectrometers to measure T_e and the concentrations of high-Z impurities; X ray crystal spectroscopy yielding high resolution spectra of impurity ions to retrieve ion temperatures from Doppler broadening and plasma rotation from the Doppler shift; and imaging systems using SXR detector arrays to measure the spatial distribution of the SXR emissivity. Multiple SXR imaging systems are often employed in a tomographic system for to measure the 2D evolution of mesoscale structures in the plasma, like MHD instabilities.

3.3.3.1. Pulse-height analysis

A pulse-height analyser features an energy resolving detector like Si(Li) diodes (lithium-drifted silicon) or high-purity germanium detectors (HPGe). The Si(Li) diodes can be used up to ~30 keV, whereas HPGe detectors can be employed up to 100 keV. Individual SXR photons from the plasma are absorbed in the semiconductor material while creating electron-hole pairs; the number of electron-hole pairs being proportional to the energy of the incoming photon. Electrons are collected by applying an electric field over the detector, which generates a voltage pulse whose pulse height is proportional to the energy of the original SXR photon. To obtain a satisfactory energy resolution, the

detectors usually need to be cryogenically cooled with liquid nitrogen. More recently, detectors that do not require cryogenic cooling (and can therefore be used in more compact systems) have been developed.

3.3.3.2. Soft X ray arrays and tomography

Free electrons have a continuum of energy states; therefore, free-free and free-bound transitions in the plasma give rise to a continuum in the radiation spectrum since they can have any wavelength. Recombination radiation can usually be neglected in the hot plasma core and therefore the continuum radiation depends on the Bremsstrahlung emissivity, which is a complicated function of the electron density n_e, temperature T_e and effective charge number Z_{eff}. Spatial and temporal variations or perturbations in the plasma (such as MHD modes) can change the profile and values of n_e and T_e locally and cause a significant change in the soft X ray emissivity. An ideal tool to study the evolution of these variations in detail is a soft X ray tomography system. Such a system is made of several independent cameras, each consisting of a soft X ray sensitive detector array (either silicon diode solid-state detectors or PIN photodiodes) viewing the plasma through a pinhole (see Fig. 3.19). The simplest tomography systems have two independent cameras but the more elaborate ones can have up to 20.

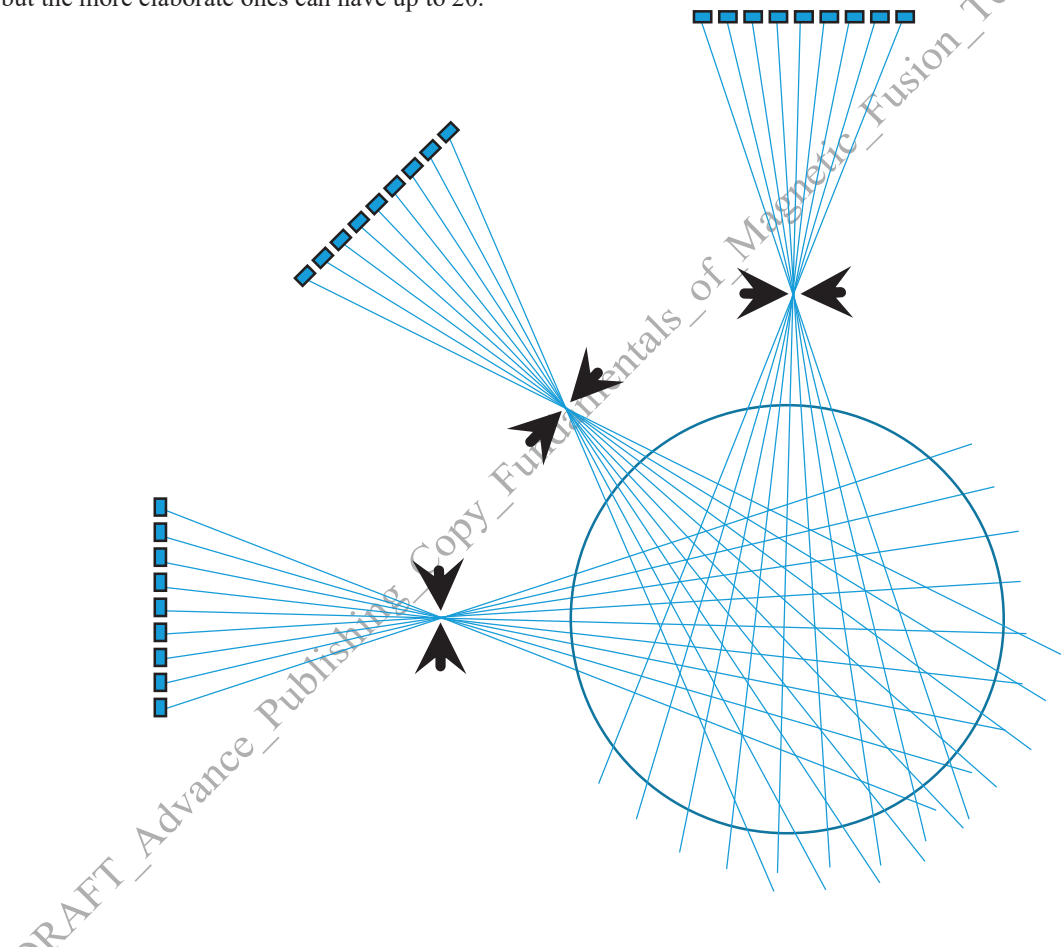

FIG. 3.19. Schematic diagram of a tomography system featuring three separate SXR pinhole cameras.

The multiple line-integrated soft X ray emissivity signals can be converted into local values of the soft X ray emissivity via tomographic reconstruction techniques. In the case of a single fan of viewing lines, the tomographic reconstruction is in principle analogous to an Abel inversion[13]. For a multiple camera tomography system elaborate reconstruction routines have been developed, with their specific advantages and drawbacks. These methods are described and compared in the suggested literature at the end of the chapter[14].

[13] Abel inversions are also used in case the plasma is observed along many parallel chords.
[14] See in particular the paper by Ingesson et al.

3.3.3.3. X ray crystal spectroscopy

X ray crystal spectroscopy is mostly used for measurements of the ion temperature and flow velocities in the plasma core, by deducing the Doppler width and shift of X ray lines emitted by highly charged ions of medium-Z elements such as argon, iron, krypton and tin. These elements may be present as indigenous impurities or added in small amounts. The origin of X ray radiation is related to an electron from the inner shell of an atom that is lost in an excitation process and subsequently replaced by an electron from the outer shell; the difference in energy is emitted as an X ray photon with characteristic wavelengths for each element. Analysis of the X ray emission spectrum provides qualitative results about elemental composition of the specimen and quantitative results on their temperature and velocities.

Many X ray crystal spectrometers are Johann spectrometers set up in the Rowland geometry (see Fig. 3.17) with a (curved) crystal instead of a grating. The angle of incidence of radiation onto the crystal and the spacing of the crystal are chosen to match the Bragg reflection condition (Eq. 3.2). To measure the Doppler widths and shifts in the wavelength range of 0.1 to 0.5 nm the spectrometers should have resolving powers $\lambda/\Delta\lambda$ of 5000 to 10000. This is often achieved by applying detectors with a high spatial resolution positioned relatively far from the crystal (typically multiwire proportional counters with spatial resolution of approximately 0.3 to 0.5 mm). In other words, the Rowland circle on which the curved crystal, the plasma observation region and the detector are positioned has a large radius – easily multiple meters.

Instead of multiwire proportional chambers, it is also possible to use a gas electron multiplier (GEM), which is another type of gaseous ionization detector. In gaseous ionization detectors, electrons released by ionizing radiation are collected and guided to a region with a large electric field. This result in an electron avalanche that will produce enough electrons to create a current that is large enough to be detected by the electronics. In multiwire proportional chambers, the large field comes from a set of thin wires with a positive high-voltage potential; these wires also collect the electrons from the avalanche and guide them towards the readout electronics. In GEMs, the large electric field is created in a set of small holes in a thin polymer sheet resulting in electron avalanches inside these holes. The ejected electrons are collected and guided towards the readout electronics.

Another novel type of detector is the medipix detector, which is based on a semi-conductor (silicon, GaAs or CdTe) sensor layer bonded to an electronics layer. Incoming radiation creates electron/hole pairs in the sensor layer. The charge of these is then collected by so-called bump bonds and processed by CMOS electronics. The electronics can measure the charge collected in individual pixels. Discriminators in the data acquisition system can be set to count event within a selected energy range, which enables full spectroscopic X ray imaging. Since the medipix detector can resolve the energy of the incoming X rays, it is in principle possible to directly observe the plasma without requiring an additional energy-dispersing element, like a crystal.

3.4. BOLOMETRY

Bolometers are used to measure the radiation losses from the plasma integrated over a wide wavelength range. Bolometers are also sensitive to particle losses. Wide-angle bolometers have been and are still applied at many confinement devices to yield a value for the total radiation losses from the plasma, which is important to understand the power balance. More recently, multiple bolometers equipped with collimators have been applied along different lines-of-sight in tomographic set-ups (see Fig. 3.19) to measure the radiated power profile.

There are two different types of bolometers. The resistance bolometer relies on the fact that the resistance of some materials is a well-defined function of temperature, which in turn is related to the power absorbed from the plasma. The resistance of the bolometer can be measured in a straightforward way by including it in a so-called Wheatstone bridge (see Fig. 3.20). To correct for temperature changes in the direct environment, one usually takes a reference measurement from a similar resistance that is not exposed to the plasma. In practice, highly compact integrated systems have been developed that are easy to implement in a multi sightline tomography set-up. Materials that are most commonly used for the resistor include gold and platinum. Under normal conditions gold is to be preferred. In fusion devices however, high neutron fluence can transmute gold into mercury, which sooner or later leads to bolometer malfunction.

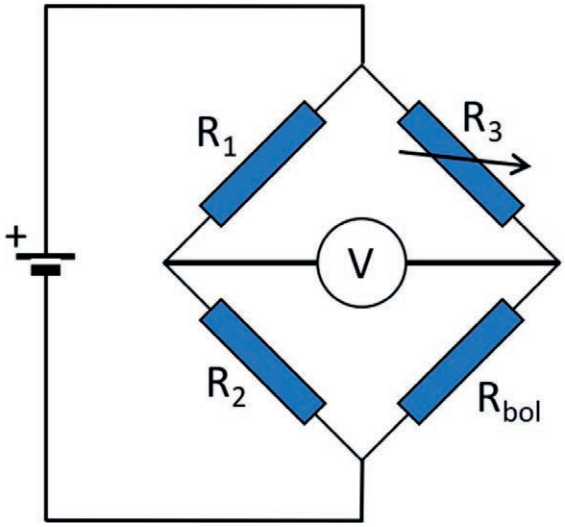

FIG. 3.20. Circuit diagram of a Wheatstone bridge. The bolometer resistance R_{bol} can be measured by changing the variable resistance R_3 such that no voltage is measured by the voltmeter. In that condition $R_2/R_1 = R_{bol}/R_3$, from which R_{bol} can be deduced.

The second type is the imaging bolometer. The principle is very simple: a thin radiation-absorbing gold foil is positioned behind a pinhole. Via the pinhole, each point on the foil is related to a unique line of sight through the plasma. The foil is instantaneously heated by the plasma. The heat pattern on the foil, which is related to the radiated power distribution in the plasma can be imaged by a 2D infrared camera. The geometry is such that the camera is positioned outside the plasma, observing the foil from the back.

3.5. PARTICLE DIAGNOSTICS

Particle diagnostics are employed in the energy range from 10 eV to 1 MeV. Neutral particle analysis (NPA) is a passive diagnostic. In the very low energy range (up to 0.5 keV) time-of-flight analyzers are often applied to measure the energy spectrum of neutral particles escaping from the plasma. This type of instrument is especially sensitive to atomic processes occurring at the edge of the plasma. At higher energies (1 to 10 keV) NPA is used to diagnose the temperature of hydrogenic ion species in the plasma core. Since the measurements are essentially line-averaged, extensive modelling is needed to obtain central values of the ion temperature. Higher–energy NPA is employed for studying fast ion populations. In large confinement devices, active techniques are used by seeding the plasma core with neutral atoms from a beam (i.e. active NPA). as otherwise the measurements of core plasma parameters would be difficult due to the background of particles that are emitted in copious amounts from the edge.

Rutherford scattering is based on the scattering of a well-collimated mono-energetic beam of neutral atoms in the plasma. The local ion temperature in the plasma can be determined from the width of the energy distribution of particles scattered over a certain angle.

CXRS, BES and MSE diagnostics are based on actively probing the plasma with a neutral beam. These systems have already been described in Sec. 3.4.2.2

Probing of the plasma with heavy–ion beams can be used to study the magnetic field and electric potential of the plasma, but it can also measure other plasma parameters. The particles injected into the plasma are usually singly charged ions of heavy isotopes like thallium, caesium or gold. Their injection energy needs to be in the range of 50 keV to several MeV to penetrate the core of the plasma. The magnetic field is determined by observing the deflection of the primary beam and a secondary beam, caused by further ionization of the injected ions. The plasma potential can be deduced from the change in energy in the secondary beam.

Beams of energetic neutral lithium atoms may be injected into the plasma to measure the magnetic field strength from the Zeeman splitting of its emission lines. The shift of the σ-component with respect to the unshifted π-component is proportional to the magnetic field strength. Injecting the beam of a dye laser, collinear with the lithium beam, and making use of the LIF effect may further increase the emission.

3.5.1. Neutral particle analysis

Most neutral particle analysers focus on measuring the ion temperature in the core of the plasma, which implies that the energy range of interest is of the same order as the ion temperature (typically 0.5 to 10 T_i). The basis of neutral particle analysis is to measure the energy spectrum of neutral particles escaping from the plasma. Although it is possible to measure the energy of neutral particles directly, in most analysers, the neutral atoms are first stripped of their electrons. This is done by letting the beam of neutral atoms pass through a stripping foil or a gas cell (stripping cell). Since most analysers are used to study hydrogenic species ^{1}H, ^{2}H (deuterium) or ^{3}H (tritium), the resulting ions are singly charged. Stripping cells are filled with gas of sufficiently high density to achieve adequate ionization of the particles while avoiding the spread of the beam by excessive scattering. Differential pumping between the stripping cell and the remainder of the analyser is in general necessary to keep the pressure in the beam line and in the analyser at tolerable levels. Stripping foils are usually ultrathin carbon foils (5 to 10 nm) that are mechanically supported by a high–transparency metallic mesh, or alternatively, free standing ultrathin diamond-like carbon films. As compared to stripping cells, stripping foils have the advantage of relaxing the vacuum pumping requirements while featuring larger acceptance solid angles. The drawback is that stripping efficiencies of foils are relatively low below 10 keV. Moreover, one needs to account for the fact that particles lose energy while passing the foil. The typical energy loss is $\Delta E \approx 4.4 \times 10^{-2} t\sqrt{E}$ (keV) for hydrogenic ions in the energy range of tens of keV, where t is the thickness of the foil in nm. After the particles are stripped, it is possible to measure their energy by deflecting them in an electrostatic field, which is generated by applying a voltage (V) across the deflection plates (see Fig. 3.21). In Fig. 3.6 the ions enter the analyser at an angle $\theta = 45°$ and follow a parabolic trajectory. The position of impact on the detector array (R), is a measure of the energy of the ion, where E is the ion energy after passage through the stripping cell and q the charge of the particle:

$$R = \frac{2\,E\,d\sin 2\theta}{q\,V}, \tag{3.3}$$

At the chosen angle $\theta = 45°$ one finds $dR/d\theta = 0$. This implies that particles with a small deflection from the ideal trajectory are focused in the detection plane.

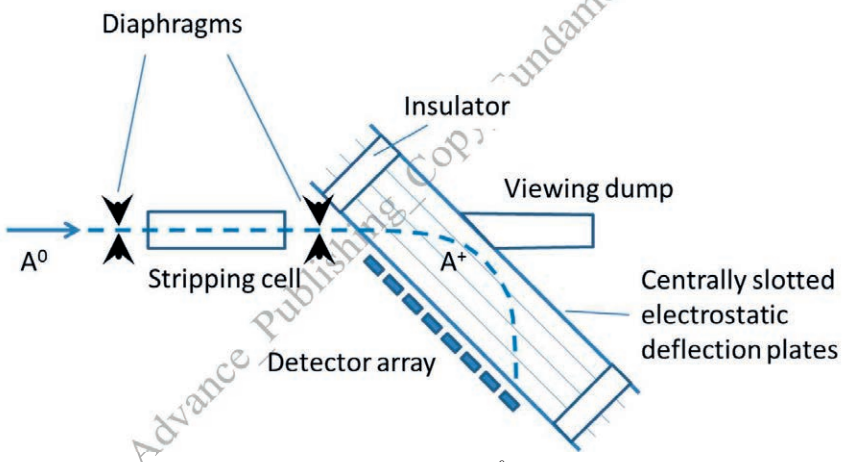

FIG. 3.21. Schematic diagram of a parallel plate electrostatic analyser. Neutral atoms A^0 enter from the left via diaphragm. They are stripped by a gas stripping cell and subsequently enter, via a second diaphragm, the electrostatic analyser made up of parallel, centrally slotted, electrostatic plates. The position where the charged ions impinge on the detector array depends on their energy.

Electrostatic analysers have been employed in a wide variety of geometries including cylindrical plate and parallel plate analysers. A limitation of the electrostatic analysers is the fact that it is not possible to distinguish different ion species, present in many contemporary plasmas. For this purpose, one can build an analyser with combined electrostatic and magnetic field (see Fig. 3.22). The charged ions are first deflected by a magnetic field with a radius of curvature dependent on the momentum of the deflected particles. In case the incoming beam contains multiple atom species, it is possible to distinguish between them by applying an electric field after the ions have left the bending magnet. The electrostatic deflection depends on the energy of the particles. Fig. 3.22 presents the basic concept of a tandem $E||B$ analyser. Some analysers are also equipped with a small accelerator section between the

stripping foil and the bending magnet. This makes it possible to shift the energy spectrum of the particles towards higher energies at which they can be detected more easily. The detectors that are used in the detector array can be either photomultipliers, channeltron detectors or channelplates.

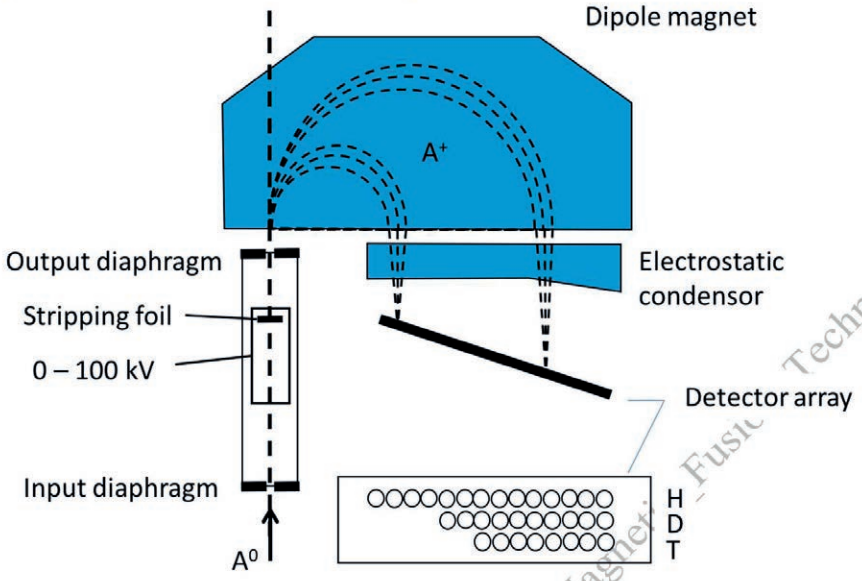

FIG. 3.22. Schematic diagram of the tandem $E||B$ analyser. Neutral atoms A^0 enter from the bottom via an input diaphragm. They are stripped by a foil and then accelerated over a voltage between 0 and 100 kV, towards the output diaphragm. Atoms that become charged by interactions in the stripping foil are first deflected by a dipole magnet, then by an electrostatic condenser. In this way, it is possible to measure both the energy and mass of the particles.

In the analyser depicted in Fig. 3.22 the magnetic and electrostatic fields are separate. It is however possible to superimpose the two fields to achieve the same effect. Measuring the energy spectrum of multiple ion species from the plasma is also possible by combining a magnetic field or an electrostatic analyser with a time-of-flight analyser. These systems make use of the fact that as a neutral or a charged particle passes through a stripping foil, secondary electrons are emitted from the foil in both forward and backward directions. One can detect these electrons, which gives a start signal for the time-of-flight measurements. The particle itself usually hits a detector at the end of the flight path, thereby generating the stop signal. An example of such a time-of-flight analyser is shown in Fig. 3.23. For simplicity, only the system detecting the secondary electrons in the forward direction is shown. Time-of-flight detectors work well if the particle flux is not too high, since it is necessary to distinguish individual particles. Typically, flight paths for particles in the range of several tens of keV are in the order of tens of centimetres. An advantage of the time-of-flight analyser is that it is based on a coincidence detection technique. Random signals, caused by neutrons or gammas for example, have therefore less impact on the measurements.

Time-of-flight techniques are also employed for detecting neutral particles with rather low energies (10 to 500 eV). These systems are based on a different time-of-flight principle. The beam of neutral atoms from the plasma is chopped into short μs long bunches by a fast rotating chopper. A detector placed 2 to 3 m behind the chopper measures the flight time spectrum of the particles within a bunch and from which the energy spectrum is derived. The system is only employed to diagnose neutral particles emerging from the very edge of the plasma where particle energies are generally low and the density of neutral atoms is high.

Passive neutral particle analysis (NPA) can still be employed at relatively small to medium-sized tokamaks provided the ions in the plasma core have a reasonable chance of becoming neutralized by charge exchange with neutral particles diffusing from the plasma edge into the core. For larger plasmas, passive NPA is not an option anymore because of the excessive attenuation of neutral particles in the plasma. Active NPA can there be employed based (in most cases) on a beam of neutral atoms injected into the plasma. The beam can be either one of the beams used for heating (see Chapter 2) or a dedicated diagnostic neutral beam. The beam helps enhancing the neutral atom population in the plasma core, and thereby the number of plasma ions neutralized via charge exchange reactions. It does not change the attenuation of neutral particles on their way from the plasma core towards the plasma edge, where they can escape. The latter effect imposes a natural limitation on how deep one can probe the plasma with neutral

particle analysers. Instead of a neutral beam it is also possible to use pellets as source of neutral particles for active NPA.

Although NPA originally served to measure the ion temperature of plasmas, many NPA diagnostics have been built to measure the energy spectrum of energetic ions that are due to neutral beam injection, radiofrequency heating, or fusion reactions. Some applications have two NPAs in series, where the first one measures the high-energy part of the spectrum (related to the fast ions that result from additional heating and/or fusion reactions), while the second is dedicated to the low-energy bulk ions.

3.5.2. Active beam scattering

A direct and straightforward technique to measure the local ion temperature in hot plasma is based on small angle (3 to 8°) Rutherford scattering of a beam of energetic neutral atoms (see Fig. 3.23). Due to the forward scattering geometry one needs to employ a very narrow pencil-like mono-energetic neutral beam to achieve a reasonable spatial resolution. Jitter in the beam energy should typically be less than 0.01%. Typical energies used in active beam scattering diagnostics lay between 10 and 50 keV.

Detection of the scattered neutral atoms can be done with a neutral particle analyser as described in the previous section. However, to get the highest possible counting rate, it is important to optimize the analyser to detect neutral atoms with energies around the energy of the diagnostic neutral beam. One way to achieve this is to preselect the relevant part of the energy spectrum with a magnetic analyser, such that neutral atoms with energies outside the relevant range will not contribute to the background signal. An ideal system to do that is the Penner 3-magnet system (see Fig. 3.23), which is an achromatic system: particles entering the achromat as a parallel beam will leave the achromat as such, irrespective of their energies. Selection of the energy window of interest is done in the middle of the central magnet where the dispersion plane is located.

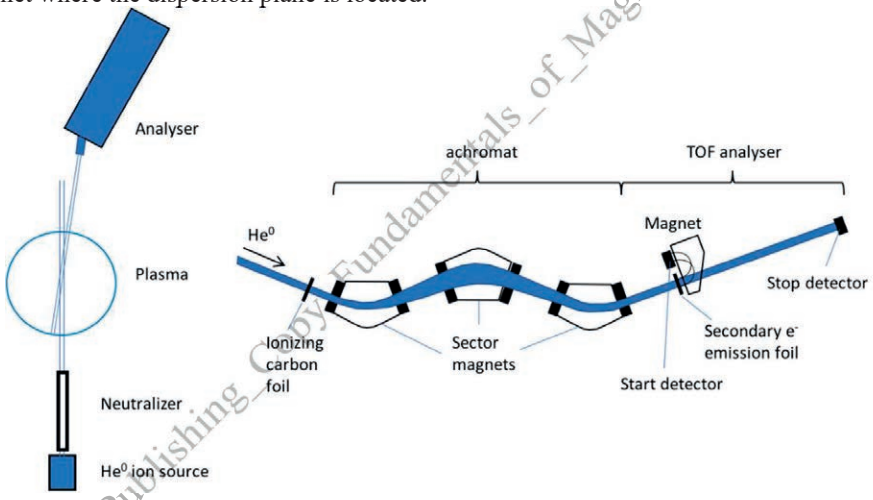

FIG. 3.23. Schematic layout of an active beam scattering experiment (left). A mono-energetic beam of neutral atoms is injected vertically from the bottom, into the plasma. The energy distribution of particles scattered over a small angle is measured by a neutral particle analyser. The scattering volume is determined by the intersection of the ion beam and the viewing cone of the analyser. Schematic layout of an analyser (right) consisting of an achromatic Penner-type 3-magnet system preselecting the energy range of interest and a time-of-flight analyser. The start signal is generated by collecting the secondary electrons that are emitted when the particles pass through a second carbon foil (collection of the electrons is done by a very small magnetic field that doesn't influence the beam ions). The stop signal is generated by the particle itself when it hits a detector.

As for NPA diagnostics, active beam scattering is limited to small and medium-sized plasmas where the incoming and scattered neutral atoms are not too strongly attenuated in the plasma. A special condition for active-beam scattering is that the beam needs to be injected (more or less) vertically into the plasma. Namely, when the beam is injected horizontally there will be an excessive background of particles that might reach the detector after having experienced several subsequent charge exchange reactions. In most modern fusion devices, a vertical orientation of the diagnostic is hard to achieve because of the presence of a divertor, located at the bottom and/or top of the vacuum chamber.

3.5.3. Heavy ion beam probe

Unlike NPA and active beam scattering (both based on diagnosing neutral particles), a heavy ion beam probe (HIBP) is based on the injection of (usually) singly charged heavy ions into the plasma. During their passage through the plasma some of the probing ions will undergo further ionizing collisions (colliding mainly with the plasma electrons). The energy difference between an ion emerging from the plasma compared to that of the original beam ion, along with the location and the angle under which the secondary ion leaves the plasma, yield information on the position of secondary ionization, the plasma potential and the poloidal magnetic field at that position. Meanwhile, the intensity of the beam of secondary particles is related to the electron temperature and density. These can be measured by simultaneously observing the double and triple-charged ions. For an HIBP to function it is important that the Larmor radius of the secondary ions be large compared to the plasma radius; otherwise the secondary particles cannot escape from the plasma, let alone be analysed. This condition can be written as:

$$ME_b/q_s^2 \geq a^2B^2/2, \tag{3.4}$$

where E_b is the initial beam energy in keV, a is the plasma radius in cm, B is the magnetic field in T, and M and q_s respectively the mass and charge of the secondary ions in atomic units. To satisfy this condition, highly energetic heavy probing ions are needed. Many HIBP set-ups feature beams of ^{133}Cs, ^{204}Tl or ^{201}Au as probing species. E_b is in the range of several tens of keVs for the smaller plasma devices, up to multiple MeVs, for the larger confinement machines.

As for active beam scattering, the energy spread in the beam should be small, typically below a few eVs. In case the HIBP system is used for fluctuation measurements this should be even better than 1 eV. The beam diameter should also be small (typical beam cross sections less than 1 cm^2) whereas the emission current density should be in the order of at least 2 to 3 mA.cm^{-2} to get high enough a signal. All these criteria are most easily achieved using a thermo-ionic source with zeolite-type emitters. These sources have a low energy spread and they are compact. They can be combined with an accelerating tube from a Van de Graaff electrostatic generator. The injector consists of an ion source, an acceleration and a focusing system, merged into a single unit. It is usually equipped with sweep plates to make it possible to scan the beam through the plasma. Many HIBP systems use an electrostatic analyzer as detector, like the one in Fig. 3.21. Sweep plates are also incorporated in most detection lines. These sweep plates, together with those in the injector make possible 2-D scans of the sample volume through the plasma.

3.6. FUSION PRODUCT DIAGNOSTICS

The field of particle diagnostics smoothly goes over and into that of fusion product diagnostics (see Fig. 3.1), which operate in the energy range from 500 keV to 14 MeV. Fusion products as tritium, protons, ^{3}He, neutrons and gammas are passively emitted by a burning plasma and their velocity distribution contains valuable information on the plasma parameters.

The neutron production rate and, hence, the neutron fluence gives a first order estimate of the ion temperature. When the neutron fluence profile, measured along a set of collimated chords, yields the neutron birth profile, from which the ion temperature profile can be derived. A problem in the interpretation of neutron measurements is the large neutron background generated by other processes. To partly overcome this, one may analyze the neutron energy spectrum. Time–of–flight analyzers with good energy resolution can be applied to measure the width of the neutron peaks around 2.45 and 14.1 MeV (arising from D-D and D-T reactions), hence providing information on the ion temperature.

Charged, highly-energetic fusion products like protons, tritium and α-particles may escape from the magnetic confinement and leave the plasma. When these escaping fast ions are detected at the plasma edge, it is possible to make a back-calculation along the trajectory of the particle to determine its birthplace.

3.6.1. Neutron diagnostics

3.6.1.1. Neutron counters

An important measurement is that of neutron emission rate as it relates to the total fusion yield. Because the neutron emission rate in a fusion device can change quickly over a large range of fluxes, detectors are needed with a fast response time and a wide dynamic range. Detectors often used for neutrons include BF_3 proportional counters, ^{3}He proportional counters and ^{235}U fission counters. These counters have a large dynamic range as they can be operated in either pulse-counting mode, for low neutron fluxes, or direct current mode, for higher fluxes. The BF_3 and ^{3}He proportional counters are based on the ^{10}B(n,α)^{7}Li and ^{3}He(n,p)^{3}T reactions, respectively. The principle is simple:

incoming neutrons undergo nuclear reactions with the background gas to produce charged particles. These particles, born with excess energies of 2.78 and 0.77 MeV respectively, ionize in turn the background gas leading to the creation of electron-ion pairs in the gas, which can be measured. Fission chambers are ionization chambers with electrodes coated with fissile material such as ^{235}U or ^{238}U (see Fig. 3.24). The gas in the chamber is ionized by fission fragments with kinetic energy in the range of 50 to 200 MeV. ^{235}U fission chambers are more sensitive to low–energy neutrons because their sensitivity is inversely proportional to the square root of the neutron energy. When equipped with moderators (used to slow down fast neutrons), they can also be employed to measure higher-energy neutrons. ^{238}U chambers have a reaction threshold of ~1 MeV and are therefore sensitive to fast neutrons only. Hard X ray and gamma-ray backgrounds can be eliminated in a relatively straightforward way by applying pulse-height discrimination techniques. One of the largest challenges in measuring the neutron emission rate resides in its absolute calibration. Two factors contribute to this:

- The fact that the neutrons emission profile is not a simple point source but a torus shaped source having a specific emission profile.
- The fact that the plasma is usually surrounded by many complicated structures such as the blankets, vacuum vessel, magnetic field coils, etc. These act as neutron absorbers and can influence and scatter the neutrons.

The calibration of neutron diagnostics is done by moving a calibrated point source through the tokamak vacuum vessel and carefully measuring the response of the detector as a function of the source's location. The calibration needs to be supported by a neutron transport code such as the Monte Carlo neutron particle (MCNP) transport code. For D-D operation of the fusion device (2.5 MeV specific neutron emission) calibration of the detectors is often done with a ^{252}Cf source. For D-T operation it is necessary to calibrate with a source of higher energy neutrons such as compact neutron generators. Since the neutron yields of ^{252}Cf sources and compact neutron generators are usually low, one can only calibrate the most sensitive detectors in pulse-counting mode. Activation detectors (see Sec. 3.7.2.2) are used for this purpose as they can integrate the signal over a relatively long time. Other less sensitive detectors then need to be cross-calibrated using the plasma as a neutron source.

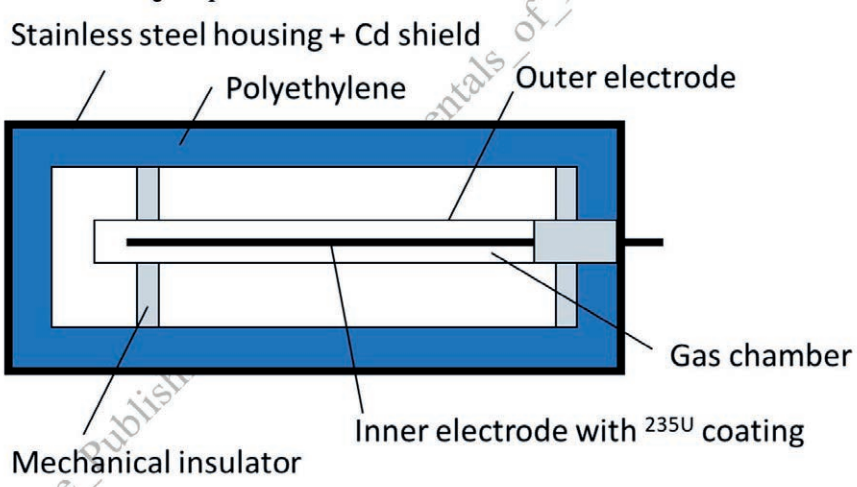

FIG. 3.24. Principle of a ^{235}U fission chamber. The polyethylene acts as moderator while a thin Cd layer surrounding the detector shields it against thermal neutrons. Fission products resulting from the impact of neutrons on the ^{235}U ionize the gas in the chamber, which is measurable because it induces a current between the inner and outer electrodes.

In future fusion devices like ITER the structure surrounding the plasma is expected to be too thick to adequately measure the neutron emission rate from a position outside the vacuum vessel. For this purpose, pencil-size microfission chambers are being developed that can be installed inside the vacuum vessel, at the end of a slit between two neighbouring blanket modules.

3.6.1.2. Activation systems

A neutron activation system can provide time-integrated measurements of the total neutron yield with a high degree of accuracy. In most activation systems foils of various materials are mounted in polyethylene capsules and brought via pneumatic transfer systems to an irradiation position close to the plasma. The neutrons induce nuclear

reactions in the solid samples resulting in an excited material that radioactively decays via gamma emission. Table 3.1 shows a few frequently used nuclear reactions, their threshold energy and the half-life of the resulting nucleus.

By simultaneously applying several material foils with different threshold energies (see Table 3.1) it is possible to distinguish the 14 MeV neutron flux from D-T reactions from the 2.5 MeV neutron flux arising from D-D reactions. In principle, one can then derive from the ratio of the two fluxes the tritium burn up ratio in D-D plasmas and the deuterium/tritium fuel ratio in D-T plasmas. Activation systems usually play an important role in the overall calibration strategy of neutron diagnostics. The relation between the neutron emission profile in the plasma and the neutron flux at the irradiation point needs to be carefully calibrated. In this calibration also, an MCNP transport calculation is indispensable.

After being exposed to the plasma for a sufficiently long time, the samples are transported by the pneumatic transfer system to a remote counting location, where germanium or NaI scintillation detectors measure the gamma rays from the activated samples. Instead of the materials listed in Table 3.1 it is also possible to use samples of fissile material such as ^{232}Th or ^{238}U. The fission products then result in delayed neutrons that can be detected by (e.g. ^{3}He or BF_3) proportional chambers.

TABLE 3.1. Nuclear reactions often used in activation measurements

Source	Nuclear Reaction	Threshold Energy (MeV)	Half-life
D-T neutrons	$^{27}Al(n,p)^{27}Mg$	2.6	9.458 min
	$^{28}Si(n,p)^{28}Al$	5.0	2.25 min
	$^{56}Fe(n,p)^{56}Mn$	4.5	2.577 h
	$^{63}Cu(n,2n)^{62}Cu$	10.9	9.74 min
	$^{93}Nb(n,2n)^{92m}Nb$	9.0	10.25 day
D-D neutrons	$^{58}Ni(n,p)^{58}Co$	1.0	70.82 day
	$^{64}Zn(n,p)^{64}Cu$	1.8	12.70 h
	$^{115}In(n,n')^{115m}In$	0.5	4.486 h

Flowing water activation measurements have also been proposed. These are based on the $^{16}O(n,p)^{16}N$ reaction in a continuous water flow. Because of the high threshold energy (10.24 MeV) this system is mainly suited for measuring unscattered 14 MeV neutrons. The counting station should be as close as possible to the plasma to still have a reasonable time resolution. The measurement is not real-time. It is done with a certain delay that depends on the average flow time from the irradiation location to the counting station.

3.6.1.3. Neutron cameras (neutron profile monitors)

Besides the total neutron yield (as measured by neutron counters and activation systems) it is also important to determine the neutron emission profile. Due to the presence of fast ions (e.g. from neutral heating beams and ion cyclotron resonance heating) the neutron emission profile is not a flux function and not completely isotropic. Neutron emission profile measurements by 2-D neutron cameras are therefore important to deduce the fast deuterium and tritium ion distributions and measure the neutron birth profile. It is also an important tool to distinguish neutrons generated in plasma-plasma from those generated in beam-plasma fusion reactions.

Neutron cameras measure the neutron emissivity along a fan of narrow chords covering the poloidal plane. Since the neutron emission profile is not isotropic, many fusion devices are equipped with at least two independent neutron cameras viewing the plasma from two different directions (in most cases horizontally and vertically). On the one hand, the detectors need to be placed as close as possible to the plasma to have the best poloidal coverage, but on the other hand the detectors need to be well screened against gamma radiation and low energy neutrons. The detectors of a neutron camera are typically mounted inside massive radiation shields and view the plasma via narrow collimation channels. Background neutron radiation (e.g. thermal neutrons) can be shielded with lithium-loaded paraffin (because of its high hydrogen content) without creating energetic gamma rays. However, since these shields do not strongly

reduce the gamma background radiation, boron–loaded concrete is often employed as additional shielding material. A single–channel detector of a neutron profile monitor is shown in Fig. 3.25.

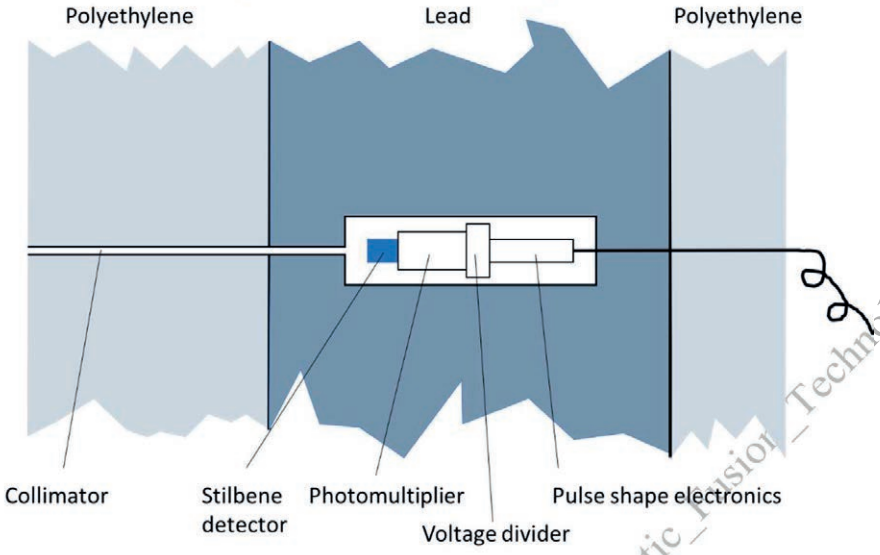

FIG. 3.25. Schematic depiction of a single sightline of a neutron profile monitor showing the detector viewing the plasma via a narrow collimation channel through lead and polyethylene shielding.

Organic scintillators (e.g. stilbene, NE213) can be employed as neutron detectors because they combine a well-known efficiency with a good time resolution. Such detectors are equipped with electronics to separate signals from neutrons from those of gammas. In determining the absolute calibration, it is important to take account of many effects such as: a) neutrons can be scattered in the collimation channels or even pass through substantial thicknesses of shielding material; b) neutrons can be collimated by one channel, but are then scattered into a neighbouring channel (neutron cross talk); c) neutrons can be scattered by the vessel wall, (viewed by a channel), which can scatter into the channel. Calibration can be improved by using a very strong neutron source combined with an MCNP transport code, as discussed before.

3.6.1.4. Neutron spectroscopy

The neutron energy distribution contains a wealth of relevant information on many plasma parameters including the ion temperature, the product of deuterium and tritium ion density, the reaction rate, the superthermal and slowing distributions, the fusion power, etc. Various spectrometers have been developed to measure the neutron energy spectrum. One of those is the time-of-flight spectrometer (see Fig. 3.26). The basic idea is to measure the time-of-flight of neutrons between two scintillators. The first scintillator is located behind a collimated neutron channel. A fraction of the neutrons undergoes collisions with protons p_H in the scintillator plastic, thereby giving rise to a recoil proton p_R and a scattered neutron n':

$$n + p_H \rightarrow p_R + n'. \quad (3.5)$$

The second scintillator is placed at a known distance L behind the first one and in turn detects a fraction of the n' neutrons scattered by the first scintillator via proton recoil. If the second scintillator is placed on a virtual sphere also going through the first scintillator, one can derive (from simple reaction kinematics) that the energy of the detected neutrons $E_n \propto 1/t_{TOF}$ is independent of the scattering angle α, where t_{TOF} is the time difference between the two detections.

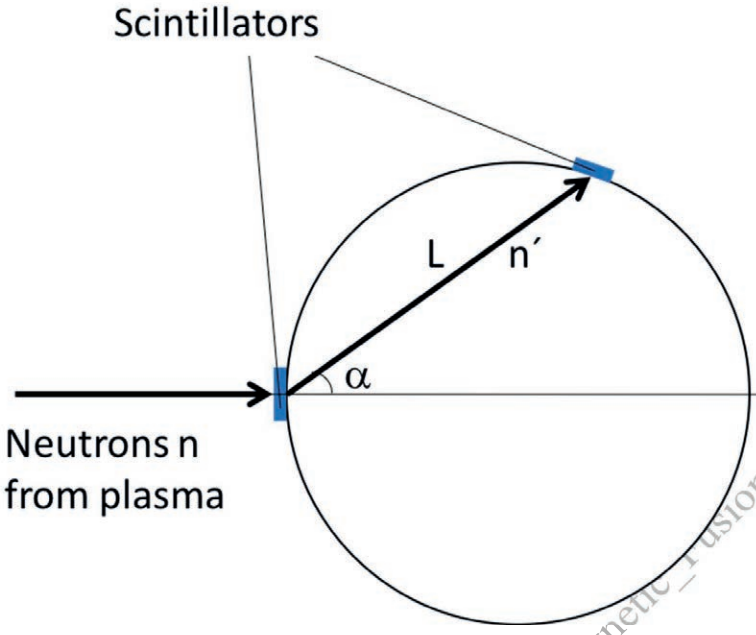

FIG. 3.26. Schematic diagram of a time-of-flight neutron spectrometer. Neutrons enter the spectrometer from the left through a collimator. The neutron energy is measured from the time-of-flight between the two scintillators. To increase the detection rate, the second scintillator is actually an annular shaped set of scintillators with the central axis of the annulus collinear to the incoming neutron beam.

In a second type of neutron spectrometer, one measures the energy of the recoil proton p_R produced in a thin target, which could be a thin sheet of polyethylene. In a magnetic proton recoil spectrometer (MPR) one detects the protons that are leaving the recoil foil in the exact forward direction, thereby guaranteeing that the energy of the recoil proton is like the energy of the neutron. The recoil protons are momentum analyzed in a magnetic spectrometer, which is rather similar in set-up to the magnetic part of the neutral particle analyzer depicted in Fig. 3.22. The magnetic field also separates the recoil protons from the neutron beam that continues straight on its trajectory. The magnetic field is configured such that protons with different energies are focused at different positions along the focal plane.

Both time–of–flight and MPR spectrometers are rather bulky. Therefore, more recently, there have been efforts to develop compact neutron spectrometers that are essentially based on a thick recoil target, measuring the deposited recoil energy via pulse height analysis. The material used for the target is typically a few centimetre thick slab of stilbene or NE213. Although in principle the neutron spectrum can be unfolded from the pulse height spectrum, a problem arises from the fact that neutrons with same energy can create recoil protons of different energy and scattering angle combinations. Using modern unfolding and analysis techniques combining pulse–height and pulse–shape analysis, it is nevertheless still possible to measure the neutron spectrum with high temporal resolution and an acceptable energy resolution. For the measurement of some plasma parameters (like the ion temperature) this might be adequate. However, for some other parameters the much better energy resolution of the time-of-flight and the MPR spectrometers might be preferred.

3.6.2. Gamma ray diagnostics

In a fusion device, fast ions reactions with plasma fuel ions or plasma impurities can lead to intense gamma radiation. There are many different kinds of such reactions, for example (p,γ), (p,p'γ), (p,α γ), (d,pγ), (d,nγ) (t, γ), etc. Analysis of the gamma-ray emission gives valuable insight into fast ion physics. The fast ions are either the result of fusion reactions or driven by neutral heating beams or ion cyclotron resonance heating. Unfortunately, a relatively continuous background of gamma-rays arising from the interaction of fusion neutrons with the structural materials surrounding the plasma is always present.

Since the gamma-ray emission is highly anisotropic, one usually employs 2D profile monitors that are rather similar in set-up to the neutron profile monitors described in Sec. 3.7.2.3. In some cases, the neutrons and gamma-rays are measured by the same system using pulse-shape discrimination techniques to separate the two types of

radiation. In some fusion machines the gamma-rays are measured by a separate system, which is still rather similar in set-up to the neutron profile monitor. As a detector, it is possible to employ amongst others NaI(Tl) crystals, NE226 or BGO scintillation detectors. Using multiple gamma-ray measurements along many individual chords, one can tomographically reconstruct the 2D gamma-ray emission. Since each kind of nuclear reaction in the plasma produces gamma-rays with specific energies, it is possible to simultaneously deduce the 2D distribution of different kinds of fast ions in the plasma.

3.6.3. Fast ion loss measurements

Ideally, fast ions such as heating ions and alpha particles should be well confined in the plasma until they have transferred their energy and slowed down. In practice, fast ions are often lost from the plasma due to various mechanisms: first orbit losses, toroidal field ripple losses, ICRH-induced losses and MHD-induced losses. Studying the properties of fast ion losses gives important clues on how to improve plasma confinement. Additionally, it is important to carefully monitor the fast ion losses as they can damage the wall of the reactor.

Fast ion loss detectors are positioned, by definition, close to the plasma facing wall (see Fig. 3.27). The most common approach is to have a small (cone–shaped) entrance slit combined with a 2D detector. A scintillator is often used for this purpose, viewed, either from the back or the front, by a CCD camera with high spatial resolution. The observed emission pattern from the scintillator gives direct information on the distribution of pitch angles and gyroradii of the fast ions. Some systems have an additional detector, like a photomultiplier, to integrate the total emission from the scintillator to have a measurement of the overall fast ion losses with high temporal resolution.

Another type of fast ion loss detector utilises nuclear activation foils. The subsequent gamma ray emission from the foil can be measured in a remote counting station. There are also proposals to measure gamma rays emitted from the backside of the foil in-situ. Due to the typical half life of the activation products these systems will measure the fast ion losses with a certain delay and not good a time resolution.

The third type of fast ion detector is the Faraday cup, which measures a current when a fast ion impinges on it. Although these systems could be geometrically similar in set-up to the scintillator based fast ion loss detector in Fig. 3.27, they are usually equipped with repeller grids to suppress secondary electron emission when the fast ions strike the cup surface. The most modern Faraday cups utilise sets of thin foils to reduce the sensitivity of the cups to neutron radiation. Since the Faraday cups are very compact it is easy to put together several individual slit-foil combinations in a single probe head.

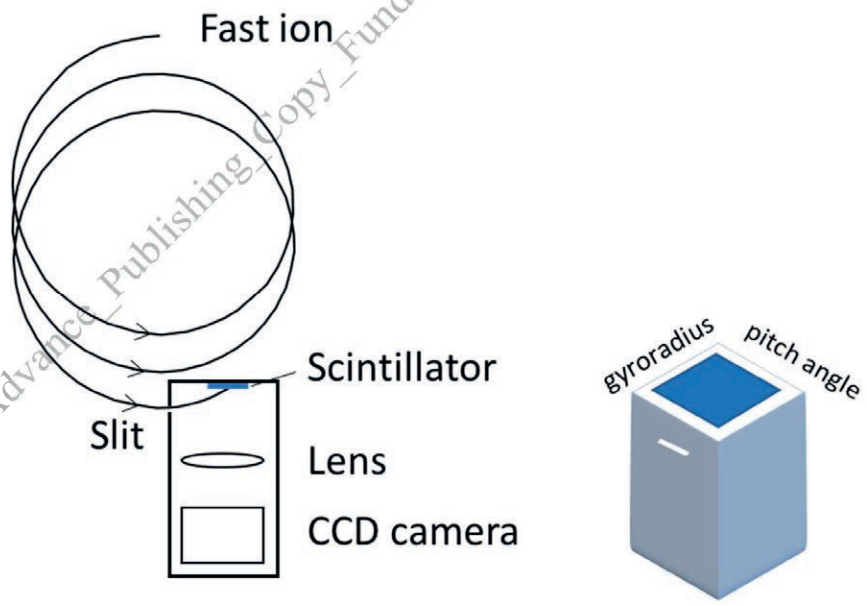

FIG. 3.27. Simplified scheme of a fast ion loss detector based on a scintillator. Fast ions on a loss trajectory enter the detector via a slit and impinge on a 2D scintillator detector. The scintillator is imaged by an optical system onto a CCD camera. From the position of impact of the fast ion on the scintillator its gyroradius and pitch angle can be deduced.

3.6.4. Confined fast ion measurements

One method to diagnose confined fast ions is by active spectroscopy. This is often referred to as fast ion D_α or FIDA spectroscopy (see Sec. 3.2.2.2). Another method to study fast ions is collective Thomson scattering (see Sec. 3.3.5.2). Here, electromagnetic radiation is scattered by the electrons in the Debye sphere of ions. Although CTS systems have been proposed in a wide wavelength range[15], applications featuring microwave gyrotrons have thus far obtained the most promising results. Indirect information on the fast ions can also be obtained from gamma-ray measurements (see Sec. 3.7.3) and neutron spectroscopy (Sec. 3.7.2.4).

3.7. FIRST WALL AND OPERATIONAL DIAGNOSTICS

Hitherto diagnostics for measuring the various plasma parameters have been presented following the order in Fig. 3.1, from low frequency to high energy. However, there are more than only plasma parameters to measure. In a fusion device, the conditions at or near the first wall, divertor and plasma facing components are also carefully monitored for machine protection. The diagnostics involved in these measurements are presented in the following. These include infrared, visible and UV measurements to monitor the plasma wall and extreme plasma edge, pressure gauges to measure total and partial pressures, residual gas analysers to detect air leaks, probes to measure plasma parameters in the scrape-off layer as well as active and passive methods to monitor the condition of the wall.

3.7.1. Infrared, visible and UV measurements of the plasma edge

3.7.1.1. Infrared cameras

Many fusion devices are equipped with infrared cameras to measure the surface temperature of plasma facing components to retrieve the heat flux deposited by the plasma and carefully monitor whether the local surface temperature does not become dangerously high. The set-up of an infra-red (IR) camera system is relatively simple, with a camera viewing the thermal emission from the plasma through a window and a limited number of optical components. For temperatures around room temperature, most signal levels are highest in the range of 8 to 12 μm. The more commonly available 3 to 5 μm detectors are well suited to monitor the higher temperatures near the divertor strike points and other areas on the plasma wall where higher temperatures can be expected; for example, near the shine-through areas of neutral beams, near limiters and protection tiles. Wavelengths below 3 μm are not useful for monitoring the wall during plasma discharges because there is generally a strong background of molecular lines from the plasma. Many optical materials have low transmission in the infrared region. Sapphire windows can be used up to 5 μm. For longer wavelengths in the range of 8 to 12 μm ZnSe windows are a good choice.

There are various choices for the infrared camera. The more traditional cameras are liquid-nitrogen cooled InSb or HgCdTe detectors that have a good sensitivity. More recently, room-temperature microbolometer arrays and quantum-well infrared photodetectors (QWIPs) have become available. The latter ones are the most sensitive, but also the most expensive. In choosing the camera one should decide between a relatively slow measurement covering the full plasma discharge or very fast measurements of transients in the plasma; for example, the heat deposition on the wall in response to an edge localized mode or a disruption. Microbolometers are in general better suited for slow measurements, which are usually done at 10 to 100 Hz, to measure time-averaged surface temperatures during the complete discharge with high spatial resolution. Digital and analogue video cameras can be used. The cameras generate a giant amount of data, generally requiring policies to decide if and how the data will be stored.

To determine the heat flux, it is necessary to calibrate the systems. Calibration of the infrared cameras can be done in various ways. One way is to calibrate the camera while the vacuum vessel is baked while simultaneously measuring the surface temperature of various representative positions in the plasma by thermocouples. The system can be calibrated in a separate optical bench, such that the transmission functions of the individual components can be determined making them easy to replace. Some calibration schemes are based on placing a hot black-body source inside the vacuum vessel during a venting period. The expected signal level from various components in the plasma depends on material properties. Carbon tiles emit an intensity that is close to that of a black-body at the same temperature but metallic tiles have a much lower emissivity. In case the emissivity of the material is unknown, it is possible to use a two-colour or multi-colour thermography system to fit a black-body spectrum to the observed intensity measurements and retrieve the temperature.

[15] In particular, CO_2 lasers at ~ 10 μm, D_2O lasers in the far-infrared and gyrotrons in the mm wavelength range.

3.7.1.2. Visible and UV cameras

Two-dimensional visible and VUV video cameras are used to monitor the 3D plasma emission in a very wide wavelength range from 100 to 900 nm. This can be for general surveillance of the vacuum vessel, but also to measure the wavelength-resolved emission of various ions in the scrape-of-layer and extreme plasma edge. One of the most common measurements is that of the H_α or D_α emission profile, which gives in general a good indication on the location of the last-closed flux surface. Visible cameras are often used for safety purposes. For example, they can monitor whether parts of the vacuum vessel get too high a temperature. They are also suited to see whether debris is falling into the plasma. Large chunks of material falling into the plasma can lead to disruptions that terminate the plasma.

In the visible and UV range one can use various types of cameras including CCDs, CMOS and charge-injection devices (CIDs). The cameras are usually placed not too far from the plasma and they need to be well shielded from electromagnetic fields, from neutron and gamma radiation. For this purpose, conventional optics and fibres are used. Calibration of the system is usually done by putting a light source of known intensity and spectral characteristics in the vacuum vessel. Components close to the plasma need to be regularly checked for their transmission characteristics. Shutters are useful to protect the plasma facing component of the system during glow discharge cleaning, boronization, etc (not so much during the plasma discharges).

3.7.2. Pressure and gas analysis measurements

The neutral pressure in a fusion device is highly anisotropic as it depends on the local recycling of the fuel ions, which is usually high in the proximity of limiters and divertors and much lower elsewhere. The anisotropy leads to pressure gradients in the toroidal 'neutral gas blanket' surrounding the plasma. Fast localized measurements of the neutral pressure are required to study the neutral gas distribution, its effect on the overall particle balance as well as its role in the detailed plasma-surface interaction processes. Localized pressure measurements are usually done with ionization gauges based on hot or cold cathodes. Another important measurement is that of the partial pressure of plasma constituents such as hydrogenic ions or helium and artificially introduced impurities such as nitrogen, neon, argon, krypton, etc. Some of these ions are introduced in the plasma edge to reduce the specific heat load that is conducted to the vessel wall and divertor targets by radiation. Since these ions have a beneficial effect only if they stay near the plasma edge, it is important to measure their partial pressures. This can be done by observing the spectral emission in the visible range with a commercial Penning gauge.

3.7.2.1. Ionization gauges

An ionization gauge senses pressure indirectly by measuring electrical ions that are produced when the gas in the gauge (in contact with the plasma chamber) is bombarded with electrons. A lower density gas results in fewer ions. Gauges are usually positioned in the divertor pumping plenums, in the divertor private flux region or in the boundary outboard of the main plasma.

In a hot cathode pressure gauge, electrons are generated by thermionic emission from an electrically heated filament and subsequently accelerated by a grid (see Fig. 3.28). They collide with gas atoms in the gauge and thereby generate positive ions. The ions are attracted to a collector; a negatively biased electrode. The current in the collector is proportional to the rate of ionization, which depends on the pressure in the system. The useful range of pressure gauges is approximately 10^{-8} to 1 Pa. Cold cathode gauges have a similar operation principle. The main difference is that the electrons are produced in a high voltage discharge. A particular difficulty in the use of ionization gauges very close to a fusion device is that the magnetic field makes the particles move in tight helical orbits around the magnetic field line direction. When the gauge is properly oriented with respect to the magnetic field one can benefit from this, as the ion collection efficiency is enhanced.

Penning gauges are cold cathode gauges that employ a magnetic field to create a mirror-like trap for ions born within them. Here again, it is possible to use the magnetic field of the fusion device to optimize the design of the gauge. However, in most applications, the gauge is positioned at some distance from the plasma and the magnetic stray field from the fusion device is screened by a thick metal casing. The time resolution of these systems is limited because of the time needed for the gas to stream from the plasma chamber to the gauge. The various constituents of the gas can be distinguished by their unique spectral signature (emission lines) in the discharge of a Penning gauge. A fusion device is therefore often equipped with a set of Penning gauges, each having a photomultiplier in combination with a narrow band pass interference filter to monitor strong, spectrally isolated emission lines.

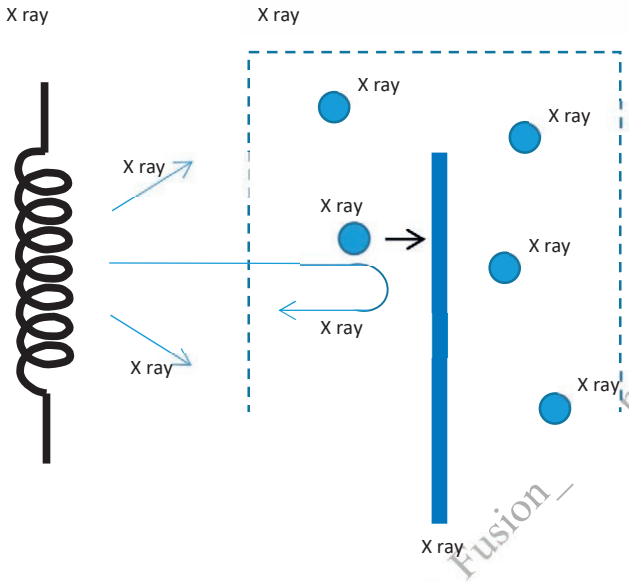

FIG. 3.28. Hot cathode ionization gauge. Electrons from an electrically heated filament are accelerated towards the chamber where they ionize the gas molecules. These are subsequently accelerated towards a negatively biased collector.

3.7.2.2. Residual gas analysis

Residual gas analysis (RGA) is a powerful technique to detect the existence of vacuum leaks, to determine global leak rate and to distinguish potential leak sources based on the measured mass spectrum of the ions. The most applied system for RGA is the quadrupole mass spectrometer (QMS; see Fig. 3.29). Particles to be analyzed are first ionized and accelerated. They are subsequently injected through a collimator into the analyzing region, which essentially contains four rods that are oriented parallel to the ion beam and electrically biased using a constant DC potential and a variable RF potential. Practically all ions in the beam will start oscillating with increasing amplitude until they eventually strike a rod and get neutralized. For each RF potential there is only one resonant mass value for which the particle doesn't hit the rod. Only in that case it can leave the analyzing region at the detector side, where it is counted by a Faraday cup or an electron multiplier. QMS detectors can be used for measuring partial pressures as low as 10^{-13} Pa.

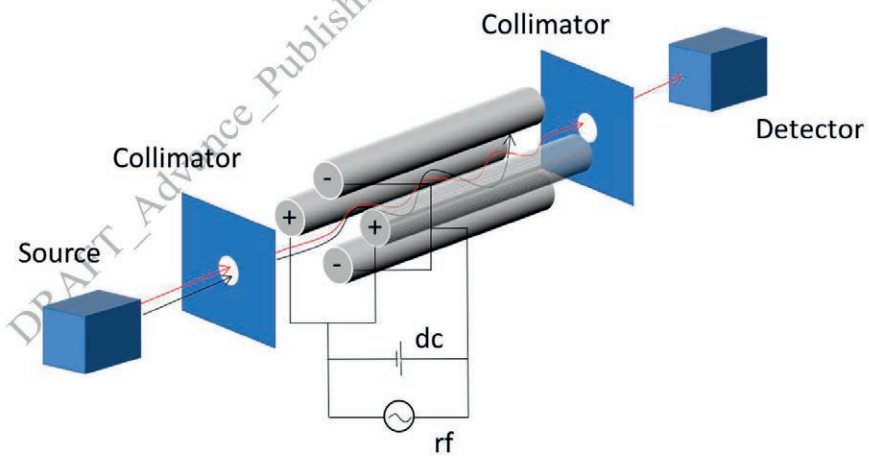

FIG. 3.29. Schematic diagram of a quadrupole mass spectrometer. Neutral particles from the plasma are first ionized then accelerated towards the analyser consisting of four rods. Resonant particles (red) can pass the analyser and be detected. Non-resonant particles (black) will hit one of the rods and will not be detected. By varying the RF frequency the system is sensitive to ions of different masses.

3.7.3. Probes

Probes are active diagnostics that are in direct contact with the plasma. They are only applicable in relatively cold plasmas or at the very edge of fusion plasma. The most applied is the Langmuir probe. The simplest probe consists of an isolated metallic pin inserted into the plasma (only the tip is not isolated). By applying a voltage to the tip, a current is drawn from the plasma. From the exponential part of the current-voltage (or I-V) characteristic, it is possible to deduce the edge plasma electron temperature and density. More elaborate probes have multiple independent tips which can be used to provide correlation measurements.

Probe measurements can also be used to obtain information on other plasma parameters like the electron density and the plasma potential. Sophisticated analyzers with electron repeller grids often measure parameters of the ion population. The logarithmic slope of the ion collection current is proportional to the ion temperature at the plasma edge.

Usually probes can only be applied at the very edge of the plasma. Otherwise, the probe could be damaged and the plasma could be affected. With reciprocating techniques, it is possible to move the probe deeper into the plasma on a periodic basis. In typically 100 ms, the probe is plunged into the plasma and pulled back.

Although the instrumentation part of probes is usually rather straightforward and simple, the interpretation of probe measurements is not. One of the main complications of probes is that they influence the plasma parameters. This effect should be carefully considered in data analysis.

3.7.4. Erosion and deposition measurements

Due to intense particle bombardment, plasma facing components and divertor components can be subject to erosion. It is important to quantify the erosion rate, as it provides some insight into the lifetime of the various components. Material that is eroded away somewhere in the fusion device is usually deposited elsewhere. This could be for instance on diagnostic components such as windows, mirrors and lenses, thereby affecting the transmission of optical systems. Erosion measurements are routinely done by placing the materials of interest at a position close to the plasma. This can be done with special lock systems, such that the materials can be frequently replaced and removed for off-line analysis with techniques as Rutherford back scattering (RBS), nuclear reaction analysis (NRA), electron recoil detection (ERD), laser-induced ablation spectroscopy (LIAS), laser-induced desorption spectroscopy (LIDS) and laser-induced breakdown spectroscopy (LIBS).

One method to measure the effective erosion/deposition rate in-situ is the quartz (piezo) crystal microbalance (QCM or QMB), which measures the mass per unit area from the change in frequency of a quartz crystal resonator. The resonance is disturbed when the mass at the surface of the acoustic resonator exhibits small changes due to erosion or deposition. A QMB is a sensitive monitor of the rate of erosion or deposition in real-time. A QMB can measure mass densities down below 1 $\mu g.cm^{-2}$ and should be mounted at a location where the conditions are similar to those of the first wall. A complication is that the piezocrystals can't operate above 573 °C. Due to the electrical and thermal stresses during a plasma discharge, QMBs are not used in real time. Instead, they are used to measure the erosion/growth of the layer between consecutive discharges. Interestingly, QMBs are not sensitive to dust as there is a good acoustic coupling between the crystal and the top layer.

Another technique to measure erosion/deposition is speckle interferometry, which in principle is sensitive to thickness changes of about 5 μm and can be utilized in real-time during the plasma discharge. It will not be explained here because it still needs to be proven in a fusion plasma environment.

3.7.5. Dust measurements

Dust created in a fusion plasma can potentially lead to safety issues. Dust can be radioactive, it can bind hydrogenic ions (tritium retention) and can potentially lead to dust explosions. It is therefore important to get a global estimate of the amount of dust. However, this picture needs to be created from local measurements. Some of the diagnostics that have been presented elsewhere in this chapter are also suited to measure dust. Many fusion devices are equipped with fast visible cameras (see Sec. 3.8.1.2). Dust particles can be observed and traced in flight with high-speed camera. In flight dust particles can be also observed parasitically with laser diagnostics like Thomson and Rayleigh scattering. Another technique is to use collectors that accumulate dust during a full measurement campaign (or part of it). The collectors are afterwards removed and dust is analysed for size distribution and amount.

Dust can be collected by electrostatic grids, reminiscent to the high-voltage grids used to terminate insects. The flat dust grid is mounted at the bottom of the fusion device. Two closely spaced conducting meanders on a printed circuit board are voltage biased. When a dust particle impinges on the grid, it temporarily short–circuits the meanders

yielding a spark during which the dust particle is almost instantaneously evaporated. This leads to a transient current flowing through the circuit. The current of the pulse is proportional to the size of the dust particle.

3.8. ISSUES OF IMPORTANCE FOR REACTORS

This chapter has so far been concentrated on diagnostic instrumentation, and not so much on the way the diagnostics are implemented onto fusion devices. In many cases, it is evident: Microwave diagnostics are usually coupled via waveguides and antennas; particle diagnostics and many fusion diagnostics via direct lines of sight; optical diagnostics via fibres, lenses and mirrors. As was mentioned in the introduction the discussion did not dwell too much into the physical principles of the various diagnostic measurements as there are ample references and text books which already cover this issue. This brief section will focus on a few implementation issues of diagnostics to reactors.

3.8.1. Application of diagnostics to fusion reactors

The environmental conditions in a fusion reactor are very unfriendly to diagnostics systems. Neutron and gamma fluxes and fluences are much higher than in present devices, giving rise to several phenomena that are completely new to the field of plasma diagnostics. These include, amongst others, radiation–induced effects on electrical and optical components, nuclear heating, swelling and transmutation. Many diagnostics that are routine at present devices can be marginally used in ITER, and will most likely be confronted to severe implementation issues on future reactors. It may be evident that the nuclear environment poses stringent demands on the engineering. To shield against neutrons streaming through ports and gaps, diagnostics need to be equipped with a labyrinth. Few exceptions apart, direct lines–of–sight will be impossible. Diagnostic viewing-lines should be equipped with a double vacuum barrier to make sure that tritium cannot escape from the fusion device in case a window or valve would fail. Diagnostic components close to the plasma will become radioactive and their replacement, requiring remote handling, will not be easy. Most likely, complete port plugs will need to be transferred to hot cells where maintenance can take place in a well screened environment. Reactors should have a high duty factor and the plasma discharges will essentially be steady state. This implies that diagnostic design should focus on robustness, reliability and stability.

In a reactor, it is important to use most of the wall surface for tritium breeding. Hence the number of access ports for peripheral heating and diagnostics need to be reduced to the bare minimum placing high demands on integration. Whenever possible, diagnostics will share joint sight lines with each other, but also with the heating and fuelling devices. Recent developments have successfully focused on combining the ECE sightline with the ECRH transmission line. It was demonstrated that it is possible to measure nanowatt signals in a megawatt environment.

A challenge lies in the will to operate the fusion reactor as close as possible to its operational limits, to achieve the highest performance. A drawback is that all kind of instabilities can easily grow, leading to a degradation or even termination of the discharge. The classical way to tackle this challenge is to add many diagnostic systems to automatically control the plasma. In future fusion reactors however, will have to cope with the fact that many diagnostics that are routine now can no longer be applied. There will be fewer diagnostics, and much less lines of sight. All this implies that control of the reactor plasma needs to rely on theoretical models of the plasma to a much higher extent than today. The latest idea is to develop a full theoretical model of the plasma (some people call it a flight simulator) equipped with many fancy synthetic diagnostics such that the exact state of the simulated plasma is well known. The idea is that the plasma control system will give feedback signals to both the reactor plasma and the flight simulator. The output of the few physical diagnostics monitoring the reactor plasma is then compared with the output of the synthetic diagnostics. Differences between the two sets will be used to adapt the feedback signal of the controller and the flight simulator (see Fig. 3.30).

3.9. DATA HANDLING

During a typical discharge of a fusion device, large amounts of data are produced by the various diagnostic systems. Since many diagnostics operate at high spatial, spectral and temporal resolution the amount of data outputted during a single discharge can run up to hundreds of gigabytes, even to several terabytes. In the long duration plasma discharges of ITER this might become even more. Therefore, it is important to set up adequate protocols to handle the data.

One of the first steps in data handling is to run an automated check to see whether there are no hardware faults in the system (e.g. no signal at all, one trace in a multi-channel diagnostic lying completely out of the rest, too much

noise, etc.), to judge whether the signal is useful at all. It is possible to incorporate a first data compression or data reduction step. Signals that are basically constant over a long time can be stored at a lower sampling frequency. Some diagnostics have a rather straightforward calibration, and this could also be automatically corrected for during data acquisition.

A next step is to search for anomalies between different diagnostic channels and/or different diagnostics. In case different diagnostics can measure the same plasma parameter one can determine whether they are consistent or one diagnostic gives results that are completely off. At a more sophisticated level one can compare the output of diagnostics with the output of theoretical models describing the plasma. This is something that will gain in importance in the coming decades, as described in Sec. 3.9.

Nowadays, data from many individual diagnostics is often first analysed to yield physical parameters. The parameters deduced from the various diagnostics are then combined to yield a unified physical picture of the plasma. In integrated data analysis (IDA), like bayesian analysis, a plasma model is fitted directly to a large range of different diagnostic data. Integrated data analysis is in general computationally intensive since it involves handling large amounts of data. It is therefore mainly a tool to achieve a better understanding of the physical processes in the plasma; the analysis is usually done within days, weeks, sometimes even months after the plasma discharge.

In the future, a completely different strategy should be followed as the main aim of a fusion reactor will be electric power production in a safe and reliable way. The main function of diagnostics will then be to adequately control the plasma. This implies that the data of the various diagnostics will be analyzed in real-time. Nowadays this is done for a limited set of diagnostics incorporated in the feedback loops, but in the future, this will hold for nearly all diagnostics. A schematic diagram of a real-time control system for a future tokamak is shown in Fig. 3.30. In a certain sense one could say that the main control loop is completely done on the tokamak flight simulator, using synthetic diagnostics. The control signals are also fed to the actuators in the tokamak and the physical diagnostic measurements are used to adapt the simulation model and to feedback the controller. The reason for implementing this strategy is that the fusion reactors will have a rather limited set of diagnostics, which will most likely not be enough to fully control the plasma. This is circumvented by the feedback on the simulation model. The model should describe the physical processes in the plasma in a relatively accurate way, but any complication should be avoided to allow the model to run almost real-time, as this is the main requirement. The limited set of diagnostics that will be operational at a fusion reactor will mainly be used to continuously benchmark the model.

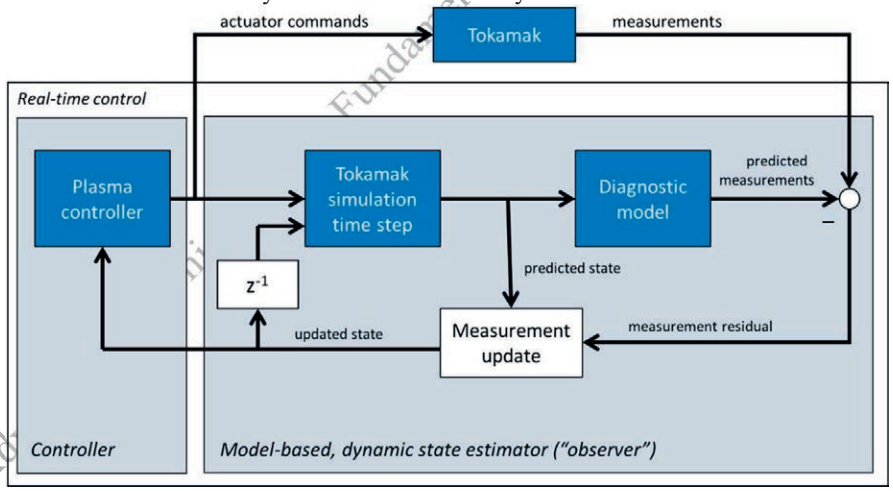

FIG. 3.30. Schematic diagram of the control system of a future tokamak device. The outputs of the plasma controller are fed to the different actuators in the tokamak as well as to a tokamak simulator involving synthetic diagnostics. The actual measurements from the tokamak are compared with the predicted measurements from the synthetic diagnostics. The differences between the two (measurement residual) is used as feedback to the controller, but is also used to update the simulation model.

ACKNOWLEDGEMENT

The writing of this chapter has been carried out within the framework of the EUROfusion Consortium and has received funding from the Euratom research and training programme 2014–2018 and 2019–2020 under grant agreement No 633053. The views and opinions expressed herein do not necessarily reflect those of the European Commission.

REFERENCES

It was a specific choice not to dilute the text in this chapter with a large amount of references. Instead the choice was to provide a list of several important text books and review papers, that are recommended for further reading.

[3.1] HUTCHINSON, I.H., Principles of Plasma Diagnostics, Cambridge University Press, Cambridge (1987).
[3.2] LOCHTE-HOLTGREVEN, W., Plasma Diagnostics, AIP Press, New York (1995).
[3.3] HARTFUSS, H.J., GEIST, T., Fusion Plasma Diagnostics with mm-Waves, Wiley-VCH Verlag GmBH (2013).
[3.4] STRAIT, E.J., FREDRICKSON, E.D., MORET, J.M., TAKECHI, M., Magnetic Diagnostics, Fus. Sci. Techn. **53** (2008) 304.
[3.5] LUHMANN, N.C., BINDSLEV, H. Jr., PARK, H., SÁNCHEZ, J., TAYLOR, G., YU, X., Microwave Diagnostics, Fus. Sci. Techn. **53** (2008) 335.
[3.6] DONNÉ, A.J.H., BARTH, C.J., WEISEN, H., Laser-Aided Plasma Diagnostics, Fus. Sci. Techn. **53** (2008) 397.
[3.7] STRATTON, B.C., BITTER, M., HILL, K.W., HILLIS, D.L., HOGAN, J.T., Passive Spectroscopic Diagnostics for Magnetically Confined Fusion Plasmas, Fus. Sci. Techn. **53** (2008) 431.
[3.8] THOMAS, D.M., McKEE, G.R., BURRELL, K.H., LEVINTON, F., FOLEY, E.L., FISHER, R.K., Active Spectroscopy, Fus. Sci. Techn. **53** (2008) 487.
[3.9] INGESSON, L. C., ALPER, B., PETERSON, B. J., VALLET, J.C., Tomography Diagnostics: Bolometry and Soft X-ray Detection, Fus. Sci. Techn. **53** (2008) 528.
[3.10] KISLYAKOV, A.I., DONNÉ, A.J.H., KRUPNIK, L.I., MEDLEY, S.S., PETROV, M.P., Particle Diagnostics, Fus. Sci. Techn. **53** (2008) 577.
[3.11] SASAO, M., NISHITANI, T., KRASILNIKOV, A., POPOVICHEV, S., KIPTILY, V., KÄLLNE, J., Fusion Product Diagnostics, Fus. Sci. Techn. **53** (2008) 604.
[3.12] LASNIER, C.J., ALLEN, S.L., BOEDO, J.A., GROTH, M., BROOKS, N.H., McLEAN, A., LaBOMBARD, B., SKINNER, C.H., RUDAKOV, D.L., WEST, W.P. and WONG, C.P.C., First Wall and Operational Diagnostics, Fus. Sci. Techn. **53** (2008) 640.
[3.13] ARSHAD, S.A., CORDEY, J.G., McDONALD, D.C., FARTHING, J., JOFFRIN, E., VON HELLERMANN, M., ROACH, C.M. and SVENSSON, J., Data Validation, Analysis and Applications for Fusion Plasmas, Fus. Sci. Techn. **53** (2008) 667.
[3.14] VAYAKIS, G., HODGSON, E.R., VOITSENYA, V., WALKER, C.I., Generic Diagnostic Issues for a Burning Plasma Experiments, Fus. Sci. Techn. **53** (2008) 699.
[3.15] MEDLEY, S.S., DONNÉ, A.J.H., KAITA, R., KISLYAKOV, PETROV, M.P., and ROQUEMORE, A.L., Contemporary Instrumentation and Application of Charge Exchange Neutral Particle Diagnostics in Magnetic Fusion Energy Experiments, Rev. Sci. Instrum. **79** (2008) 011101.
[3.16] DONNÉ, A.J.H., et al., Progress in the ITER Physics Basis, Chapter 7: Diagnostics, Nucl. Fusion **47** (2007) S3.

Chapter 4

PLASMA CONTROL AND DATA ANALYSIS

Wolfgang Biel
Forschungszentrum Jülich GmbH
Germany
Ghent University
Belgium

Geert Verdoolaege
Ghent University
Belgium

4.1. DIAGNOSTIC AND CONTROL SYSTEM OF A DEMO TOKAMAK REACTOR

According to the European long term strategy towards fusion energy, a demonstration fusion reactor (DEMO) is foreseen as the single step between the ITER experiment and a commercial fusion power plant. DEMO should deliver significant net electrical power into the grid by the mid-21st century, achieve tritium self-sufficiency, and allow for a safe extrapolation towards an economically viable commercial fusion power plant [4.1]. Within the currently pursued DEMO project, the baseline design is a tokamak with a predominantly inductive long pulse operation (a few hours) and several hundred megawatts of net electrical output power.

The current development of the European DEMO follows a conservative approach [4.2] using only moderate physics and technology extrapolations beyond the status of ITER. This approach is chosen in order to facilitate a timely development under the boundary conditions of limited resources and taking into account the construction delays of ITER, which are shifting the schedule for large scale experimental validation of any major new developments towards the mid-2030s. Specifically, it is currently assumed that the plasma scenario of the European DEMO reactor will provide a confinement quality near the standard ELMy H-mode (confinement quality $H \approx 1.0$) [4.3] but without edge localized modes (ELMs) or only low energy ELMs below the threshold for wall damage. Furthermore, the European DEMO reactor should be operated at a high core plasma radiation fraction $P_{rad}/P_{heat} \approx 0.6$ to 0.7 to limit the power flowing towards the divertor and at a high plasma density to facilitate detached plasma operation in the lower single-null divertor. The typical time-averaged auxiliary heating power would be in the order of 50 MW or less, mainly used for plasma control purposes with only a minor impact on the pulse duration via current drive. Additional details on the current physics and technology basis and their gaps can be found in [4.4]. It is important to note that some of the key features of the DEMO plasma scenario and technology are still not well defined, nor have they so far been simultaneously demonstrated in reactor relevant conditions. Therefore, at the current stage of the DEMO studies, the development of the diagnostic and control system (D&C) can only be pursued in a generic way considering the significant uncertainties concerning the final plasma scenario and machine properties.

The first tokamak experiment producing significant fusion power will be ITER. Given the plasma parameters and the nuclear environment of the ITER machine, which both represent an important step from smaller experimental tokamaks towards DEMO, the ongoing developments for the ITER diagnostic and control system are an important basis for any considerations towards DEMO D&C. The ITER diagnostic suite under development [4.5, 4.6] has to serve the needs for both plasma control and physics investigations in a plasma experiment with predominant alpha particle heating and moderate neutron fluences up to damage levels in the order of one displacement per atom (dpa) near the first wall. Engineering challenges for the realization of ITER diagnostics [4.7, 4.8, 4.9], in particular the nuclear aspects [4.10], have led to the development of important concepts such as the port plug based integration approach, the maintenance of diagnostic components via remote handling and the selection of irradiation-hard functional materials for diagnostics components.

In addition to the open issues towards the DEMO physics basis and the definition and validation of the plasma scenario, the development of the plasma diagnostic and control system for DEMO is facing several significant challenges, which go far beyond ITER [4.11]. Specifically, the DEMO D&C system should provide high reliability since any loss of plasma control may result in a loss of confinement or even in a disruption, which can cause significant damage to the inner wall or other components of the machine. High accuracy of the D&C system is also needed to operate DEMO near its operational limits, where the power output of the reactor is maximized. Fast reactions of the D&C system are required, especially in case of unforeseen events (e.g. component failure, or radiation increase

following impurity ingress into the core plasma). On the other hand, space restrictions for the implementation of diagnostic components in the blanket (optimization of the tritium breeding rate) and adverse effects acting on the diagnostic front-end components (neutron and gamma radiation, heat loads, erosion and deposition) will be much stronger than on ITER. This will limit the performance of measurements where the capabilities of the available actuators for plasma control (poloidal field coils, auxiliary heating and fuelling) are limited as well. To improve the controllability of the DEMO plasma, in view of the limited available diagnostics and actuators, advanced control techniques will be employed, aiming to provide either a fast state description of the plasma based on the measured data, or even deliver model-based predictions towards optimized actuator trajectories [4.12].

As part of the European DEMO conceptual design studies, the development of the D&C system has recently been launched within the work package DEMO diagnostic and control (WPDC) [4.11]. During the first two years of the project, an initial understanding of the prime choices of diagnostic methods and actuators applicable to DEMO has been obtained. Subsequently, an initial version of the DEMO systems requirements document (SRD) for the diagnostic and control system has been issued [4.13]. Simulations are now being developed for several control issues to prepare the physics models for future advanced control schemes and provide some quantitative verification of the controllability of the DEMO plasma. At present, the D&C concept only addresses the stationary burn phase of the discharge. The ramp-up and ramp-down phases, the heating-up towards the burn phase, as well as the control of instabilities and emergency actions (e.g. disruption mitigation or fast shut down) will be investigated in more detail at a later stage of the project.

This chapter is structured as follows: In Section 2, the challenges and limitations towards the integration of the necessary plasma control diagnostics in DEMO are discussed and some requirements and first conclusions relevant to the control system are formulated. In Section 3, the initial DEMO D&C concept is presented, addressing only the stationary (burn) phase at the current stage of development. After this, Section 4 gives an overview on the foreseen diagnostic systems and presents some key features related to their integration into DEMO. In Section 5, the status of the foreseen actuators and their performance properties is briefly summarized. Critical open issues are discussed in Section 6, which is followed by a summary and conclusions.

4.1.1. Challenges for diagnostic integration on DEMO

The integration of diagnostics for DEMO plasma control is facing the following challenges [4.11]:

- Only limited space is available in the machine (in-vessel) for the integration of diagnostic components and sightlines: First, DEMO has to achieve a tritium breeding rate greater than one, which in turn requires that most of the inner surface of the torus has to be covered by the breeding blanket. Second, the number of ports and other openings is limited, and it has to be shared with many other systems, such as heating and current drive, remote handling, gas fuelling and pumping.
- Any maintenance of in-vessel components within the nuclear environment of DEMO has to be performed by remote handling and is therefore technically challenging, expensive and time-consuming. To achieve the high overall availability required for DEMO, all in-vessel components should be designed for a high degree of reliability and durability such that the need for scheduled and non-scheduled maintenance is minimized.
- All forward-mounted components in DEMO are subject to nuclear irradiation (neutrons, gammas) resulting in volumetric heat loads, transmutation and displacement damage (dpa). These conditions imply restrictions in the choice of materials and require specific design choices such as the application of active cooling. Moreover, any in-vessel front-end diagnostic components having an open sightline towards the plasma (e.g. diagnostic mirrors) are subject to bombardment by energetic neutral particles originating from charge exchange collisions in the plasma, as well as impurities released from the wall. Hence, diagnostic components on DEMO will have to be selected according to their robustness and mounted in remote (protected) locations, which leads to limitations in the applicability and performance of the diagnostic methods.
- The provision of any penetrations in the machine for diagnostic or actuator access to the plasma represents a specific challenge for the design of the involved components (especially for the first wall or divertor). Here, mechanically stable and well cooled structures are needed to be able to accept the high heat loads originating from neutron and gamma radiation, plasma particles and plasma radiation) and the mechanical loads arising e.g. from eddy currents during transients.
- The complex task of reliably controlling the DEMO plasma near the operational limits[16] can only be fulfilled if accurate and timely information about the state of the core, edge, X-point and divertor plasma is available. For normal plasma operation, a reduced set of measurements may be sufficient if control oriented plasma models

[16] e.g. density limit, radiation limit, wall load limit.

can describe all possible evolutions of the plasma. However, in view of the risk of unforeseen events such as the sudden failure of major components (e.g. coolant ingress or a quench in superconducting magnets) or the sudden increase of plasma radiation following impurity ingress into the core plasma (dust particles, etc.), it remains an open question at this time to what degree future control oriented models will be able to cover all possible evolutions of the plasma. At the current stage of the DEMO D&C project, it is therefore assumed that the information on the plasma state is based on sufficiently detailed measurements and the application of advanced control oriented models.

- Since quantitative data on the reliability (mean time between failures) of the DEMO diagnostics is not available, it is currently assumed that the number of installed channels (for all foreseen methods) is typically twice the minimum number of required measurements. Depending on the reliability and on the risk of running into severe damage or even into safety relevant problems (to be determined by future R&D), this tentative redundancy factor of two may have to be adjusted in future (note that fission power plants have up to 5 independent cooling systems while only one operational system is needed).

Based on the challenges above, the following requirement can be formulated:

All in-vessel and in-port components of diagnostics and actuators have to be mounted in sufficiently remote (protected) locations, using robust designs and resilient materials to maximize their lifetime (minimize maintenance needs and the resulting downtimes). In principle, the goal is to achieve maintenance-free operation of in-vessel components over (at least) the lifetime of the blanket, i.e. two full-power years (fpy) for the starter blanket (designed for a neutron fluence of 20 dpa) and 5 fpy for the second blanket (50 dpa). For ex-vessel components, the requirements for maintenance-free operation can somewhat be reduced provided any necessary maintenance actions can be performed within a short time and with low effort without compromising the overall target availability of DEMO. Of course, since there will always remain a risk for in vessel diagnostic component failure, all components have to be compatible with maintenance via remote handling. In the following, the status of the development of the DEMO D&C system is summarized with respect to control tasks, front-end components and materials, and integration approaches.

4.1.2. Initial version of the DEMO diagnostic and control concept

The current initial DEMO diagnostic suite, addressing the stationary ("burn") phase of the plasma, has been defined based on a coarse listing of the main DEMO plasma control issues summarized in Table 4.1. The key elements of the DEMO plasma control strategy for the stationary part of the discharge ("burn phase"), including the current understanding on diagnostics, actuators and control margins, are summarized in the following. They can be grouped into the three headlines: equilibrium control, kinetic control and the control of instabilities and events.

TABLE 4.1: Control issues and related diagnostics suite and actuators on DEMO, updated version based on [4.11].

Control issue	Operational limits	Main diagnostics	Main actuators and counter-measures
Equilibrium control			
Plasma current	q_{95} limit (safety factor)	Magnetic coil based diagnostics and Hall probes	Central solenoid auxiliary heating
Plasma position and shape, including vertical and horizontal stability	Local wall loads (FW and divertor) max Δz / VDE disruption	Ex-vessel magnetic diagnostics MW reflectometry, ECE in-vessel magnetic diagnostics neutron/gamma diagnostics IR polarimetry/interferometry	PF coils CS coils Auxiliary heating Gas injection
Kinetic control			
Plasma density (edge rather than core)	Density limit	MW reflectometry IR polarimetry/interferometry Plasma radiation Neutron/gamma diagnostics	Gas injection Pellet injection Pumping system
Plasma radiation, impurity mixture, Z_{eff}	Radiation limit LH threshold	Spectroscopy + radiation measurements U_{loop}	Impurity gas injection Auxiliary heating
Fusion power	Local wall loads (FW and divertor) LH threshold	Neutron/gamma diagnostics FW/blanket and divertor power (for calibration only)	Main plasma density Impurity gas injection Auxiliary heating
Divertor detachment and heat flux control	LH threshold local wall loads in the divertor	Divertor thermo-currents Spectroscopy + radiation measurements Thermography	PF coils Gas injection Pellet injection Pumping system
Plasma pressure	Beta limit	Magnetic diagnostics Density and temperature diagnostics	Auxiliary heating Gas injection

Control of instabilities and events			
(MHD) plasma instabilities	Various (→ disruptions)	MW reflectometry, ECE IR polarimetry/interferometry magnetic diagnostic neutron/gamma diagnostics	Auxiliary heating ECCD PF coils
Impurity events	Radiation limit Density limit	Spectroscopy and radiation measurements	Auxiliary heating Gas injection
Component failure	Various	Various	(redundancy)
Disruption mitigation	Various	Microwave diagnostics Magnetic diagnostics Spectroscopic and radiation measurements	Matter injection to distribute wall loads and act against runaways

4.1.2.1. Equilibrium control

Plasma position and shape depend on the interplay between magnetic forces and kinetic plasma pressure. More specifically, the horizontal plasma position is related to vertical field, plasma current and pressure, while the vertical plasma position in the elongated configuration (defined by the attractive forces acting from PF coils located above and below the plasma) is in principle unstable and needs to be monitored and controlled on a time scale faster than the vertical instability. Thus, the prime actuators for position and shape control are the poloidal field coils and the central solenoid (via the plasma current and via stray fields); however, the auxiliary heating (increase of heating power) and the plasma fuelling (affecting confinement properties) may also influence the plasma position and shape. The primary choice of diagnostics for position and shape control in tokamaks are (traditionally) in-vessel magnetic diagnostics. The control concept for ITER follows the same approach, see e.g. [4.14] and references therein. Coil based measurements provide a signal proportional to the time derivative of the magnetic field, and hence the signals need to be integrated over time. However, during the long stationary burn phase, the raw signals to be integrated are essentially zero. This means that any spurious voltages originating from irradiation effects [4.10] could appear like a steady "drift" of the magnetic configuration, which should be corrected before using these signals as input for plasma control. Based on currently available neutronics calculations for DEMO [4.15], the predicted fluence behind the DEMO blanket (inboard side) will be up to 10^{26} neutrons per square meter (~10 dpa), exceeding the ITER levels by up to two orders of magnitude.

Several irradiation-induced effects that could disturb signals from magnetic sensors have been thoroughly investigated for ITER. Specifically, a thermo-electric voltage can be generated via transmutation in the conductor, which is known as the radiation-induced thermoelectric sensitivity (RITES) [4.10]. Since this effect evolves slowly with the accumulated fluence over the period of operation, it could (to some extent) be corrected based on the baseline signal level measured prior to the start of a DEMO discharge. Another important effect is the parasitic voltage induced by thermal gradients inside the sensor (temperature-induced electromotive force, TIEMF) [4.10]. These could in principle be minimized by optimizing the sensor design and sensor cooling such that a fairly constant temperature distribution can be maintained over the sensor during operation. For the low-temperature co fired ceramics (LTCC) coil design developed for ITER, a temperature drop of less than 1 K has been predicted based on simulations [4.16], which translates into a typical spurious voltage of 0.1 to 0.5 μV [4.17]. Finally, the signals transmitted via mineral insulated (MI) coaxial cables can be disturbed by the radiation-induced electromotive force (RIEMF) effect, which generates a current or voltage across the insulator via charged particles created by gamma or neutron reactions [4.10]. Considering the large neutron fluences on DEMO and the long discharge duration over which all the spurious signal contributions will be integrated, it should be expected that the signals from in-vessel magnetic sensors will be accordingly stronger influenced by irradiation-induced effects as compared to the ITER sensors. Ex-vessel magnetic sensors are shielded by the thick vacuum vessel, hence experience irradiation effects which are about three orders of magnitude lower than those felt by the in-vessel sensors located behind the blanket [4.15]. On the other hand, the eddy current shielding by the vacuum vessel will slow down the signals measured by ex-vessel magnetic sensors, such that the measured signals are too slow for the control of fast events [4.18].

During long plasma pulses, the time-integration of even the smallest offset voltages in the electronics connected to magnetic coil sensors may lead to spurious signals which appear to be drifting with time. Therefore, as a complementary approach, the installation of Hall sensors is foreseen. These sensors provide raw signals proportional to the magnetic field rather than its time derivative. However, those signals have only small amplitudes which are temperature dependent. The limitations for the application of Hall sensors under irradiation levels relevant for DEMO are currently unknown.

The current approach for DEMO plasma position and shape control pursues a risk mitigation strategy: Fast in-vessel measurements from magnetic coil based sensors are foreseen, complemented by measurements from microwave diagnostics (reflectometry and electron cyclotron emission). In-vessel Hall sensors may be added if their durability in DEMO relevant irradiation levels can be shown. In addition, ex-vessel magnetic measurements (both coil based and Hall sensor based) will be available to monitor slow changes of the magnetic configuration and provide a basis to correct the apparent drifting of in-vessel magnetics coil signals arising from irradiation damage. Finally, infrared interferometry/polarimetry and neutron/gamma diagnostics may also contribute to plasma position and shape control. More specifically, IR interferometry/polarimetry may be used during the ramp-up and ramp-down phases of the discharge, when the plasma cross section is not fully developed and hence the plasma edge is too far from the reflectometry antennae to obtain useful data. In the nuclear burn phase, neutron/gamma diagnostics may contribute in defining the position of the plasma centre (roughly corresponding to the current centroid), which would be a useful amendment to the information obtained from reflectometry monitoring of the position of the plasma boundary.

The plasma current (edge safety factor q_{95}) will be controlled based on signals from magnetic sensors (ex-vessel coils and Hall sensors) measuring the related poloidal field. In the case of a pulsed DEMO tokamak the actuators are given by the central solenoid coil and a limited auxiliary current drive. The edge safety factor should be kept precisely in the desired range with a relatively small control margin since it belongs to the characteristic quantities of the plasma scenario and it is related to the susceptibility of the plasma to certain MHD instabilities [4.19]. Additional ex-vessel magnetic measurements are foreseen to diagnose the diamagnetic energy and the loop voltage. Substantial future R&D is needed to better determine the limits of the durability (lifetime) of in-vessel magnetics by irradiation testing and modelling, to find out in how far the spurious voltages arising from these effects can be corrected for, or whether a sudden malfunction of these sensors should be expected, e.g. by swelling, cracking or disconnection of cables, and to optimize the designs and locations of sensors accordingly.

4.1.2.2. Kinetic control

For DEMO, a moderately peaked radial plasma density profile with a pedestal near the plasma edge (separatrix) is predicted [4.21, 4.22]. Understanding the Greenwald density limit [4.23] as a limit applying to the plasma edge density, the pedestal top density should remain below the Greenwald limit. Reflectometry is foreseen as the primary diagnostic to measure the plasma density in the gradient region, while the central values will be derived using infrared interferometry/polarimetry. The measured radial profiles from radiation power and neutron flux measurements may contribute to perform a consistency check of the measured density profiles. Primary actuators for density control are pellet and gas injection. It is understood that the overall pumping speed and efficiency can only slowly be adjusted on purpose, depending somewhat on the actual divertor plasma conditions. The size of the density-limit control margin will depend on the achievable accuracy of the control system. It is currently assumed that the density at the pedestal top should stay below 80 to 85% of the Greenwald limit.

According to the current understanding of plasma confinement, the plasma pressure predicted in DEMO will remain safely below the beta limit. Therefore, a rigorous control of the plasma beta is not a priority at this stage. It is however planned to derive a coarse electron temperature profile from electron cyclotron emission measurements (ECE) and to analyse radial profiles of gamma and neutron spectra together with high resolution X ray spectra from the plasma centre, and to obtain the ion temperature distribution. The knowledge of plasma density and temperature profiles will allow consistency-checks of the fusion power and radiation power profiles in the plasma, thus enhancing the inherent redundancy and consistency of the information on the plasma state and improving the robustness of the control concept.

For a stable plasma operation in H-mode, the power loss P_{loss} across the separatrix towards the divertor should exceed the H-mode threshold P_{LH} [4.24]. On the other hand, divertor protection requires keeping the local power densities impinging onto the divertor target below the damage threshold, which pushes towards reducing P_{loss} as much as possible. These two conflicting requirements on the loss power can only be simultaneously fulfilled by providing accurate measurements of the plasma heating power (ionic part of fusion power $P_{\mathrm{fus,ion}}$, and auxiliary power P_{ext}) and the core plasma radiation power $P_{\mathrm{rad,core}}$, and controlling their difference according to

$$P_{\mathrm{loss}} = P_{\mathrm{fus,ion}} + P_{\mathrm{ext}} - P_{\mathrm{rad,core}} = f_{\mathrm{LH}} P_{\mathrm{LH}} \ ,$$

where the enhancement factor f_{LH} should be kept slightly above unity for a stable H-mode operation. To fulfil this condition for a DEMO tokamak with ~2 GW thermal power and an LH power threshold in the order of 100 to 150 MW, the core radiation power typically has to amount 60 to 70% of the total plasma heating power. This makes the quantity P_{loss} a small difference of two big numbers, with significant uncertainty arising from the limited measurement accuracies for both P_{heat} and $P_{\mathrm{rad,core}}$. The power balance and core radiation level can be adjusted by using impurity gas injection into the plasma core, fuel injection and auxiliary heating. The latter is also applicable if a fast increase in heating power is needed (e.g. to counter-act an unwanted increase of plasma radiation and reduction of P_{loss} after an impurity event). To provide some accuracy and consistency check for these quantities, the measurements of the total radiation power should be accompanied by a detailed spectroscopic analysis together with on-line modelling of the various contributions to core plasma radiation using the measured plasma density and temperature profiles as input. Since a long lasting- absolute calibration of the total radiation power diagnostics appears infeasible (mirror and detector aging, etc.), occasional H-L back-transitions, purposely induced by core impurity injection, may serve to perform a relative "calibration" of the control circuit for P_{loss} with respect to the H-mode threshold power. The total fusion power can be deduced from the neutron flux measurements, which can be absolutely calibrated against data from activation foils and the slow but accurate measurement of the total thermal power based on the flow and temperatures of the blanket and divertor coolants.

If a certain toroidal plasma rotation would be required to maintain the plasma scenario, the toroidal ion velocity could be accessed via the Doppler shift of high resolution X ray spectra provided that the observation direction has a

toroidal inclination angle of more than 15 degrees against the poloidal plane. In this case, NBI heating would be the prime actuator to apply torque to the plasma.

Within the divertor, the heat flux density to each of the target plates has to be kept below the damage threshold. The current baseline foresees a detached plasma state in front of the divertor, where the plasma temperature near the divertor target plate is smaller than ~3 eV and the particle density is accordingly high. Under such conditions, the plasma is only partially ionized and a predominantly neutral) particle zone exists in front of the target plates distributing the impinging heat loads onto a larger area. The proposed approach for divertor control measurements is threefold: First, the divertor thermo-currents will be measured. Those are related to the sheath voltage at the target plate and hence should drop to almost zero under conditions of low plasma temperature near the target plates. Second, a detailed spectroscopic analysis of the divertor plasma in front of the inboard and outboard target plates is foreseen to identify the existence and location of the ionization front of the detached plasma. For this analysis, the details regarding the decisive spectroscopic signature (selection of spectral lines or line shapes to be monitored, geometry of sightlines) will be defined once a detailed control-oriented model of the divertor plasma becomes available. As a third approach, infrared thermography will be employed to measure the local temperature distribution along the target plate. The latter two measurements will be implemented via first mirrors installed in the equatorial ports to avoid installing optical components in the dusty divertor environment. The prime actuators for divertor plasma control are gas or pellet injection (impurity and fuel) into the divertor, and the control of upstream (pedestal top) plasma conditions. The interrelation between H-mode control and divertor power control, the partially contradicting requirements, the non-linear and indirect approaches for measurements, and the rapid development of wall damage (erosion and melting) in case of failure makes this part of the DEMO plasma control one of the most challenging.

4.1.2.3. Control of instabilities and events

Instabilities and (unforeseen) events are of major concern for the operation of DEMO since they can lead to disruptions, which in turn have a significant potential to damage the machine. Extensive studies on JET have shown that a fraction of several percent of disruptions remains without a clear explanation [4.25], and that a fraction of several percent of upcoming disruptions is recognized too late for any effective mitigation actions to take place [4.26]. A few more general issues on disruptions are listed in Section 6. From a control point of view, it is important to work towards an early and reliable recognition of plasma conditions which may lead to a disruption to provide means of prevention or mitigation, if it cannot be avoided.

Present-day disruption diagnostics [4.27] will all be available on DEMO but their latency will be somewhat larger than on medium sized experimental tokamaks (like AUG or TCV) because of the retracted mounting position of certain sensors behind the blanket (see details below). The feasible reaction time for disruption mitigation will also be longer on DEMO since the matter injection system (e.g. scattered pellet injector or massive gas injection system) will have to be installed in a protected location behind the blanket to ensure sufficient lifetime and reliability in the neutron environment. It will remain an important open issue for the further development of the DEMO physics basis [4.4] to devise a plasma scenario with sufficiently reduced disruptivity to develop the DEMO device as a whole towards stable operation with almost no disruptions and achieve a design which provides a certain level of resilience towards the disruptions that cannot be avoided.

High confinement plasma scenarios with a large gradient in plasma pressure near the separatrix often show edge localized modes (ELMs), i.e. an instability which periodically expels up to 20 percent of the pedestal energy within a short time scale towards the plasma-wetted parts of the first wall and the divertor. To estimate the situation for DEMO, assume a typical pedestal energy of $W_{\mathrm{ped}} \approx 300$ MJ, an ELM duration of $\tau_{\mathrm{ELM}} \approx 0.2$ ms and an ELM energy deposition width at the divertor of ~20 cm (i.e. spreading of the energy deposition in the divertor by a factor 4 as compared to the stationary heat distribution [4.28]). Under these assumptions, the maximum heat impact factor amounts to $\eta_{\mathrm{ELM}} \gg 0.2\, W_{\mathrm{ped}}/A_{\mathrm{eff}}/\sqrt{\tau_{\mathrm{ELM}}} \gg 240\ \mathrm{MJ} \cdot \mathrm{m}^{-2} \cdot \mathrm{s}^{\frac{1}{2}}$, which exceeds the surface damage limits for bulk tungsten [4.29] by a factor 40 to 80. ELM mitigation factors of this magnitude within ELMing discharges have not yet been experimentally demonstrated over long periods of time [4.30]. Clearly, the avoidance or mitigation of ELMs down to tolerable levels represents a significant challenge for plasma control, aiming for reliable operations over long periods. It is currently assumed that a plasma scenario which is either free from ELMs or features only small ELMs will become available for DEMO such that ELM mitigation techniques can be applied to meet the requirements for maximum transient loads to the divertor and first wall. Candidate actuators for ELM mitigation are the pellet injection and edge magnetic perturbations induced by error field coils [4.30, 4.31].

Within the current WPDC project, the specific developments towards the control of core MHD instabilities are still at an early stage. Clearly, a good spatial coverage by diagnostics with high temporal and spatial resolution will be needed to be able to detect any MHD modes early enough. In addition to the in-vessel coil based magnetic sensors

described in the above, a dense coverage of the core plasma with microwave reflectometry and/or ECE measurements is foreseen. Infrared interferometry/polarimetry and even the neutron/gamma diagnostics may contribute as well for mode detection; the latter one in particular for slowly evolving modes (e.g. neo-classical tearing modes, NTMs).

Finally, impurity events represent a major concern for DEMO control since the addition of a few milligrams of tungsten (the dominant first wall element) to the core plasma can already drive the radiation levels to the limit and trigger a disruption. Fast detection of changes in the tungsten radiation level in the plasma edge region is foreseen via VUV spectroscopy. Possible counter-measures include the reduction of impurity seeding and the increase of auxiliary heating. The first numerical studies have been undertaken [4.32] and will be further refined to explore the boundary conditions under which the plasma operation can be maintained in case of impurity events.

4.1.3. Initial suite of diagnostics for DEMO plasma control

This section exposes the methods and channels comprising the initial DEMO diagnostic suite. Preliminary integration strategies are also discussed.

4.1.3.1. Microwave diagnostics (reflectometry and ECE)

Microwave reflectometry will be used to measure the plasma density in the gradient region and assess the position of the plasma boundary (gap control), while ECE will provide the plasma (electron) temperature profile. Additionally, both measurements are well-suited for the fast detection of MHD modes and instabilities in the plasma. The frontend components for microwave reflectometry and ECE measurements consist of horn antennae and waveguides made of EUROFER (ferritic steel) with a tungsten coating (for protection and improved electrical conductivity). The irradiation conditions and thermal loads will be like those of the blanket first wall (the antennae are only slightly retracted from the first wall level).

For microwave reflectometry, many antennae will be implemented into two full poloidal sectors (i.e. 2 × 16 locations, each with 4 to 6 antennae). These will serve for position and shape control (gap control) as well as the determination of the plasma density profile (control of the pedestal top density against the density limit). They will also contribute to MHD detection at least in the outer radial region of the plasma. Near the plasma mid-plane, the single pair approach for emitting and receiving antennae will provide good spatial resolution. However, the curvature of the plasma (incidence angle variations) will cause significant problems for the operation and accuracy of reflectometry measurements near the upper and lower side.

The primary integration approach implements the so-called dummy poloidal section concept [4.33], i.e. a full banana-shaped housing with toroidal dimension of 20 to 30 cm carrying the antennae and routing the waveguides towards a vertical port. This dummy poloidal section might be integrated with an entire breeding blanket sector. Whenever the blanket will be exchanged, the microwave waveguides will have to be disconnected near the vertical port. The entire breading blanket sector is then removed together with the dummy poloidal sector by a procedure like that used for the blanket banana exchange. A new breading blanket sector is then inserted and, finally, the waveguides are reconnected to the extensions via the vertical port.

For the ECE temperature profiles and MHD control measurements, a sufficient spatial resolution can only be obtained when measuring from the outboard mid-plane side of the plasma [4.34]. Accordingly, the ECE antennae will be integrated into equatorial ports. Two slim drawers in different equatorial port plugs are foreseen to host the ECE antennae and route the waveguides to the backside, with feedthroughs near the port plate. Additional ECE channels are needed near the ECRH launchers for mode detection and control. For this purpose, it is proposed to integrate two ECE channels into each of the ECRH port plugs using a scheme like that used for the port based ECE antennae described above.

4.1.3.2. Magnetic coil based diagnostics

As discussed above, magnetic coil based diagnostics have a wide range of applications comprising the measurement of plasma position and shape, diamagnetic energy, plasma current, loop voltage and the detection of MHD modes and instabilities. A large number (~360) of coil based magnetic diagnostics (e.g. Mirnov coils, saddle coils) will have to be integrated into the machine in between the blanket backside and the vacuum vessel to provide measurements with sufficient time resolution to be used for plasma position and shape control, and to contribute to MHD mode detection. Such magnetic sensors consist of cabling and metallic housing as well as ceramic insulators. However, the durability of these sensors still needs to be assessed regarding the long-term stability of the measured signals. Under DEMO conditions, fluences up to 10^{25} neutrons per square meter (~10 times the ITER value) are expected behind the blanket on the outboard side, while up to 10^{26} neutrons per square meter are expected on the inboard side. The temperature range is in the order of 300 to 400°C (water-cooled blanket) or 400 to 500°C (He-cooled blanket). The

adverse effects arising from the irradiation of the magnetic coil based sensors (RITES, TIEMF) will be accordingly higher than on ITER and will result in spurious voltages (e.g. from thermoelectric effects), which will be integrated together with the magnetic signals over plasma pulses more than 10 times longer than for the $Q = 10$ scenario on ITER. Moreover, the nuclear heating of the connecting cables for these sensors needs to be assessed.

Low temperature co-fired coils (LTCC) technology has recently been proposed as a more reliable alternative to the standard concept of mineral insulated cable (MIC) coils. LTCCs rely on gold-based metallic pastes for the conducting lines on a substrate of insulating ceramic material. The sensor housing provides mechanical support and the electrical connections. The connection system for the in-vessel coils should meet the following functional requirements:

1) mechanical attachment to the supporting structure (backside of the blanket or vacuum vessel);
2) electrical connection to the in-vessel wiring;
3) heat transfer to the supporting structure.

The primary integration scheme for these magnetic pick-up or saddle coil diagnostics would be to mount the sensors at either the backside of normal blanket modules or the backside of dummy poloidal sectors shared with the microwave diagnostics. All cabling would be routed along the backside of the breading blanket sector (or dummy sector) towards the feedthroughs at the vertical port. As compared to mounting the sensors at the inner vessel wall, these approaches would have the advantage that a replacement of the complete systems would be possible during any blanket exchange (disconnecting all cables, taking out the bananas, installing new bananas and reconnecting the cables). Integration details like cable attachments, (passive?) sensor and cable cooling, and the durability against forces during disruptions are still to be defined.

Another large number of magnetic coil based diagnostics will be mounted outside the vacuum vessel[17]. Due to eddy-current shielding from the vessel, these sensors will have a time resolution which has been shown to be insufficient for the control of fast events (e.g. vertical displacement events, VDEs), thus cannot replace the in-vessel sensors [4.18]. Ex-vessel sensors will rather be used as a slow but precise backup measurement, which can e.g. be used for calibration purposes of the in-vessel diagnostics (e.g. integrators). The ex-vessel coil based diagnostics comprise pick-up or saddle coils, Rogowski coils for plasma current measurements, diamagnetic loops to measure the diamagnetic energy of the plasma, and flux loops for the measurement of the loop voltage.

The main adverse effect caused by irradiation on the in-vessel magnetic coil sensors is the development of small spurious currents or voltages (caused e.g. by thermoelectric effects), which are superimposed to the low signals originating from changes in the plasma. Integrating these signals over long pulse durations may lead to a loss of information over time (e.g. those may appear as drifting values of plasma position). It may be investigated whether such effects can be overcome using pairs of sensors with alternating winding orientations, or by on-line recalibration based on signals from undisturbed ex-vessel sensors or by alternative diagnostics such as reflectometry.

It should be noted here that on ITER quite a few additional in-vessel magnetic sensors will be mounted for technical purposes such as the measurement of halo or eddy currents in the blanket or divertor modules, which may be generated by disruptions. Such sensors are not treated in this text since they are not required by the plasma diagnostic and control concept for normal operation. However, should such sensors be needed on DEMO, they will be subjected to strong deterioration from irradiation effects hence their implementation would not be straightforward.

4.1.3.3. Hall sensors

Up to 240 in-vessel Hall sensors may be integrated into the machine with a similar technical approach as for the in-vessel magnetic coil based sensors. As compared to coil based magnetic measurements, Hall sensors do not need any time integration of signals hence could provide stable measurements of the magnetic field over long periods of time. However, technical issues with the temperature dependence of the Hall constant and with the low signal voltage need to be addressed [4.35]. Specifically, an accurate measurement of the local temperature of the sensor is needed to correct for the temperature dependence of the Hall constant. Thus, for each Hall sensor, a total of six cable wires have to be provided. Like for the coil based magnetic diagnostics, the long-term applicability of in-vessel Hall sensors will depend on their durability against DEMO relevant loads, which still needs to be demonstrated. In addition, up to 360 ex-vessel Hall sensors are foreseen to provide long-term stable signals without suffering from the degradation arising from neutron irradiation, however at the expense of a reduced time resolution due to the eddy current shielding from the thick vacuum vessel.

The metallic Hall sensors in question consist of a thin metal film (e.g. bismuth, gold, molybdenum) on a ceramic substrate (Si3N4, AlN or Al2O3) and the cabling (copper with ceramics insulators). As for the in-vessel coil based sensors, the typical expected fluences are up to 10^{25} neutrons per square meter on the outboard side and up to 10^{26}

[17] Ex-vessel sensors do not present any in-vessel integration issues hence will not be covered in detail in this section.

neutrons per square meter on the inboard side. The temperature range is in the order of 300 to 400°C (water-cooled blanket) or 400 to 500°C (helium-cooled blanket).

A preliminary experimental assessment of the endurance of Hall sensors based on high-temperature nano-sized metal gold and molybdenum films has been performed. The results confirm the reliable stability of the signals in a DEMO-relevant radiation environment up to fluences of 10^{24} neutrons per square meter and demonstrate that such values remain below the operational limit. For the future, irradiation testing at an appropriate neutron source will be needed for fluences up to 10^{25} and 10^{26} neutrons per square meter, which are the relevant values for a sensor located behind the DEMO blanket at the outboard and inboard side, respectively.

The integrated magnetics approach [4.36, 4.37], which combines a magnetic coil and a Hall sensor into one construction, will minimize the influence of the negative effects arising from each kind of sensor, namely: the spurious voltages caused by the radiation effects in the magnetic coils based sensors and the temperature dependence of Hall constant in the Hall sensors. Prototypes of integrated magnetics with semiconductor Hall sensors have been tested in JET within the radiation-hard Hall probes project [4.38] under the EFDA JET-EP2 enhancement programme.

4.1.3.4. Spectroscopic and radiation measurements

For power exhaust and burn control, a precise measurement of the radiated power in core, edge, X point-region and divertor plasma is mandatory. Furthermore, for detachment control, the existence of an ionization front in the divertor plasma has to be monitored via detailed spectroscopic analysis of the plasma. This analysis may also yield information on the local tungsten erosion in the divertor, which needs to be minimized to achieve a high availability of DEMO. Direct measurement of the divertor target temperature via thermography would be quite desirable as an alternative route for heat load control. However, the required observation angles (> 30 degrees against the target surface) will not be achievable by far distance viewing if a divertor dome of usual dimensions is installed (due to shadowing). For all divertor views, it remains to be clarified how far one can rely on the toroidal symmetry of divertor radiation, i.e. how many toroidal locations should be monitored such that any overloading of one of the divertor targets can be safely excluded.

To facilitate the feedback-control of the influx of gaseous seed impurities (for radiation control) the intensities of the impurities' most prominent spectral lines should be measured; preferably from the edge plasma, where the fastest response of signals can be achieved (at impurity transport time scales). Central accumulation of high-Z impurities can be identified based on intensity ratios between spectral lines radiated from plasma core and plasma edge, respectively. This requires the use of core X ray spectroscopy to access relevant ionization stages at the high plasma temperatures in DEMO. Finally, the foreseen first wall protection limiters may need to be monitored with respect to wall loads, erosion and wall temperature. The latter measurement may also serve as an additional input to control the plasma shape and position (using the criterion of equal loads on all limiters).

The most vulnerable front-end components of spectroscopic and radiation diagnostics are the first mirrors, which serve to transmit the light from the plasma towards the backside of the machine, where secondary mirrors may be located to guide the light towards detectors or spectrometers located outside of the vacuum vessel. Considering the large fluences expected on DEMO, the deterioration of mirror surfaces by erosion and deposition of plasma particles can only be minimized by mounting the mirrors behind long thin ducts with a large length-to-diameter L/D. According to recent modelling results [4.39], the eroded layer can be kept smaller than about one tenth of the wavelength per full power year if a duct with a ratio of $L/D > 30$ is used in the infrared range, $L/D > 40$ in the visible range and $L/D > 50$ in the VUV wavelength range. Additionally, the nuclear heating of the mirrors should be reasonably limited to preserve the integrity of the optical imaging, even when assuming metallic mirrors with active cooling. These erosion and nuclear heating issues practically rule out the use of mirrors mounted in forward position. Under these conditions any wide-angle viewing or imaging optical schemes seem unfeasible (e.g. the ITER wide-angle viewing system or the ITER core CXRS diagnostics). Within the DEMO plasma, profile information or a wide coverage of large areas can only be accomplished by installing several individual narrow (large L/D) sightlines with all first and secondary mirrors mounted in backward positions.

For any of the above spectroscopic and radiation measurements, a large number of individual sightlines will be needed to achieve the spatial coverage required for all foreseeable plasma conditions and obtain the level of redundancy needed to ensure a reliable operation of the machine. Each of the foreseen (~150) sightlines consists of a straight metallic duct (with metallic baffles), typically 3 to 5 cm in open diameter and 1 to 2 m in duct length. For most sightlines, a first metallic mirror will also be installed behind the duct. The mirror surface materials have to be defined according to the wavelength range of interest. For the visible wavelength range under erosion-dominated conditions, single-crystalline rhodium appears to be a promising option providing high reflectivity even when removing a surface layer up to 1 μm [4.40]. In the vacuum ultraviolet range, gold and platinum are prime mirror

materials providing high reflectivity down to 15 nm, under near normal incidence conditions, and down to ~1 nm, under grazing incidence conditions. In the case of X ray spectroscopy, a perfect crystal (quartz or silicon) will serve as the most forward component, where the distance to the first wall could be in the range of 3 to 6 meters in duct length so that radiation induced damage should be of minor importance. It remains to be defined whether radiation power measurements will use mirrors, which will depend on the location of the sightlines and the choice and location of the detectors. In all cases, mounting the detectors outside the vacuum vessel would facilitate their replacement in case of failure.

At the location of mounting of the metallic first mirrors (behind the blanket) the typical expected fluences are up to 10^{25} neutrons per square meter (outboard side). The temperature range is in the order of 600 to 700 K (water-cooled blanket) or 700 to 800 K (He-cooled blanket).

For many of the sightlines, in particular those involving X ray, VUV and total radiation measurements, high-vacuum extensions are needed up to the detector since the radiation would otherwise be absorbed by e.g. windows or the gas in the beamline. Together with the neutron/gamma diagnostics, this results in over 100 vacuum extensions beyond the port plates. Window-type interfaces near the port plates may only be applicable for the visible and infrared sightlines if a reasonable technical solution for the windows can be found. If not, vacuum extensions may at least be applicable to most of the visible and infrared sightlines.

4.1.3.5. Polarimetry/Interferometry

IR laser interferometry and/or polarimetry is foreseen for the measurement of the central plasma density. The general layout of the beams will either follow the ITER toroidal interferometer/polarimeter (TIP) approach [4.41] or the ITER poloidal interferometer/polarimeter (PoPola) [4.42] approach.

The front-end components would consist of metallic mirrors (high reflectivity in the IR range[18]) mounted at 0.6 to 2 m behind the first wall and protected by a long straight duct, i.e. a metal tube with metallic baffles. At the location of the port plates or further out (e.g. when using a vacuum extension) an IR window (e.g. a diamond window) will be needed for each incoming laser beam.

If the toroidal interferometer concept is chosen for DEMO, each beam's first mirror and end mirror (retroreflector) will be in different ports (equatorial, vertical or both) with oblique sightlines through the plasma. Restricting ourselves to the use of equatorial ports would effectively limit this approach to provide only 3 to 4 physically different sightlines (due to shadowing from the central column). A few more physically different sightlines may become available if the retro-reflectors are mounted in one of the vertical ports. These oblique sightlines in the equatorial and vertical ports will occupy a relatively large space. These could block the insertion of radial "drawers" into a major part of the port plug. A factor two of redundancy in the number of sightlines should be foreseen.

If the poloidal interferometer approach is taken, a fan of rays could be implemented in a (almost) poloidal plane with ducts integrated into a small slice of volume (20 cm in the toroidal direction) within an equatorial port plug containing all first mirrors. The end mirrors (retro-reflectors) would be mounted behind the blanket at the high field side (HFS). Since the duct length on the inboard side would be limited by the blanket thickness (~60 cm), the HFS mounting of retro-reflectors would result in a smaller L/D ratio (given a beam diameter and required lateral alignment tolerances), hence a lesser mirror protection. Furthermore, the opportunities for maintenance on the HFS would be more restricted as compared to the port based mounting. However, the poloidal beam arrangement would provide the advantage of having a larger radial coverage of the plasma, which would allow the use of these measurements for vertical plasma control e.g. during the start-up and ramp-down phases of the discharges when the plasma cross section is not fully developed and reflectometry measurements would suffer from the large distance between the plasma and the antennae.

4.1.3.6. Neutron/gamma diagnostics

For the measurement and control of the fusion power, a neutron flux measurement will be implemented comprising a set of 2× 10 horizontal sightlines (equatorial ports) and an additional set of 2×10 sightlines from the vertical port (wider coverage of radial range, and coverage of Shafranov shift effects), where the factor two provides some redundancy. During the burn phase, these measurements may also contribute to the plasma position control. In addition, the D/T ratio and ion temperature can be deduced from neutron/gamma spectroscopy. Initial assessment of the performances of these neutron flux monitors indicates that the fusion power can be calculated with a relative error of less than a few percent on a time scale of less than 10 ms, and that the neutron emissivity profile can be reconstructed up to 0.9 normalized poloidal flux coordinates with the same time resolution and a relative error less than 1%. At the

[18] Candidate materials need to be selected.

same time, DT ratio and ion temperature can be determined with a time resolution of 1 second. It remains to be clarified whether the additional gamma-ray spectroscopic measurements can be taken by using (sharing) the sightlines of the neutron flux measurement (without a significant reduction of their performance), and which measurement performance could be achieved. The front-end of each channel consists of a long duct less than 7 cm in inner diameter. A detector (or a series of detectors) will be mounted at the far end of each collimator, outside the bio-shield, at a distance greater than 15 m from the front collimator. EUROFER is considered as the main material for the collimator tube surrounded by boron carbide B4C. The composition of the collimator towards the detector can include material for in-scattered neutron moderation (concrete) doped with thermal neutron absorbers and gamma-ray attenuator material. The sightlines can be integrated in a poloidal plane such that the space occupation in the ports is minimized. Specifically, the sightlines from the equatorial port can be integrated into drawers. At the location of the detectors (several meters away from the first wall), the irradiation levels are low enough such that no adverse effects on the detectors are expected.

4.1.3.7. Divertor thermo-current measurement

For the DEMO power exhaust control, the thermo-current has to be measured at several divertor target plates. This measurement can be used as a reliable indicator of plasma detachment since the sheath voltage, and hence the thermo-current, should vanish under low plasma temperature conditions in front of the divertor target. This principle of plasma detachment control has been successfully demonstrated on the ASDEX upgrade tokamak [4.43]. On DEMO, such measurement requires the use of (ceramics) insulators to electrically isolate the divertor cassette (or major parts of it) against the vacuum vessel. The durability of these insulators under the neutron load conditions in the DEMO divertor area has to be verified. The temperature range is in the order of 500 to 600 K (assuming a water-cooled divertor). The integration issues for this measurement are limited to the divertor target, cassette and divertor (lower) plugs.

4.1.4. Actuator properties as relevant to plasma control

The essential actuators available for plasma control are the magnet system (poloidal field coils and central solenoid), the auxiliary heating system, and the gas injection (fuel and impurity gases) and pumping system. The main properties are qualitatively summarized below. Six poloidal field (PF) coils will be installed on DEMO to control the equilibrium (plasma shape and position), which depends on the magnetic field configuration together with the plasma pressure profile. The central solenoid (CS) coil provides most of the flux needed to drive the plasma current over the projected burn time of 2 hours. The CS coil consists of several sectors in a “pan-cake” like arrangement, which can be controlled independently. The total available flux will be in the range of several hundreds of volt-seconds, while the maximum rate of change will be designed such that a toroidal electric field of 0.3 $V.m^{-1}$ can be sustained for a few seconds to facilitate the ignition of the discharge. For the case of a fast (emergency-type) ramp-down of the plasma current, a power limitation in the order of 100 MW and a voltage limitation in the order of 5000 volts for the CS coils correspond to a minimum ramp-down time in the order of 10 to 20 seconds. The auxiliary heating system to be installed on DEMO is not yet fully defined. The main control tasks of the auxiliary heating system are the following:

- Heating during the plasma initiation and current ramp-up, including overcoming the H-mode threshold.
- Burn control, impurity control and instability control during all plasma phases.
- Plasma handling in case of unforeseen events such as impurity events or component failures.
- Wall conditioning, if applicable.

It is generally assumed that the auxiliary heating system will include an electron cyclotron resonance heating (ECRH) subsystem comprising 50 to 100 gyrotrons, launchers and the corresponding transmission lines. It may also include a neutral beam injection (NBI) subsystem, consisting of two to three NBI boxes, as well as an ion cyclotron resonance heating (ICRH) subsystem, a lower hybrid (LH) heating subsystem, or both. The final suite of heating systems will depend on the details of the plasma control requirements, which in turn depend on the details of the DEMO plasma scenario that are not fully defined yet.

4.1.5. Critical open issues: Avoidance and mitigation of disruptions

One of the most critical issues for the operation and control of the DEMO plasma is the avoidance and mitigation of disruptions. Extrapolating from JET [4.44] and ITER [4.45], in a disruption on DEMO up to 50% of the thermal plasma energy of ~1 GJ would be released to the first wall within the short thermal quench period of ~1 ms. If this energy is distributed over the entire first wall area (~2000 m^2) with an inhomogeneity factor of 3 to 4 — usually referred to as the case of perfect disruption mitigation — the resulting heat impact factor amounts

$\eta = W_{\mathrm{th}}/A_{\mathrm{eff}}/\sqrt{\tau_{\mathrm{TQ}}} \sim 30\ \mathrm{MJ}\cdot\mathrm{m}^{-2}\cdot s^{\frac{1}{2}}$. This represents about half of the value needed for bulk tungsten melting starting from the DEMO operational temperature (300 to 500°C), but significantly exceeds the limit for surface crack formation. It remains a subject of future R&D to determine how many of such events the first wall and divertor of DEMO could withstand. Obviously, since even well mitigated disruptions on DEMO may lead to large area wall damage, disruption avoidance should have highest priority on DEMO. In the following, a brief list of the main root causes for disruptions is presented and the envisaged counter-measures from the point of view of DEMO control are explained:

1) The vertical plasma position in a divertor tokamak is, in principle, unstable. The plasma current centroid is subject to attractive forces from both poloidal field coils, located above and below the plasma, which grow inversely proportional to the distance from the centroid to the respective coils. If a deviation from the nominal plasma position is recognized too late, the counter-action by the poloidal field coils may come too late to prevent the plasma from touching the wall and (eventually) disrupting. The risk for this type of disruptions can be minimized by limiting the plasma elongation and shaping — which unfortunately reduces the fusion performance — and by optimizing the control system with respect to performance (accuracy and speed) and reliability of measurements and actuators.
2) Various types of MHD instabilities can occur causing a loss of confinement quality and eventual disruptions. This concern is particularly important when operating the plasma near the operational limits of the machine. Clearly, these paths to disruptions can be avoided by providing means for early and reliable recognition of any evolving instability and by defining the plasma parameters with sufficient margins against operational limits.
3) Failures of the control system (component or system failure) may also lead into disruptions. Here, a systematic improvement of the reliability of all parts of the control system is needed. Depending on the achievable level of reliability, a certain level of redundancy with respect to both the number of systems and channels and the number of methods should be installed.
4) In principle, disruptions arising from human error in the operation of DEMO and its control system should be minimized by operating DEMO within a single stable discharge scenario only. However, before this ideal point can be reached, many components will need to pass rigorous testing and validation procedures, and many operational issues will first have to be demonstrated on ITER. The commissioning phase of DEMO will then have to follow a step-by-step approach, where the operational parameters will be gradually adjusted towards their final values.
5) Unforeseen events, e.g. big impurity events, wall damage with coolant ingress or the quench of a superconducting magnet are a matter of concern. Beyond a certain size or speed of the event, the disruption cannot be avoided at all and the control system could only (if at all) reduce but not avoid the damage. Therefore, the minimization of the risk of such events should have high priority in the DEMO design, which means aiming for robust and reliable components, low wall loads and a low amount of accumulated dust.

In designing DEMO, the choices aiming to reduce the likelihood of the above-mentioned disruption causes will be constrained by cost. It should also be noted that the operation of DEMO during the commissioning phase may be subject to a higher disruptivity since the necessary fine-tuning procedure towards the final stable plasma regime with good performance will include a final experimental verification at operational conditions which will be realized for the first time; and naturally associated with a certain failure rate.

4.1.6. Summary and conclusions

The development of the diagnostic and control system for a future tokamak demonstration fusion reactor (DEMO) is a challenging task, which comprises a variety of physics and technology elements with interfaces to many areas of the overall DEMO design. The requirements for reliable and stable plasma control on DEMO are much higher than on any existing fusion device since DEMO should achieve a certain overall availability and because of the risk of severe damage to the inner DEMO wall in case of plasma disruptions and other transient events. A limited set of diagnostics and actuators will be available to control the DEMO plasma scenario, the detailed parameters of which are not yet fully defined. Novel integrated control techniques may help achieve a reliable control based on a limited set of measurements and actions, in particular by providing an accurate forecast on the evolution of the plasma state based on sophisticated modelling.

Obtaining a quantitative understanding of DEMO control is a prerequisite to achieve the required control reliability. For this purpose, the performance of control components and the overall control system has to be analysed by quantitative simulations and, where needed, validation experiments on the feasibility of specific approaches.

For many plasma parameters, the DEMO operational point will have to obey control margins (distance from operational limits), the size of which will depend on the achievable accuracy of the control system. In this regard, the

feasibility of the DEMO control system will have a strong impact on the overall DEMO design since larger control margins lead to a lesser fusion power, which could only be compensated by enlarging the dimensions of the tokamak. An iterative approach should thus be followed, wherein the DEMO physics and technology basis, the design details and the development of the diagnostic and control system are pursued in parallel.

4.2. BAYESIAN DATA ANALYSIS IN FUSION EXPERIMENTS

Magnetic confinement fusion experiments generate large quantities of complex data. At a basic level, the data reflects the state of the machine and plasma, enabling a safe and reliable operation of the device, i.e. well within the design limits of the machine and compatible with the scientific goals of the experiment. In addition, the data is an essential ingredient to interpret the experiment at a higher level, increasing the physical understanding of the various plasma processes and their interaction with the device.

In a fusion reactor, most of the data will be used for machine operation. The main criteria will be safety and plasma performance, maximizing the fusion output. Modelling codes produce even more data, which needs to be compared to the experimental results. Depending on the requirements, different analysis techniques are needed to extract as much useful information as possible from the raw data. This ranges from very basic tools for signal resampling or motion correction in images to more advanced statistical analysis or pattern recognition methods. As the available computing power increases, real-time high-level data analysis also starts to become feasible for plasma control.

The throughput volume and complexity of fusion experimental data demand special attention for the analysis. As an illustration, the JET experiment presently generates ~55 GB of data per pulse and ITER will produce up to 1 TB in each discharge. The complexity of the data has two fundamental causes: the fusion plasma is an extremely complex physical system and a hostile environment, difficult to probe. Put differently, the variables characterizing the plasma usually interact in an intricate, nonlinear way and their measurements can be affected by considerable uncertainty. Furthermore, different diagnostics may provide information on the same plasma quantity, resulting in a certain degree of redundancy that can be exploited for the purpose of integrated data analysis, but may also entail issues of data consistency and heterogeneity. Modern information science can play an important role in the improvement of data accuracy and robustness and the unravelling of useful physical quantities or relations from the data.

Curiously, modern tools from probability theory and machine learning have only recently been applied in fusion experiments and remain uncommon. The situation is quite different in other data-intensive disciplines of the physical sciences (e.g. high energy physics, astronomy and ecology), where advanced techniques have been part of the common practice for many years. Therefore, in fusion science the development and application needs to be stimulated of state-of-the-art techniques based on probability theory and machine learning to address complex data analysis problems. The goal should be to raise the part of the scientific process related to data analysis to the same high level as the experimentation, modelling and theory building.

This section will have a closer look at some basic techniques from Bayesian probability theory and integrated data analysis (IDA) that have recently entered fusion science. We do not strive for comprehensiveness, rather mean to give a flavour of several typical methods and references to further readings, which will hopefully prove useful to the beginning practitioner.

4.1.6.1. Frequentist and Bayesian approaches to probability

We begin the discussion with a short note about the view we choose to adopt on probability. Over time, various interpretations of probability have been proposed, the most popular by far being the frequentist and the Bayesian approaches. Both interpretations come with their associated set of methods and tools, although practices vary across disciplines (e.g. social sciences vs. physical sciences). In addition, there exist various flavours of Bayesian thinking, some of which are half frequentist and use frequentist terminology. However, in the physical sciences and fusion in particular, the objective Bayesian point of view has come to prevail. In the spirit of [4.46, 4.47], this approach considers probability theory as an extension of logic to uncertain propositions. The theory is based on a set of common-sense axioms (or desiderata), including the basic requirement of consistency. In other words, different observers should arrive at the same conclusions when provided the same information. From this point of view, a probability always depends on two pieces of information: the proposition or hypothesis A, the probability of which is sought, and the information B, conditioning the probability. The standard notation used to denote such a probability is $P(A|B)$ and corresponds to a real number in the interval $[0,1]$ expressing the plausibility of A provided B is true. Put differently, it is a measure of the extent to which B implies A. As such, a probability denoted by $P(.|.)$ always has

two slots that need to be filled to produce a meaningful numerical output. The conditioning information B can be a problem statement, some measured data or any other available background information. The whole of information on which a probability statement is conditioned is often summarized by the generic symbol I, e.g. $P(.|I)$. Specific additional information conditioning the probability may be stated explicitly, e.g. $P(.|B,I)$.

The classical frequentist definition of probability is based on the frequency of an event in the long run and necessitates identical repeats of experiments or ensembles of the system under study. As such, it contrasts with the Bayesian interpretation, which enables a direct evaluation of the probability of any statement or single event. Examples include the probability of the plasma density in a fusion machine being within certain bounds or the probability that a plasma is in the H mode. In the Bayesian view, probabilities are useful whenever there is a general lack of certainty, e.g. regarding the details of plasma particle trajectories causing fluctuations in the macroscopic quantities or the electron thermal motion in a detector introducing noise in the measurement. No appeal is made to any notion of 'randomness' and although the term 'random variable' occurs in some Bayesian literature, we will avoid it. Neither will we follow the habit of using capital letters to denote random variables since, from our point of view, the information carried by any physical variable is subject to uncertainty. Furthermore, while the concept of a statistic as a function of the data is technically well-defined, its definition is not required in Bayesian analysis. Indeed, whereas the field of statistics is essential for frequentist inference and some practitioners of (partly) Bayesian methods use the term 'Bayesian statistics', frequentist terminology is better not used to avoid confusion. This approach is adopted by several excellent textbooks on Bayesian probability theory geared to physicists; see [4.47, 4.48, 4.49, 4.50].

4.1.6.2. Bayesian diagnostic modelling and integrated data analysis

An important application of Bayesian probability theory (BPT) that has gained considerable use within the fusion community can be found in fusion diagnostics modelling. This practice is motivated by the frequent and substantial uncertainties entering the derivation of physical quantities from raw (measured) data, often a voltage at a sensor. Without proper measures, these uncertainties can enhance and complicate the total uncertainty on the quantity of interest, deteriorating the quality and reliability of the result. In extreme cases the result may become meaningless, which, for instance, may occur in the calculation of profiles from line-integrated measurements through an inversion technique. Not only is this problem heavily underdetermined (multiple solutions fit the data), but the noise on the line-integrated measurements also propagates through the inversion and generally worsens the result. Limiting the number and smoothness of the solutions by regularization techniques is the standard solution, but further improvements are often possible. BPT offers a solid and coherent framework for better profile reconstruction. It consistently handles any kind of uncertainty by assigning probabilities (or probability distributions) and manipulating them using a set of well-defined rules. One of these is Bayes' rule — hence the designation 'Bayesian probability theory' — which will be introduced below. The result of a Bayesian calculation is a probability (distribution) for the quantity of interest or a hypothesis, depending on the available information.

A related application is integrated data analysis (IDA), involving the combination of heterogeneous data sets from multiple sources, such as fusion diagnostics. By modelling each diagnostic in the Bayesian framework, a probability for a specific plasma quantity can be derived that is consistent with the data from all diagnostics involved in the analysis. So, in case multiple diagnostic measurements contain information on a certain plasma quantity (e.g. interferometry and Thomson scattering on the electron density of a plasma), it becomes possible to exploit the advantages of each diagnostic, hence improving the quality of the estimate for the desired plasma quantity. This quality can be reflected in smaller error bars, higher resolution or enhanced robustness, since the analysis involves information from diagnostics that are based on different measurement principles or different hardware components.

4.1.7. Concepts of Bayesian probability theory

In this section, some basic concepts from Bayesian probability theory are introduced. This is done in the context of a simple example involving the estimation of the parameters of a normal distribution based on suitable prior information and the repeated measurement of a physical quantity.

4.1.7.1. Bayes' rule

In fusion, as in many scientific activities, one does not have direct access to the physical properties of the plasma. Instead, the experimentalist devises a measurement technique for a diagnostic, which returns numbers (usually voltages) that are related to the quantity of interest. If the properties of a physical system were known precisely, together with the full details of the measurement process, the corresponding measurement values could be computed straightforwardly. This would require the measurement process to be encoded in a mathematical model: the forward model (see Section 4.2.6). However, since the microscopic details of the physical system and the measurement process

are unknown, the raw measurement itself is never a truly precise number.[19] It may nevertheless be possible to model this uncertainty by assigning a probability for the measured value to lie within certain bounds. Representing the measurement by a real number x, it is convenient to introduce the probability density function (PDF) of x.[20] The PDF is usually denoted $p(x|I)$, where $p(x|I)\mathrm{d}x$ can be interpreted as the probability to find the measurement value between x and $x + \mathrm{d}x$, given the background information I.[21] Strictly speaking, for continuous variables, the term distribution function refers to the cumulative distribution function; it is nevertheless used colloquially to denote the PDF. To indicate that a variable x is assumed to be distributed according to (or sampled from) the model with PDF $p(x|I)$, one writes $x \sim p$. By convention, a PDF is always normalized to 1 ('certainty'), meaning that, when integrating over the full range of the variables, the result should be 1. One of the most common models is the normal or Gaussian distribution, the density function of which is the well-known function:

$$p(x|\mu,\sigma,I)=\frac{1}{\sqrt{2\pi}\sigma}\exp\left[-\frac{(x-\mu)^2}{2\sigma^2}\right]. \tag{4.1}$$

This is often written as $x \sim \mathcal{N}(\mu,\sigma^2)$, where μ is the mean (expectation value) of the distribution and σ the standard deviation. Note that, in the Bayesian spirit, the PDF has explicitly been written as a two-slot function $p(x|\mu,\sigma,I)$, where the second slot emphasizes that the probability density can only be calculated for known values of μ and σ. Any additional information (e.g. the fact that it is a Gaussian distribution) has been summarized in the symbol I. With the same knowledge, the probability that x is found to lie within two given bounds can be calculated by integration (involving the error function erf). Again, it is important to stress that, in characterizing the uncertainty in x, the concept of randomness has not been invoked. We simply do not know x exactly, although we claim that we have a certain idea where x can be found with appreciable probability. This viewpoint does not exclude the practical situation of a series of measurements of x, where one realization of x appears to be unrelated to any other, and where most values lie close to μ in a pattern that can be summarized by (4.1). This feature is related to the frequentist interpretation of probability. However, in the Bayesian view, the frequency distribution is an observed consequence of the underlying characteristics of the system rather than the basis for the definition of probability. The measurement uncertainties that can be described by probability models such as (4.1) are often referred to as stochastic or statistical uncertainties. This is opposed to systematic uncertainties, which result in a 'deterministic' deviation of the result from the 'correct' measurement.

An entirely different question concerns the assignment of probabilities to the parameters μ and σ, given a set of measurements for the variable x, denoted by $\boldsymbol{x}$. The solution, known as Bayes' rule or Bayes' theorem, is generally credited to Thomas Bayes (1763) and Pierre-Simon Laplace (1812). This is a direct consequence of the well-known product rule of probability theory, which in this context reads

$$p(\boldsymbol{x},\mu,\sigma|I) = p(\boldsymbol{x}|\mu,\sigma,I)p(\mu,\sigma|I). \tag{4.2}$$

Of course, the same rule also yields

$$p(\boldsymbol{x},\mu,\sigma|I) = p(\mu,\sigma|\boldsymbol{x},I)p(\boldsymbol{x}|I),$$

which, together with (4.2), results in Bayes' rule (applied to the current example):

$$\overbrace{p(\mu,\sigma|\boldsymbol{x},I)}^{\text{posterior}} = \frac{\overbrace{p(\boldsymbol{x}|\mu,\sigma,I)}^{\text{likelihood}}\overbrace{p(\mu,\sigma|I)}^{\text{prior}}}{\underbrace{p(\boldsymbol{x}|I)}_{\text{evidence}}}. \tag{4.3}$$

Thus, the rules of probability theory naturally enable the inversion of a probability. Determining appropriate values for the quantities of interest —μ and σ —from (4.3) is referred to as the task of parameter estimation. This task will be discussed in more detail below, still in the context of a normal distribution. Bayes' rule can also be interpreted in terms of a learning process. In this sense, the distribution of the parameters μ and σ is considered before the data is acquired: the so-called prior distribution, indicated in (4.3). The prior can be obtained from background knowledge about the problem or other experiments. Alternatively, one may choose an uninformative prior, which, as the term implies, allows adopting a maximally ignorant point of view before performing the experiment. However, one should be careful in keeping the problem well-posed (or identifiable), i.e. there should be sufficient information in the data and the prior to estimate the parameters with reasonable accuracy (e.g. the discussion in [4.51]). Various criteria and

[19] At a certain point, one also hits the rather philosophical question of whether there is such a thing as an 'exact value' of a (microscopic) physical quantity.

[20] We will treat only continuous variables here. This represents the most common situations in physical sciences.

[21] We will follow the common slight abuse of notation of using the symbol p to denote a specific model (e.g. Gaussian) of the probability density of a specific variable or, in general, the probability density of a variable, possibly unknown or unspecified.

methods exist to assign uninformative prior distributions, including invariance under basic transformations (e.g. translations and rotations), maximum entropy distributions in the presence of specific pieces of testable information (e.g. knowledge of the mean of a distribution), smoothness-ensuring priors for regularizing ill-posed problems and others (see [4.48, 4.49] for practical advice and [4.47] for more in-depth discussions). Whether one chooses an uninformative or informative prior, in the objective Bayesian view the prior distribution is not a subjective judgment by an individual scientist, but rather the result of quantifying the available prior information. In this sense, two individuals, given the same information prior to the experiment, should arrive at the same prior distribution, hence should obtain the same conclusions. Many practitioners use a very pragmatic rule to assign prior distributions, which is related to the analytical tractability of the posterior. This gives rise to the so-called conjugate priors, described for instance in [4.52]. However, one could object that more objective prior information is to be preferred over a criterion based on computational ease, especially as the likelihood and the experimental setup also depend, to some extent, on 'subjective' choices.

Continuing with the example of inferring the parameters of a normal distribution, a series of n measurements could next be performed, here described by $\boldsymbol{x}$. We will assume, given a common μ and σ, that the measurements are performed independently from each other. Fixed system parameters μ and σ imply stationary system and measurement conditions. Under these assumptions, the joint distribution of $\boldsymbol{x}$, conditioned on μ and σ, factorizes into a product of marginal distributions for each of the x_i components of $\boldsymbol{x}$ ($i = 1 \ldots n$):

$$p(\boldsymbol{x}|\mu,\sigma,I)=\prod_{i=1}^{n}\frac{1}{\sqrt{2\pi}\sigma}\exp\left[-\frac{(x_i-\mu)^2}{2\sigma^2}\right]. \tag{4.4}$$

This is the likelihood distribution. According to (4.3), the product of the likelihood and the prior is proportional to the posterior distribution for the quantities of interest, given the available information encoded in $\boldsymbol{x}$ and I; in the present case μ and σ. In this respect, an important observation is that, in estimating μ and σ, normalization of the posterior is irrelevant. Only the posterior's dependence on μ and σ matters, since it determines the shape of their joint distribution. For this reason, the denominator in (4.3) is irrelevant in the context of parameter estimation and may be absorbed in a proportionality constant. The denominator is referred to as the evidence since it gives the probability of the data in light of the background information, which includes knowledge about the model used for the physical and measurement systems. This term provides evidence for the model and becomes important in comparing different models. In the Bayesian approach, the task of model selection is also performed according to Bayes' rule; we will not go deeper into this topic here, but the reader may refer to [4.49].

4.1.7.2. Uniform prior distribution

Coming back to the parameter estimation problem, an adequate prior distribution has to be chosen. Let us suppose for a moment that very reliable information about the typical measurement error is available, allowing an approximation which fixes σ at a known value σ_e. This fact is included in the background information I. Eq. (4.3) can then be rewritten as the problem of determining μ from the available information. With a uniform prior distribution, it is assumed that the only prior information about μ is that it lies within some reasonable bounds: $\mu \in [\mu_{\min}, \mu_{\max}]$. For example, suppose the variable μ stands for the core electron density in a fusion device during steady-state (flat top) operation. In such case, μ can be estimated to lie within reasonable bounds, e.g. $\mu \in [10^{19}, 10^{20}]\ \mathrm{m}^{-3}$, suggesting a relatively uninformative uniform prior distribution, which, properly normalized, reads:

$$p(\mu|I) = \begin{cases} \dfrac{1}{\mu_{\max}-\mu_{\min}}, & \text{if } \mu \in [\mu_{\min}, \mu_{\max}], \\ 0, & \text{otherwise.} \end{cases}$$

This reflects the limited information available about μ before making any measurements. In fact, it is possible to pretend complete prior ignorance, in which case one would assign a uniform prior to the entire real line (via a limit process). While such a prior cannot be normalized, it suffices that the posterior be normalizable. In fact, if the interval $[\mu_{\min}, \mu_{\max}]$ is taken to be sufficiently wide, the effect of the uniform prior can simply be absorbed in the proportionality constant of the posterior. As a result, the posterior distribution $p(\mu|\boldsymbol{x}, I)$ is essentially determined by the likelihood in (4.4), which can be rewritten as follows:

$$p(\mu|\vec{x}, I) \propto \exp\left[-\frac{\sum_{i=1}^{n}(x_i-\mu)^2}{2\sigma_e^2}\right]. \tag{4.5}$$

Defining the sample average $\bar{x}$ and sample variance $\overline{(\Delta x)^2}$ as is customary,

$$\bar{x} \equiv \frac{1}{n}\sum_{i=1}^{n} x_i, \qquad \overline{(\Delta x)^2} \equiv \frac{1}{n}\sum_{i=1}^{n} (x_i - \bar{x})^2,$$

(4.5) can be written explicitly as a distribution for μ. Indeed, by expanding the sum of squares in (4.5) and subtracting and adding the term $2n\bar{x}^2$, it is easy to bring the posterior for μ into the form:[22]

$$p(\mu|\boldsymbol{x}, I) \propto \exp\left\{-\frac{1}{2\,\sigma_e^2/n}\left[(\mu - \bar{x})^2 + \overline{(\Delta x)^2}\right]\right\}. \tag{4.6}$$

The last term within the exponential does not depend on μ, thus may again be absorbed in the proportionality constant of the posterior, so that

$$p(\mu|\boldsymbol{x}, I) \propto \exp\left[-\frac{(\mu - \bar{x})^2}{2\,\sigma_e^2/n}\right]. \tag{4.7}$$

Clearly, the posterior for μ is also normal. It has a mean value $\bar{x}$ and a standard deviation $\sigma_e/\sqrt{n}$, which corresponds to the intuition that the error bar on a measured quantity should decrease when it is defined as the average over a large number n of repeated measurements. The normal likelihood PDF (4.1) – with mean $\mu = 10$ and standard deviation $\sigma_e = 2$ – is plotted in Fig. 4.1. A histogram based on $n = 20$ data points sampled from this distribution is also depicted (this data set will be used repeatedly later on). The marginal (normalized) posterior density (4.7) for μ, based on these data and a uniform prior with bounds at infinity is also shown.

FIG. 4.1. The normal likelihood PDF (4.1) for the variable x with μ=10 and σ_e = 2. A histogram of 20 samples constructed from this likelihood, and the resulting posterior PDF (4.7) for μ based on a given σ_e and a uniform prior, are also plotted.

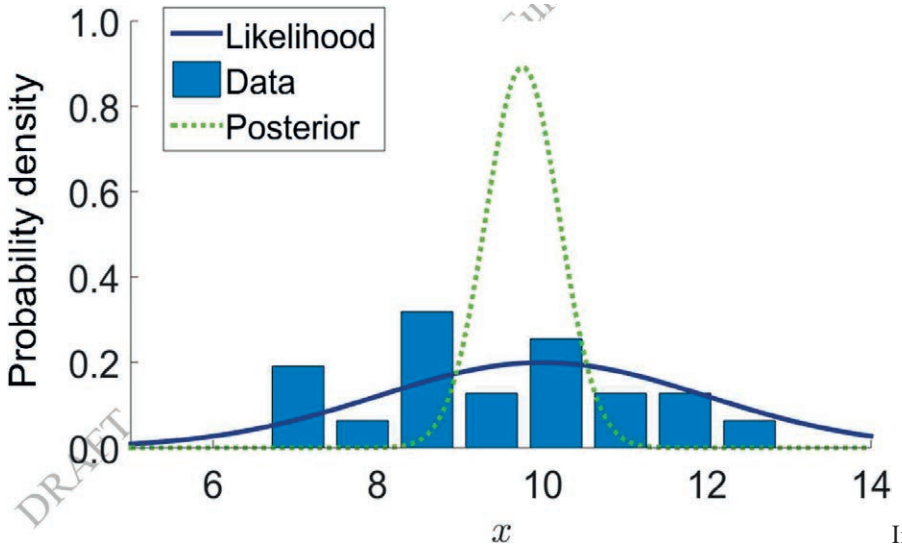

In retrospect, the best estimate for μ in terms of the sample average could have also been obtained by applying the maximum likelihood method (ML). This well-known frequentist rule states that a PDF parameter can be estimated by maximizing the likelihood of the data with respect to that parameter. In the context of the present example – in which the likelihood is given by (4.4) – this means that μ is assigned to the value that maximizes the probability density of the data. Under the assumption that the data is a representative sample of the proposed likelihood distribution, it indeed seems to be a good strategy to maximize the probability of observing the data that was in fact observed. It can then easily be verified

[22] This step is based on the well-known trick called 'completing the square'.

that the result is the sample average $\bar{x}$.[23] Note that, in maximizing a PDF, it is often analytically simpler and numerically more stable to look for the maximum of the logarithm of the distribution. Furthermore, the same result is obtained when maximizing the posterior (4.5) with respect to μ. This Bayesian technique is called the maximum a posteriori (MAP) method. In the present example, MAP yields the same result as the maximum likelihood method. This is a consequence of choosing a uniform prior and is definitely not always the case. Moreover, in the present example, the posterior distribution is Gaussian, therefore symmetric around the mean. As a result, the value of μ for which the PDF is maximum, called the mode of the distribution[24], coincides with the mean. The situation would have been different had we taken an asymmetric likelihood. Summarizing a distribution by its mean may thus yield a (considerably) different result compared to using the mode.[25]

Many practitioners introduce extra levels in the prior distribution by parameterizing them by so-called hyper-parameters. The hyper-parameters follow a hyper-prior distribution and, in principle, the hyper-prior could be modelled by hyper-hyper-parameters, and so on. Some problems are particularly well described by such a hierarchical description: think for example of the average plasma density in multiple tokamaks, in a single machine and in a single discharge.

4.1.7.3. Normal prior distribution

We are now interested in solving the same problem given a more informative prior distribution. Suppose that, before starting the experiment, there are reasons to believe that the value of μ should lie in the vicinity of μ_0. An earlier similar experiment might have pointed this out.[26] We wish to update our state of knowledge concerning μ as additional data $\boldsymbol{x}$ comes in from a new experiment. Obviously, the exact value of μ is not known. If it were, new experiments would be superfluous. A normal prior distribution with mean μ_0 and known prior standard deviation τ might suitably reflect our prior information. Together with the likelihood in (4.4), which is assumed to have a known standard deviation σ_e, it yields the following posterior for μ:

$$p(\mu|\boldsymbol{x}, I) \propto \exp\left[-\frac{\sum_{i=1}^{n}(x_i-\mu)^2}{2\sigma_e^2}\right] \times \exp\left[-\frac{(\mu-\mu_0)^2}{2\tau^2}\right].$$

After expansion, omitting the factors which do not depend on μ and completing the square, one recovers a normal posterior with mean μ_n and variance σ_n^2:

$$\mu_n = \sigma_n^2\left(\frac{n}{\sigma_e^2}\bar{x} + \frac{1}{\tau^2}\mu_0\right) \qquad \text{and} \qquad \sigma_n^2 = \left(\frac{n}{\sigma_e^2} + \frac{1}{\tau^2}\right)^{-1}.$$

The posterior mean μ_n is a weighted average of the prior mean μ_0 and the sample average $\bar{x}$. It should also be noted that, with increasing number n of observations, the influence of the prior distribution on the posterior becomes less pronounced and the posterior eventually reduces to (4.7). This observation is fairly common but it would be misleading to conclude that the prior distribution does not matter; in fact:

- Prior probabilities are an intrinsic part of Bayesian probability theory, enabling a coherent framework of learning from experience and new data.
- Including prior information is particularly important when high-quality data is scarce.
- Prior distributions are an effective instrument to regularize ill-posed problems (e.g. tomographic inversion).
- Some problems do not follow the common rule that the prior becomes less important as more data arrives, e.g. regression analysis with substantial measurement errors in both the response and predictor variables, see [4.49].

4.1.7.4. Unknown standard deviation

Until now, the standard deviation σ_e (measurement error bar) in the likelihood distribution was assumed to be known. While this is usually the case in fusion science,[27] it does not need to be so. Taking σ unkown in Eq. (4.4) is a viable option, on condition that the data or the prior distribution provide information on σ. In the present example, this is guaranteed by taking repeated measurements, which naturally provide information on σ through their fluctuating behavior. We will thus impose a maximally uninformative prior for both the mean and standard deviation,

[23] By setting the derivative of (1.4) with respect to μ equal to zero and solving for μ.
[24] A PDF may have multiple local maxima, in which case it is called multimodal. However, we will not deal with this challenging case here.
[25] Curiously, some distributions do not even have a well-defined mean. This is the case for the Cauchy distribution mentioned in Section 4.2.5.
[26] It should be noted that, normally, the data for the current experiment should not be used for constructing the prior as this would violate Bayes' rule.
[27] The diagnostician often specifies an estimate for the error bar based on experience.

reflecting our prior state of ignorance. Here, the different character of the μ and σ variables comes into play. Indeed, whereas μ conveys information about the location of the Gaussian distribution's peak, σ is related to the measurement scale of the variable x. For location variables (e.g. μ), a uniform prior is uninformative. However, for scale variables such as σ, it can be shown that a more uninformative prior is Jeffreys' scale prior

$$p(\sigma|I) \propto \frac{1}{\sigma}, \tag{4.8}$$

which is defined on the interval $]0, +\infty[$. A motivation for this scheme can be found in the invariance of prior information under coordinate transformations, see [4.49]. The PDF (4.8) is again an improper prior as it cannot be integrated over $[0, +\infty]$. We will thus have to ensure that the posterior is normalizable. Going back to the uniform prior assigned to μ, by analogy with (4.6), the joint posterior for the variables μ and σ is given by

$$p(\mu, \sigma|\boldsymbol{x}, I) \propto \frac{1}{\sigma^n} \exp\left[-\frac{(\mu - \bar{x})^2 + \overline{(\Delta x)^2}}{2\,\sigma^2/n}\right] \times \frac{1}{\sigma}. \tag{4.9}$$

Note that, since this is a posterior for both μ and σ, the leading factor $1/\sigma^n$, appearing in the normalized expression of the posterior, had to be introduced. The last factor $1/\sigma$ is Jeffreys' prior. A contour plot of this distribution (when normalized) is shown in Fig. 4.2; it was obtained from the same 20-points data set used before.

We now introduce another essential tool of (Bayesian) probability theory known as marginalization. For continuous distributions, it consists in integrating the joint distribution over one or several variables or parameters. In the present example, this issue arises when there is no interest in deriving an estimate of σ, rather one only wishes to assess the probability of statements related to μ. In addition, for practical purposes, it is more convenient to plot the marginal posterior distribution of μ than the joint distribution of two (or more) variables. A parameter that is instrumental in the description of a problem, but in which one is not particularly interested, is called a nuisance parameter. Integrating out a nuisance parameter from a distribution is the marginalization step and results in the marginal distribution of the remaining parameters. In the present case, the standard deviation σ can be integrated out of the posterior (4.9):

$$\begin{aligned} p(\mu|\boldsymbol{x}, I) &= \int_0^{+\infty} p(\mu, \sigma|\vec{x}, I)\, \mathrm{d}\sigma \\ &\propto \int_0^{+\infty} \frac{1}{2}\left[\frac{(\mu - \bar{x})^2 + \overline{(\Delta x)^2}}{2/n}\right]^{-\frac{n}{2}} s^{\frac{n}{2}-1} e^{-s}\, \mathrm{d}s \\ &= \frac{1}{2}\Gamma\left(\frac{n}{2}\right)\left[\frac{(\mu - \bar{x})^2 + \overline{(\Delta x)^2}}{2/n}\right]^{-\frac{n}{2}}. \end{aligned}$$

In the second step, the variable $s \equiv \left[(\mu - \bar{x})^2 + \overline{(\Delta x)^2}\right]/(2\,\sigma^2/n)$ has been introduced. The result is given in terms of the gamma function $\Gamma(.)$. Proper normalization of this expression yields the following PDF:

$$p(\mu|\boldsymbol{x}, I) = \frac{\Gamma\left(\frac{n}{2}\right)}{\sqrt{\pi\overline{(\Delta x)^2}}\,\Gamma\left(\frac{n-1}{2}\right)}\left[1 + \frac{(\mu - \bar{x})^2}{\overline{(\Delta x)^2}}\right]^{-\frac{n}{2}}. \tag{4.10}$$

Finally, a change of variables is made:

$$t \equiv \frac{(\mu - \bar{x})^2}{\sqrt{\overline{(\Delta x)^2}/(n-1)}}. \tag{4.11}$$

Since this cannot affect the probabilities, it holds that[28]

$$p(t|\boldsymbol{x}, I)\, \mathrm{d}t \equiv p(\mu|\boldsymbol{x}, I)\, \mathrm{d}\mu.$$

From this, one can compute the density in terms of t:

$$p(t|\boldsymbol{x}, I) = \frac{\Gamma\left(\frac{n}{2}\right)}{\sqrt{(n-1)\pi}\,\Gamma\left(\frac{n-1}{2}\right)}\left[1 + \frac{t^2}{n-1}\right]^{-\frac{n}{2}}.$$

This is the PDF of Student's t-distribution with parameter $\nu = n - 1$. Owing to the transformation (4.11), this distribution is centred around zero, corresponding to the location of the sample average $\bar{x}$ in (4.10). Hence, the corresponding result from frequentist statistics is obtained, where it is also proved that the variable t — the

[28] When changing variables in probability densities, one should always take into account the effect of the respective volume elements (in this case $\mathrm{d}t$ and $\mathrm{d}\mu$).

standardized population mean — follows a t-distribution. In this context, $\nu = n - 1$ is the number of degrees of freedom of the distribution. By this, it is understood that every data point provides a degree of freedom. The total is reduced by one because the standard deviation is unknown and will be estimated from the data. The PDF (4.10) is shown in Fig 4.2. Owing to its heavy tails, the t-distribution still allows a reasonable probability density for values of μ relatively far from the sample average $\bar{x}$, as compared to the Gaussian posterior (4.7) for μ. On the other hand, as the number of measurements increases, the Student t-distribution approaches a normal distribution. Indeed, starting from (4.10) one obtains:

$$p(\mu|\boldsymbol{x}, I) \overset{n\gg1}{\longrightarrow} \frac{1}{\sqrt{2\pi\ \overline{(\Delta x)^2}/n}} \exp\left[-\frac{(\mu-\bar{x})^2}{2\ \overline{(\Delta x)^2}/n}\right].$$

In frequentist statistics, the standard deviation $\sqrt{\overline{(\Delta x)^2}/n}$ of this limiting distribution is often referred to as the 'standard error' corresponding to $\bar{x}$. Note the resemblance with (4.7). Naturally, the mean can also be marginalized from the joint posterior (4.9) by integrating over μ between $-\infty$ and $+\infty$:

$$p(\sigma|\boldsymbol{x}, I) = \int_{-\infty}^{+\infty} p(\mu, \sigma|\vec{x}, I)\ \mathrm{d}\mu \tag{4.12}$$

$$\begin{aligned}
&\propto \int_{-\infty}^{+\infty} \frac{1}{\sigma^{n+1}} \exp\left[-\frac{(\mu-\bar{x})^2 + \overline{(\Delta x)^2}}{2\,\sigma^2/n}\right] \mathrm{d}\mu \\
&= \frac{1}{\sigma^{n+1}} \exp\left[-\frac{\overline{(\Delta x)^2}}{2\,\sigma^2/n}\right] \int_{-\infty}^{+\infty} \exp\left[-\frac{(\mu-\bar{x})^2}{2\,\sigma^2/n}\right] \mathrm{d}\mu \\
&\propto \frac{1}{\sigma^n} \exp\left[-\frac{\overline{(\Delta x)^2}}{2\,\sigma^2/n}\right].
\end{aligned}$$

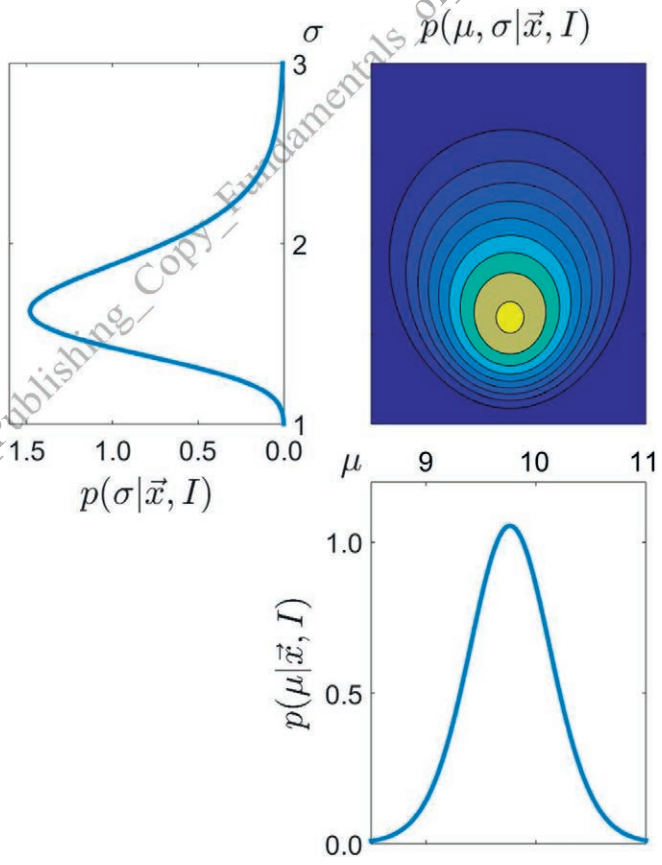

FIG. 4.2. Contour plot of the joint distribution $p(\mu, \sigma|\boldsymbol{x}, I)$, together with the corresponding marginal distributions $p(\mu|\boldsymbol{x}, I)$ and $p(\sigma|\boldsymbol{x}, I)$ for the 20-point data set.

Substituting $X \equiv n\,\overline{(\Delta x)^2}/\sigma^2$ (i.e. $\mathrm{d}X = -2n\,\overline{(\Delta x)^2}/\sigma^3\,\mathrm{d}\sigma$) one gets

$$p(X|\boldsymbol{x}, I) \propto X^{\frac{n}{2}-\frac{3}{2}}\,\mathrm{e}^{-\frac{X}{2}},$$

which is also depicted in Fig. 4.2 (normalized). Defining $k \equiv n-1$ and normalizing, this becomes the familiar χ^2 distribution with $k = n-1$ degrees of freedom:

$$p(X|\boldsymbol{x}, I) = \frac{1}{2^{\frac{k}{2}}\Gamma\left(\frac{k}{2}\right)} X^{\frac{k}{2}-1}\,\mathrm{e}^{-\frac{X}{2}}.$$

4.1.7.5. Laplace approximation

When the posterior is not a standard distribution, the Laplace (or saddle-point) approximation offers a convenient study tool, typically applied in the vicinity of the mode. Originally intended to approximate integrals, the Laplace approximation is based on a Taylor expansion of the logarithmic PDF around the mode. For instance, expression (4.10) – maximum at $\bar{x}$ – yields to second order:

$$\ln[p(\mu|\boldsymbol{x}, I)] \approx \ln[p(\bar{x}|\boldsymbol{x}, I)] + \frac{1}{2}\left.\frac{\mathrm{d}^2(\ln p)}{\mathrm{d}\mu^2}\right|_{\mu=\bar{x}} (\mu-\bar{x})^2$$

$$= \ln\left[\Gamma\left(\frac{n}{2}\right)\right] - \ln\left[\Gamma\left(\frac{n-1}{2}\right)\right] - \frac{1}{2}\ln\left[\pi\overline{(\Delta x)^2}\right] - \frac{n}{2\overline{(\Delta x)^2}}(\mu-\bar{x})^2.$$

On the original scale, one thus finds

$$p(\mu|\boldsymbol{x}, I) \approx \frac{\Gamma\left(\frac{n}{2}\right)}{\Gamma\left(\frac{n-1}{2}\right)} \frac{1}{\sqrt{\pi\overline{(\Delta x)^2}}} \exp\left[-\frac{(\mu-\bar{x})^2}{2\,\overline{(\Delta x)^2}/n}\right]. \tag{4.13}$$

On the right-hand side of (4.13) a Gaussian PDF is recognized. The apparently incorrect normalization can be traced back to the exclusion of the higher order terms. However, expression (4.13) can still provide a good approximation to the shape and the typical width of the distribution. The quality of this approximation clearly depends on the similarity of the PDF to a Gaussian close to its mode. One should also bear in mind that this approximation only works near the mode (e.g. not in the tails of the distribution). The standard deviation of the Gaussian distribution suggested by (4.13) is given by the 'standard error' $\sqrt{\overline{(\Delta x)^2}/n}$. Of course, the properly normalized normal distribution is recovered in the limit $n \to +\infty$, where $\Gamma\left(\frac{n}{2}\right)/\Gamma\left(\frac{n-1}{2}\right) \to \sqrt{n/2}$. More generally, one sees that the standard deviation σ_{L} of the Laplace approximation is related to the curvature of the logarithmic PDF by

$$\sigma_{\mathrm{L}} = \left[-\left.\frac{\mathrm{d}^2(\ln p)}{\mathrm{d}\mu^2}\right|_{\mu=\bar{x}}\right]^{-1/2}.$$

This is always well-defined since the second derivative is evaluated at the maximum of the PDF. Similarly, one could try to approximate the χ^2 distribution around its mode by a normal distribution. Looking at (4.12), the mode of the distribution for σ is seen to lie at $\sqrt{\overline{(\Delta x)^2}}$. The normal approximation at the mode has a standard deviation given by

$$\sigma_{\mathrm{L}} = \left[-\left.\frac{\mathrm{d}^2(\ln p)}{\mathrm{d}\sigma^2}\right|_{\sigma=\sqrt{\overline{(\Delta x)^2}}}\right]^{-1/2} = \sqrt{\frac{\overline{(\Delta x)^2}}{2n}}.$$

Judging from Fig 4.3, in the present case study, this approximation is reasonable around the mode but worsens in the tails of the distribution. For larger n the approximation improves as the χ^2 distribution approaches a Gaussian.

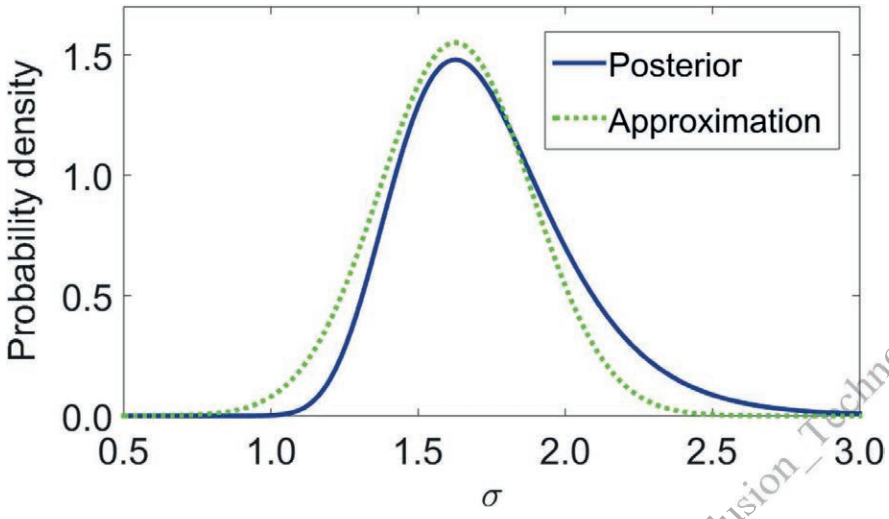

FIG. 4.3: Marginal posterior distribution for σ according to (4.12) and the corresponding Laplace approximation by a normal distribution around the mode of the posterior.

The Laplace approximation can be extended to the case of a joint distribution of multiple variables, i.e. a multivariate distribution. Summarizing the set of variables by the vector-valued variable $\boldsymbol{\theta}$ with components $\theta_1, \theta_2, \ldots, \theta_p$,[29] one can obtain the following approximation for the distribution of $\boldsymbol{\theta}$ around its mode $\boldsymbol{\theta}_0$ [4.48]:

$$p(\boldsymbol{\theta}|\boldsymbol{\theta}_0, I) \propto \exp\left[\frac{1}{2}(\boldsymbol{\theta}-\boldsymbol{\theta}_0)^{\mathrm{t}}\,[\nabla\nabla(\ln p)]_{\boldsymbol{\theta}=\boldsymbol{\theta}_0}(\boldsymbol{\theta}-\boldsymbol{\theta}_0)\right].$$

Here, $\nabla\nabla\,(\ln p)$ represents the (symmetric) Hessian matrix of partial second derivatives of the logarithmic PDF. Evaluated at the maximum of the PDF, this term is minus the inverse of the covariance matrix Σ_{L} of the approximating normal distribution:

$$\Sigma_{\mathrm{L}} = -\left\{[\nabla\nabla(\ln p)]_{\boldsymbol{\theta}=\boldsymbol{\theta}_0}\right\}^{-1}.$$

Even when the Laplace approximation is not adequate, it can still be used to find the maximum (mode) of the distribution in case an analytical expression for the mode cannot be found. This leads to the well-known Newton-Raphson numerical optimization procedure [4.48].

4.1.8. Monte Carlo computational methods

When performing Bayesian calculations, the joint posterior distribution of a set of variables $\boldsymbol{\theta}$ is not always available in a closed form (even when unnormalized). Moreover, in general, it may not be possible to devise an effective approximation by a Gaussian distribution. When the forward model or the prior distribution introduce strong nonlinearities, the resulting posterior might be significantly skewed, heavy-tailed or multimodal (multiple local maxima). In such cases, numerical techniques may be required to get an idea of the shape of the distribution or to calculate its moments. Another practical issue arises when the marginal distribution of a (set of) variable(s) is required, e.g. when a nuisance parameter needs to be integrated out. To address such problems, arbitrary probability distributions need to be integrated in potentially high-dimensional spaces (e.g. tens or hundreds of variables). Various methods have been developed to tackle the issue of integration. We will here briefly concentrate on two of the most popular, i.e. importance sampling and Markov chain Monte Carlo simulation [4.48, 4.49, 4.53].

4.1.8.1. Importance sampling

In importance sampling, the goal is to calculate the expectation $\mathbb{E}_p[f(\boldsymbol{\theta})]$ of a function $f(\boldsymbol{\theta})$ over a (typically multivariate) probability distribution $p(\boldsymbol{\theta}|I)$ defined over a domain $\mathcal{D}$:

$$\mathbb{E}_p[f(\boldsymbol{\theta})] \equiv \int_{\mathcal{D}} f(\boldsymbol{\theta})\, p(\boldsymbol{\theta}|I)\, \mathrm{d}\boldsymbol{\theta}.$$

[29] Throughout this section, we assume that vectors are column vectors and use the corresponding notation for multiplication with matrices and the dot product between vectors.

The function f might be vector-valued, in which case the expectation operator acts component-wise. For instance, if f is the identity function ($f(\boldsymbol{\theta}) \equiv \boldsymbol{\theta}$) then the expectation of $\boldsymbol{\theta}$ itself is calculated. If it is easy to draw samples $\boldsymbol{\theta}_i$ ($i = 1 \ldots n$) from $p(\boldsymbol{\theta}|I)$, then by the law of large numbers $\mathbb{E}_p[f(\boldsymbol{\theta})]$ can be approximated by the sample average:

$$\mathbb{E}_p[f(\boldsymbol{\theta})] \approx \frac{1}{n}\sum_{i=1}^{n} f(\boldsymbol{\theta}_i). \tag{4.14}$$

However, p might be difficult to sample from or f might be non-negligible in only a small region $\mathcal{A}$ in $\mathcal{D}$. In the latter case, the approximation in (4.14) can be very inefficient, as the majority of samples drawn from p barely contribute to the sum. The algorithm hence wastes most of its time in regions of $\mathcal{D}$ outside $\mathcal{A}$ — an issue that becomes even more pressing in a high-dimensional space. To solve this problem, it may be possible to generate samples from a distribution $q(\boldsymbol{\theta}|I)$ that approximates p reasonably well over the part of the domain where $f(\boldsymbol{\theta})\, p(\boldsymbol{\theta}|I)$ is appreciable. In that case, one simply writes

$$\mathbb{E}_p[f(\boldsymbol{\theta})] = \int_{\mathcal{D}} f(\boldsymbol{\theta})\, p(\boldsymbol{\theta}|I)\, \mathrm{d}\boldsymbol{\theta} = \int_{\mathcal{D}} \frac{f(\boldsymbol{\theta})\, p(\boldsymbol{\theta}|I)}{q(\boldsymbol{\theta}|I)} q(\boldsymbol{\theta}|I)\, \mathrm{d}\boldsymbol{\theta} = \mathbb{E}_q\left[\frac{f(\boldsymbol{\theta})\, p(\boldsymbol{\theta}|I)}{q(\boldsymbol{\theta}|I)}\right]$$

As a result, the expectation of f over p is derived by calculating the expectation over q and correcting by the weighting factor $p(\boldsymbol{\theta}|I)/q(\boldsymbol{\theta}|I)$. This is possible if $q(\boldsymbol{\theta}|I) > 0$ when $f(\boldsymbol{\theta})\, p(\boldsymbol{\theta}|I) \neq 0$. Hence, given samples $\boldsymbol{\theta}_i$ ($i = 1 \ldots n$) from $q(\boldsymbol{\theta}|I)$, the expectation of f over p can be approximated by the following Monte Carlo average:

$$\mathbb{E}_p[f(\boldsymbol{\theta})] \approx \frac{1}{n}\sum_{i=1}^{n} \frac{f(\boldsymbol{\theta}_i)\, p(\boldsymbol{\theta}_i|I)}{q(\boldsymbol{\theta}_i|I)}, \qquad \boldsymbol{\theta}_i \sim q(\boldsymbol{\theta}|I).$$

To avoid wasting time in unimportant regions of $\mathcal{D}$, one should ensure that q is small where $f(\boldsymbol{\theta})\, p(\boldsymbol{\theta}|I)$ is small and vice versa; hence the name importance sampling: the sampling mainly occurs where $f(\boldsymbol{\theta})\, p(\boldsymbol{\theta}|I)$ is important. As a matter of fact, the best q are (roughly) proportional to fp. This means that the variance of q should be smaller than that of p. Importance sampling can thus be used as a variance reduction method in Monte Carlo integration. A (multivariate) normal distribution can often make an acceptable q, but a good choice generally requires considerable experience.

In Bayesian analysis, p and/or q might be known up to a normalizing constant; say $p_{\mathrm{u}} \equiv cp$ and $q_{\mathrm{u}} \equiv bp$, with c and b constants. In such case, importance sampling can be used as follows (with $q(\boldsymbol{\theta}|I) > 0$ wherever $p(\boldsymbol{\theta}|I) > 0$). Indeed, as n becomes large, the numerator converges to $\frac{c}{b}\,\mathbb{E}_p[f(\boldsymbol{\theta})]$ while the denominator approaches c/b.

$$\mathbb{E}_p[f(\boldsymbol{\theta})] \approx \frac{\frac{1}{n}\sum_{i=1}^{n} f(\boldsymbol{\theta}_i)\, p_{\mathrm{u}}(\boldsymbol{\theta}_i|I)/q_{\mathrm{u}}(\boldsymbol{\theta}_i|I)}{\frac{1}{n}\sum_{i=1}^{n} p_{\mathrm{u}}(\boldsymbol{\theta}_i|I)/q_{\mathrm{u}}(\boldsymbol{\theta}_i|I)}, \qquad \boldsymbol{\theta}_i \sim q_{\mathrm{u}}(\boldsymbol{\theta}|I).$$

4.1.8.2. Markov chain Monte Carlo simulation

Markov chain Monte Carlo (MCMC) is a collective term for a set of techniques to generate samples (i.e. to simulate) from probability distributions. In case of multiple variables, hence multivariate distributions, arbitrary subsets of variables can be considered. As such, MCMC offers a convenient way to integrate distributions for marginalization, expectation value calculation and cases in which other numerical integration techniques would fail or take a prohibitively long time to complete. Here, we briefly present two common MCMC techniques: Gibbs sampling and the more general Metropolis-Hastings (M-H) algorithm. Both are very simple algorithms, although various practical issues might arise in their implementation and interpretation, which, again, may require some experience. A major advantage of these sampling techniques is that the distribution to be sampled from only needs to be known up to a multiplicative factor. This means that it does not have to be normalized, which is clearly interesting in Bayesian analysis.

Suppose we wish to generate samples from an arbitrary multivariate distribution for a vector–valued variable $\boldsymbol{\theta}$ with components $\theta_1 \ldots \theta_p$. The distribution is called the target distribution and its density is denoted by $\pi(\boldsymbol{\theta}|I)$. The Gibbs sampling algorithm makes this possible, provided the conditional distribution of each component θ_j is known or can easily be sampled from. Note that, in general, this is much easier than sampling from the marginal distribution of any θ_j given the joint distribution, as the latter requires integration. Indeed, the conditional distribution of θ_j is given by

$$p\left(\theta_j\middle|\theta_1,\dots,\theta_{j-1},\theta_{j+1},\dots,\theta_p,I\right)=\frac{\pi(\boldsymbol{\theta}|I)}{p(\theta_1,\dots,\theta_{j-1},\theta_{j+1},\dots,\theta_p|I)}. \tag{4.15}$$

The denominator is just a normalization factor, independent of θ_j. It is therefore not needed for inference concerning θ_j, which is very convenient as it represents a marginal distribution that could otherwise only be determined by integration over θ_j — exactly what we try to avoid. Hence, the unnormalized conditional distribution of θ_j is simply the slice of the known joint distribution $\pi(\boldsymbol{\theta}|I)$ that can be obtained when fixing all θ_k with $k\neq j$. In the case of (4.9), the distribution of μ, conditioned by σ, is given (up to a multiplicative constant) by

$$p(\mu|\sigma,\boldsymbol{x},I)\propto\exp\left[-\frac{(\mu-\bar{x})^2+\overline{(\Delta x)^2}}{2\,\sigma^2/n}\right]\propto\exp\left[-\frac{(\mu-\bar{x})^2}{2\,\sigma^2/n}\right].$$

We have recovered (4.7) in its unnormalized form (conditioning on σ_e is absorbed in I). In general, it may not be easy to sample the conditional distribution in (4.15). When it is possible, one can use the Gibbs sampler.

The idea behind the Gibbs sampler is to create a Markov chain of points $\boldsymbol{\theta}^{(t)}$ labelled by a 'time' parameter t. The chain moves from one state to another by sequentially selecting new values $\theta_j^{(t+1)}$ for each of the components of $\boldsymbol{\theta}^{(t+1)}$. This is done by sampling from the distribution of each $\theta_j^{(t+1)}$, conditional on the most recent value of the other components. In accordance with the Markov property of the chain, the new state does not depend on the states before time t. Starting from an arbitrary state $\boldsymbol{\theta}^0$, it can be proved that the chain will eventually converge to the target distribution $\pi(\boldsymbol{\theta}|I)$. Put differently, the chain generates samples from the (approximate) joint distribution $\pi(\boldsymbol{\theta}|I)$. However, quite remarkably, any subchain associated to a subset of $\boldsymbol{\theta}$ components generates samples from the corresponding marginal distribution. The set of samples $\left\{\theta_j^{(t)}\right\}$, corresponding to any θ_j, contains samples from the marginal distribution $p\left(\theta_j\middle|I\right)$ of θ_j, for all times t after the chain has converged. The Gibbs sampling algorithm is summarized as follows:

At $\boldsymbol{t=0}$: start from $\boldsymbol{\theta}^{(t)}=\left(\boldsymbol{\theta}_1^{(t)},\boldsymbol{\theta}_2^{(t)},\dots,\boldsymbol{\theta}_p^{(t)}\right)$

repeat[30]

$$\begin{aligned}
&\boldsymbol{\theta}_1^{(t+1)}\sim\boldsymbol{p}\left(\boldsymbol{\theta}_1\middle|\boldsymbol{\theta}_2^{(t)},\dots,\boldsymbol{\theta}_p^{(t)},\boldsymbol{I}\right)\\
&\boldsymbol{\theta}_2^{(t+1)}\sim\boldsymbol{p}\left(\boldsymbol{\theta}_2\middle|\boldsymbol{\theta}_1^{(t+1)},\dots,\boldsymbol{\theta}_p^{(t)},\boldsymbol{I}\right)\\
&\vdots\ \boldsymbol{\theta}_j^{(t+1)}\sim\boldsymbol{p}\left(\boldsymbol{\theta}_j\middle|\boldsymbol{\theta}_1^{(t+1)},\boldsymbol{\theta}_2^{(t+1)},\dots,\boldsymbol{\theta}_{j-1}^{(t+1)},\boldsymbol{\theta}_{j+1}^{(t)},\dots,\boldsymbol{\theta}_p^{(t)},\boldsymbol{I}\right)\\
&\vdots\ \boldsymbol{\theta}_p^{(t+1)}\sim\boldsymbol{p}\left(\boldsymbol{\theta}_p\middle|\boldsymbol{\theta}_1^{(t+1)},\dots,\boldsymbol{\theta}_{p-1}^{(t+1)},\boldsymbol{I}\right)
\end{aligned}$$

end

It is important to note that, as a value is sampled for component θ_j at time $t+1$, the PDF is conditioned on the most recent values of the components $\theta_1\dots\theta_{j-1}$, sampled at $t+1$. If feasible, one may sample from the joint conditional distribution of several combinations (blocks) of variables at the same time, i.e. the components θ_j do not need to be treated individually through their univariate marginal distribution.

Implementation of the Gibbs sampler can be straightforward in relatively simple problems, but more complex situations may require special care. In any case, a number of samples at the beginning of the chain (the burn-in period) has to be discarded until the chain converges. A variety of convergence diagnostics exist. However, for simple problems, a visual inspection of the time traces of each component θ_j can give a good impression. After convergence of the chain, the subsequent samples can be used to study the marginal distributions of (combinations of) the components θ_j. Furthermore, sample (Monte Carlo) averages of the components or any function thereof can be used as estimates of the corresponding expectation values over the target distribution, or any of its marginal distributions. For instance, assuming that the chain is run for n iterations after converging at time t_c, estimates of the mean and variance of component θ_j are given by

$$\bar{\theta}_j=\frac{1}{n}\sum_{i=1}^{n}\theta_j^{(t_\mathrm{c}+i)},\qquad\qquad\overline{(\Delta\theta_j)^2}=\frac{1}{n}\sum_{i=1}^{n}\left(\theta_j^{(t_\mathrm{c}+i)}-\bar{\theta}_j\right)^2.$$

The number n of samples required to attain a certain precision in such Monte Carlo averages depends on the problem at hand. However, it should be understood that the Gibbs algorithm returns a chain of strongly correlated samples. Usually, the adverse effect of autocorrelation on the precision of Monte Carlo averages can be mitigated by

[30] Here, the notation '∼' stands for 'take a sample from'.

running the chain for a sufficiently long time. Nevertheless, in some situations, a systematic deviation from the true moments of the target distributions can be difficult to reduce and more sophisticated techniques may be needed [4.49].

We end the section on computational methods by mentioning the Metropolis-Hastings (M-H) algorithm, useful in case the conditional distribution of subsets of variables is not easily sampled from. The M-H algorithm forms a Markov chain by sampling from a proposal distribution, which depends on the current state of the chain and is chosen to be easily sampled from. Somewhat like importance sampling, M-H then introduces a correction to better approximate the target distribution, by rejecting some of the samples generated from the proposal distribution (similar to another useful Monte Carlo technique called rejection sampling). Again, one may choose to update the state by sampling each component θ_j sequentially, or group variables in one or multiple blocks. Under appropriate (easily fulfilled) conditions, the chain will converge to the target distribution and the sub-chain corresponding to any component θ_j will sample from the corresponding marginal distribution.

The performance of the M-H sampler depends on the choice of the proposal distribution. A uniform distribution is a straightforward choice, but it is often more effective to take a distribution that is centred on the most recent state of the chain. A common strategy is to sample a new value $\theta_j^{(t+1)}$ from a univariate Gaussian with mean given by $\theta_j^{(t)}$. Equivalently, one may sample the whole new state $\boldsymbol{\theta}^{(t+1)}$ in a single step from a multivariate Gaussian centred at $\boldsymbol{\theta}^{(t)}$. The chain then moves through the sample space as a random walk. Nevertheless, the advantage of not sampling all components at the same time is that they can have different proposal distributions. Denoting the target distribution by $\pi(\boldsymbol{\theta}|I)$ and the individual proposal distributions by $q_j\left(\eta\middle|\boldsymbol{\theta}^{(t)}\right)$, the algorithm goes as follows:

At $\boldsymbol{t=0}$, start from $\boldsymbol{\theta}^{(t)}=\left(\theta_1^{(t)},\theta_2^{(t)},\dots,\theta_p^{(t)}\right)$

repeat

for $\boldsymbol{j=1}$ to $\boldsymbol{p}$

$$\boldsymbol{y}\sim \boldsymbol{q_j}\left(\boldsymbol{\eta}\middle|\boldsymbol{\theta_1^{(t+1)}},\boldsymbol{\theta_2^{(t+1)}},\dots,\boldsymbol{\theta_{j-1}^{(t+1)}},\boldsymbol{\theta_j^{(t)}},\boldsymbol{\theta_{j+1}^{(t)}},\dots,\boldsymbol{\theta_p^{(t)}},\boldsymbol{I}\right)$$

$$\boldsymbol{\theta_j^{(t+1)}} == \begin{cases} \boldsymbol{y}, \text{ with prob. } \boldsymbol{\rho}\left(\boldsymbol{y},\boldsymbol{\theta_1^{(t+1)}},\boldsymbol{\theta_2^{(t+1)}},\dots,\boldsymbol{\theta_{j-1}^{(t+1)}},\boldsymbol{\theta_j^{(t)}},\boldsymbol{\theta_{j+1}^{(t)}},\dots,\boldsymbol{\theta_p^{(t)}}\right) \\ \boldsymbol{\theta_j^{(t)}}, \text{ with prob. } \boldsymbol{1-\rho} \end{cases},$$

where $\boldsymbol{\rho}\left(\boldsymbol{y},\boldsymbol{\theta_1^{(t+1)}},\boldsymbol{\theta_2^{(t+1)}},\dots,\boldsymbol{\theta_{j-1}^{(t+1)}},\boldsymbol{\theta_j^{(t)}},\boldsymbol{\theta_{j+1}^{(t)}},\dots,\boldsymbol{\theta_p^{(t)}}\right)\equiv$

$$\equiv \min\left\{\boldsymbol{1},\frac{\boldsymbol{\pi}\left[\boldsymbol{\theta_1^{(t+1)}},\boldsymbol{\theta_2^{(t+1)}},\dots,\boldsymbol{\theta_{j-1}^{(t+1)}},\boldsymbol{y},\boldsymbol{\theta_{j+1}^{(t)}},\dots,\boldsymbol{\theta_p^{(t)}},\boldsymbol{I}\right]}{\boldsymbol{\pi}\left[\boldsymbol{\theta_1^{(t+1)}},\boldsymbol{\theta_2^{(t+1)}},\dots,\boldsymbol{\theta_{j-1}^{(t+1)}},\boldsymbol{\theta_j^{(t)}},\boldsymbol{\theta_{j+1}^{(t)}},\dots,\boldsymbol{\theta_p^{(t)}},\boldsymbol{I}\right]}\right.$$

$$\left.\times\frac{\boldsymbol{q_j}\left(\boldsymbol{\theta_j^{(t)}}\middle|\boldsymbol{\theta_1^{(t+1)}},\boldsymbol{\theta_2^{(t+1)}},\dots,\boldsymbol{\theta_{j-1}^{(t+1)}},\boldsymbol{y},\boldsymbol{\theta_{j+1}^{(t)}},\dots,\boldsymbol{\theta_p^{(t)}},\boldsymbol{I}\right)}{\boldsymbol{q_j}\left(\boldsymbol{y}\middle|\boldsymbol{\theta_1^{(t+1)}},\boldsymbol{\theta_2^{(t+1)}},\dots,\boldsymbol{\theta_{j-1}^{(t+1)}},\boldsymbol{\theta_j^{(t)}},\boldsymbol{\theta_{j+1}^{(t)}},\dots,\boldsymbol{\theta_p^{(t)}},\boldsymbol{I}\right)}\right\}$$

end

end

The function ρ, called the acceptance probability, is not a probability density but a function that returns a probability, which depends on the proposal y and the current state of the chain. From the expression of the acceptance probability, it is clear that neither π nor the q_j need to be normalized. If a proposal is not accepted the state of the chain remains unchanged. Furthermore, the proposal densities q_j are often chosen to obey a symmetry condition causing them to cancel from the proposal density.[31] Moreover, in many cases, the q_j do not depend on components other than θ_j. Take a simple Gaussian proposal density for example, i.e.

$$q_j\left(\eta\middle|\theta_j^{(t)},I\right)\propto\exp\left[-\frac{\left(\eta-\theta_j^{(t)}\right)^2}{2\sigma_j^2}\right],$$

for a given standard deviation σ_j (knowledge of which is incorporated in I). By tuning σ_j for each q_j, one can adjust the average step size and, indirectly, the acceptance probability. From the definition of ρ and assuming symmetric proposal densities, one notices that the proposed sample is always accepted if it increases the value of the target density π. By virtue of this property, the algorithm spends most of its time sampling from regions where the target density is appreciable. Nevertheless, even when the proposal leads to a decrease of the target density, there is a nonzero probability that the sample will be accepted. This allows the algorithm to sufficiently explore the sample space, causing the chain to converge. It also prevents the sampler from getting trapped in local density maxima, which is especially

[31] In that case, the sampler follows the Metropolis algorithm.

useful when the density is multimodal. For the same reasons, it is sometimes useful to adopt a proposal density that has heavier tails than the normal distribution, e.g. a Cauchy distribution. Like the Gaussian proposal density, the Cauchy distribution is symmetric in its arguments and most proposals will occur in the neighbourhood of the current state. However, owing to its heavier tails, it increases the chances of occasional transitions to states located far from the current one.

As for the Gibbs sampler, implementation of the M-H algorithm is straightforward for simple problems but issues may arise in more complex situations. Acceptance of the proposal y with probability ρ is equivalent to accepting it whenever $u < \rho$, where u is a sample from a uniform distribution in the interval $[0,1]$ (a probability). As mentioned before, the acceptance probability of each variable can be adjusted by tuning the proposal densities. If the acceptance rate is too low or too high, exploration of the sampling space will be inefficient. The acceptance probabilities should thus be monitored while the chain is run. A level of ~50% is usually considered for a univariate target distribution. In higher dimensions it is ideally lower, yet higher than 20%.

4.1.9. Integrated data analysis

4.1.9.1. Introduction

Up to now, one of the main applications of Bayesian probability theory to fusion data analysis has been in diagnostic modelling, to estimate physical quantities from raw data [4.51, 4.54]. This approach, called integrated data analysis (IDA), has two important characteristics. First, great care is taken in studying the uncertainties entering the diagnostic data, the calibration and the physical model upon which the measurement technique is based. Quantification of the uncertainties is accomplished by probability distributions leading to a (joint) distribution of the physical quantities of interest. In technical terms, one starts from the prior distribution of the quantities, updating them into a posterior distribution via Bayes' theorem, after acquiring the data using the diagnostic. The Bayesian approach intrinsically takes care of the propagation of errors through the measurement model. It is applicable even in a complex chain of calculations from the raw data to the calibrated physical quantities. In general, this is far beyond the point where the standard rules of Gaussian error propagation break down. It should be stressed that a proper analysis of uncertainty propagation can not only affect the error bars on the final quantities, but also the mean values of the quantities themselves. Bayesian analysis may also improve the robustness of certain algorithms prone to uncertainty accumulation, such as tomography.

Bayesian inference can be applied to individual diagnostics, but a better approach is to consider sets of diagnostics and model the interdependencies to exploit their synergies. This is the second most important characteristic of IDA using Bayesian probability theory: data from highly heterogeneous sources can be incorporated in a single self-consistent analysis. On the one hand, this approach is useful in the (common) case in which the estimate of a physical quantity depends on the measurements of multiple diagnostics. An example can be found in the determination of the electron density profile from interferometry, which requires knowledge of the magnetic equilibrium. Instead of sequentially calculating the equilibrium, using it as input for an inversion based on the interferometry measurements, the data from both diagnostics can be included in a single probabilistic model. This results in a single joint posterior for all parameters, some of which may be of direct interest, while others (nuisance parameters) can be marginalized. On the other hand, in fusion plasmas, it often happens that several physical quantities can be measured in multiple ways. For instance, the local electron density can be inferred from interferometry, Thomson scattering, lithium beam spectroscopy, etc. Again, the IDA framework allows the data to be combined in a single analysis. Information gathered by entirely different principles thus contribute to the knowledge of a single physical quantity. This generally leads to synergies combining the strong points of each diagnostic, e.g. spatial or temporal resolution and spatial coverage. At the same time, inconsistencies between diagnostics might be resolved, e.g. by properly modelling any sources of systematic uncertainty [4.51]. Synergies may also be possible in less obvious combinations of diagnostic information. An example is the joint determination of electron density and temperature from Thomson scattering and soft X ray diagnostics [4.55]. Other interesting examples and methodology regarding IDA can be found in [4.56, 4.57, 4.58]. Combination of diagnostics will become even more important in DEMO, where a limited set of diagnostics will be available to monitor the plasma state.

4.1.9.2. The IDA recipe

We now sketch a general picture of an implementation of IDA to combine data from two diagnostics. Suppose we wish to infer a scalar high-level physical quantity Q from diagnostics A and B, which both provide information on Q (e.g. the local or global plasma density, temperature, impurity concentration, etc.). Specifically, let us assume that a single measurement performed by diagnostic A (or B) results in raw data in the form of a single number x_A (or x_B).

By raw data, we mean the information that comes directly from a sensor, usually a voltage, which in principle has not been processed nor calibrated. It helps to think of the analysis in terms of a stream of information or data from the raw measurements (the source) all the way down to the high-level quantities of interest (downstream). In practice, the analysis may also start at a later point in the data stream, for instance after calibration or combination with other data sources (e.g. atomic data). However, in general, the results will benefit from an analysis modelling all 'individual' sources of uncertainty in a way that is as detailed as possible. Put differently, a detailed quantification of uncertainty sources is generally a better approach than a rougher quantification of the uncertainty further down the data stream.[32] The mathematical description of this data stream is precisely the forward model, where 'forward' is understood as the upstream direction. The forward model represents the classic chain of calculations from the (physical) variables describing the system under study, for instance Q, up to the variables describing the raw data. It is called 'forward' because typically the variables describing the system are hidden, and one can only try to infer them based on the measured data, which is the inverse problem. If the hidden variables were known exactly, the data could be predicted through the forward model (also assumed to be exact). The likelihood distribution thus quantifies the probability density of predicting specific data if the hidden variables were known. The hidden variables are usually referred to as the 'parameters' of the system. They typically include quantities of interest as well as nuisance parameters.

Continuing with the example, we will assume that the forward model for diagnostic A depends on the quantity Q, and possibly an additional set of parameters $\vec{\theta}_A$, which may or may not be of interest. These parameters describe additional details of the physical system (or the measurement process) and, for now, we assume them to be known. This information is encoded in the forward model $f_A(Q, \boldsymbol{\theta}_A)$, which would exactly predict the data point x_A, should it be able to describe the measurement process in a deterministic way. Likewise, the forward model for diagnostic B can be written as $f_B(Q, \boldsymbol{\theta}_B)$. Of course, in reality, the forward models encode the measurement process only to a certain degree of accuracy and detail. As a result, one can only make statements about the probability of measuring a certain data set, given the parameters of the system. The corresponding probability densities are modelled through the likelihood distribution, which usually involves the difference between the data predicted by the forward model and the measured data. Let us focus on the common case of a Gaussian distribution, for which the likelihood for diagnostic A becomes

$$p_A(x_A|Q, \boldsymbol{\theta}_A, \sigma_A, I_A) = \frac{1}{\sqrt{2\pi}\sigma_A} \exp\left\{-\frac{[x_A - f_A(Q, \boldsymbol{\theta}_A)]^2}{2\sigma_A^2}\right\}, \tag{4.16}$$

and likewise for B. A measure of uncertainty in the form of the standard deviation σ_A of the distribution has been introduced, assumed to be known for the moment. Now suppose that a number n_A of measurements is carried out by means of diagnostic A, under the assumption that Q, $\boldsymbol{\theta}_A$, σ_A and all the other background information I_A stays the same. These numbers are denoted by $x_{A,i}$ $(i = 1 \dots n_A)$, or $\boldsymbol{x}_A$ in short. By assumption, the $x_{A,i}$ can be seen as samples drawn from distribution (4.16). Furthermore, assume that, conditional on Q, $\boldsymbol{\theta}_A$, σ_A and I_A, the individual measurements $x_{A,i}$ are mutually independent. This corresponds to the common experience of repeated measurements fluctuating around a mean value in a seemingly random fashion. These fluctuations are then called 'measurement noise', which is usually due to a combination of microscopic fluctuations in both the physical system (the plasma) and the measurement system (the diagnostic hardware). We adopt similar assumptions and notations for diagnostic B. The diagnostics are also taken to be independent, whereby it is assumed that Q can be derived by a traditional analysis from either A or B. This means that $\boldsymbol{x}_A$ and $\boldsymbol{x}_B$ are independent, hence the joint likelihood of the data factors into a product of the marginal likelihoods (conditional on the model parameters and summarizing I_A and I_B by I): [33]

$$\begin{aligned} p(\boldsymbol{x}_A, \boldsymbol{x}_B|Q, \boldsymbol{\theta}_A, \boldsymbol{\theta}_B, \sigma_A, \sigma_B, I) = \\ = (2\pi)^{-(n_A+n_B)/2} \sigma_A^{-n_A} \sigma_B^{-n_B} \\ \times \exp\left\{-\frac{1}{2\sigma_A^2}\sum_{i=1}^{n_A}\left[x_{A,i} - f_A(Q, \boldsymbol{\theta}_A)\right]^2 - \frac{1}{2\sigma_B^2}\sum_{i=1}^{n_B}\left[x_{B,i} - f_B(Q, \boldsymbol{\theta}_B)\right]^2\right\}. \end{aligned} \tag{4.17}$$

Up to now we have assumed that the parameters $\boldsymbol{\theta}_A$, $\boldsymbol{\theta}_B$, σ_A and σ_B are known before the experiment. We now focus on the more realistic case in which this information is not given. In such case, $\boldsymbol{x}_A$ and $\boldsymbol{x}_B$ are used to determine Q and their fluctuation properties provide information on σ_A and σ_B. This is to be combined with the prior information.

[32] In reality, by the time the data is registered as numbers in an acquisition memory, the data will have already passed through an electronic circuit. However, to keep the analysis tractable, one usually makes abstraction of such details. The circuit can simply be treated as a source of uncertainty (electronic noise).

[33] On the microscopic level one would find dependencies between data points and diagnostics. Such dependencies are almost completely washed out at the level of diagnostic measurements, therefore (1.17) is still a good approximation.

However, information regarding $\boldsymbol{\theta}_A$ and $\boldsymbol{\theta}_B$ will need to be obtained from other sources, i.e. other experiments. If these experiments result in a trustworthy distribution for $\boldsymbol{\theta}_A$ and $\boldsymbol{\theta}_B$, it can be used as a prior distribution, which is then combined with the likelihood (4.17) following Bayes' rule (4.3). On the other hand, it may be necessary to include these additional experiments in the Bayesian analysis, meaning that their measurement process is encoded in an additional likelihood. For demonstration purposes, we assume that $\boldsymbol{\theta}_A$ consists of two scalar parameters $\theta_{A,1}$ and $\theta_{A,2}$ and leave $\boldsymbol{\theta}_B$ unspecified. Furthermore, we assume that additional information regarding $\theta_{A,1}$ is available through a third, conditionally independent experiment C (not necessarily a plasma diagnostic). Apart from $\theta_{A,1}$, the associated forward model $f_C(\theta_{A,1}, \boldsymbol{\eta})$ will depend on a set of additional parameters $\boldsymbol{\eta}$. We will assume that sufficient information regarding the model parameters $\boldsymbol{\eta}$ is given through prior information.[34] We choose again a Gaussian likelihood distribution, with standard deviation σ_C, assuming n_C measurement points in a vector $\boldsymbol{x}_C$:

$$p(\boldsymbol{x}_C|\theta_{A,1}, \boldsymbol{\eta}, \sigma_C, I_C) = (2\pi)^{-n_C/2}\sigma_C^{-n_C} \exp\left\{-\frac{1}{2\sigma_C^2}\sum_{i=1}^{n_C}\left[x_{C,i} - f_C(\theta_{A,1}, \boldsymbol{\eta})\right]^2\right\}. \tag{4.18}$$

The joint posterior distribution for the integrated experiment is the distribution of all parameters entering the problem (including $\vec{\eta}$), conditioned by the data from the three experiments A, B and C. Incorporating all background information in I, Bayes' rule yields:

$$p(Q, \boldsymbol{\theta}_A, \boldsymbol{\theta}_B, \sigma_A, \sigma_B, \boldsymbol{\eta}, \sigma_C|\boldsymbol{x}_A, \boldsymbol{x}_B, \boldsymbol{x}_C, I) \propto p(\boldsymbol{x}_A, \boldsymbol{x}_B, \boldsymbol{x}_C|Q, \boldsymbol{\theta}_A, \boldsymbol{\theta}_B, \sigma_A, \sigma_B, \boldsymbol{\eta}, \sigma_C, I)\, p(Q, \boldsymbol{\theta}_A, \boldsymbol{\theta}_B, \sigma_A, \sigma_B, \boldsymbol{\eta}, \sigma_C|I).$$

The prior density is now factored, meaning that (before any data has been acquired) all parameters are considered to be mutually independent.[35] This is a common assumption in Bayesian analysis, unless there is information that some of the parameters are *a priori* related in a certain way. In factoring the likelihood, one has to be careful since $\boldsymbol{x}_A$ and $\theta_{A,1}$ are interdependent. Furthermore, $\boldsymbol{x}_B$ and $\boldsymbol{x}_C$ can be separated from the other data, leading to the following result:

$$\begin{aligned} p(Q, \boldsymbol{\theta}_A, \boldsymbol{\theta}_B, \sigma_A, \sigma_B, \boldsymbol{\eta}, \sigma_C|\boldsymbol{x}_A, \boldsymbol{x}_B, \boldsymbol{x}_C, I) \propto\ & p(\boldsymbol{x}_A|Q, \boldsymbol{\theta}_A, \sigma_A, I)\, p(\boldsymbol{x}_B|Q, \boldsymbol{\theta}_B, \sigma_B, I)\, p(\boldsymbol{x}_C|\theta_{A,1}, \boldsymbol{\eta}, \sigma_C, I) \\ & \times p(Q|I)\, p(\boldsymbol{\theta}_A|I)\, p(\boldsymbol{\theta}_B|I) p(\sigma_A|I)\, p(\sigma_B|I)\, p(\boldsymbol{\eta}|I)\, p(\sigma_C|I). \end{aligned}$$

Note that, in the likelihood densities on the right-hand side, a few unnecessary dependencies have been suppressed. For instance, when $\boldsymbol{\theta}_A$ is given together with Q and σ_A, there is no need to specify $\boldsymbol{\eta}$ and σ_C, as the density of $\boldsymbol{x}_A$ is completely determined through (4.16).[36] Considering (4.17) and (4.18), the joint posterior becomes

$$\begin{aligned} p(Q, \boldsymbol{\theta}_A, \boldsymbol{\theta}_B, \sigma_A, \sigma_B, \boldsymbol{\eta}, \sigma_C|\boldsymbol{x}_A, \boldsymbol{x}_B, \boldsymbol{x}_C, I) \propto\ & \sigma_A^{-n_A}\sigma_B^{-n_B}\sigma_C^{-n_C} \\ & \times \exp\left\{-\frac{1}{2\sigma_A^2}\sum_{i=1}^{n_A}\left[x_{A,i} - f_A(Q, \boldsymbol{\theta}_A)\right]^2 - \frac{1}{2\sigma_B^2}\sum_{i=1}^{n_B}\left[x_{B,i} - f_B(Q, \boldsymbol{\theta}_B)\right]^2 - \frac{1}{2\sigma_C^2}\sum_{i=1}^{n_C}\left[x_{C,i} - f_C(\theta_{A,1}, \boldsymbol{\eta})\right]^2\right\} \\ & \times p(Q|I)\, p(\boldsymbol{\theta}_A|I) p(\boldsymbol{\theta}_B|I) p(\sigma_A|I)\, p(\sigma_B|I)\, p(\boldsymbol{\eta}|I)\, p(\sigma_C|I). \end{aligned}$$

It remains to specify the prior densities. If little prior information is available besides the expected range of a quantity, a uniform prior usually works well and Jeffreys' scale prior can be used for the standard deviations. At the next stage, a joint posterior can be approximated or samples can be drawn from it using simulation techniques. As mentioned before, the converged sub-chains generated by Gibbs sampling or M-H correspond to the respective marginal distributions. From this, the expectation value corresponding to a (set of) parameter(s) can be calculated, together with estimates of error bars, based, for instance, on the sample standard deviations. In the present case, the marginal distribution of Q will provide the desired result.

We have given the general outline of an IDA, which, in principle, can cover much more complex situations. For instance, the reconstruction of local plasma quantities from line-integrated data can be formulated as a problem of inference. In fact, this approach is usually less prone to reconstruction errors than classic techniques since it does not involve an explicit inversion (this is the job of Bayes' theorem). The parameters of interest are then those characterizing the local profile or field (e.g. spline parameters). The smoothness of the solution can be encoded as prior information, e.g. the Fisher information prior [4.49]. However, in complex problems, one should always be

[34] For instance, if one of the parameters in model C is the speed of light c, it is, fortunately, not necessary to include an experiment that will estimate the speed of light for our Bayesian analysis. Instead, we can take this information for granted through a prior distribution on c. Moreover, in the particular case of c, the value of the parameter is known to such great precision that it would not make a significant difference in our analysis to simply plug the known value into the likelihood for experiment C.

[35] This is no longer the case after performing the experiments!

[36] The situation is different for a probability density like $p(\boldsymbol{x}_A|Q, \sigma_A, \boldsymbol{\eta}, \sigma_C, I)$, for $\boldsymbol{x}_A$ logically depends on the knowledge of $\boldsymbol{\eta}$ and σ_C through $\boldsymbol{\theta}_A$.

careful that the problem remains identifiable, i.e. that sufficient information is available to determine all parameters unambiguously. If the data does not provide information on a certain parameter of the system, then its prior distribution should be sufficiently informative (e.g. a normal distribution).

4.3. REFERENCES

[4.1] ROMANELLI, F., Fusion Electricity — A roadmap to the realisation of fusion energy (2013), https://www.euro-fusion.org/wpcms/wp-content/uploads/2013/01/JG12.356-web.pdf
[4.2] FEDERICI, G., et al., Fusion Engineering and Design 109–111 (2016) 1464–1474.
[4.3] DOYLE, E. J., et al., "Plasma confinement and transport", Nucl. Fusion **47** (2007) S18–S127.
[4.4] WENNINGER, R., et al., Nucl. Fusion **57** (2017) 016011.
[4.5] COSTLEY, A., et al., Rev Sci. Instrum. **70** (1999) 391–396.
[4.6] DONNE, A. J. H., et al., Nucl. Fusion **47** (2007) S337–S384.
[4.7] WALKER, C. I., et al., Rev. Sci. Instrum. **75** (2004) 4243–4246.
[4.8] COSTLEY, A., et al., Fus. Engin. Des. **74** (2005) 109–119.
[4.9] WALSH, M., et al., IEEE 24th Symp. on Fusion Engineering (2011).
[4.10] VAYAKIS, G., et al., Fus. Sci. Technol. **53** (2008) 699–750.
[4.11] BIEL, W., et al., Fusion Engineering and Design **96–97** (2015) 8–15.
[4.12] FELICI, F., et al., Plasma Phys. Contr. Fusion **54** (2012) 025002.
[4.13] ZAGAR, K., et al., System requirements document (SRD) for the DEMO diagnostic and control system (2016), https://idm.euro-fusion.org/?uid=2MNK4R
[4.14] ZABEO, L., et al., Fusion Engineering and Design **89** (2014) 553-557.
[4.15] FISCHER, U., et al., Fusion Engineering and Design **109-111** (2016) 1458-1463.
[4.16] PERUZZO, S., et al., IEEE Transcations on Plasma Science **44** (2016) 1704.
[4.17] PERUZZO, S., et al., Fusion Engineering and Design **88** (2013) 1302–1305.
[4.18] PIRONTI, A., ARIOLA, M., et al., WPDC final review meeting (internal report) (2016).
[4.19] HENDER, T., et al., Nucl. Fusion **47** (2017) S128.
[4.20] ARIOLA, M., PIRONTI, A., Magnetic Control of Tokamak Plasmas, 2nd ed., Springer (2016).
[4.21] GREENWALD, M., et al., Nucl. Fusion **47** (2007) L26.
[4.22] ZOHM, H., et al., Nucl. Fusion **53** (2013) 073019.
[4.23] GREENWALD, M., A new look to tokamak density limits, Nucl. Fusion **28** (1988) 2199.
[4.24] MARTIN, Y. R., et al., Journal of Physics: Conference Series **123** (2008) 012033.
[4.25] DE VRIES, P., et al., Survey of disruption causes at JET, Nucl. Fusion **51** (2011) 053018.
[4.26] VEGA, J., et al., Results of the JET real-time disruption predictor in the ITER-like wall campaigns, Fusion Engin. Design **88** (2013) 1228.
[4.27] MARASCHEK, M., et al., Path-oriented early reaction to approaching disruptions in ASDEX Upgrade and TCV in view of the future needs for ITER and DEMO, Plasma Phys. and Contr. Fusion (2017) (accepted).
[4.28] PITTS, R.A., et al., Journal of Nuclear Materials **438** (2013) S48–S56.
[4.29] LOEWENHOFF, Th., et al., Fusion Engineering and Design **87** (2012) 1201–1205.
[4.30] LANG, P.T., et al., Nucl. Fusion **53** (2013) 043004.
[4.31] EVANS, T.E., et al., Journal of Nuclear Materials **438** (2013) S11–S18.
[4.32] JANKY, F., et al., Simulation of burn control for DEMO using ASTRA coupled with Simulink, Fusion Engin. Design **123** (2017) 555–558.
[4.33] MALAQUIAS, A., et al., IEEE transactions on plasma science **46** 2 (2018) 451–457.
[4.34] RISPOLI, N., et al., Fusion Engineering and Design **123** (2017) 628–631.
[4.35] DURAN, I., et. al., Fus. Engin. Design **123** (2017) 690–694.
[4.36] BOLSHAKOVA, I., HOLYAKA, R., GERASIMOV, S., Procede de mesure du champ magnetique quasi-statique, France Patent FR2887991 (2007).
[4.37] BOLSHAKOVA, I., HOLYAKA, R., GERASIMOV, S., Method for measuring quasi-stationary magnetic field, Great Britain Patent GB2427700 (2009).
[4.38] BOLSHAKOVA, I., QUERCIA, A., COCCORESE, V., et al., IEEE Transactions on Nuclear Science **59** (2012) 1224–1231.
[4.39] TOKAR, M. et. al., Nucl. Materials and Energy **12** (2017) 1298–1302.
[4.40] LITNOVSKY, A., et al., First direct comparative test of single crystal rhodium and molybdenum mirrors for ITER diagnostics, Fusion Engineering and Design **123** (2017) 674–677.
[4.41] VAN ZEELAND, M.A., et al., Rev. Sci. Instrum. **84** (2013) 043501.
[4.42] DONNÉ, A.J.H., et al., Rev. Sci. Instrum. **75** (2004) 4694.
[4.43] KALLENBACH, A., et al., Divertor power load feedback with nitrogen seeding in ASDEX upgrade, Plasma Phys. Control. Fusion **52** (2010) 055002.
[4.44] LEHNEN, M., et al., Nucl. Fusion **53** (2013) 093007.
[4.45] LEHNEN, M., et al., J. Nucl. Materials **463** (2015) 39–48.
[4.46] COX, R.T., The Algebra of Probable Inference, Johns Hopkins Press, Baltimore, MD (1961).

[4.47] JAYNES, E.T., Probability Theory. The Logic of Science, Cambridge University Press, Cambridge (2004).
[4.48] SIVIA, D.S., SKILLING, J., Data Analysis: A Bayesian Tutorial, second edition, Oxford University Press, Cambridge (2006).
[4.49] VON DER LINDEN, W., V. Dose and U. von Toussaint, Bayesian Probability Theory. Applications in the Physical Sciences, Cambridge University Press, Cambridge (2014).
[4.50] GREGORY, P., Bayesian Logical Data Analysis for the Physical Sciences: A Comparative Approach with Mathematica Support, Cambridge University Press, Cambridge (2005).
[4.51] VERDOOLAEGE, G., et al., Potential of a Bayesian Integrated Determination of the Ion Effective Charge via Bremsstrahlung and Charge Exchange Spectroscopy in Tokamak Plasmas, IEEE Trans. Plasma Phys. **38** (2010) 3168–3196.
[4.52] GELMAN, A., CARLIN, J.B., STERN, H.S., DUNSON, D.B., VEHTARI, A., RUBIN, D.B., Bayesian Data Analysis, 3rd Edition, Chapman & Hall/CRC, Boca Raton, FL (2013).
[4.53] GILKS, W.R., RICHARDSON, S., SPIEGELHALTER, D.J., eds., Markov Chain Monte Carlo in Practice, Chapman & Hall/CRC, Boca Raton, FL (1996).
[4.54] FISCHER, R., et al., Bayesian modelling of fusion diagnostics, Plasma Phys. Control. Fusion, **45** (2003) 1095–1111.
[4.55] FISCHER, R., et al., Integrated data analysis of fusion diagnostics by means of the Bayesian probability theory, Rev. Sci. Instrum. **75** (2004) 4237–4239.
[4.56] RATHGEBER, S., et al., Estimation of profiles of the effective ion charge at ASDEX Upgrade with Integrated Data Analysis, Plasma Phys. Control. Fusion **52** (2010) 16.
[4.57] FISCHER, R., et al., Integrated data analysis of profile diagnostics at ASDEX Upgrade, Fusion Sci. Technol. **58** (2010) 675–684.
[4.58] SVENSSON, J., et al., Modelling of JET Diagnostics Using Bayesian Graphical Models, Contrib. Plasma Phys. **51** (2011) 152–157.

Chapter 5

MAGNETIC CONFINEMENT

J. L. Duchateau

Institute for Fusion Research by Magnetic Confinement,CEA

France

In fusion devices, large magnetic fields are needed to confine the plasma. Such fields are efficiently generated by superconducting magnets. The history of superconductivity and that of fusion cross paths at the beginning of the eighties. Nowadays, several large-scale superconducting machines are in operation. The main characteristics of the magnet system required by these machines are illustrated by ITER, the world's largest fusion experiment, presently under construction. After an introduction to applied superconductivity, this chapter emphasises the design of large magnet systems for the fusion environment. For this purpose, a review is carried out, providing an analytical approach to the issues at stake, supported in many cases by numerical calculations. A survey is made about the different materials being considered for present day and for future reactors. The main design principles for the components of cable in conduit conductors — a specific high current, high field conductor adapted to the fusion environment — are explained. A quench is a fast–propagating superconducting-to-resistive transition. As it occurs, a large amount of magnetic energy will quickly be extracted into external resistors to protect the magnet system. The issue of quench detection is critical to fusion superconducting magnets due to the high voltages and the inherent pulsed operation of the tokamak, which remains by far the most mature reactor configuration considered for future power plants.

5.1. SUPERCONDUCTING MAGNETS FOR MAGNETIC CONFINEMENT FUSION

In experimental fusion systems, large magnetic fields are needed to confine the plasma [5.1]. The generation of the required field in large vacuum chambers — such as that of ITER (835 m^3) — is achieved using superconducting magnets. This constitutes one of the main technological challenges to be tackled towards a commercial reactor.

5.1.1. From JET to Tore Supra and ITER

Until the beginning of the eighties, all fusion magnet systems used resistive silver alloyed copper conductors with good mechanical properties and endure the large electromagnetic stresses. This was still possible due to the small size of the machines and their pulsed, not-steady state, mode of operation. The largest machine of this type ever built is the joint European torus (JET), which requires more than 1 GW of power to energize its magnet system. This large power can only be produced using flying wheel generators, which in turn is only possible due to the short duration of the plasma discharges (10 to 30 s). The following expression is given for the toroidal field (TF) magnet system resistive power P, where J_{cu} is the current density in copper (~10 A mm^{-2}), L is the TF magnet turn length, B_t is the plasma magnetic field and R is the tokamak major radius:

$$P_{\text{resis}} = 2p\,\frac{r_{\text{cu}}\,J_{\text{cu}}\,L\,B_{\text{T}}\,R}{m_0} \tag{5.1}$$

By design, ITER remains a pulsed machine and the electrical power necessary to energize the whole system using resistive magnets (P = 2 GW for 500 s) cannot reasonably be obtained from the electric grid. The high power required by resistive magnets and prospective steady state machines pushed the plasma physics community towards the development of superconducting magnet systems in experimental fusion machines. Superconductivity was first introduced in small tokamaks such as T-7 (R = 1.22 m) in 1978 in the Soviet Union and TRIAM (R = 0.8 m) in 1990 in Japan, using Nb_3Sn. Today, all major magnetic confinement fusion experiments (shown in Table 5.2) are superconducting. Six machines are presently in operation — Tore Supra [5.2] in France, LHD [5.3] in Japan, EAST [5.4] in China, KSTAR [5.5] in Korea, W7-X [5.6] in Germany and SST-1 [5.7] in India — and two more are under construction — JT-60SA [5.8] and ITER [5.9].

The first major experiments employing superconductors were Tore Supra in France (R = 2.4 m) and T-15 [5.10] in the Soviet Union. Both machines ramped magnetic fields up to 9 T for which the classical use of 4.2 K NbTi conductors did not meet the requirements. The debate went on at the end of the seventies about two possible choices:

- The use of niobium-tin (Nb_3Sn) conductors cooled by a forced flow of helium to ~4 K.

- The use of niobium-titanium (NbTi) conductors with pressurized helium, bath cooled at 1.8 K by the means of a new cryogenic technology developed at CEA, in France.

The insufficient industrial maturity of Nb_3Sn technology clearly appeared during the acceptance tests of the TF system of T-15. Resistive parts in the magnets prevented the steady state operation of the tokamak, decommissioned in 1991. This was again seen by a large international fusion experiment at Oak Ridge national laboratory [5.23] where six large coils were tested introducing forced flow refrigeration. One of those was made of Nb_3Sn and again showed resistive parts.
At the beginning of the eighties, the main design objective for the TF system of Tore Supra was to push forward the application of the NbTi: a cheap superconducting material that is insensitive to mechanical strain and suitable to high fields (9 T). For this purpose, superfluid helium bath, at a temperature of 1.8 K and a pressure of 1 bar, was used as coolant for the first time at industrial level. The industrialization of 1.8 K refrigeration techniques, at this occasion, has been a real breakthrough, enabling higher fields on superconducting NbTi magnets.

TABLE 5.1: Power requirements for Tore Supra, JET and ITER in case of selection of copper magnet systems [5.15].

Fusion Machine (Pulse duration)	Major Radius (m)	Plasma Volume (m^3)	Plasma Magnetic Field (T)	Fusion Power (MW)	Electrical power TF system (copper coils) P_{resis} (MW)
TS (1000 s)	2.4	24	4.5	0	~150 (superconducting system was selected)
$JET_{upgrade}$ (10 s)	2.96	100	4	~20	~500 (copper magnets)
ITER (500 s)	6.2	837	5.3	~400	~800 (superconducting system in construction) ~20 in cryoplant [5.11]

TABLE 5.2: Superconducting machines in fusion by magnetic confinement [5.15].

Name	Nature	Major Radius R (m)	Maximum Field cond. (T)	Stored Energy TF (MJ)	Superconducting Material/ T_{op} (K)	Operationstatus
TS	Tokamak	2.4	9	600	NbTi/1.8	Since 1988
LHD	Heliotron	3.9	6.9	920	NbTi/5	Since 1998
EAST	Tokamak	1.7	5.8	400	NbTi/5	Since 2006
KSTAR	Tokamak	1.8	6.7	470	Nb_3Sn and NbTi/5	Since 2008
SST-1	Tokamak	1.1	4.2	56	NbTi/5	Since 2015
W7-X	Stellarator	5.5	5	620	NbTi/4	Since 2015
JT-60SA	Tokamak	3.	5.65	1060	NbTi/5	Expected in 2020
ITER	Tokamak	6.2	11.8	40000	Nb_3Sn and NbTi/5	Expected in 2025

5.1.2. The ITER adventure

It is not possible to cover the description of all tokamaks presented in Table 5.2. The superconducting magnet system of a large tokamak will therefore be illustrated by that of ITER. The ITER adventure was initiated at a meeting in Geneva in November 1985. At that meeting, Ronald Reagan and Mikhail Gorbachev agreed to encourage an international collaboration aiming to master fusion energy. However, it was only in 1991 that four initial parties (Europe, Russia, Japan and the United States) embarked on a six years project with a dedicated team: ITER was born.

The ITER organization was later extended to three more parties (India, Korea, and China) and the construction of the machine officially started in 2006 at the Cadarache site in the south of France.
To prove the feasibility of thermonuclear fusion as a source of energy, ITER is taking a major leap forward from the most performing fusion machines ever built: JT-60 in Japan and JET in Europe. For example, JET's major radius[37] is 3 meters in dimension, while a radius of 6.2 meters has been selected for ITER. By extrapolation from the scaling laws developed on JET and the other machines, ITER will achieve its goal by sustaining a stable discharge for up to 500 seconds, producing 400 MW of fusion power with an energy amplification ratio[38] Q of 10.
To fulfil its mission, ITER will deal with many unprecedented technological challenges. These challenges concern the design and commissioning of the plasma facing components, the high-power plasma heating sources and the very large sized components. Among the latter, the commissioning of the superconducting magnet system is one of the most remarkable. Deeply buried at the very heart of the tokamak, the superconducting magnet system is the true backbone of the machine, and repairs to its components are hardly conceivable, let alone a few protruding joints. The quality assurance process during fabrication is therefore conducted in such a way as to avoid any possible fault.
The 838 m^3 ITER plasma (a torus with a 12.4 m diameter and a 21 m^2 cross section) burning at 100 million kelvins will be confined by the machine's superconducting magnet system, which will operate at a temperature of 5 K. The magnet system represents about 30% of the cost investment of ITER.

5.1.2.1. An engineering approach of ITER dimensioning

The electrical power associated to the refrigerator needed to compensate for all losses at cryogenic temperatures can be estimated about 25 MW. This value is to be compared to the 2 GW of power required by an equivalent resistive system.
It is important to try to link the objectives of ITER to its main engineering parameters, namely R, the major radius, a, the plasma minor radius and B_t, the toroidal field at the centre of the plasma (Eq. 5.2). Given this relation and a target fusion power P_{fus}, the pair (R, B_t) is selected in tight connection to calculations of cost, required magnetic flux for inductive mode, availability of technology and accessibility of the plasma through ports. To satisfy the objectives of ITER, the pair was chosen as R = 6.2 m and B_t = 5.3 T. Due to the toroidal shape of the device, the magnetic field increases (from the centre of the plasma to the conductor on the magnet system) by a factor greater than two, which imposes the use of Nb_3Sn for the ITER TF system.

$$P_{fus} \sim \frac{R^3 B_t^4}{A^4} \quad \text{, where A = R/a.} \tag{5.2}$$

The design of the magnet system of a tokamak reactor is also tightly linked to the mechanics of the system. The main principles of mechanical design for the tokamak can be found in [5.13]. A key part of the ITER TF structure is the vault formed by 18 TF inner legs, which is dimensioned to resist the centring and hoop stresses associated with the large Laplace forces in place. The vault is composed at 80% of steel and insulating material while the superconductor itself only occupies 4% of the total cross section. This example emphasizes the dominating role of the supporting structures.

5.1.2.2. The superconducting magnet system for ITER

Mainly the ITER magnetic field is composed by three major systems shown in Fig. 5.1 and described in Table 5.3. The following discussion is intended as a short summary of the ITER documentation concerning the design of its magnet system, which is thoroughly reviewed in [5.9] and [5.24].

[37] Radius of the plasma torus.
[38] The energy amplification factor (Q) is the ratio of the output fusion power to the input heating power.

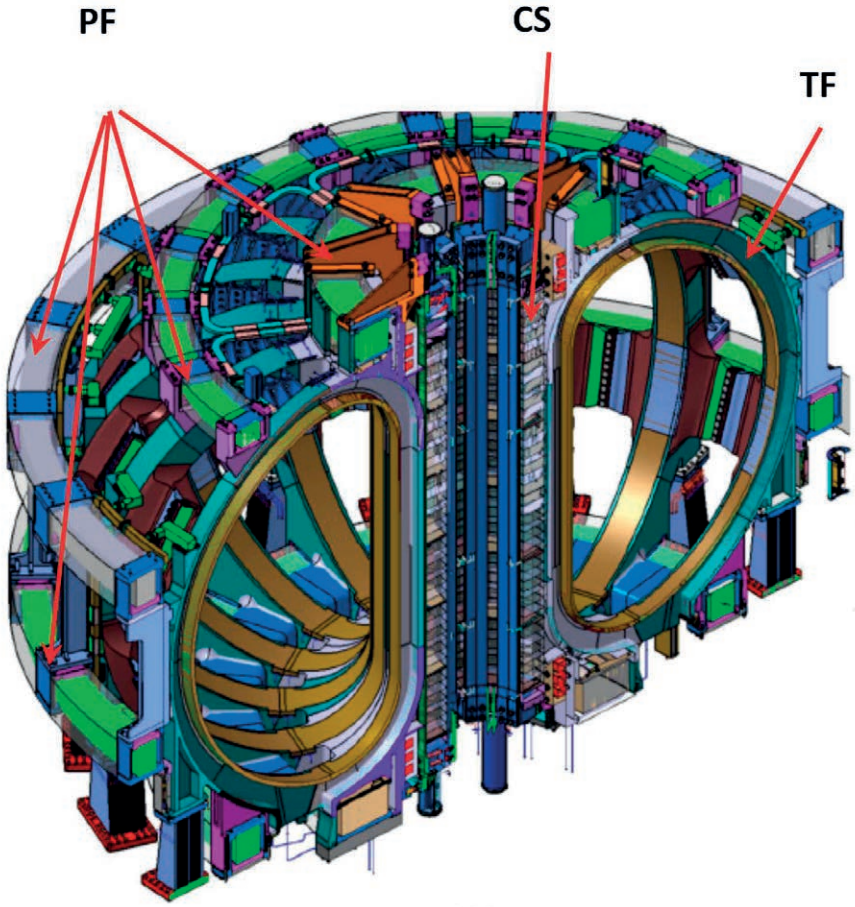

FIG. 5.1. The three major components of the ITER superconducting magnet system (Courtesy of the ITER organization, [5.9])

- The toroidal field (TF) system providing the main magnetic field to confine the particles.
- The central solenoid (CS) providing the inductive flux to ramp and shape the plasma current.
- The poloidal field (PF) system allowing stabilization and positioning of the plasma current.

Table 3: Main characteristics of the ITER superconducting systems.

System	Energy (GJ)	Peak Field (T)	Total Mat (MA)	Cond. Length (km)	Weight total/strand (t)
TF	41	11.8	164	82.2 (Nb_3Sn)	6540/396
CS	6.4	13	147	35.6 (Nb_3Sn)	974/118
PF	4	6	58.2	61.4 (NbTi)	2163/224
Correction coils		4.2	3.6	8.2 (NbTi)	85/5

All ITER magnets are wound from cable in conduit conductors (CICC), which are described in Section 5.3. The properties of the superconducting materials used in each system are described in Section 5.2. Protection against sudden irreversible losses of superconductivity known as quenches is presented in Section 5.4. It is to be noted that the TF system is a DC system while the PF and the CS systems are superconducting pulsed coils, posing new challenges for applied superconductivity.

5.1.3. The ITER TF system: double pancakes inserted within steel plates

The TF system is the most important magnet system in ITER. It is composed of 18 D-shaped Toroidal Field Coils (TFC) like the ones shown in Fig. 5.2. Each coil consists of a winding pack enclosed in a thick steel case. The winding pack is a bonded structure of 7 double pancakes, each inserted within a steel radial plate. It includes 134 turns of reacted and insulated CICC. The total length of the five regular double pancake is 760 metres but the two side double pancakes are shorter. The double pancakes are reacted for two weeks within large ovens at 850K. They are insulated after reaction and transferred into the plates. The name of this production process is Wind-React-Transfer. This phase is a true challenge due to the brittleness of Nb_3Sn after heat treatment. The coil terminals (two per winding pack) are formed after winding. They protrude from the lower curved part of the TFCs in the form of 6 double pancake joints (linking adjacent double pancakes) and corresponding helium feeder manifolds.

When energized alone, the TF system is submitted to large magnetic forces, mainly a hoop and a centring force. These magnetic forces induce primary stresses, which are contained by multiple large steel structures (conductor jacket, plates, casings). The overall current density in the TF inner leg is therefore driven by the large section of structural steel, limiting the overall current density in the range of 11 $A \cdot mm^{-2}$. The thickness of the TF coil in the radial direction is therefore driven by the structures and not by the superconductor.

In modern superconducting tokamaks, operated or under construction, the centring force is contained by wedging the inner legs of the coils, forming a vault as presented in Fig. 5.2. During plasma operation, secondary stresses are induced in the TF coils due to their interaction with the coils of the PF system, leading to out-of -plane stresses. They are contained by wedging the outboard region with specific mechanical structures such as the outer-inter coil structures (OIS) and pre-compression rings shown in Fig. 5.2.

The hydraulic length of the regular pancakes on ITER is just about 380 meters, or half of the conductor unit length. This is achieved by design of the cooling helium inlets located on the inner surface (plasma side) of the coil at the double pancake. Cold helium is thus supplied in the high field inner region where most of the nuclear heating is concentrated. It cools the two pancakes in parallel and exits through the joints located on the outer surface (cryostat side) of the coil at the bottom curved part. An 8 $g \cdot s^{-1}$ helium massflow is circulating in the conductor.

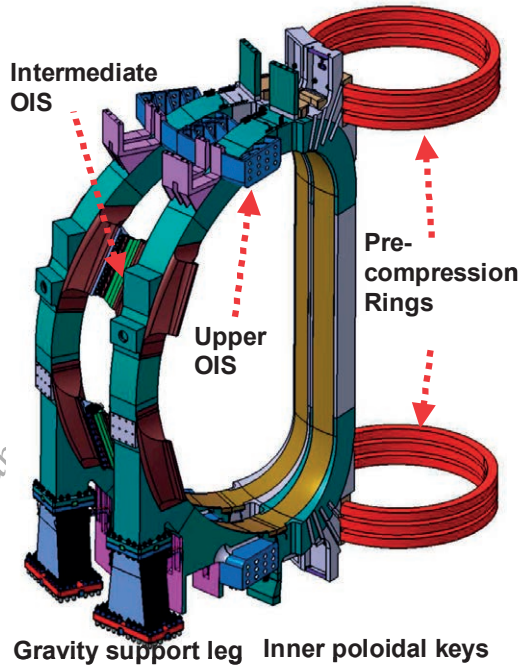

FIG. 5.2. The ITER TF system with highlights on the mechanical structure set up to resist out of plane loads (Courtesy of the ITER organization [5.9]).

5.1.4. Validation of the magnet system design: the ITER model coils

Significant international effort was put into the design, manufacture and testing of two model coils during the preparation phase of ITER (1997–2002) [5.12]:

- An ITER central solenoid coil model was manufactured by the US and Japan. Europe collaborated in the fabrication of the conductor and the model was tested at the JAERI facility in Japan.
- An ITER toroidal field coil model was manufactured and tested at FZK facility in Europe. The European community also fabricated the conductor.

The model coil experiments (2000 to 2002) played a major role to test the behaviour of Nb_3Sn CICCs at ITER relevant scales. Unexpected degradation of performance was found due to the great sensitivity of Nb_3Sn strands to strain. This point will be further explained in Section 5.3.5. The strain is mainly due to the differential thermal contraction arising between steel and Nb_3Sn during cooling from the reaction temperature of 900 K to 5 K. Additional strains, including a bending strain, were identified during the model coil experiments. The bending strain can be related to the Lorentz force loading the strands at nominal current. The sensitivity of Nb_3Sn strands to strain is not yet fully modelled and the characteristics to be adjusted (void, twist pitches, cabling patterns, cycling) remain under investigation. The design of the ITER CICCs was adapted, especially the CS CICC submitted to cycling in operation, to account for these effects.

5.1.5. DEMO: the next step to ITER

The next step to ITER will be DEMO: a fusion reactor that should typically provide 500 to 1000 MW of electric power. Its construction could start in the thirties, after ITER has delivered the relevant results in the deuterium tritium operational phase.

There is now an important European activity related to DEMO coordinated by EUROFUSION [5.14]. The aim of DEMO is to create a reactor featuring near ignition operation, tritium autonomy and a net electrical power output of several hundreds of megawatts. In a pragmatic approach, a pulsed version of DEMO (2 to 3 hours pulse length), looking like an extrapolation of ITER to larger dimensions, is being considered. The plasma magnetic field would be in the same range as that of ITER for a major radius of approximately 9 meters.

This solution would not require the use of high temperature superconductors and the magnet system would have the same characteristics as that of ITER using CICC TF coils in casings arranged as a vault. However, the magnet design will certainly be revised to simplify the TF cooling, which could be achieved by drastically shielding the TF system from nuclear heating, improving the casing's cooling and increase the temperature margin around 2 K. Note that the expected electrical power needed for the DEMO magnet refrigerator is low, around 25–30 MW.

As for ITER, the dimensions and optimal parameters of such a machine will be determined by an integrated approach. In addition, new constraints imposed by exploitation of the reactor will play a strong role in the design and commissioning of DEMO.

5.2. INTRODUCTION TO APPLIED SUPERCONDUCTIVITY

5.2.1. Superconductivity [5.1, 5.16]

For liquefying helium and for the first observation of the extraordinary property of zero electrical resistance exhibited by certain materials (superconductors) below a certain critical temperature[39] T_c, Dutch physicist Heike Kammerlingh-Onnes was awarded the 1911 Nobel prize in physics. Trains "flying" above their tracks by magnetic levitation, electricity storage in giant magnetic coils, electro-technical machines and power transmission cables with virtually no Joule losses and magnetic fields delivering high resolution images of the internal structure of the human body, are few of the dreams generated by superconductivity, since its discovery in 1911.

Besides zero electrical resistance, the materials discovered by Kammerlingh–Onnes[40] possess another remarkable property, discovered in 1933 by German physicists Walter Meissner and Robert Ochsenfeld: the Meissner effect. Ignoring the London penetration depth, superconductors can be said to exhibit perfect diamagnetism. In other words, the superconducting material fully expulses its internal magnetic field up to a certain critical field value B_{c1}. Herein

[39] The critical temperature at which a type I superconductor becomes superconductive varies with the isotopic mass of the compound.

[40] Also known as type I superconductor.

lies the second obstacle hampering the development of superconductor applications: superconductivity is lost above a critical magnetic field strength.

For many years physicists thought that there was only one type of superconductivity (type I) and that the magnetic anomalies observed in some samples were solely due to the presence of impurities. In the 1950s however, Russian physicists Vitaly L. Ginzburg and Lev D. Landau came up with a theory for a second kind of superconductors, which was later confirmed by Russian-American physicist Alexei Abrikosov in 1957. Type II superconductors exhibit a completely different type of magnetization characterized by a mixed state that allows them to retain their superconducting properties even in intense magnetic fields and up to B_{c2}. Abrikosov, Ginzburg and the anglo-american physicist Anthony J. Leggett were awarded the 2003 Nobel prize in physics for their research in superconductors.

In 1957 American physicists John Bardeen, Leon N. Cooper and John R. Schrieffer published their theory of superconductivity, for which they received the 1972 Nobel prize in physics. The Bardeen–Cooper–Schrieffer (BCS) theory describe electrons as moving through the crystal lattice as Cooper pairs (two electrons with opposite spins). The pairs behave as spin-zero bosons and condense into a single quantum state by a phonon interaction. It is this electron-phonon interaction that explains resistivity and superconductivity. Ion, in response to the passage of an electron (10^6 m · s^{-1}), moves thereby creating an area of positive charge, which is maintained after the passage of the electron. This attracts another electron that pairs up with the first. It thereby resists the Coulomb repulsion but not the thermal agitation, which explains why above a critical temperature, superconductivity vanishes.

The BCS theory, which applies to 'conventional' low temperature superconductors (LTS), does not apply to superconductivity at relatively high temperatures. For instance, it does not apply at liquid nitrogen temperature 77 K (or –196°C) and a fortiori at ambient temperature[41]. In 1987, German physicist Johannes G. Bednorz and Swiss physicist Karl A. Müller were awarded the Nobel Prize in physics for their work on high temperature superconductors (HTS). They discovered a lanthanum based copper oxide perovskite material with superconducting properties at temperatures in the range of 35 K (–238°C). By replacing lanthanum with yttrium, particularly in $YBa_2Cu_3O_7$, the critical temperature was significantly increased, within the cuprate superconductors. HTS are all type II superconductors.

5.2.2. Critical field and Critical temperature

Critical fields (B_c) and critical temperatures (T_c) of the most common superconducting materials are presented in table 5.4. Experimental results have shown that a parabolic law (Eq. 5.3) can relate the critical field of a given material to its critical temperature, as that given in Fig. 5.3 for NbTi.

$$B_c = B_{c0}\left[1 - \left(\frac{T}{T_c}\right)^2\right] \tag{5.3}$$

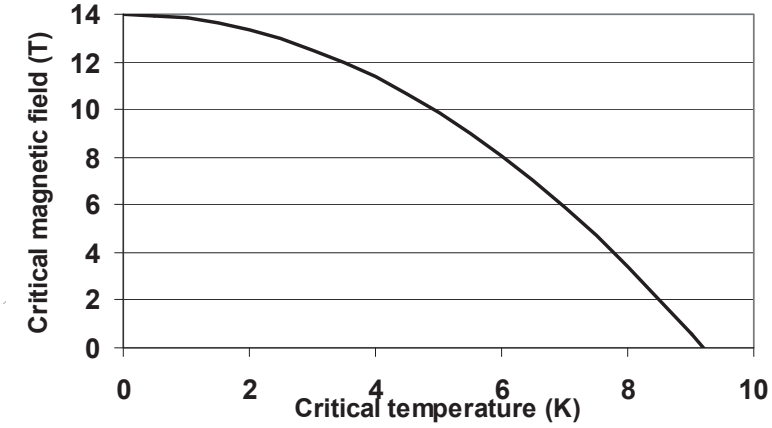

FIG. 5.3. Illustration of relationship between critical field and critical temperature for NbTi.

[41] The 77 K threshold was reached by compounds such as Y-Ba-Cu-O and the current records stands at around 165 K at high pressure, and 138 K at atmospheric pressure.

TABLE 5.4: Critical fields and temperatures of the most important superconducting materials.				
Type	Material	T_c (K)	B_{c1} (mT) 0 K	B_{c2} (T) 0 K
I	Al	1.18	10.5	
	Sn	3.72	30.5	
	Pb	7.18	80.3	
	Hg	4.15	41.1	
II	Nb	9.25	240	0.26
	NbTi	9.5	10	14
	Nb_3Sn	18	7	25.5
	Nb_3Al	19		42
	Nb_3Ge	23		37
	$PbMo_6S_8$	15		60
	MgB_2	39		?
	$Yba_2Cu_3O_2$	93		140
	$Bi_2Sr_2Ca_2Cu_3O_{10}$	110		184
	$Tl_2Ba_2Ca_2Cu_3O_{10}$	125		75
	$HgBa_2Ca_2Cu_3O_{10}$	133.5		

5.2.3. Applications of superconductivity: the NbTi era

While type I superconductivity does not present any great potential for application, only two kinds of type II superconducting materials are industrially mature for real world application: Niobium-titanium NbTi (T_c = 9.2 K) and Niobium-tin Nb_3Sn (T_c = 18 K). Unfortunately, these materials are LTS and only present their superconducting properties when cooled to liquid helium temperatures (4.2 K). HTS were supposed to lead the way to higher temperature superconductivity. Unfortunately, HTS are ceramics which makes production costly and mechanically difficult. Until now, there have been nearly no real commercial applications of HTS in power devices but many prototypes for transformers, motors and power cables in several cities [5.17].

Type II superconductors can withstand very strong magnetic fields and are able to carry extraordinarily high current densities up to a third critical value labelled J_c, the critical current density, that varies with the magnetic field as shown in Fig. 5.4. This was at the origin of the development of the first superconducting magnets[42]. In fact, applications requiring large magnetic field in a large volume, for instance magnetic resonance imaging, nuclear magnetic resonance (NMR), particle physics and fusion, predominantly use type II superconductors. The most popular material used for such purposes is NbTi, a cheap material with very good mechanical properties. The yearly production of NbTi is in the range of 1500 to 3000 tons with a typical price of 150–200 € per kilogram.

Superconductivity also significantly decreases electric power consumption, even considering the cryogenic efficiency of the facilities. One watt dissipated at 4.2 K requires a minimum consumption of 200–300 watts at ambient temperature in the largest industrial power plants.

[42] The current densities that can be generated in superconducting regimes are huge in comparison with what can be achieved with domestic or industrial electro–technical applications (around 10 $A \cdot mm^{-2}$).

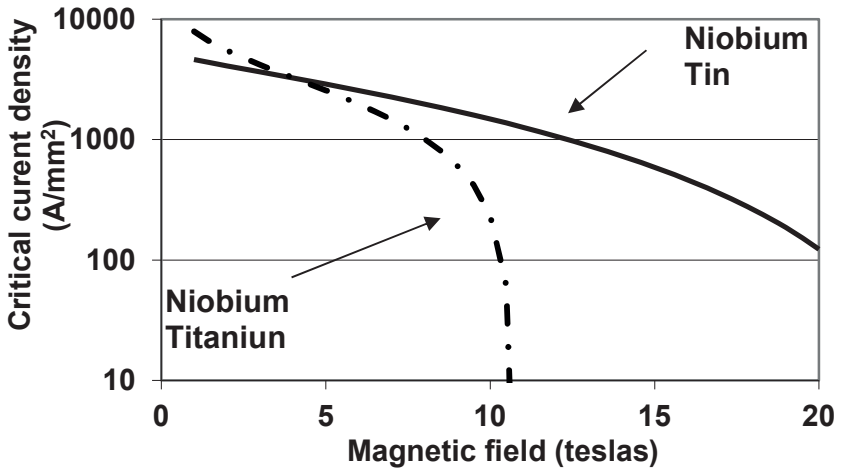

FIG. 5.4. Critical current densities as a function of the magnetic field for the two most commonly used superconducting materials: NbTi and Nb_3Sn.

As can be seen in Fig. 5.4, Nb_3Sn may operate at higher magnetic fields than NbTi. The current commercial record is held by a system developed by Bruker, operating at 23 T and Nb_3Sn for nuclear magnetic resonance (NMR), which plays a determining role in matter and life sciences. Nb_3Sn was discovered before NbTi, but it is about 4 times more expensive. The formation of the crystallographic structure of Nb_3Sn, known as A15, requires heat treatment for two weeks divided in several stages. The final stage typically lasts for 200 hours and requires temperatures around 850K. When reacted, Nb_3Sn becomes very brittle and cannot be manipulated easily without affecting critical properties of the material. It is also highly sensitive to strain contrary to NbTi. The yearly production of Nb_3Sn, around 20 tons, linked to NMR magnets has increased due to ITER project during the recent period. The cost is significantly higher than for NbTi, about 500 €/kg.

ITER requirements for magnetic fields higher than 10 T imposed the use of Nb_3Sn for both the TF and CS systems. More than 500 tons of Nb_3Sn strands are needed in ITER. This presents a true challenge for the Nb_3Sn industry.

The brittleness of Nb_3Sn required the development of the so-call wind react and transfer method for ITER. Components such as double pancakes in the TF system are reacted within dedicated moulds in large furnaces. After the heat treatment, the double pancakes are slightly unwound to be insulated and transferred into the final radial plates. This very delicate process was first tested at a reduced scale during the ITER model coil programme (Figs 5.5 and 5.6) and being refined for the industry.

It can be noted that HTS have found an interesting application for current leads in superconducting magnets. For instance, all current leads at the large hadron collider are made of HTS. It is also the case for the current leads of the ITER magnet system and most fusion machines, which make use of Bi-2223 HTS, sparing about 1 kW of cryogenic power at 4 K. HTS materials are being considered on the long term for fusion reactors [5.18], as they offer large temperature margins which could greatly simplify the magnets' cooling system.

FIG. 5.5. Insulation of a pancake during the model coils programme (Courtesy of EFDA Ref. 5.30).

FIG. 5.6. Heat treatment of a pancake during the ITER model coils programme (Courtesy of EFDA Ref 5.30).

5.2.4. Superconducting strands

Superconducting conductors are the result of a specific electrical engineering design for operation at very low temperature named cryoelectricity. The elementary strands, also known as composites, have shapes much like those of the conductors made of copper or aluminium strands. To manufacture kilometres of conductor, it is necessary to press billets of 100 to 200 kg. After extrusion, the material is drawn to the specified diameter in the range of a millimetre.

Within the strands, the superconducting filaments are divided and twisted to limit the losses due to inter-filament coupling under AC magnetic fields. The filaments are arranged within a copper matrix, which occupies a substantial part of the section and plays an important role for stabilization and protection of the strand in case of a quench.

These characteristics are visible in Fig. 5.7 featuring the simplest existing strand used in magnetic resonance imaging. Fig. 5.8 and Fig. 5.9 respectively show a Nb_3Sn strand and a NbTi strand developed respectively by the European industry and the Chinese industry for ITER. These strands require very fine filaments with diameters of 5 to 10 µm.

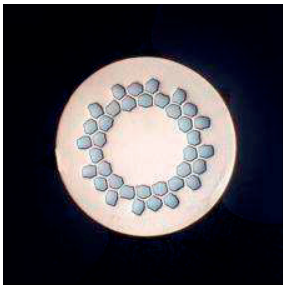

FIG. 5.7. NbTi strand for MRI (ϕ = 1mm, Courtesy of Alstom)

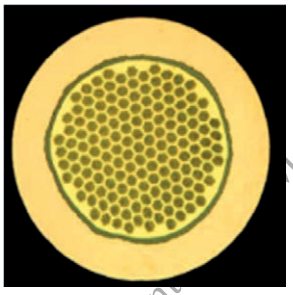

FIG. 5.8. ITER Nb_3Sn strand (ϕ = 0.82 mm, BAS). (Courtesy of the ITER Organization)

FIG. 5.9. ITER NbTi strand for (ϕ = 0.73 mm, WST)
(Courtesy of the ITER Organization)

Large magnets require high currents. As in conventional electrical engineering, it is necessary to build cables made of several transposed strands to enable the best possible current distribution. The ITER cables are cable in conduit conductors made of roughly 1000 strands.

Strand plating is compulsory to avoid sintering during the heat treatment of Nb_3Sn. Strand plating also play an important role in avoiding high coupling losses under varying magnetic fields. The material used for Nb_3Sn strand plating is chromium. A trade-off is made between a sufficient resistivity to limit the losses and a sufficiently low resistivity for current redistribution inside the cable between strands in case the critical current is exceeded in some part of the cables, which is likely to happen. Nickel plating, performed after the production of the strand, is the reference solution for the ITER NbTi strands. Unfortunately, Ni plating imposes the complex operation of removing the plating during the manufacture of the connexions. An alternative could have been the use a CuNi barrier inside the strand as for the NbTi strands of JT-60SA's TF system.

5.2.5. Critical current density

When current circulates in a superconductor, a Lorentz force is applied to the vortices or fluxoids in which the magnetic field is trapped. In an ideal type II superconductor, there are no means to prevent the fluxoids of the mixed state from moving and thus generating an electrical field. This is the so-called flux flow regime. In commercial superconductors such as NbTi and Nb_3Sn, methods have been developed to pin the fluxoids, preventing their movement. The pinning sites are associated with the α phase of titanium in NbTi and with the grain joints in Nb_3Sn. At critical current density J_c, the Lorentz force exceeds the pinning force and the flux flow regime, which is associated with heat dissipation. In this sense, the critical current density characterizes the capacity of the superconducting material to carry current.

5.1.5.1. The I-V curve

The critical current (I_c) of a multifilamentary wire can be determined from the I-V curve for a short sample of length l. For LTS, the critical current density J_c is defined by an electrical field E_c of 10 μV.m^{-1}. An index n can also be defined characterizing the transition. The electrical field E in a superconductor is given by Eq. (5.4), J being the current density in the superconductor:

$$E = E_c (J/J_C)^n \quad (5.4)$$

For Nb_3Sn, the non-copper current density J_{noncu} is substituted by J_c to account for the presence of bronze and barriers materials, which are required by Nb_3Sn but do not carry any current (Eq. 5.5), where A_{NbTi} is the NbTi section; and A_{noncu} is the non-copper section.

$J_c = I_c / A_{NbTi}$ (for NbTi) $\quad J_{noncu} = I_c/A_{noncu}$ (for Nb_3Sn) (5.5)

From these definitions, the voltage (V) across a short sample of length l is described by Eq. (5.6) and illustrated in Fig. 5.10 for 100 mm of a typical NbTi wire at 5 T having a critical current of 400 A and a value of n equal to 30. A critical current of 400 A is observed for a voltage of 1 μV, according to the definition.

$$V = E_C \, l \left(\frac{I}{I_C}\right)^n \quad (5.6)$$

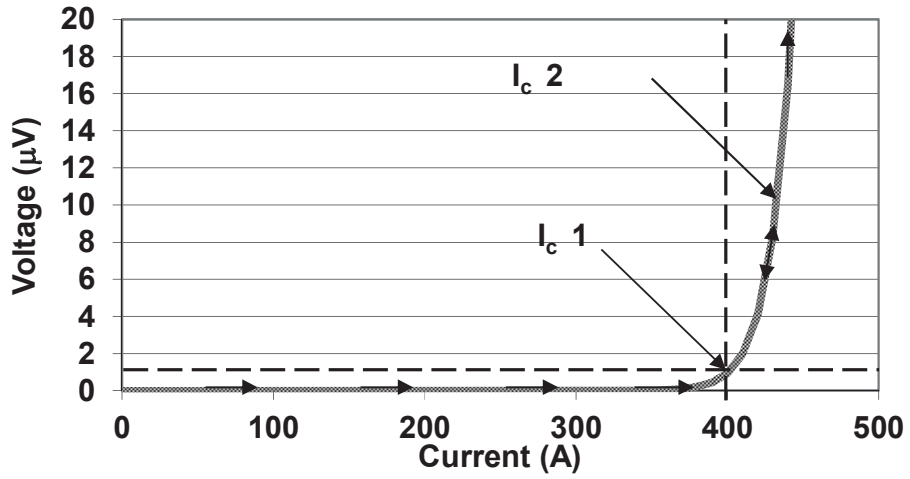

FIG. 5.10. Typical I-V curve of a NbTi wire at 5 T having a critical current of 400 A and a value of n equal to 30.

The n index is a quality indicator for NbTi conductors. Low values of n can be associated with heterogeneities of the filament sections or sausaging of the filaments along the strand. The n index is a decreasing function of the critical current. At high magnetic fields or high temperatures n is low. For instance, values in the range of 30 are expected at 5 T. The n index can be calculated between point 1 (V_1 = 10 μV.m^{-1}) and point 2 (V_2 = 100 μV·m^{-1}) according to Eq. (5.7).

$$n = \frac{\log V_2/V_1}{\log I_2/I_1} \quad (5.7)$$

As can be observed in Fig. 5.10, there is a first reversible part of the transition but beyond a certain value of E_0 the transition to normal sate is irreversible. This is only indicative and there is no absolute rule. The location of the transition point is affected by characteristics such as the amount of copper in the strand or the nature of cooling.

5.1.5.2. I-V testing of a strand sample

The VAMAS is the standard mandrel used by the fusion technology community to compare results from different laboratories and companies. It has a typical diameter of 30 mm and supports ten turns of wire (approximately one meter in length), which is enough to suppress end effects, which can appear on samples of shorter lengths. The experimental setup for strand testing is presented in Fig. 5.11, where approximately one meter of strand is wired around a VAMAS mandrel. Two central voltage taps across one turn are used for critical current determination corresponding to a length of about 100 mm. For Nb_3Sn testing, a special titanium mandrel fitted for heat treatment at 850K can be used. The sample is inserted into the bore of a magnet and characterized at 4.2 K in a helium bath. In certain laboratories, adapted internal cryostats allow measurements at different temperatures.

FIG. 5.11. VAMAS mandrel

5.1.5.3. I-V testing of an ITER conductor sample: The SULTAN test facility.

Conductor qualification and quality control tests for ITER are carried out at the SULTAN facility [5.19], CRPP Switzerland (see Fig. 5.12). A magnetic field of up to 11 T is produced by a split coil configuration in the bore of which the sample is inserted. SULTAN samples (see Fig. 5.13) are hairpin samples, with two ~3.6 m long legs, with a high field zone of ~400 mm, somewhat like the last cable twist pitch. Samples are tested in pairs with joints at the top and bottom, and are instrumented with voltage taps and temperature sensors at various locations. Measurements can be done either at a fixed temperature increasing the current (critical current measurement) or at a fixed current varying the temperature (current sharing temperature measurements). Measurement campaigns have highlighted possible non-equipotential voltage gradients in the jacket cross section for which the voltage is no longer taken at a specific point but averaged from an array of 6 probes azimuthally disposed on the jacket. In addition, AC loss and stability tests can be performed on the conductors.

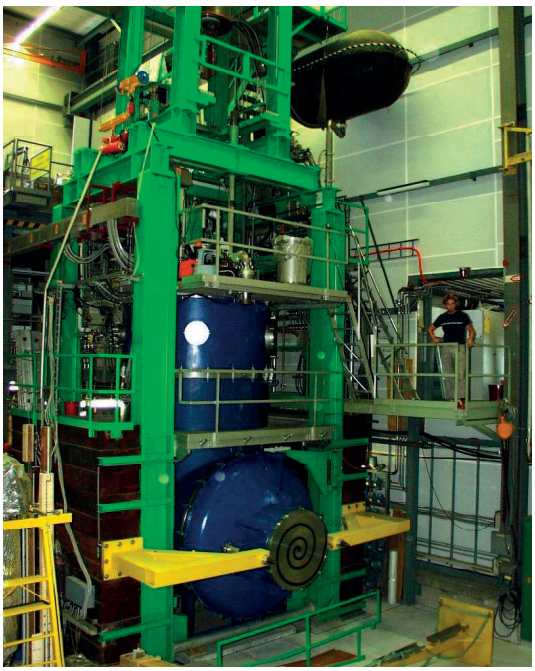

FIG. 5.12. The SULTAN test facility
(Courtesy of Swiss Plasma Center Ref. 5.19)

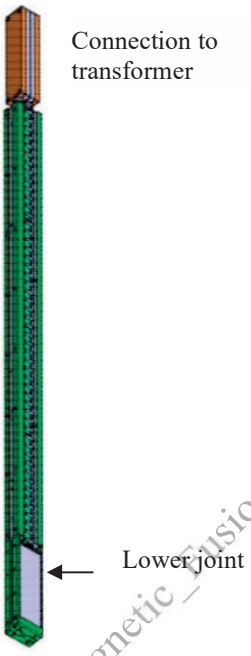

FIG. 5.13. Sultan sample
(Courtesy of Swiss Plasma Center Ref. 5.19)

5.2.6. Parameterization of critical current density

For design and quality assurance purposes, the properties of superconducting materials are parameterized. For example, J_c is a function of magnetic field and temperature, and for Nb_3Sn, J_{noncu} is additionally sensitive to strain. Parameterization of such dependencies is necessary to correctly estimate the temperature margin and losses. The parameters are obtained in dedicated test facilities where samples (c.f. Fig. 5.11) are tested with fine control over temperature, magnetic field and strain.

5.1.5.4. Parameterization of niobium-titanium

The following parameterization (Eqs 5.8 and 5.9) is used for NbTi in fusion programmes such as ITER and JT-60SA. A detailed explanation is given in [5.20].

$$J_c(B,T) = \frac{C_0}{B}\left[1-\left(\frac{T}{T_{c0}}\right)^{1.7}\right]^g \left[\frac{B}{B_{c2}(T)}\right]^a \left[1-\left(\frac{B}{B_{c2}(T)}\right)^b\right] \quad (5.8)$$

$$B_{c2}(T) = B_{c20}\left[1-\left(\frac{T}{T_{c0}}\right)^{1.7}\right] \quad (5.9)$$

J_c as given by Eq. (5.8) is plotted in Fig. 5.14 for a temperature range relevant to the TF system in JT-60SA, including the temperature margin. The following parameters for Eqs. (5.8) and (5.9) are typically used for JT-60SA TF conductor:

C_0=1.22 10^{11} A.T^{-1}.m^{-2}, B_{c20}=14.93 T, T_{c0}=8.7 K, α=0.9, β=1.2, γ=1.94.

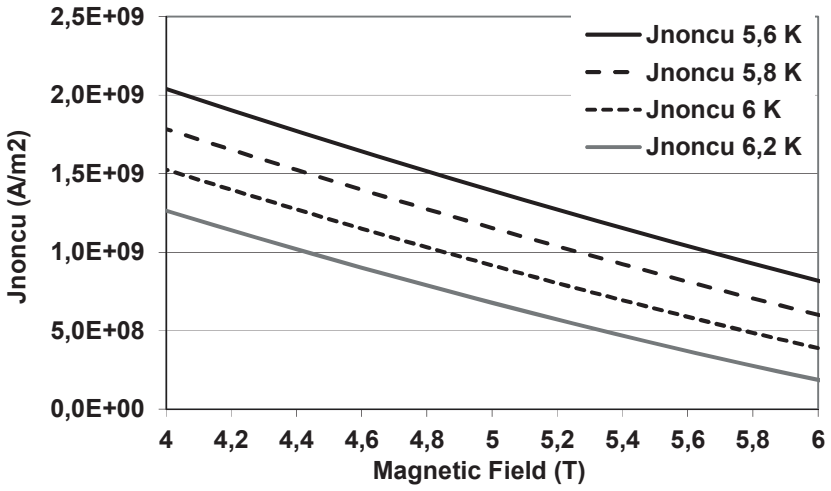

FIG. 5.14. Critical current density for JT-60SA NbTi superconducting material.

5.1.5.5. Parameterization of Nb_3Sn

Similarly, a detailed parameterization of Nb_3Sn has been defined for ITER, which can be found in [5.21]. Figure 5.15 shows the influence of the magnetic field and the temperature on J_{noncu}.

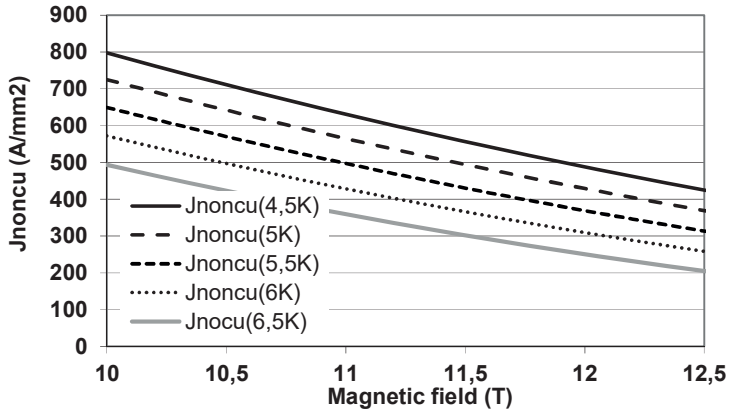

FIG. 5.15. Typical non-copper current density in ITER Nb_3Sn superconductors.

5.2.7. Temperature margin, current sharing temperature and load line

In a fusion project, the notion of temperature margin ΔT_{margin} is very important. From an operating temperature T_{op}, ΔT_{margin} is defined as the increase in temperature, which produces the system transition to normal state. ΔT_{margin} can be adjusted by changing the section of superconducting material so that external disturbances (for example a plasma disruption) will not bring the coil to transition. ITER's CS and TF coils typically use a temperature margin of 0.7 K. ITER's NbTi PF system uses a ΔT_{margin} of 1.5 K.

5.1.5.6. Current sharing temperature T_{cs}

The current sharing temperature (T_{cs}) is defined in (Eq. 5.10) for Nb_3Sn[43], where I is the current in the superconductor. T_{cs} is associated with the current and not be confused with T_c. For a magnet being operated at a temperature T_{op}, T_{cs} is such as: $\Delta T_{margin} = T_{cs} - T_{op}$.

$$J_{noncu}(B_{op}, T_{cs}, e) = \frac{I}{A_{noncu}} \quad (5.10)$$

5.1.5.7. Load line and temperature margin

ΔT_{margin} can be evaluated graphically using the superconducting material's parameterization, the load line of the coil and the effective maximum field on the conductor. This method is illustrated in Fig. 5.16 for Nb_3Sn. Eq. (5.11) describes the load line of the coil.

$$B_{eff} = kI \quad (5.11)$$

For the ITER TF system, B_{eff} = 11.2 T. The load line crosses the I_c (5.8 K) line at 68 kA, the ITER TF nominal curent. This means that T_{cs} = 5.8 K for T_{op} = 5 K and thus ΔT_{margin} = 0.8 K.

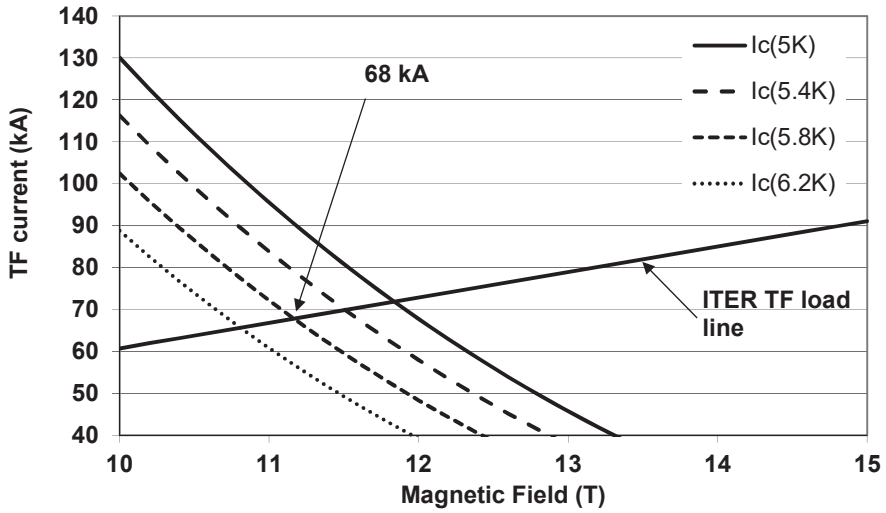

FIG. 5.16. Illustration of T_{cs} calculations for the ITER TF system.

5.2.8. Superconducting materials in ITER

In the framework of the ITER project, 514 tons of Nb_3Sn and 309 tons of NbTi will be produced [5.22], [5.24]. The strand specifications, most of which have been described in the preceding section, are given in Tables 5 and 6. The residual resistivity ratio (RRR) of a copper strand is defined as the ratio of the copper resistivity at 4 K to the copper resistivity at 300 K. The copper strands in ITER are made of oxygen free high conductivity (OFHC) copper. The resistivity of ITER OFHC copper is presented as a function of temperature in Fig. 5.17, showing a characteristic plateau at 4.2 K associated with the RRR.

[43] The same kind of definition can be made for NbTi.

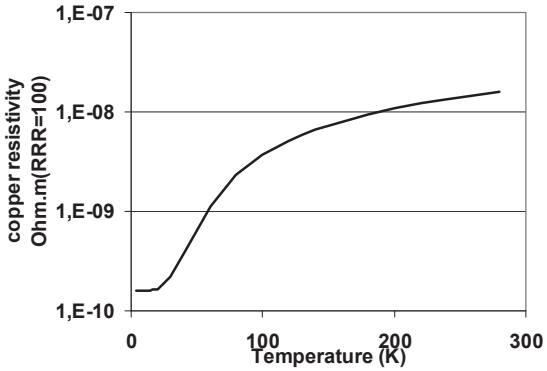

FIG. 5.17. Resistivity of OFHC copper as a function of temperature (RRR=100).

TABLE 5.5: Specification of chromium-plated, Nb_3Sn strands for the ITER TF coils.

Item	Requirement
Superconductor type	Nb_3Sn
Minimum piece length	1000 m
Un-reacted, Cr-plated strand diameter	0.820 ± 0.005 mm
Twist pitch	15 ± 2 mm (right hand)
Cr plating thickness	2.0 +0 -1 µm
Cu-to-non-Cu volume ratio	1.0 ± 0.1
RRR of Cr-plated strand (273 to 20 K)	> 100 (after heat treatment)
Minimum critical current at 4.22 K and 12 T	190 A
Resistive transition index at 4.22 K and 12 T (as measured on ITER barrel)	> 20 in the 0.1 to 1 $\mu V \cdot cm^{-1}$ range
Maximum Hysteresis loss per strand unit volume at 4.22 K over a ± 3 T cycle	500 $mJ \cdot cm^{-3}$

TABLE 5.6: Specification of Nickel-plated, NbTi-based ITER strands.

Item	Strand Type 1	Strand Type 2
Superconductor type	NbTi	NbTi
Minimum piece length	1000 m	1000 m
Ni-plated strand diameter	0.730 ± 0.005 mm	0.730 ± 0.005 mm
Twist pitch (right hand)	15 ± 2 mm	15 ± 2 mm

Ni plating thickness	2.0 +0 -1 μm	2.0 +0 -1 μm
Cu-to-non-Cu volume ratio	1.6 -0.05/+0.15	2.3 -0.05/+0.15
Filament diameter, D_{fil}	≤ 8 μm	≤ 8 μm
Inter-filament spacing, S_{fil}	≥ 1 μm	≥ 1 μm
RRR of Ni-plated strand (between 273 and 10 K)	> 100	> 100
Minimum critical current, I_{Cmin}, at 4.22 K and B_{ref}	≥ 306 A (B_{ref} = 6.4T)	≥ 339 A (B_{ref} = 5.0T)
Resistive transition index 4.22 K	> 20 in the 0.1 to 1 μV.cm^{-1} range at B_{ref} = 6.4 T	> 20 in the 0.1 to 1 μV.cm^{-1} range at B_{ref} = 5.0 T
Maximum Hysteresis loss per strand unit volume at 4.22 K over a ± 1.5 T cycle	55 mJ.cm^{-3}	45 mJ.cm^{-3}

5.3. THE CABLE IN CONDUIT CONCEPT FOR CONDUCTORS

Most superconducting magnets are dry magnets, which means that the conductor is not directly in contact with the coolant, e.g. magnetic resonance imaging, nuclear magnetic resonance magnets, and the detectors of the CERN LHC, Atlas and CMS. It is almost the case for the beam magnets of the LHC despite some wetting by the superfluid helium. Cryostable magnets — which allow T_c to be temporarily exceeded on long lengths and recovery at the operating temperature — do not exist in practice. An exception is the Tore Supra TF system, which operates in a superfluid helium bath.

The magnets of ITER, EAST, KSTAR, W7-X, SST-1 and JT-60SA are forced flow cooled magnets due to the very high voltages and currents carried by the coils and the important cryogenic losses. These losses are absorbed by the cryogenic system while maintaining the temperature. CICC is used in all tokamaks with superconducting magnets except Tore Supra. In principle, any kind of forced flow conductor should be able to sustain a high voltage to the ground but CICC is also well adapted for fast heat deposition (such as the one caused by a plasma disruption) allowing a limited temperature increase. The ITER coils, for instance, require high currents (70 to 80 kA) and very high voltages (10 kV to ground for the PF and CS systems in normal operation considering the envisaged plasma scenarios in ITER). This is due to the size of the magnetic systems, which led to CICC as the best choice in the present state of superconducting technology.

The CICC concept was introduced in 1975 by M. Hoenig at the Massachusetts Institute of Technology, USA. Since then, numerous prototype coils have been made of CICC, but the experience with magnet systems employing this type of conductor is limited. The Westinghouse coil (CICC shown in Fig. 5.18) was the first large sized coil employing CICC. It was built with a Nb_3Sn conductor in the framework of the “large coil task”, an R&D programme related to fusion [5.23]. Its performance was unfortunately limited by some spreading out of a resistive phase in the magnet.

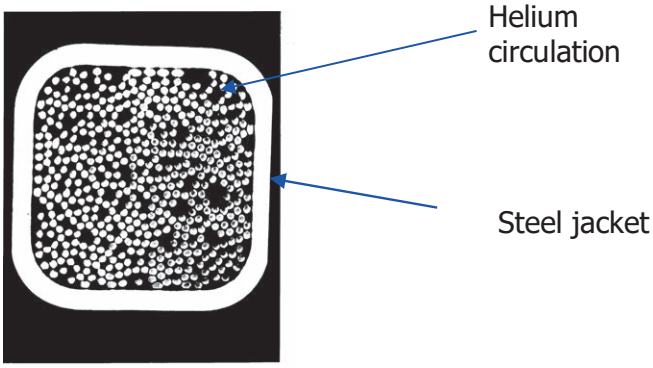

FIG. 5.18. CICC 1988 (20.8 mm x 20.8 mm, 20.7 kA, 9 T Ref. 5.23).

A CICC is made by cabling several stages of superconducting and copper strands and compacting the cable inside a conduit generally made of stainless steel. The CICC for ITER and JT-60SA are composed of several components, which can be seen in Fig. 5.19 and Fig. 5.20: superconducting strands, copper strands, steel bandages, helium, and a steel conduit. In a project like ITER [5.24], the optimum composition of the conductor components is calculated using certain design criteria, mainly:

- The temperature margin of the conductor associated with the critical energy deposition accepted by the conductor determines the superconducting section.
- The required copper section to protect the cable in case of a quench.

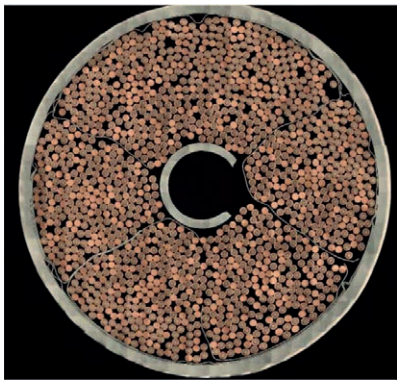

FIG. 5.19. The ITER TF dual channel CICC 68 kA, 11.8 T, Φ = 39.7 mm (Courtesy of the ITER Organization Ref. 5.24).

FIG. 5.20. The JT-60SA TF CICC 25.7 kA, 5.65 T, 18 × 22 mm²(cable) (Courtesy of JT-60SA Ref. 5.8).

To keep the temperature constant, heat loads from all sources (W_{hl}) are removed from the coils by circulating a mass flow ($\dot{m}$) through the conductor. This requires pump work to compensate for the viscous pressure losses and a heat exchanger where the power is extracted from the system as depicted in Fig. 5.21.

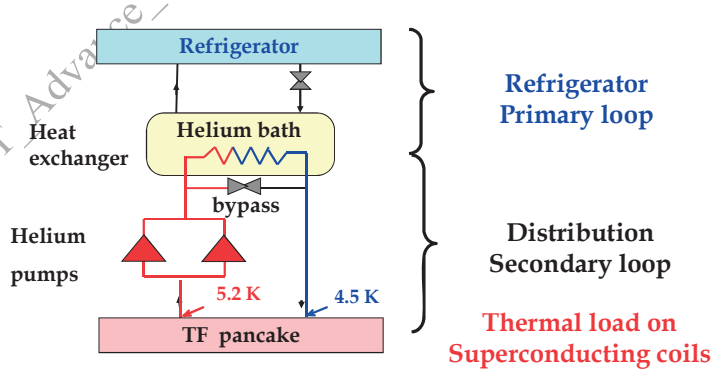

FIG. 5.21. Cryogenic loop associated with forced flow.

5.3.1. Fusion magnets: fast energy deposition and CICC temperature margin

CICC benefits from the very high volumetric heat capacity of helium[44] to limit the temperature excursion during fast energy depositions (see Table 5.7). This is particularly well illustrated in the case of constant power heat deposition, where the composite section behaves adiabatically within one time constant τ_{comp}[45] and its temperature excursion is then damped by the volumetric heat capacity of helium as demonstrated for the case of JT-60SA CICC in Fig. 5.22. For any kind of disturbance existing in tokamaks, calculations can be performed with a classical thermo-hydraulic code such as GANDALF [5.26].

TABLE 5.7: Comparison between enthalpies of metallic materials and helium at 4.5 K.

Material	Enthalpy for a temperature excursion of 2 K starting from 4.5 K (kJ·m^{-3})
Copper	2.7
Nb_3Sn	7.4
A316 (steel)	40
helium (constant volume)	640
helium (local enthalpy)	1660
helium (enthalpy at constant pressure)	2270

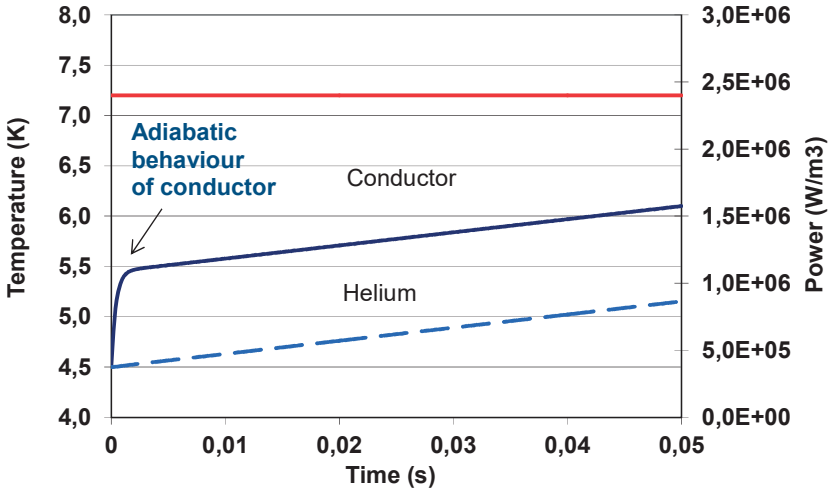

FIG. 5.22. Temperature excursion in JT-60SA NbTi CICC (constant power heat deposition).

According to [5.25], the analytical solution for the NbTi composite temperature (supposed uniform) can be obtained for a constant heat power deposition. The critical energy W_c, which is the largest acceptable energy deposition to stay in superconducting state, may also be derived. This is applied to the case of JT-60SA in table 5.8. The analytical expression of the composite temperature T_{comp} for a constant heat power deposition Q_0 (W·m^{-3}) is given as a function of time in Eq. (5.12) and Eq. (5.13). C_{comp} is the composite volumetric heat capacity of (J·m^{-3}K^{-1}), A_{comp} is the composite section (m^2), P is the wetted strand perimeter (m) and h is the heat transfer coefficient to helium (W·m^{-2}K^{-1}).

$$T_{comp}(t) = T_0 + \left(\frac{Q_0}{C_{comp}}\right)(t_{He} + t)t_{comp}/t_{He} \qquad (5.12)$$

[44] About 500 times the volumetric heat capacity of metallic materials.
[45] A very short time!

$$t_{comp} = \frac{C_{comp}A_{comp}}{hP},\ \tau_{\mathrm{He}} = \frac{C_{\mathrm{He}}A_{\mathrm{He}}}{hP} \quad (5.13)$$

In this case, a simple expression (Eq. (5.14) is given for the critical energy W_c (J·m^{-3}) referring classically to the composite volume. W_c is also dependent on Δt, the time during which this energy is deposited. It ca be seen that W_c is proportional to the temperature margin and very linked to the helium enthalpy.

$$W_c = C_{\mathrm{He}}(T_{cs} - T_0)(1 - a_0)\frac{void}{1-void} \quad a_0 = \frac{1}{1+\frac{Dt}{t_{He}}} \quad (5.14)$$

TABLE 5.8: Critical energy (W_c) for JT-60SA TF CICC (Constant power heat deposition Δt = 50 ms).

h	τ_{He}	τ_{comp}	α_0	W_c
600 W.m^{-2} K	72 ms	0.45 ms	0.59	102 mJ/cm^{-3}
1000 W.m^{-2} K	43 ms	0.27 ms	0.46	135 mJ/cm^{-3}

Sudden heat depositions may happen during plasma disruptions causing losses in the superconducting strands, when fast magnetic field variations (within 50 to 100 ms) affect the whole coil over lengths well above several meters. The cable in conduit conductor provides an adequate solution to this problem by offering:

- A local helium enthalpy reservoir.
- A very high wetted perimeter of superconducting strands via subdivided access to the reservoir.
- Low AC losses in the conductor by time constant control through the contact resistance between strands.

5.1.6. Cryogenic loss removal by forced flow of helium

The helium mass flow circulating through the conductor limits the temperature increase due to thermal losses, residual nuclear heating and AC losses generated by the varying magnetic fields of a plasma discharge. CICC can be made with one helium channel or two channels like those of ITER. The central channel helps keeping the pressure drop at an acceptable level when the hydraulic length of conductor is large, as it is in ITER. In the latter case, helium circulates at two different velocities in the central channel and in the strand region. It can be considered in first approximation that a single fluid is circulating in the CICC with an average velocity, provided the heat exchange is good and thus the temperature in the two regions is the same. The average fluid velocity v is given by (Eq. 5.15), where $\dot{m}$ is the total helium mass flow rate, $\bar{r}$ is the average helium volumetric mass and A_{He} is the total helium section.

$$v = \frac{\dot{m}}{\bar{r}\,A_{\mathrm{He}}}. \quad (5.15)$$

A typical mass flow in ITER CICC is in the range of 10 g·s^{-1} and the residence time of helium in the coil can be very long (2250 s in the case of the ITER TF system where the pancakes' hydraulic length is about 380 meters). Helium is injected at a pressure of roughly 5 bars, and a temperature between 4.5 K and 5 K. The equation governing the heat power in such a circuit is Eq. (5.16), where ΔH is the enthalpy variation between the helium inlet and outlet, Q_{hl} is the DC power losses along the circuit and $\dot{m}$ is the helium mass flow.

$$Q_{hl} = \dot{m}DH \quad (5.16)$$

To calculate the pressure drop ΔP along the hydraulic length, it can be considered that the helium mass flow is distributed between the two channels of the CICC. This distribution establishes an equal pressure drop along the two channels given by Eq. (5.17), where f is the friction coefficient, L_{h} is the hydraulic length, ρ_{He} is the helium volumetric mass and d_{h} is the hydraulic diameter of each channel. Writing the equilibrium enables to calculate the mass flow distribution between the two channels and the pressure drop.

$$DP = \frac{f L_{\mathrm{h}} \dot{m}^2}{2\bar{\rho}_{\mathrm{He}} d_h A_{He}^2} \quad (5.17)$$

Illustration: the ITER TF cable (see Fig. 5.23)

ITER TF cables have an 8 mm (inner diameter) central channel. The thickness of the spiral is 1mm. The injection temperature is typically 5 K at an inlet pressure of 5 bars. The main hydraulic characteristics are presented in Table 5.9, showing how different the two channels are from each other.

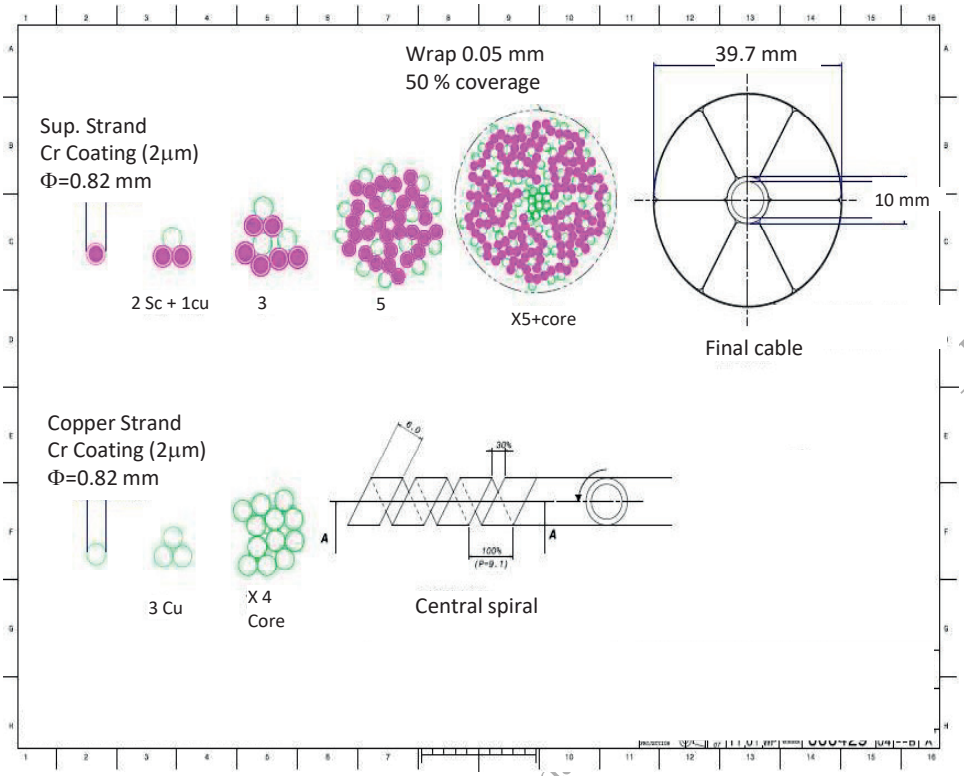

FIG. 5.23. Main design characteristics of the ITER TF CICC (Courtesy of the ITER organization).

TABLE 5.9: Hydraulic characteristics of the two channels in the ITER TF CICC.

	Central region	Annular region
Helium section	50.3 mm^2	344 mm^2
Wetted perimeter	25.1 mm	4040 mm
Hydraulic diameter	8 mm	0.34 mm
Mass flow	4.9 $g.s^{-1}$	3.1 $g.s^{-1}$
Reynolds number	2.12 10^5	843
Friction factor	0.058	0.28
Pressure drop	261 $Pa.m^{-1}$	261 $Pa.m^{-1}$

5.1.7. Pump work

The cryogenic heat load Q_{hl} from all sources is removed from the coils by circulating a mass flow $\dot{m}$ through the conductor to keep its temperature constant. This requires a pump work Q_{circ} to compensate for the viscous pressure losses corresponding to a cryogenic power (Eq. 5.18), where $\dot{m}/\rho_{He}$ is the volumetric flow circulated in the conductors, ΔP is the pressure drop which is forced by the circulating pumps and η_{circ} is the efficiency of pumping.

$$Q_{\text{circ}} = \frac{\dot{m}\Delta P}{\mathrm{r_{He}h_{circ}}} \quad (5.18)$$

The two main sources of heat on the 4.5 K refrigerator are therefore Q_{hl} and Q_{circ}, where Q_{hl} is the heat load on the magnet system and Q_{circ} is the circulation heat load. Q_{circ} is a direct function of Q_{hl} as the mass flow $\dot{m}$ is chosen according to the power Q_{hl}, which is to be removed to keep the superconductor temperature margins constant (Eq. 5.16). Q_{circ} is also related to the design of the magnet conductor and to the associated pressure drop characteristics.

Illustration: Estimation of the pump work of the ITER TF system

The pressure drop ΔP_{circ} along the total length of an ITER TF pancake can be calculated by multiplying the pressure drop per unit length by the total length of the conductor pancake (380 m): $\mathrm{D}P_{\text{circ}} = 380\frac{\mathrm{D}P}{L} \sim 10^5$ Pa. The total mass flow circulating along the 18 TF coils, each made up of 14 pancakes is:
$\dot{m} = (8 \times 14 \times 18)\ \mathrm{g}{\cdot}s^{-1} = 2020\ \mathrm{g} \cdot s^{-1}$. According to (5.18), this yields a required pumping power Q_{circ} of 2.6 kW if the efficiency of the circulation process is estimated as $\eta_{\text{circ}} = 0.6$.

5.1.8. Cable in conduit conductor design

The current density inside the CCIC cable is linked to the sections of its different components:

- A_{noncu}, the so-called non-copper section.
- A_{cu}, the copper section.
- A_{He}, the helium section.
- A_{add}, the additional metallic materials sections such as the internal spiral and the wrappings.

The sections for the ITER TF cable are presented in Table 5.10. It is to be noted that the A_{noncu} section is relatively small compared to A_{cu} and A_{He}.

TABLE 5.10: Overall current density in ITER TF cable.

Type of material in the cable (cable diameter: 39.7 mm)	Section (mm^2)	Relative occupation
Helium	422.9	30%
Total copper	508.3	41%
Non-copper	235.3	19%
Wrappings, spiral	71.3	6%
Total	1238	100%
J_{cable} ($A{\cdot}mm^{-2}$) 68 kA	55 $A{\cdot}mm^{-2}$	

A_{cu} plays a major role in the protection of the cable; its design, presented in the Section 5.4.2, is mainly focused upon this purpose. A_{He} plays an important through its large enthalpy; it is meant to eliminate cryogenic losses by forced flow of helium and to stabilize the CICC in case of sudden heat deposition. The void fraction in the strand region of the CICC is kept low to mechanically stabilize the brittle superconducting material. Void fractions in the range of 29% are currently prescribed for Nb_3Sn while 34% is considered acceptable for NbTi CICC.
The A_{noncu} section is determined by Eq. 5.19. In the following expression, B is the magnetic field, I cable current, T is the temperature and ε is the material strain (not to be considered for NbTi). The worst combination of B and T has to be considered in this operation.

$$I = A_{\text{noncu}}\, J_{\text{noncu}}(B, T, e) \quad (5.19)$$

If the parameterization of J_{noncu} is known (see Sections 5.2.6.1 and 5.2.6.2), A_{noncu} can be derived from estimated design temperature and magnetic field. The temperature is determined by adjusting A_{noncu} to respect $\Delta \mathrm{T}_{\text{margin}}$ and ensure the expected critical energy (see Section 5.3.2).

$$T = T_{\text{inliet}} + DT_{\text{tl}} + DT_{\text{JT}} + DT_{\text{add}} + DT_{\text{margin}}$$

In this expression, ΔT_{tl} is temperature increase due to thermal loads (AC losses + nuclear heat) while ΔT_{JT} is the temperature increase due to Joule Thomson discharges along the CICC. ΔT_{add} is the temperature gradient between the central tube and annular zone. Finally, ΔT_{margin} is the temperature margin.

Illustration: Application to the ITER TF system

For the ITER TF systems, T_{inlet} = 4.5 K, $\Delta T_{tl} + \Delta T_{JT} + \Delta T_{add}$ ~ 0.5 K and ΔT_{margin} = 0.7 K (disturbances included). The considered point is the TF inner leg on the plasma side.This yields a dimensioning temperature of T = 5.7 K. Due to the large size of the CICC, the magnetic field is not homogenous across the conductor cross section. The twisted strands oscillate between B_{min} and B_{max} due to the self-field of the conductor (see Fig. 5.24). The value B_{max} is thus too conservative for the calculation of A_{noncu} and an intermediate value is usually taken between B_{min} and B_{max}, depending on the n value B_{eff}. The non-copper section of the CICC can be dimensioned at this intermediate effective magnetic field value B_{eff}, which can be calculated using Eq. (5.20) if the electrical field of the conductor is taken as the average electrical field of the section of conductor. E_c is the reference electrical field for the critical current — also called the critical electrical field — and n is the transition index.

$$E = \frac{E_c}{A_{comp}} \int_{A_{comp}} \left[\frac{J}{J_{noncu}(B,T,e)}\right]^n dS = E_c \left[\frac{J}{J_{noncu}(B_{eff},T,e)}\right]^n \quad (5.20)$$

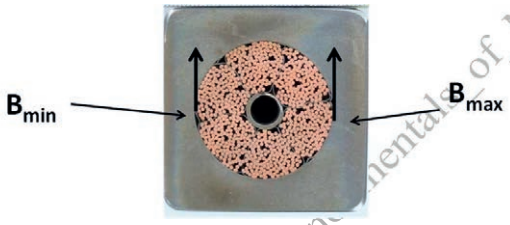

FIG. 5.24. Magnetic field gradient across an ITER CS conductor type.

Among A15 superconducting materials, Nb_3Sn is the most sensitive to strain. Strain sensitivity has long been investigated in Nb_3Sn strands with special attention on longitudinal (and axial) compressive strains. A compressive strain $\varepsilon_{thermal}$ naturally appears during cooling from the reaction temperature of 900 K down to the cryogenic temperature of 5 K due to the differential thermal contraction between the Nb_3Sn filaments and the copper strand matrix in a multi filamentary composite. The compressive strain is even stronger in CICC such as those of ITER due to the large steel jacket section and the associated differential thermal contraction. In general, the effective strain can be described as the sum of two components:

- The thermal strain $\varepsilon_{thermal}$ (differential thermal contraction between the steel jacket and Nb_3Sn during cooling).
- The strain due to the magnetic pressure ε_p(BI).

The latter component is to be attributed to the Lorentz force on the cable arising from the carried current. The Lorentz force applies to each strand and accumulates over the length of the cable. This effect is therefore linked to the size of the cable, which is large, and supposed to be proportional to BI. The role of the ε_p(BI) component was noted during the testing of the ITER model coils (2000 to 2002) as an unexpected degradation in performance, which could be scaled to about one kelvin of temperature margin degradation. This finding motivated the new design of higher performance Nb_3Sn conductor strands for ITER. During a crash programme, samples from all potential producers were tested at the SULTAN test facility and it was shown that a decrease of the cable void fraction from 33% to 29% was favourable to mitigate the effects of the magnetic pressure strain. It was recently discovered, that tightening the twist of the first two stages of the CICC could mechanically stabilize the conductor and avoid degradation over cycles. From a theoretical point of view, a full model of the total strain on the conductor (ε) is hardly possible. The total strain is compressive and applied to the strand but it is also a bending strain, which means that it is not uniform across a strand. In some cases, it is even possible for only certain parts of the strand to be in tension, causing the filaments to break.

This non-uniformity of strain raises a question about the method used to estimate the effective strain (ε) which should be considered in strand performances estimations and design of the CICC. As a matter of fact, there is no precise way to measure strain and it is usually taken as an adjusted parameter in the performance tests conducted at the SULTAN facility. The effect of the strain on strand performances is very high. A typical effective strain can be taken in the range of –0.75%, corresponding to more than a 50% degradation of the non-copper current densities in the composites. This explains the large degradation experienced by Nb_3Sn strands in CICC due to large void fraction (> 30 %), which allows bending under thermal contraction and Lorentz forces.
A third (beneficial!) component corresponding to the hoop strain (ε_{op}) — and associated with the Lorentz force in the coil — is added to the effective strain. ε_{op} is non-uniform along the conductor but is thought to slightly relax the compressive strain, especially in the CS coil (~0.1%). It is not clear, however, if this strain will be fully transferred from the jacket to the cable.

5.4. QUENCH PROTECTION IN FUSION MAGNETS

A quench is a quick irreversible transition from superconducting to normal state. In a CICC the resistive power appearing in the normal zone is transferred into helium. The expansion of the helium is the vector of the quench propagation in two directions. This propagation is characterized by a propagation velocity (one front). The quench can be triggered by different sources and magnets are designed such as to avoid quenches considering all possible internal and external loads. Overloads, which can appear during faults such as short circuits, non-opening of current breakers or unmitigated quenches are typically the most difficult to handle. The ITER coils which carry high currents (40 to 70 kA) are superconducting. Despite all precaution, margins taken to avoid quenches during plasma operation, their occurrence may not be completely ruled out. Possible causes for ITER coil quenches are listed in Table 5.11. There is not much experience in the protection of pulsed superconducting systems (such as the ITER PF and CS systems) and large inductive voltages appearing across the coils during operation make quench detection particularly challenging.
The detection and action time (τ_{da}) is the time between the initiation of a quench and the triggering of the fast safety discharge (FSD). An FSD (with current time constant τ) is triggered to extract the magnetic energy from the coil into external dump resistors. τ_{da} is small enough to limit the temperature increase in the coil, protecting it from damage, but high enough to filter out the electrical disturbances [5.27].
The eventuality of a quench is considered during the design phase of a superconducting magnet by dealing with:

- The design of the conductor itself.
- The maximum voltage to ground in a quench.
- The speed of quench detection.
- The presence of a direct current breaker.

Depending on the magnets, several solutions are possible to protect the magnet system. These are to be envisaged during the early stages of the project. In ITER magnets and fusion magnets in general, the most probable faults are related to leaks and high voltages.

TABLE 5.11: Possible quench sources in superconducting magnets.

Cause of quench	Illustration
Deterioration of insulation	Can occur during a FSD or in pulsed operation. Fault of insulation to ground in terminal or bus bars. Faulty or aged insulation. This can cause an arc.
Loss of coolant	Breakdown in refrigeration plant. Should trigger a decrease of the coil current.
Conductor quench	Unpredicted weakness or overestimation of conductor critical properties. Degradation of Nb_3Sn over cycles.
Loss of insulation vacuum or poor cooling of the TF casing	Triggers coil temperature rise.

Conductor movement or local crack in epoxy	Common in particle physics magnets training.
External causes	Beam losses in particle physics or plasma disruptions in fusion, other plasma events.
Mechanical	Under-designed or degradation of structural components can cause a quench under Lorentz forces.

High voltages

In DC magnets[46], significant voltages to ground only appear during FSDs and magnets often suffer from FSDs erroneously triggered by faulty sensors. During ITER normal operation, voltages greater than during FSDs will exist in the CS and PF systems, especially during the start-up phase of the plasma. Typical voltage to ground values in ITER are given in table 5.12.

TABLE 5.12: Typical voltages to ground in ITER magnet systems.

Coils	Energy [GJ]	Voltage to ground [kV] (Normal operation)	Voltage to ground [kV] (FSD)
TF	41	0	4
CS	6	~10	5
PF	4	~10	3 to 5

The most serious electric failure in superconducting magnets is arcing, which can either short circuit two neighbouring conductors or permanently damage parts or between conductor and ground. The severity of the damage is related to the amount of energy stored within the coil, part of which is dissipated in the arc. In fact, the configuration of fusion coils designed to tackle the problem of insulation failure imposed the use of cable in conduit conductors.
High voltage insulation is wrapped around the conductor to provide a true electrical barrier that allows for tests before applying filling materials such as epoxy resin. Epoxy resin is not sufficient on its own as it may contain undetected voids. Therefore, before impregnation, insulation layers made of Kapton are provided around the conductor, allowing for the tests. The TF winding packs are surrounded by insulation (fibre glass reinforced epoxy resin) and inserted into a stainless-steel casing. The insulation is externally covered by a conducting paint providing an equipotential voltage.
Illustrating the high voltages present in ITER, the feeder system consists of 31 units distributed around the tokamak, each weighing ~50 tons and being 30 to 40 m long. Each feeder is a complex subassembly that connects a coil (electrical power, helium, instrumentation) to the main containment building. The feeder contains two NbTi bus bar conductors. At each end of the feeder, a bus bar connects the coil to its warm terminals through HTS current leads. The bus bars are particularly sensitive subcomponents operating at low field but generally submitted to high voltage to ground, thus requiring special care.
All surfaces exposed to the cryostat vacuum have a hard ground connection. Currents flowing in potential ground shorts are limited by the grounding system of the power supply.
One of the non planar coil of W7-X is shown in Fig. 5.25. On the lower side of the image, an area is visible emerging from the rest of the magnet. This corresponds to electrical and hydraulic connections, like those of ITER, where the insulation is painted in conductive grey paint. Regarding fabrication, this area is particularly delicate. During the fabrication and tests of the W7-X coils, different kinds of insulation failures were detected in this area and could be eliminated as access, even difficult, is however possible for repair.
The insulating properties of helium are very dependent on pressure. At the very low helium pressures of the cryogenic vacuum, the helium insulating properties are very good. As the pressure increases (e.g. in case of a leak), the insulation is degraded towards the so-called Paschen minimum, which is reached at a characteristic value of pressure times the distance of the electrodes.

[46] Most superconducting systems and tokamak TF systems use DC magnets.

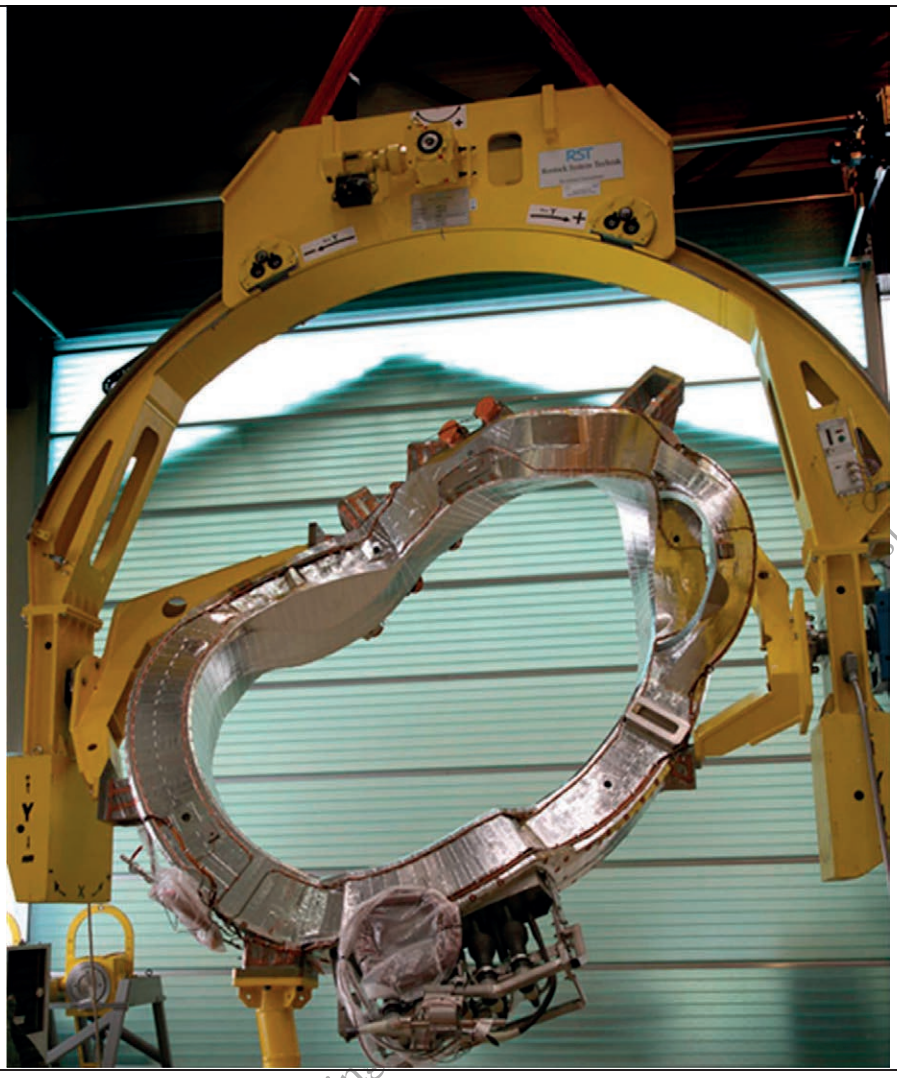

FIG. 5.25. W7-X non planar coil showing the connection region in the lower part (Copyright: IPP [5.6]).

In normal operation, coil vacuum is held between 10^{-5} and 10^{-6} mbar. Below 10^{-3} mbar, the breakdown voltage of helium is about 10 kV. Therefore, in normal operation, there is no risk of an arc even in the case of a breach in insulation. In summary, the risk only exists in case of double fault: vacuum degradation and an insulation breach.
After fabrication at room temperature, the magnets can be tested in degraded vacuum (Paschen condition) to detect eventual cracks or breaches in the insulation and avoid primary insulation defects. Contrary to bath cooled magnets, magnets with cable in conduit conductors are subject to a specific risk of leaks. Leaks will not happen inside the winding pack where the conductor is impregnated, leaving practically no void. Leaks are likely to appear in connections zone such as visible in Fig. 5.25.

5.1.9. The hot spot criterion

As soon as a quench starts, heat is dissipated with an associated temperature rise in the coil. This temperature increase is a function of the current decay due to the dump of the current density and copper content. The calculation of the temperature increase (Eq. 5.21) is classically made on the highly pessimistic assumption that the starting quenched point (cell) behaves adiabatically. The cell only involves the cable materials (A_{cu} and A_{noncu}) and not the helium; its calculation requires knowledge of the average resistivity of the cell in Ωm ($\rho=\rho_{cu}/\eta_{cu}$), the average current density in

the cell (J) in $A \cdot m^{-2}$, the average volumetric density of the cell (γ) in $kg \cdot m^{-3}$, the average specific heat capacity (C) in $J \cdot kg^{-1}.K^{-1}$ and the ratio of copper in the cell (η_{cu}).

$$\rho(T)J^2(t)\mathrm{d}t = g\,C(T)\mathrm{d}t \qquad (5.21)$$

According to the hot spot criterion, the maximum temperature (T_{max}) at the end of the current decay should not exceed 250 K. To achieve this goal, it is necessary for the conductor design to answer to two coupled questions:

- What is the amount of copper in the conductor?
- What is the time constant assuming exponential decay of the current?

Eq (5.21) can be rewritten in a more convenient way (Eq. 5.22). In this expression, U(T) is a function of the temperature only characterizing the section electrical and thermal properties (see Fig. 5.26).

$$\int_0^{¥} J^2(t)\mathrm{d}t \;<\; \int_{T_0}^{T_{max}} \frac{g\,C(T)}{r(T)}\mathrm{d}t = U(T_{max}) \qquad (5.22)$$

$J = J_0$; $t < \tau_{da}$ $\quad J = J_0\, e^{-t/\tau}$; $t > \tau_{da}$.

Classically, quench detection is performed over a time lapse τ_{da} during which the current is constant (details will be given in Section 5.4.3.1). Following the detection of a quench, a fast safety discharge of the current is initiated with a time constant τ:

Illustration: Estimation of FSD time constant for the ITER TF system given a detection delay τ_{da} of 2 s.

The total strand section A of the TF conductor (see table 5.10) is typically made of copper (67%) and non–copper (33%). Following design criteria, T_{max} is adjusted to remain below 250 K. The function U(T) for an ITER TF coil is plotted in Fig. 5.26. Supposing a copper RRR of 100 and a magnetic field of 12 T, it can be found that:

A = 743 mm^2; I = 68 kA; U (T_{max}) = 6.4 10^{16} $A^2s.m^{-2}$; J_0= 91 $A.mm^{-2}$
Therefore τ can be calculated according to Eq. (5.23).

$$J_0^2\,(\tau_{da} + \tau/2) = U(T_{max}) \Rightarrow \tau = 2[(U(T_{max})/J_0^2) - \tau_{da}] = 11\ s \qquad (5.23)$$

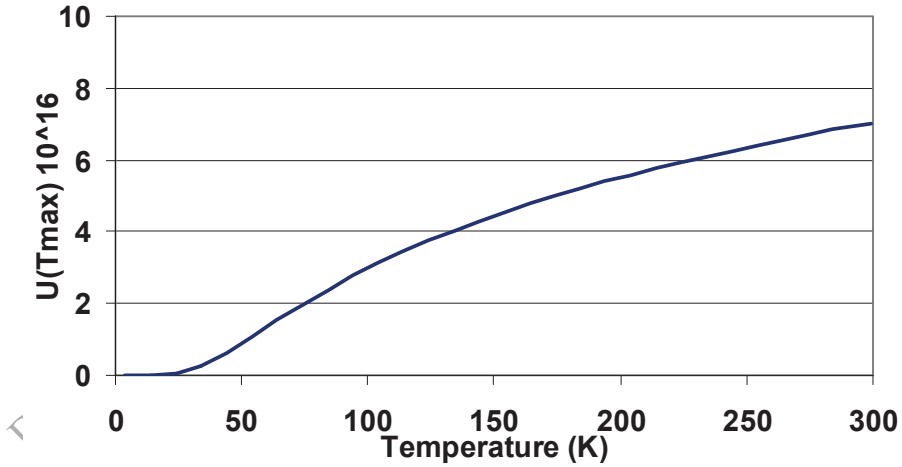

FIG. 5.26. U(T) function for an ITER TF conductor at 12 T.

5.4.3 The quench protection circuit

The ideal superconducting magnet is "self-protecting", dumping its stored energy into its own winding in case of a quench. This feature can be required e.g. in magnets for imaging, which have no electrical link with the room

temperature environment. Self-protecting magnets usually feature high normal zone propagating velocities to avoid local overheating. In case of a quench, the major risk is to dissipate all the stored magnetic energy of the coil just into the quenched zone, which has a limited extension, causing its burn. Ideally, if the whole magnet is quenched, the stored energy is uniformly dissipated over the winding pack, which is quite acceptable. Therefore techniques exist allowing an auto acceleration of the quench spreading it all over the magnet. In practice, this form of passive protection is limited to small coils (e.g. for MRI and NMR magnets) with low stored energy and low current density, in which case the voltage across the coil is null.

In case of a large stored energy, dumping through an external resistor, is the most appropriate solution. It is used in large magnets for particle physics (detectors) and fusion. The principle consists in dissipating most of the magnetic energy outside the magnet to prevent the hot spot from reaching temperatures above the maximum allowed. Fig. 5.27 illustrates the main components of the quench protection circuit (QPC) implementing this technique. The cryogenic superconducting magnet is connected to the warm electrical circuit by two current leads situated in ○ and ○. In normal operation, the current breaker is closed and short circuiting the resistor. Once the quench is detected by the sensors, the current breaker opens, the power supply is short circuited and the stored energy is dissipated into the external resistor R_e.

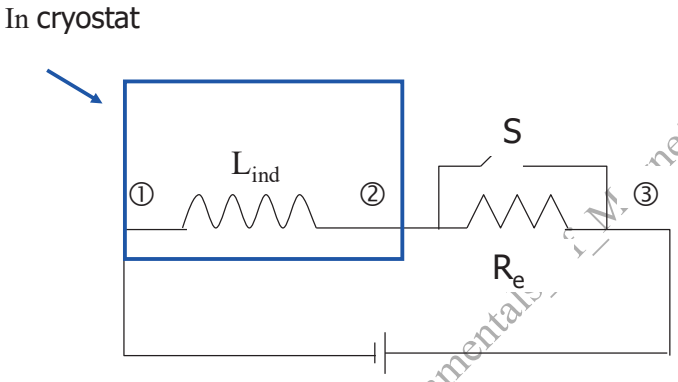

FIG. 5.27. Elementary quench protection circuit using an external resistor including the superconducting magnet characterized by its inductance L_{ind}, the external resistor R_e, the current breaker S and the power supply PS.

The maximum voltage across the coil terminals ($V_{b,max}$) is a parameter of great importance. It is directly linked to the maximum voltage to ground ($V_{g,max}$). It is generally possible to ground the resistor such that $V_{g,max} = V_{b,max}/2$. Neglecting the small internal resistance in the coil (compared to the external resistance), it is possible to write the equation of the current during a FSD:

$$L_{ind}\, dI/dt + R_e\, I = 0 \quad \Rightarrow I = I_0\, e^{-t/\tau} \tag{5.24}$$

$$\tau = L_{ind}/R_e \tag{5.25}$$

$$V_{b,max} = R_e\, I_0 \tag{5.26}$$

5.4.3.1Maximum voltage across the coil during fast safety discharges

It is possible to find a more general expression for $V_{b,max}$ by noting that the maximum voltage across the coil is proportional to the stored energy W_{mag} and inversely proportional to the current and the FSD time constant (5.27). Figure 5.28 shows the voltage distribution in the circuit.

$$V_{b,max} = 2\frac{W_{mag}}{I_0 t} \tag{5.27}$$

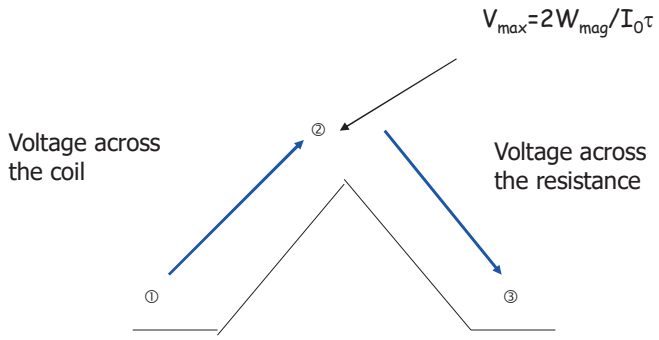

FIG. 5.28. Voltage distribution in the coil and the external resistor during a FSD neglecting the internal resistance of the coil.

Impact of $V_{b,max}$ on current breakers (or switches), the acquisition system and the insulation.

Whatever technology is chosen for the components, commuting the DC current into the resistor bank using a vacuum current breaker, there is an upper limit on $V_{b,max}$ ($V_{limit,cb}$). This upper limit is typically in the range of 3 kV. If this limit needs to be exceeded, several components will be connected in series. Therefore, it is recommended to adjust $V_{b,max}$ such that $V_{b,max} < V_{limit,cb}$.

Some of the sensors, particularly voltage sensors, are submitted to $V_{g,max}$ during operation. Specialists in acquisition systems have shown that the limit in acceptable voltage to ground for standard systems is ~3.5 kV. The value of $V_{g,max}$ is also the driving factor in insulation issues, especially in the terminals. Roughly speaking, the complexity of a project scales with $V_{g,max}$. On ITER, the value of $V_{g,max}$ is set typically to 10 kV, offering an unprecedented challenge as compared to values in the range of 2 kV in most existing projects.

5.4.3.2 Voltage reduction by coil subdivision

In most fusion projects, coil subdivision is implemented to reduce the voltage. The voltage of a project is driven by the stored magnetic energy, the nominal current and the time constant of the safety discharge (Eq. 5.28) The time constant is linked to the copper content and (indirectly) to the current density in the cable (which is to be kept as high as possible). When possible, an efficient way to reduce the project's voltage is to subdivide the coils, leaving discharge resistors in between them (see Fig. 5.29). In tokamaks, the TF system is composed of a finite number of identical coils, which makes the configuration suitable to this technique. The system is naturally divided into a maximum number of elements corresponding to the total number N_G of TF coils. The price to pay is an increased number of current leads. Applying coil subdivision to the TF system yields:

$$V_{g,max} = \frac{W_{mag}}{N_G I_0 t} \qquad (5.28)$$

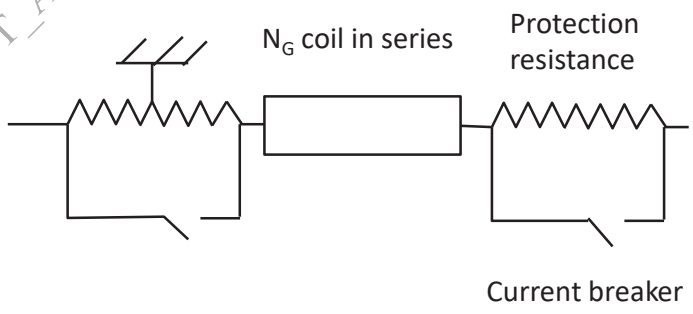

FIG. 5.29. Quench protection circuit with coil subdivision.

Illustration: Application to JT-60SA

The total number of TF coils is 18. The coils are electrically divided in three groups of 6 coils. For W_{mag} = 1 GJ, τ = 10 s and I_0 = 25.6 kA, V_{gmax}= W_{mag} / (3 I_0 t) = 1.3 kV. In Fig. 5.30, the current and voltage decays in the JT-60SA TF system are illustrated for the classical case of a constant stainless steel resistance [5.29].

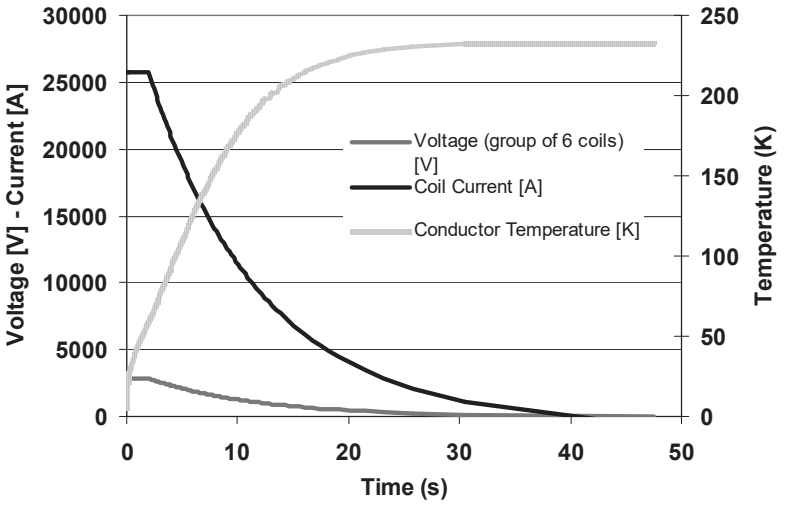

FIG. 5.30. Hot spot temperature as a function of time for the JT-60SA TF system.

Illustration: Application to Tore Supra

The total number of TF coils is 18. The coils are electrically divided into 18 groups as to limit the voltage as much as possible. The price to be paid is to have 18 pairs of current leads. For W_{mag}=600 MJ, τ=120 s and I_0=1400 A, $V_{g,max}$=W_{mag}/18$I_0\tau$ = 200 V.

5.4.3.3 Voltage reduction by variable resistance

In ITER and W7-X, variable resistors (the resistance increases with temperature) have been included to alter the decay law of current and voltage [5.28]. In Eq. (5.23), R_e is no longer constant in time. With this modification, the current decay is no longer exponential.
In Fig. 5.31, the current and voltage decays are schematically illustrated for the W7-X stellarator TF system. In this case, the variable resistance is made of Nickel. The maximum voltage across the coil is only 6.7 kV since it is not reachable at the beginning of the FSD when the current is maximum (Eq. 5.24), but only later when the current is lower. The current decay is no longer exponential. This method thus provides means to limit the project FSD voltage while keeping a sufficiently low effective time constant for an appropriate boundary on the temperature increase. However, the price of a nickel resistor is far larger than one of made stainless-steel.

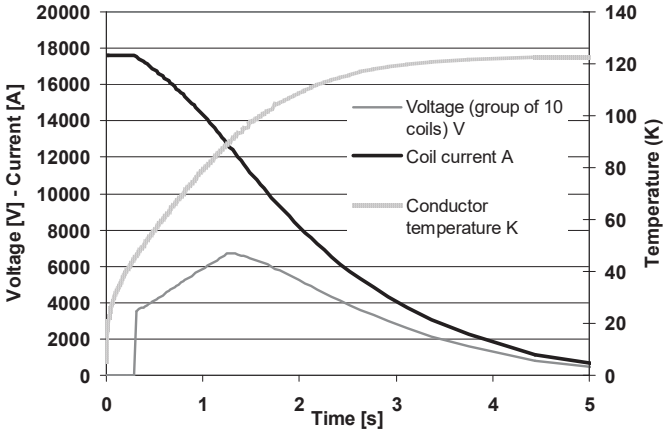

FIG. 5.31. Hot spot temperature as a function of time for W7-X's TF system.

5.4.3.4 Components of the quench protection circuits

In the following, the main components of the QPC are presented.

(a) Current breakers

The core component of a quench protection circuit is usually a DC circuit breaker allowing the current to be discharged into resistors upon activation and closed during normal operation. In superconducting fusion magnet systems, most solutions are based on existing industrial vacuum current breakers. These solutions are progressively becoming impractical due to the higher current and voltage regimes in the latest machines. A short review can be consulted in [5.29].

In Tore Supra [5.2], the first large tokamak with superconducting toroidal field magnets, the protection system (1.5 kA / 3.5 kV during the initial commissioning) implements six AC three-pole circuit breakers diverting the DC current into serially connected resistors. The QPC is a single commutation circuit as presented in Fig. 5.27.

For W7-X [5.28], a solution (20 kA / 8 kV) based on a DC industrial mechanical circuit breaker from the railway industry was selected for the current breaker to seize the opportunity of an existing industrial solution. However, due to the high nominal current, bypass switches (S1) are required to sustain the current in normal operation. The QPC is thus a double commutation circuit schematically presented in Fig. 5.32. This means that the current is commuted into the resistor R_e in two phases. Prior to the detection of a quench, current is circulating in S1, which can sustain a continuous 20 kA current but is incapable of opening the current. In a first phase, the current is commutated through S2, which is not designed to sustain the continuous current but may open the current at the rated voltage. In a second phase the current breaker S_2, which is not able to continuously pass the current, is opened. Both switches are doubled in series for redundancy. In case of non-opening, an exploding fuse is activated.

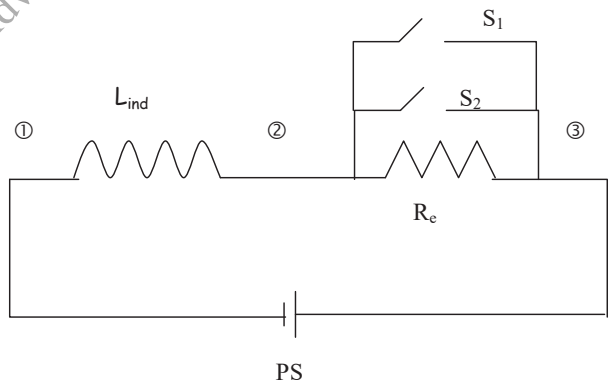

FIG. 5.32. Double commutation circuit for W7-X.

The requirements on the ITER current breakers (70 kA / 24 kV) are even much more severe than for those of W7-X. Schematically, an appropriate current commutation unit of the W7-X kind (Fig. 5.32) has been developed. The current opening is achieved by discharging a counter-pulse capacitor creating an artificial current null in the current breaker arc chamber which has needed an important development.

For JT-60SA (25.7 kA / 3.5 kV), the reference solution [5.29] implements static (semiconductor) circuit breakers[47] instead of the conventional vacuum current breakers. This solution is particularly attractive as it offers fast, arc-less, current interruption, does not require a counter-pulse network and because static current breakers are almost maintenance-free.

(b) The discharge resistors

Discharge resistor banks for superconducting magnets can be located far away from the superconducting system. During a FSD, the magnetically stored energy of the magnet system is dissipated into the resistor bank, dimensioned to accept the energy with an acceptable heating of the bank. The resistor bank of Tore Supra is shown in Fig. 5.33 is cooled by natural air convection during the FSD.

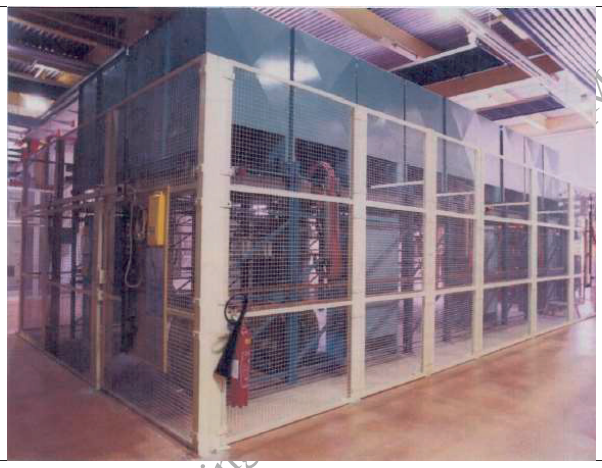

FIG. 5.33. The stainless-steel resistor bank of Tore Supra.

5.4.4 Quench detection in fusion magnets

5.4.4.1 Selection of quench detection parameters

In case of a quench, an FSD with a current time constant τ is triggered to extract the magnetic energy of the coil into external dump resistors, thus protecting the coil. Quench detection using voltage measurements across the coil is likely to be the fastest technically available solution. In Tore Supra other detectors based on temperature and pressure have been implemented and were possible due to the bath cooled system [5.2]. Specific processing is required to discriminate the inductive voltage (due to the variations of the magnetic field) from the resistive voltage (which needs to be detected). As a matter of fact, any false positive should be avoided, which would entail a severe perturbation in the operation of the reactor. This problem, proper to long-pulsed large superconducting systems, makes detection particularly challenging.

The main phases in the detection process are illustrated in Fig. 5.34 for a typical ITER TF system signal starting from quench initiation. The parameters of the detection parameters have also been indicated:

- The voltage threshold (V_t) above which a quench is detected.

[47] Turn-on / turn-off controllable semiconductors such as gate turn-off (GTO) thyristors, insulated gate bipolar transistors (IGBT) or IGCTs.

- The holding time (τ_h) during which V_t is continuously exceeded before the current breaker is opened and a FSD is initiated.

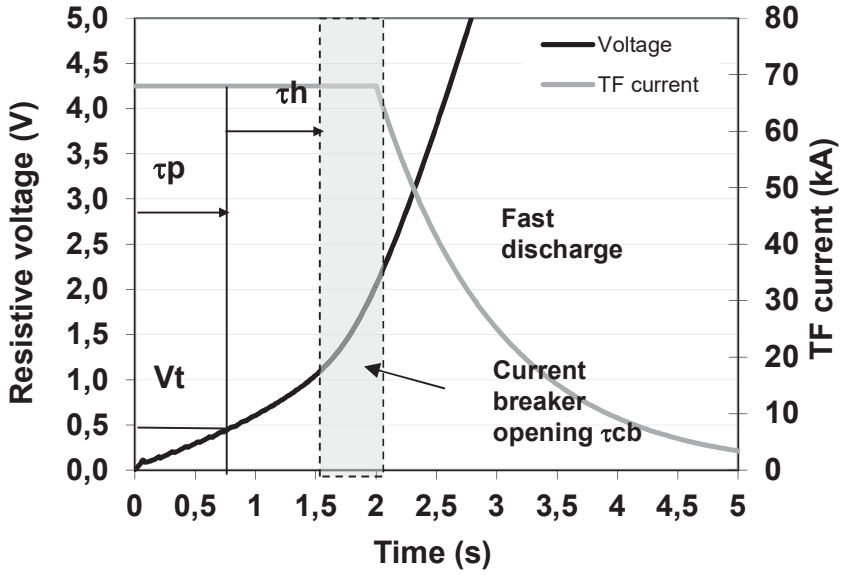

FIG. 5.34. Main parameters of quench detection illustrated for a typical resistive signal in the ITER TF system.

The total detection and action time (τ_{da}) corresponds to the time during which the current stays constant in the conductor after quench initiation and is used to apply the hot spot criterion (Section 5.4.2). τ_{da} is the sum of three terms: the holding time (τ_h), the propagating time before reaching the voltage threshold (τ_p) and the time to open the current breaker (τ_{cb}).

$$\tau_{da} = \tau_p + \tau_h + \tau_{cb} \quad (5.29)$$

The holding time τ_h is tightly linked to the duration of the inductive disturbance signal. τ_p depends on the hypothesis related to the quench event, i.e. the amount of energy deposited, the length of the initial quenched length (L_q) and the duration of the energy deposition. For example, a quench initiated in the inner leg of the ITER TF with $L_q = 1$ m within 0.1 s (typical duration of a plasma disruption) can be modelled using GANDALF [5.26]. A typical resistive voltage of 0.5 V is reached after 0.8 s corresponding to 7 meters of quenched length (see Fig. 5.35). An analytical approximation for the detection voltage is given by the following expression [5.27], where ρJ is the electrical field in the initial quenched cell:

$$V_t(t) = r\,J(L_q + 2v_p t) \quad (5.30)$$

After the quench starts, v_p, the propagation velocity, is an increasing function of L_q and the volumetric power in the CICC; it is also a decreasing function of the temperature margin. Typical values of 2 m.s^{-1} and 3 to 4 m.s^{-1} can be respectively found, using Gandalf, in the high field region of JT-60SA and in the ITER TF and CS systems. v_p is classically the characteristic one-front propagation velocity inside the conductor. Note that the propagation generally displays two fronts, explaining the factor "2" in (Eq. 5.30).

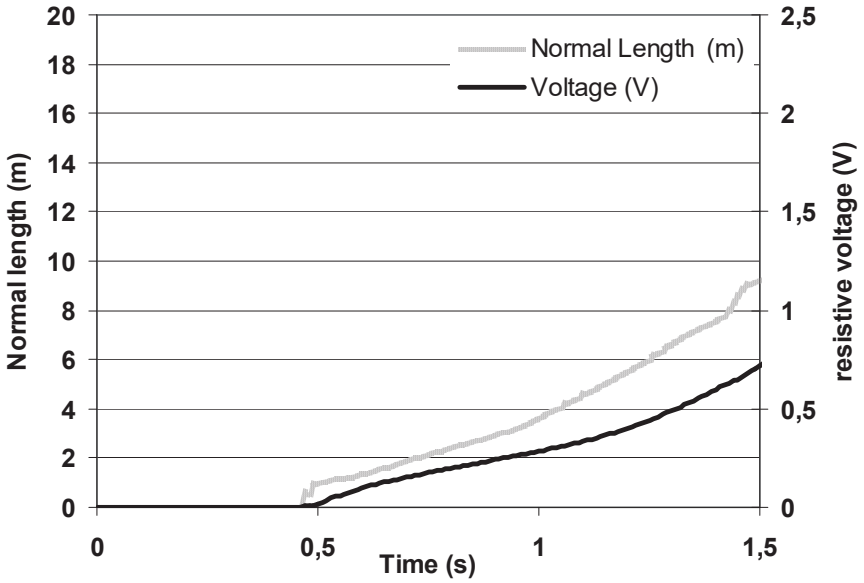

FIG. 5.35. GANDALF simulation of the propagation of a quench inside the inner leg of the ITER TF system.

By considering τ_{da} and the time constant τ of the FSD, consistency requires that the classical adiabatic hot spot criterion be respected (see Section 5.4.2). In ITER, this imposes a maximum temperature of 250 K at the point where the quench has been initiated.

5.4.4.2 Compensation of the inductive part of the voltage

The voltage across the coil or a part of the coil consists of a resistive voltage and an inductive disturbance voltage (Eq. 5.31). R_{quench} is the resistance of the normal zone to be detected, I(t) is the current carried by the quenching sub-element, L_{ind} is the self-inductance of the coil and M_j refers to the mutual inductances between the quenching sub-elements and the other magnetic field generating elements with associated current I_j(t). For instance, the mutual inductance of a TF coil with the other TF coils, the PF coils and the plasma.

$$V(t) = R_{\text{quench}}(t)I(t) + L_{\text{ind}}\frac{\mathrm{d}I(t)}{\mathrm{d}t} + \sum_j M_j \frac{\mathrm{d}I_j(t)}{\mathrm{d}t} \qquad (5.31)$$

Voltages induced in the ITER systems are associated with the plasma discharges and other plasma events. To discriminate the resistive voltage appearing in the coil during a quench, from the inductive voltage present in operation, the usual method is to balance the coil voltage with a “symmetric" coil. Note that the inductive voltage is not a phenomenon restricted to pulsed coils in magnet systems for fusion, but always present during any superconducting magnet energization.
This usual method cannot be applied to ITER magnets. Methods for balancing inductive signals are succinctly described in the following Sections. There are described more in details for ITER magnets in [5.31].

(a) The classical bridge circuit

The classical bridge circuit shown in Fig. 5.36 illustrates the balance between the inductive signals. The coil is made of two identical parts with respective equivalent inductances L_1 and L_2 and carrying the same current *I(t)*. The quench resistance *r(t)* is growing in the case when the middle point of the coil is available. The inductive part of the measured voltage (*V*) can be suppressed as presented in Fig. 5.36. In general, *V* is given by Eq. (5.32).

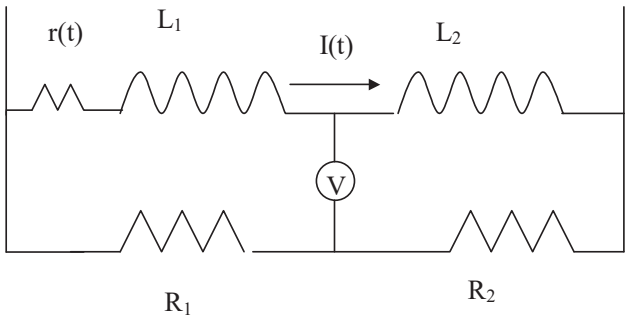

FIG. 5.36. The classical bridge circuit

$$V(t) = \frac{R_2}{R_1+R_2} L_1 \frac{\mathrm{d}I(t)}{dt} - \frac{R_1}{R_1+R_2} L_2 \frac{\mathrm{d}I(t)}{dt} + \frac{R_2}{R_1+R_2} rI(t) \quad (5.32)$$

To suppress the inductive noise, it is possible to adjust R_1 and R_2 such that:

$$\frac{R_2}{R_1+R_2} L_1 \frac{dI(t)}{dt} - \frac{R_1}{R_1+R_2} L_2 \frac{dI(t)}{dt} = 0 \text{ Þ } R_2 L_1 = R_1 L_2.$$

Equation (5.32) can then be rewritten as:

$$V(t) = \frac{R_2}{R_1+R_2} rI(t) \quad (5.33)$$

(b) Other methods to balance the inductive voltage

There is an intrinsic first order symmetry between the coils of a tokamak's TF system, neglecting the dissymmetry introduced by the other systems. This symmetry can be exploited to suppress the inductive voltage, combining two TF coils into a system like the one presented in the previous section. In this case, the resistance values of the bridge (R_1 and R_2) can be very close to each other. Such a system is used in Tore Supra and KSTAR. R_1 and R_2 are adjusted during the commissioning of the TF system. It is however impossible to use this method for the ITER CS system because the 6 modules are magnetically non-identical, powered separately and magnetically coupled in individually different ways to the PF system, the plasma and other pulsed subsystems.

Another model, synthetized in Fig. 5.37, consists in opposing the voltage across each of the 60 double pancakes to the average voltage of the two neighbouring double pancakes. The so-called central difference average voltage (CDA) ΔV is monitored for each double pancake. The balance coefficients α and β are used to compensate for magnetic dissymmetry in the sub-elements, which is not negligible among the ITER CS modules (Eq. 5.34).

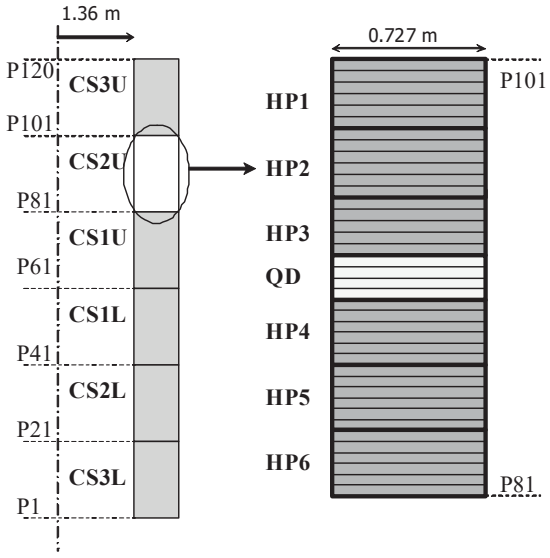

FIG. 5.37. Overview of a ITER CS cross section (left). Cross section of CS2U (right). Each module is divided into 6 hexa-pancakes and one quad-pancake.

Each CS module is divided into 6 hexa-pancakes and one quad-pancake. Using a code providing precise magnetic field calculations it is possible to predict the residual inductive signal from Eq. (5.34) along a reference scenario of ITER. It can be then calculated, that the residual signal is always below 0.55 V during a reference scenario, which leads to select 0.55 V as the threshold level V_t.

$$DV_{DPi} = V_{DPi} - \frac{a\,V_{DPi+1} + b\,V_{DPi-1}}{2} \qquad (5.34)$$

5.4.4.3 The co-wound tape

The best solution to balance the inductive voltage of the monitored circuit is to use co-wound tape, which follows the exact same path as the conductor and therefore sees the same flux variations. The co-wound tape is to be carefully insulated from the jacket of the conductor. Co-wound tape for the ITER TF system is shown in Fig. 5.38.

The electric principle behind the co-wound tape is shown in Fig. 5.39. The residual inductive voltage, given by Eq. (5.35), can be very low if the inductive coupling between the conductor and the tape is considered perfect. The drawback of such a solution is the risk to introduce additional complications in the fabrication of the conductor and a new source of insulation leaks. In addition, it is to be noted that signal pickups in the co-wound tape, associated with poloidal field variations, are simply unavoidable and different from the signal pickups experienced by the cable.

$$\Delta V = V_2 - V_1 = R_{quench}\,I_{cond} \qquad (5.35)$$

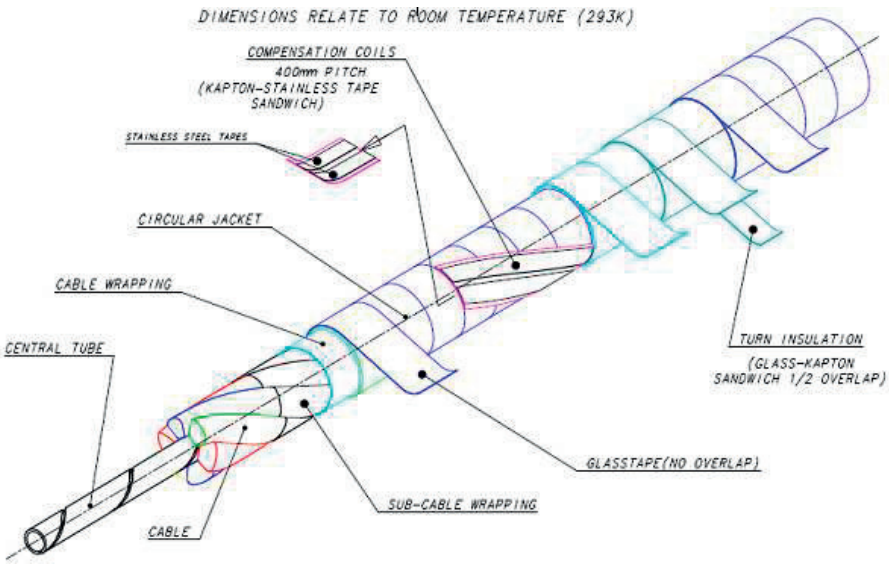

FIG. 5.38. ITER TF conductor showing two redundant co-wound tapes located within the insulator (Courtesy of the ITER Organization).

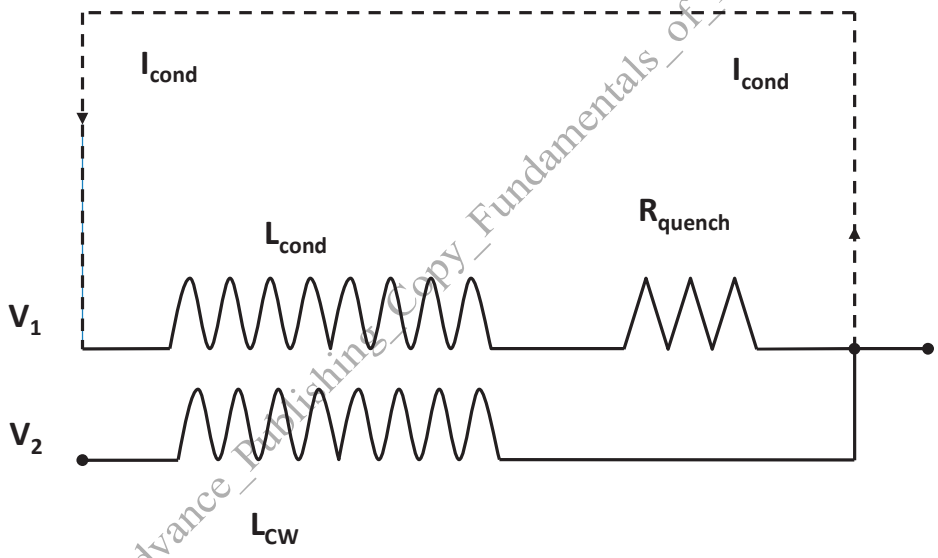

FIG. 5.39. Monitoring of a quench detection system using co-wound tape.

5.5. CONCLUSION

Today, superconductivity is classically present in large fusion projects. Very low temperature components, in the range of 4 K, are accommodated next to high temperature plasmas. A largely positive experience with large fusion superconducting magnets, showing no major counter indications and good reliability, has been accumulated throughout the years with machines such as Tore Supra, LHD, EAST and KSTAR and the ITER model coils. The magnet system typically represents 30% of the cost investment of a fusion experiment, which emphasizes its importance.

The attention is now focused upon W7-X, which has started operations at the end of 2015. The magnet system of W7-X, presently operating around 70 % of the nominal current, will reach full nominal current in 2019-2020.

The production of conductor and coils for the NbTi JT-60SA TF system in Europe is now completed and the coils have been delivered at Naka (Japan). The production of the TF coils was split between ENEA (ASG, Italy) and CEA (GE, France). Cryogenic tests of all the coils have been successfully completed at CEA Saclay in France in 2018. The assembly of JT-60SA has started on site.

The main challenge nevertheless remains the construction of the ITER magnet system. While the procurement of conductor is now completed, the construction of the different magnet systems is in progress. The first magnets were

produced and the first module of the CS system will be tested in the US in 2020. The fabrication is a challenge due to the size, weight and heat treatment of the components. The commissioning of the magnet system will have to confirm the expected properties for the magnet system with 500 tons of Nb_3Sn for the first time.
The test content for the commissioning of a large system such as the ITER magnet system (minimizing the risks) is a big issue and concerns in particular proper superconductor properties, insulation (10 kV to the ground), pulsed mode, leak detection as well as quench detection adjustment. Careful observation of the superconducting machines in operation (EAST, KSTAR, W7-X) or in commissioning (JT-60SA) is crucial to the preparation for ITER commissioning.

NOMENCLATURE

a	Tokamak minor radius (m)
A	Tokamak aspect ratio
A_{cu}	Copper section in cable (m^2)
A_{He}	Total helium section in cable (m^2)
A_{NbTi}	NbTi section in cable (m^2)
A_{noncu}	Non-copper section in cable (m^2)
B_c	Critical magnetic field (T)
B_t	Magnetic field at plasma centre (T)
B_{max}	Maximum magnetic field in the magnet (T)
B_{eff}	Effective magnetic field in the magnet (T)
C_{He}	Helium volumetric heat capacity ($J.m^{-3}$)
d_h	Hydraulic diameter (m)
ε	Nb_3Sn strain
ΔT_{margin}	Temperature margin for cable design (K)
ΔP	Pressure drop along the considered hydraulic length (Pa)
E_c	Critical electric field ($V.m^{-1}$)
h	Heat transfer coefficient ($W.m^{-2}.K^{-1}$)
I_{TF}	Conductor current (A)
J_c	Critical current density ($A.mm^{-2}$)
J	CICC (copper + non-copper) current density ($A.m^{-2}$)
J_{noncu}	Non-copper current density in a cable ($A.m^{-2}$)
L	TF system D length (m)
L_h	Hydraulic length (m)
L_q	Quenched initial zone (m)
$\dot{m}$	Helium mass flow in a cooling circuit ($kg.s^{-1}$)
P_{fus}	Reactor fusion power (MW)
P_{resis}	Resistive power in a copper TF (MW)
Q_0	Heat power deposition into a composite ($W.m^{-3}$)
Q_{circ}	Cryogenic power for the circulating pumps (W)
Q_{hl}	Cryogenic losses on a circuit (W)
R_e	Circuit external resistance (Ω)
ρ_{cu}	Copper resistivity (Ωm)
ρ_{He}	Helium volumetric density ($kg.m^{-3}$)
T_c	Critical temperature (K)
T_{cs}	Current sharing temperature (K)
T_{op}	Operating temperature (K)
τ_{comp}	Composite time constant (s)
τ_{He}	Helium time constant (s)
τ_{da}	Detection and action time constant (s)
τ_p	Propagation time (s)
τ_h	Holding time (s)
τ_{cb}	Current breaker opening time constant (s)
V	Voltage (V)
v_p	Quench propagation velocity (one front) ($m.s^{-1}$)
W_c	Critical energy per composite section ($J.m^{-3}$)
W_{mag}	Magnetic stored energy in a magnet (MJ)

5.6. REFERENCES

[5.1] ROGALLA, H. and KES, P.H., "100 years of superconductivity development" 2012 CRC press
[5.2] DUCHATEAU, J.L., JOURNEAUX J.Y., GRAVIL, B., "Tore Supra toroidal superconducting system" Fusion Science and Technology 56 (2009), 1092.

[5.3] MOTOJIMA, O., et al., “Progress of plasma experiment and superconducting technology in LHD" Fusion Eng. Des. 81 (2006), 2277.
[5.4] WU, S., and the EAST Team, “An overview of the EAST project” Fusion Eng. Des., 82, (2007), 463.
[5.5] OH, Y.C., et al., “Commissioning and initial operation of KSTAR superconducting tokamak” Fusion Eng. Des. 84 (2009), 344.
[5.6] WEGENER, L., “Status of Wendelstein 7-X construction” Fusion Eng. and Des. 84 (2009), 106.
[5.7] PRADHAN, S., "First operational results with SST-1 system magnet and its cryogenics" Physics Procedia 67 (2015) 756.
[5.8] ZANI, L., et al. "Design of JT-60SA magnets and associated experimental validation" IEEE Trans. Appl. Supercond. **21** 3 (2011), 520.
[5.9] MITCHELL, N., et al., “The ITER magnet system” IEEE Trans. Appl. Sup. **18** 2 (2008), 435.
[5.10] CHERNOPLENKOV, N.A., “The System and Test Results for the Tokamak T-15 Magnet” Fusion Eng. Des. 20 (1993), 1938.
[5.11] SERIO, L., “Challenges for cryogenics at ITER” Advances in cryogenic engineering Transactions of CEC 55 (2010), 651.
[5.12] MITCHELL, N., “Summary, assessment and implications of the ITER model coil test results” Fusion Eng. Des. 66-68 (2003), 971.
[5.13] DUCHATEAU, J.L., et al., "Conceptual integrated approach for the magnet system of a tokamak reactor" Fusion Eng. Des. 89 (2014), 2606.
[5.14] FEDERICI, G., et al. "Conceptual integrated approach for the magnet system of a tokamak reactor" Fusion Eng. Des. (2014), 882.
[5.15] “Handbook of applied Superconductivity” Edited by B. Seeber Institute of Physics Publishing 1998
[5.16] WILSON, M., “Superconducting magnets” Clarendon Press Oxford 1983
[5.17] MELHEM, Z., "High temperatures superconductors (HTS) for energy applications" Woodhead Publishing Limited (2012)
[5.18] FIETZ, W.H., "Application of HTS for fusion" Fusion Eng. Des. 86 (2011), 1365
[5.19] BRUZZONE, P., “Upgrade of operating range for sultan test facility” IEEE Trans. Appl. Supercond. **12** 1 (2002), 520.
[5.20] BOTTURA, L., “A practical fit for the critical surface of NbTi” IEEE Trans. Appl. Sup. 22 (2012), 1054.
[5.21] BOTTURA, L., "J_c (B, T, ε) Parameterization for the ITER Nb_3Sn production" IEEE Trans. Sup. 19 (2009), 1521.
[5.22] PONG, I., et al., “Worldwide benchmarking of ITER internal tin Nb_3Sn and NbTi strand tests facilities” IEEE Trans. Appl. Sup. 22 (2012), 4802606.
[5.23] BEARD, D.S., et al., “The IAEA Large Coil Task,” Fusion Eng. Des.,**7** (1988)
[5.24] DEVRED, A., et al., “Status of ITER conductor and production” IEEE Trans. Appl. Supercond. 22 (2012), 4804909.
[5.25] DUCHATEAU, J.L., “New Considerations About Stability Margins of NbTi Cable in Conduit Conductors” IEEE Trans. Appl. Sup. 19 (2009), 55.
[5.26] BOTTURA, L., "A numerical model for the simulation of quench in the ITER magnets" J. Comp. Phys. 125 (1996), 26.
[5.27] DUCHATEAU, J.L., et al. “Quench detection in ITER superconducting systems” Fusion Science Technology 64 (2013), 705.
[5.28] MONNICH, T., RUMMEL, T., **“**Production and Tests of the Discharge Resistors for Wendelstein 7-X**”** IEEE Trans. Appl. Sup. 16 (2006), 1741.
[5.29] GAIO, E., et al, “Conceptual design of the quench protection circuits for the JT-60SA superconducting magnets” Fusion Eng. Des. 84 (2009), 804.
[5.30] ULBRICHT, A., et al., "The ITER toroidal field model coil" Fusion Eng. Des. 73 (2005), 189.
[5.31] COATANEA , M., et al. "Electric quench detection in ITER magnet systems" IEEE Trans. Appl. Sup. 25 (2015), 4202507.

Chapter 6

PLASMA FACING COMPONENTS

Lorenzo Boccaccini
Karlsruhe Institute of Technology
Germany

A Gen-I fusion power plant prototype is outlined in Fig. 6.1. The architecture is based on the ITER design: a D–T tokamak with a single null divertor configuration. The picture shows the tokamak after removing the cryostat vessel, the thermal shield and external devices (heating systems, coolant piping equipment, vacuum pumps, etc.). The main coil system is shown in light blue: namely 16 D shaped toroidal field (TF) coils and six poloidal field (PF) coils. The central solenoid (CS) was also removed from the picture for simplicity. Some structural components are also represented, such as the equatorial supports of the TF coils required for mechanical stability against the magnetic forces acting among the coils. Inside this magnetic cage, the vacuum vessel is represented in dark grey. External access to the vacuum vessel is only possible through a series of ports located at different positions around the machine. In this configuration, each sector[48] features three ports: a vertical, an equatorial and a lower port (in light green). The ports are used to replace in-vessel components and provide access for piping, heating systems or diagnostics.

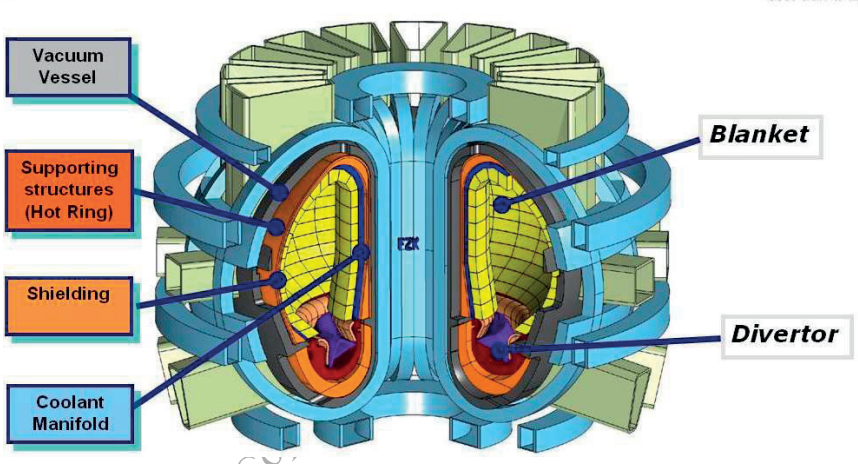

FIG. 6.1. Vision of a fusion power plant based on the ITER configuration. Courtesy of KIT.

All of which is located inside the vacuum vessel constitutes the thermonuclear core of the reactor, where the fusion plasma burns. The materials between the plasma and the vacuum vessel walls are called in-vessel components. The plasma facing surface of these components is called the first wall. The main in-vessel component is the blanket (in yellow), which covers ~85% of the first wall and collects most of the neutrons and heat coming out of the plasma. The blanket is responsible for tritium breeding and electricity production by heat removal using a high-temperature coolant. It also shields the magnets and vacuum vessel from heating and radiation damage. The second largest in-vessel component is the divertor (red and violet), located in the lower part of the vacuum vessel. The divertor defines the plasma edge and removes impurities, including the helium ash produced in fusion reactions. Additional subsystems distribute the coolant (piping and manifolds), extract tritium from the blanket, support the blanket and divertors, enhance the nuclear shielding or provide additional functions like pellet fuelling, edge localized mode (ELM) mitigation or gas puffing.

[48] A torus portion delimited by two adjacent TF coil midplanes.

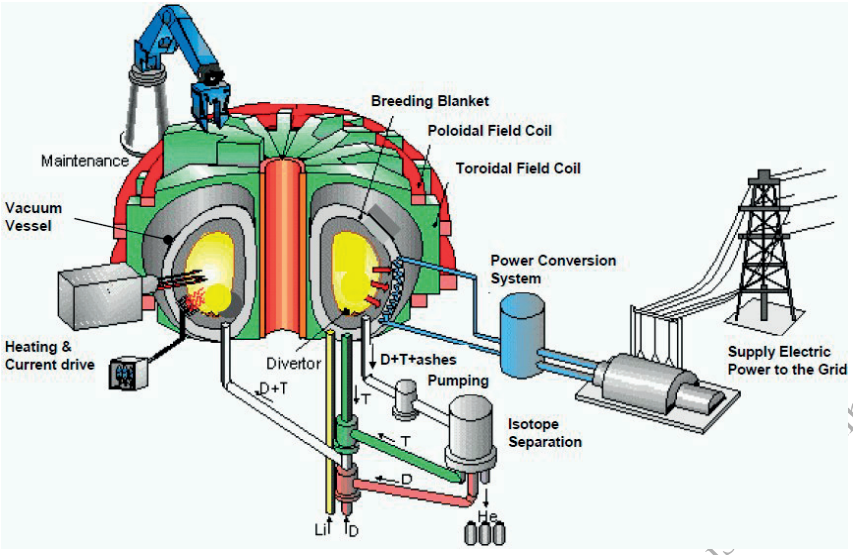

FIG. 6.2. Fusion power plant auxiliary systems.

The major auxiliary systems related to the magnets, the blanket and the divertor are shown in Fig. 6.2. The power conversion system uses a high-temperature coolant for electricity production. The heating and current drive (H&CD) system supplies energy to the plasma and sustains its internal magnetic field. The fuel cycle uses the divertor to remove fusion reaction products, the blanket for tritium production, and the isotope separation system to separate deuterium, tritium and light hydrogen. The maintenance system performs scheduled and unscheduled replacements of in-vessel components. Further details can be found in [1], which presents a complete documentation of the power plant conceptual study conducted by the European fusion development agreement (EFDA) from 1999 to 2004. Summaries of this work can also be found in [2]. An overview of recent design strategies for the EU DEMO can be found in [3] and [4].

6.1. THE IN-VESSEL CORE CONFIGURATION

The core of a burning fusion reactor should be very well isolated (avoiding heat losses), for which the magnetic field is shaped into onion shell like surfaces. However, the plasma particles will drift across these surfaces from the core to the external regions. The plasma flux can contact the first wall of the vacuum vessel, damaging its surfaces, cooling down and contaminating the plasma with sputtered particles from the first wall. This outward drift of plasma particles is nevertheless important to remove helium from the plasma core — avoiding energy losses by fuel dilution — and maintain the thermonuclear reactions. For this purpose, helium ions should be pumped in 5 up to 10 times the energy confinement time. This high removal rate can only be obtained if the helium ion flux at the plasma edge is highly compressed as it enters the vacuum pumping channels. The pumped limiter and the divertor configurations have been developed to define the plasma edge, to avoid uncontrolled interactions with plasma facing components and to remove helium ash and impurities [5].

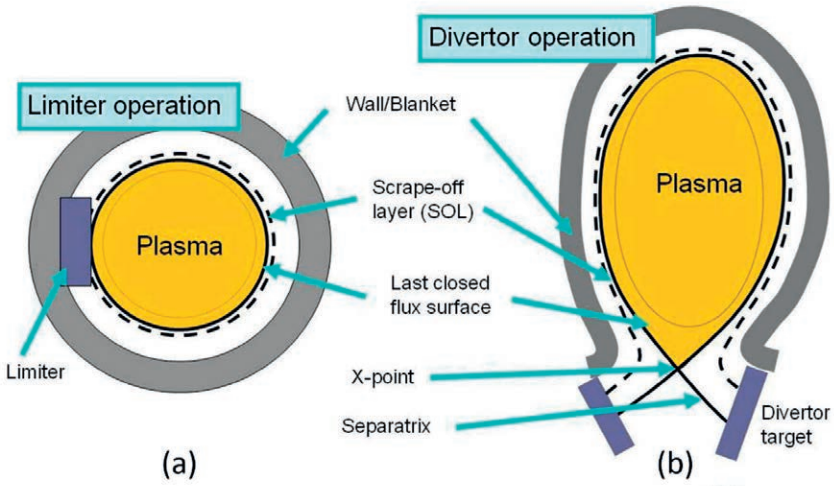

FIG. 6.3. Edge plasma in the limiter and divertor operation modes. Courtesy of KIT.

The pumped limiter, illustrated in Fig. 6.3(a), is the simplest configuration. A part of the first wall surface — called the targets — is designed to touch the plasma, interrupting the closed magnetic lines of the plasma core. The last closed flux surface — also known as the Separatrix — defines the confined zone of the plasma core. Magnetic surfaces outside the Separatrix are said to be open as they collide with the target. Particles drifting outside the Separatrix terminate their movement along the magnetic surface at the limiter target, where they lose their kinetic energy and get neutralized. The targets can be shaped (limiter blades) to produce a compression of the neutralized plasma particles where the channels of the pumping system are located. The zone outside the Separatrix, in which the escaping particles follow the edge of the plasma before colliding with the target, is called the Scrape Off Layer (SOL). In the SOL, the movement of the charged particles is mainly along the spiral magnetic lines in the toroidal direction. The corresponding parallel flux is maximum at the separatrix and decreases monotonically with distance. Unfortunately, the simple pumped limiter is not very efficient at pumping and removing impurities. Since the targets are close to the plasma edge, re-ionized particles can re-enter the plasma core. For this reason, modern tokamaks operate in the more efficient divertor configuration.

Divertor configurations are created by the magnetic field of external currents interacting with the equilibrium magnetic field of the tokamak. Different types are possible, but the most common is the axisymmetric poloidal divertor, where the poloidal magnetic field component is diverted by external toroidal currents[49]. In this configuration, shown in Fig. 6.3(b), the separatrix forms a singular point, the X point, where two magnetic field lines intersect. As in the pumped limiter configuration, the SOL region is made of open magnetic field lines where the motion of charged particles is parallel. In a burning plasma, the corresponding (parallel) heat flux can reach hundreds of megawatts per square meter in the first five centimetres, decaying under 10 MW/m^2 after only 15 cm. The SOL flux profile is determined by the balance between parallel and perpendicular fluxes. The profile is usually peaked in the equatorial region, broadening after the X point. Outside the separatrix, the field is guided into a divertor chamber up to the divertor targets where the particles escaping the plasma core deposit their power and get neutralized. The intersection of the Separatrix with the target surface in a vertical plane is called the strike point. The effective heat flux entering the plate is mostly determined by the incidence angle between the magnetic field line and the target plate. Incidence angles of few degrees can be achieved, reducing the effective flux on the divertor target by a factor of ten. In the divertor configuration, the impurities ejected from the targets are further away from the plasma core and adequate shaping of the targets can produce an effective compression of the neutralized particles, improving the pumping performance of the vacuum system.

[49] Those currents are generated by a proper configuration of PF coils.

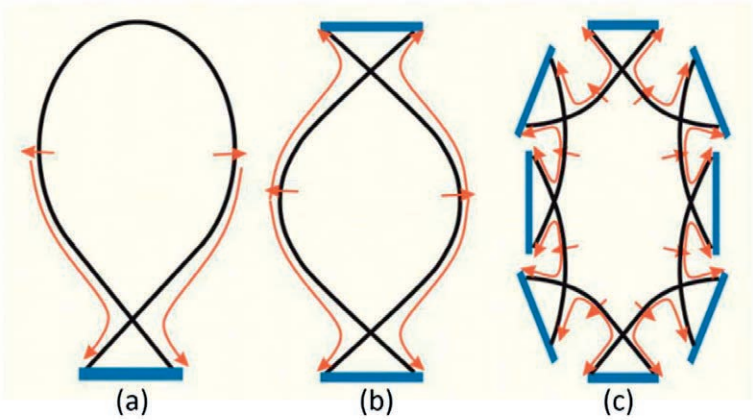

FIG. 6.4. Schematics of (a) single null, (b) double null and (c) island divertors.

Another advantage of divertor operation is to have D shaped plasmas, which facilitate the high confinement mode (H mode). The H mode was first demonstrated on the axially symmetric divertor experiment (ASDEX) in 1982 [6] and eventually adopted by most modern tokamaks. For example, JET (UK) and DIII-D (USA) were retrofitted, while JT-60 (Japan) was adapted to the divertor geometry of the ASDEX. Today's fusion experiments such as ASDEX upgrade (Germany), TCV (Switzerland), KSTAR (South Korea), EAST (China) or WEST (France) operate with divertors. ITER is also designed to operate with a divertor. Different configurations can be realized according to the number of X points. Beyond the single null configuration (only one X point), shown in Fig. 6.4(a), the magnetic field of a tokamak can be shaped into a double null configuration; see Fig. 6.4(b). In this setup, a second divertor in the upper region allows a better repartition of the power load but also occupies more space needed for tritium breeding blankets. Stellarators use the island divertor configuration, Fig. 6.4(c), in which there can be up to ten X points [7].

The power flow in a single null tokamak reactor is outlined in Fig. 6.5, identifying the major heat loads expected on blanket and divertor components. The calculations developed for EFDA DEMO 2050 are presented as an example [8]. The power balance is done in stationary conditions, i.e. the flat part of a 2.5 h pulse for 2 GW of fusion power. Eighty percent of this power (1.6 GW in this example) is in the kinetic energy of the neutrons, leaving the core without any significant reaction with the plasma. The 14 MeV neutron flux at the first wall surface has a peak in the equatorial region (~1.2 peaking factor in this example) starting from an average value of 1.3 MW/m^2. The neutrons react with the structures surrounding the plasma, releasing energy as heat and producing even more by exothermal nuclear reactions. About 4/5 of the neutron energy is released in the blanket structures (breeding blanket and supporting components) and another fifth is deposited in the divertor region. The fusion energy associated with α particles (400 MW) together with the energy injected by the heating systems (50 MW in this example) constitute the so-called plasma power exhaust. Alpha particles have strong interactions in the plasma region. Part of that energy is directly radiated from the plasma core as high energy photons (e.g. Bremsstrahlung and synchrotron radiation) and absorbed at the surface of plasma facing components. In our example, this corresponds to ~210 MW and an average heat flux of 0.175 MW/m^2.

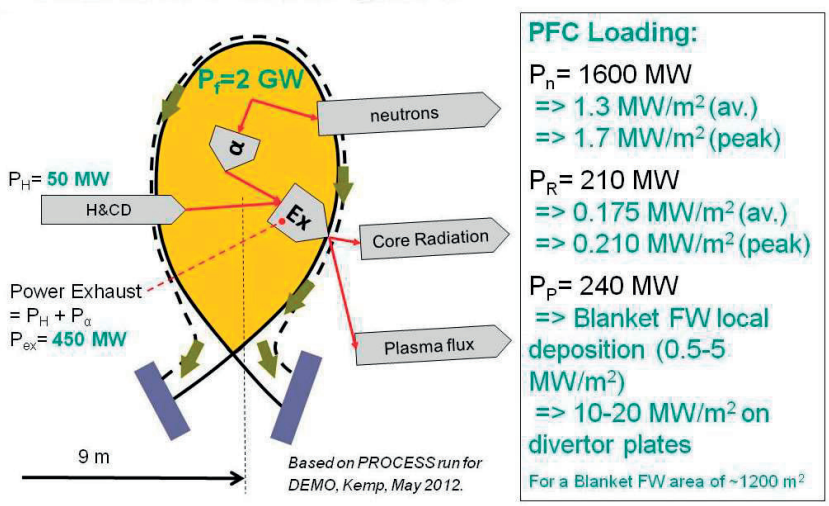

FIG. 6.5: Power flow in the DEMO reactor. Courtesy of KIT.

The remaining energy (~240 MW) is carried by the plasma flux to the SOL. In an ideal case, this energy is completely deposited on the divertor targets, resulting in a large flux concentrated on a small surface but protecting the rest of the first wall. Several mechanisms have been observed in tokamaks suggesting that an interaction of this flux with localized zones of the entire first wall is possible anywhere. Such mechanisms are present in stationary or quasi-stationary conditions, like ELMs or convective transport. They are aggravated during transients such as disruptions, vertical displacement events (VDE), runaways electrons or start-up. Present knowledge of these interactions and the large uncertainties oblige engineers to design the entire first wall with huge protective factors. For example, the ITER first wall is currently designed to withstand a maximum heat flux of 1 to 5 MW/m^2 [9].

For DEMO and FPP the load distribution derived from present knowledge is unsatisfactory in terms of peak values (in particular on the divertor plates) and uncertainties (up to an order of magnitude). Several mechanisms have been proposed to modify the present power distribution, e.g. by increasing the core radiation, consequently decreasing the energy available to the SOL plasma flux. Kallenbach discusses the possibility of enhancing core radiation flux by impurity seeding (Ar or Kr) in [10]. The limits of this technique are to be assessed and extended up to 90% of core radiation. In particular, more work is required to understand the effects of impurity seeding on energy confinement. Seeding technology has also been used in the divertor region to reduce the energy peak at the target. Divertor plasma can be seeded with e.g. nitrogen to locally enhance line radiation. The neutral cloud near the target plates interacts with the incident stream causing a detachment of the plasma from the solid target. In this regime, momentum losses due to recombination (radiative and three body) and charge exchange of hot ions with cold neutrals increase the plasma density and reduce the temperature at the target. This allows higher upstream operating temperatures, a more efficient pumping of the helium ash, less sputtering at the solid target and therefore less impurities. In experiments where plasmas become fully detached, detachment stabilization on both targets can be challenging. The influx of neutral particles (especially impurities) into the confined plasma can cause high radiation levels, which can result in thermal instability of the whole plasma. The phenomenon leading to such instabilities — known as multifaceted asymmetric radiation from the edge (MARFE) — needs to be avoided.

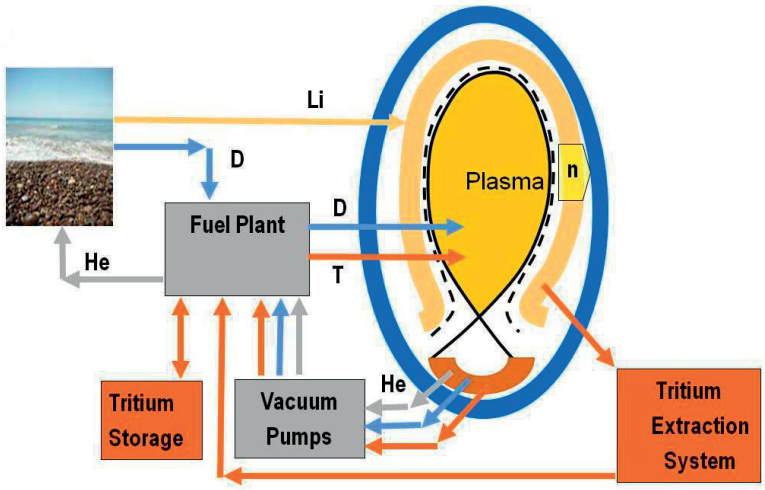

FIG. 6.6. Inner (plant, vacuum vessel, vacuum pumps) and outer (plant, vacuum vessel, tritium extraction system) fuel cycles. Courtesy of KIT.

The last topic of this section concerns the function of blankets and the divertor within the fuel cycle; depicted in Fig. 6.6. The thermonuclear fuel, deuterium and tritium, needs to be supplied to the plasma. In a reactor, deuterium and tritium pellets[50] will be injected at high velocity into the plasma to replace the fuel consumed by fusion reactions. Deuterium is abundant in nature: in ocean water the H/D ratio is ~6500, i.e. 150 ppm. As deuterium is already used in nuclear technology, e.g. CANDU reactors[51], industrial processes are available for extraction and isotopic enrichment. On the contrary, tritium is rare. The world tritium inventory amounts less than 30 kg, produced as by-products of heavy water reactors due to n-absorption of deuterium. At full power a fusion power plant requires ~150 g of tritium per day per gigawatt of power installed. To satisfy the fuel necessities of a power plant, it is therefore necessary to produce tritium onsite. Moreover, an initial tritium charge of several kilograms is required for start-up, until the system can use its own production. The currently available resources allow only a few DEMO plants in this century [11].

Tritium is produced by neutrons−lithium reactions in the blanket and extracted to make fuel pellets at the plant. The part of the fuel cycle involving the blanket is an essential feature of FPPs called the outer cycle. Since ITER does not produce tritium, the outer cycle is not present in its fuel plant. The inner cycle is the loop that starts from the fuel plant, injects tritium in the plasma and extracts the resulting helium and unburned D–T mixture from the vacuum vessel as input flow to the fuel plant. Since only a small fraction of the injected fuel is burned (burnup fraction of 1% in ITER and expected greater 2.5% in FPPs), large quantities of deuterium and tritium will be present in the exhaust with helium. The divertor is therefore an integral part of the inner cycle. Deuterium and tritium are to be reused for pellets production, while helium is removed. Recent developments on the fuel cycle of EU DEMO can be found in [12].

6.2. PLASMA IN-VESSEL COMPONENTS INTERACTION

In a reactor, plasma interacts with the surrounding in-vessel structures. Components exposed to the plasma are primarily damaged by interaction with the plasma flux from the core. Most of the damage can be attributed to sputtering, which causes a rapid erosion of plasma facing surfaces. This is especially true at the divertor or limiter targets used for plasma neutralization. In addition, transients like unmitigated ELMs or plasma disruptions considerably increase the erosion rate of plasma facing components.

Most components suffer from cumulated neutron flux and heat releases. Magnets are critical components in which small neutron fluxes and modest fluences can cause a system wide failure of the reactor. Heat loads, causing fatigue and creep, are another source of damage to the materials. Combined effects of radiation and heat, like swelling, degrade the materials even further. Component damage results in safety and operational issues, for example dust production. Finite component lifetimes require blanket and divertor replacements during scheduled maintenance periods.

[50] Fuel pellets are prepared in the fuel plant using deuterium and tritium.
[51] CANDU stands for Canadian deuterium uranium reactor.

6.2.1. Plasma–edge interactions with the first wall

Considering the interaction of the SOL flux with the surrounding in-vessel components, one of the most important phenomena is the sputtering effect. Sputtering denotes a process in which atoms are ejected from a solid target due to energetic particle bombardment. This process can lead to a significant erosion of target materials and the production of large amounts of impurities. Table 6.1 reports sputtering data related to typical plasma ions and self-sputtering. In general, the selection of plasma facing materials (PFM) is a compromise between its effect on the plasma as an impurity (i.e. energy confinement decrease) and its threshold energy (expected amount of the impurities). Despite being a deleterious (high Z) impurity, tungsten has very high threshold energies making it a suitable PFM. It is presently the only candidate considered for EU DEMO [13].

TABLE 6.1. Threshold energies (eV) for typical plasma facing materials sputtered by hydrogen, deuterium, tritium and helium ions. The last column shows the effect of impurity ions of the same element on these surfaces. The table reports average values from different sources for comparison purposes only.

	H	D	T	^{4}He	SELF
Beryllium	27	24	28	33	-
Graphite (C)	10	10	13	16	30
Titanium	44	36	28	22	41
Iron	64	40	37	35	35
Molybdenum	164	86	50	39	54
Tungsten	400	175	140	100	70

Unmitigated ELMs, plasma position excursions or runaway electrons during disruptions can deposit huge amounts of energy on PFMs over short periods of time and cause melting. Aggravating conditions can also impact the design, e.g. exposure to a high fluence of high energy neutrons. Furthermore, thermal quenches from electromagnetic transients, mechanical impulses and runway electrons will also contribute to the load [14]. The damage induced in the materials (including helium production) adds up to the erosion limiting the lifetime of in-vessel components.

6.2.2. Neutron interaction

The intensity of the 14 MeV neutron flux is reduced as it moves away from the core and interacts with the shields and blanket. Inside the materials, the decay law is almost exponential. In a typical reactor, the blanket reduces the fast neutron flux by ~1/10. A good shield further reduces the flux by an order of magnitude for each decimetre of thickness. Nevertheless, this damage can be severe for superconducting magnets, even at very low fluxes (e.g. heat generation) and fluences (cumulative damage in material structure). In ITER, the total neutron fluence experienced by first wall components will not exceeded 0.3 MW·a·m^{-2}, even if the component remained in the reactor the entire lifetime of the machine. Twenty five times greater cumulative fluences are envisaged for the current EU DEMO over its entire lifetime (~7 MW·a·m^{-2}). Up to 60 MW·a·m^{-2} are hypothesized for the future FPPs studied in the EU power plant conceptual studies (PPCS) [15].

Neutron damage mainly consists in displacements per atom (dpa) in the lattice and the production of transmutation products (e.g. appm-He). Both effects can produce changes in the mechanical (e.g. hardening, embrittlement) and physical properties (e.g. thermal conductivity) of PFMs. Contrary to fission reactors, large amounts of helium are produced in fusion materials by high energy neutrons (the corresponding reactions have thresholds in the MeV spectrum). Helium can form bubbles and enhance cavity formation [16]. This effect is strongly dependent on the microstructure of the materials. Steels with a face centred cubic (fcc) structure are very sensitive to swelling, limiting their use to less than 20 dpa. Body centred cubic (bcc) ferritic and ferritic–martensitic steels have been proposed for their relatively good stability under fission neutron irradiation with very low swelling [13].

An important constraint on the lifetime of blanket components is the nuclear burnup of breeder materials. At present, the lifetime of a solid breeder is almost comparable to that of the steels used as structural materials. Note that this limitation is only important for solid breeders and beryllium since liquid breeders can be chemically purified, and burned elements replaced, while operating.

6.2.3. Cyclic and high temperature loads

Lifetime limitations are also related to mechanical stress in the components, subject to cycling loads (fatigue) at high temperature (creep). Table 6.2 reports the required values for the DEMO blanket in the European programme. The first series of blankets can survive 20 dpa, while the second one can withstand 50 dpa. In this example the reactor has a pulse length of approximately 2 hours.

TABLE 6.2: Lifetime requirements for the EU DEMO blanket.

First wall damage	Number of cycles	Creep time
20 dpa	5800	11700 h
50 dpa	14500	29000 h

6.2.4. Dust formation

As a result of the damage suffered by the PFM, a large amount of dust can accumulate in the vacuum vessel[52]. The production of dust in fusion reactors will play an important role in determining their safety and operational performance. Safety concerns related to dust include radiological hazard, chemical toxicity and chemical reactivity. For example, the greatest concern about tungsten dust is its radiotoxicity due to its high activation. Dust is also hazardous if combustible gas is generated by interaction with the coolants (e.g. hydrogen from a water–beryllium reaction) or air from a vacuum leak. For this reason, the maximum amount of in-vessel dust should be limited. The 100 kg level was introduced early in the ITER engineering design activities. Similar limitations will be necessary for DEMO.

Several mechanisms are responsible for dust generation in fusion devices. These include blistering and fracturing of deposited layers, reactive species generation in edge plasmas, arcing, explosive ejection and brittle destruction of surface imperfections, as well as the nucleation of vaporized materials [17]. Any of these mechanisms can be dominant depending on the circumstances. Due to safety implications, the survey of dust accumulation and the development of dust removal technologies are essential features and potential show-stoppers. Direct measurements seem impossible. A global assessments of erosion sources based on local erosion and dust measurements has therefore been proposed. Promising dust removal techniques include cyclone vacuum cleaning, laser ablation or shockwaves, and electrostatic collection [18].

6.2.5. Component damage and replacement

The relation between the overall lifetime of the plant and that of the components determines the frequency and the modality of replacements. Structures like the vacuum vessel, cryostat or the magnets are designed to last for the entire lifetime of the plant. Their replacement (if ever possible) is related to very long and unscheduled maintenance operations. Other components have much shorter lifetimes, e.g. the first wall, breeder zone, divertor targets, and some of the associated shielding and supporting structures. For these components, replacements at scheduled maintenance times is required. Component lifetime is a key parameter to maximize the availability of the FPP. An efficient maintenance system also contributes to this effect. Considering the high radioactivity inside the vacuum vessel, these operations can only be done by remote handling devices; discussed in Chapter 11. Fig. 6.7 shows that the limit between permanent and replaceable components is somewhere inside the vessel. This limit depends on the design parameters of the components and the reactor itself.

[52] We mainly refer to tungsten as it is the first choice material for DEMO plasma facing components. In ITER beryllium is the prevalent material for the blanket.

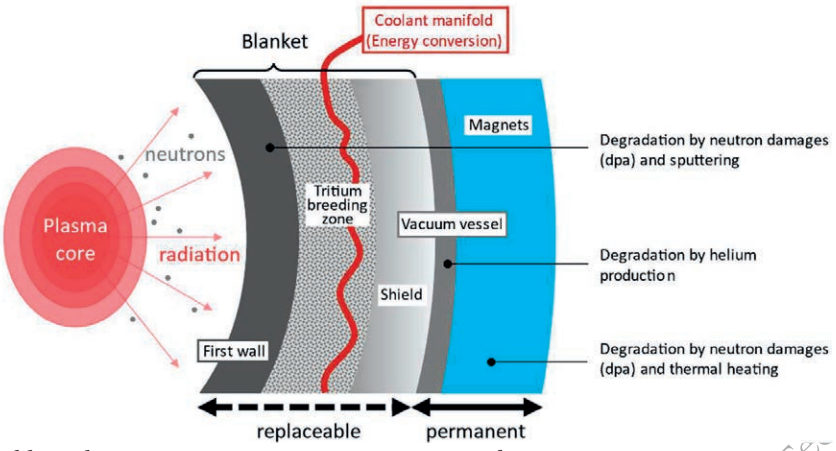

FIG. 6.7. Replaceable and permanent components in a magnetic fusion reactor.

6.3. BLANKETS

This section presents the principles of blanket design. Following a brief history of the blanket programme, the functions and requirements of this system are described. Different types of blanket, blanket materials (structure, breeder and coolant) and examples of blanket designs are discussed.

6.3.1. Blanket Programmes

6.3.1.1. European Union

In Europe, the blanket programme started early in the seventies. The first blanket concepts were proposed for international projects such as the international tokamak reactor (INTOR) or the next European torus (NET). From 1994 to 2000, modern blanket concepts were developed for DEMONET; but this configuration was not the result of a coherent reactor study, rather an agreed set of geometrical and loading conditions proposed to compare different blanket designs. DEMONET resulted in two blanket concepts that became the EU reference for DEMO and for the ITER test in the framework of the international test blanket programme [19]. The two concepts were:

- the helium cooled pebble bed (HCPB), a helium cooled concept with a solid breeder proposed by KIT [20] and
- the water cooled lithium lead (WCLL), a liquid breeder developed at CEA [21].

In the DEMONET framework, a dual coolant lithium lead (DCLL) concept was also developed at KIT [22]. However, this concept was not selected for the following EU breeder blanket programme. This concept found a renewed interest at the University of California in San Diego and was further developed under the USA ARIES programme.

Another important step in blanket development was the EU PPCS started in 2000 and concluded in 2004 [15]. In this study, focus was made on possible fusion power plant configurations that could achieve the full set of requirements for a mature reactor in terms of economic viability (cost of energy) and safety (no evacuation or geological waste storage required). Reactors based on the HCPB (Mod-B, [23]), the WCLL (Mod-A, [24]) and the DCLL (Mod-C, [25]) blankets were adapted and improved to explore the performance limits according to the above-mentioned objectives and requirements. During the PPCS, a major change happened in the EU breeding blanket programme. Driven by a budget reduction, it was decided to converge the designs of the solid and liquid breeder blanket. Priority was given to the possibility of testing both breeders, for which large uncertainties in the behaviour were present. Exclusive use of helium cooling, compatible with both breeders, was thereafter required [26]. A two year joint study performed by KIT and CEA provided a cooling architecture adaptable to both breeders. An upgraded HCPB [27] and a brand new HCLL concept [28] became the reference for EU DEMO blanket and the ITER test blanket programme. In a short DEMO study carried out from 2006 to 2008, HCLL and HCPB were used to design the EU DEMO configuration. In 2007, Fusion for Energy (F4E) was constituted with aims to procure the EU test blanket module (TBM) for ITER. F4E took the leadership in blanket development while the European fusion laboratories (EFL) continued their work as contractors. However, almost all direct DEMO activities were stopped; continued at low level through the TBM programme.

The fusion programme restarted in the EFL in 2011 with the constitution of the power plant physics and technology (PPPT) department at the European fusion development agreement (EFDA). At this new stage in development, a strategy was defined in the European Roadmap [29]. The Roadmap describes the actions needed and the challenges ahead of the delivery of several megawatts of electrical energy by a DEMO FPP around 2050. This new strategy caused a large reorganization of the European fusion programme: the EFDA was replaced by the EUROfusion consortium, formed by the EFL. For blanket development, this required a choice of concepts, materials and technologies for the machine described in the Roadmap, as well as the choice of the right blanket development strategy towards a commercial FPP. The EUROfusion programme is about to conclude its pre-conceptual design. The conceptual phase will be completed by 2030. The following engineering phase will culminate with the construction of EU DEMO before 2050 [30].

6.3.1.2. International cooperation

International partnership in fusion involving the USA, Japan, the Russian Federation (former USSR) and the EU began in the seventies with INTOR. Each country developed at that time its own blanket concepts based on their own roadmaps for the development of fusion energy. The USA developed important studies in the ARIES[53] programme such as:

- the dual coolant lithium–lead (DCLL) [31] [32] or
- the self-coolant lithium–lead [33].

Japan followed-up in the nineties with a water-cooled solid breeder blanket developed at JAEA for the Japanese DEMO programme [34]. Several blanket concepts – ranging from fluid metal to molten salt designs – were also investigated by Japanese universities. In 2006, China, Korea and India joined Europe, Japan, Russian Federation and USA in ITER and the IEA agreement on fusion technology. In the last 13 years, these countries have developed their own roadmaps to fusion and proposed new blanket concepts. The Chinese roadmap foresees the Chinese Fusion Engineering Test Reactor (CFETR) as an intermediary step between ITER and DEMO to develop and test blanket concepts, e.g. water cooled solid breeders [35] and a helium cooled blanket [36]. Korea has proposed a steady state fusion demonstration reactor (KDEMO), with preference for a water cooled solid breeder concept [37]. Helium cooled versions are also developed as TBM for ITER [38].

6.3.1.3. ITER

The physics goal of ITER is to study a burning fusion plasma. However, technologically, ITER will be the paradigm for the development and licencing of the main system of future FPPs. Several systems will directly profit from the development of ITER e.g. the magnets, the inner fuel cycle, but not the blanket. Even though the blanket system has been studied for several decades and different concepts have been proposed, and investigated, a breeding blanket will not be present in the very first burning plasma device. In fact, ITER has been designed to use a relatively low amount of tritium in its entire lifetime (< 20 kg), using the production of CANDU reactors. In ITER, the breeding blanket is replaced by a shielding blanket whose sole purpose is to remove the nuclear heat and shield the vacuum vessel and magnets from neutrons. Hence, the ITER blanket design is not relevant to a reactor: the adopted materials can only withstand low neutron fluences (< 0.3 $MWa.m^{-2}$), the outlet temperature of the coolant (< 150°C) is too low for an efficient electrical power production and no tritium is bred. In ITER, breeding will only be tested in the form of test blanket modules (TBM), in the framework of the international test blanket programme. A TBM is a blanket mock-up with a dimension of less than 1 m^3 and an exposed surface of less than 1 m^2. Six TBMs can be inserted through the three equatorial ports adapted for this use (see Fig. 6.8). Table 6.3 lists the blanket concepts to be tested in ITER.

TABLE 6.3. Blanket concepts to be tested as ITER test blanket modules (status 2017).

Location	Country	Label	Description
ITER Port 2	China	HCCB	Solid breeder blanket with helium cooling [39].
	India	LLCB	Lithium lead blanket with ceramic breeder in dual coolant configuration [40].
ITER Port 16	EU	HCLL	Liquid metal breeder blanket with helium cooling [41], [42].

[53] A multi-institutional research activity with the mission to "perform advanced integrated design studies of the long-term fusion energy embodiments to identify key R&D directions and to provide visions for the fusion program.".

	EU	HCPB	Solid breeder blanket with helium cooling [41], [43].
ITER Port 18	Japan	WCCB	Solid breeder blanket with water cooling [44].
	South Korea	HCCR	Solid breeder blanket with helium cooling and neutron reflector [38].

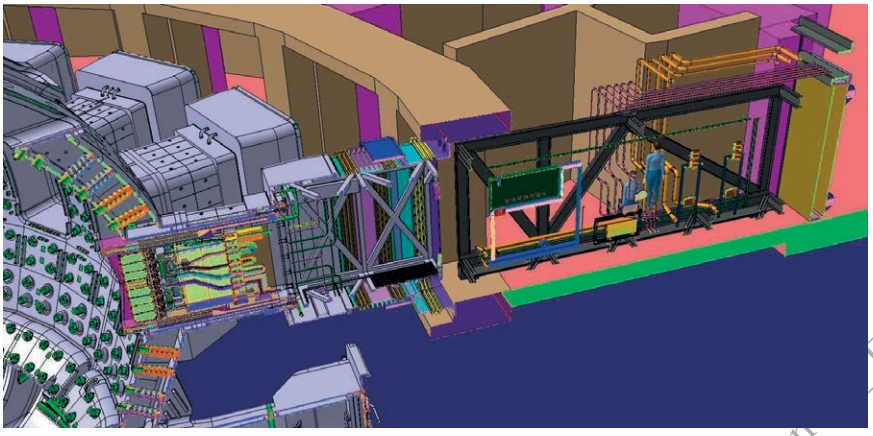

FIG. 6.8. Example of blanket integration to an ITER equatorial port.

6.3.2. Blanket functions and requirements

The breeding blanket is an essential component in future reactors. It will provide the breeding capability for tritium self-sufficiency, remove heat at high temperature for efficient electricity generation and contribute to the protection of magnets and other external systems from high energy neutron irradiation. The blanket is a complex system requiring an adequate combination of materials, manufacturing and cooling technologies in its design, considering neutronics, thermomechanical, electromechanical, thermohydraulic, fluid-dynamical, magnetohydrodynamic, radiation and safety aspects. It requires, as a first step, the correct identification of all requirements, keeping in mind the large uncertainties. The choice of a configuration, allowing economically viable FPPs and a well-defined roadmap to the necessary materials and technologies is one of the hottest topics in preparation for DEMO. It will be a trade-off among different (sometimes competing) requirements like tritium production, safety in normal and off-normal conditions, reduction of activated waste, electricity production efficiency and development strategy.

6.3.2.1. Tritium self-sufficiency

The primary function of the breeding blanket is to ensure the tritium self-sufficiency of the reactor. In a full power day, a fusion reactor consumes ~152 g of tritium for each gigawatt of fusion power installed. The same amount should be produced per day to maintain the fuel cycle, with a margin to compensate for losses and provide reserves. Any blanket concept thus needs an accurate neutronic assessment to demonstrate a positive neutron balance. Since only one neutron is generated per fusion reaction, and since a part of the neutrons will be absorbed by elements other than Li or escape the blanket, the balance can only be kept greater than one with neutron multiplication. This balance is usually quantified by the tritium breeding ratio (TBR), i.e. the ratio between the tritium atoms generated in breeder and the tritium consumed in thermonuclear reactions.

Blanket coverage should be maximized to reduce neutron losses. The blanket usually covers more than 80% of the surface surrounding the plasma, while the remaining surface is reserved for the divertor cavity and the integration of other in-vessel systems. In principle, the divertor zone should be designed to contribute to tritium breeding. However, a blanket structure behind the divertor cassette is rather inefficient and the complications in designing the divertor would greatly increase. Penetrating through the blanket, external H&CD systems and diagnostics further reduces the coverage by several percentage points. Parasitic neutron absorptions should be reduced by minimizing the amount of neutron absorber materials, especially in the plasma facing region of the blanket where breeding takes place. An efficient mechanical design, with large coolant manifolds moved behind the breeding zone, helps reducing neutron absorptions in structural materials.

Since losses cannot be avoided, neutron multiplication is an essential part of the breeding process. The ^{7}Li isotope, present in the natural lithium composition (92.5 at.% ^{7}Li and 7.5 at.% ^{6}Li) can produce an additional neutron for each tritium atom. Unfortunately, the reaction cross section is small while the energy threshold is high, meaning that this process only works when combining lithium to other blanket materials with very low neutron absorption (e.g. vanadium as structural material). A more effective way to produce additional neutrons is to replace ^{7}Li with a more effective neutron multiplier and increase the relative amount of ^{6}Li that has a very high cross section at the lower energies. More effective multipliers are beryllium and lead. The former is mostly used in combination with solid breeders (e.g. Li_2O, Li_4SiO_4, Li_2TiO_3). The latter forms a eutectic lithium–lead (15.8 at. %Li) that is liquid above 235°C, providing the necessary neutron multiplication and tritium production in a single material. The optimal ^{6}Li enrichment depends on the breeder concept: solid breeders using Li_4SiO_4 usually necessitate a 50% enrichment. A 70% enrichment level is needed with Li_2TiO_3, which has a lower lithium density. Eutectic lithium–lead (usually PbLi) only works satisfactorily with very high ^{6}Li enrichment at ~90%.

The effective TBR needed to supply the fuel cycle is dependent on design, requirements and the expected performance. It should account for tritium trapping in materials, losses and decay. Old US studies (see [45] and [46]) recommend an effective TBR ~1.05, including the production of a new charge of tritium at the end of the reactor life able to start a new FPP. Neutronic calculations are routinely performed for entire reactor designs to guarantee an adequate TBR [47]. The calculated TBR should always be larger than the effective value to account for:

- uncertainties in the calculations (simplifications and cross section data);
- ^{6}Li burnup from start of life to the end of life of the blanket;

Increasing factors between effective and calculated TBR of 8 to 10% are considered to cope with uncertainties and provide enough margin, especially in initial design phases where some of the reactor subsystems are ill-defined, which can incur in future loses of blanket coverage.

6.3.2.2. Heat removal

Referring to Section 6.1, three main heat sources should be considered in designing the breeder blanket:

- The volumetric heat caused by neutrons.
- The surface heat from plasma core and edge radiation.
- The SOL particles interaction.

Neutrons constitute the main source of heat in the blankets. This heat is typically released through the blanket with an exponential decay from the plasma facing surface to the vacuum vessel. Neutron wall loads of 1 to 3 MW/m^2 (typical reactor configurations), result in power density peaks of less than 25 MW/m^3. This is a relatively low value compared to typical core values of 100 MW/m^3 in light water (fission) reactors. The neutron poloidal distribution is peaked around the equatorial plane, with maximum values on the outboard surface. Typical peaking factors of 1.2 to 1.4 have been calculated for common plasma configurations. Core radiation — mainly synchrotron radiation and Bremsstrahlung — constitutes a surface source for the blanket first wall with values corresponding to a 1/4 of the neutron wall load and similar peaking factors. The additional heat load from interactions of SOL particles with the first wall remains ill-defined. In many blanket designs and past studies this contribution is neglected, assuming the plasma control systems of a post ITER device will keep the total surface loading from radiation and particles under a reasonable value. However, new findings in SOL physics led to the ITER first wall panel design, recognizing that the impact of the SOL on the first wall was underestimated in DEMO design studies [48].

The ITER first wall cannot be used for a breeder blanket, which requires a thinner wall to maintain the delicate neutron balance. In recent years a “limiter protection” was developed to control and reduce the heat loads in EU DEMO [49]. Limiters are separate first wall components that protude into the plasma. Placed at particular locations along the wall, they intecept the plasma flux before it can impact and damage the blanket. New analyses have calculate the dimensions, number and (poloidal, toroidal) positions of several limiters. They will occupy just a few percent of the first wall surface and withstand transient, which can develop during plasma start up and shut down. Due to their loading, cooling and remote handling, limiters will be designed like divertor target plates. Moderate loads from the SOL plasma will still impact the blanket, dimensioned to sustain 1 MW/m^2. A protective layer of tungsten (a few mm) is considered to cope with erosion.

The complete definition of blanket heat loads will necessitate a precise specification of the requirements considering all transients and local hot spots. The present, pre-conceptual level, design usually considers nominal values. Table 6.4 lists the set of heat load requirements used in EU studies.

TABLE 6.4. Heat load conditions used in EU design studies.

	DEMONET [19]	PPCS [1]	DEMO PPPT (pre-conceptual)
Neutron wall load, max [MW/m^2]	3.0	2.5	1.2
Surface flux, max [MW/m^2]	TBD	TBD	0.3
SOL interaction [MW/m^2]	TBD	TBD	Localized hot spot
Total Surface flux (2+3), max [MW/m^2]	0.5	0.5	< 1
Pulse lengths	Steady state	Steady state or long pulses (~8h)	2 h
First wall coating	none	none	2mm-W

The heat removed from the blanket is converted in an electrical power generator or used by industrial processes, such as hydrogen production. Considering that the blanket system collects more than the 82% of the thermal energy produced by the reactor, the selection of the primary heat transfer system coolant and parameters is a key design choice. As one major design targets is to maximize the production of energy — hence reducing the cost of electricity — it is important to maximize the outlet temperature of the blanket coolant. Helium and liquid metal cooling can be used provided the development of materials suitable to high temperature operation in a fusion environment; see also Chapter 8.

6.3.2.3. Lifetime

As described in Section 6.2.5, blanket components have limited lifetimes. Several limiting factors are directly related to irradiation damage, like dpa, swelling and transmutations. Mechanical design is limited by fatigue and creep, allowable values of which are in turn affected by irradiation. Localized erosion of the first wall by SOL particles and helium production in permanent structures can also be limiting. For instance, a few appm of helium can form cracks in the materials, affecting the quality of the new welds.

In any case, the estimated lifetime of blankets is much less than the total lifetime of the plant such that replacements of the entire blanket systems must be foreseen in the general FPP architecture. In fission reactors, the blanket replacement is a scheduled maintenance that corresponds to refuelling operations. The plant is stopped and cooled, and the vacuum vessel is opened to exchange all or part of the blankets. This operation together with the replacement of the divertor cassettes will require several months and impact the total availability of the plant. Availability considerations combined with the cost of the components themselves are strong economic arguments to increase blanket lifetime, thereby reducing the cost of electricity. For reference, an average availability of 0.75 (used in many reactor studies) is considered a very optimistic value. An increased component lifetime would also reduce the amount of radioactive waste that will have to be treated, further reducing the overall costs. For waste reduction, radial zoning of the blanket system can be adopted. From plasma to the vacuum vessel, the outermost blanket and shield can be permanent or semi-permanent like the adjacent vacuum vessel. In such case, only the internal blanket ring needs regular replacements.

6.3.2.4. Neutron Shielding

Some components, like the magnets, require efficient shielding from high neutron fluxes to ensure their integrity throughout their lifecycle. Others, such as EUROFER structural materials, need to stay below a given number of displacements per atom. Table 6.5 lists parameters and requirements that are usually considered for the design of blanket systems.

TABLE 6.5. Parameters and requirements for the design of blanket systems [50].

Parameter	Value
Lifetime neutron fluence of epoxy insulators [1/m²]	1×10^{22}
Lifetime peak fast neutron fluence (E>0.1 MeV) to the Nb_3Sn superconductor [1/m²]	1×10^{22}
Lifetime peak fast neutron fluence to the ternary Nb_3Sn superconductor [1/m²]	1×10^{22}
Peak displacement damage to copper stabilizer, or maximum neutron fluence, between TF coil warmup [1/m²]	$1 – 2 \times 10^{21}$
Peak nuclear heating in winding pack [W/m³]	50
Helium production for the starter blanket life time (2 full power years) in the area where re-welding for the second blanket is necessary [appm]	1

6.3.2.5. Tritium: releases and inventories

Tritium is breed, processed and consumed in the fusion reactor. Considering the radiological hazards of tritium, releases and inventory limits are major nuclear protection goals. The plant containment strategy ensures that chronic and accidental releases are minimized. For chronic releases, a limit of 2.5 mg/d HTO (~0.38 mg/d T) is compatible with an off-site dose of 25 μSv/y. As the tritium production is in the order of hundreds of grams per day, the release rate should be more than 100 000 times lower. Among all possible release paths from the breeder material to the environment, the most critical is through the coolant to the steam generator (heater) that couples the primary to the secondary loop.

To avoid accidental releases that would require an evacuation of the population, the maximum power plant inventory is generally limited to 1 or 2 kg. Since the blanket is part of the coolant and breeder systems, tritium control is a major requirement that should be considered by design. Tritium inventories in the different blanket subsystems and materials should be assessed and limited. Issues can arise from trapping mechanisms in the coolant and breeders.

6.3.2.6. Electromagnetic loading

The in-vessel components of magnetic fusion reactors are subjected to large standing electromagnetic fields (~8 T from the DEMO TF coils) and transients (~20 T/s in a typical plasma disruption). Huge (Lorentz) forces can be generated in electrically conducting structures, which represent critical design loads for these components. In addition, the ferritic martensitic steels proposed as structural materials (e.g. EUROFER) are ferromagnetic. This affects the resulting value of the magnetic field, increasing the effect of disruptions, causing additional large static forces [51].

6.3.3. System architecture

The blanket system is the main in-vessel component, both in terms of dimensions and functions. As such, the general architecture of an FPP is greatly constrained by the need to support blanket functions and requirements. This section addresses the impact of blanket exchange requirements on FPP architecture. The replacement of in-vessel components constitutes one of the great unsolved challenges of fusion engineering and design, if the overall availability of the plant is to be kept at an acceptable level. The three main architectures proposed in power plant studies are:

- The large module system (LMS)
- The vertical maintenance system (VMS)
- The large port system (LPS)

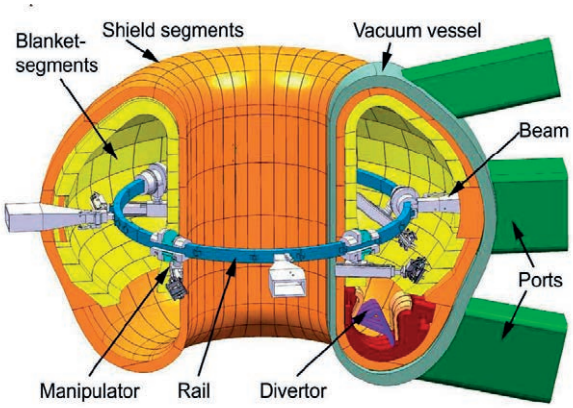

FIG. 6.9. Reactor design for the large module system adapted to a DEMO configuration; courtesy of KIT.

The large module system (LMS) is derived from the ITER system. The ITER blanket is divided into small modules, directly attached to the vacuum vessel. An in-vessel robot is used to attach and detach the mechanical connections of these modules, to cut and re-weld the hydraulics connections and to move the module in and out of the vacuum vessel. The coolant distribution system manifold is also connected to the vacuum vessel[54]. The water pipes are routed through the upper ports outside the vacuum vessel. The LMS is complemented by a divertor cassette maintenance system on a rail supported from the lower ports; see Section 6.4.2. An adaptation of this system to a DEMO reactor is shown in Fig. 6.9. The blanket system is segmented in large modules whose dimensions are limited by the load capability of the robot and the port dimension (about 300 in this design).

The ITER system has been developed for a low availability machine, in which scheduled in vessel replacements are foreseen only for the divertor cassettes. Its application to a power plant is questionable, mainly due to the large number of units to be replaced and the challenge of achieving re-weldable connections inside the vacuum vessel, between a removable module and a permanent manifold system attached to the vacuum vessel. Moreover, the level of radiation inside the vacuum vessel after shutdown seems incompatible with the electronic control of the replacement robot.

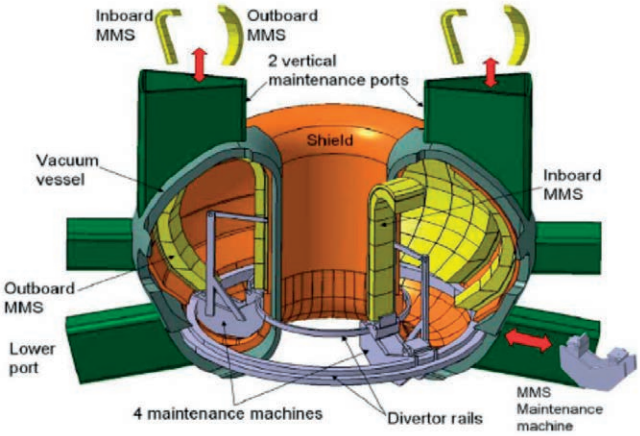

FIG. 6.10. Reactor design for a vertical maintenance system; courtesy of KIT.

For these two reasons, an alternative scheme was developed in the NET study, which relies on vertical ports. Implementation of the vertical maintenance system foresees a segmentation of the blanket system into 5 vertical segments per sector: 2 inboard segments (IBS) and 3 outboard segments (OBS). A vertical opening at the top of the vacuum vessel allows the extraction of all segments and provides space to route all necessary piping; see Fig. 6.10. The remote handling sequence for the extraction of the damaged blanket segments consists in:

1) opening of the vertical port;

[54] A relatively low differential thermal expansion (~50 K) makes this design possible.

2) cutting the pipe coming from the segments and freeing the port duct;
3) vertical extraction of the middle OBS;
4) extraction of the lateral OBS[55];
5) extraction of the IBSs, which is first be moved radially and toroidally to reach a position under the vertical port opening for vertical extraction.

The inverse sequence is foreseen for the insertion of the new blanket segments. The divertor is generally excluded from this type of maintenance. Single null configurations usually have a separate cassette-based maintenance system, for example in ITER. The VMS is one of the most popular concepts for DEMO and FPP maintenance. Studied since the 1980s, it is currently the favored concept in EU power plant studies as it provides a conceptual solution to several key issues:

- The need to drastically reduce the replacement time, minimizing the number of replaceable units and reducing in-vessel handling operations of hydraulic, mechanical and electrical connections. The standard VMS concept in a 16 sector reactor requires 80 segments.
- Access to the removable parts and their connections while providing protection against neutron heating and damage. This requirement calls for moving the connections to outer parts of the in-vessel region, beyond the shielding structures. Re-weldable connections should be particularly well protected from helium-producing reactions. In the VMS, the hydraulic connections of the segments are placed in the vertical access port; a region of simple access and low radiation field.
- The VMS reduces the nuclear exposure of remote handling devices needed to cut and reweld connections and move the blanket segments. Note that the impact of the γ radiation field on DEMO remote handling operations and machinery will be orders of magnitude more severe in comparison to ITER.

The studies have also highlighted drawbacks and issues related to this concept, including but not limited to:

- High precision in handling very large and heavy components through relatively small access ducts; where the extraction of a segment requires a succession of movement in toroidal, radial and poloidal directions with additional rotation of the component respect to the vertical axis. This is especially true for in-vessel movements, where additional motions could be necessary depending on the attachment system. The kinematics need to be studied in detail, as in-vessel remote handling seems essential.
- Removable units need to be mechanically attached to the vacuum vessel to withstand several large loads; e.g. electromagnetic loads. The design of this attachment system is complicated by the thermal mismatch between the inner power core at high temperature and the outer power core that can be fixed to the vacuum vessel at a lower temperature; usually 100 to 150°C.
- The maintenance scheme doesn't allow a selective replacement of segments; e.g. in case of unscheduled maintenance due to component failure. Excepting the mid OBS all segments have to be removed before accessing the faulty one.
- The opening of all ports for replacement poses issues that are often underestimated [52]. The opening a single port is a major undertaking due to the multiple operations it entails (opening the confinement barrier, removing pieces of shield and pipes, cutting the closure plates and installing a double port system) and their conformity to the safety regulations in force.
- The external logistic to transfer a large segment between the reactor and the hot cell facility (HCF) is also very demanding; e.g dimension of the casks.
- HCF requirements in terms of space, time and equipment seem generally demanding. If segment refurbishment is not required as a scheduled operation, certain constraints can be relaxed. Precise requirements for the recycling of irradiated materials are still incomplete and variants at each step of the maintenance system can have very different outcomes.

[55] The segment is moved toroidally to allow a vertical extraction.

- H&CD or control diagnostic are assumed to be allocated to dedicated vacuum vessel ports and their maintenance is assumed to be based on the port plug approach. Conflicts with the segmentation of the power core and the pipe routing have already been identified.

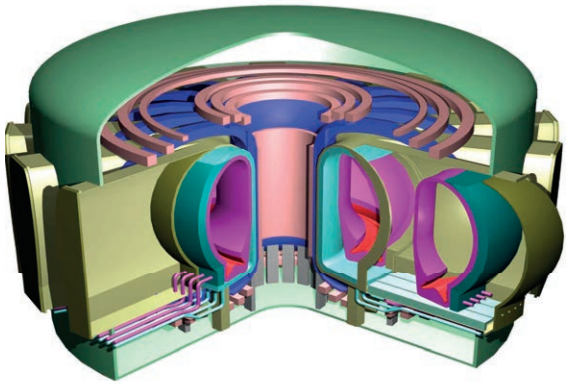

FIG. 6.11. Reactor design for a large port system; courtesy of KIT.

The large port system approach, shown in Fig. 6.11, has been proposed to maximize the advantages of the VMS, in particular:

- A drastic minimization of the number of removable units. Applied to a 16 sector reactor, the standard LPS concept requires only 16 removable units.
- Accessibility and protection of the connections. In this concept the main mechanical and hydraulics connection for the sectors are in the outboard structure of the blanket, well behind the main shielding structures.
- No need for in-vessel remote handling machines. This can be a strong advantage considering the very high γ dose in the torus.
- Simplification of the extraction procedure. The sectors are very large removable units. Their replacement only requires a single straight radial extraction–insertion movement. The units are supported on rails by the floor, allowing a reliable and precise motion.

To realize this concept the entire reactor configuration should be reconsidered proposing. Entire sectors — blanket and divertors and their ancillary systems are combined together — are to be pulled out in a single radial straight motion between two adjacent toroidal field coils. The extraction of a whole sector is geometrically possible by radially enlarging the TF coils in the outboard region so that the distance among adjacent vertical legs of the TF coils is larger than the sector width, while allowing the PF coils to move to the upper or lower cryostat region to avoid interference with the extraction pattern of the sectors. The vacuum vessel port should also be dimensioned to allow the sector extraction. The LPS concepts is one of the most studied concepts for DEMO and FPP maintenance. The LPS was also adopted by most of the major US (ARIES-RS and ARIES-AT) and Japanese (DREAM, CREST and SlimCS) power plant studies. Single in-vessel components (blankets and divertors) are replaced from the transverse (toroidal) direction. This radical solution has its own drawbacks and issues mainly related to:

- A particular configuration of the magnet system to allow the extraction of each sector through corresponding horizontal port. In particular, the design of the TF coils needs to be enlarged in the outboard radial direction, which could result in an increased capital cost (~10%). Another engineering challenge is the support of the turnover forces on the outer TF legs where supporting structure are difficult to place. The layout of the PF coils should also be adapted to the necessity of high horizontal ports. Raising the PF coils to the upper region or lowering them to the bottom region increases their distance from the plasma core and the manget current requirements.
- Vacuum vessel design is complicated by (i) the remote handling and helium-tight sealing of large closure plates, the (ii) integration of large ports on the toroidal structure, and (iii) the realization of port flanges in very restricted space.

- The design of transport casks and related handling equipment for very large removable units.
- The removable units include components of different lifetime classes. To reduce the waste and reuse the less irradiated subcomponents, several operations of refurbishment can be performed in hot cell facilities. This implies remote disassembly of used sectors, dividing waste and reusable components, and the assembly of new sectors, using new and irradiated parts. A modular design of the removable units can simplify the operations.
- Each removable unit has to be mechanically attached to the vacuum vessel to withstand large loads (e.g. electromagnetic loads) during reactor operation. Several solutions, including radial rails or flanges, need to be studied in detail.
- The opening of very large ports is a major undertaking due to the several operations that have to be done — e.g. opening of confinement barrier, removing pieces of shield and pipes, cutting of closure plates, installing a double port system — and their conformity to the safety regulations in force.
- The external logistic to manage the transfer of the large sectors between the reactor and the HCF is very demanding. The impact on the HCF requirements in terms of space, time and equipment has not been studied in detail.

In the present EU DEMO design stage the plant architecture adopts a variant of the vertical maintenance system; details can be found in [53].

6.3.4. Blanket concepts and classification

Blanket systems have been studied for several decades and different concepts have been investigated worldwide. The classification of blanket concepts is generally based on the choice of (breeder, structural and coolant) materials, the primary cooling configuration or the tritium extraction process.

6.3.4.1. Breeding materials and neutron multipliers

According to Section 6.3.2.1, lithium can be used for breeding as pure metal or as a compound, in liquid or solid form. The form (liquid or solid) leads directly to a major classification of blanket concepts in two broad categories, namely solid breeder and liquid breeder. This distinction has a large impact on the requirements and the processes involved. For example, the tritium extraction in a solid breeder is usually achieved by a gas purge that transfers the tritium outside the vacuum vessel into dedicated removal units that separate tritium from the carrier gas. In liquid breeders, the entire breeder needs to be circulated through extraction units, outside the vacuum vessel, where tritium is removed from the liquid breeder by means of e.g. vacuum permeators or gas stripping.

Solid breeders remain in the reactors for the entire lifetime of the blanket. The deterioration of their characteristics (e.g. mechanic or neutronic) can thus reduce the blanket lifetime. On the contrary, liquid breeders are chemically controlled and purified in the external loops. For example, the Li burnup degradation can be controlled by adding fresh lithium and removing transmutation products from the materials.

Typical solid breeders include lithium oxide (Li_2O) and ternary ceramics such as lithium orthosilicate (Li_4SiO_4), metatitanate (Li_2TiO_3), metazirconate (Li_2ZrO_3) or alluminate ($LiAlO_3$). The selection of the most suitable solid breeder is a trade-off among different, often contrasting, requirements, also very dependent on the chosen blanket architecture. A high lithium density is desirable to achieve compact configurations and ease the need for enrichment. Materials from which the tritium is quickly released and extracted are favourable to avoid the build-up of a large tritium inventory in the breeder and reduce the amount needed to start the reactor. The time constant of this process is known as the tritium residence time.

A critical item in the design of a solid breeder is temperature control. Most of the phenomena related to breeder operation are temperature dependent, e.g. the tritium residence time, swelling, thermal and mechanical properties and chemical compatibility. The temperature profiles setups should remain unchanged for the entire lifetime of the blanket. Good thermal properties (e.g. high thermal conductivity, low expansion coefficient) in a large temperature window are therefore important to obtain a satisfactory thermal design of the breeder zone. If the breeder has no specific structural requirements, fragmentation and swelling should be minimized to keep purge capabilities and temperature control.

The operation of the breeder should be compatible with the surrounding materials, i.e. steel. Compatibility up to 550°C (at the interface) is usually provided, ensuring a baseline for the design of the breeder containment. Compatibility during accidents should also to be considered. For example, water used as coolant can react violently

with pure lithium and, to a smaller extent, with lithium compounds. Good hygroscopic properties help reduce the handling requirements, avoiding the use of protection gas.

Other important selection criteria are activation characteristics. Elements, like aluminium and zirconium, that can produce long lived activation products tend to be avoided, even if they are otherwise attractive. For all remaining compounds, the fulfilment of these criteria is tied to very strong specifications related to the level of long lived activation products. The impurity level should be strongly controlled to reduce the final activation, reduce the amount of waste and allow the recycling of expensive materials (e.g. highly enriched lithium). Table 6.6 lists the main properties of typical solid breeders.

TABLE 6.6. Properties of solid breeder materials. For comparison, the properties are given at an average temperature of ~500°C.

	Li_2O	Li_2TiO_3	Li_2ZrO_3	Li_4SiO_4	y-$LiAlO_2$
Density [g/cm^3]	0.94	0.43	0.38	0.51	0.27
Thermal conductivity [W·m^{-1}·K^{-1}]	4.7	2.4	0.75	2.4	2.4
Thermal expansion [-]	1.25	0.8	0.50	1.15	0.54
Reaction with water	very	less	less	little	little
Residence time [h]	0.03	4	0.01	10	50
Swelling					
Melting point [°C]	1430	1550	1615	1250	1610

Over the last decade, blanket developers have focused almost exclusively on Li_4SiO_4 and Li_2TiO_3 in form of pebble beds. Both materials ensure a low activation, high operational temperatures, good tritium release, and easy manufacturing and recycling routes. They can be used up to ~920°C with enough safety margins from any major change of state, i.e. melting.

Li_2TiO_3 is not sensitive to moisture, simplifying handling. From a design point of view its lower thermal expansion reduces the build-up of stresses during the heating phase and possible gap formation during the cooling. Li_4SiO_4 has a higher lithium density, which is a great advantage from a neutronics point of view. Only Li_2O can offer a higher lithium density, but its poor mechanical properties at high temperature result in major drawbacks. Fabrication and recycling routes have been defined and demonstrated for both reference materials: Li_4SiO_4 pebbles are usually produced by melting spray process, while Li_2TiO_3 pebbles are made by sintering. Specifications for DEMO (e.g. control of impurities) have been formulated and the production of both ceramic materials has reached a semi-industrial level with a peak capacity of few hundred kilograms per year. The characterization of these ceramics in out-of-pile conditions is almost complete, including chemical compatibility with EUROFER and purge gases, thermomechanical properties, high-temperature long term behaviour and tritium release characteristics; state of the art design information is now available [54]. More recently, ~20 mol% of Li_2TiO_3 has been added to the initial melting of Li_4SiO_4, increasing the mechanical characteristics of the pebbles while maintaining a simple fabrication process. This comes at the expense of a moderate increase of the melting temperature [55]. Liquid breeders used in the reactor are mainly pure lithium, the eutectic Pb-15.8%Li (usually shortened as PbLi) and molten salts such as FLiBe (LiF-BeF_2) and FLiNaBe (LiF-NaF-BeF_2). In general, the composition of these alloys and compounds include a neutron multiplier element (lead or beryllium) to optimize the neutron balance. Table 6.7 presents the major properties of these materials

TABLE 6.7. Major properties of liquid breeder materials. The values reported in are given at an average temperature of ~500°C, for comparison purposes only. The data was obtained from PbLi database review [56], FLiBe and Li database review [57] and FLiNaBe database review [58].

	Lithium	PbLi	FLiBe	FLiNaBe
Reference composition (mol%)	pure lithium (metal)	Eutectic alloy: ~15.8% Li	0.67% LiF - 0.33% BeF_2	0.31% LiF - 0.31% NaF - 0.38% BeF_2
Melting point [K]	~454	~508	~732	~600

Density [kg·m^{-3}]	485	~9600	~2005	2200
Electrical resistivity [Ωm]	3.5×10^{-7}	1.3×10^{-6}	$\sim 0.7 \times 10^{-2}$	-
Thermal conductivity [W·m^{-1}·K^{-1}]	50	17	~1	~0.70
Specific heat [J·kg^{-1}· K^{-1}]	4394	190	~2380	~2200
Viscosity [Pa·s]	3×10^{-4}	3.4×10^{-4}	1.5×10^{-2}	$\sim 15 \times 10^{-4}$

For liquid breeders, the melting temperature is an important parameter to avoid risks of solidification, compromising the cooling and tritium extraction. Liquid breeders are particularly interesting since they can be used, simultaneously, as coolants in advanced blanket concepts; refer to Section 6.3.4.4.

The eutectic lithium–lead alloy PbLi has a lesser breeding capability than pure lithium. However, it is favoured for its lower chemical activity; it is stable in air and mildly reacting with water. The issue here is related to the use of water as coolant. In case of accidents, a contact between lithium and water would result in a violent exothermal reaction with hydrogen production. Issues related to the use of PbLi include the corrosion of pipes and blanket structures, the lack of an efficient tritium extraction and purification process, the control of tritium leakage and permeation into coolants. Irradiated PbLi should also be controlled for polonium and other transmutation products. Moreover, PbLi requires up to 90% of ^{6}Li enrichment to minimize the radial thickness of the breeder zone.

As discussed in Section 6.3.2.1, a neutron multiplier is necessary for tritium self-sufficiency in practically all blanket concepts. For solid blankets, beryllium is the natural choice since it is solid in the temperature range of interest. It can be used in the form of pebble beds, as in ceramic breeders, or in rods. Three main issues should be considered: degradation of the mechanical properties, reactivity with steam and air, and tritium retention.

The first issue is tied to a specific design choice as beryllium tends to become brittle during irradiation. If beryllium is used in large blocks, these blocks could break with consequences on the effective thermal conductivity (temperature control). Pebble beds are less sensitive to fragmentations.

The second and third issues pose general safety concerns. An accidental contact with steam would produce hydrogen and become exothermal beyond 600°C. Due to the simultaneous formation of tritium and helium during irradiation, tritium can be trapped in helium bubbles, which can grow inside beryllium grains. By this mechanism, kilograms of tritium could have accumulated in the beryllium inventory at EoL (depending on temperature level and neutron doses). For these reasons, the recent EU HCPB beryllium has been substituted by a beryllide ($Be_{12}Ti$), which is less reactive with steam and retains less tritium. In liquid breeders, the neutron multiplication function is carried out by elements that are part of the alloy or compound (mainly lead and beryllium). The addition of beryllium blocks has been proposed in a few liquid metal concepts (especially pure lithium or molten salts) to enhance the multiplication capability of the breeder.

6.3.4.2. Coolants

The coolant choice is driven by several sets of requirements. Its function as the primary heat transfer system (removing more than 80% of the thermal energy produced by the fusion reactor) is a major selection factor. The coolant should remove heat at high temperature, (> 300°C) for efficient electricity generation, or (beyond 700°C) industrial processes such as hydrogen production. In addition, the coolant should not jeopardize the neutron balance. For this purpose, the best solution might use the breeder itself (in liquid form) as a coolant. Another important issue is the compatibility of the coolant with other blanket and reactor materials in operational and accidental cases. For example, corrosion could require the use of a complicated coating technology to protect the attacked surfaces of structural materials. Safety concerns include possible reactions with structural or breeding materials at high temperature, fire hazards or hydrogen production followed by an explosion. Four categories of coolants have been considered in FPP conceptual designs:

- Water, e.g. pressurized water reactor (PWR, ~280 to 330°C) and supercritical water (> 374°C).
- Gases, mainly helium.
- Liquid metals (breeder and coolant), e.g. lithium or the eutectic PbLi.

- Molten salts (breeder and coolant), e.g. FLiBe or FLiNaBe.

Water is an exceptional coolant allowing high heat transfer coefficients; e.g. with turbulence promoters such as the swirl or the Hypervapotron [59][60]. Water has a high thermal capacity and a sufficiently high density allowing heat transport with low temperature differences, using relatively small volumes. Its availability is practically unlimited. However, water is limited by its temperature range if the coolant is liquid and a margin to evaporation is needed (< 335°C). These conditions are fulfilled by the PWR cycle, where temperatures are between 285 and 335°C at a controlled pressure of 15.5 MPa.

Beyond ~22 MPa and 374°C water exists as a supercritical fluid; this range has found very little success in fission and fusion technology due to severe corrosion issues with steels requiring chemical control. The main disadvantage of water comes from its poor compatibility with other fusion materials; e.g. chemical compatibility with breeders and multipliers like lithium, PbLi and beryllium that can contact water in accidental conditions. For instance, at high temperatures, reactions with metals like beryllium or tungsten can be prohibitive for safety reasons; e.g. hydrogen production. Another example is the temperature window mismatch with structural materials like ferritic or ferritic-martensitic steels potentially reducing component lifetime under irradiation; see Section 6.3.4.3. Water is also a neutron moderator and thus plays an important role in the neutronic balance of an FPP. The parasitic absorption of water coolant should be carefully considered in the neutronics analysis. Water is also subjected to nuclear activation under neutron irradiation: isotopes of N arise from O leading to high gamma and neutron emissions with short half-lives (4 to 7 seconds). Finally, water can trap tritium by isotopic exchange. Its removal requires an expensive decontamination process of the whole inventory (~300 t).

Unlike water, helium is adaptable to a wide range of temperatures. It is therefore compatible with practically all materials used in fusion reactors. It can be employed up to very high temperatures, increasing power generation efficiency. However, the cooling properties of helium are comparatively poor. For heat transfer applications, the low density is partially compensated using high pressures (8 to 10 MPa) and velocities (up to 80 m/s). High velocity yields acceptable heat transfer coefficients at the high heat flux surfaces (e.g. the first wall) but sometimes produces large pressure drops, requiring huge pumping power for circulation. This reduces the power conversion efficiency, compromising the advantage of a high temperature coolant. Nevertheless, suitable working points exist, with pumping powers in the range of 5% of the extracted heat. Helium has practically no neutron interaction, which can be favourable to the neutron balance. Nevertheless, the considerable volume necessary for channels and manifolds produces large void fractions in the breeding zone. This void fraction complicates the shielding of in-vessel components. For example, as pipes are transparent to neutrons, a special (dog legs) design is required to avoid neutron streaming, resulting in an increased thickness of in-vessel components. Tritium extraction from helium is not difficult. However, the safety risk of tritium permeation in components such as steam generators can place strict requirements on the maximum tritium partial pressure in the coolant. This can penalize the system economically and require complex coolant purification systems or antipermeation barriers. The availability of helium in the next decades is uncertain. As the production of helium is tied to the extraction of natural gas, the decrease of this natural resource will probably cause a shortage in helium supplies and impact helium technology worldwide.

Liquid metals, such as lithium and PbLi, are attractive coolants that can cumulate the functions of a coolant with those of a breeder, simplifying the overall power plant concept and maximising the neutronic balance for tritium production. The production of tritium in the coolant opens large issues for tritium extraction and control. If the first is mostly an economical issue[56], the second is a safety concern; i.e. large quantity of hydrogen circulating within a high temperature coolant. In spite of its excellent cooling features (high density, high thermal conductivity, low operational pressure), the use of liquid metal in magnetic confinement devices is limited by magnetohydrodynamic (MHD) interactions, which compromise (or even nullify) all potential advantages. The situation is worsened if electrically conducting materials (like steel) are used in the pipe structure containing the liquid metal. The electrical paths are closed, and the circulating currents induce high magnetic pressure drops and turbulence suppression. The use of liquid metal coolants thus requires non-conducting structural materials, like SiC_f /SiC, or the provision of a very effective insulating layer on the inner surfaces of the conducting ducts. Further issues are related to the compatibility of liquid metal coolants with FPP materials. In normal conditions, PbLi and lithium have corrosion issues with steels. Lithium is very dangerous in accidental conditions if it contacts air or water. PbLi can also reacts with steam. Both lithium and PbLi are solid at room temperature and pressure. Both materials require special provisions to avoid their solidification in the components during off normal operation or accidents.

Like liquid metals, molten salts can simultaneously function as breeder and coolant with the additional advantage of a lower electrical conductivity. This allows their use in the FPP magnetic field with conducting steel ducts. Typical

[56] Tritium extraction from lithium is rather challenging.

materials considered for this scope are FLiBe or FLiNaBe. FLiBe is not flammable and does not react with air or water. Low tritium inventory and low working pressures are favourable characteristics. Obstacles include a very low thermal conductivity, a high kinematic viscosity (Prandtl-number) and an unimpressive breeding capability, calling for the addition of a neutron multiplier. Chemical stability is one of the major issues; especially under electric fields (electrolysis) or irradiation (radiolysis). FLiBe is rather aggressive to several structural materials with the formation of hydrogen fluoride. Control over hydrogen fluoride synthesis in the FLiBe stream is therefore required. Blanket concepts have been proposed, notably in the APEX study [61] and for the Japanese reactor FFHR [62]. FLiNaBe molten salt (BeF2-LiF-NaF) was proposed for its lower melting point (240°C). However, FLiNaBe has an even lower tritium breeding capability, requiring the addition of a neutron multiplier (e.g. solid beryllium).

6.3.4.3. Structural materials

Suitable structural materials should feature a high neutron damage resistance (swelling and dpa), good neutronic properties (low absorption), chemical compatibility with the breeder and coolant, good thermomechanical properties and a reduced activation. As such, few materials could ever be considered promising for blanket application. Among these, even fewer have been developed for qualification in a fusion environment. For Gen-I reactors only certain grades of steels have could conceivably reach maturity. Other materials have been proposed for their peculiar characteristics, e.g. vanadium alloys, which offer exceptionally low neutron absorptions and combine almost ideally with pure lithium. Ceramics, like silicon-carbide (SiC) fibres–SiC matrix compounds, have also been proposed. Their low electrical conductivity allows for liquid metal coolants. Table 6.8 compares the critical properties of these structural materials.

TABLE 6.8. Comparison of structural materials considered for fusion application. Compiled for comparison reason, this table presents only average values in the temperature windows of interest.

	AISI-316L	EUROFER	V Alloy	SiC_f/SiC
Temperature range [°C]	250 to 500	~300 to 550	400 to 700	700 to 1000
Density [kg/m^3]	~7980	7798	6100	2500 to 3000
Coef. of thermal expansion [10^{-6}]	17.5 to 18.5	11.2 to 12.1	10.3	4.0
Thermal conductivity [W·m^{-1}·K^{-1}]	15	33.4 to 32.4	28	~15
Max. allowable stress, S_m [MPa]	122 to 108	169 to 117	220	140
Young's modulus [GPa]	180 to 165	203 to 184	125 to 138	200
Poisson number [-]	0.27	0.3	0.36	0.18
Magnetic permeability [H/m]	1	39 to 53	-	-
Electrical resistivity [Ωm]	7.5×10^{-7}	5 to 8×10^{-7}	7.4×10^{-7}	2×10^{-4}

Blankets for DEMO and Gen-I FPPs should be compatible with structural materials that will be qualified for licensing in a relatively short time frame (20 to 30 years). Only certain grades of steels have reached a suitable level of qualification to be compatible with this time frame. The main requirements for blanket structural materials are radiation hardness and low activation. Acknowledging these requirements, the EU and the Japanese fusion programmes have been developing ferritic–martensitic steels since the nineties; see Chapter 8. In the EU, this grade of steel was developed under the name EUROFER [63].

EUROFER is a reduced activation ferritic–martensitic (RAFM) steel. RAFM steels are alloys whose main composition is derived from modified 9Cr–1Mo steel, where high activation elements such as Mo and Nb are replaced by equivalent[57] low activation elements (e.g. W, V and Ta). The presence of high activation residual elements (like Co) is kept as low as possible. Ferritic–martensitic steels present good resistance against neutron damage (dpa and swelling) and offer relatively good thermomechanical properties as compared to austenitic steels. This material allows the design of fusion components that can withstand high neutron fluxes. A target ~70 dpa is considered for Gen-I power plants ensuring enough availability of the blanket system for economic viability. The performance is expected to double in future FPPs. The temperature range of application is presently between 300 and 550°C, where the lower limit is mainly dictated by the increase of the ductile to brittle transition temperature under irradiation and the upper limit by the loss of strength. The ductile to brittle transition temperature of these steels tends to increase under irradiation, especially below ~350°C. It can reach room temperature levels after little irradiation [64]. An EU database

[57] Equivalent in terms of the required micro-structural and mechanical properties.

of material properties and design criteria is under preparation to facilitate blanket structural design in beginning of life conditions. Extension to end of life conditions is only estimated and validated by fission reactor irradiations. The qualification of EUROFER for DEMO applications will need an additional assessment of the effects of helium production, associated to the fusion spectrum. Additional irradiation programmes have been requested to this end. Neutron sources such as the international fusion materials irradiation facility (IFMIF) [65] or DONES [66] will simulate the effects of 14 MeV neutrons at high fluence, producing damage above 20 dpa and relevant amounts of helium. The present production[58] has been optimized in terms of operational temperature window for the EU helium cooled blanket concepts. EUROFER shows a good chemical compatibility with Li_4SiO_4, Li_2TiO_3 and beryllium up to 550°C; corrosion with PbLi becomes relevant beyond 450°C. The ferromagnetic properties of EUROFER play an important role in the design of the DEMO blankets and the ITER TBM. In ITER, the presence of the ferromagnetic TBM in a prevalently non-magnetic environment needs to be accounted for in controlling the plasma to compensate local distortions of the confining magnetic field. This could require a reduction of the total amount of RAFM during high performance plasma operations [67]. In DEMO, the effect of a completely ferromagnetic blanket ring will be assessed to establish the loads in transient and static conditions. Mechanical loads caused by disruptions will also be affected by the magnetic properties of these steel that produce a local enhancement of the magnetic field [51].

Austenitic steels (e.g. AISI 316L) are widely used in existing tokamaks and foreseen for the ITER shielding blanket. They are very well suited for water cooling in terms of corrosion and ductility at lower temperatures and do not required heat treatment processes after welding, simplifying blanket replacement operations (i.e. welding of pipe connections). However, their use in a true reactor environment is questionable because of their shorter lifetime under neutron irradiation and relatively poor thermomechanical characteristics.

Vanadium alloys have been proposed in the past as an ideal structural material for lithium blanket concepts. In fact, vanadium presents an exceptionally low neutron absorption, allowing blanket concepts without an added neutron multiplier and using lithium at its natural isotopic composition. Vanadium alloy (V_4Cr_4Ti) has been proposed as the structural material because it can accommodate high heat loads and operate in a range of temperatures of ~400 to 700°C. It also has several attractive features such as good mechanical properties at high temperatures, high neutron fluence capability, low degradation under neutron irradiation, good compatibility with blanket materials, low decay heat, low waste disposal rating and adequate strength to accommodate the electromagnetic loads during plasma disruption events. The limited use of vanadium alloy has raised concerns related to the qualification of this material. For first generation reactors, vanadium alloy is not considered any more.

As discussed in Section 6.3.4.2, the use of liquid metal coolants is strongly limited by MHD phenomena. Indeed, liquid metal coolants can only be applied provided electrically non-conducting structures. Ceramic materials, like silicon carbides, have therefore been proposed in advanced blanket concepts. As a composite (SiC fibre in Sic matrix, SiC_f/SiC) silicon carbide has good resistance against neutron damage and allows very high operational temperatures (~1000°C). However, the thermomechanical properties of this material (particularly its thermal conductivity) are not exceptional. Even special SiC fibres harbouring values above 10 $MW.m^{-1}.K^{-1}$, shows a typical degradation to much lower values after relatively short irradiations. The material presents good compatibility with PbLi, ceramic breeders, beryllium and helium over a wide range of temperatures. Manufacturing is an additional issue. Provided a successful validation for fusion reactor conditions, SiC_f/SiC could be considered for Gen-II FPPs.

6.3.4.4. Cooling and tritium extraction configuration

Another major classification criterion is related to cooling and the tritium extraction processes. A rough classification distinguishes:

1. An independent loops configuration, in which coolant and breeder are strictly separated. A dedicated loop for the breeder collects and transfers tritium to an external extraction plant. This loop usually operates at a much lower pressure than the cooling loop (lower mass flow and negligible heat removal function). A separate coolant loop removes the heat generated in the blanket. In this scenario, tritium contamination in the coolant (e.g. permeation between adjacent coolant and breeder regions or from plasma ion implantation) is a parasitic effect that should be minimized and controlled by design.
2. A self-coolant configuration, in which the tritium carrier is the coolant itself. A liquid breeder is used to delivers heat and tritium outside the blanket system. In this configuration the loop fulfils stringent tritium removal and extraction requirements handling large quantity of tritium within a high temperature carrier.

[58] EUROFER is already produced at an early industrial scale.

3. A dual coolant configuration, which foresees two independent loops. The first loop is dedicated to cooling, while the second combines coolant and tritium transport functions using a liquid breeder.

The HCLL blanket is one of the most studied concepts. Fig. 6.12(a) shows the "independent loop" configuration of such blanket. In this scheme, the coolant function is entirely performed by the helium loop, at high pressure (~8 MPa) and temperatures (300 to 500°C). A steam generator transfers the heat power to a secondary Rankine cycle for electrical power generation. Tritium contamination in the helium loop is controlled by a coolant purification system that keeps the tritium partial pressure compatible with the operational release requirements; see Section 6.3.2.5. The breeder zone is filled with PbLi, which flows at a few centimetres per second through an independent loop. PbLi transports the tritium produced in the blanket out of the vacuum vessel for extraction (e.g. gas stripping flow).

A typical self-cooled blanket is shown in Fig. 6.12(b). The breeding and cooling functions are fulfilled by a single PbLi loop, owing to the use of SiC as structural material. The loop transfers heat (700 to 1100°C) and tritium outside the blanket system to a tritium extraction unit (e.g. vacuum permeator). A helium–helium heat exchanger transfers the power to a Brayton Cycle (viable in this temperature range). A noteworthy example of this blanket design is the self-cooled lithium–lead (SCLL) described in [68].

A dual coolant system is illustrated in Fig. 6.12(c). This example is the dual cooled lithium–lead blanket (DCLL) described in [69]. The coolant loop contains helium in a temperature range (300 to 500°C) compatible with EUROFER and removes ~50% of the heat. A separate loop uses PbLi as breeder and coolant. The design of the breeder zone and the use of SiC (thermally and electrically insulating PbLi and steel) allow a flow of PbLi at higher temperatures (500 to 700°C). A two-stage heat exchanger transfers the heat to a secondary helium loop connected to a Brayton cycle.

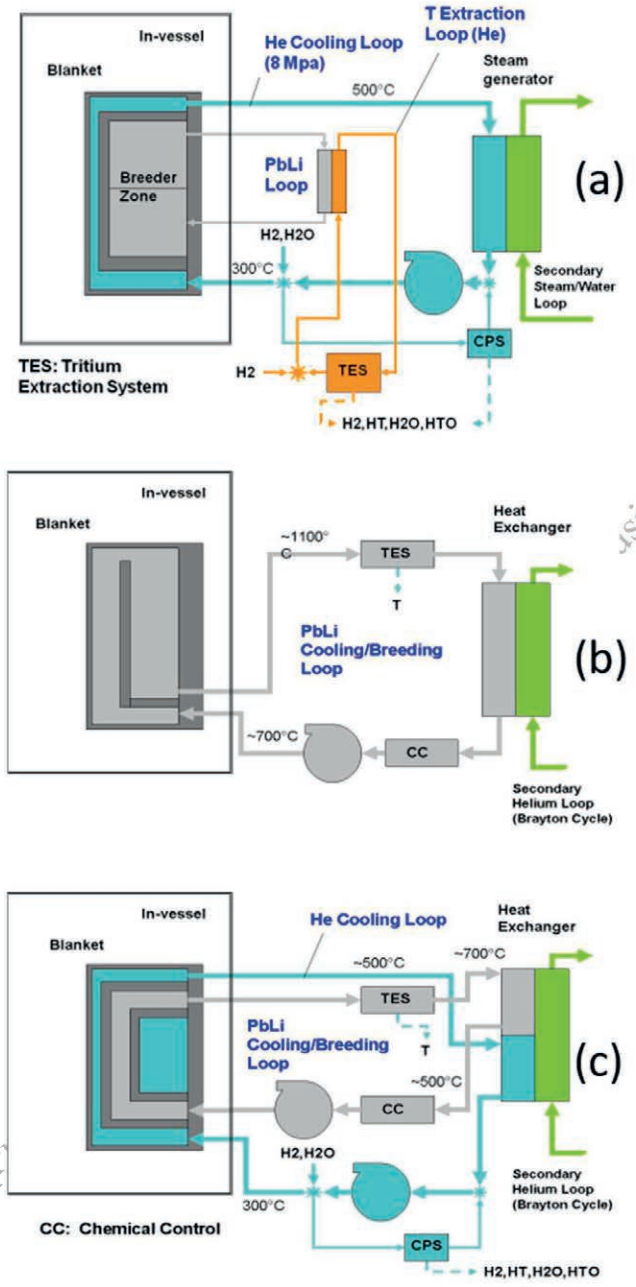

FIG. 6.12. (a) Helium cooled pebble bed blanket system (example of an independent loops configuration); (b) self-coolant lithium lead blanket system; and (c) dual coolant lithium–lead blanket. Courtesy of KIT.

6.3.5. Proposed blanket designs

Table 6.9 lists the major blanket designs proposed and studied worldwide, summarizing the foreseen materials and processes combination. As explained in Section 6.3.1.1, two blanket concepts are considered in the pre-conceptual design of EU DEMO, namely the HCPB and the WCLL. Both solutions are based on the use of EUROFER as structural material (i.e. operational temperatures between 300 and 550°C) and adopt the "independent loop" architecture. These concepts differ in their choice of breeders and coolants.

TABLE 6.9. Main blanket technologies proposed and studied worldwide.

Blanket design	Structure	Breeder	Multiplier	Coolant & tritium extraction
HCPB (EU) [23]	EUROFER	Li4SiO4 (Li_2TiO_3)	Be, BeTi	He, independent loops
HCLL (EU) [28]	EUROFER	PbLi	PbLi	He, independent loops
DCLL (US, EU) [25], [69]	EUROFER	PbLi	PbLi	He and PbLi, dual coolant
WCLL (EU) [24]	EUROFER	PbLi	PbLi	H_2O, independent loops
WCSB (Japan, China and South Korea) [34]	F82H (RAFM)	Li_2TiO_3	Be, BeTi	H_2O, independent loops
SCLL (US, EU) [33], [68]	SiC/SiC_f	PbLi	PbLi	PbLi, self-coolant
AHCPB (EU) [70]	SiC/SiC_f	Li4SiO4 (Li_2TiO_3)	Be, BeTi	He, independent loops
Li/V-SC (US)[71]	V (alloy)	Li	Be	Li, self-coolant

Fig. 6.13 illustrates the concept of a HCPB blanket. The HCPB uses helium as coolant (300 to 500°C) with a pressure of ~8 MPa. The helium flows along small channels supplied by a system of manifolds behind the blanket. The first wall removes direct surface heat (up to 1 MW/m^2) while cooling plates in the breeding zone remove the volumetric heat. The breeding zone itself is a sandwich of cooling plates, breeder material and the neutron multipliers. Both breeder and neutron multiplier are purged by an independent low pressure low velocity helium flow meant to extract the tritium from the blanket.

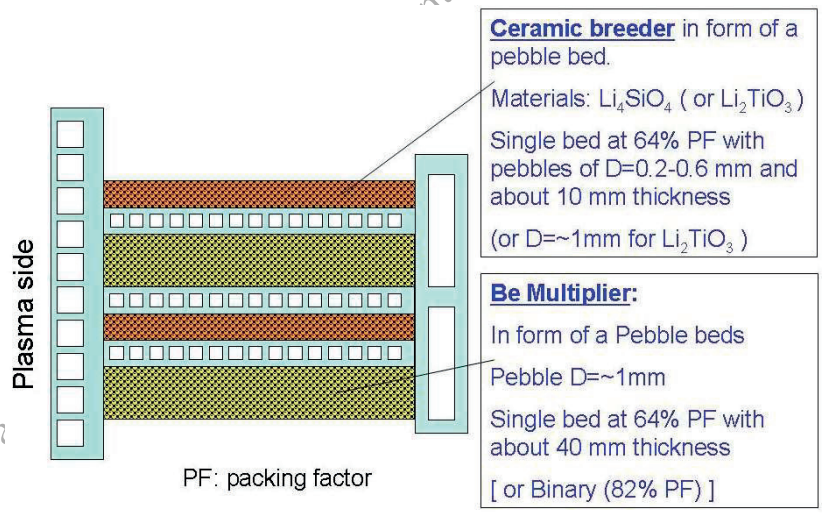

FIG. 6.13. *Conceptual scheme for the HCPB blanket. Courtesy of KIT.*

The breeder material is a ternary ceramic breeder (Li_4SiO_4 or Li_2TiO_3), used in the form of a pebble bed. This stabilises the thermal properties of the bed making it less sensible to further fragmentations, but also reduces the effective thermal conductivity compared to the base material. The maximum temperature is, by design, 920°C. The design maximizes and controls the average temperature of the bed to increase tritium release and reduce inventory over the entire lifecycle. Hydrogen is added to the helium stream up to a partial pressure of ~100 Pa, in order to enhance tritium extraction from the ceramic pebbles. Beryllium is used as neutron multiplier in a 4:1 (weight) ratio to the ceramic breeder.

Tritium permeation in the coolant is a major safety concern due to the large interface with pebble beds and coolant systems (~13,000 m^2 in the whole reactor) at a maximum temperature of ~550°C. From the coolant, tritium

can reach the steam generator and permeate to the water side, where it is easily released into the environment. The HCPB concept has several features that help reduce the risk associated to tritium permeation:

a) The tritium partial pressure on the bed side (driving permeation) can be reduced by purging from the plasma side to the rear part.
b) The tritium partial pressure increases in the ceramic breeder beds from practically zero to a maximum under 1 Pa at the output (rear). The tritium partial pressure at this interface can be reduced increasing the mass flow during the purge. However, this countermeasure will increase hydrogen recirculation. It could also enhance the pressure drops of the purge flow.
c) On the helium coolant side, a coolant purification system (CPS) is needed to maintain a low tritium partial pressure in the loop. A reduction of this partial pressure limits permeation of tritium into the steam generator. The achievable partial pressure depends on the influx of tritium in the coolant and the economically viable size of the CPS.
d) Permeation can further be reduced by adding H_2 and H_2O to the helium coolant, maintaining a stable oxide layer on the CPS (and steam generator) coolant side producing a modest permeation reduction factor.

If methods (a), (b), (c) and (d) were insufficient, permeation barriers in form of coating layers should be considered. These would likely cause major modifications to the general concept.

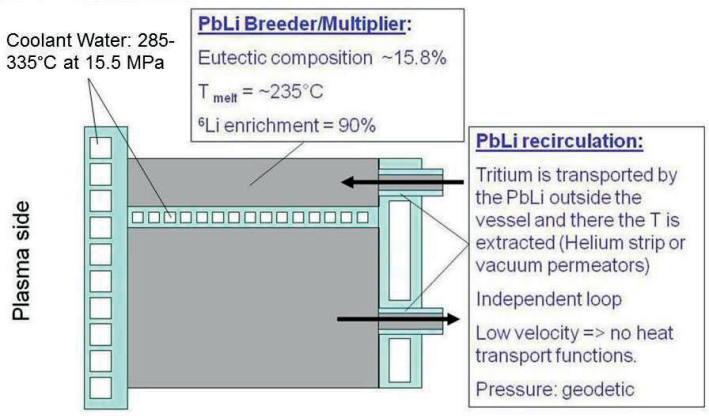

FIG. 6.14. *Conceptual scheme for the WCLL breeder blanket. Courtesy of KIT.*

Fig. 6.14 illustrates the WCLL concept. In the WCLL blanket, the first wall and breeding zone are cooled by water flowing through small channels or tubes in PWR conditions: 285 to 325°C at a pressure of 15.5 MPa. The remainder of the box is filled with liquid PbLi for tritium breeding and neutron multiplication. The liquid breeder is recirculated to extract tritium outside the vessel[59]. A recirculation pattern is provided inside the blanket box from an inlet collector to an outlet. Within the magnetic field, the liquid metal can only be recirculated at very low velocity (a few mm/s). No more than 10 recirculations of the PbLi inventory are typically foreseen per day to keep the MHD effects at an acceptable level, avoiding negative impacts in pumping power and tritium extraction.

Tritium control in WCLL presents its own set of issues. The low transit velocity of PbLi and the poor solubility of tritium could cause an accumulation in the breeder. Large tritium partial pressures are therefore likely to appear at the cooling plate interface, driving permeation. In this context, tritium transport modelling is complicated by several phenomena, including tritium solubility in PbLi, MHD effects on the PbLi flow, tritium diffusion velocity and tritium trapping in PbLi. However, once tritium reaches the coolant, it is trapped in water. The inventory thus continuously increases until the threshold for safe operation of the reactor is reached and a replacement of the coolant is required. The contaminated water is then treated as waste in a separate facility. To mitigate this scenario, a CPS can be used within the coolant loop for water detritiation. This process is limited by the achievable treatment rate considering a realistic CPS dimensioning and energy consumption, making water substitution the only practical solution. A drastic reduction of tritium permeation could be achieved in WCLL by coating the EUROFER. R&D is ongoing to demonstrate the feasibility and lifetime of this technology under operational conditions (e.g. irradiation).

[59] Tritium coming from the tritium extraction unit is pretreated and sent to the fuel cycle.

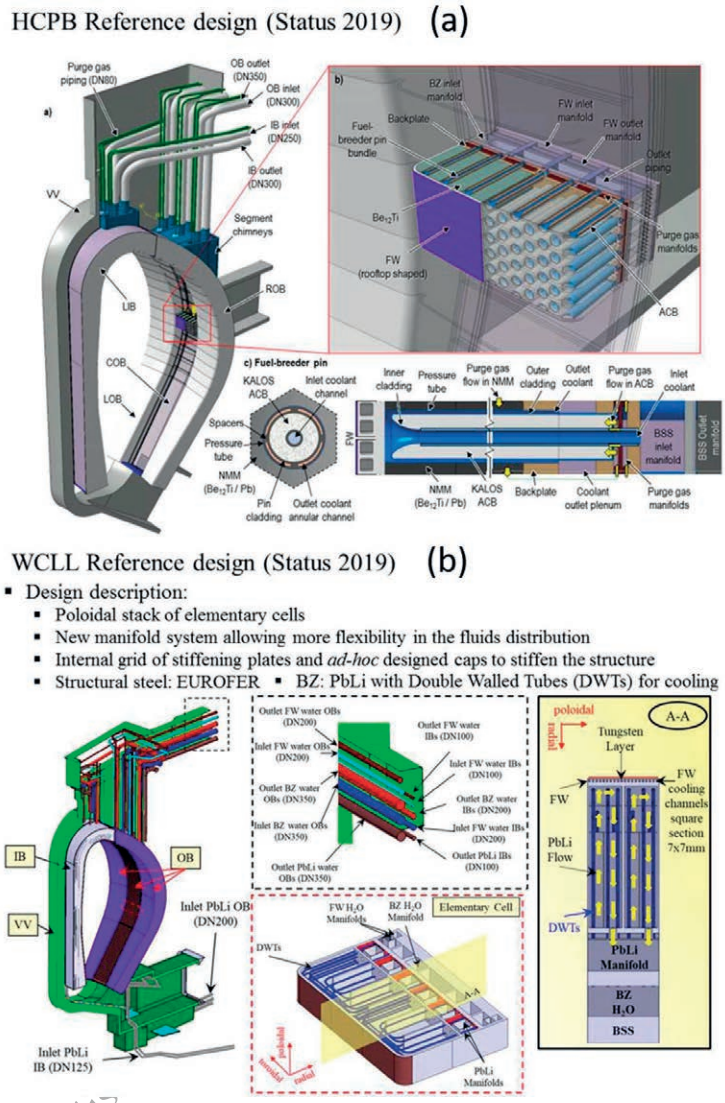

FIG. 6.15. Blankets in the EU DEMO (Status 2019): a) HCPB DEMO (courtesy KIT); b) WCLL DEMO (courtesy ENEA). For further explanations consult [72] and [73].

Finally, Fig. 6.15 shows the HCPB and WCLL systems conceived in the 2019 EU DEMO design. The suitability of these blanket systems to the conceptual design of EU DEMO is under assessment [30].

6.4. DIVERTOR

Present day tokamaks and stellarators adopt divertor configurations to solve the issues of the plasma edge; i.e. a large part of the exhaust power is concentrated, or "diverted", as plasma flux onto localized regions at the plasma core boundary. In these regions, ionized particles are neutralized (they become neutrals) and removed from the vacuum chamber. Neutralization of the plasma flux usually happens by impact on solid plates. The FPP component used for this purpose is also called the divertor. From an engineering point of view, the issue is to cope with the high energy density of this flux, with peak values in the hundreds of MW/m^2 at the boundary of the separatrix. The ITER divertor is considered the most promising starting point for power exhaust management in future reactors.

6.4.1. Divertor functions and requirements

Following the description made in Section 6.1, the main functions of the divertor are to extract helium and other impurities from the plasma and to remove the associated heat. To fulfil its purpose the divertor needs reliable targets, able to remove large heat loads. The targets will be shaped to compress the neutrals into a dedicated region where they can be pumped out efficiently, avoiding their return to the plasma core.

For an efficient reactor, the heat removed by the divertor should be used for electricity production. This is, of course, not a requirement for ITER and may not even be requested of Gen-I reactors. However, usage of the fusion energy collected by the divertor (15 to 20% of the total according to PPCS) will become increasingly important towards the economical exploitation of fusion reactors.

Like the blanket, the divertor shields the vacuum vessel and the magnets from heat and neutron damage. The question of component replacements is therefore as important as for the blanket. Divertor components will be damaged by neutrons (dpa and helium production) and by direct interaction with the plasma flux at the targets (e.g. erosion). Their lifetime will largely be determined by the adopted configuration, geometry and materials. For present technology, the lifetime of divertors with solid targets is estimated to be much shorter than that of the blanket. A very effective replacement system is then needed to keep the maintenance time compatible with the required availability of the machine. As far as safety requirements are concerned, an approach like that used in the blanket can be speculated for the divertor. Analogous safety relevance classification and waste management considerations can therefore be made.

Finally, considering the difficulties of tritium self-sufficiency, it may be important to consider the neutrons that flow into the divertor cavity for breeding. In fact, 15% of the wall surface is occupied by the divertor with a corresponding loss of blanket coverage and breeding capability. Concepts have been proposed to include breeder materials into the divertor or in complementary structures behind the targets. While breeding is usually not required of the divertor, configurations requiring multiple divertors (e.g. double null tokamaks) may not have a choice. This additional requirement would complicate the engineering design with additional features for tritium extraction and control.

6.4.2. The ITER divertor

Considering the importance of ITER as the first example of a burning fusion machine, the design and the technical solutions proposed for the divertor system are considered paradigmatic for the development of EU DEMO and FPPs. The reference configuration was developed at the end of the nineties by modelling the divertor plasma for different target geometries, with validation tests in JET [74]. It was found that the peak power load on the vertical targets strongly depends on the existence of a V shaped geometry near the strike zone. Such a configuration confines neutral particles in the V channels and aids partial plasma detachment. The importance of an efficient particle exchange between the inner and outer divertor channels via neutral gas in the private flux region was also demonstrated. Since the neutral pressure in the inner divertor is normally higher than in the outer region, the resultant gas flow between the channels increases the neutral-induced energy loss in the outer channel.

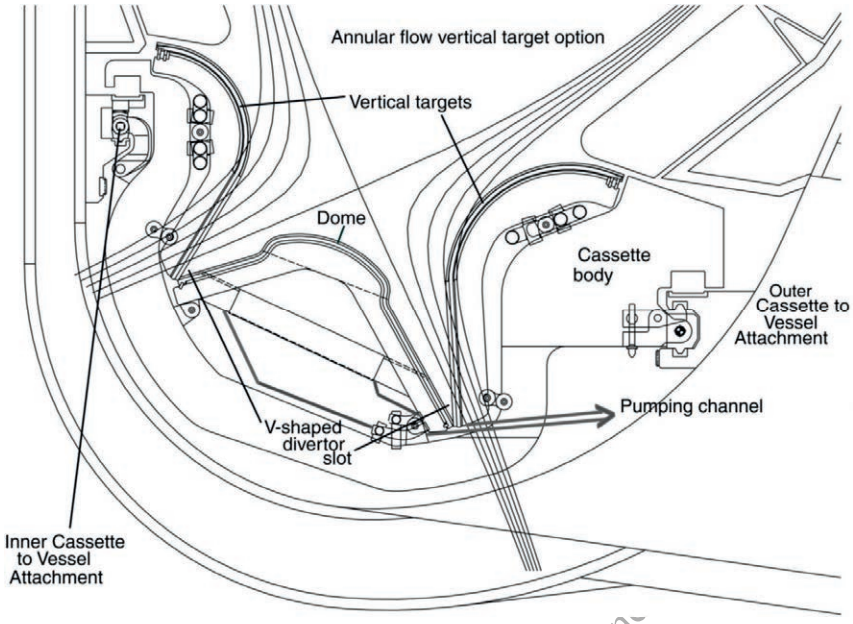

FIG. 6.16. The ITER divertor configuration[60].

The ITER divertor configuration, shown in Fig. 6.16, is a vertical target and baffle with an open private flux region and a dome below the X point. The vertical target is inclined to intercept the magnetic field lines of the separatrix at an acute angle. Together with the lower end of each vertical target, a neutral particle reflector plate forms the V shape. The baffle is designed to provide a factor 10^4 reduction of the neutral particle pressure between the divertor and the main chamber and a tenfold reduction in the private flux regions above and below the dome. The baffle is formed by the upper part of the divertor vertical targets and the divertor dome; it constitutes a toroidally continuous high heat flux surface following the 6 cm flux surface (measured at the outer plasma equator).

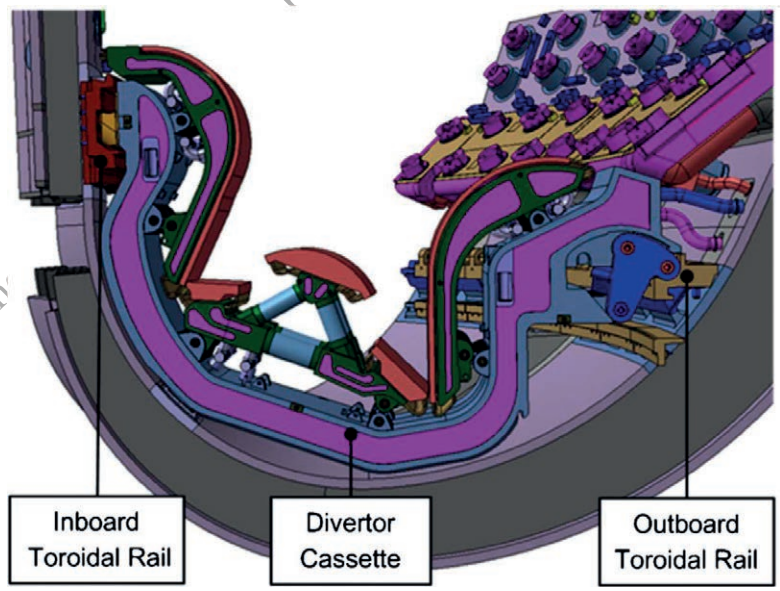

FIG. 6.17. Attachment system to vacuum vessel rails.

[60] https://www-pub.iaea.org/MTCD/publications/PDF/csp_008c/pdf/iter_3.pdf

In ITER, the divertor is composed of 54 cassettes each about 12 t — three cassettes per sector disposed toroidally on the bottom region of the vacuum vessel. The cassettes are supported by two toroidal rails attached to the vacuum vessel, one in the inboard region and the other in the outboard region; see Fig. 6.17.

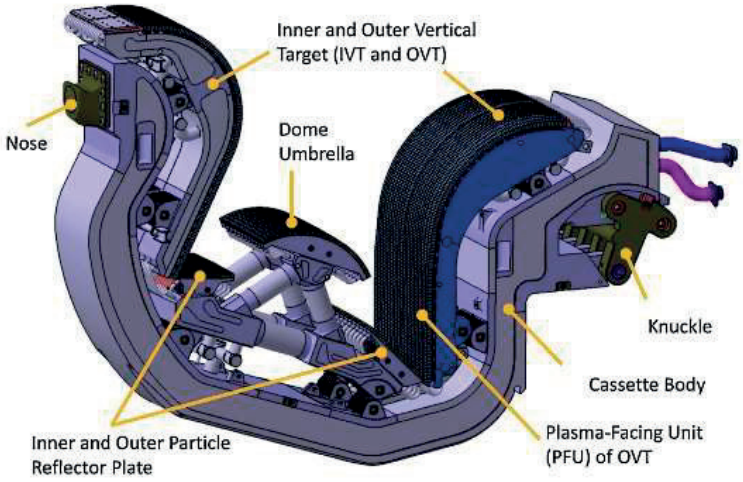

FIG. 6.18. The ITER full-tungsten divertor [75].

The ITER divertor shown in Fig. 6.18. is the result of recent studies adopting a full tungsten design [75]. Previous versions using carbon fibre composite armour for the high heat flux regions are described in e.g. [76]. Referring to Fig. 6.18 the divertor is composed of a supporting body, the target plates (inboard and outboard) and the private zone (dome umbrella and reflector plates). The divertor cassette body is a large stainless steel structure (~10 t) supporting the targets, delivering water for nuclear heat removal and shielding the vacuum vessel and magnets. It supports the attachment systems (nose and knuckle) and provides elasticity to the component by acting as a precompressed spring between the rails. The inner and outer vertical targets are the plasma facing components. Their primary function is to intercept the SOL plasma. They are divided in two: a curved zone, part of the baffle region, and a plane one, the plasma facing unit, where the strike point intercepts the target. The plasma facing units are disposed at a small angle with respect to the separatrix (15 to 25° in the poloidal–radial plane), to increase the heated area and reduce the local steady state peak flux to ~10 MW/m^2. The dome protects other divertor components from the plasma and constitutes a barrier — preventing neutrals in the private region to reach the X point — helping to create the baffle region of the divertor.

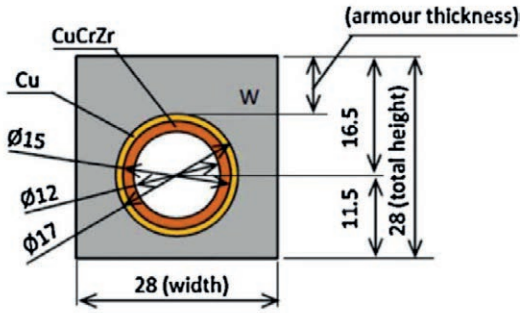

FIG. 6.19. Tungsten monobloc configuration of the ITER plasma facing units [75]. A copper alloy (CuCrZr) tube is surrounded by tungsten blocks (28x28x12 mm^3).

The design of plasma facing units is particularly challenging. ITER parameters require the removal of a 10 MW/m^2 stationary load, up to 20 MW/m^2 during slow transients. The heat transfer components use the monobloc configuration, shown in Fig. 6.19, in which a copper alloy (CuCrZr) tube is surrounded by tungsten blocks. The pipe sustains a flow (~10 m/s) of pressurized water (~4 MPa) in the temperature range of 100 to 150°C [76]. Between the pipe and the monoblocs, a compliant layer accommodates the differential expansion mismatches of casted copper. To

increase the heat transfer performance of water, a swirl tape is inserted in the tube causing a spiral movement of water in the channel, enhancing the critical heat flux limit, providing a 50% margin during 20 MW/m^2 transients. The tungsten monoblocs protect the pipes against plasma interaction: ~8 mm in thickness are proposed on the plasma side as a compromise between limiting the surface temperature and the need to cope with erosion[61]. In each target, the monobloc channels are oriented in the poloidal direction and receive the coolant from below.

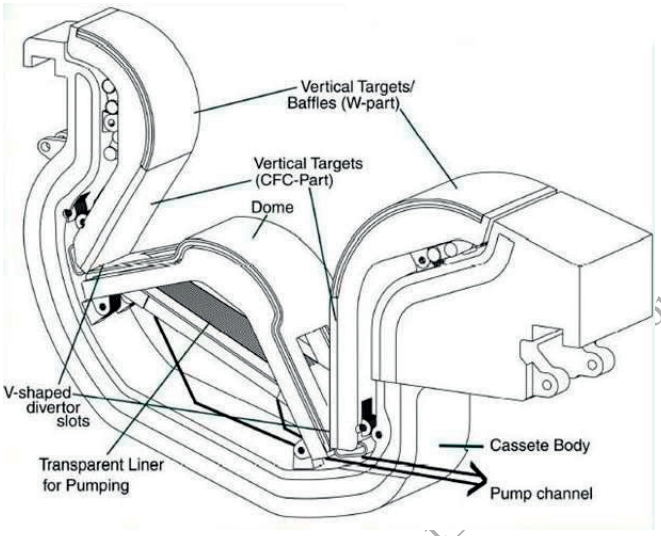

FIG. 6.20. Pumping system integrated in the divertor a connection to the pump channel.

The pumping features of the divertor are shown in Fig. 6.20: neutrals are compressed in the baffles towards the bottom of the V channels, driven to the private region (under the dome) on to the pump channel, connected through the lower vacuum vessel port to the pump system.

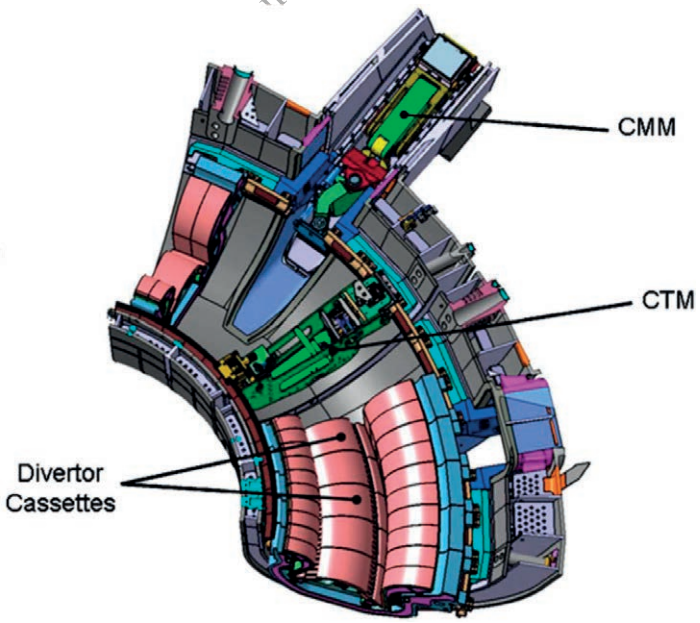

[61] A sacrificial layer is added to increase the lifetime of the component.

FIG. 6.21. The cassette multifunctional mover (CMM) provides radial transportation of cassettes and equipment through the divertor maintenance ports while the cassette toroidal mover (CTM) transports the divertor cassettes toroidally along the vessel [78].

Finally, Fig. 6.21 illustrates the cassette replacement system. Subject to high erosion and the uncertainties of plasma operations, the ITER divertor system is designed for 5 replacements (3 scheduled and 2 unscheduled) over the twenty year experimental programme. The replacement time for the whole system should be limited to six months [77]. Three equidistant lower ports are foreseen to achieve these specifications. Each port is used to replace one third of the cassettes. The replacement systems are remotely handled, relying on the use of robotized transporters (known as cassette movers) which are assisted by dexterous man-in-the-loop telemanipulators capable of deploying and operating a variety of mobile tools. The replacement operation starts with the extraction of the cassette directly in front of the maintenance port by means of a radial mover. Toroidal movers are used to collect the cassettes positioned left and right of the maintenance port and allow for their radial extraction [78]. The inverse sequence is used for the insertion of the new divertor cassettes.

6.4.3. DEMO and Gen-I fusion power plan divertor

Power exhaust handling is one of the critical design points for DEMO. As described in Section 6.1, the in-vessel components of DEMO and FPPs will experience cumulative neutron fluences over 20 times larger than their ITER counterparts. They will also be exposed to plasma particle sputtering for longer periods. Since an FPP requires a large availability (over 75%) — to compete on the electricity production market — the lifetime of the divertor becomes a critical issue. Even provided a quick and reliable replacement system, the minimum lifetime requirement for FPP components is ~2 full power years to achieve the availability target (considering a neutron load of ~1 MW/m^2).

The long list of divertor requirements has been discussed in Section 6.6.1. Considering the necessary performance, it is no surprise that few divertor concepts (with a chance to satisfy all requirements) have been proposed and developed. The ITER concept, described in Section 6.4.3, seems a good starting point for DEMO, while improvement attempts have been made to meet the required performance (2 full power years at 1 MW/m^2) [79]. These efforts are summarized in [80], which considers a water-cooled target suitable for the EU DEMO 2050 that can be integrated to an ITER-like cassette divertor. The study is preliminary but aims to confirm the monobloc design, to choose a reference material for the target (W-Cu-CuCrZr) and to increase the water temperature (inlet at 200°C with a pressure of 5 MPa and flow velocity of 20 m/s). The study also considers the substitution of AISI-306 with EUROFER as the cassette body structural material to reduce the amount of activated waste.

Nevertheless, radiation damage in copper and low coolant temperatures hinder the integration of such coolant loop into the electricity generation system. For this reason, extensive research has been conducted in KIT (with additional studies in the USA) for an ITER-like helium-cooled divertor[62]. The KIT concept has been developed for more than ten years and a large body of literature has been published describing its progress [81]. The motivation behind this concept is to enable high temperature materials by helium cooling. This allows for the integration of the divertor coolant loop to the electricity production system. This solution thereby allows a high power conversion efficiency. Helium also increases the safety characteristics of the reactor by eliminating water cooled in-vessel components altogether (provided a helium cooled blanket). Accidental water–metal reactions with production of hydrogen are thereby precluded. Challenges are shifted onto the poor heat transfer characteristics of helium cooling technology requiring sophisticated configurations and a high pumping power. The KIT concept is illustrated in Fig. 6.22, where the key plasma facing component (the finger) is described. Inlet helium at 600°C is directed through a steel insert (cartridge) towards the plasma side. Small holes in the insert cup produce jets of helium on the external thimble. The impingement (local velocity ~200 m/s) produces heat transfer coefficients up to 6×10^4 W·K^{-1}·m^{-1}. The material of the thimble is the critical element of design. It should have a very high thermal conductivity (to remove a load of ~10 MW/m^2) and, at the same time, be able to contain helium at high pressure (~10 MPa). A tungsten–lanthanum alloy has been suggested for this scope, which can operate above 600°C. Tungsten tiles brazed onto the tungsten–lanthanum thimble constitute the armour part of the component. The supporting part, under the thimble, is high temperature steel. Fingers have already been manufactured and tested out-of-pile with high temperature coolant under electron beam loadings up to 10 MW/m^2. A record of 1000 cycles has been achieved in these tests. Data for tungsten and tungsten alloy under irradiation are scarce but a rapid increase of embrittlement under irradiation has already been observed in some samples for temperatures below 800°C.

[62] Casette concept with solid targets.

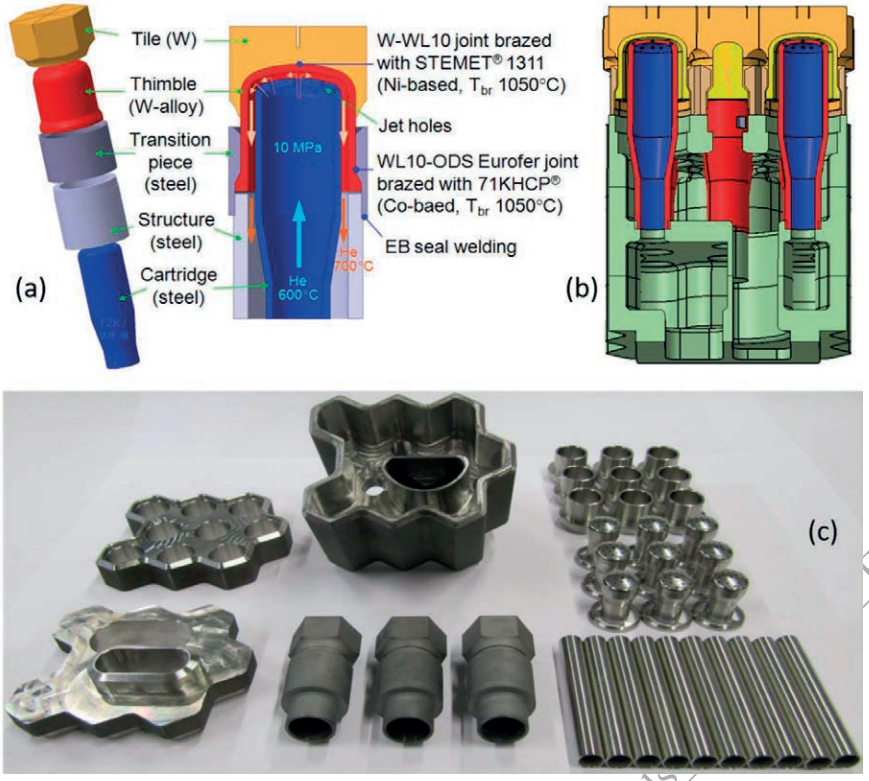

FIG. 6.22. The KIT helium cooled divertor concept: (a) design of a finger; (b) design of a 9-finger module; (c) manufacturing of a 9-finger module [81].

The main difficulty with solid-target divertor concepts is to cope with material damage. In fact, very few materials can withstand high heat and neutron fluxes simultaneously (though in very limited operation conditions). For this reason, radical alternatives have been proposed such as liquid surface divertors, evaporating divertors or even flowing pebble divertors.

Liquid surface divertors use liquid metals (e.g. PbLi, lithium, tin, gallium) or molten salts (e.g. FLiNaBe) to create a flowing surface at the target. They are attractive because they can sustain higher heat fluxes than those present in ITER. Some challenges for this concept are: MHD instability in the liquid flow needed to maintain the target, evaporation of the liquid with possible contamination of the plasma, reduced efficiency in removing helium and hydrogenous species from the vacuum chamber (i.e. ash exhaust or tritium−deuterium recirculation). Although several studies have considered these concepts (e.g. APEX and ALPS), the technology seems to remain at an early stage of development [82].

FPP requirements in terms of heat flux removal and plasma damage are at the limit of present technology and material development. Different strategies are followed to try to overcome this issue. From the engineering side, further developments of the ITER divertor configuration, processes and technologies should provide a better understanding of the issues at stake. Ultimately, the operation of ITER in the 2030s will be the proof of principle for this concept. Another interesting field of development is in the production and characterization of new materials; for example, materials engineered with nanopowder or composite promise an enhanced performance for divertor applications. On the plasma physics side, alternative approaches are under investigation to reduce the heat flux at the divertor targets. In addition to the seeding technology (in the plasma core or near the divertor targets) mentioned in Section 6.1, alternative magnetic configurations are studied to stretch the magnetic field lines at the divertor targets or to distribute the flux on additional targets. Examples of these technologies are the Super-X and the Snowflake divertor configurations. Another possibility is to implement a reliable sweeping of the strike point, spreading the power load over a wide surface, thus reducing the peak. Judging upon the technology development over the last 30 years, the task of achieving a fully satisfactory divertor concept for a fusion power plant will remain a challenging undertaking for the next decades.

6.5. REFERENCES

[1] MAISONNIER, D., et al., Final Report of the European Fusion Power Plant Conceptual Study (PPCS), EFDA-RP-RE-5.0, European Fusion Development Agreement (2005).
[2] MAISONNIER, D., et al., DEMO and fusion power plant conceptual studies in Europe, Fusion Engineering and Design **81** (2006) 1123–1130.
[3] FEDERICI, G., et al., European DEMO design strategy and consequences for materials, Nuclear Fusion **57** (2017) 092002.
[4] FEDERICI, G., et al., DEMO design activity in Europe: Progress and updates, Fusion Engineering and Design **136** (2018) 729–741.
[5] FINKEN, K.H., Edge Physics, Divertors, Pump Limiters, Transaction of Fusion Science and Technology **45** (2004).
[6] ASDEX TEAM, The H-Mode of ASDEX, Nuclear Fusion **29** (1989).
[7] FENG, Y., et al., Physics of island divertors as highlighted by the example of W7-AS, Nuclear Fusion **46** (2006) 807–819.
[8] KEMP, R., Demo Design Summary, EFDA-IDM-2L2F7V, European Fusion Development Agreement (2012).
[9] MITTEAU, R., et al., Heat loads and shape design of the ITER first wall, Fusion Engineering and Design **85** (2010) 2049–2053.
[10] KALLENBACH, A., et al., Plasma surface interactions in impurity seeded plasmas, Journal of Nuclear Materials **415** (2011) 19–26.
[11] PEARSON, R.J., ANTONIAZZI, A.B., NUTTALL, W.J., Tritium supply and use: a key issue for the development of nuclear fusion energy, Fusion Engineering and Design, **136** (2018) 1140–1148.
[12] DAY, C., GIEGERICH, T., The Direct Internal Recycling concept to simplify the fuel cycle of a fusion power plant, Fusion Engineering and Design **88** (2013) 616–620.
[13] STORK, D., et al., Developing structural, high-heat flux and plasma facing materials for a near-term DEMO fusion power plant: The EU assessment, Journal of Nuclear Materials **455** (2014) 277–291.
[14] BOCCACCINI, L.V., KALLENBACH, A., An Integrated View on Plasma Power Exhaust and In-vessel Components, (Proc. Int. Workshop MFE Roadmapping in the ITER Era, Princeton, 2011).
[15] MAISONNIER, D., et al., The European Power Plant Conceptual Study, Fusion Engineering and Design **75–79** (2005) 1173–1179.
[16] KLIMENKOV, M., MÖSLANG, A., MATERNA-MORRIS, E., Helium influence on the microstructure and swelling of 9% Cr ferritic steel after neutron irradiation to 16.3 dpa, Journal of Nuclear Materials **453** (2014) 54–59.
[17] J.P. SHARPE, D.A. PETTI, H.-W. BARTELS, A review of dust in fusion devices: Implications for safety and operational performance, Fusion Engineering and Design **63–64** (2002) 153–163.
[18] S. ROSANVALLON at al.: "Dust limit management strategy in tokamaks", Journal of Nuclear Materials **390–391** (2009) 57–60.
[19] GIANCARLI, L., DALLE DONNE, M., DIETZ, W., Status of the European breeding blanket technology, Fusion Engineering and Design **36** (1997) 57–74.
[20] DALLE DONNE, M., (Ed.) European DEMO BOT solid breeder blanket, KfK-5429, Forschungszentrum Karlsruhe (1994).
[21] FÜTTERER, M.A., et al., Further improvements of the water-cooled Pb–17Li blanket, Fusion Engineering and Design **58–59** (2001) 523–527.
[22] S. MALANG, K. SCHLEISIEK, (Eds) Dual coolant blanket concept, KfK-Report 5424 Forschungszentrum Karlsruhe (1994).
[23] HERMSMEYER, S., MALANG, S., FISCHER, U., GORDEEV, S., Lay-out of the He-cooled solid breeder model B in the European power plant conceptual study, Fusion Engineering and Design **69** (2003) 281–287.
[24] SARDAIN, P. et al., Power plant conceptual study WCLL concept, Fusion Engineering and Design **69** (2003) 769–774.
[25] NORAJITRA, P., et al., Conceptual design of the dual-coolant blanket in the frame of the EU power plant conceptual study, Fusion Engineering and Design **69** (2003) 669–673.
[26] BOCCACCINI, L.V., et al., Materials and design of the European DEMO blankets, Journal of Nuclear Materials **329–333** (2004) 148–155.
[27] HERMSMEYER, S., et al., Revision of the EU Helium cooled pebble bed blanket for DEMO (Proc. 20th IEEE/NPSS Symposium on Fusion Engineering, San Diego, 2005).
[28] LI-PUMA, A., et al., Breeding blanket design and systems integration for a helium-cooled lithium–lead fusion power plant, Fusion Engineering and Design **81** (2006) 469–476.
[29] ROMANELLI, F., A roadmap to the realization of fusion energy, Fusion Electricity, European Fusion Development Agreement (2012).
[30] FEDERICI, G., et al., Overview of the DEMO staged design approach in Europe, Nuclear Fusion **59** (2019) 066013.
[31] TILLACK, M.S., MALANG, S., High performance LiPb blanket (Proc. 17th IEEE/NPSS Symposium on Fusion Energy, San Diego, 1997).
[32] TILLACK, M.S., et al., Fusion power core engineering for the ARIES-ST power plant, Fusion Engineering and Design **65** (2003) 215–261.

[33] RAFFRAY, A.R., et al., High performance blanket for ARIES-AT power plant, Fusion Engineering and Design **58–59** (2001) 549–553
[34] TOBITA, K., et al., Design study of fusion DEMO plant at JAERI, Fusion Engineering and Design **81** (2006) 1151–1158.
[35] LIU, S., et al., Progress on design and related R&D activities for the water-cooled breeder blanket for CFETR, Theoretical & Applied Mechanics Letters **9** (2019) 161–172.
[36] LEI, M., et al., Conceptual Design of a Helium-Cooled Ceramic Breeder Blanket for CFETR, Fusion Science and Technology **4** (2015) 772–779.
[37] KIM, K., et al., Design concept of K-DEMO for near-term implementation, Nuclear Fusion **55** (2015) 053027.
[38] CHO, S., et al., Overview of Helium Cooled Ceramic Reflector Test Blanket Module development in Korea, Fusion Engineering and Design **88** (2013) 621.
[39] FENG, K., et al., New progress on design and R&D for solid breeder test blanket module in China, Fusion Engineering and Design **89** (2014) 1119–1125.
[40] CHAUDHURI, P., et al., Status and progress of Indian LLCB test blanket systems for ITER, Fusion Engineering and Design **87** (2012) 1009–1013.
[41] BOCCACCINI, L.V., et al., Present status of the conceptual design of the EU test blanket systems, Fusion Eng. Des. **86** (2011) 478–483.
[42] AIELLO, G., et al., HCLL TBM design status and development, Fusion Engineering and Design **86** (2011) 2129–2134.
[43] CISMONDI, F., et al., HCPB TBM thermomechanical design: assessment with respect codes and standards and DEMO relevancy, Fusion Engineering and Design **86** (2011) 2228–2232.
[44] ENOEDA, M., et al., Development of the Water Cooled Ceramic Breeder Test Blanket Module in Japan, Fusion Engineering and Design 87 (2012) 1363–1369.
[45] SAWAN, M.E., ABDOU, M.A., Physics and technology conditions for attaining tritium self-sufficiency for the DT fuel cycle, Fusion Engineering and Design **81** (2006) 1131–1144.
[46] EL-GUEBALY, L.A., MALANG, S., Toward the ultimate goal of tritium self-sufficiency: Technical issues and requirements imposed on ARIES advanced power plants, Fusion Engineering and Design **84** (2009) 2072–2083.
[47] FISCHER, U., at al., Methodological approach for DEMO neutronics in the European PPPT programme: Tools, data and analyses, Fusion Engineering and Design **123** (2017) 26–31.
[48] MITTEAU, R., et al., The design of the ITER first wall panels, Fusion Engineering and Design **88** (2013) 568–570.
[49] MAVIGLIA, F., et al., Wall protection strategies for DEMO plasma transients, Fusion Engineering and Design **136A** (2018) 410–414.
[50] FISCHER, U., et al., Neutronics requirements for a DEMO fusion power plant, Fusion Engineering and Design **98** (2015) 98–99.
[51] MAIONE, I. A., VACCARO, A., Analysis of electromagnetic loads on EU-DEMO inboard and outboard blanket vertical segments. Fusion Engineering and Design, 89 (2014) 1314–1318.
[52] MAISONNIER, D., European DEMO design and maintenance strategy, Fusion Engineering and Design **83** (2008) 858–864.
[53] KEEP, J., WOOD, S., GUPTA, N., COLEMAN, M., LOVING, A., Remote handling of DEMO breeder blanket segments: Blanket transporter conceptual studies, Fusion Engineering and Design **124** (2017) 420–425.
[54] ZMITKO, M., et al., Development and qualification of functional materials for the European HCPB TBM, Fusion Engineering and Design **136-B** (2018) 1376–1385.
[55] KNITTER, R., et al., Fabrication of modified lithium orthosilicate pebbles by addition of titania, Journal of Nuclear Materials **442** (2013) 433–436.
[56] MAS DE LES VALLS, E., et al., Lead–lithium eutectic material database for nuclear fusion technology, Journal of Nuclear Materials **376** (2008) 353–357.
[57] GIERSZEWSKI, P., MIKIC, B., TODREAS, N., Property Correlations for Lithium, Sodium, Helium, FLiBe and Water in fusion Reactor applications, PSFC-RR-80-12, MIT Publication (1980).
[58] SERRANO-LÓPEZ, R., FRADERA, J., CUESTA-LÓPEZ, S., Molten salts database for energy applications, Chemical Engineering and Processing: Process Intensification, **73** (2013) 87–102.
[59] EZATO, K., SUZUKI, S., DAIRAKU, M., AKIBA, M., Experimental examination of heat removal limitation of screw cooling tube at high pressure and temperature conditions, Fusion Engineering and Design **81** (2006) 347–354.
[60] PASCAL-RIBOT, S., SAROLI, A.-F., GRANDOTTO, M., SPITZ, P., ESCOURBIAC, F., 3D numerical simulations of Hypervapotron cooling concept, Fusion Engineering and Design **82** (2007) 1781–1785.
[61] WONG, C.P.C., et al., APEX advanced ferritic steel, FLiBe self-cooled first wall and blanket design, Journal of Nuclear Materials **329–333** (2004) 1599–1604.
[62] SAGARA, A., et al., Design and development of the FLiBe blanket for helical-type fusion reactor FFHR, Fusion Engineering and Design, **49-50** (2000) 661–666.
[63] VAN DER SCHAAF, B., The development of EUROFER reduced activation steel, Fusion Engineering and Design **69** (2003) 197–203.
[64] GAGANIDZE, E, SCHNEIDER, H.-C., DAFFERNER, B., AKTAA, J., High-dose neutron irradiation embrittlement of RAFM steels, Journal of Nuclear Materials **355** (2006) 83–88.

[65] KNASTER, J., et al., IFMIF, a fusion relevant neutron source for material irradiation current status, Journal of Nuclear Materials **453** (2014) 115–119.
[66] IBARRA, A., et al., The European approach to the fusion-like neutron source: the IFMIF-DONES project, Nuclear Fusion **59** (2019).
[67] PORTONE, A., ROCCELLA, M. , ROCCELLA, R., LUCCA, F., RAMOGIDA, G., The ITER TF coil ripple: Evaluation of ripple attenuation using Fe insert and of ripple enhancement produced by TBM, Fusion Engineering and Design **83** (2008) 1619–1624.
[68] GIANCARLI, L., et al., In-vessel component designs for a self-cooled lithium-lead fusion reactor, Fusion Engineering and Design **69** (2003) 763–768.
[69] S. MALANG, A.R. RAFFRAY, N.B. MORLEY, An example pathway to a fusion power plant system based on lead–lithium breeder: Comparison of the dual-coolant lead–lithium (DCLL) blanket with the helium-cooled lead–lithium (HCLL) Fusion Engineering and Design **84** (2009) 2145–2157
[70] BOCCACCINI, L.V., FISCHER, U., GORDEEV, S., MALANG, S., Advanced Helium Cooled Pebble Bed Blanket with SiCf/SiC as structure material, Fusion Engineering and Design, **49-50** (2000) 491–497.
[71] GOHAR, Y., MAJUMDAR, S., SMITH, D., High power density self-cooled lithium–vanadium blanket, Fusion Engineering and Design **49–50** (2000) 551–558.
[72] HERNÁNDEZ, F., et al., Advancements in the Helium-Cooled Pebble Bed Breeding Blanket for the EU DEMO: Holistic Design Approach and Lessons Learned, Fusion Science and Technology, **75** (2018) 352–364.
[73] DEL NEVO, A., et al., Recent progress in developing a feasible and integrated conceptual design of the WCLL BB in EUROfusion project, Fusion Engineering and Design (in press).
[74] JANESCHITZ, G., et al., Overview of the divertor design and its integration into RTO: RC-ITER, Fusion Engineering and Design **49–50** (2000) 107–117.
[75] HIRAI, T., et al., ITER tungsten divertor design development and qualification program, Fusion Engineering and Design **88** (2013) 1798–1801.
[76] MEROLA, M., et al., European contribution to the development of the ITER divertor, Fusion Engineering and Design **66–68** (2003) 211–217
[77] ESQUÉ, S., et al., Progress in the design, R&D and procurement preparation of the ITER Divertor Remote Handling System, Fusion Engineering and Design, **89** (2014) 2373–2377.
[78] PALMER, J., et al., The design and development of divertor remote handling equipment for ITER, Fusion Engineering and Design **82** (2007) 1977–1982.
[79] FEDERICI, G., Overview of EU DEMO design and R&D activities, Fusion Engineering and Design **89** (2014) 882–889.
[80] VISCA, E., et al., Assessment of an ITER-like Water-Cooled Divertor for DEMO, (Proc. IEEE 25th Symposium on Fusion Engineering, San Francisco, 2013).
[81] NORAJITRA, P., Divertor Development for a Future Fusion Power Plant, KIT Scientific Publishing (2011).
[82] NYGREN, R., et al., Design Integration of Liquid Surface Divertors, Fusion Engineering and Design **72** (2004) 223–244.

Chapter 7

FUSION NEUTRONICS

Ulrich Fischer
Karlsruhe Institute of Technology, Institute for Neutron Physics and Reactor Technology
Karlsruhe, Germany

The D-T fusion reaction produces an α particle and a neutron, and releases a nuclear binding energy of 17.58 MeV. According to the momentum conservation law, 80% of this energy is transferred to the neutron; neutrons born in the plasma chamber of a D-T fusion reactor are thus emitted with a kinetic energy of 14.1 MeV. Neutrons have no charge and are therefore not affected by the electro-magnetic fields of the tokamak. They propagate through the materials surrounding the plasma chamber and undergo various nuclear reactions with the atomic nuclei of that matter.

Fusion neutronics is concerned with the transport of the 14 MeV fusion neutrons through matter, which includes the mathematical representation of the propagation process and all nuclear interactions. The nuclear interactions result in the generation of secondary particles including neutrons and photons, subject to further transport, and charged particles, which are assumed to be locally absorbed and contributing to the nuclear heating of the material. The interactions also affect the atomic nuclei which can be transmuted into other nuclei, stable or radioactive. The chemical composition of the considered materials therefore changes during irradiation; a radioactive inventory is built-up and may represent a radiation hazard.

Fusion neutronics can deal with all these phenomena. Neutron and photon transport is described with a probabilistic or deterministic approach, which provides the neutron and photon distributions in space and phase (energy and angle). With this distribution, nuclear reaction rates can be calculated provided the associated nuclear cross-sections are available. Tritium breeding can thus be evaluated and optimized for a given material configuration, the nuclear heat generated and deposited in the materials can be calculated and the transmutation and activation of all materials as well as the radiation induced damage can be assessed.

The scope of fusion neutronics thus includes tasks of superior importance to reactor design, which also strongly affect safety and materials issues. The fundamental task of neutronics is, however, to provide the phase-space distribution of neutrons and photons for a given material configuration. The principles which are necessary to accomplish this task are presented in the following Sections: 7.2 and 7.3. Applications to reactor design and material issues are presented in Sections 7.4 and 7.5, respectively.

7.1. NUCLEAR INTERACTION PROCESSES

7.1.1. Neutron induced reactions

There are two principal types of neutron induced interaction processes taking place in a (D-T) fusion reactor and accounted for in neutronics:

- Elastic neutron scattering.
- Neutron absorption.

Elastic scattering is the process in which a neutron collides with an atomic nucleus and both the neutron and the atomic nucleus can be represented as hard spheres. Elastic scattering can thus be described by classical mechanics. Energy and momentum are exchanged per the respective conservation laws. A high energy neutron transfers in this way kinetic energy to the colliding nucleus in thermal equilibrium. The neutron loses kinetic energy, i.e. it is slowed down or moderated to a lower energy; the lighter the mass of the colliding nucleus, the larger the loss in energy. The maximum energy transfer, where M is mass of the nucleus, m_n is the mass of a neutron and E_n is the initial kinetic energy of the neutron, is given by:

(7.1)

$$\Delta E_{\max} = E_n \cdot \left[1 - \left(\frac{M - m_n}{M + m_n}\right)^2\right]$$

Low mass nuclei are thus efficient neutron moderators. If there is a large amount of low mass material present in a fusion reactor, 14 MeV neutrons will be quickly slowed down and the neutron spectrum will be moderated. This affects both the tritium breeding and the neutron radiation shielding discussed later in this section. Most efficient neutron moderators are hydrogenous materials such as water or hydrides.

Neutron absorption is a nuclear process in which the neutron is absorbed by the colliding nucleus $X(A, Z)$ forming a new so-called compound nucleus $X(A+1, Z)$. A is the mass number; Z is the nuclear charge. This process is entirely

described by the laws of quantum mechanics. The compound nucleus is highly excited due the release of the neutron's binding energy upon it's absorption. It is therefore unstable and decays by the emission of various particles (or radiation). The emission of photons results in the product nucleus $X(A, Z+1)$. This reaction is generally denoted as (n, γ) reaction. It is the source of photon radiation in fusion reactors. A prominent example is the (n, γ) reaction on ^{56}Fe which produces the stable ^{57}Fe isotope and releases 7.65 MeV of energy. (This reaction is also the dominating parasitic reaction of a fusion reactor employing steel as structural material).

The emission of one or two neutrons from the compound nucleus results in the product nuclei $X(A, Z)$ or $X(A, Z-1)$, respectively. This process is in general accompanied with the emission of gamma radiation. The reaction is called inelastic because the kinetic energy of the incident neutron is converted into electromagnetic radiation energy. Inelastic scattering reactions on heavier mass nuclei can transfer high energy neutrons to lower energies like elastic scattering processes on low mass nuclei. (n, 2n) reactions like those on ^{9}Be or on Pb-nat are utilized to multiply neutrons: an incident high energy neutron produces 2 secondary neutrons of lower energy. Most blanket designs for (D-T) fusion reactors rely on the use of neutron multiplier materials (such as beryllium or lead) to compensate for the parasitic neutron losses and achieve sufficient tritium breeding.

The emission of charged particles (p, D, T, ^{3}He, α) produces nuclei with lower atomic numbers (Z-1 or Z-2). Charged particles are generally not transported but locally absorbed. This means that their kinetic energy is assumed to be entirely transferred to the material (as heating energy) at the location of the reaction. The most prominent example of a charged particle reaction in a fusion reactor is the ^{6}Li(n, α)t breeding reaction, which produces a triton and an α particle with an energy release of 4.78 MeV.

Which process happens depends on the nucleus colliding with the neutron and its energy. In general, this cannot be predicted. A probability of each process happening can be given instead. This information is conveyed by the nuclear cross-section.

7.1.2. Nuclear cross-sections

The nuclear cross-section is a fundamental quantity describing the interactions of neutrons and atomic nuclei. Within the scheme of classical mechanics, the nuclear cross-section indicates the cross-section area of the nucleus that has to be hit by a neutron for an interaction to take place. This roughly holds for elastic scattering processes. However, in general, the nuclear cross-section indicates the probability that an interaction takes place. This is due to the quantum mechanical nature of the nuclear interaction process and does not generally depend on the actual (geometric) cross-sectional area of the nucleus[63]. The reaction rate R — which gives the number of nuclear reactions taking place (per cm^3 per second) in a certain reaction volume irradiated by neutrons — can be formulated as follows:

(7.2)

$$R\left[\mathrm{cm^{-2}s^{-1}}\right] = \sigma\left[\mathrm{cm^2}\right] \cdot N\left[\mathrm{cm^{-2}}\right] \cdot n\left[\mathrm{cm^{-3}}\right] \cdot v\left[\mathrm{cm \cdot s^{-1}}\right] = \sigma\left[\mathrm{cm^2}\right] \cdot N\left[\mathrm{cm^{-2}}\right] \cdot \Phi\left[\mathrm{cm^{-2} \cdot s^{-1}}\right] = \Sigma\left[\mathrm{cm^{-1}}\right] \cdot \Phi\left[\mathrm{cm^{-2} \cdot s^{-1}}\right]$$

Here N is the number density of the material irradiated by neutrons with of density n. Φ is the neutron flux density given by the number of neutrons, from all directions, crossing an area of 1 cm^2 per second. Σ is the so-called macroscopic cross-section which gives the probability that a reaction takes place per cm of pathway and has units of a reciprocal length[64]. σ is the microscopic cross-section, generally referred to as the nuclear cross-section, and has units of barns (10^{-24} cm^2). The nuclear cross-section depends on the considered nucleus, the neutron energy and the reaction channel. It is a characteristic of the atomic nucleus and cannot be artificially modified[65].

A high reaction rate for a specific reaction (e.g. a reaction leading to the production of tritium) requires a nuclide showing a high nuclear cross-section for the (n, t) reaction channel — as compared to other possible reaction channels on the same nuclide — and its irradiation with neutrons of the energy at which this cross-section is highest. The reaction probability can further be increased, of course, if the atomic density can be increased. (This means an increase in the macroscopic cross-section Σ and a decrease in the average mean free path λ for the same microscopic cross-section σ). This strategy can be applied if an isotope of a given material is naturally less abundant and can be enriched (e.g. ^{6}Li to produce tritium from lithium or ^{235}U for thermal fission of uranium fuel).

Examples of neutron cross-sections are shown in Figs 7.1 to 7.4 as functions of the neutron energy. Looking at the tritium production cross-section of ^{6}Li (see Fig. 7.1), a significant increase in the ^{6}Li(n, t) reaction rate can be

[63] This quantity can be (formally) derived as a *cross-section area* and has therefore units of length square.

[64] The inverse of Σ, is called the average mean free path λ and gives the distance a neutron travels before it interacts with a nucleus.

[65] In equation (7.2) for the reaction rate R, the microscopic cross-section σ has been derived as the proportionality constant assuming R is proportional to the atomic number density N and the neutron flux density Φ.

obtained by moderating the fast 14 MeV neutrons to lower energies. The associated cross-section at thermal energy (0.025 eV) is five orders of magnitude higher than at 14 MeV[66].

Tritium production from the ^{7}Li(n, n'α)t reaction, on the other hand, suffers from a rather high reaction threshold around 3 MeV. In a fusion reactor, it is thus very difficult to achieve a ^{7}Li(n, n'α)t reaction rate which can ensure tritium self-sufficiency. This matter will be further discussed in Section 7.4.

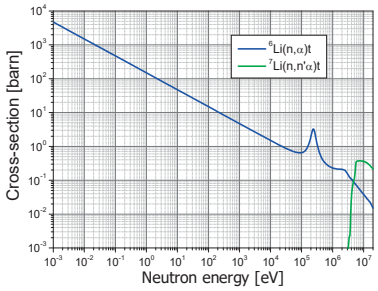

FIG. 7.1. Neutron induced cross-section of Tritium production of ^{6,7}Li as a function of neutron energy.

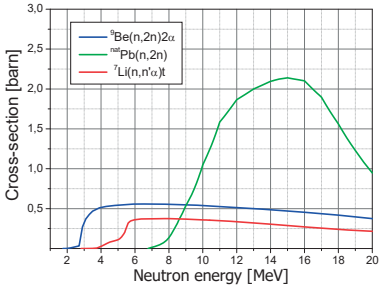

FIG. 7.2. Neutron induced cross-section of (n, 2n) reaction (Be and Pb) as a function of neutron energy.

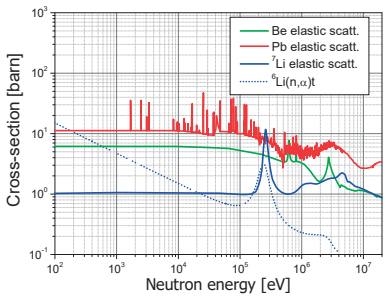

FIG. 7.3. Neutron induced elastic scattering cross-section as function of neutron energy.

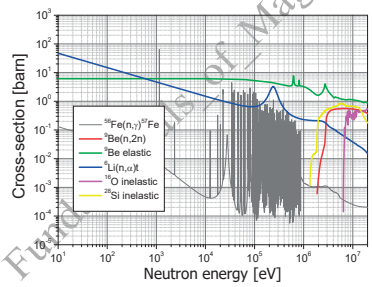

FIG. 7.4. Neutron induced cross-section as a function of neutron energy of important reactions.

The (n, 2n) cross-section comparison (Fig. 7.2) shows the big advantage of beryllium for 14 MeV neutrons multiplication. Although the cross-section is low compared to that of lead, the reaction threshold around 2 MeV is very low for a (n, 2n) reaction. This is a unique and inherent feature of ^{9}Be, formally composed of two α particles with an extra neutron, which can easily be kicked out (The binding energy of a neutron is ~6 to 8 MeV and thus the (n, 2n) reaction, except for ^{9}Be). After a (n, 2n) reaction on ^{9}Be, a neutron of lower energy can initiate another (n, 2n) reaction on ^{9}Be. As a result, the multiplication factor for 14 MeV neutrons can be greater than two in a beryllium configuration. This feature, together with a high moderator quality, a low absorption cross-section and an extremely low activation make beryllium a superior candidate for solid neutron multiplier in a fusion reactor.

The comparison of some elastic cross-sections (Fig. 3) shows the dominance of lead for this interaction process. This results in many scattering processes taking place in Pb without any significant energy losses. Accordingly, there is a high fast neutron flux level when employing lead in a large amount as neutron multiplier, e. g. as the Pb-Li eutectic alloy used in liquid metal blankets (see Section 7.4).

The comparison of other important cross-sections (Fig. 7.4) demonstrates the competitive behaviour of the relevant reaction channels, strongly varying over the relevant neutron energy range. The parasitic neutron absorption in ^{56}Fe, e. g. which proceeds via the (n, γ) reactions, mostly takes place in the resonance region between 10 keV and ca. 1 MeV. This means that moderated systems, (such as those using beryllium) are more affected by this effect than fast systems (as those based on lead). Inelastic reactions (e.g. on ^{16}O and ^{28}Si, two constituents of ceramic breeders)

[66] However, in a fusion reactor, many other materials can parasitically absorb neutrons during the slowing-down process.

can display rather high values around 14 MeV and dominate other competing reactions (except the elastic scattering). This is a detrimental effect for a breeder blanket since 14 MeV neutrons are also turned into neutrons of lower energy by the inelastic reaction and may thus be absorbed, preferably in the resonance region of the $^{56}Fe(n, \gamma)$ reaction. Those neutrons are lost and need to be compensated by a neutron multiplier.

Secondary neutron and photons, emitted in the reactions with 14 MeV neutrons, show distinctive energy distributions. This is demonstrated by the example of lead irradiated with 14 MeV neutrons in Figs 7.5(a) and 7.5(b) for neutrons and photons, respectively. The neutron emission spectrum shows a broad continuous distribution up to ~5 MeV with a peak around 1 MeV. This energy range is populated by neutrons evaporated from the equilibrium state of the compound nuclei. Other nuclear processes, such as pre-equilibrium and direct processes, and elastic scattering at 14 MeV contribute to the energy range above 5 MeV. The energy spectrum of secondary photons, shown in Fig. 7.5(b), extends up to ~24 MeV as confirmed by the measurements also displayed in the figure. It is thus evident that the 14 MeV neutron coming from the (D-T) fusion plasma can generate a very hard gamma radiation which has high penetration power and needs to be shielded.

FIG. 7.5(a). Neutron emission spectrum.

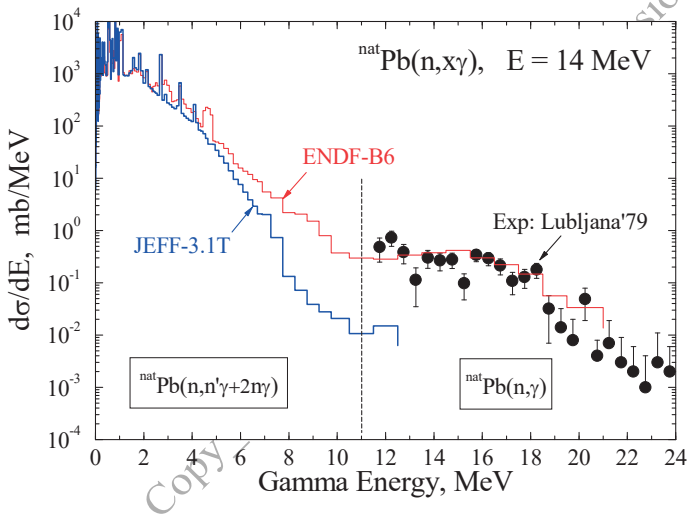

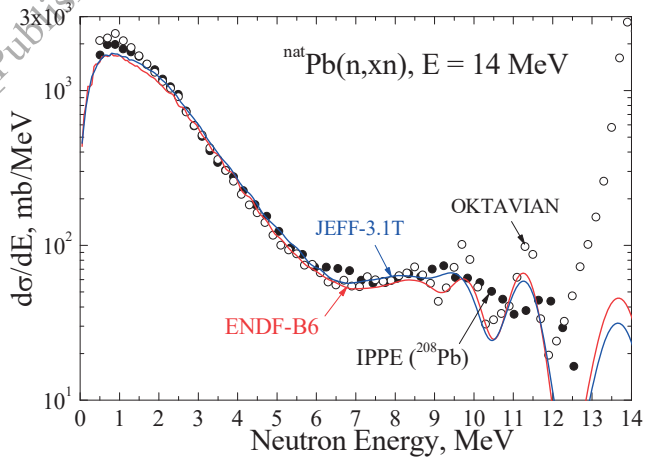

FIG. 7.5(b). Photon emission spectrum

The emission spectra shown in Fig. 7.5 are for single processes due to a 14 MeV neutron colliding with a lead nuclei, i.e. the spectra show the probability distribution for the energy of neutrons or photons emitted from lead after a reaction with a 14 MeV neutron. The secondary neutrons and photons will then further react with the nuclei of the matter present in the system. Taking into all the reactions in a neutron transport simulation will result in a neutron spectrum such as that shown in Fig. 7.6 for the first wall of a DEMO reactor. Fig. 7.6 reveals that the neutron spectrum, due to the many elastic and inelastic scattering events letting neutrons pass back and forth through the first wall, is already degraded at the first wall. Typically, the 14 MeV neutron peak accounts for less than 25 to 30% of the first wall neutron spectrum. The comparison to a neutron spectrum in the high flux reactor (HFR) Petten[67] shows that (except for the 14 MeV peak) the spectra are not too different. In the HFR, a spectrum is formed by neutrons emitted in the fission process (fission spectrum) while in the fusion reactor the spectrum below the 14 MeV neutron peak is formed by the many (n, xn) reactions and the elastic interactions taking place around the entire reactor.

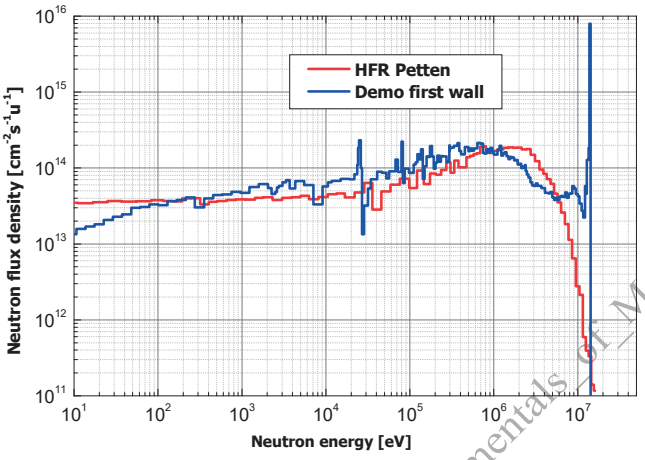

FIG. 7.6. Neutron flux spectra in a fusion power reactor (DEMO first wall) and a fission reactor (HFR Petten).

The nuclear data required for fusion neutronics analyses comprise neutron cross-sections for neutron transport calculations (absorption and total cross-sections as function of the neutron energy, neutron emission cross-sections as function of incident neutron energy, secondary energy and scattering angle), cross-sections for photon transport calculations (neutron induced γ-production cross-sections and associated photon emission spectra as function of the incident neutron energy, γ-interaction cross-sections as function of the photon energy) and finally nuclear data to calculate reaction rates: the so-called nuclear responses as functions of the neutron energy (e.g. tritium production, energy deposition, gas production, activation and transmutation, and radiation induced damage). Nuclear data evaluations provide such data based on nuclear model calculations and experimental cross-section data. The data are compiled in nuclear data libraries using the international standard evaluated nuclear data file (ENDF) format. Nuclear data libraries suitable for fusion neutronics applications contain cross-section data for all nuclides of interest to fusion technology comprising all nuclear reactions and all data types (as specified above) over the entire neutron energy range from 20 MeV down to 10^{-3} eV. Such data libraries are provided e. g. by the European joint evaluated fusion and fission file project (JEFF), the American evaluated nuclear data file, B (ANDF/B) series, and the Japanese evaluated nuclear data library (JENDL) libraries. A dedicated nuclear data library tailored for fusion technology applications has been developed under the auspices of the IAEA/NDS with the international fusion evaluated nuclear data library (FENDL). Version FENDL-2.1 [7.1], assembled in 2004, serves as the current reference data library for ITER nuclear design analyses. A recent major update led to FENDL-3.0 which includes, among others, an extension in the energy range up to 150 MeV and the complete co-variance data required for uncertainty analyses [7.2].

[67] An experimental reactor operated by EURATOM in Petten, the Netherlands.

7.2. PARTICLE TRANSPORT IN MATTER

The knowledge of nuclear cross-section data is a pre-requisite to solve the mathematical transport problem which describes the propagation of particles through matter. There are two different methodological approaches for its solution:

1) The deterministic approach, which represents a macroscopic description of a particle ensemble and is governed by the Boltzmann transport equation,
2) and the probabilistic approach, which is a microscopic description of the real physical processes undergone by a single particle during its lifetime.

7.2.1. The Boltzmann transport equation

Particle transport on the macroscopic level is governed by the Boltzmann transport equation. In a general time-independent formulation it is an integro-differential equation for the angular neutron flux density, where the following definitions apply: $\Psi(\boldsymbol{r}, E, \boldsymbol{\Omega})$ is the angular neutron flux density (in $cm^{-2} \cdot s^{-1} \cdot sr^{-1}$), $\boldsymbol{r}$ is the position vector, E is the primary neutron energy, E' is the secondary neutron energy, $\boldsymbol{\Omega}$ is a unit vector in the particle flight direction, $\sum_{\text{tot}}(E, \boldsymbol{r})$ is the total macroscopic cross-section, $\sum_s(\boldsymbol{r}, E' \rightarrow E, \boldsymbol{\Omega}' \rightarrow \boldsymbol{\Omega})$ is the scattering kernel and $Q(\boldsymbol{r}, E, \boldsymbol{\Omega})$ is the neutron source term:

(7.3)

$$\boldsymbol{\Omega} \cdot \nabla\Psi(\boldsymbol{r}, E, \boldsymbol{\Omega}) + \Sigma_{\text{tot}}(E, \boldsymbol{r}) \cdot \Psi(\boldsymbol{r}, E, \boldsymbol{\Omega}) = \int_0^{4\pi} \mathrm{d}\boldsymbol{\Omega}' \int_0^{\infty} \mathrm{d}E' \cdot \Sigma_s(\boldsymbol{r}, E' \rightarrow E, \boldsymbol{\Omega}' \rightarrow \boldsymbol{\Omega}) + Q(\boldsymbol{r}, E, \boldsymbol{\Omega})$$

The Boltzmann transport equation is essentially a balance equation in an infinitesimal phase space element: the particle losses through leakage (first term on the left side) and nuclear interactions (absorption and scattering in other directions, second term on the lefts side) are equal to the particle gains through in-scattering processes from other directions and energies (first term on the right side) and the direct generation of source particles (second term on the right side).

This equation needs to be solved for the angular neutron flux density. For this purpose, simplified equations can be derived for 1 and 2-D geometries and highly-symmetric geometries such as spheres, slabs and cylinders. The energy dependence also needs to be simplified by averaging the nuclear cross-sections over specified energy intervals; the so-called group cross-sections σ^g are used instead of continuously varying cross-sections:

(7.4)

$$\sigma^g = \frac{\int_g \sigma(E)dE}{\int_g \Phi(E)dE} \qquad \Phi^g = \int_g \Phi(E)dE$$

Where the neutron flux density ϕ is used as weighting function; ϕ^g is the associated neutron group flux, which is obtained by integrating the energy dependent neutron flux density of the energy group g; and the group cross-section is given an input to the transport equation. An assumption is thus made for the neutron flux density $\phi(E)$ used as weighting function.

The transport equation, in its multi-group approximation, needs to be solved for all energy groups. The quality of the approximation depends, to a large extent, on the number of energy groups included. For fusion applications, 175 energy groups are typically used, spanning from 20 MeV down to 10^{-3} eV. The cross-section data provided by nuclear data libraries (such as FENDL) is thus processed by special computer codes for the multi-group application with deterministic transport codes. Suitable group data libraries, generated in 175 energy groups using a typical fusion weighting spectrum are available in most of the nuclear data libraries mentioned above.

There are many non-commercial computer codes available to solve the Boltzmann transport equation in one-, two- and three-dimensional geometry. Those can be obtained from the NEA data bank of the OECD [7.3] or the radiation safety information computational centre (RSICC) [7.4]. However, they are not ideal for fusion applications since they are generally incapable of representing the complex geometry of a tokamak. A recent advanced approach based and the application of the finite elements method in the commercial ATTILA code makes use of tetrahedral meshes generated from computer aided design (CAD) geometry models enabling a very precise representation of the tokamak geometry. However, all deterministic codes require group cross-sections, thus can only approximate the strong energy dependence of the neutron cross-section data.

7.2.2. Monte Carlo simulation of neutron transport

The nuclear interactions undergone by neutrons propagating through matter are of true stochastic nature. Interactions take place following the quantum-mechanical probabilities included in the nuclear cross-section data. The Monte Carlo method takes advantage of this fact and simulates the history of a particle on the microscopic level considering all stochastic processes from the particle's birth to its death. It is a true simulation of the random walk of a neutron from its birth in a (D-T) fusion reaction to its absorption in a nuclear reaction or leakage out of the considered geometry. Two advantages make the Monte Carlo method superior for applications in fusion neutronics:

1) There are no geometrical limitations. Any arbitrary 3-D configuration of any complexity can be modelled. Geometry cells are pre-defined as solids or bounding surfaces using combinatorial geometry.
2) The nuclear cross-section can be used in the continuous energy representation as they are given in nuclear data libraries. No group data need to be used and thus no approximation is required.

The accuracy of the Monte Carlo method is practically only limited by the statistical error associated with the calculated responses and the uncertainty of the nuclear data. Many histories are generally required to ensure sufficient statistical accuracy. This particularly applies for the calculation of local responses or high resolution space and energy distributions. Nowadays, the required computational effort can easily be provided by the available advanced computer technology. With the use of large computer clusters, Monte Carlo particles can be run in parallel on as many processors as available. The wall clock-time for a heavy Monte Carlo can thereby amount to a few hours or a day.

7.2.2.1. Particle Tracking

The Monte Carlo particle transport simulation is based on the particle tracking technique outlined in Fig. 7.7. In a (D-T) fusion reactor, a source neutron is released (born) in the plasma chamber. In the Monte Carlo simulation, the position of the neutron's birth place is first sampled[68] based on the source distribution provided by plasma physics calculations. The energy of the source neutron is then sampled based on a given energy distribution of (D-T) neutrons[69]. The source neutron is then emitted into a direction sampled by assuming an isotropic emission.

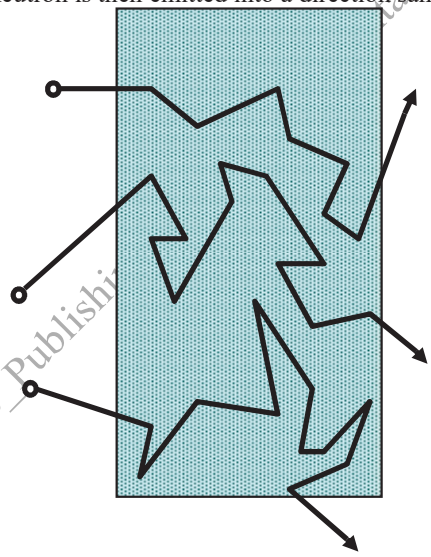

FIG. 7.7. Particle tracking scheme.

The neutron is assumed to travel along a straight line until it collides with an atomic nucleus. The distance to the site of this collision is sampled through the following equation:

(7.5)

$$p(x)\mathrm{d}x = \exp\left(-\sum_{\mathrm{tot}} x\right) \cdot \sum_{\mathrm{tot}} \mathrm{d}x$$

[68] In this context, *sampling* refers to the application of a random number generated by a suitable algorithm called the random number generator.

[69] That's usually a Gaussian distribution with peak value at 14.1 MeV.

$p(x)dx$ denotes the probability that a neutron will undergo a collision when moving an infinitesimal distance dx in the considered material, i.e. $p(x)$ is the associated probability density function. By definition, this probability is given by the product of the total macroscopic cross-section Σ_{tot} and the distance dx. The probability that the neutron reaches x along its free flight path without interaction is given by the transmission factor $e^{-\Sigma_{tot} \cdot x}$. Therefore, the probability that the neutron will collide next at x is $P = \int_0^x e^{-\mathrm{Stot} \times x'} \mathrm{S}_{\mathrm{tot}} dx' = 1 - e^{-\Sigma_{tot} \cdot x}$. A random number between 0 and 1 is generated and assigned to P, thus the distance x can be calculated by inversion of the above equation. If a material boundary is between two collision sites, first the distance to this boundary along the free flight path is calculated, next the distance of the next collision is calculated assuming the material of the starting site. If this distance is larger than the distance to the boundary, the collision will take place on the other side of the boundary in the neighbouring material cell.

With the collision site sampled, the material (e. g. steel in a homogeneous mixture) is sampled, then the element (e. g. Fe in steel), the nuclide (e. g. ^{56}F), and finally the reaction type (absorption, elastic scattering, etc.). The generation of secondary particles is sampled (neutron or photon or none), its energy and the flight direction. If a particle is dead, meaning that it has disappeared either by an absorption reaction or by explicit killing (e. g. when coming to a region with zero importance) the next particle's history is started. This procedure is continued until the user specified number of histories has been completed. It is, of course, up to the user to make sure that the number of particle histories is sufficient for the nuclear responses he wants to compute.

7.2.2.2. Monte Carlo estimators

The nuclear responses are macroscopic quantities which need to be related to microscopic events that can be scored or tallied during the Monte Carlo simulation. Examples of such events are the number of particles crossing a specified surface, the number of particle paths in a cell, or the number of collisions, etc. Monte Carlo estimators are used to relate in various ways those microscopic events to nuclear responses. One of the most important is the track length estimator of the particle flux. It relates the total track length of a particle in a cell (cf. Fig. 7.8) to the flux in that cell, as shown in the following.

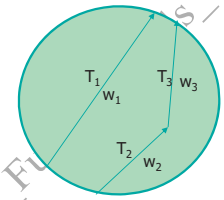

FIG. 7.8. Particle track lengths T_1, T_2 and T_3 in a cell with volume V and associated particle weights w_1, w_2 and w_3.

The neutron flux density F (in cm^{-2}s^{-1}) can be defined as:

(7.6)

$$\Phi = n \cdot v = \text{neutron-volume} \cdot v = \text{neutron-volume} \cdot v \cdot t \Delta\Delta t$$

$$= \frac{\text{neutrons} \times v \times \Delta t}{\text{volume} \times \Delta t} = \frac{(\text{total particle track length})}{(\text{volume} \times \Delta t)}$$

In other words, summing up the lengths of all particle tracks in a cell and dividing by the cell volume gives the average particle flux in a time interval (Δt) within the cell. The particle track length estimator is the most commonly used tally in Monte Carlo neutron transport simulations. It yields the neutron flux density when multiplied by the neutron source intensity (given in units of s^{-1}). Reaction rates in a material cell (in cm^{-3}s^{-1}) can also be obtained by multiplying the track length estimate of the neutron flux density by the nuclear cross-section of the reaction under consideration and the atomic number density. When multiplying the reaction rate by the heating number[70], the nuclear heating in a material cell can be calculated (usually given in MeV · g^{-1}). This quantity can be converted into a power density of the material (in units of W · cm^{-3}) after normalization to the absolute neutron source intensity.

7.2.2.3. Error Estimation

Tallying for nuclear response on the microscopic level is done for single events. Many statistically significant events need thus to be accumulated to obtain statistically reliable results. To judge the statistical quality of a tally, an

[70] The heating number is the energy deposited per reaction in the material under consideration.

estimation of the statistical error needs to be provided by the Monte Carlo calculation. The tally provides an estimate of the mean value of some quantity x:

(7.7)

$$\bar{x} = \frac{1}{N}\sum_{j=1}^{N} x_j$$

Where N is number of particle histories. The variance of this quantity, a measure of the dispersion of the x_j values around the mean, is:

(7.8)

$$S_x^2 = \frac{1}{N-1}\sum_{j=1}^{N}(x_j - \bar{x})^2 = \frac{1}{N-1}\sum_{j=1}^{N}(x_j^2 - \bar{x}^2)$$

The standard deviation σ is the positive square root of the variance and error of the mean defined as follows:

(7.9)

$$S_{\bar{x}} = \sqrt{\frac{S_x^2}{N}}$$

The result of a Monte Carlo estimate of quantity x is thus reported as: $x = \bar{x} \pm S_{\bar{x}}$ and the relative error is defined as: $R = \frac{S_{\bar{x}}}{\bar{x}}$. According to the central limit theorem, as N approaches infinity, there is a 68% chance that the true result will lie in the range $\bar{x}(1 \pm R)$, i. e. within 1σ, and a 95% chance within 2σ.

The figure of merit FOM = $1/(R^2T)$ is a useful quantity used to judge the behavior of a tally, where T is the computer time spent on the simulation, which scales linearly with the number of particle history. Hence, the FOM should approach a constant value for a tally to become statistically reliable.

7.2.2.4. ***Monte Carlo geometry***

The Monte Carlo approach for transport simulations allows the user to represent the geometry of the reactor in as many details as needed, without any significant simplification or approximations. It requires, however, to define the model at every point in space that a particle could reach in the simulation. The 3-D volumes of the model, called cells, are defined by their bounding surfaces using combinatorial geometry with surfaces and primitive bodies such as spheres, cylinders, cones, tori, etc. A cell number is assigned to each 3-D volume and a material number is assigned to each cell. The material composition within a cell is assumed to be uniform and homogeneous. That is, the material cells need to be defined to represent heterogeneities of the geometry as required and suitable for the neutronics simulation.

The Monte Carlo code MCNP, developed by Los Alamos national laboratory (LANL) in the USA, [7.5] is the standard code used in fusion neutronics applications. MCNP can handle surface types of 1st order (planes), 2nd order (spheres, cylinders, cones, ellipsoids, hyperboloids, paraboloids, general quadrics) and 4th order (elliptical and circular tori). The geometry is defined by Boolean operations (intersections, unions, complements) on the algebraic half-spaces defined by the surface sense (inside, outside a closed surface or above, below a plane). A simple example is shown in Fig. 7.9.

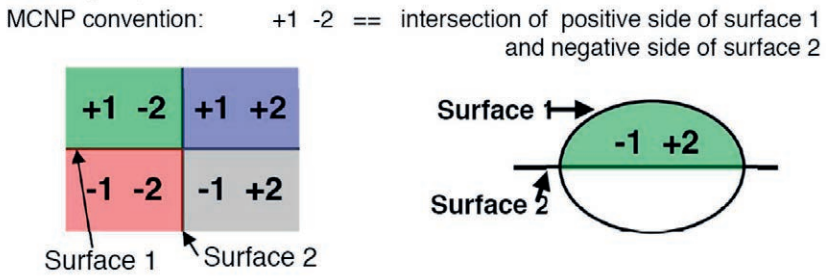

FIG. 7.9. Definition of geometry cells (3-D volumes) by Boolean operations on algebraic half spaces [7.6].

Any complex geometry can be accurately modelled by simple operations on primitive bodies. The manual modelling of a complex 3-D geometry for Monte Carlo transport simulation is however tedious, time consuming and error prone. A promising way to overcome this bottleneck is to make use of available CAD geometry data in the Monte Carlo calculations. This can be achieved by either converting the CAD data into the geometry representation used by Monte Carlo codes, or by the direct tracking of Monte Carlo particles on the CAD geometry. Several software tools have been developed over the past decade to allow the use of CAD geometry data in Monte Carlo transport calculations. These include conversion tools like MCAM [7.7] and McCAD [7.8], and the DAG-MCNP code [7.9] employing a modified particle tracking algorithm directly on the CAD geometry.

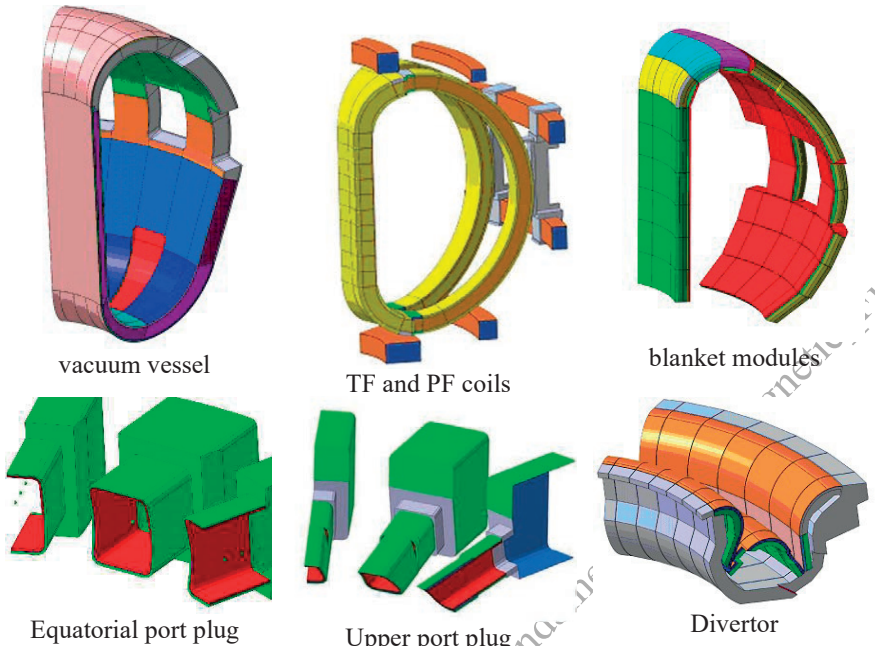

FIG. 7.10. Components used to construct a CAD neutronics model of ITER.

Engineering CAD models are, in general, not clean enough to be used in neutronics simulations; they typically contain overlaps and gaps that need to be removed. Furthermore, void space is not defined in CAD models but mandatory for Monte Carlo simulations. This is accounted for in the conversion by adding void space, generated by a dedicated algorithm. As an example, Fig. 7.10 shows components of an ITER torus sector which have been adapted from engineering CAD models to neutronics simulations geometries [7.10].

Fig. 7.11 shows (on the left side) the CAD model for neutronics simulations, which has been created from the components in Fig. 7.10 for an ITER torus sector of 40°. On the right side of Fig. 7.11, the converted MCNP model is shown in a 2-D cut.

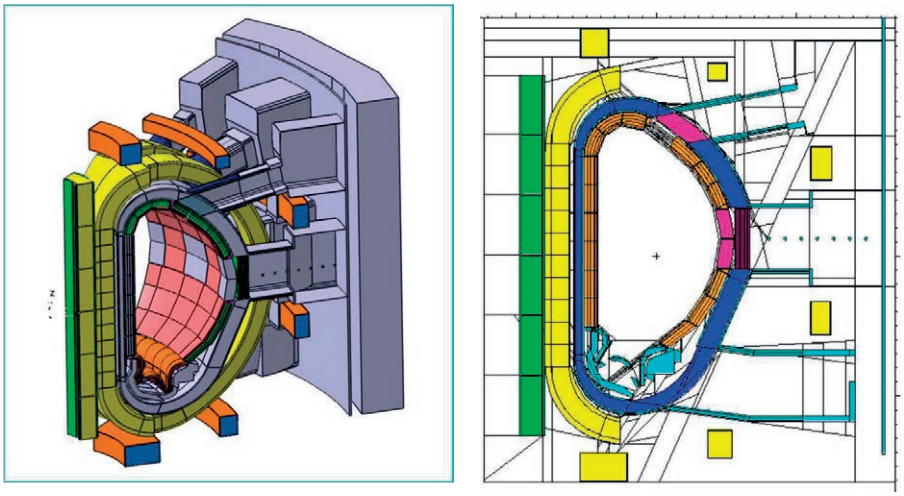

FIG. 7.11. MCNP 40° torus sector model (2-D cut, right side) generated from the CAD neutronics model (left side) by the conversion software McCAD.

Fig. 7.12 shows an example of a DEMO reactor model which has been constructed with the CAD software CATIA for a 11.25° torus sector and converted by the McCAD software into MCNP geometry. The model includes breeder blanket modules arranged around the plasma chamber to provide tritium breeding, a requirement for reactor operation.

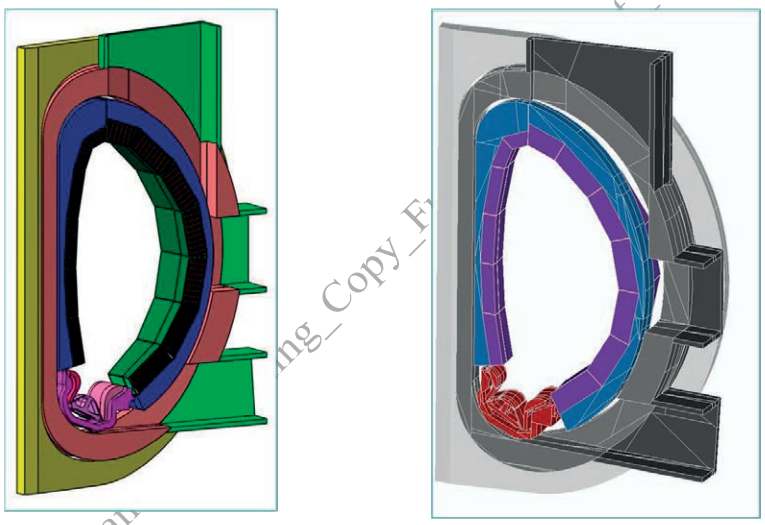

FIG. 7.12. Model of a DEMO reactor with integrated blanket modules, CAD neutronics model (left) and converted MCNP model (right).

7.2.2.5. Normalization and specification of nuclear responses

In general, the results of a Monte Carlo calculation are relative to one source neutron (per second) and normalized to the total number of source neutrons N_ϕ produced (per second) in the plasma. N_ϕ can be calculated from the fusion power P_{fus} and E_{fus} = 17.58 MeV, the energy released per (D-T) fusion reaction:

$P_{\text{fus}} = N_\Phi \cdot E_{\text{fus}}$

For example, in a 1 GW fusion power reactor a possible value of N_ϕ is 10^3 MW/17.58 MeV = 3.55×10^{20} s^{-1} source neutrons per second. Any tally reported by the Monte Carlo calculation needs to be multiplied by this number to get absolute values for the nuclear responses.

The neutron wall loading (NWL), given in the units $MW \cdot m^{-2}$, denotes the fusion neutron power loaded to the first wall per unit area. It accounts for direct (virgin) 14 MeV neutrons coming from the plasma and impinging on the

first wall without any interactions. Under this definition, the NWL can be translated into a current density of 14 MeV source (direct) neutrons, denoted as J_{14}, impinging on the first wall:

(7.10)

$$1\,\mathrm{MW}\cdot\mathrm{m}^2 = \frac{M\cdot 1\mathrm{eV}}{10^4\mathrm{cm}^2\cdot 1.6\cdot 10^{-19}\mathrm{s}} = 6.241\cdot 10^{14}\,\frac{\mathrm{MeV}}{\mathrm{cm}^2\mathrm{s}}$$

$$J_{14} = \frac{6.241\cdot 10^{14}}{14.06\ \mathrm{MeV}}\cdot\frac{\mathrm{MeV}}{\mathrm{cm}^2\cdot\mathrm{s}} = 4.439\cdot 10^{13}\mathrm{cm}^{-2}\mathrm{s}^{-1}$$

A neutron wall loading of 1.0 MW · m^{-2} thus corresponds to a source (uncollided) neutron current density of 4.4 × 10^{13}cm^{-2}.s^{-1} at the first wall. The NWL depends on the fusion power, the spatial neutron source distribution and the shape of the first wall surface relative to the plasma neutron source. The NWL is calculated for a voided model of the considered reactor by scoring the number of source neutrons impinging on the first wall from the plasma side. Neutrons entering space regions other than the plasma chamber and the void space in front of the first wall are killed as they do not contribute to the NWL. In the Monte Carlo calculations, the neutron importances are thus set to zero in all geometry cells except the plasma chamber. By definition, the Monte Carlo NWL can be obtained using an estimator for the current. With the MCNP code, it is the F1 tally which counts the number of neutrons crossing a specified surface (e.g. the first wall):

(7.11)

$$\mathrm{NWL} = \mathrm{F1}\times N_f\,/A_{\mathrm{FW}}.$$

Where A_{FW} is the area of the first wall in squared metres. The NWL is typically a little less than 1 MW·m^{-2} (ITER) to ~3 MW·m^{-2} in a reactor. When multiplied by the irradiation time T_{irrad}, the so-called first wall neutron fluence (FWNF) is obtained: FWNF = NWL × T_{irrad} with the irradiation time given in years[71].

The FWNF is often used as a criterion for the lifetime of the first wall, blanket modules and other components since it is related to the accumulated radiation induced damage and gas production. Typical values for a power reactor are in the range of 7 to 15 MW · a · m^{-2}. ITER is designed as a low fluence experimental device and will achieve FWNFs under 0.3 to 0.5 MW · a · m^{-2}.

The neutron flux density ϕ can be calculated by the Monte Carlo technique at a surface (like the first wall) or as a volume averaged value in a cell using the track length estimator introduced in Section 7.3.2.2. The latter is a basic quantity used to calculate reaction rates of any kind in a given volume. The MCNP code provides the F4 tally as an estimate of the average flux in a cell. More precisely, it gives the average fluence in a cell (in units of cm^2) referring to one source neutron per second. With the cell volume V_{cell} (given in cm^3) the (absolute) neutron flux density ϕ_{cell} averaged over the cell volume is then obtained (in the proper units of cm^{-2} · s^{-1}) according to:

(7.12)

$$f_{\mathrm{cell}} = F4\times\frac{N_f}{V_{\mathrm{cell}}}$$

MCNP's F2 tally scores the number of particles crossing an area independent of the flight direction. The neutron flux density ϕ_{FW} at the first wall can thus be calculated by specifying an F2 tally for the first wall surface. With the first wall area A_{FW} given in units of cm^2, ϕ_{FW} is obtained in units of cm^{-2} · s^{-1} by:

(7.13)

$$f_{FW} = \mathrm{F2}\times\frac{N_f}{A_{\mathrm{FW}}}$$

Typical values of ϕ_{FW} are in the order of 10^{15} cm^{-2} · s^{-1} for a power reactor and 2 to 3 × 10^{14} cm^{-2} · s^{-1} in ITER. In general, the total neutron flux density exceeds the direct 14 MeV neutron current density at the first wall by an order of magnitude. This is due to the many scattering events a neutron undergoes in the blanket and the other material components. As a result, on average, a neutron crosses the first wall multiple times and will be scored as many times for the total neutron flux density.

Nuclear heating of the materials is due to the deposition of kinetic energy on the atomic nuclei as result of their interaction with primary and secondary neutrons, secondary charged particles and gammas. The energy deposition can be described by the kinetic energy release in materials (KERMA) factor. The KERMA factor $K_{i,j}$ (in units of MeV ·

[71] The symbol [a] stands for annum.

barn) describes the transfer of kinetic energy to the nuclide of type *j* in a nuclear reaction of type *i* as a function of energy per reaction, where $E_{kin,i,}$ is the kinetic energy transferred to the nuclide *j* in a nuclear reaction of type *i*.

(7.14)

$$K_{ij} = \sigma_{i,j} \cdot E_{kin,i,j}$$

The nuclear heating rate *H* (in units of $W \cdot cm^{-3}$) can thus be calculated by the following equation, where $E_{con} = 1.6021 \times 10^{-13}$ [J · MeV] is the conversion factor and *N* is the number density of the considered material. Indices have been omitted for convenience:

(7.15)

$$H\ [W/cm^3] = K\ [MeV/reaction] \times N\ [cm^{-3}] \times \sigma\ [cm^2] \times \Phi_{cell}\ [cm^2\ s^{-1}] \times E_{con}$$

MCNP provides a dedicated tally (F6) for the energy deposited in the material (in units of $MeV \cdot g^{-1}$) given the track length estimation for the cell flux. The nuclear power density can then be calculated as follows:

(7.16)

$$P\ [W/cm^3] = F6\ [MeV/g] \times \rho\ [g/cm^3] \times N_\phi\ [s^{-1}] \times E_{con}\ [J/MeV]$$

Here ρ denotes the mass density of the considered material. The total nuclear power P_{tot} produced in a cell, in a component or the entire reactor system can be obtained on this basis by simply setting the volume of the cell(s) to unity (This is an implicit integration of the power density over the cell volume).

(7.17)

$$P_{tot}\ [MW] = F6\ [MeV] \times N_\phi\ [s^{-1}] \times E_{con}\ [J/eV]$$

With the total nuclear power production, the energy multiplication factor M_E of the reactor system can also be obtained. The energy multiplication factor M_E typically varies between 1.1 and 1.3 depending on the materials used in the reactor. This means that 10 to 30% more energy is produced in the blanket and other components than that provided by the 14 MeV fusion neutrons.

(7.18)

$$M_E = \frac{total\ nuclear\ power\ generated\ in\ reactor}{fusion\ neutron\ power}$$

$$M_E = \frac{total\ energy\ deposition\ per\ source\ neutron}{14\ MeV}$$

$$= \frac{F6\ [MeV]}{14\ MeV}$$

The highest energy multiplication is obtained for systems employing beryllium as neutron multiplier. Such systems also provide the highest neutron multiplication.

7.2.2.6. Neutron source modelling

In a Monte Carlo calculation, source neutrons are sampled from a probability distribution reproducing the source density *s.* The neutron source distribution in the plasma chamber can be described by a parametric representation derived from plasma physics [7.11]; the neutron source density $s(a)$ is given by:

(7.19)

$$s(a) = \left[1 - \left(\frac{a}{A}\right)^2\right]^P, 0 \le a \le A$$

Where A is the plasma minor radius. The exponent P depends on plasma physics modelling assumptions and generally is between 3 and 4. The parameter a fixes a contour line of constant source density; it also corresponds to a magnetic flux line, which can be described in a parametric representation:

(7.20)

$$R = R_0 + a\cos(t + \delta \sin t) + e\left[1 - \left(\frac{a}{A}\right)^2\right]$$
$$z = Ea \sin t$$

Here, R is the radial distance to the torus axis, z is the poloidal distance to the torus mid-plane, R_0 is the plasma major radius, δ is the plasma triangularity, δ_0 is the maximum plasma triangularity and e is the Shafranov factor, which denotes an outward shift of the magnetic surfaces. This distribution is coded into a source subroutine which can be linked to the Monte Carlo code for sampling the generation and emission of 14 MeV source neutrons in the plasma chamber of the (D-T) fusion reactor.

7.3. NUCLEAR DESIGN ISSUES

A (D-T) fusion reactor relies on the availability of tritium, which decays with a half-life of 12.3 years, thus needs to be produced in a dedicated blanket covering the plasma chamber as much as possible. The principal function of a blanket is to breed enough tritium for self-sufficiency of the reactor. Proof of tritium self-sufficiency is a high priority task in fusion technology which is conducted by neutronics using the proper methods, tools and data.

Another function of the blanket is to convert the nuclear energy — deposited in the blanket materials by the 14 MeV fusion neutrons and the various nuclear reactions in place — into heat. The nuclear heating data, including the total nuclear power generation and the spatial distribution of the nuclear power density in the various materials, can also be calculated for the thermal-hydraulic layout of the blanket by neutronics calculations.

A third function of the blanket is to attenuate the neutron radiation impinging on the first wall. The breeder blanket needs to be optimized for tritium production and therefore shows, in general, a very poor shielding performance[72]. The breeding blanket of a fusion reactor is therefore backed up by a dedicated radiation shield optimized for shielding performance. This is again a task for neutronics, which includes the proof that the provided attenuation is sufficient to protect the super-conducting magnets from the (neutron and gamma) radiation penetrating the shield.

During operations, every component of a fusion reactor is subject to different levels of neutron and photon radiation. The materials of those components become activated to different extents, depending on their compositions, the radiation levels and the assumed operational scenario. The material activation has an impact on safety issues during reactor operation, shut-down periods and (on the long-run) the handling of the nuclear waste. Material activation and the related nuclear properties such as decay heat or emitted ionizing radiation can be predicted by neutronics and activation analyses. In this context, the task is to minimize the radio-activity inventory in the short and the long-term radiation hazard potential. This requires the assessment of the activation behaviour of the selected materials (e.g. steel with varying elemental compositions. Finally, it is important to ensure that plant personnel can safely access specific areas of the facility to perform maintenance work. This requires a proper radiation dose assessment of the concerned areas during full operation and shut-down periods. Such assessments can also be provided by means of neutronics and activation analyses given the necessary computational tools and nuclear data.

The resulting neutronics requirements were specified for a DEMO fusion power plant in Ref. [7.12]. A more recent paper provides and update on the tritium breeding requirements for a DEMO as considered lately in the European fusion programme [7.13].

7.3.1. Tritium breeding

Tritium will be bred in the blankets of D-T reactors for fuel self-sufficiency. This can be achieved by the (n, t) reaction which produces a triton per absorbed neutron. The neutron released by the (D-T) fusion reaction has to be absorbed by a stable nuclide from a suitable material, which should occur naturally in a sufficient amount; the (n, t) reaction of the nuclide(s) in question should also feature a sufficiently high cross-section.

Such pre-conditions immediately lead to lithium, which occurs in two stable isotopes: ^{6}Li and ^{7}Li of relative natural abundances of 7.5 and 92.5 2-D, respectively. Both lithium isotopes produce tritons with neutrons in the energy

[72] The neutron flux is typically attenuated in less than an order of magnitude by a breeding blanket (see Section 7.4.5).

range of the fusion neutrons: ^{6}Li(n, α)t + 4.786 MeV, ^{7}Li(n, n'α)t − 2.467 MeV. The associated nuclear cross-sections were discussed in Section 7.2 and shown in Fig. 7.1. The preference for the ^{6}Li(n, α)t reaction in tritium production is evident: There is no reaction threshold as for ^{7}Li(n, n'α)t and the cross-section strongly increases with decreasing energy. Actually, there are only two materials, pure lithium metal and Li_2O, which allow sufficient tritium breeding for self-sufficiency utilizing the ^{7}Li(n, n'γ)t reaction without additional neutron multiplier. The use of any other lithium compound relies on the ^{6}Li(n, α)T reaction for tritium production and thus requires a neutron multiplier.

The material will be arranged around the plasma chamber such that the incident fusion neutron is, with high probability, absorbed on the breeder in a *useful* reaction, i.e. the (n, t) reaction. In fact, the blanket also contains structural material, in general steel, and coolant to remove the heat. Parasitic neutron absorptions will occur and, consequently, less than one triton may be produced per incident fusion neutron. To compensate for the parasitic absorptions, additional neutrons need to be supplied through multiplication, e. g. through (n, 2n) reactions. In addition to breeder, structural and coolant materials, the blanket will thus incorporate a suitable neutron multiplier like beryllium or lead.

Tritium breeding capacity has to be proven by realistic neutronic calculations. This requires, first and foremost, a suitable computational method such as the Monte Carlo technique, qualified for fusion neutronics applications. Secondly, a realistic model of the fusion reactor with sufficient details about the blanket geometry has to be provided. Finally, high quality nuclear data has to be made available. The prediction of the calculation needs to be checked against benchmark experiments to ensure that they are reliable within some uncertainty margin. Such benchmark experiments have been performed on mock-ups of the European concepts for a helium cooled lithium lead (HCLL) and a helium cooled pebble bed (HCPB) blanket using 14 MeV neutron generator facilities at ENEA, Frascati, and TUD (Dresden) [7.14].

The quantity which indicates the tritium self-sufficiency is called the tritium breeding ratio (TBR). It is the ratio, per second, between the number of tritons produced in the entire blanket and the number of fusion neutrons produced in the (D-T) plasma. The TBR can be calculated as per

(7.21)

$$TBR = \frac{\int N_{^{6}Li} \cdot {}^{^{6}Li}\sigma_{n,\alpha} \Phi dV + N_{^{7}Li} \cdot {}^{^{7}Li}\sigma_{n,n'\alpha} \Phi dV}{N_{\Phi}}$$

Here, N_ϕ is the number of source neutrons produced in the (D-T) plasma, as defined in Section 7.3.2.5. With this definition, the requirement for tritium self-sufficiency translates into TBR ≥ 1.0. This is a pre-condition for any (D-T) fusion power reactor which will be proven by realistic neutronic calculations. The actual requirement is even stronger because of tritium losses (e. g. in the fuel cycle), deficiencies in the applied model and uncertainties in calculations and data to be accounted for. To this end, an uncertainty margin is usually imposed on the TBR, resulting in a requirement of (at least) TBR ≥ 1.05 [7.15].

To achieve a TBR greater than or equal to 1.0 in a fusion reactor, the neutron losses will be compensated by either utilizing the ^{7}Li(n, n'α)t reaction for the tritium production or additional neutron multipliers. With the ^{7}Li(n, n'α)t reaction, a triton is produced without consuming a neutron. The associated cross-section is, however, not very large and shows a reaction threshold around 3 MeV, see Fig. 7.1. If the breeder contains additional constituents, the competing nuclear reactions may become so large that tritium breeding cannot be achieved. This is the case for all breeder materials except Li and Li_2O which can be utilized in liquid metal and solid breeder blanket configurations, respectively. Any other breeder material, compound or alloy, requires additional neutron multipliers in the blanket to provide an extra neutron via the (n, 2n) reaction. Such neutron multiplier materials will have low neutron absorption cross-sections (to avoid parasitic absorptions) and high (n, 2n) cross-sections with low reaction thresholds, if possible.

Beryllium is the multiplier material with the highest neutron multiplication power. With a pure beryllium assembly of sufficient size, the neutron multiplication factor can even be greater than two. This is due to the low threshold of the ^{9}Be(n, 2n)2α reaction at 1.75 MeV (Fig. 7.2): A neutron emitted through a (n,2n) reaction can have sufficient energy[73] to initiate another (n, 2n) reaction on Be. Another beneficial property of beryllium is its low mass, which results, together with the low neutron absorption cross-section, into a high moderator quality. This is in turn advantageous to enhance the tritium breeding capability of a blanket utilizing the ^{6}Li(n, α)t.

Lead features a higher (n, 2n) cross-section than beryllium (Fig. 7.2) but also has a high reaction threshold around 7 MeV; the neutron multiplication power of lead is thus inferior to that of beryllium. In general, lead is used in

[73] Well above the reaction threshold!

breeding blankets in the form of Pb-Li liquid metal alloys. Other potential neutron multipliers show either a worse multiplication power which, in many cases, is not sufficient (e.g. Zr) or result in hazardous activation products which need to be avoided in a fusion power plant (e.g. Bi). These considerations lead to breeding blanket conceptual designs based on either liquid metals or solid breeder materials:

Liquid metal blankets: pure lithium metal, generally enriched in ^{6}Li up to ~30 2-D, is utilized as breeder material. In such a case, there is a significant contribution of the ^{7}Li(n, n'α)t reaction in tritium production. The use of liquid lithium; however, presents safety concerns for the operation of a fusion power plant. For this reason, among others, a eutectic Pb-Li alloy has been proposed and developed for liquid metal breeder blankets. Such an alloy is favoured since it combines the tritium breeding and the neutron multiplication capabilities of lithium and lead, respectively. The Pb-Li eutectic alloy with 15.8 2-D Li requires; however, a high ^{6}Li enrichment — in general 90at% — to ensure sufficient tritium breeding. The liquid metal can also be used as coolant but will then have to be circulated at high velocities. This in turn causes high pressure drops due to MHD (magneto hydrodynamic) effects induced in the flowing liquid metal by the high magnetic fields of the tokamak. To avoid such problems, liquid metal blankets can be cooled by high pressure helium gas or water. The liquid metal can then be circulated slowly for tritium extraction. A helium cooled lithium lead blanket concept is the actual reference solution for a liquid metal blankets in the European fusion programme [7.16]. To achieve a TBR above unity, liquid metal blankets require a comparatively large blanket thickness, typically between 60 and 80 cm. This applies for both for lithium and Pb-Li for the following reasons. Lithium has a rather low total neutron cross-section for fast neutrons and a low atomic density. This results in a rather high average mean free path in the order of 15 to 20 cm. Lead on the other hand, has a large elastic scattering cross-section and a high mass. This results in multiple (sequential) scatterings of neutrons without significant loss of kinetic energy until a (useful) absorption in the Li-alloy takes place.

Solid breeder blankets: examples of potential breeder materials are ceramics such as Li_4SiO_4, Li_2TiO_3, Li_2ZrO_3 or Li_2O, which are most commonly employed in the form of small sized pebbles in the blanket to reduce thermal stresses and facilitate tritium release during operation. Ceramics with a high lithium density such as Li_4SiO_4 or Li_2O are favoured for their superior tritium breeding potential. With the exception of Li_2O, solid breeder materials require an additional neutron multiplier. For its superior properties, beryllium is the preferred neutron multiplier. It is almost exclusively in all design concepts developed for a solid breeder blanket. Li_2O is not considered in most solid breeder blanket designs due to its hygroscopic properties and its thermal instability at elevated temperatures. Solid breeders require ^{6}Li enrichment to ensure sufficient tritium breeding, typically in the range of 30 to 60at%. With beryllium for neutron multiplication, only a small blanket thickness is required, typically 30 to 50 cm. The geometric arrangement and dimensioning of the beryllium multiplier and breeder material is subject to optimization based on neutronics analyses. A helium cooled pebble bed blanket concept [7.16], using Li_4SiO_4 pebbles for the tritium production and beryllium pebbles for neutron multiplication is the reference solution for a solid breeder blanket in the European fusion programme. A typical scheme for such a blanket concept is briefly described in the following to demonstrate the methodology applied for neutronic optimization.

7.3.2. Helium cooled pebble bed breeder blanket concept

The HCPB blanket employs Li_4SiO_4 ceramics (or alternatively Li_2TiO_3) as breeder material and beryllium as neutron multiplier. Both the breeder and the beryllium are used in the form of mono-disperse pebble beds. The Li_4SiO_4 ceramic pebbles have a diameter in the range of 0.2 to 0.6 mm, and the beryllium pebbles of 1 mm; the resulting effective volume fraction (packing factor) of the pebble beds is ~63%. For sufficient tritium production, the ceramic breeder needs to be enriched in ^{6}Li. Due to the lower lithium density, a higher enrichment is required for Li_2TiO_3 ceramics, as shown in Fig. 7.15. Neutron multiplier and breeder material are arranged in a heterogeneous array of Be and Li_4SiO_4 ceramics pebble bed layers separated by thin cooling plates as outlined in Fig. 7.13. (The coolant is provided by high pressure helium gas). The volume ratio of Be and breeder ceramic is about 4:1 which is close to the optimal ratio indicated by the neutronics analyses. The pebble beds run in the radial direction, perpendicular to the first wall, with a horizontal or vertical orientation. From a neutronics point of view, such a configuration acts almost like a homogeneous Be/ceramic configuration. True heterogeneous solutions are also feasible with the pebble beds running parallel to the first wall. Such a configuration requires a thorough optimization including several iterations as shown below.

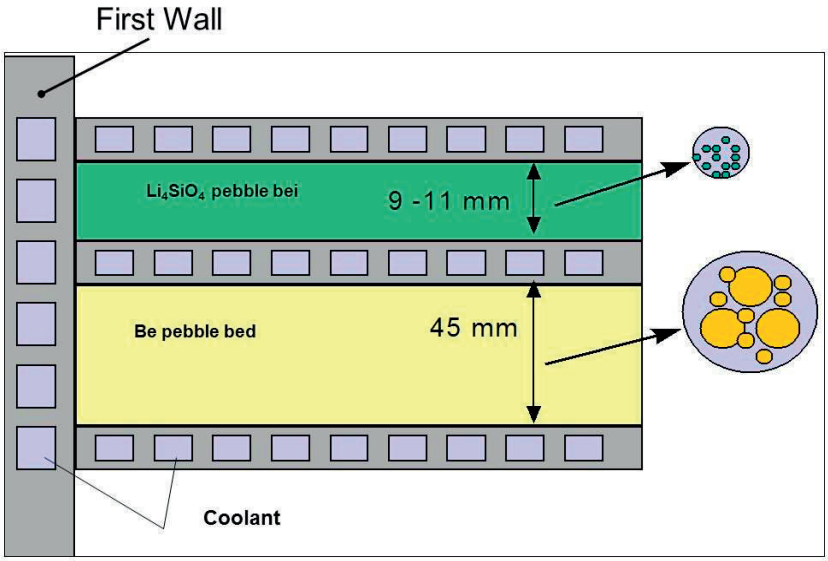

FIG. 7.13. Schematic view of the HCPB blanket design concept.

Beryllium, the breeder ceramics, the structural material and the coolant are the major constituents of a fusion power reactor based on the HCPB concept. Beryllium provides neutron multiplication by $^{9}Be(n, 2n)2\alpha - 1.57$ MeV and moderates the neutrons by the elastic scattering process. These reactions also contribute to the nuclear heating of the blanket. The Li_4SiO_4 ceramic provides tritium breeding by the reaction $^{6}Li\ (n, \alpha)t + 4.78$ MeV. The ^{6}Li enrichment is in the range 30 to 40at% as shown below. $^{6}Li\ (n, \alpha)t$ is the main source of nuclear energy in the blanket. The structural material is assumed to be the reduced activation ferritic-martensitic (RAFM) steel EUROFER, with an iron content of ~90 weight %: the main nuclear reaction on the steel structure is thus $^{56}Fe(n, \gamma)^{57}Fe + 7.65$ MeV, which is also the major parasitic neutron absorption reaction in the system. On the other hand, this reaction significantly contributes to the heat generation due to the high release of nuclear binding energy.

7.3.3. Modelling and optimzation of a HCPB type DEMO reactor

Fig. 7.14 shows an example of a MCNP model developed for a HCPB type DEMO reactor [7.17]. The reactor is in the so-called double null configuration with two plasma X points and two divertors at the bottom and top of the plasma chamber. Breeder blanket modules are arranged around the plasma chamber on the outboard and the inboard sides, as well as behind the (very simple) divertor plates. The enlarged insert shows the detailed geometry of an outboard blanket module with first wall, beryllium (pink colour) and breeder pebble bed layers (yellow) and cooling plates.

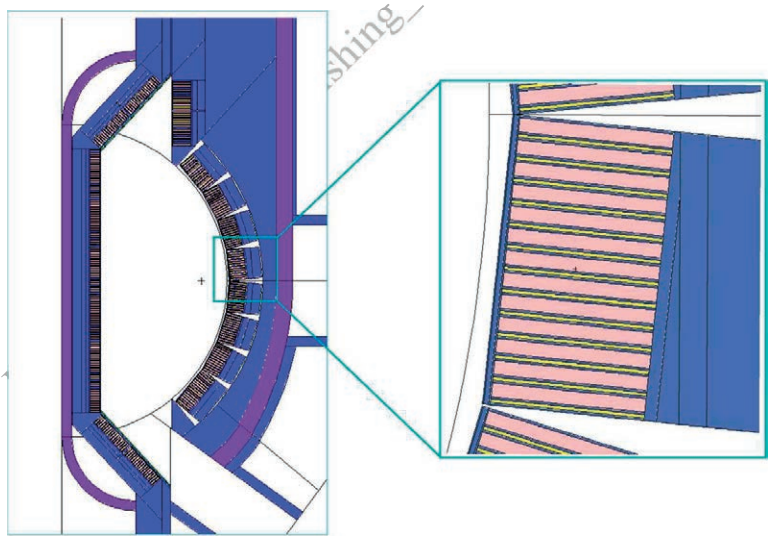

FIG. 7.14. MCNP model of a HCPB type DEMO reactor (vertical cut through the 11.25° torus sector model).

In this case, the main subjects of optimization are the ratio of Be and breeder ceramics pebble bed height, the (vertical) height of the latter, the (radial) length of the pebble beds, and the ^{6}Li enrichment. As an example, Fig. 7.15 shows the TBR as a function of the ^{6}Li enrichment, calculated for the reference pebble bed height of 10 mm for the breeder material candidates Li_4SiO_4, Li_2TiO_3, and Li_2TiO_3. This result indicates that the breeding capability of the Li_4SiO_4 ceramics is superior to the that of Li_2TiO_3 and Li_2TiO_3. This is mainly due to the higher Li density of Li_4SiO_4. As can be seen in Fig. 7.15, the TBR target range of 1.10 to 1.15 specified for this DEMO configuration can be achieved with a ^{6}Li enrichment of 30 to 45at% with the Li_4SiO_4 breeder ceramic. To achieve this goal, Li_2TiO_3 and Li_2TiO_3 would require enrichment levels of 50 to 65at% and 55 to 75at%, respectively.

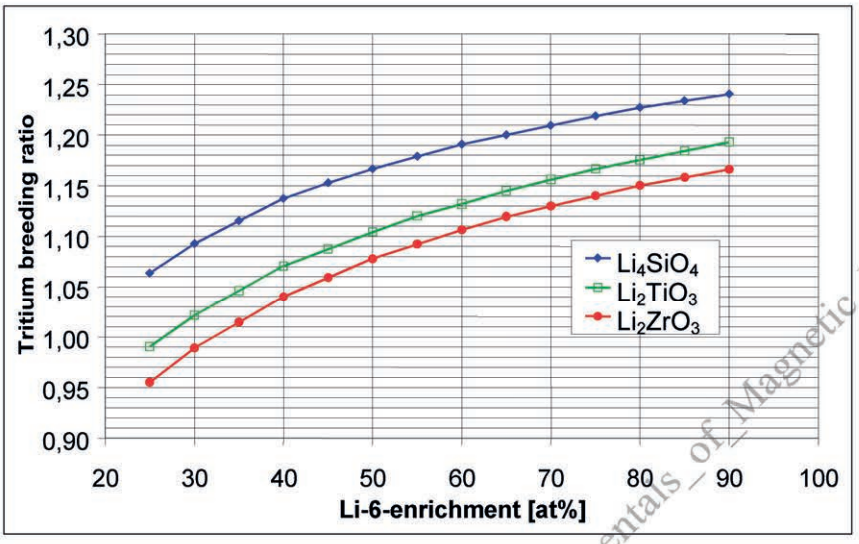

FIG. 7.15. HCPB type DEMO: TBR as function of the ^{6}Li enrichment for the breeder candidate materials Li_4SiO_4, Li_2TiO_3, and Li_2TiO_3.

Fig. 7.16 shows another MCNP model of a HCPB type power reactor [7.18], developed for the European power plant conceptual study (PPCS) [7.19]. This model is used to analyse and optimize the heterogeneous Be/breeder ceramics configuration with the pebble beds running parallel to the first wall. This configuration offers many degrees of freedom for optimization: each single pebble bed can be varied in thickness, and in case of the breeder, the ^{6}Li enrichment. The total number of pebble beds can be varied as well. Such variations will be performed iteratively together with thermal-hydraulic analyses ensuring the maximum temperature in the middle of the pebble beds is not exceeded[74]. An optimized configuration is shown in Table 7.1.

[74] This temperature is very sensitive to the height of the pebble bed and should be determined with great care.

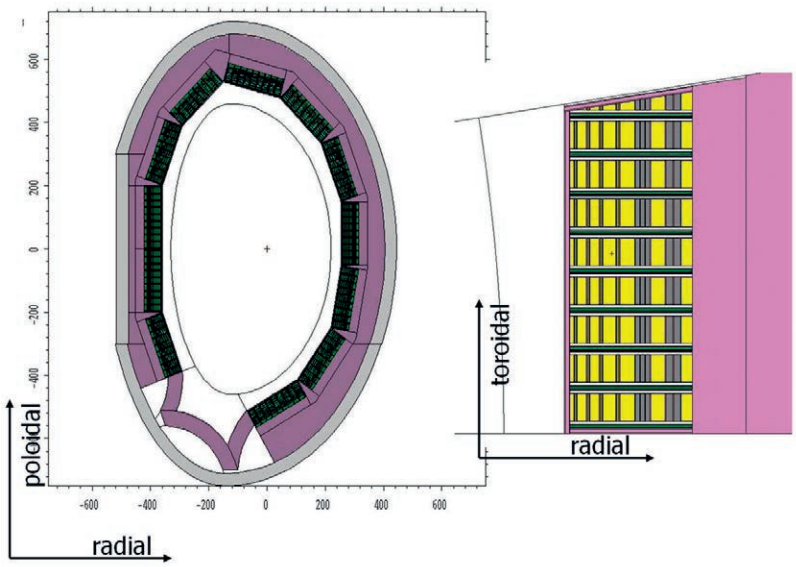

FIG. 7.16. MCNP model of a power reactor employing a HCPB blanket with pebble beds parallel to the first wall.

TABLE 7.1. Optimized radial build of the HCPB blanket with pebble beds parallel to the first wall.

Material	Be	CB (*)	Be	CB	Be	CB	Be	CB	Be	CB	Be	CB	Be
thickness [mm]	20	11	50	11	50	12	70	15	80	3x24	80	2x38	50
Li-6 [at%]		60		60		60		60		90		90	

(*) CB = Ceramics Breeder.

The resulting TBR for this configuration is at 1.15 which is sufficiently high for tritium self-sufficiency with a large uncertainty margin. A high ^{6}Li-enrichment is however required as well as a large blanket thickness of ~70 cm. This also results in a high beryllium mass inventory (~440 tons) for the considered PPCS-type power reactor. Since the beryllium world resources are scarce, the Be mass inventory will be minimized. This calls for a HCPB blanket solution with pebble beds perpendicular to the first wall. Fig. 7.17 shows two variants of such a configuration. Variant B is advantageous in terms of beryllium savings due to the replacement of the rear part of the Be pebble beds by breeder ceramics; it allows the Be mass inventory can be reduced from 412 to 284 tons without significantly affecting the neutron multiplication and tritium breeding (see Table 7.2). For example, when replacing the rear 15 cm of the Be pebble beds by breeder ceramic pebbles, the neutron multiplication decreases from 1.68 to 1.66 while the TBR remains at 1.14.

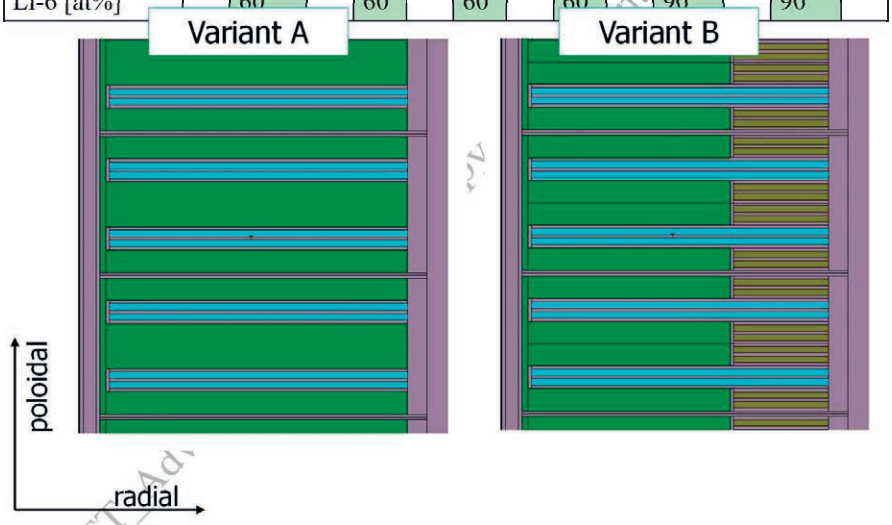

FIG. 7.17. HCPB blanket variants with pebble beds perpendicular to the first wall. This design employs two double containers with breeder ceramic per compartment. The radial length of the structure is 46 cm and the poloidal height of the breeder pebble bed is 10 mm.

The nuclear power generation and the nuclear power density distribution are calculated by a Monte Carlo calculation using the tally definitions presented in Section 7.3.2.5. Figures 7.18 a and b show radial profiles of the nuclear power density calculated for the HCPB design variants with pebble beds vertical and perpendicular to the first wall, respectively. The power densities are given for individual materials: beryllium, the breeder ceramics and the steel structure. The highest power density is in the breeder ceramics due to the $^{6}Li(n, \alpha)t$ reaction dominating all other reactions taking place in the system. While the power density profiles are continuous and smooth for the HCPB variant with the pebble beds running perpendicular to the first wall, they show sharp peaking values when the beds are arranged parallel to the first wall. This also affects the maximum power density which is significantly higher in the latter case.

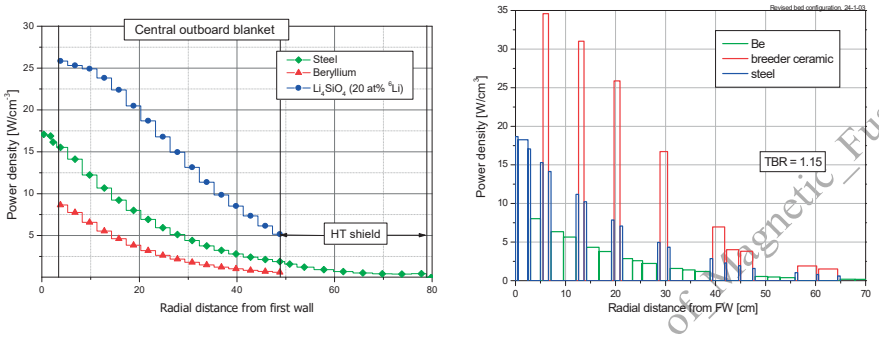

(a) *(b)*

FIG. 7.18. Radial power density profiles for HCPB blanket variants with pebble beds running perpendicular (a) and parallel (b) to the first wall. The profiles are shown for the central outboard blanket module. The values are normalized to a fusion power of 3300 MW, assumed in the PPCS for reactor model B [7.18].

Examples of nuclear power generation in a fusion reactor are given in Table 7.2 for the HCPB and the HCLL variants [7.20]. By breaking-down the total into components it is shown that 85% to 90% of the power is produced in the blankets while no more than 1.5% and 3% comes from shield and vacuum vessel, HCPB and HCLL variant, respectively. The high energy multiplication factor in the HCPB blanket is due to the use of beryllium.

	HCLL	HCPB
Blanket	1914	2277
Manifolds	58	47
Shield and vacuum vessel	65	39
Divertor	188	167
Total	2225	2530
Global energy multiplication	1.17	1.33

TABLE 7.2. Nuclear power production in MW and energy multiplication factors of the HCPB/HCLL variants of DEMO for a fusion power of 2385 MW [7.20].

7.3.4. Neutron wall loading and neutron flux spectra

The neutron wall loading, defined in Section 7.3.2.5, is of primary importance for the engineering design of reactor components subject to the intense 14 MeV neutron radiation emitted from the D-T plasma. The NWL distribution is calculated with MCNP for the voided torus sector model by scoring the number of source neutrons crossing a closed surface following very closely the first wall and covering the divertor opening at the bottom of the plasma chamber. The NWL shows a pronounced poloidal profile due to the spatial variation of the neutron source

intensity and the shape of the first wall adapted to the plasma contour. The example shown in Fig. 7.19 is for a HCLL-type DEMO reactor with 2385 MW of fusion power [7.21]. The average NWL is 1.76 MW · m^{-2}. The peak values reach up to 2.11 and 1.90 MW · m^{-2} at the outboard and inboard torus mid-plane, respectively.

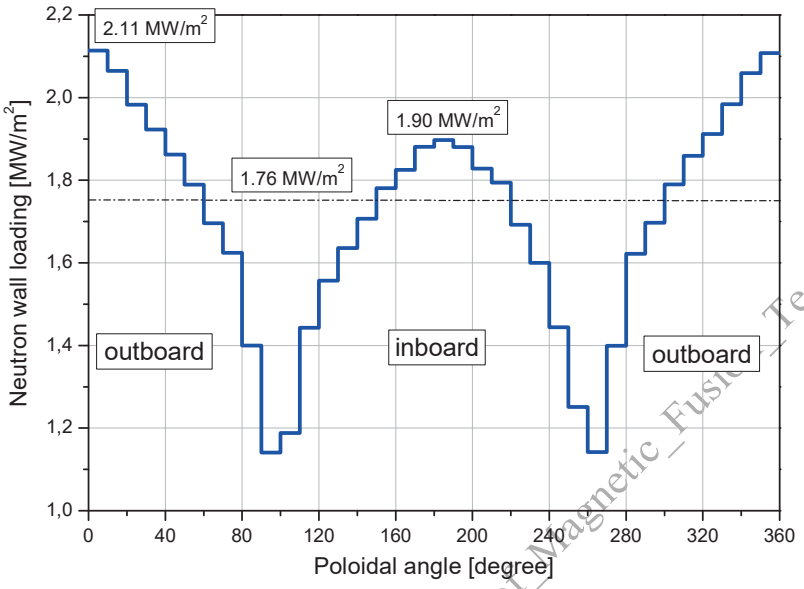

FIG. 7.19. Poloidal profile of the neutron wall loading (NWL) to the first wall of a DEMO reactor (with 2385 MW of fusion power).

The neutron wall loading refers to (D-T) source neutrons only. The 14 MeV neutrons colliding with the atomic nuclei of the material components are scattered in all directions. As a result, scattered neutrons of lower kinetic energy cross the first wall many times. The neutron flux spectrum on the first wall is therefore composed of the 14 MeV neutrons (typically 25 to 30%) and scattered neutrons, which form the spectrum below the source peak. The number of scattered neutrons and the shape of the spectrum depends mainly on the materials used in the plasma facing components, particularly the blanket materials. Fig. 7.20 shows, as an example, the first wall spectra of a HCLL and a HCPB based power reactors. The differences come from the different nuclear properties of the materials involved, in particular lead (HCLL) versus beryllium (HCPB), as discussed previously. The neutron spectrum of the HCPB DEMO is significantly degraded due to the neutron moderation effect of beryllium. Lead, on the other hand, does not moderate neutrons.

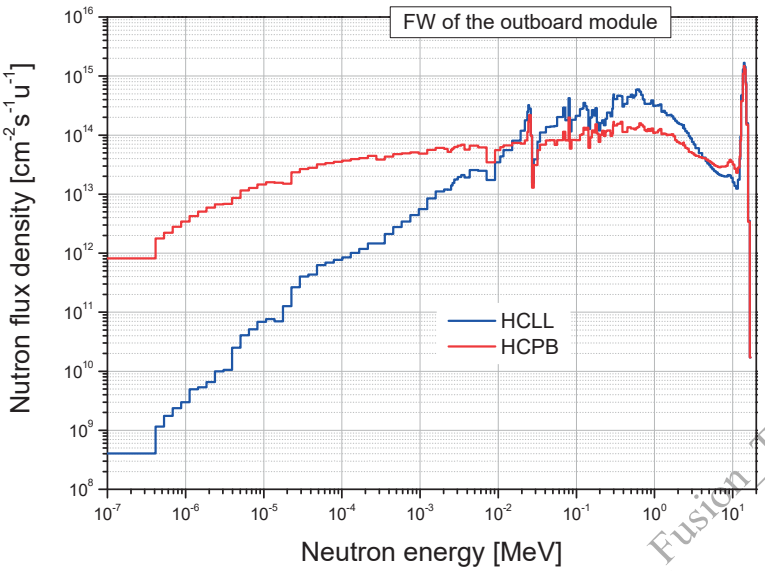

FIG. 7.20. Neutron spectra at the first wall of a power reactor (2385 MW fusion power) based on HCLL and HCPB blankets for the Tritium breeding [7.20].

7.3.5. Radiation Shielding Issues

The shielding performance of breeder blankets is, in general, very low. The neutron flux density is attenuated in less than an order of magnitude from 10^{15} cm^{-2} · s^{-1} at the first wall to 10^{14} cm^{-2} · s^{-1} at the back wall of the blanket. The breeding blanket will thus be backed by a dedicated radiation shield, which needs to be optimized for shielding performance.

There are two essential shielding requirements for a fusion reactor: first, the re-weldability of components, connections and pipes made of steel such as the vacuum vessel, and, second, the protection of the superconducting toroidal field (TF) coils. Based on existing data, the current assumption is that re-welding of stainless steel should be successful at He concentrations below 1 appm. The same limit is assumed for the accumulated He production of components, which need to be re-welded during their life-time as for example coolant feeding pipes. Another crucial value for in-vessel components is the displacement damage accumulation, which, together with the operating temperature, will determine the component lifetime and has an impact on the choice of material. A target limit of 70 dpa (displacements per atom) is assumed for the DEMO first wall made of EUROFER steel.

TABLE 7.3. Recommended radiation design limits for super-conducting coils in ITER and DEMO.

	ITER	DEMO(*)
Integral neutron fluence for epoxy insulator [m^{-2}]	1×10^{22} ≅ 10^7 Gray	**1×10^{22}**
Peak fast neutron fluence (E>0.1 MeV) to the Nb_3Sn superconductor [m^{-2}]	1×10^{23}	
Peak fast neutron fluence to the Nb_3Sn ternary superconductor [m^{-2}]	$0.5 – 1 \times 10^{22}$	1×10^{22}
Peak displacement damage to Cu stabilizer or max. neutron fluence between TFC warm-ups [m^{-2}]	$1–2 \times 10^{21}$ ≅ $0.5–1 \times 10^{-4}$ dpa	**$1–2 \times 10^{21}$**
Peak nuclear heating in winding pack [W.m^{-3}]	1×10^3	**$< 0.05 \times 10^3$**

(*) Based on D. Maisonnier, P. Sardain, EFDA Memo, December 2006, and revisions by G. Federici and J.-L. Duchateau, December 2011.

The most crucial radiation loads to the TF-coil are the fast neutron fluence to the superconductor, the peak nuclear heating in the winding pack, the radiation damage to the copper insulator and the radiation dose absorbed by the epoxy resin insulator. The related radiation design limits are also used to assess the shielding efficiency which needs to be met at the inboard mid-plane of the reactor where the space available for shielding is minimal. Table 7.3 shows state-of-the-art radiation design limits for ITER and DEMO.

The TF coils are protected from the penetrating radiation by the blanket, the shield and vacuum vessel. All three should be optimized for an efficient attenuation of the radiation. This includes both the material composition and total thickness of the shielding system. A good shielding performance can be achieved by combining an efficient neutron moderator (i.e. a hydrogenous material such as water or a hydride) and a good neutron absorber (steel, tungsten). In this way, fast neutrons are efficiently slowed down and captured by the absorber material in the resonance range (Fe, W) or the thermal energy range (e.g. using boron). The total thickness of the blanket shield system is typically in the range of 110 to 120 cm for a power reactor. The thickness of the vacuum vessel supposed in ITER is, in general, 35 cm. It consists of two 5 cm thick steel plates at the front and the back, and a 25-cm thick shielding mixture in between, which is typically composed of 60% borated steel and 40% water. If required, this shielding mixture can be replaced by a more efficient one such as water/tungsten or tungsten carbide (WC). Assuming an efficient shielding material composition of tungsten carbide, steel and water, the shield preceding the vacuum vessel will have a thickness of ~30 cm. A typical radial build, as elaborated for a fusion power reactor based on the HCLL breeder blanket concept, is shown in Table 7.4.

TABLE 7.4. Typical radial build for a fusion reactor based on the HCLL breeder blanket concept (Inboard and outboard builds given at torus mid-plane) [7.21].

Component	Inboard thickness (mm)	Outboard thickness (mm)	Material composition
First wall armor	2	2	W
First wall	30	30	EUROFER 63.5%, He 37.5%
Breeding zone	475	775	Heterogeneous, EUROFER structure, He coolant, Pb-15.8Li, 90% ^{6}Li
Manifold	300	400	LiPb 5%, EUROFER 28%, He 67%
Shielding	300	400	WC 65%, EUROFER 10%, H_2O 25%
Vacuum vessel	350	650	SS316 61%, H_2O 37%, B 2%
TF coil casing	60	60	SS316

For such a configuration, Fig. 7.21 shows the radial profiles of the fast, total and low energy neutron flux densities from the first wall to the TF-coil. As can be seen, the neutron flux is attenuated by less than an order of magnitude across the 45-cm thick blanket module. A strong attenuation of ~6 orders of magnitude is provided by the shield and the vacuum vessel due to the material composition and dimensions. Fig. 7.22 shows the corresponding profiles of the nuclear power density in the Pb-Li and the steel structures. At the font of the TF coil, the power density is ~1 $W \cdot m^{-3}$, thus well below the limit of the peak value specified for the magnet (see Table 7.3).

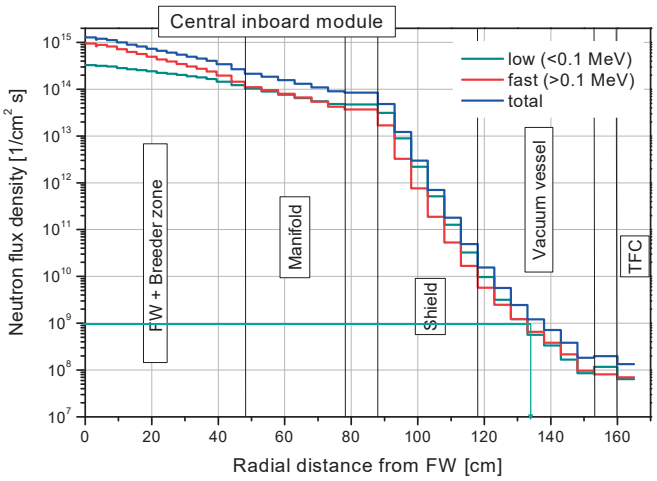

FIG. 7.21. Radial profiles of the neutron flux densities across the inboard mid-plane of an HCLL-type Demo reactor.

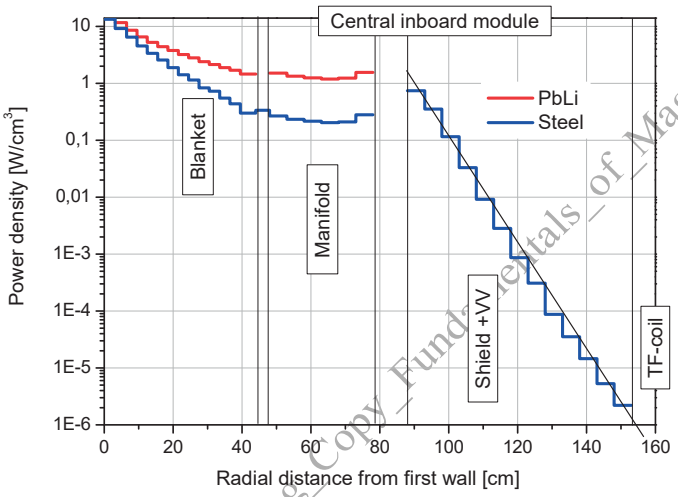

FIG. 7.22. Radial profiles of the nuclear power densities across the inboard mid-plane of an HCLL-type DEMO reactor.

Radial profiles of the helium production and displacement damage accumulation in the steel structure are shown in Fig. 7.23. At full power, the maximum helium production per year in the steel of the shield and in the vacuum vessel amount to 0.1 and 2 × 10^{-3} appm, respectively. The displacement damage accumulation in the steel of the shield and the vacuum vessel isn't crucial either. For instance, a level of 1 dpa is achieved at the front of the shield after 10 years at full power, while the vacuum vessel will be subjected to no more than 2 × 10^{-4} dpa per full power year due to the efficient protection provided by the 30-cm thick preceding shield. Both components, shield and vacuum vessel, could thus be operated over the full anticipated lifetime of an HCLL type DEMO.

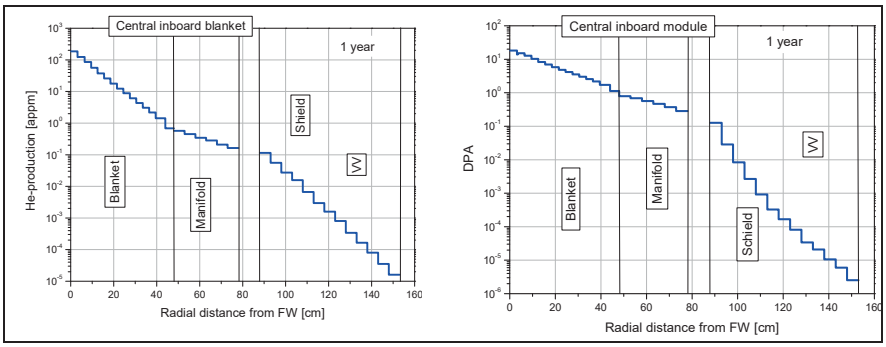

FIG. 7.23. He gas production (left) and displacement damage accumulation (right) in the steel structure of an HCLL-type DEMO reactor. Radial profiles across the inboard mid-plane are constructed assuming 1 full power year of operations at 2385 MW.

REFERENCES

[7.1] ALDAMA, D.L., TRKOV, A, FENDL-2.1: Update of an evaluated nuclear datalibrary for fusion applications, Report INDC(NDS)-467 (December 2004)

[7.2] http://www.iaea-nds.iaea.org/fendl3

[7.3] http://www.oecd-nea.org/dbprog/

[7.4] http://rsicc.ornl.gov/

[7.5] X-5 Monte Carlo Team, MCNP - A General Monte Carlo N-Particle Transport Code Overview and Theory (Version 5, Vol. I), Los Alamos National Laboratory, Report LA-UR-03-1987 (24 April 2003) (Revised 10/3/05)

[7.6] BROWN, F., LANL, MCNP lectures

[7.7] LU, L., LEE, Y.K., ZHANG, J., et al, Development of Monte Carlo automatic modelling functions of MCAM for TRIPOLI-ITER application, Nucl. Instrum. Methods Phys. Res. Sect. A, **605** (2009) 384–387

[7.8] GROSSE, D., FISCHER, U., KONDO, K., LEICHTLE, D., PERESLAVTSEV, P., SERIKOV, A., Status of the McCad geometry conversion tool and related visualisation capabilities" for 3D fusion neutronics calculations, Fusion Engineering Design, online available at http://dx.doi.org/10.1016/j.fusengdes.2013.02.146

[7.9] WILSON, P., TAUTGES, T., KRAFTCHECK, J., SMITH, B., HENDERSON, D., Acceleration techniques for the direct use of CAD-based geometry in fusion neutronics analysis, Fusion Engineering and Design **85** (2010) 1759–1765

[7.10] FISCHER, U., IIDA, H., LI, Y., LOUGHLIN, M., SATO, S., SERIKOV, A., TSIGE-TAMIRAT, H., TAUTGES, T., WILSON, P., WU, Y., Use of CAD generated geometry data in Monte Carlo transport calculations for ITER, Fusion Science and Technology **56** (2009) 702-709.

[7.11] FAUSSER, C., LI PUMA, A., GABRIEL, F., VILLARI, R., Tokamak D-T neutron source models for different plasma physics confinement modes, Fusion Engineering and Design **87** (2012) 787-792

[7.12] FISCHER, U., BACHMANN, C., PALERMO I., PERESLAVTSEV, P., VILLARI R., Neutronics requirements for a DEMO fusion power plant, Fusion Engineering and Design **98-99** (2015) 2134-2137

[7.13] FISCHER, U., BOCCACCINI, L.V., CISMONDI, F., COLEMAN, M., DAY C., HÖRSTENSMEYER, Y., MORO, F. PERESLAVTSEV, P., Required, achievable and target TBR for the European DEMO, Fusion Engineering and Design **155** (2020) 111553

[7.14] BATISTONI, P., ANGELONE, M., FISCHER, U., KLIX, A., KODELI, I., LEICHTLE, D., PILLON, M., POHORECKI, W., VILLARI, R., Neutronics experiments for uncertainty assessment of tritium breeding in HCPB and HCLL blanket mock-ups irradiated with 14 MeV neutrons, Nuclear Fusion **52** 8 (2012) 083014

[7.15] GUEBALY, L. El, MALANG, S., Towards the ultimate goal of tritium self-sufficiency: Technical issues and requirements imposed on ARIES advanced power plants, Fusion Engineering and Design **84** (2009) 2072-2083.

[7.16] FISCHER, U., BATISTIONI, P., BOCCACCINI, L.V., GIANCARLI, L., HERMSMEYER, S., POITEVIN, Y., EU Blanket Design Activities and Neutronics Support Effort, Fusion Science and Technology **47** (2005) 1052-59

[7.17] FISCHER, U., LEICHTLE, D., TSIGE-TAMIRAT, H., Neutronics characteristics of a solid breeder blanket for a fusion power demonstration reactor. Jahrestagung Kerntechnik '99, Karlsruhe, 18.-20. May 1999 Bonn: INFORUM GmbH (1998) 553-56.

[7.18] FISCHER, U., PERESLAVTSEV, P., HERMSMEYER, S., Neutronic design optimisation of modular HCPB blankets for fusion power reactors, Fusion Engineering and Design **75-79** (2005) 751-757.

[7.19] CHEN, Y., FISCHER, U., PERESLAVTSEV, P., WASASTJERNA, F., The EU Power Plant Conceptual Study – Neutronic Design Analyses for Near Term and Advanced Reactor Models, Forschungszentrum Karlsruhe, Report FZKA-6763 (April 2003)

[7.20] FISCHER, U., GROSSE, D., PERESLAVTSEV, P., STICKEL, S., TSIGE-TAMIRAT, H., WEBER, V., Neutronics Design Analyses of Fusion Power Reactors Based on a Novel Methodological Approach, Fusion Engineering and Design **84** (2009) 323-728.
[7.21] FISCHER, U., PERESLAVTSEV, P., GROSSE, D., WEBER, V., LI PUMA, A., GABRIEL, F., Nuclear design analyses of the helium cooled lithium lead blanket for a fusion power demonstration reactor, Fusion Engineering and Design **85** (2010) 1133-1138.

Chapter 8

MATERIALS FOR FUSION REACTORS

Sehila Maria González de Vicente
International Atomic Energy Agency
Vienna, Austria

Guido Van Oost
Ghent University, Department of Applied Physics
Belgium
National Research Nuclear University "MEPHI"
Moscow, Russia
National Research University "MPEI"
Moscow, Russia

Jan Willem Coenen
Forschungszentrum Jülich
Germany

Andrey Litnovsky
Forchungszentrum Jülich
Germany

Dmitry Terentyev
Belgian Nuclear Research Centre SCK.CEN
Mol, Belgium

Modern radiation damage research started with the installation of the first nuclear fission reactors in the USA. Already in 1946, Enrico Fermi pointed out that 'The success of nuclear technology will depend critically on the behaviour of materials in the intense radiation fields of the reactors'. Materials determine in a fundamental way the performance and environmental attractiveness of a fusion reactor: through the size (power fluxes to the divertor, neutron fluxes to the first wall); economics (replacement lifetime of critical in-vessel components, thermodynamic efficiency through operating temperature, etc.); plasma performance (erosion by plasma fluxes to the divertor surfaces); robustness against off-normal accidents (safety); and the effects of post-operation radioactivity on waste disposal and maintenance [1][2]. Materials constitute a key issue on the path to fusion power reactors. There is a strong need for materials which (a) are resistant to irradiation by a typical fusion neutron spectrum, (b) can operate at the highest possible temperatures, to allow for a good plant thermal efficiency, and (c) are as low activation as possible, to ease the public acceptance of fusion as a future energy source.

Radiation damage relates to the initial disturbance of a material under irradiation and arises from the interaction of incident particles (e.g. fission neutrons, fusion neutrons, high-energy protons, electrons and heavy ions) with the atoms (electrons and nuclei) of a target material (see Section 8.6). This interaction depends on the mass, electrical charge and energy of the incident particles, as well as on the properties of the target material. The incoming particles can lose their energy in the target through different types of processes:

(a) inelastic interactions with the target electrons, leading to ionization and/or excitation and therefore to electronic losses. In metals, the perturbation usually relaxes rapidly and leads (mainly) to heat dissipation;
(b) elastic collisions with the target nuclei, leading to atomic displacements or atomic displacement cascades (the displacement threshold energy is strongly dependent on the material and, for crystalline materials, on the surface crystallographic orientation with respect to the incoming particle);
(c) capture of the incoming particles by the target nuclei, leading to nuclear transmutation reactions and therefore to the production of impurities such as helium and/or hydrogen gas atoms as well as the transmutation of chemical elements such as tungsten to rhenium (see also Section 1.2.2.1). The products of such reactions are often unstable and decay by particle emission to different chemical species that may include radionuclides. Both emitted and residual nuclei are point defect impurities in the lattice. At elevated temperatures, they may diffuse through the lattice, cluster, and participate in precipitation reactions.

For a given material different types of incident particles yield differences in the structure of the atomic displacement cascades, and differences in the rate of production of impurities. In the case of electrons, usually no collision cascade occurs (i.e. one Frenkel pair is produced per electron). In the case of ions, only a relatively thin layer

close to the surface is irradiated, in an inhomogeneous way. Fission neutrons produce very few helium and hydrogen, while high-energy protons produce large amounts of impurities, including gas and metallic impurities.

Key irradiation parameters include the accumulated damage or irradiation dose, expressed in grays (Gy), the fluence or number of 'dpa' (displacements per atom, i.e. the number of times an atom is displaced from an equilibrium atomic site for a given fluence), the damage rate or dose rate (in dpa·s^{-1}) and the rates of production of the impurities (e.g. He/dpa and H/dpa ratios). The unit dpa is typically used to express material lattice damage by neutrons. Given a neutron flux, the dpa is material dependent.

Several critical phenomena are known to occur when neutrons are incident on material surfaces. The knowledge of the severity of the interactions is established in irradiations with fission neutrons, where radiation "hardening", radiation embrittlement, radiation swelling and radiation-induced thermal creep and high temperature helium embrittlement of grain boundaries have been measured. These primarily result from the displacements of atoms within the lattice following inelastic neutron-atom collisions and result in the formation of self-interstitial atoms and vacancies in the lattice that diffuse and aggregate to create a variety of extended defect complexes.

Radiation damage engenders radiation effects (see Section 8.6). The final microstructure of irradiated materials results from a balance between environmental conditions, especially radiation damage and thermal annealing, and stress-strain histories. It is therefore dependent on the initial composition and microstructure of the material and on the irradiation conditions, which define the initial radiation damage, as well as on the temperature of the material under irradiation. These microstructural changes are more stable than the initial damage and lead to an evolution of the properties referred to as 'radiation effects' (changes in dimensions, chemical composition, physical and mechanical properties).

Possible changes in the physical properties are a decrease of electrical conductivity (especially at low temperatures), thermal conductivity (especially for ceramic materials, see Section 8.3.3), or both. Changes in the mechanical properties include hardening (referred to as 'radiation hardening'), embrittlement effects, loss of creep strength (known as radiation enhanced creep), or combinations of these. Void formation may engender a macroscopic increase in the volume of the irradiated material, a phenomenon referred to as 'void swelling', leading to a loss of dimensional stability. Void swelling is an isotropic increase in the volume of a material due to irradiation-induced void (cluster of vacancies) growth. Irradiation creep and irradiation growth may also occur, as well as irradiation-assisted stress corrosion cracking. In addition, irradiated materials may become radioactive due to the formation of radioactive chemical elements by nuclear transmutation reactions.

Irradiation effects are strongly dependent on the temperature of the material under irradiation. Metals and alloys with a 'body-centred-cubic (bcc)' crystal lattice structure, including iron and ferritic steels (see Section 8.2.1), and tungsten, show better resistance to prolonged irradiation, in terms of much lower swelling and lower embrittlement (loss of elasticity, deformability, or both, of a material, making it brittle), than metals with face-centred-cubic (fcc) lattices. At low temperatures (e.g. below 673 K for steels), radiation hardening and embrittlement effects imply a loss of ductility, a loss of fracture toughness and an increase in the ductile-to-brittle transition temperature (DBTT) in the case of body-centred cubic (bcc) materials such as the ferritic/martensitic steels and the ferritic steels, their oxide dispersion strengthened (ODS, see Section 8.3.1.2) variants and refractory metallic materials (see Section 8.2.2). This increase in DBTT determines the minimum service temperature. An intermediate temperature range (e.g. 573 to 773 K for steels) usually corresponds to a peak in swelling. At higher temperatures (e.g. above 873 K for steels), irradiation-enhanced precipitation, bubble coarsening and creep effects arise. The critical temperatures mentioned in parentheses are strongly dependent on the material and the irradiation conditions.

Irradiation-induced degradation of the physical and mechanical properties and loss of the dimensional stability are the main factors limiting the choice of candidate materials for fusion-power reactors. In addition to an acceptable resistance to radiation damage, the materials should show high performance, high thermal stress capacity, compatibility with the coolant(s) and the other materials, a long lifetime, a high reliability, adequate resources, ease of fabrication at a reasonable cost, and a good safety and environmental behaviour. The residual radioactivity of a large amount of exposed material is an important concern and will govern the handling methods, dictate the recycling scenarios, storage periods and the overall waste management (see Chapter 1). The materials R&D strategy that considers these limitations has led to the development of the so-called 'low activation' or 'reduced activation' materials (see Section 8.2.1). R&D activities on materials for fusion-power reactors are focused on plasma facing, functional and structural materials [2] [1] [3] [4] and relate to the development of new high-temperature, radiation resistant materials, the development of coatings that will act as erosion, corrosion, permeation and electrical or magneto- hydrodynamic barriers, the characterization of candidate materials in terms of mechanical and physical properties, the assessment of irradiation effects, compatibility experiments, the development of reliable joints, and the development and validation of design rules. Magnetohydrodynamic (MHD) effects occur in a conducting liquid

flowing in a magnetic field and include flow laminarisation (and reduced heat transfer at the wall) and increased pressure drops due to the Lorentz force generated by the magnetic field which opposes the liquid metal flow.

In parallel to these activities, several designs for first wall/breeding blanket and divertor components (see Chapter 6) are being investigated in the different ITER member countries.

Almost everything that is known about material degradation in intense neutron fluxes comes from fission research (essentially moderate energy) neutrons. There are however good reasons to suppose that the effects of the high-energy fusion neutrons will be worse for a given neutron flux. One factor is that the inelastic lattice damage collisions become at least an order of magnitude more probable at high neutron energies. But the main factor is that primary knock-on atoms from fusion neutron collisions have correspondingly more energy, which directly leads to more displacements. Moreover, beyond a few MeV of incident energy, the neutrons interact with the lattice atoms resulting in transmutation products, helium and hydrogen.

ITER's primary mission is to demonstrate net thermal power production and the self-sustained burn of a fusion plasma at the reactor scale. However, it will not operate with a sufficiently high component temperature or duty cycle to provide an adequate proving ground for the materials used in constructing the first wall or handling the heat fluxes from the plasma. A higher duty cycle, obtained by operating very long duration or steady-state burning plasmas, is a prerequisite to obtain sufficient fluences of both the high-energy fusion neutrons to test the damage performance of in-vessel structural and high-heat-flux (HHF) materials, and the exhaust plasma ions to test intrinsic power handling and erosion properties of the HHF materials.

In ITER, the materials will be subject to much less severe environmental conditions than in DEMO and future fusion power reactors. For instance, the accumulated damage at the end of life should reach 3 to 5 dpa and the maximum temperature should be ~800 K (first wall conditions). Therefore, from the beginning of the ITER project, the general strategy was to use industrially available materials. However, the specific ITER operational conditions - for instance in terms of irradiations conditions, temperature range and mechanical stresses - required some modifications to several existing materials, by composition refining and thermo-mechanical treatments, to meet specific strength and safety requirements [5] [6].

As described in Chapter 6, the plasma facing components (first wall, divertor) and the breeding blanket components (see figure 8.1) will be exposed to the most severe operational conditions in a fusion reactor. The first wall will consist of a structural material attached to a plasma facing (or armour) material. The breeding blanket will consist of a neutron multiplier, a tritium breeding material, one or several coolants, and a structural material to separate and contain the different service materials. Both neutron multiplier and tritium breeding materials are called functional materials. The divertor will consist of a structural material (heat sink) containing a coolant and supporting a plasma facing (or armour) material.

Three types of materials (treated in Sections 8.3, 8.4 and 8.5) are therefore of primary concern: the plasma facing materials, which will serve as an armour for the underlying materials, the functional materials, which will have one or several functions (e.g. tritium breeding, neutron multiplication, optical transmission, etc.), and the structural materials, which will support the basic structure of the reactor.

Materials for the test blanket modules (TBM) are treated in Chapter 6; waste management issues in Chapter 1.

8.1. CLASSES OF IRRADIATED MATERIALS

The materials which require a degree of nuclear hardness for a fusion power plant can be divided into categories by the *missions* they themselves fulfil [1]; these are:

- **Structural Materials,** which provide the structures (walls, base-plates, etc.) for the in-vessel components, principally the breeding blanket (see Chapter 6 and below), the divertor cassette structure (see Chapter 6) and the vacuum vessel (see 8.2).
- **Plasma Facing materials,** which provide the 'first wall' armour exposed to plasma impingement on the breeding blanket and the divertor; see Section 8.4.
- **High-heat flux materials,** which allow for the efficient conduction of heat fluxes to the in-vessel coolant channels, especially in the divertor of a reactor where the heat fluxes will amount to several 10s of $MW \cdot m^{-2}$ (demanding a high-heat flux capability of the armour); see Section 8.4 and Chapter 6.
- **Functional materials,** which will have one or several functions (e.g. tritium breeding and neutron multiplication in the breeding blanket, optical transmission, etc.); see Section 8.3 and Chapter 6.

The internal components of a fusion reactor (see figure 8.1) will experience a variety of operating conditions related to temperature, temperature gradients, the local radiation dose, the dose rate, and the neutron energy spectrum. These parameters will have a significant impact on the materials selections and development. The lifetime of the

components will be determined by the resistance of functional materials as well as the resistance of plasma facing and structural materials.

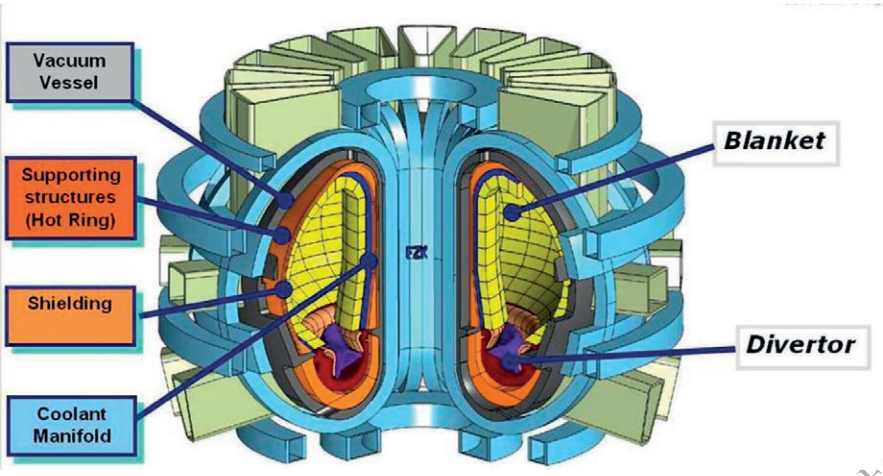

FIG. 8.1. Simplified schematics of the main types of components and materials that will be exposed to the most severe environmental conditions in a fusion power reactor (Courtesy of KIT).

8.2. CANDIDATE STRUCTURAL MATERIALS

The reliability and service lifetime of structural materials determine, to a large extent, the economics (in terms of cost of electricity), safety, environmental attractiveness and hence the overall commercial feasibility of fusion energy (see also Chapter 1). Structural materials will operate at elevated temperatures for extended lifetimes under severe conditions, characteristic of a fusion power reactor. The major areas of concern include thermal stress, mechanical stress, irradiation-induced deformation (irradiation creep and swelling), and chemical compatibility with coolants and tritium breeding materials (requiring fundamental information on corrosion and mass transfer behaviour). Within the topic of mechanical stress, several subtopics emerge which are of high importance, including plastic instability or overload conditions (determined from tensile properties of unirradiated and irradiated material over a range of test conditions), cyclic behaviour (determined from fatigue and crack growth tests), time dependent deformation (creep-rupture properties), and irradiation-induced embrittlement (determined from fracture toughness measurements)[1].

One of the most serious risks for structural materials comes from low-temperature embrittlement under neutron irradiation. Most commonly-used structural materials are ductile at normal temperatures, i.e. they have a ductile–brittle transition temperature below 273 K. Neutron irradiation shifts this DBTT to 'unusable' levels (i.e. DBTT above ~293 K), but the effect is known to depend on the temperature at which the irradiation occurs. This arises because the stability against embrittlement (and other radiation-induced mechanical problems) is provided by recombination of defects within the lattice, and this is a kinetic phenomenon, controlled by the thermally activated formation, dissolution and migration of the various radiation defects. Thus, irradiation effects at higher temperatures (where the definition of higher is material-dependent) can be annealed out. This leads to the concept of a 'temperature operating window' defined by radiation embrittlement and high-temperature thermal creep or other phenomena, which is very important for a potential structural material in a reactor because the demands of technology and engineering employed in the in-vessel design of the reactor place limits on the acceptable mechanical properties of the materials and their time dependence [2].

- The qualification of structural materials is a fundamental challenge due to:
  - High temperatures.
  - High levels of neutron irradiation.
  - High mechanical stresses.
  - High thermo-mechanical stresses.

- The thermodynamic efficiency of a reactor depends on:
  - The difference between the temperature of the coolant at the exit of the reactor and the temperature of the coolant at the entrance of the reactor.
  - These temperatures are mainly limited by the temperature window for use of the structural materials.

- The temperature operating window for use of the structural materials is mainly limited by their mechanical resistance under irradiation. The lower limit is determined by radiation-induced hardening and embrittlement. The higher limit is determined by creep resistance.

- Key issues for materials selection relate to physical, mechanical, chemical and neutronic properties such as:
  - High strength at high temperatures.
  - High surface heat capability: high thermal conductivity, low coefficient of thermal expansion. Surface heat capability is the product of the maximum allowable heat flux and the wall thickness ($W \cdot m^{-1}$).
  - Good resistance to radiation damage.
  - Compatibility with coolants.
  - Compatibility with other materials.
  - Long lifetime.
  - High reliability.
  - Adequate resources and easy fabrication.
  - Good safety and environmental behaviour (e.g. corrosion).
- Main candidate materials have a chemical composition that is based on low activation elements (e.g. iron, chrome, vanadium, titanium, tungsten, silicon and carbon):
  - Reduced activation ferritic/martensitic (RAFM) steels (8.2.1.1).
  - Oxide dispersion strengthened (ODS) RAFM steels (8.2.1.2).
  - Oxide dispersion strengthened RAF steels (8.2.1.3).
  - Tungsten-based alloys (8.2.2.1).
  - Vanadium-based alloys (8.2.2.2).
  - SiC/SiC_f ceramic composites (8.2.3).

Structural materials for breeder blankets are also treated in Chapter 6. Additional details can be found in [2], [7], [8], [9], and references therein.

.

8.2.1. Reduced activation steels and their oxide dispersion strengthened (ODS) variants

For structural materials, the reduced activation ferritic/martensitic (RAFM) steels are currently the most technologically mature option for the in-vessel structures of the proposed fusion power reactors. Advanced (or enhanced) next generation higher performance steels offer the opportunity for improvements in fusion reactor operational lifetime and reliability, superior neutron radiation damage resistance, higher thermodynamic efficiency, and reduced construction costs. The two main strategies for developing improved steels for fusion energy applications are based on (1) an evolutionary pathway using computational thermodynamics modelling and modified thermomechanical treatments (TMT) to produce higher performance RAFM steels and (2) a technologically novel, higher risk, potentially higher payoff approach based on powder metallurgy techniques to produce very high strength oxide dispersion strengthened steels capable of operating up to very high temperatures and with a potentially very high resistance to fusion neutron-induced property degradation [10].

8.2.1.1. Reduced activation ferritic/martensitic (RAFM) steels

The development of ferritic/martensitic steels for application in fusion devices emanates from the limitations of the austenitic stainless steels and the promising high dose experience with ferritic/martensitic steel fuel cladding in liquid metal cooled fast fission reactors.

Austenitic steels (e.g. 316L stainless) suffer from severe helium embrittlement at elevated temperatures and swell to a degree that is not acceptable for fusion reactor components. The performance of ferritic/martensitic steels in both swelling and helium embrittlement resistance is superior to that of austenitic steels. Ferritic/martensitic steels also exhibit a better surface heat capability (maximum allowable heat flux times wall thickness) than austenitic steels, favourable cost, availability and service experience, and their good compatibility with aqueous, gaseous, and liquid metal coolants permits a range of design options.

At the same time, ferritic/martensitic steels with alloying elements such as chromium, some tungsten, vanadium and tantalum activate little compared to conventional austenitic stainless steels with nickel and molybdenum, while manganese-stabilized austenitic stainless steels are not attractive due to high decay heat (safety) concerns.

RAFM steels contain elements selected to minimize fusion neutron production of highly radioactive and volatile nuclides during short time periods (relevant for public safety during accidents) and longer-lived radioactive isotopes that decay to low levels (e.g. suitable for recycling or shallow land burial) in the timeframes required by the waste management scenario (typically within 100 years following reactor shutdown) [11].

It has been demonstrated that it is feasible to produce RAFM steels on an industrial scale with sufficiently low impurity levels. Industry has also proven to be able to reproduce the required quality. The promise remains to produce low activation varieties that allow recycling within a century (see Chapter 1). The production of RAFM steels with even stricter impurity control is technically feasible, but requires fabrication equipment used for high purity steels only. The main investigated RAFM steels for fusion power reactors include the Chinese low activation martensitic (CLAM) steel, the European EUROFER-97 alloy (see Chapter 6), the Japanese F82H and JLF-1 alloys, and the Russian RUSFER-EK-181 alloy. F82H (Fe-8Cr-2W-0.2V-0.04Ta) and EUROFER-97 (Fe-9Cr-1W-0.2V-0.12Ta) are the RAFM steels which currently have the largest databases and have demonstrated feasibility in preparing the various required shapes, e.g. thin to thick plates, piping and tubing [11].

- Favourable properties:
  - Lower activation than austenitic stainless steels.
  - Good surface heat capability (maximum allowable heat flux times wall thickness; 5.4 $kW \cdot m^{-1}$ at 673 K; three times that of stainless steels).
  - Good resistance to helium-induced embrittlement and void swelling at $T \geq 673$ K (1 vol.% per 100 dpa compared to 1 vol.% per 10 dpa in stainless steels).
  - Favourable cost, availability, service experience.
  - Good compatibility with aqueous, gaseous, and liquid metal coolants.
- Main problems:
  - Body centred cubic (bcc) structure: DBTT = 183 K for EUROFER-97.
  - Limited strength at high temperatures: drop in tensile strength at ~823 K, strong reduction in creep strength at $T \geq 873$ K, significant softening under cyclic loading.
  - Irradiation-induced hardening and embrittlement effects at $T < 673$ K: loss of ductility, increase in DBTT, loss of fracture toughness.
  - Production of high amounts of helium and hydrogen.
  - Joining: more difficult to weld than austenitic stainless steels.
  - Limited database at high irradiation doses.
  - Effects of ferromagnetic properties on the plasma confinement (considering spatial inhomogeneity). It is currently considered that the ferromagnetic nature of high-Cr steels will not pose a major problem.
  - Narrow temperature operating window: 623 to 823 K.

Presently, several applications of RAFM steel near the plasma of fusion devices are prominent in Chinese, European, Japanese, Russian and US fusion power plant designs (see Chapter 1). First wall designs exist with RAFM steel as structural material and either a coating or tile-like armour elements on the plasma facing side of the structure. Several breeding blanket designs (see Chapter 6) use RAFM steel as structural material. Main European divertor designs also use RAFM steel as structural material, but in that case the need for higher operating temperatures is eminent.

Prospective fusion power plant designs put pressure on the materials aim at increasing the operating temperatures from 825 to ~1000 K. All structures (first wall, breeding blanket, divertor) would benefit from this temperature increase, resulting in a significant fusion power plant efficiency increase. The issue of higher temperature strength is thus strongly felt in the RAFM development, but in the short term the major effort is put on the successful operation of the TBMs (Chapter 6) implementing first generation RAFM steels (see Chapter 6). The demonstration of fabrication techniques resulting in reliable operations in ITER is therefore high on the priority list of the international fusion programmes.

Tensile and creep property data is sufficiently abundant to derive the allowable stresses for RAFM steels; the physical properties are also well documented. It should be possible to refine the composition of RAFM steels to improve their high-temperature mechanical properties (in particular their creep strength) and therefore their upper operational temperature. While the strength of the RAFM steel wrought products is well established, the mechanical properties of welded joints vary considerably.

Several irradiation campaigns on RAFM steels have been performed, are ongoing and are also planned worldwide: (1) low dose irradiation (less than 1 dpa) to support the modelling of radiation damage and radiation effects (see Section 8.6), (2) medium dose irradiation (up to 15 dpa) to constitute an engineering database for TBM design, and (3) high dose irradiation (up to 200 dpa) for applications in the first demonstration fusion power reactor (DEMO) and subsequent fusion power plants.

Post-irradiation experiments (PIE) on RAFM steels include mainly hardness tests, tensile tests, creep tests on small pressurized tubes, low cycle and high cycle fatigue tests, fatigue crack growth rate measurements, punch tests, fracture tests including Charpy impact tests as well as dynamic and static fracture toughness tests on bend bars and compact tension specimens. Microstructural examinations include mainly scanning and transmission electron microscope (TEM) observations, positron annihilation spectroscopy (PAS) and small angle neutron scattering (SANS) experiments.

Radiation effects on RAFM steels are well documented up to 15 dpa for all kinds of product forms and welded joints. The general result is that neutron irradiation at temperatures below ~673 K leads to strong hardening and embrittlement effects that include loss of ductility - characterized by a strong reduction in uniform elongation (the total elongation remaining quite large) - an increase in the DBTT, and a loss of fracture toughness. An additional tensile hardening is measured when cyclic temperature changes are performed during the irradiation. Because of neutron irradiation at 300 K, the irradiation-hardening rate of RAFM steels saturates at ~1.5 dpa, while at 575 K the irradiation-hardening rate decreases continuously with increasing irradiation dose. The rate of DBTT increase is strongly dependent on the product form and decreases with increasing irradiation dose. Following irradiation at temperatures above 675 K, very little hardening is measured. The DBTT shift also appears to be strongly reduced. It seems that at low doses the DBTT shift (ΔDBTT) is correlated with the tensile hardening (ΔH) at least in the case of neutron irradiation performed at ~473 K, i.e., at relatively low temperatures and in the absence of helium. This indicates that reduction of hardening should be effective in reducing the DBTT shift. At higher irradiation doses, the relationship between both parameters appears less evident.

Improvement of normalizing and tempering heat treatment conditions may help to minimize irradiation-induced effects. On the other hand, annealing of irradiated materials may lead to the suppression of radiation damage resulting from atomic displacements and the subsequent recovery of the original physical and mechanical properties (such as the DBTT). However, irradiation may also cause precipitate evolution, which could be difficult to recover using conventional heat treatments at intermediate temperatures. In addition, helium gas produced by nuclear transmutation reactions could also be difficult to recover, especially if located at the grain boundaries in the form of helium bubbles.

Possible gas atom effects are still a matter of controversy. The effects of helium and hydrogen on the physical and mechanical properties of RAFM steels are mainly investigated by means of implantation of high energy ions, boron or nickel doping, or the use of spallation neutron sources (see Section 8.5.1), or both. However, these methods represent relatively poor simulations of the production of gas atoms by nuclear transmutation reactions. Usually in dual- and triple-beam irradiation, only a relatively thin layer close to the surface is irradiated in an inhomogeneous way, and confounding effects due the proximity of free surface sinks are sometimes observed. Boron and nickel doping cause undesirable effects, since the composition of the material is changed, potentially leading to the formation of atypical phases during irradiation. In addition, boron and nickel elements often concentrate in peculiar areas, e.g. at the grain boundaries, favouring the production of helium in these areas. High-energy protons and mixed spectra, made of high energy protons and spallation neutrons, produce too high $He \cdot dpa^{-1}$ and $H \cdot dpa^{-1}$ rates with respect to fusion irradiation conditions, as well as metallic impurities whose effects on mechanical properties may become important at high irradiation doses.

Helium has also a significant impact on void swelling. For a given irradiation dose, void swelling resulting from dual-beam irradiation with iron and helium ions is much more important than void swelling produced by high-dose neutron irradiation in a fast reactor at temperatures above 675 K. In addition, the incubation dose for void swelling is much lower for ion irradiation than for neutron irradiation.

The effect of hydrogen isotopes on the mechanical properties of RAFM steels is another important concern. RAFM steels have a rather high susceptibility for hydrogen embrittlement, with threshold concentrations for transition from ductile to completely brittle behaviour.

Compatibility of RAFM steels with pressurized water, super-critical pressurized water, liquid Pb-Li, liquid lithium and the molten salt Flibe (Chapter 6, Section 6.3.4) has been investigated for application in TBMs as well as in fusion power reactors. RAFM steels exhibit a good resistance to corrosion by water, including super-critical pressurized water. It seems that water-cooled components of RAFM steels could be safely operated, at least under proper coolant chemistry control and low-to-moderate dose neutron irradiation. The compatibility of RAFM steels with flowing eutectic Pb-Li is a concern for dual-coolant tritium breeding blanket concepts. It has been shown that the resistance of RAFM steels to corrosion by flowing Pb-Li strongly depends on the flow rate and temperature. Therefore, it appears that coatings protecting RAFM steels against corrosion by liquid Pb-Li could be needed in the case of TBM concepts including the use of liquid Pb-Li.

Coatings have to be developed for RAFM steels to be used in fusion power reactors, which need to meet one or several of the following requirements (see also Section 8.3.3): (i) electrically insulating coatings to mitigate MHD effects in liquid metal type blanket concepts, (ii) tritium barriers to reduce tritium permeation, (iii) tritium containment

barriers to reduce tritium release to the environment, (iv) corrosion barriers to allow higher temperature operation, (v) helium coolant containment barriers to reduce helium leakage into the plasma chamber. Candidate tritium permeation barriers and barriers against corrosion by liquid Pb-Li include thin tungsten alumina (Al_2O_3) and erbia (Er_2O_3) coatings, produced by physical vapour deposition (PVD) for instance, as well as iron-aluminium multi-layered coatings with alumina as the top layer produced either by the hot dip aluminizing process or by chemical vapour deposition (CVD) of aluminium followed by oxidation or various plasma spraying processes. Millimetre-thick tungsten coatings produced by CVD or plasma spraying, for instance, are envisaged to protect the first wall (made of RAFM steel) against erosion, high temperatures, thermal shocks, etc.

8.2.1.2. Oxide dispersion strengthened (ODS) RAFM steels

Advanced high-performance ODS steels are being developed as structural materials for the longer term. ODS steels are sometimes called 'nanostructured ferritic alloys'(NFAs) in recent literature. Oxide dispersion strengthened steels are reinforced with a stable dispersion of uniformly distributed small (nanoscale) oxide particles. Such materials exhibit an improved creep resistance at elevated temperatures. As the upper temperature for use of RAFM steels is presently limited by a drop in mechanical strength at ~823 K, R&D is going on to develop RAFM steels with high strength at higher operating temperatures, mainly using stable oxide dispersion, usually yttria (Y_2O_3; see 8.4.3.1). Oxides are being used because their formation free energy is larger than that of sulfides, nitrides and carbides, and among them, yttria is one of the most thermodynamically stable phases. Furthermore, yttria is chemically more stable than titania (TiO_2) and less sensitive to neutron irradiation-induced activation than alumina (Al_2O_3). In addition, the numerous interfaces between the matrix and the oxide particles are expected to act as sinks for the irradiation-induced defects. As helium is essentially insoluble in metals, there is a strong tendency for it to form bubbles that can significantly degrade mechanical properties. A strategy to effectively manage helium is to provide a high density of internal interfaces to serve as helium bubble nucleation sites and vacancy-interstitial recombination centres. Main R&D activities aim at finding a compromise between good tensile and creep strength and sufficient ductility, especially in terms of fracture toughness.

- Favourable properties:
  - Increase in tensile strength with respect to EUROFER-97, even if a strong drop occurs in the temperature range of 823 to 923 K.
  - Increase in creep strength with respect to EUROFER-97.
  - Ductility like that of EUROFER-97 in the temperature range RT-450 to 823 K is reasonable.
  - The Y_2O_3 particles remain stable under irradiation and heat treatment, at least under the conditions investigated up to now.
  - The numerous interfaces between matrix and oxide particles are expected to act as sinks for irradiation-induced defects: helium bubble nucleation sites thus suppressing growth of helium bubbles, vacancy-interstitial recombination centres thus suppressing the accumulation of radiation induced microstructures.
- Main problems:
  - Body centred cubic structure: DBTT at 373 K in the unirradiated state; can be reduced by thermomechanical treatments.
  - Processing by powder metallurgy: coarse oxide particles with non-uniform size and spatial distribution, residual porosity, time-consuming, expensive. Processing by hot extrusion and typical thermo-mechanical treatments: non-isotropic grain shape.
  - Lack of joining techniques.
  - Poor knowledge of full characterization of pre-irradiation behaviour.
  - Stability of Y_2O_3 particles under irradiation and heat treatment.
  - Full characterization of effects of irradiation.
  - Operating temperature window up to 923 K.

ODS RAFM steels show a good resistance to oxidation, much better than that of conventional martensitic steels and like that of austenitic stainless steels as well as a good resistance to water corrosion. Few results are presently available concerning their resistance to radiation damage. It seems that neutron irradiation at intermediate temperatures to a few dpa yields radiation hardening but no significant loss of ductility. The dislocation structure and oxide particles were found to be relatively stable under fast neutron irradiation between 593 and 773 K to doses in the range of 2.5 to 15 dpa. As expected, with respect to RAFM steels, ODS RAFM steels show a much higher capacity for hydrogen and helium trapping caused by the smaller grain size and the presence of yttria particles in the RAFM steel matrix.

The ODS RAFM steel welding potential is under evaluation. The feasibility of joining ODS-EUROFER and EUROFER by diffusion welding has been demonstrated. New technologies, such as friction stir welding and pressurized resistance welding might solve the limitations of fusion welds. Limiting the maximum stir weld process temperature to 0.8 times the melting temperature produces defect free joints in ODS-EUROFER and other ODS steels. The stir method still has geometry limitations, but these could be reduced with further development.

As an alternative to the manufacturing of ODS steels by powder metallurgy, strengthening of martensitic steels by more conventional processing techniques (e.g. melting, casting, hot working, cold working, etc.) is being investigated. A special thermo-mechanical treatment of martensitic steels produces many small precipitates (precipitation strengthening). These steels exhibit strength and ductility as good as those of the best experimental ODS steels. An increase in creep-rupture life has been observed to commensurate with the increase in tensile strength.

8.2.1.3. Oxide dispersion strengthened (ODS) RAF (fully ferritic) steels

The potential of (high-Cr)12-14Cr ODS steels for increasing the operating temperatures up to ~1073 K is being investigated. If sufficient yttrium is added, optimal consolidation temperature and titanium content lead to steels with a high density of nanoclusters enriched with Y,Ti and O. Such ODS ferritic steels show excellent high temperature tensile and creep strength, as well as a very favourable oxidation resistance. Most of the R&D activities focus on the characterization of commercial ODS ferritic steels in the unirradiated and irradiated states, as well as on the development of new ODS RAF steels for fusion applications. These materials exhibit very promising mechanical properties, i.e. higher strength and lower DBTT values than the best available ODS RAFM steels. As compared to commercial ODS ferritic steels, these materials also exhibit a much higher creep strength at 1075 K due to a much finer distribution of Y-Ti-O nanoclusters.

Favourable properties:

- Excellent high temperature tensile strength.
- Excellent high temperature creep strength.
- Excellent oxidation behaviour.
- Promising results of neutron-irradiation at 693 K to 200 dpa (nanostructured ferritic alloy MA957): swelling like that of RAFM steels, tensile strengths unaffected, elongations slightly degraded, oxides resistant to radiation damage.
- The numerous interfaces between matrix and nanoclusters are expected to act as sinks for irradiation induced defects: helium bubble nucleation sites, vacancy interstitial recombination centres.

Main problems:

- Body centred cubic structure: work is in progress to reduce the DBTT.
- Processing by powder metallurgy: coarse oxide particles with non-uniform size and spatial distribution, residual porosity (Hot Isostatic Pressing, HIPping), anisotropic properties (hot extrusion), time-consuming, expensive. Processing by hot extrusion and typical thermomechanical treatments: non-isotropic grain shape.
- Lack of joining techniques.
- Poor knowledge of full characterization of pre-irradiation behaviour.
- Stability of Y-Ti-O nanoclusters under irradiation and heat treatment?
- Full characterization of the effects of irradiation.
- The upper operating temperature is increased by ~473 K with respect to RAFM steels.

8.2.2. Refractory metallic materials

The term refractory refers to the quality of a material that retains its strength at high temperatures. Refractory metals are characterized by their extremely high melting point, which lies well above those of iron and nickel. Refractory metallic materials include group V-A metals (V, Nb, Ta) and group VI-A metals (Cr, Mo, W). When the refractory metals are defined as metals melting at temperatures above 2123 K, twelve metals constitute this group: tungsten, rhenium, osmium, tantalum, molybdenum, iridium, niobium, ruthenium, hafnium, zirconium, vanadium, and chromium. Rhenium is the most recently discovered refractory metal, and its rarity makes it the most expensive of the refractory metals.

Refractory materials are chemically and physically stable at high temperatures. They are thus extraordinarily resistant to heat, thermal shock and wear. However, refractory metals are usually poorly resistant to oxidation and corrosion. Group V-A metals are much easier to fabricate than group VI-A metals but are more sensitive to interstitial solute gathering effects. Both groups have bcc structures and are prone to low-temperature brittle fracture associated with the presence of a DBTT. Poor low-temperature manufacturability and extreme oxidizability at high temperatures are shortcomings of most of the refractory metals.

Application of these metals usually requires a protective atmosphere, an ultrahigh vacuum or a coating. Refractory metals are used in lighting, tools, lubricants, nuclear reaction control rods, vacuum furnace technology, as catalysts, as well as for their chemical or electrical properties. Because of their high melting pointhttp://en.wikipedia.org/wiki/Melting_point, refractory metal components are usually not fabricated by casting, but by powder metallurgy. Refractory metals can be worked into wires, ingots, bars, sheets or foils.

Under neutron irradiation, refractory metals and alloys show severe embrittlement effects and a decrease of electrical and thermal conductivity, the latter leading to an increase in thermal stresses. R&D activities for application in fusion power reactors focus on tungsten-base materials (and vanadium based alloys), due to their reduced activation under neutron irradiation. Refractory alloys are being explored for plasma facing component structures and armours such as the first wall, divertor and blanket structures.

8.2.2.1. Tungsten-based materials

Research on tungsten has been focused on plasma facing applications [12]. For the divertor plasma facing components, tungsten is currently the material of choice for state-of-the-art technology, and it has been specified for use in ITER. Despite its brittle nature at lower temperatures (even after relatively light, ~1 dpa irradiation it has a DBTT of ~973 K), tungsten is favoured because of its high sputtering threshold for hydrogen ion bombardment, its consequently low erosion, and for its low retention of tritium, important to the minimization of mobilisable radioactive inventories in the tokamak reactor vessel. In addition, tungsten has a low level of long-lived transmutation products from neutron bombardment. Due to its numerous favourable properties, tungsten is the leading candidate armour material for a DEMO divertor and first wall, although the specific anisotropic microstructure of tungsten materials limits the applicability. Examples of tungsten-base materials include pure W, W-Re alloys, W-Cu pseudo-alloys, WL10 (W-1 wt.% La_2O_3), WVM (potassium doped W); wt is the weight percentage.

Favourable properties (pure W):

- High strength at high temperatures: it has the highest melting point of all metals and alloys (3683 K).
- Good surface heat capability (11.3 $kW \cdot m^{-1}$ at 1273 K).
- Good resistance to erosion.
- Does not suffer from high activation.
- Tritium retention properties.

Main problems:

- The inherent low fracture toughness at all temperatures associated with a high DBTT.
- Specific anisotropic microstructure of tungsten materials limits their applicability.
- High fabrication costs due to the brittleness of tungsten.
- Low ductility (deformability) and sensitivity to production history.
- Creep rate and strength between 973 K and 1573 K.
- Strong irradiation-induced embrittlement effects at T < 973 K: the irradiation-induced increase of DBTT is not yet known and could yield a DBTT value well above 873 K.

- The production by transmutation nuclear reactions of considerable amounts of osmium and rhenium (plus Hf, Ta, etc.) under neutron irradiation, which causes the formation of a brittle (intermetallic) sigma phase.
- Limited knowledge about irradiation effects in general.
- Joining of tungsten-base alloys to (ODS) RAFM steels.
- Operating temperature window: 1173 to 1573 K.

Perspectives:

- It is usually considered that tungsten is most suited for special purposes (e.g., plasma facing materials, coatings) due to its low ductility at low and intermediate temperatures.
- The development of tungsten-based alloys for high temperature structural applications is still at its very beginning. Tungsten-based alloys are candidate materials for structural applications in the high temperature region of plasma facing components, such as the 'high heat flux and high temperature heat removal units' of DEMO-relevant helium cooled divertor concepts.
- Development of advanced alloys: W-(0.3-0.7) wt.% TiC plastic working (e.g. hot forging rolling) after HIPping improves significantly the ductility at room temperature by reducing the grain size from 2.0 to ~0.5 μm.
- Development of nanocrystalline materials: Severe plastic deformation, electro-deposition. They are expected to show improved ductility and resistance to radiation damage, as grain boundaries act as sinks for irradiation-induced defects.
- Development of coatings: Thick W coatings (plasma spraying, chemical vapour deposition) to protect the structural material against first wall conditions. Thin W coatings (physical vapour deposition) as barrier against corrosion by liquid Pb-Li.

8.2.2.2. Vanadium-based materials

The emphasis of the worldwide R&D efforts is put on the V-Cr-Ti system containing 4–5 wt.% Cr and 4–5 wt.% Ti, in particular on the reference composition V-4Cr-4Ti and V-5Cr-5Ti alloys, but a number of alternative compositions and processing routes are being explored in an attempt to achieve improved performance. Vanadium base alloys are very attractive due to their low activation and good high temperature strength and surface heat capability (6.4 $kW \cdot m^{-1}$ at 675 to 875 K). They also exhibit a low DBTT in the unirradiated state (~66 K for unirradiated V-5Cr-5Ti), constant strength and good ductility in the temperature range of 475 to 1145 K, better creep resistance than the RAFM and austenitic stainless steels (up to 875 K for short durations), good fatigue resistance at room and intermediate temperatures, negligible irradiation-induced embrittlement at T > 675 K, good swelling resistance, and good compatibility with purified helium and liquid metals. Vanadium alloys, ODS RAFM steels and SiC/Si_f ceramic composites (see Section 8.3.3) are the three major candidate low activation structural materials.

Favourable properties:

- Low activation.
- Good surface heat capability (6.4 $kW \cdot m^{-1}$ at 673 to 873 K).
- DBTT at 73 K (unirradiated V-5Cr-5Ti).
- Good high temperature strength: constant strength and ductility in the range of 473 to 1073 K.
- Better creep resistance than the RAFM and austenitic stainless steels (up to 873 K and for short durations).
- Good fatigue resistance at room and intermediate temperatures.
- Negligible irradiation-induced embrittlement at T > 673 K.
- Good swelling resistance.
- Good compatibility with purified He and liquid metals.

Main problems

- Strong affinity for pickup of solute impurities such as oxygen (oxidation), carbon and nitrogen (dynamic strain aging at 673 to 973 K): matrix embrittlement, reduced compatibility with liquid lithium.
- High solubility, diffusivity and permeability of tritium; embrittlement at low temperatures.
- Severe thermal creep at high temperatures.
- Strong irradiation-induced embrittlement effects at T below 673 K.
- MHD effects (see Section 8.1) in relationship with the use of liquid lithium.
- Welding in an inert atmosphere.
- Lack of industrial maturity.
- Effects of irradiation-induced high He content?
- Effects of irradiation-induced formation of precipitates.
- Operating temperature window: 673 to 973 K.

Perspectives:

- Vanadium-based alloys remain very attractive due to their low activation and high surface heat flux capability.
- Solutions for use in fusion reactors:
    - To decrease the impurity level.
    - To develop reliable, fully adherent, corrosion barrier, self-healing insulator coatings (for liquid lithium blanket options).
    - How to improve the high T creep behaviour?
    - How to limit the effects of neutron irradiation?
    - Effects of irradiation-induced high He content?
    - To develop permeation barriers for impurity pickup.

The use of vanadium-base alloys for fusion applications requires reducing the impurity level, improving the high temperature creep behaviour, developing fully adherent, self-healing and robust MHD insulator coatings, and eventually finding a way to limit the effects of neutron irradiation. Knowledge about the influence of interstitial impurities such as oxygen, carbon and nitrogen on tensile, creep and fracture properties is not sufficient. Low temperature ($\leq$ 725 K) properties can be improved by removing oxygen, carbon and nitrogen, but the high-temperature creep strength is then reduced. Concentrations of interstitial impurities can be controlled by small additions of silicon, aluminium or yttrium. In particular, the addition of yttrium was found to be effective in reducing the oxygen level. High purity, large-scale V-4Cr-4Ti-Y ingots have been successfully produced by levitation melting, and V-4Cr-4Ti alloys with reduced impurity level appear to have sufficient creep strength to be used in the long-term self-cooled (with lithium) breeding blanket concept at temperatures up to ~1023 K. However, ideally, elements such as oxygen, carbon and nitrogen should be considered as alloying elements in vanadium, analogous to carbon in steels, rather than undesirable impurities. To achieve this goal, a much better control of these elements will be required. There is also a strong need for exploring alternative alloying elements and multiphase microstructures for improved creep performance and helium management, since the sink strength of V-4Cr-4Ti, for instance, for helium trapping may not be adequate.

Ultra-fine grained V-(1.6–2.6)Y alloys (in weight percent) with nano-sized Y_2O_3 and YN particles appear to be effective in reducing environmental and irradiation-induced embrittlement effects. However, these alloys exhibit a lower tensile strength than V-4Cr-4Ti alloys above 1200 K due to grain boundary sliding and lower solution hardening. The addition of 2.1 wt.% Ti to the V-1.7 wt.%Y alloy reduces significantly the decrease in high temperature tensile strength, and this positive effect tends to increase with temperature. Internal oxidation of Zr-containing vanadium-based alloys yields the formation of ultrafine ZrO_2 particles, which lead to an increase in low and high temperature strength of the alloys, their room temperature ductility remaining sufficiently high. It is thought that the upper temperature for use of vanadium based alloys could be increased by ~373 to 473 K using such method. As vanadium-based alloys are naturally oxidized, the retention and desorption behaviour of helium and hydrogen isotopes may

depend on the oxidised state of the surface. The diffusion behaviour of tritium in a V-4Cr-4Ti alloy has been investigated in detail. It is thought that tritium inventory in vanadium-base alloy blanket structures should be a minor issue for the self-cooled (with lithium) breeding blanket concept, because of the low tritium partial pressure in lithium.

Changes in mechanical properties due to the formation of precipitates under irradiation at high temperatures are a key issue. The precipitation behaviour seems to be affected by long range diffusion of oxygen. Concerning the effects of diffusion of interstitial impurities such as oxygen and nitrogen on the precipitation behaviour of Ti,(O,N,C), it seems that the precipitation rates under ion irradiation are determined by the initial impurity level and by the flux of oxygen that invades from the surface under irradiation.

In the case of the long-term self-cooled (with lithium) breeding blanket concept, a vital issue is to reduce the MHD pressure drop due to the Lorentz force generated by the magnetic field, which opposes the lithium flow. An insulator coating on the inside of the lithium flow channel is a possible approach to solve this issue. The coating will have a high electrical resistance to reduce the MHD pressure drop and a high chemical stability in liquid lithium (which is very reactive at high temperatures). Candidate coating materials include AlN, CaO, $CaZrO_3$, Y_2O_3 and Er_2O_3 ceramics. Thin erbia coatings prepared by PVD exhibit a good compatibility with liquid lithium at 1073 K, at least for exposure times up for 1000 to 2000 hours. Irradiation is one of the most important factors affecting their electrical insulating performance. It seems that degradation of insulating performance, due to radiation-induced electrical conductivity (RIC), depends weakly on temperature and will not prevent the achievement of the required performance in the high temperature and radiation environment of the breeding blanket. Multilayer coatings also appear promising: a vanadium based alloy layer could prevent lithium from interacting with the underlying ceramic insulating layer (e.g. Er_2O_3).

8.2.3. SiC/SiCf ceramic composites

SiC fibre reinforced SiC matrix ceramic composites (SiC/SiC_f) have attractive properties for functional and structural applications. SiC/SiC_f ceramic composites exhibit several advantages including (1) the ability to operate with good mechanical properties at temperatures much higher than steels (up to 1273 to 1473 K), with little reduction in strength up to 1273 K , which offers potential increase in fusion reactor efficiency; (2) an inherent low level of long-lived radioisotopes, which reduces the radiological burden of the structure; a (3) perceived tolerance against neutron irradiation up to very high temperatures, as bulk SiC exhibits moderate swelling at intermediate temperatures (up to ~1273 K). The peak temperature of void swelling in bulk SiC could be ~1848, or more.

The chemical composition, density, elastic constants, thermal conductivity and neutron irradiation resistance are different for SiC fibres and bulk SiC. With respect to SiC/SiC_f ceramic composites, the brittle characteristics of bulk SiC, such as low fracture strain and toughness, still impose severe limitations to its practical application. Development of high purity, dense, nanostructured bulk SiC with improved ductility is being investigated by compacting nanometric SiC powder particles using a series of successive processes including cold isostatic pressing, sintering and either HIPping or spark plasma sintering. The high thermal conductivity of SiC/graphite composites also offers potential for improved thermo-mechanical performance of SiC-base materials.

There exist many different SiC/SiC_f materials: they are currently at an early stage of development and are constantly evolving. The chemical composition, density, elastic constants, thermal conductivity, neutron irradiation resistance are different for SiC fibres and bulk SiC. With respect to SiC/SiC_f ceramic composites, the brittle characteristics of bulk SiC, such as low fracture strain and toughness, still impose severe limitations to its practical application.

Favourable properties:

- Very low activation (facilitating waste disposal and safety concerns).
- Much higher operating temperatures than steels (up to 1373 K).
- Little reduction in strength up to 1273 K (notion of failure is different from that in metallic materials).
- Good tolerance against neutron irradiation: bulk SiC exhibits moderate swelling in the range 423 to 1173 K.

Main problems:

- Low surface heat capability (2 $kW \cdot m^{-1}$ at 1073 K), dependent on processing conditions, type of fibres and fibre architecture.
- Structural stability under thermal loading.
- Strong irradiation-induced reduction in thermal conductivity, especially at low temperatures.
- Strong irradiation-induced reduction in fracture toughness.
- High He and H production rates under irradiation: swelling of 10.8 vol.% at room temperature for bulk SiC, associated with a crystalline to amorphous phase transition.
- Irradiation-induced damage is permanent (debonding).
- Limited knowledge about irradiation effects in general and especially irradiation creep.
- Development of joining techniques.
- Leakage of helium gas coolant into the fusion plasma, as most of the available SiC/SiC_f ceramic composites are still porous and anticipated to be vulnerable to widespread microcracking.
- Development of appropriate tritium barriers.
- Corrosion resistance under flowing liquid Pb-Li at high temperatures (up to 1373 K).
- Fabrication of large components.
- Structural design methodology.
- Operating temperature window: 873 to 1273 K.

Perspectives:

- SiC/SiC_f ceramic composites offer potential increase in fusion reactor efficiency (high operating temperatures).
- Whereas recent progress was driven by the availability of almost stoichiometric fibres with higher thermal conductivity and higher thermal stability, the next step will be to tailor the properties of the composite to the specific application by choosing the appropriate fibre architecture, fibre to matrix interface and densification processes.
- So far, focus of international fusion materials R&D activities has been on structural applications.
- However, the very first in-vessel application should probably be as a thermal and electrical barrier (flow channel insert) to insulate the RAFM steel from flowing liquid Pb-Li in the dual-coolant breeding blanket concept. This requires:
    - The design of a SiC/SiC_f composite material with stoichiometric fibres.
    - A good density to prevent liquid metal infiltration.
    - A high in-plane strength.
    - A thermal conductivity as low as possible through the thickness.
    - A high resistance against corrosion by liquid metal.
    - A high electrical resistance to minimize MHD pressure drop after ~100 dpa.
    - A 2-D fibre texture is recommended since low thermal and electrical conductivities

The operating ranges of various structural materials are summarized in figure 8.2 **[13]**.

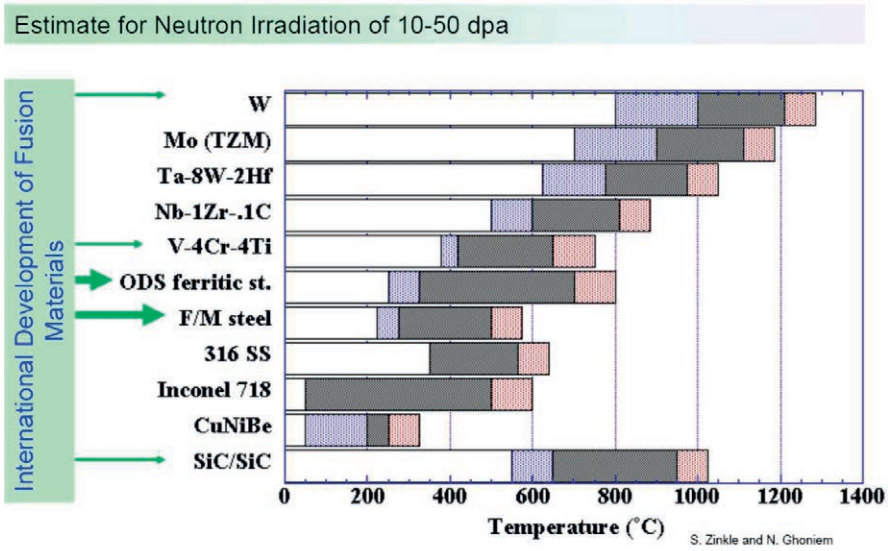

FIG. 8.2. Operating temperature windows (based on radiation damage and thermal creep considerations) for refractory alloys, Fe(8–9%)Cr ferritic-martensitic steel, Fe–13%Cr oxide dispersion strengthened ferritic steel, Type 316 austenitic stainless steel, solutionized and aged Cu–2%Ni–0.3%Be, and SiC/SiC composites. The light shaded bands on either side of the dark bands represent the uncertainties in the minimum and maximum temperature limits ***[13]***.

8.3. CANDIDATE FUNCTIONAL MATERIALS

The qualification of functional materials is also very demanding. Their mechanical resistance under irradiation is presently considered of no primary concern. However, material properties like the tritium release behaviour, thermal conductivity and structural integrity after prolonged neutron irradiation are important concerns as compared to structural materials, orders of magnitude more hydrogen and helium gas atoms will be generated in functional materials, e.g. in beryllium-type neutron multipliers and lithium ceramic-type tritium breeders. The irradiation resistance of other functional materials for diagnostics, such as ceramic insulators, dielectric and optical windows, optical fibres or complete sensor assemblies, is also an important concern.

Functional materials play important roles in the harsh irradiation environment of fusion power reactors. Irradiation modifies properties of functional materials both dynamically and irreversibly. Electronic excitation results in the formation of electronic defects and bulk thermal heating in general and in some cases in structural changes through a radiolysis (at high doses). It also causes modifications of the stability of defect complexes and in an increase of the mobility of point defects and ions. Radiation damage affects the microstructure of functional materials, resulting in changes of dimensions and mechanical and functional properties.

The qualification of functional materials is complex. Different functional materials are used for different purposes in a fusion machine: neutron multipliers, tritium breeding materials, ceramic insulators, dielectric and optical windows, optical fibres, and complete sensor assemblies. Their mechanical resistance under irradiation is presently not considered of primary concern. However, properties like the tritium release behaviour, the thermal conductivity or the entire structural integrity after prolonged neutron irradiation, are important concerns.

Selection of functional materials is very limited as it relies mainly upon the properties required by the envisaged function. The lack of adequate functional materials meeting the very high temperature design window is an important issue for fusion power reactors. Component lifetimes will be determined by the resistance of functional materials as well by the resistance of plasma facing and structural materials.

8.3.1. Tritium breeding materials

The tritium-breeding ratio (TBR) is defined as the amount of tritium generated by the breeding blanket of a deuterium-tritium fusion reactor divided by the amount of tritium burned in the reactor. A tritium-breeding ratio larger than unity is necessary for self-sufficient fuelling. The readers are referred to Chapters 6 and 10.

8.3.2. Neutron multiplier materials

The use of a neutron multiplier material is required to improve the TBR value. Beryllium and lead are the main candidate neutron multiplier materials via nuclear reactions of the type Be(n,2n) and Pb(n,2n), respectively. Lead has a higher cross-section for the (n, 2n) reaction for neutrons with an energy over 10 MeV, while beryllium multiplies neutrons over a much wider neutron energy range. The threshold energy for the (n, 2n) reaction is also much higher in lead, and thus a harder neutron spectrum is required for the lead multiplier. Further details are provided in chapters 6 and 7.

Therefore, beryllium has been selected as neutron multiplier for several breeding blanket concepts. Key issues concerning the use of beryllium relate to its compatibility with structural materials, tritium retention (following neutron irradiation atomic tritium appears to be dissolved in the beryllium lattice, while molecular tritium is contained in helium bubbles or small clusters in the vicinity of dislocations), high reactivity with water vapour (leading to hydrogen gas generation) and oxygen, large swelling and creep under neutron irradiation at high temperatures (typically 1175 K) and extreme brittleness after irradiation. In addition, beryllium is hazardous to human beings, beryllium natural resources are very limited and beryllium is therefore very costly. However, beryllium shows a good corrosion resistance against liquid lithium which is very important for the self-cooled (with lithium) breeding blanket concepts. In addition, high purity grades of beryllium became available, and 1 mm pebbles have been successfully produced from such materials. A major reason for using pebble beds in solid breeder blankets arises from the high-volume void fraction that provides accommodation space for swelling, as the DEMO end-of-life helium content in beryllium will be very high, equal to ~20.000 appm.

Beryllides like $Be_{12}Ti$ and $Be_{12}V$ may be more suitable as neutron multiplier materials in fusion power reactors as they exhibit a higher melting point, faster tritium release, much lower swelling and better chemical stability (i.e., lower chemical reactivity with air, steels and hot water) than pure beryllium. When exposed to water vapour, the chaotic breakaway reaction, which is known to take place at the surface of beryllium, does not occur at the surface of $Be_{12}Ti$, and the amount of water that reacts with this material is much smaller than in the case of beryllium. However, while fabrication routes and properties of beryllium are well established, there is still a lack of knowledge for beryllides.

8.3.3. Optical components, Dielectric materials and Coating Materials for Blankets

Behind the first wall protection are the materials in which radiation effects due to neutron and gamma flux interaction are dominant. Critical among these are the insulating materials (mainly oxides) used in magnetic coils, heating systems, and safety and control diagnostics. These applications strongly rely on the DC and AC/RF electrical and optical properties of the materials and associated components. The functional integrity of such systems is a key factor in the performance and reliability of the machine, and will only be ensured by the dependability of the materials used.

Beyond ITER (dose under 10 GGy) the expected first wall doses will increase up to 150 dpa for power plants. However, due to the first wall loading limit, the dose rates will probably be very similar. Hence ionizing dose rates ranging from less than 1 $Gy.s^{-1}$ to ~1000 $Gy.s^{-1}$, and displacement dose rates from under 10^{-11} to ~10^{-8} $dpa \cdot s^{-1}$ are expected for the numerous dielectric materials. This will lead to ionizing doses over 200 GGy, and displacement doses of many dpa.

Under these conditions the initial behaviour of the required dielectric materials will be very like ITER, but as damage accumulates changes are expected in the dose rate effects on physical properties. For the considerably higher doses (Gy and dpa – displacement per atom) an important influence of extended defects and structural damage is expected leading to changes in the physical and thermomechanical properties. Furthermore, nuclear reactions introduce transmutation products “impurities”, which will become important for DEMO and fusion power plants (FPP); see table 1 [14] [15].

TABLE 8.1. *Estimated maximum appm per year transmutation products for alumina. Based on 1 $MW.m^{-2}$ 1st wall loading.*

	H	He	C	N	Na	Mg	Si
ITER	29	50	62	3.4	7	44	1
DEMO	774	1340	1660	91	187	1170	27
FPP	1470	2550	3150	173	355	2220	51

8.3.3.1. Optical components and materials

Optical components (mirrors, windows, lenses, optical fibres, and optical coatings) are related to operational control and safety. They are present in diagnostics systems required for the analysis of optical radiation from the plasma. In fact, almost half of the ITER plasma parameters will be measured by optical or laser-based diagnostics (or both) over a range of wavelengths from the X ray region, vacuum ultraviolet, visible, infrared, to the millimetre electron cyclotron emission (ECE) region [16] [17] [18]. Such components are also needed for remote maintenance (remote handling systems) and to enable visual inspection and control to be carried out during any in-vessel operations. Optical fibres could simplify the design and maintenance for many applications, although their use is limited by radiation induced absorption and luminescence which, due to the length, are far more severe than for windows and lenses. In general, fibres, lenses, windows, and prisms will quickly degrade in high gamma and neutron dose rate regions near the first wall due to radiation induced optical absorption, emission, or both [16] [18] [19] [20]. Hence, they cannot be used as plasma facing components.

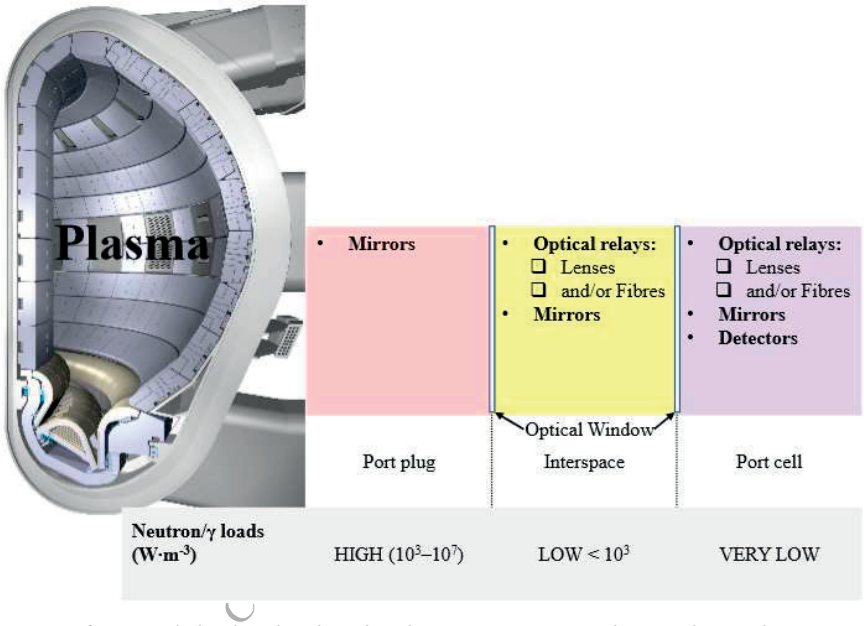

FIG. 8.3. Schematic view of neutron/γ loads related to the plasma position. Based on oral contribution "Radiation Hardness Testing of Functional Materials for Future Fusion Reactors" by R. Vila and S. M. Gonzalez de Vicente presented at the ISFNT - 11, 2013, Barcelona, Spain.

(a) Mirrors

Mirrors are essential components of optical methods for plasma diagnostics in a fusion reactor. They also serve as steering systems near the first wall, for example in electron cyclotron heating. Mirrors will be the components facing the highest radiation levels. According to their position, they can be classified into first mirrors (plasma facing mirrors) and secondary mirrors, located in dog-leg shielding ducts of different lengths (see Fig. 8.4).

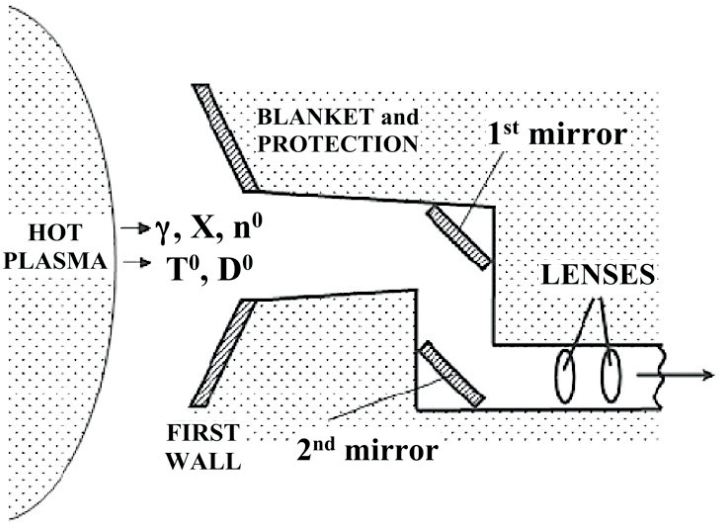

FIG. 8.4. Schematic layout of optical measurement components [17].

The first mirror brings the required radiation wavelengths out of the reactor vessel for analysis, and is the nearest diagnostics component to the plasma [21]. The neutron, gamma, and charge exchange atom (CXA) fluxes at first mirror positions will be about one order of magnitude less than those at the first wall [16]. For this harsh environment, metallic mirrors (polycrystalline bulk metal mirrors, metal films on metal substrate mirrors, and monocrystalline metal mirrors) are the main candidates. In the case of the secondary mirror, the use of dog leg shielding labyrinths reduces the neutron and gamma irradiation levels by at least three orders of magnitude relative to the first wall value, while the CXA flux at the secondary mirror surface will be negligible. This important reduction in the radiation level allows for the use of high reflectivity dielectric mirrors.

FIG. 8.5. Radiation enhanced corrosion of mirrors. Courtesy of E. Hodgson (CIEMAT, Spain).

(b) Windows

The ITER diagnostic systems will use more than 100 window assemblies on the primary and secondary vacuum boundaries [16]. For windows (as well as lenses and fibres) over the vacuum ultraviolet (VUV) to the near infrared (NIR) region, radiation induced optical absorption (RIA) and light emission or radioluminescence (RIL) impose severe limitations on the use of any optical material within an intense radiation field [22]. RIA is a function of fluence (dose): both ionization and displacement damage produce a build-up of defects (impurity and vacancy related) in the transparent insulator materials that generally result in transmission loss due to broad absorption bands in the UV to IR range. RIL, in contrast, is a function of flux (dose rate) and is caused by excitation of impurity and vacancy defects through electron and hole ionization production.

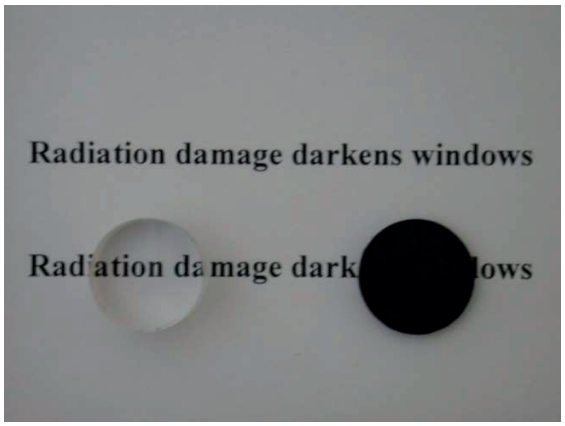

FIG. 8.6. Example of radiation reduction of transmission. Courtesy of E. Hodgson (CIEMAT, Spain).

For the UV–Visible–IR range, sapphire (Al_2O_3) and high purity fused silica (SiO_2) are the main candidates for optical diagnostic and remote handling systems (windows, lenses, optical fibres) as these materials show relatively high radiation hardness in terms of maintaining transmission under high levels of ionizing radiation (beyond 10 $Gy \cdot s^{-1}$) and atomic displacements (over 10^{-10} $dpa \cdot s^{-1}$) to doses above 10^{20} neutrons per square meters and over 1 MGy (see annex for basic radiation data), at elevated temperatures (100 to 200 ºC) [23] [24] [25] [26] [27] [28] [29] [30] [31] [32] [33] [34] [35] [36].

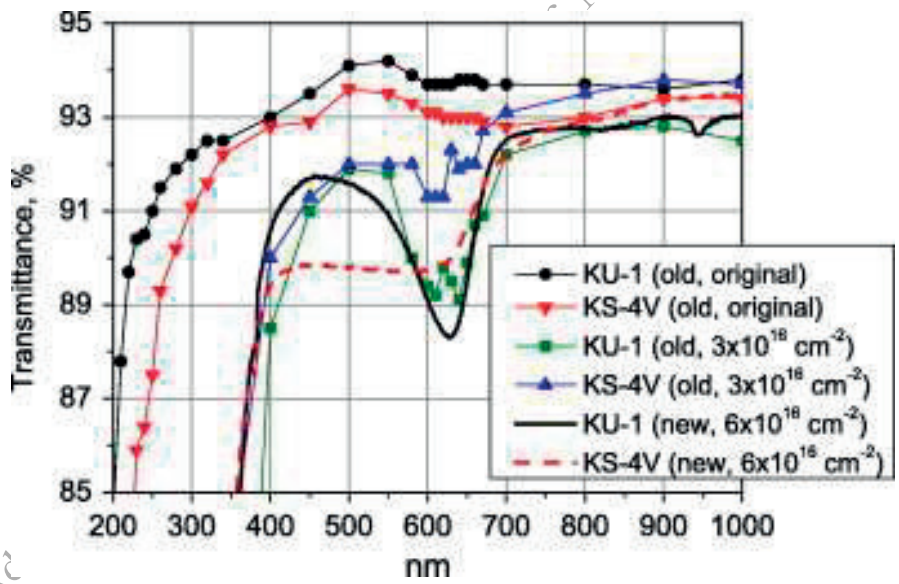

FIG. 8.7. Detailed transmittance of fused silica irradiated to 6 × 10^{16} cm^{-2} [30].

In the IR range, there are limited data about absorption and transmission loss for neutron irradiated IR materials such as Ge, Si, ZnSe, ZnS, CaF_2, BaF_2 and YAG [37] [38] [39] [40] [41] [42] [43] [44] [45] [46] [47]. Such materials are required for IR diagnostics, and are important for example to provide real-time monitoring of first wall temperature [48]. An alternative to these materials with limited transmission bandwidths and different radiation sensitivities is CVD diamond, which offers superior transmission properties from the visible to the mm wave (electron cyclotron resonant heating) region [49]. The CVD diamond now available for window applications has not only excellent mechanical and thermal properties but also considerable radiation hardness up to ~10^{-4} dpa [49] [50] [51] [52].

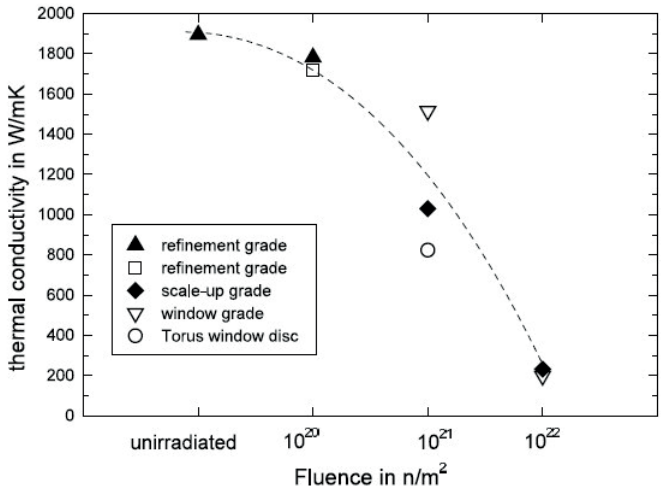

FIG. 8.8. Thermal conductivity of neutron irradiated CVD-diamond [49].

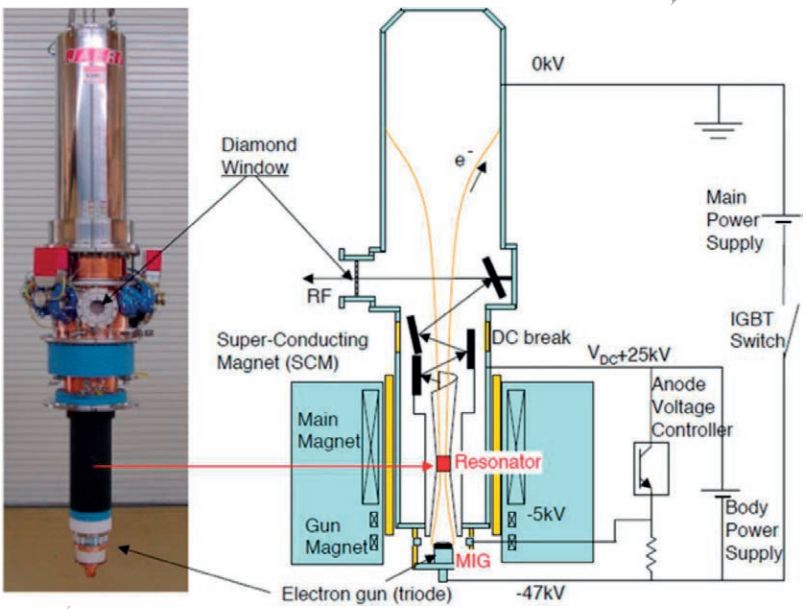

FIG. 8.9. Picture of the high power 170 GHz gyrotron in JAEA with a water-cooled diamond window [53].

As a final comment, it is important to stress that optical windows act as confinement barriers for tritium and other radioactive products, and that the effect of radiation on tritium diffusion mechanisms need to be assessed for any chosen material [54].

(c) Optical fibres

Optical diagnostic systems need complex pathways to provide adequate shielding for the different components (mirrors, lenses, windows) required to bring the light signals out of the vacuum vessel. The possibility that optical fibres might reduce this complexity, at least for part of the length, is well known [55] [56]and the design viability has been demonstrated on TFTR and JET [57] [58]. Although fibres might simplify the design and maintenance of many diagnostics (and remote handling applications), due to the length of the optical path, RIA and RIL are far more severe in the case of optical fibres than for windows.

Different optical fibres have been examined to assess RIA and RIL, the influence of hydrogen loading and jacketing material, as well as high temperature operation and annealing, and photo-bleaching using high intensity

lasers to recover transmission. Metal jacketing has allowed fibre operation at higher temperatures, as well as the possibility of post-irradiation annealing of the radiation induced defects. The most radiation resistant fibres tested to date are made of hydrogen loaded pure silica materials (KU1 and KS-4V from the RF, STU from Heraeus) drawn into aluminium jacketed 200 µm core-diameter fibres at FORC (Fibre Optics Research Centre, Moscow) [59]. Figure 8.10 shows the results for these fibres irradiated in the BR2 fission research reactor (SCK.CEN, Mol, Belgium) at 50 ºC, for doses up to ~5×10^{20} neutrons per square meter and 8 MGy. The ability for optical fibres to operate in a nuclear environment and maintain their transmission properties in the IR make possible using them as real-time and integrating dosimeters, operating at low level (~1 $Gy.s^{-1}$ to 1 kGy dose range) in inaccessible areas [60].

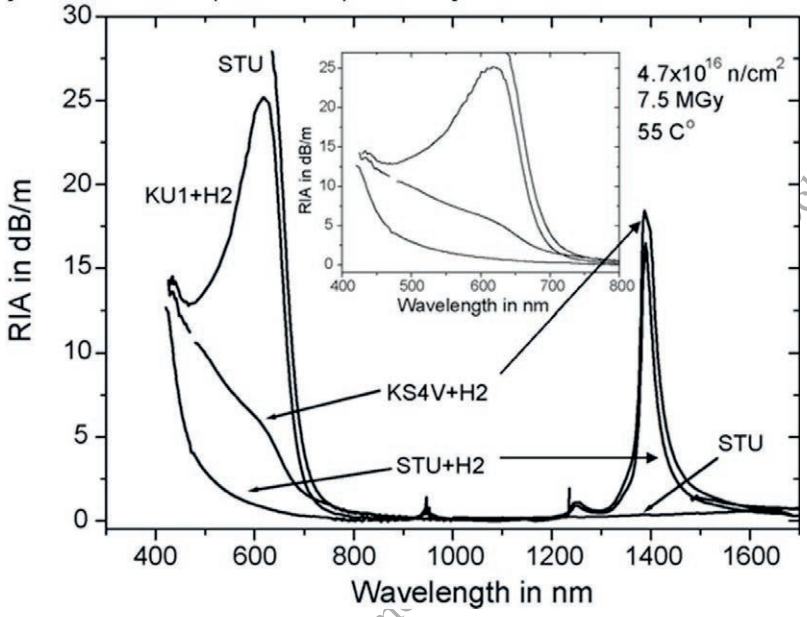

FIG. 8.10. Spectral comparison of the RIA response due to fission reactor irradiation. The lowest absorption is measured in the hydrogen treated STU [59].

8.3.3.2. Dielectric Materials

Dielectric materials will be required for numerous systems and components where electrical insulation for DC and AC/RF (Hz to GHz) is necessary. These include diagnostics, H&CD (NBI, IC, LH, and EC), and RH systems (see Chapters 2 and 11). These will need insulating materials ranging from simple supports, feedthroughs, stand-offs, mineral insulated cables, and wire insulation, to large NBI insulators and RF windows. For these applications, the thermophysical properties of immediate concern (i.e. at the onset of operation) are electrical resistance (usually discussed in terms of electrical conductivity, the inverse of resistivity), dielectric loss and permittivity, and thermal conductivity. Any reduction in the electrical resistance of the insulator material in these components may give rise to problems such as signal loss or impedance change, and (of greater concern) an increase in Joule heating. Similarly, for the AC/RF applications an increase in dielectric loss tangent gives rise to an increase in absorbed power within the insulator. Adequate thermal conductivity and cooling is needed to avoid catastrophic over-heating and thermal runaway. Typical property requirements are an electrical conductivity less than or equal to 10^{-6} $S\cdot m^{-1}$ (10^{6} Ωm), loss tangent below 10^{-4}, and high thermal conductivity (~30 to 1000 $W.m^{-1}.K^{-1}$ depending on the use). For those materials which satisfy and maintain the desired thermophysical property requirements, possible degradation of mechanical strength with operation time (dose) needs to be considered. Furthermore, components such as feedthroughs and RF windows also act as tritium barriers. The main candidate material for many of the applications is Al_2O_3 and is also the one which has been most extensively studied within the fusion programme, both in the polycrystalline alumina form and as single crystal sapphire. Furthermore, for more specific applications MgO, BeO, $MgAl_2O_4$ (spinel), Al N, CVD-diamond, and SiO_2 have also been studied [14] [16] [22] [56] [55].

(a) Electrical conductivity

Three potential types of electrical degradation in a radiation environment are recognized: these are radiation-induced conductivity (RIC) and radiation-induced electrical degradation (RIED), and surface electrical degradation [16] [22]. Of these three types of degradation, radiation induced modification of the insulator conductivity by RIC and

RIED has been extensively examined regarding fusion applications [14] [22]. RIC is sufficiently "well understood", and the available data indicate that this type of electrical degradation can be accommodated by the ITER design, using suitable available materials with electrical conductivities under 10^{-6} $S \cdot m^{-1}$ for ionizing dose rates above 10^3 $Gy \cdot s^{-1}$. RIC is strongly affected by defect and impurity content, both of which can decrease the effective lifetime of electrons excited into the conduction band by ionizing radiation and hence a reduction in RIC. This has been observed for alumina with different total impurity contents [61]. There is data indicating that RIC may be reduced with irradiation time (dose) from measurements done on neutron irradiated alumina [62], and possibly during in-reactor RIED experiments [63]. Neutron irradiation causes not only an increase in defect concentration but also a build-up of transmutation products (impurities). Although still not fully understood, RIED is potentially far more serious than RIC and has been reported under certain conditions to permanently increase, i.e. degrade, the electrical conductivity under irradiation [14] [22]. In alumina (Al_2O_3), for which most work has been performed, RIED is observed as a permanent increase or degradation of the electrical conductivity when an electric field is applied during irradiation at moderate temperatures (600 to 800 K).

8.4. CANDIDATE PLASMA FACING MATERIALS

8.4.1. Loading conditions

In addition to the neutron damage, the high heat flux (HHF) and plasma facing metals undergo bombardment by the ions and neutrals leaving the plasma. This is particularly virulent in a tokamak's divertor strike zones, where the heat flux can reach values over 20 $MW \cdot m^{-2}$ and the plasma particle flux can reach values over 10^{24} $m^2 \cdot s^{-1}$. In these cases, there will be a high level of sputtering and erosion of the material surface. Robustness against this damage (which will eventually erode the surface of the divertor and require a replacement) is the key parameter in the selection of divertor materials.

Copper alloys are considered as the material for the HHF heat sinks in the water-cooled divertor design. Their most serious issues relate to the rapid loss of ductility under irradiation at temperatures under 453 K (operating temperature should be kept above 473 K). This may necessitate composite material development.

The plasma facing components (PFCs: first wall and divertor, see Chapter 6) in existing and future fusion devices are strongly affected by plasma material interaction processes. On the one hand, these mechanisms have a strong influence on the plasma performance, and on the other hand, they have major impact on the lifetime of the plasma facing armour and the joining interface between the plasma facing material and the heat sink. Besides physical and chemical sputtering processes, high heat quasi-stationary fluxes during normal and intense thermal transients are of serious concern for the engineers who develop reliable wall components. In addition, the material and component degradation due to intense fluxes of energetic neutrons is another critical issue in D-T burning fusion devices which requires extensive R&D.

The divertor will be subject to intense thermal loads during plasma operation with power densities up to ~20 $MW \cdot m^{-2}$ for next step tokamaks. These requirements impose high demands on the selection of qualified materials and reliable fabrication processes for actively cooled PFCs. Besides the quasi-stationary heat loads, short transient thermal pulses (disruptions, ELMs, VDEs) with deposited energy densities in the order of several tens of $MJ \cdot m^{-2}$ are a serious concern for tokamak reactors. The most serious of these events are plasma disruptions whereby a considerable fraction of the plasma energy is deposited on a localized surface area in the divertor strike zone; the time scale of these events is typically in the order of milliseconds. Although a dense cloud of ablation vapor will form above the strike zone, only partial shielding of the divertor armour from incident plasma particles will occur. Consequently, thermal shock induced crack formation, vaporization, surface melting, melt layer ejection, and particle emission induced by brittle destruction processes will limit the lifetime of the components. In addition, dust particles (neutron activated or toxic metals or tritium enriched carbon) are a serious concern form a safety point of view. Instabilities in plasma positioning (vertical displacement events, VDE) may also cause irreversible damage to plasma facing components, particularly to the metallic wall armour.

Irradiation induced material degradation due to the impact of 14 MeV neutrons in D-T burning plasma devices is another critical issue, both from a safety point of view and with respect to component lifetime. Next step thermonuclear confinement devices such as ITER with an integrated neutron fluence in the order of 1 dpa (displacements per atom)[75] do not pose any unsolvable material problems. However, in future devices such as DEMO or in commercial fusion reactors with integrated neutron wall loads of 80 to 150 dpa, new radiation resistant materials should be developed and tested under realistic conditions. Due to the lack of an intense 14 MeV neutron source (see

[75] For low-Z materials 1dpa corresponds to approx. 10^{25} neutrons per square meter.

Section 8.5), complex neutron irradiation experiments are being performed in material test reactors to quantify the n-induced material damage. These tests provide a valuable data base on the degradation of thermal and mechanical parameters; in addition, the thermal fatigue and thermal shock performance of irradiated high heat flux components are other important issue for the engineering design, the licensing and the safe operation of future fusion reactors.

The design of PFCs involves diverse branches of science: (i) atomic and molecular physics (ionization, dissociation, and photon radiation of plasma and impurity species), (ii) surface physics (sputtering, chemical erosion, hydrogen trapping and release, and surface segregation), (iii) materials science (radiation damage, thermal fatigue, stress corrosion, creep, bonding, and hydrogen trapping), (iv) engineering science (stress management, heat transfer, and component design). Successful PFCs will be robust and forgiving and will operate very close to the limit of catastrophic failure. For further details, readers are referred to the discussion provided in [64].

8.4.2. Liquid metals

The success of magnetic fusion reactors strongly depends upon handling the challenging issues of power and particle exhaust. Tungsten is widely used in existing fusion devices for plasma facing components (PFCs). Tungsten will also be used in the ITER divertor due to its high thermal conductivity, low sputtering yield and high melting point. However, even in the absence of neutron irradiation, conventionally available tungsten suffers from cracking due to its high ductile-to-brittle transition temperature (DBTT). It is estimated that the thermal load limit for a solid tungsten divertor is ~5 to 20 $MW \cdot m^{-2}$, which is almost an order of the magnitude lower than what is expected in a 3 GW fusion reactor [65] [66] [67]. Growing efforts are thus being devoted to the development of advanced tungsten-based materials (Section 8.4.3).

An alternative to solid plasma facing components is the use of liquid metals such as lithium. Liquid metals offer the benefits of the self-healing properties of liquid surfaces and the possibility of in situ replacement of surfaces exposed to the plasma by capillary forces. The vapor shielding effect provides plasma facing component (PFC) resilience against transients and neutron loading. Liquid metal PFCs also feature fuel retention capability, a critical issue for the tritium inventory and general safety in fusion reactors. However, the use of these materials in fusion reactors depends on the degradation of the discharge performance due to enhanced plasma contamination by impurities. Fortunately, recent experiments have shown a strong reduction of retention with increasing lithium temperature and demonstrated the release of retained hydrogenic species by thermal treatment.

The first lithium wall conditioning experiments were conducted in the nineties on the tokamak fusion test reactor (TFTR) in Princeton, USA, showing improved core confinement. Since then, the use of lithium in fusion devices significantly increased worldwide. Lithium has also gained in popularity as a plasma facing material (PFM) [65] [68] [69] [67], and will be used in fusion neutron sources (see 8.5.2.). However, compared to solid materials PFCs, liquid metal PFCs are far less investigated in the fusion community. Liquid lithium related issues include:

- Liquid lithium exhibits a large hydrogen isotope trapping coefficient, which on the other hand makes it a perfect candidate material for particle exhaust facilitating tritium extraction. On the other hand, large hydrogen solubility leads to lower recycling at the plasma edge, which may not be compatible with reactor operations. However, lower recycling and lower edge density increases edge temperatures and reduces the temperature gradient, which may help reduce electron turbulence and enhance plasma confinement [70] [71]. To keep the edge density low the fuel must be injected into the core plasma and not introduced by gas puffing, e.g. by injection of cryogenic DT pellets [72].
- The use of flowing liquid metal PFCs allows for continuous recirculation and PFC regeneration in a closed loop complete lithium circulation system (not just the use of the latent heat properties of melting lithium) with a collector for liquid metal waste and unused fuel. This approach avoids dust formation and the issues related to embrittlement caused by helium, volumetric swelling, material structural disintegration, neutron induced long term damage as well as tritium retention in the material [73] and Chapter 10. However, no realistic concept exists.
- Extraction technologies for the recovery of hydrogenic species captured by lithium must be verified on large scale lithium-loop systems separating lithium impurities, recovering deuterium and tritium, and recycling clean lithium back to the plasma-material surface. Co-deposition of lithium with hydrogen isotopes can lead to the accumulation of lithium hydrides and large quantities of tritium. Liquid lithium's high thermal capacity and low atomic number holds a great promise for high thermal load handling and low plasma contamination [65]. Evaporated lithium becomes ionized very rapidly and is seen to reduce the heat load of the divertor by radiation losses. As lithium gets ionized very quickly the penetration of lithium to the core of the plasma is very low and does not induce radiation losses in this region. Lithium is compatible with steel and refractory

materials. However, liquid lithium's melting point casts doubts over its compatibility with a tungsten first wall, which will be heated to high temperatures (773 to 973 K) to keep it conditioned [65] [74] [66]. The liquid lithium divertor, on the other hand, is kept at temperatures in the range of 473 to 723 K to keep the lithium liquid at a low evaporation rate

- Despite all these benefits, the hot tungsten first wall is expected to retain varying amounts of lithium and lithium-related impurities. This calls for the investigation of the amount of retained fuel within the lithiated tungsten and the possible enhancement of sputtering [65] [69].

Two main approaches are presently available for the application of liquid lithium as a divertor material, with different degrees of maturity. The first approach directly employs fast moving liquid lithium within the vacuum vessel (e.g. IFMIF, see Section 8.5). This can be implemented as free falling curtains or using special trenches with a self-pumped flow, using thermoelectric magnetohydrodynamics to remove heated lithium and replenish it at a lower temperature. However, there exist great uncertainties related to the behavior of free-surface liquids (with no extra holding force but gravity) in a strong magnetic field and vapors interacting with the edge plasma, particularly during transient events.
Therefore, a second approach employing capillary porous systems (CPS) has been developed in Russia. CPS make use of large surface tensions to stabilize and force the liquid metal through the porous mesh [65]. The tension forces also act as a capillary pump that replenishes the liquid metal. This allows good coverage of the PFC with low risk of splashing and droplet formation and offers surface replenishing capability. The thickness of the liquid metal film coating the porous matrix remains to be investigated as a function of liquid metal properties, operational conditions and topography of the mesh. Molybdenum is presently considered as the primary substrate material for its corrosion resistance and wettability for liquid lithium. However, the underlying substrate may be exposed to plasma due to the destruction of the lithium layer. Therefore, the synergy of helium plasma irradiation and liquid lithium corrosion on molybdenum is to be evaluated. Although the CPS concept is promising in terms of relative simplicity of implementation and testing, the understanding of its power handling capabilities is still limited, especially during transient events as well as concerning the role of vapor shielding. The power exhaust by heat conduction to the substrate is not sufficient and hybrid systems based on conduction, evaporation cooling and plasma radiation are required.
Besides lithium, tin (Sn) has more recently been proposed as a PFM. Lithium (atomic number 3, atomic weight 6.9, melting point 453 K, boiling point 1603 K) and tin (atomic number 50, atomic weight 118.7, melting point 505 K, boiling point 2875 K) exhibit a very different behavior. For instance, tin is compatible with tungsten, but incompatible with steel and with molybdenum above 1073 K. The operating window of tin is also much larger owing to its lower vapor pressure at a given temperature and allowing higher heat loads on the surface. However, the main attractive of liquid tin is its low hydrogen retention. Despite its advantages, the wettability of tin is lower than that of lithium and it has been observed that oxide reduction is required to improve the wetting conditions for tin when coupled to CPS systems [65]. In any case, more R&D is needed.
Lithium-tin alloys are also being investigated for candidate alternatives in power exhaust handling solutions for future reactors. These alloys offer unique properties in terms of evaporation, fuel retention and plasma compatibility. It is recommended to use molybdenum instead of steel, which otherwise dissolves in tin.
A wide range of innovative liquid metal PFC concepts have been proposed for DEMO and FPPs. However, issues of tritium retention, core impurity accumulation and material compatibilities impose strict power and temperature ranges which are not yet clearly established. For further details consult [65] and references therein.

8.4.3. Advanced materials

8.4.3.1. Development of self-passivating tungsten-based alloys

(a) Safety mission for materials in a fusion power plant

Future fusion power stations like DEMO will require a new level of understanding in fusion physics [75] and represent an unprecedented challenge in managing fusion power exhausts [76]. Plasma facing first wall components in DEMO will have to withstand the unprecedented particle fluence, intensive plasma radiation and the highest neutron fluences. All these parameters are by several orders of magnitude higher than in any existing and prospective experimental fusion reactor, including ITER [77] [78]. This makes the realization of fusion power plant an outstanding technological challenge.

Several material advantages such as a high melting point, a low retention of the radioactive tritium, a high ductility at elevated temperatures, and a moderate activation under neutron impact make tungsten (W) a prime candidate to be used in future fusion power plants. At the same time, the material evaluation for the application in DEMO clearly shows an inability of any existing plasma-facing materials to withstand the combination of plasma,

radiation and neutron power loads. This harsh reality requires the development of new advanced plasma-facing materials.

In addition to high operational limits, safety is paramount for future fusion power plants. In case of a severe accident (see Chapter 1) such as the so-called loss-of-coolant accident (LOCA), tungsten plasma-facing components could reach temperatures of 1473 K due to the nuclear decay heat in absence of a coolant [5]. In case of simultaneous air ingress, the neutron-activated tungsten (W) forms the volatile oxide WO_3, leading to the sublimation of radioactive volatile species into the environment. The modelling estimates the release of 10 to 100 kg of sublimated material per hour [79] leading to the complete mobilization of the tungsten first wall within one to two months after an accident, which is unacceptable.

(b) Advanced self-passivating tungsten-based alloys

Advanced tungsten based self-passivating, so-called "smart", alloys were introduced to address the above-mentioned issues [80]. The smart alloy is supposed to adjust its behaviour to the environmental conditions. During regular plasma operation, the alloying elements will be removed due to preferential sputtering by plasma ions, Fig. 8.11-left. As a result, the plasma will face an almost pure tungsten surface. In case of an accident, the alloying elements remaining in the bulk creating their own dense protective oxide scale, thus preventing the sublimation of tungsten, figure 8.11-right. Extensive studies of smart alloy systems have been undertaken worldwide [81] [82] [83].

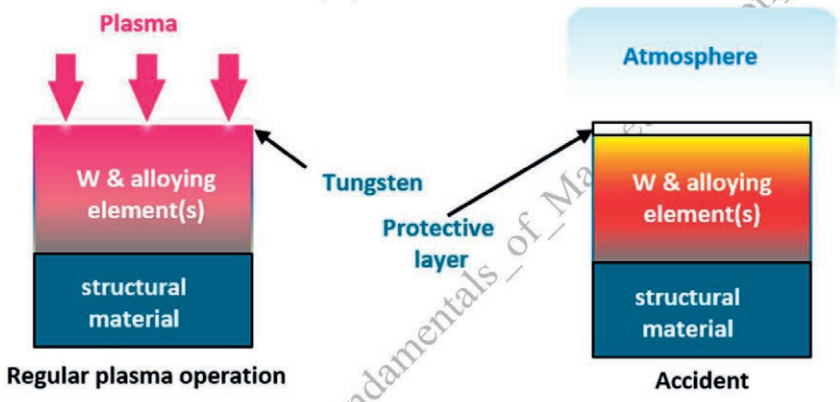

FIG. 8.11. The scheme of operation of smart alloys during regular plasma operation and accidental conditions.

There are several requirements imposed on the selection of alloying elements for a fusion power plant; those:

1. must allow for a small volume increase due to oxidation,
2. must possess low activation,
3. should have a high melting point,
4. should provide a good adhesion to the substrate.

(c) Role of yttrium

Presently, the most advanced alloying systems contain chromium (Cr) as a passivating element. The chromium-containing tungsten-based smart alloys feature rather high melting points of ~3000 K making them attractive candidates for an application as plasma-facing materials in DEMO. At the same time, the long-term passivation of the W-Cr alloy could not be realized due to the mechanical instability of the formed oxide layer for this binary system and the formation of tungsten-containing oxides on its surface after long-term exposures. To resolve this issue, the introduction of a third, so-called "active" element is advantageous. Introduced in small amounts into the alloy system, active elements can dramatically improve the performance of the system. Intensive research was conducted with different alloying elements. Yttrium (Y) is one of the most efficient active elements, well-known from the research on steels. The main properties of yttrium-containing alloys are shown schematically in figure 8.12. According to present knowledge:

- Yttrium is supposed to occupy the inter-grain locations enhancing the diffusion of Cr necessary for the formation of the protective oxide layer [84] [85], Fig. 8.12a.

- Yttrium stimulates inter-grain oxidation leading to smooth, well-adhering protective alloys with suppressed pore formation [85] [86] [87] [88], figure 8.12b.
- Due to its high chemical reactivity, yttrium is likely to bind the impurities, which may otherwise de-stabilize the formation of the oxide layer [89], Fig. 8.12c.

Yttrium is also known for its dense [90] and chemically stable oxide [91]. These properties bring additional advantages to yttrium-containing alloy systems.

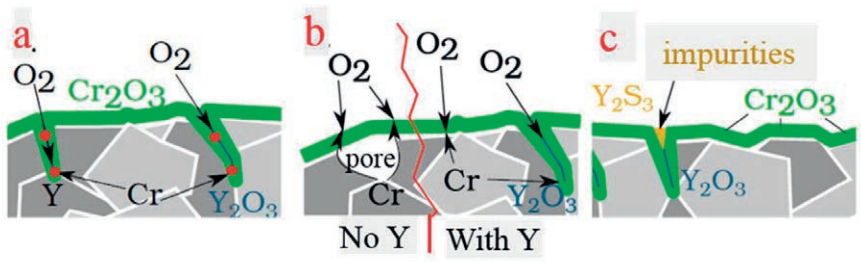

FIG. 8.12. Effects of yttrium on oxide formation: 1) formation of stabilizing oxide pegs 2) segregation on grain boundaries and prevention of pores and 3) trapping of impurities and avoidance of nucleation sites [79].

(d) Smart alloy research and development

The research and development of smart alloys consists of three main stages:

I. At an initial stage, the prospective smart alloy systems are produced in the form of thin films, with the typical thicknesses between 1 and 10 µm, which can be produced very fast, ~1 to 3 hours. At the same time, the thickness of such a system allows for short studies of oxidation properties and is therefore crucial for the initial evaluation of a given elemental composition.

II. The most promising thin film candidate alloy systems are then chosen as a basis for bulk sample production. Bulk samples are usually produced following a powder-metallurgical route. They usually have dimensions of several millimetres to several centimetres allowing for long-term and lifetime studies of their performance.

III. The best bulk smart alloy samples undergo performance tests. Presently, performance tests comprise the exposure of samples to steady-state deuterium plasmas under DEMO-relevant plasma parameters followed by the oxidative study of plasma-exposed samples, thus covering both performance under regular plasma operation of the power plant as well as under accidental conditions.

During the oxidation, the mass change of the sample is usually recorded. In case of passivation, an oxidation process is driven by the diffusion of oxygen and alloying elements through the protective layer. If the protective layer is stable and there is no cracking or delamination, the mass change Δm is proportional to the increase in oxide volume. Since oxidation is controlled by diffusion, the increase of the volume is proportional to the diffusion depth of oxidation:

$$L \sim (Dt)^{1/2} \qquad (1)$$

where D is the diffusion coefficient and t is the oxidation time [10]. It can be inferred from equation (1) that the change of the volume and the corresponding mass change is proportional to the square root of time, demonstrating the so-called “parabolic behaviour”.

(e) Production of smart alloy systems

Presently, the main purpose of bulk smart alloy samples is to ensure a large reservoir of alloying elements guaranteeing the passivation for the entire lifetime of the first wall in DEMO. At the same time, the developed bulk alloys should have a thickness in the order of the first wall cladding expected in DEMO i.e. 2 mm [92]. As seen on thin films [79] [93], the homogeneity of the smart alloy plays a crucial role in obtaining the passivating behaviour. Therefore, providing an as homogenous as possible distribution of alloying elements is crucial. Several processes, like re-crystallization, lead to crystal growth thus degrading the required homogeneity. Therefore, re-crystallization must be prevented, if possible. The production of bulk smart alloys consists from two main stages:

1) the mechanical alloying of the elementary powders and

2) the sintering of the alloyed powder.

The decisive advantage of mechanical alloying is in its ability to produce an alloyed material as a powder at room temperature. It is much a more controllable way of producing alloys than baking. On the other hand, the mechanical alloying is a rather long process, taking tens of hours to obtain the alloyed powder. Nevertheless, the production of smart alloys usually starts with mechanical alloying. The elementary powders are milled together under an argon atmosphere using a planetary mill system. The aim of this stage is to create a solid solution of tungsten and alloying element(s).

There are different ways of realizing the second stage of production of the smart alloy systems. In [94] [95] and [96], bulk smart alloy samples were produced using hot isostatic pressing (HIP). The recent results obtained on such bulk W-Cr-Y systems however, demonstrate the massive transport of tungsten through the protective oxide layer [95]. The inhomogeneity of the elemental distribution along such samples may be responsible for the noticed degradation of oxidation resistance in comparison with that of the thin film samples. At the same time, the investigations performed with thin films, show perfect passivation with dense protective Cr_2O_3 layer for a time limited by the Cr reservoir. The afore mentioned studies suggest the crucial role of the highest homogeneity of the elements along the alloy together with the smallest possible granularity of the alloy.

Therefore, recent efforts have concentrated on finding the sintering technique(s) capable of producing the most homogenous alloy systems, approaching thin films in their homogeneity and grain size. To attain the required homogeneity, an alternative technique was applied to produce bulk smart alloy systems: spark plasma sintering (SPS) also known as field-assisted sintering technology (FAST) [97]. In FAST, the powder is placed in a graphite die between two graphite punches, which apply uniaxial pressure during the thermal treatment. The maximal pressure is typically under 100 MPa, meanwhile the maximum temperature of the FAST process is ~2473 K. Joule heating, caused by the pulsed DC current with low voltage and high intensity (10^3 A), occurs through the graphite system. The main advantages of FAST are:

1. High heating rates: heating rates faster than 373 K per minute are typically achieved in FAST due to the pulsed DC current. This is highly beneficial for the reduction of the time spent by the sample at high temperatures. High heating rates allow attaining the desired temperature faster, thus minimizing the residence time at high temperatures. This decreases the risk of undesirable corresponding grain growth, which deteriorates the homogeneity required for an efficient suppression of oxidation.
2. Pressure: uniaxial pressure during the thermal cycle promotes the densification, reducing the maximal temperature required to fully densify the material.
3. Reduction of time: the fast heating rates and short isothermal holding time (~ min) to densify a material reduce the time that the sample is at high temperature. This saves a lot of energy and allows for the tailoring of the final microstructure, by reduction or inhibition of the grain growth.
4. Ability to operate below the recrystallization temperature: The reduction of the maximal temperature due to the uniaxial pressure and the DC current leads to densified materials at lower temperatures than the alternative sintering techniques. As a result, it is possible to densify materials below the recrystallization temperature and avoid the degradation of certain compounds.

Several bulk smart alloy samples were produced with the FAST technique featuring different FAST parameters: heating ramp, maximum temperature and a holding time at maximum temperature. These studies demonstrated that avoiding the holding time and imposing the steepest temperature ramp enabled the achievement of a very fine structure with compact sub micro-grains under 200 nm in size and the finest Y distribution along the boundaries of the formed grains (see Fig. 8.13). The oxidation resistance of produced FAST samples was investigated under identical oxidation conditions and described in detail in [98]. The mass change due to oxidation and eventual sublimation of oxidized material are shown for pure W samples. Thin film smart alloys along with two FAST samples is presented in Fig. 8.14.

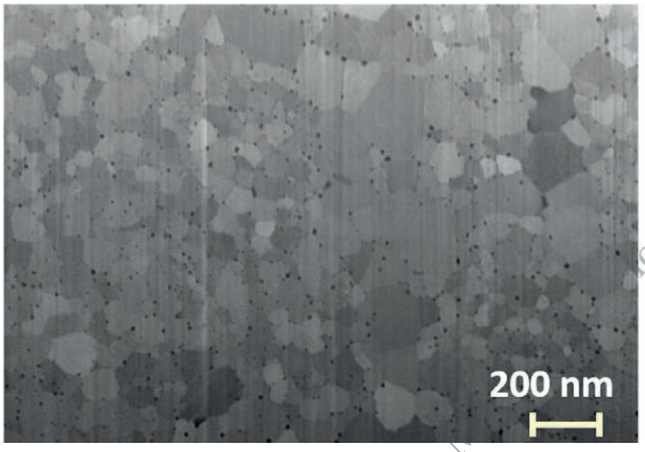

FIG. 8.13. Grain structure of a sample produced using the FAST technique [98].

From Fig. 8.14, it can be noted that the sample FAST 6 — which was produced with a temperature ramp of 200 K per minute without any holding time and with the maximum temperature of 1733 K — demonstrates the achievement of an unprecedentedly low oxidation rate.

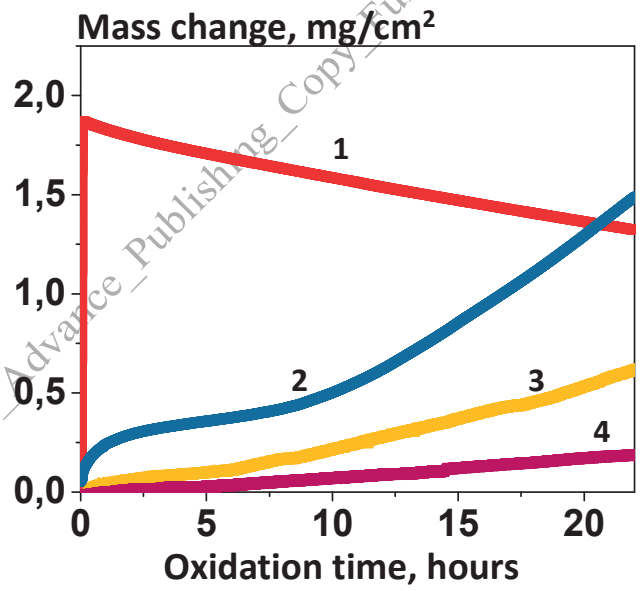

FIG. 8.14. Mass change during the oxidation process: 1) for the pure thin film W sample, 2) for the reference thin film W-11.6Cr-0.6Y smart alloy, 3) for FAST 1 sample and 4) for FAST 6 sample. Oxidation took place in an atmosphere consisting of 80 vol.% of Ar + 20 vol. % of O_2 at 1 bar and 1273 K [98].

(f) Performance tests: plasma exposure and accidental conditions

Since smart alloys are to be used as PFCs in DEMO, their plasma performance is very important. Having achieved the production of bulk smart alloy systems with good oxidation properties on a time scale of hours, the development of performance tests became crucial. The first such combined test was recently performed using two FAST samples: SA1 and SA2. It is crucial to assess under DEMO-relevant conditions:

1. The sputtering rates of smart alloys.
2. The preferential sputtering of alloying elements by plasma ions and its effect on the oxidation resistance.
3. The evolution of surface roughness during plasma exposure.

Plasma tests of the bulk W-Cr-Y systems have started very recently. The first plasma exposure was conducted in an identical manner as the recent study of the W-Cr-Ti system described in [98]. Two FAST samples and two pure W samples manufactured according to ITER specifications [99] were used for a direct comparison. Series of pre-characterizations were made on all studied samples, including:

1. weight measurements for the evaluation of sputtered materials,
2. SIMS measurements to understand the initial elemental composition,
3. stylus profiler measurements of surface roughness (R_a) were made on several locations,
4. SEM scans were made to investigate the initial morphology of the surface, and
5. FIB measurements were performed to study grain size and homogeneity, and to make the markers needed for the direct evaluation of sputtered material.

Smart alloy and pure tungsten reference samples were installed in the sample holder and exposed to steady-state deuterium plasma in the PSI 2 linear plasma device [100], shown in figure 8.15. Plasma parameters were evaluated using a moveable Langmuir probe. Electron temperature T_e ranged between 6 and 8 eV, depending on radial position. Biasing was applied to the sample holder so that the energy of impinging ions was ~220 eV. The samples were actively heated to a temperature of 893 to 923 K. Ion energy and the temperature during exposure provided a conservative estimate of the environment expected in DEMO [92]. The total exposure duration was 4 hours 36 minutes. The accumulated fluence was $1x10^{22}$ ions per square centimetre. A summary of the results is provided in table 8.1. From this data, it can be confirmed that the mass loss of both pure W samples and smart alloys was nearly identical. The removed material after exposure accounted for ~450 nm for the pure W samples (W1 and W2) and for ~870 nm for smart alloys SA1 and SA2. The surface roughness increased from ~20 to ~50 nm on most the studied locations. The newly developed bulk W-Cr-Y systems (even at this early stage of development) already demonstrated a very good plasma performance.

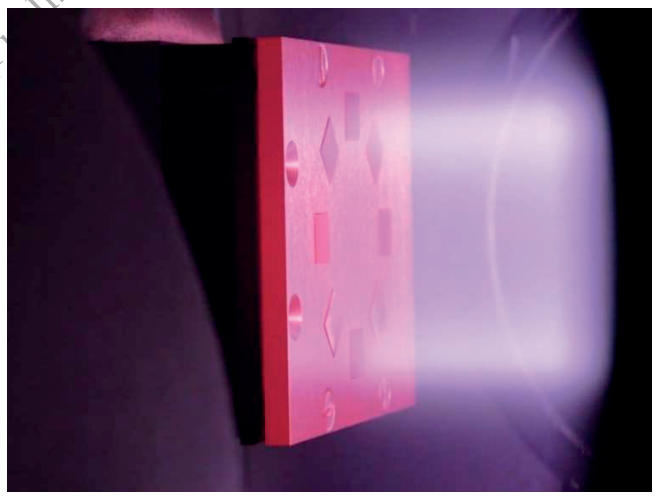

FIG. 8.15. Exposure of smart alloys and pure tungsten samples in steady-state deuterium plasma of the PSI 2 linear device. A side view of the heated tungsten and smart alloy samples is presented, mounted into the holder and glowing during plasma exposure.

As a next step to evaluate the impact of plasma on the oxidation resistance, one of the plasma-exposed smart alloy samples underwent isothermal oxidation at 1273 K in a gas mixture containing 20 vol. % of O_2 and 80 vol.% of Ar at 1 bar. The results of this oxidation and their comparison with data from non-exposed FAST sample is presented in Fig. 8.16. In addition, the oxidation curve for pure W along with the oxidation curves of the previous W-Cr-Ti systems reported earlier in [98] are provided in Fig. 8.16.

TABLE 8.2. Main parameters of exposed pure tungsten and smart alloy samples

Sample	Mass loss [μg]	$R_{a,\ before}$ [nm]	$R_{a,\ after}$ [nm]	Eroded material [nm]
W1	1200±10	30±7	141 ±55	460
W2	1093±10	24±8	52± 49	440
SA1	1287±10	22±5	46±25	860
SA2	1223±10	24±9	47±32	870

The analysis of the obtained dependencies showed a decrease of oxidation resistance after plasma exposure calling for further optimization of smart alloy systems. At the same time, the results obtained with W-Cr-Y systems are by far superior to those obtained with the W-Cr-TI alloys, representing a very promising result.

(g) Summary

New advanced tungsten-based smart alloys are needed to ensure the intrinsic safety of DEMO and future fusion power plants. Smart alloys should combine acceptable plasma performance with suppressed oxidation in case of an accident. The research program on smart alloys is presently focused on studies of W-Cr-Y systems. First studies made on film smart alloys demonstrate a remarkable 10^5-fold suppression of oxidation as compared to that of a pure tungsten.

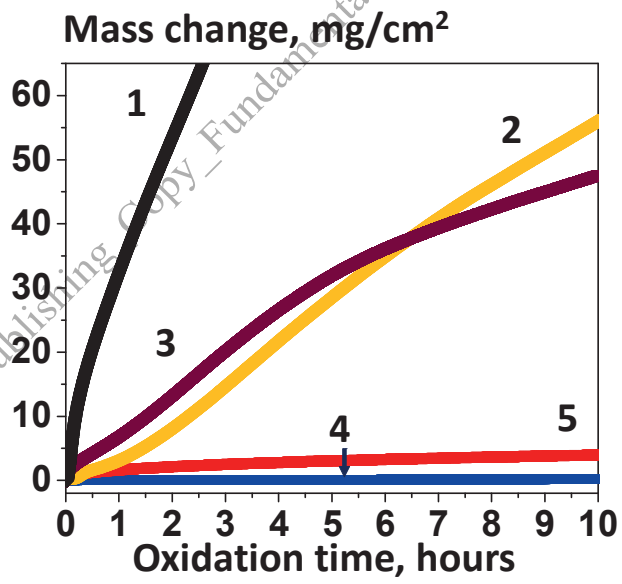

FIG. 8.16. Mass change during the oxidation process: 1) for the pure W sample, 2) for the reference W-10Cr-2Ti smart alloy [98], 3) for the W-10Cr-2Ti smart alloy exposed in plasma [98], 4) for the reference W-11.6Cr-0.6Y smart alloy and 5) for the W-11.6Cr-0.6Y smart alloy exposed to plasma. Oxidation took place in an atmosphere consisting from 80 vol.% of Ar + 20 vol. % of O_2 at 1 bar and 1273 K[98].

The first bulk smart alloy samples of DEMO-relevant size have become available. The newest mechanically alloyed powder is sintered using a field-assisted sintering technique (FAST). Bulk samples with 99.8% of nominal density featuring a fine sub micro-grain structure with grains 100 to 200 nm in size and a homogenous distribution of

yttria along the W-Cr grain boundaries were obtained. The measured oxidation resistance was clearly superior, even in comparison with the reference thin film systems.

Fast progress in smart alloy R&D has made a start in the combined testing of the newly developed alloy systems. These tests comprise the exposure of alloys to steady-state deuterium plasma followed by the controlled oxidation of the exposed samples. During one such exposures in the linear plasma device PSI 2, smart alloy samples were studied together with pure W samples under identical plasma conditions. The exposure temperature (~903 K) and the energy of impinging ions (220 eV) provided conditions for a rather conservative estimate of the performance of smart alloys under DEMO-relevant conditions. During the exposure, smart alloys exhibited the same mass removal by plasma as a pure tungsten samples. Volumetric loss of smart alloy (850 nm) was about twice as much as that of pure tungsten (460 nm), as expected due to a larger volume of chromium and preferential sputtering of alloying materials at a higher sputtering rate than that for an W matrix.

The subsequent oxidation of the exposed smart alloy sample revealed a superior oxidation resistance in comparison with the former ternary W-Cr-Ti system. At the same time, the oxidation resistance of plasma-exposed the W-Cr-Y slightly degraded as compared with non-exposed sample calling for further optimization of the smart alloy systems.

(h) Outlook

Very fast progress in the research and development of advanced material systems, such as smart alloys, has allowed the start of the performance tests both in DEMO-relevant plasma environment and under accidental conditions. Despite very promising first results, further progress will likely be challenging. The smart alloy systems have now reached the next level of maturity, allowing to directly address their lifetime in the power plant. High-fluence plasma facilities, like Magnum-PSI are now able to obtain DEMO-relevant parameters. The first pilot lifetime studies have started very recently. Further improvements are required both in the detailed understanding of sputtering in smart alloys as well as in the optimization of their performance during multi-month oxidative exposure.

Plasma compatibility needs to be further tested. In future plasma exposures, a gas seeding will be performed to study its effect on sputtering rates and on the morphology of smart alloys. New oxidation exposures will be performed in humid air atmospheres to approach the accidental conditions in DEMO. The necessary improvement of the thermo-mechanical properties of smart alloy systems will be studied. Furthermore, the effect of neutron irradiation on the properties of smart alloys is to be investigated in the future.

8.4.3.2. Advanced materials for a damage resilient divertor concept and DEMO

(a) Introduction

Tungsten (W) is currently the main candidate material for the first wall and the highly-loaded components of fusion reactor divertors as it is resilient to erosion, has the highest melting point among candidate materials, shows a rather benign behaviour under neutron irradiation and a low tritium retention. Extensive work has been done to qualify current materials with respect to these issues for ITER, especially for Was first wall and divertor material [101] [78]. For the next step devices like DEMO/FPP the limits on power exhaust, availability, lifetime and fuel management are much more stringent. Extensive studies and materials programs [102] [103] [104] [105] [106] [107] have already been performed. It is assumed that the boundary conditions [13] to be fulfilled for the materials are in many cases above the technical feasibility limits as they are set today [101] [78].

Efforts to establish new advanced plasma-facing material-options are moving forward [78] focusing on crack resilient materials with low activation, minimal tritium uptake, long lifetime and low erosion. The operational gap between materials for cooling structures, e.g. Cu, and the plasma-facing materials needs to be bridged [78] [108].

Many of these materials base their advanced properties on the use of a composite approach. With the incorporation of fibres, energy dissipating mechanisms, like ductile deformation of fibres, fibre pull-out, and crack bridging.

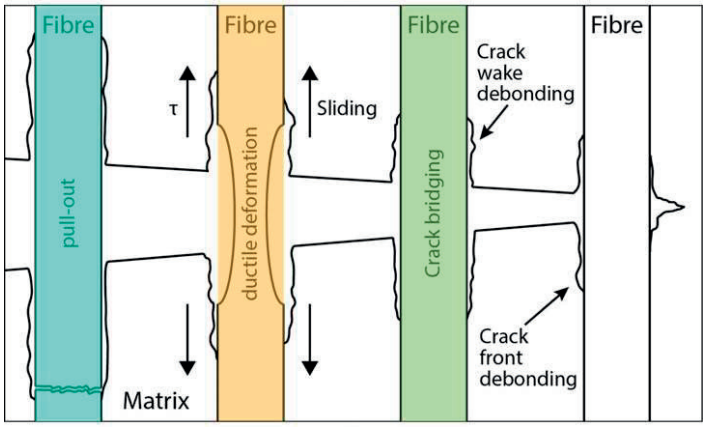

FIG. 8.17. Energy dissipation mechanisms typically considered in W_f/W and other fibre-reinforced composites [109] and facilitating bridging and deflection [110] [111] [112].

An additional difficulty encountered in a fusion power plant implementing W is the formation of radioactive and highly volatile W-oxide (WO_3) compounds during accidental air ingress. To suppress the release of W-oxides, W-based self-passivating alloys can be incorporated into the composite approach [80] [113] [114] [115] [116]. Here the focus lies on the powder-metallurgical production route for W_f/W as a plasma-facing-material.

(b) Tungsten-Fibre Reinforced Tungsten

To overcome the brittleness issues of W, a W-fibre enhanced W-composite material (W_f/W), incorporating extrinsic toughening mechanisms can be used. Various methods of building and constructing W_f/W composites, either via CVD [117] [118] or powder metallurgical processes [119] [120] are available. Based on the work presented in [117] [118] [119] [120] [121] [109] and previous work, the basic proof of principle for CVD & powder metallurgical W_f/W has been achieved. It can be expected that using doped W-wires, even at elevated temperatures (above 1500 K), W-fibres will keep their ductility [122], hence all mechanisms described above may function [109]. Should the fibres however lose their ductility due to neutron embrittlement and high temperature [123] [124], the pull-out of fibres and the crack deflection should still be able to maintain pseudo-ductility. In W_f/Cu the embrittlement due to high temperature can likely be neglected, neutrons, however, will remain important.

Powder Metallurgical Production

For powder-metallurgical production, the homogenous introduction of powder between the fibres is required for good material properties. Short fibres are thus preferred in contrast to e.g. woven preforms or parallel long fibres.

FIG 8.18. 2.5 µm W_f/W sample produced by FAST with random distributed fibre and an yttria interface between fibres and matrix

A sample of W_f/W is shown in figure 8.18, as-produced by powder metallurgical. A sample with 40 mm diameter and a height of 5 mm was produced based on FAST [125]. Potassium doped W-fibres with 150 µm

diameter and 1.5 mm length (OSRAM), together with pure W-powders (OSRAM) (average particle size 5 µm) were used as raw materials.

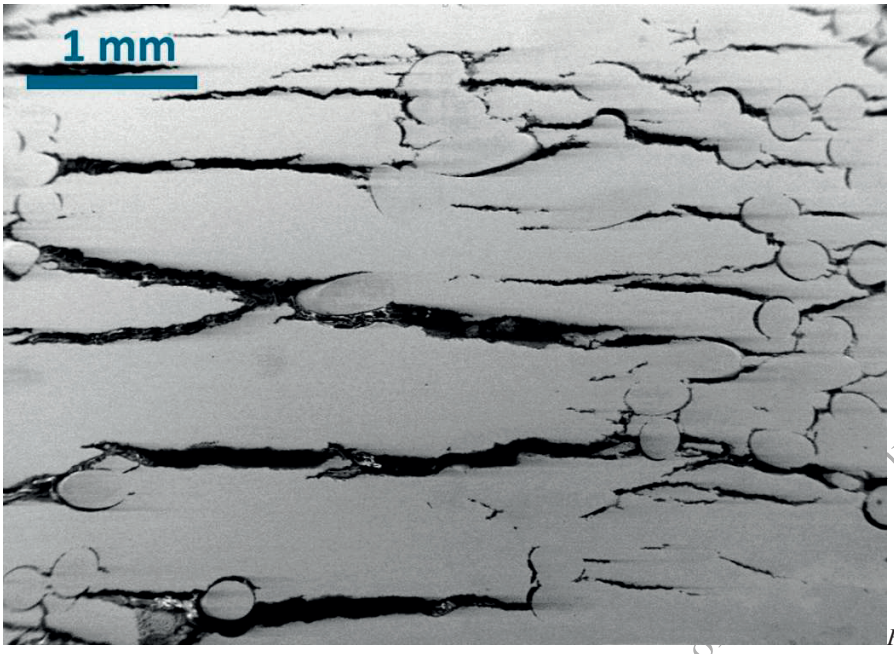

FIG. 8.19. Microstructure of W_f /W generated by dry pressing and subsequent pressure-less sintering.

Dry pressing of a fibre/powder mixture and subsequent pressure-less sintering would be the cheapest and simplest process, by which W_f/W production would have been sped up significantly. Therefore, our first experiments were conducted in this direction. Using a press with an instrumented cylindrical floating die [126], the fibre/powder mixture was compacted using a maximum pressure of 700 MPa reaching a relative density of 78%. Subsequently, the resulting green part was sintered in a W-tube furnace under a H_2 atmosphere at 2273 for 1 h.

The resulting microstructure (cf. Fig. 8.19) shows distinctive cracking by shrinkage of the compacted powder, whereas the fibres are already at final density. From these results, it is evident that additional external pressure during sintering of W_f/W is required to get a dense and crack-free sample. FAST provides such additional compaction during sintering.

For the material consolidation with FAST the fibres and powders were mixed homogeneously before sintering to produce a W_f/W sample with a random fibre distribution and orientation. A density of ~94% was achieved after applying the sintering process at 2173 K (4 min) and 60 MPa (heating rate 200 K per minute). In addition to the large samples, some samples with 20 mm diameter for mechanical testing were produced based on the same parameters with varying compositions. Two kinds of W-powders were used: Pure W-powder (OSRAM) (average particle size 5 µm) and the so-called smart W-alloy powders (W-12Cr-0.5Y, provided by CEIT). The fibre size is also chosen differently in this case (240 µm × 2.4 mm). In all cases, a fibre-volume-fraction of 30% was used. The samples have been prepared to establish if and how pseudo-ductility can be achieved in the case of a randomly distributed short fibre W_f/W.

Fibre & Interface Optimization

As part of the development of W_f/W, the choice of the fibre and the interface material can be crucial. With respect to the fibre, the choice of a sag-stabilized potassium doped fibre means that some ductility can be retained [109]. Interface research on a variety of interlayers and their properties has been performed [127] [128] [129] [130] [131] [132] [133] including alumina, erbia and yttria (Y_2O_3). The interface properties and stability needs to be established during the powder metallurgical production process. For fusion applications, a non-activating material must be chosen for the fibre-matrix interface [78]. Yttria has been proposed as an ideal candidate interface material for the W_f/W composite due to its several advanced properties: good thermal and chemical stability, high mechanical

strength and hardness. Yttrium oxide is proposed in W_f/W and is also used for permeation barrier coatings. For the material samples presented here the Y_2O_3 layers were deposited by a Prevac magnetron sputtering system from an yttrium metal target. Oxygen was injected into the argon atmosphere as the reactive gas so that Y_2O_3 could be formed.

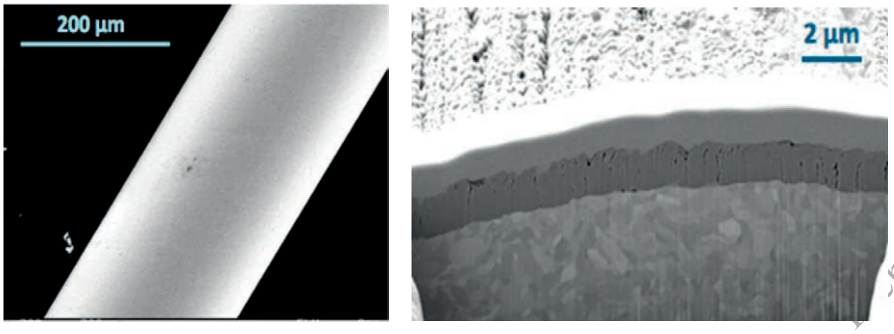

FIG. 8.20. The figure shows in (left) the SEM image of a single coated fibre with an yttria interface, while (right) is a FIB cut showing the yttria interface structure before consolidation

Figure 8.20 shows an individual fibre coated with yttria before adding it to the powder for W_f/W production. Various interface thicknesses have been used during the various development steps of W_f/W. 1 µm was established as a feasible thickness for the CVD production route [109] [134] [135]. For the powder metallurgical route, both FAST and HIP, sintering under high pressures and temperatures has led to the understanding [119] that potentially a thicker interface is required. The FAST process adds additional complications as electrical insulation, pressure and temperature on the interface can cause thin interfaces to dissipate [136] [137] [138]. Here 2.5 µm thick yttria is needed for a viable interface.

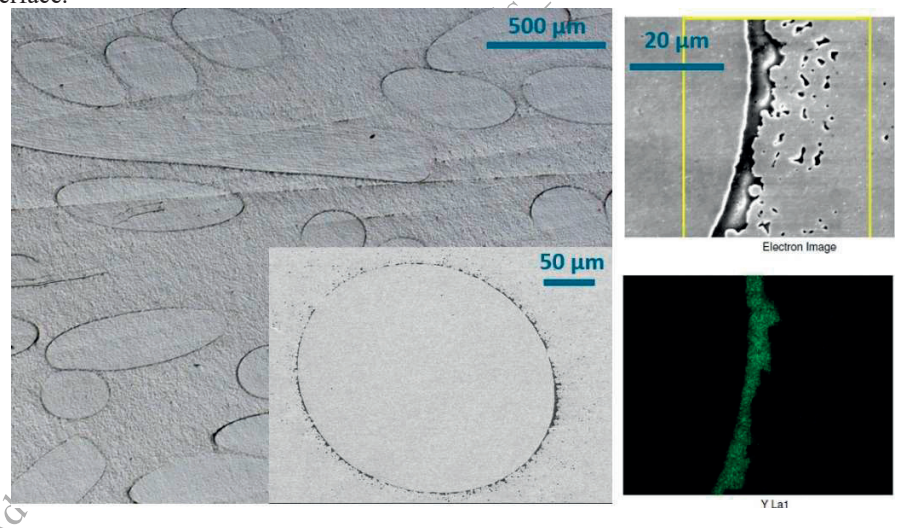

FIG. 8.21. Yttria interface on W-fibre in PM-W_f/W after consolidation (l) Fibre and Interface after consolidation (r) EDX Map showing Yttrium in the interface

Figure 8.21, shows a fibre after consolidation of the W_f /W, as described in the above. The impact of the FAST process can be clearly identified. After FAST, the interface is far thinner and shows the indentation marks of the surrounding powder. Figure 8.21-right clearly shows that yttria (green signal) is remaining and hence the interface around the fibre is intact. Additional interface materials are also being tested.

Pseudo-Ductile Behaviour

The crucial point when considering W_f/W for applications is to establish its pseudo-ductile behaviour based on extrinsic toughening mechanismsand eventually show improved mechanical behaviour during operational conditions. The three mechanisms introduced in displacement (a.u.) tested material samples can be identified in

figure 8.17. Small (18 mm × 2 mm × 4 mm) three-point bending test samples were produced and a pre-not for stable crack initiation was introduced. Utilizing an Instron 3342 universal testing machine (Instron GmbH), load displacement curves were taken and fracture surfaces produced to determine if the desired behaviour could be reached. Figure 8.22 presents four typical load displacement curves. In arbitrary units, the behaviour of two pure W 2.5 µm yttria Wf/W samples is shown together with one self-passivating (W-12Cr-0.5Y) W_f/W sample measurement. In addition, the catastrophic failure of a pure W sample is shown. In all three Wf/W cases crack initiation is observed after which an increased load can still be handled. This is a clear indication of pseudo-ductility in this simple model-system. Material qualification now needs to make sure that potential failure modes like cracking [139] can be overcome for future divertor materials and components. Figure 8.23 shows details of the cracked surface and highlights the individual mechanisms presented in figure 8.17.

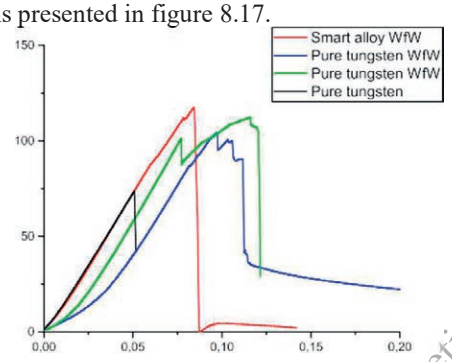

FIG. 8.22. Force displacement curves. 3pt bending tests of PM-W_f/W.

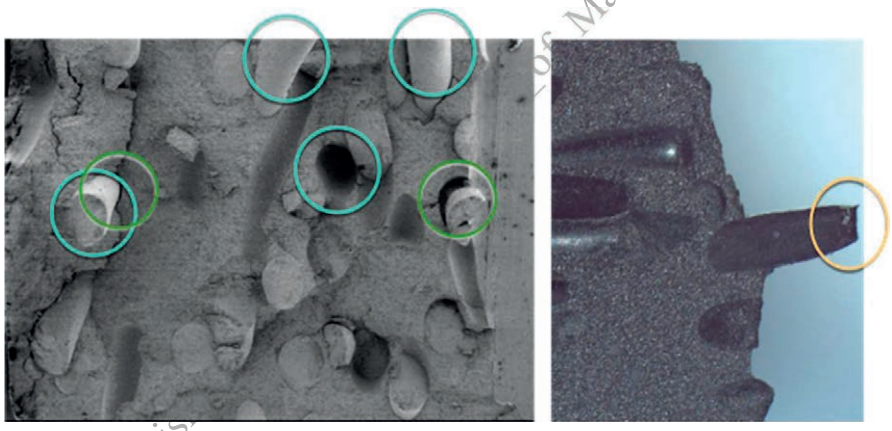

FIG. 8.23. Fracture Surface of W_f/W (Circle colours refer to figure 8.17).

All three mechanisms, ductile deformation of fibres, crack deflection and pull-out can be observed. Based on these promising results further materials development needs now to establish the actual material parameters like fracture toughness and ultimate tensile strength.

8.4.3.3. A new divertor Component

FIG. 8.24. Component design incorporating W_f/W and W/Cu solutions at various points in the structure [121] [140].

When trying to improve the performance of the divertor, not only the PFM or the armour are important but also the cooling structure and potential joints in the component, and hence several material concepts often need to be combined [78] [141]. A component [78] [141] [98]could comprise of tungsten fibre-reinforced tungsten (W_f/W) [109] [119] [120] [121], smart W-alloy as the matrix material [113] [114] [115] [142], a copper-based advanced cooling-tube (e.g. W-reinforced copper, W_f/Cu) [143] and integrated permeation barrier layers (e.g. yttria) [128] [144].

Figure 8.24 shows a small variety of options that could be used based on conventional ITER-like divertor designs. The top row assumes a copper cooling structure and a flat tile of W for the armour material. The copper tube

can be strengthened by introducing fibres and the mechanical stresses on the copper structure reduced by a gradual transition between Cu and W. Results on W/Cu new materials are reported in [103] [98] [143].

It is essential that the exhaust capability of an advanced component is like conventional designs and does in addition show resilience against e.g. embrittlement, failure due to thermal stresses and cyclic loading. We hence propose to utilize the W_f/W composite approach together with W-alloying concepts to maximize the potential of W-based-PFCs on top of the advanced cooling options. The lifetime influenced by erosion, creep, thermal fatigue, and embrittlement, needs to be compatible to the requirements from steady state operation. This means that erosion determined by the top layer needs to be close to pure W. Potentially various options introducing the composite need to be considered. Thermal stress analysis can give hints at locations within the component where a potential application of W_f/W is indicated by high stress and crack probability [139].

8.4.3.4. Outlook

Two manufacturing paths for W_f/W are now open: powder metallurgy and CVD. The presented approach allows for quick prototyping and testing of new material combinations, fibres, interfaces and alloys. It has been shown that pseudo-ductile behaviour works in short fibre powder metallurgical W_f/W. However, W_f /W on its own cannot solve the issues of heat-exhaust in the divertor of a future fusion power plant. Here, improvements to the typically used copper cooling structure need to be considered. Together, both technologies can be used to develop improved divertor components. Here, rigorous testing and qualification is required with respect to heat-exhaust, thermal fatigue, cyclic loading and plasma wall interaction. It is planned to have prototype components available within five years for application in existing fusion devices. To establish material performance under irradiation powder metallurgical W_f/W samples (cf. figure 8.18) are earmarked for irradiation in a nuclear reactor starting in 2017.

8.5. FUSION MATERIALS IRRADIATION FACILITIES

Currently there is no neutron source with a high enough flux to mimic irradiation conditions relevant to those experienced by the first wall of a fusion reactor. Nevertheless, highly valuable information can be obtained from existing irradiation sources, materials test reactors, fast neutron reactors and ion accelerators. Partial information is provided by these irradiation facilities that can be used to select main materials candidates for DEMO fusion reactors and evaluate their performance under limited conditions. Modelling is an indispensable tool to interpret all the available information and build a test matrix of experiments to be carried out in a dedicated fusion neutron source (see Section 8.6).

8.5.1. Current irradiation facilities

In the absence of a dedicated high-intensity 14 MeV neutron source, materials science and development must rely on the experimental simulations of fusion environments using several presently available devices, namely:

- Fission reactors with fast or mixed neutron spectra.
- Electrostatic accelerators in single, dual or triple beam configuration.
- Spallation neutron sources.
- Cyclotrons.

8.5.1.1. Fission reactors and spallation neutron sources

The irradiation damage conditions for iron within the present and planned "neutron-facilities" are compared with DEMO conditions in table 8.3 (adapted from [145] [146] [147])

***TABLE 8.3**. Neutron fluxes, atom displacement rates, He and H productions in DEMO FW, in the high flux test module (HTFM) of the proposed IFMIF (40MeV, 2x125 mA), in the SINQ target, in the reflector in the European spallation source (ESS), in a material testing reactor (MTR) of present generation, high flux reactor (HFR), in the fast neutron reactor BOR60, and in the Jules Horowitz reactor (JHR): a new-generation MTR under construction in France.*

Irradiation parameters		DEMO FW 1-3MW/m^2	IFMIF HFTM	SINQ	ESS rigs reflector	HFR Position F8	JHR	HFIR	BOR60 Position D23
Total flux	n	1.3×10^{15}	5.7×10^{14}	2.7×10^{14}	6.5×10^{14}	3.8×10^{14}	2.5×10^{15}	10^{15}	2.3×10^{15}

(cm^{-2} s^{-1})	p		0	2.6×10^{14}	2.5×10^{12}	0	0	0	0
Damage [dpa·fpy^{-1}]		15–30	20–55	30	5–10	2.5	16	20	20
H, appm·fpy^{-1}		600–1240	1000–2400	11000	160–360	1.9	10.6		14
He, appm·fpy^{-1}		125–320	250–600	2600	25–60	0.8	4.4	12	5.8
appm-H·dpa^{-1}		40–41	35–54	350	33–36	0.8	0.7		0.70
appm-He·dpa^{-1}		8–11	10–12	85	5–6	0.3	0.3	0.6	0.29

The chief advantages associated with neutron irradiation facilities such as fission test reactors include the ability to perform a wide range of bulk property measurements on irradiated materials, utilizing irradiation volumes up to several litres for sodium-cooled fast spectrum test reactors and water-cooled mixed-spectrum reactors. A wide range of temperatures (333 to 1773 K) can be achieved in capsules introduced at these materials testing reactors (MTR) by direct contact with the coolant or by utilization of mixed gases of varying thermal conductivity between the specimens and the reactor coolant. Damage levels up to ~50 dpa can be achieved over 2 to 4 years in the highest power mixed spectrum reactors, and up to ~100 dpa can be achieved over similar times in fast reactors [147]. Some of the disadvantages for existing fission neutron irradiation facilities include:

1) a non-prototypic neutron irradiation spectrum compared to D-T fusion spectra (resulting in low co-generation of H and He due to lower neutron fluxes at energies above ~5 MeV where (n, p) and (n, α) threshold reactions are initiated in many elements);
2) different damage accumulation rates, which may also give rise to different types of damage through the dose rate effects as well as a slower accumulation of damage (maximum dose rates less than anticipated in fusion first walls, (cf. table 3), which can limit the practical maximum achievable dose levels; and
3) difficulties in accurately controlling the irradiation temperature or perform in-situ measurements in some facilities, or both.
4) Specimens produced are activated and need special facilities for experimentation.

Despite these drawbacks, fission reactors have provided the materials science and technology community with extremely valuable data on radiation effects that have been extensively used to develop radiation resistant materials, even for fusion application, especially reduced activation ferritic/martensitic (RAFM) steels [148]. Spallation sources can provide highly-valuable information about microstructural evolution and mechanical property degradation that may be induced at very high transmutant helium and hydrogen concentrations (~1000 appm-He, ~5000 appm-H). But, as in the case of fission neutron irradiation facilities, the irradiation spectrum differs from the D–T fusion irradiation conditions as the high-energy neutron tail associated with spallation neutron facilities introduces very high primary knock-on atom energies, and increased H, He (table 8.3) and solid solute transmutation rates that may alter microstructural evolution and mechanical properties, particularly for higher doses in excess of 10 dpa. It should be also noted that, even in the European spallation source (ESS) reflector rig where the irradiation conditions are the closest to those of fusion, they remain not prototypical for fusion. Spallation neutron sources also introduce a pulsed irradiation environment, the impact of which is anticipated to be small to moderate depending on the specific material and irradiation temperature. Finally, precise control of irradiation temperature in spallation targets is difficult due to the very high beam heating (proportional to the instantaneous accelerator beam current) that is subject to frequent beam trips and other fluctuations [147].

8.5.1.2. Ion beam accelerators

Ion beam accelerators have long been used to produce displacement damage in materials for detailed microstructural characterization studies as it is discussed in detail in this paper back from 1990 [149]. One to three electrostatic accelerators in the range of a few hundreds of kV to a few MV can be coupled to operate in single-, dual- or triple-beam configurations: one accelerator creating ballistic damage, the second in a dual-beam configuration or the second and third in a triple-beam configuration serving to simultaneously implant relevant transmutation elements such as He and H [150]. Some of these facilities are also equipped with a transmission electron microscope allowing for in-situ examination of damage accumulation during irradiation [151]. Implantation of transmutation elements other

than H and He can be carried out provided that the ion source is available. Table 4 presents the main such facilities worldwide.

TABLE 8.4. *Ion beam facilities dedicated to materials irradiation in the range of a few hundred kV to a few MV.*

Ion beam facilities	*Accelerator voltage*	*Configuration*
Electron Beam Research Facility at Texas A&M	*10 MeV electron beam linear accelerators (LINAC) – 5 MeV, X Ray linear accelerator*	*Dual-beam*
Michigan Ion Beam Laboratory (MIBL)	*3MV – 1.7 MV – 400 kV*	*Triple-beam*
Sandia's Ion Beam Analysis Laboratory	*6 MV – 3 MV*	*Dual-beam*
Los Alamos Ion Beam Materials Lab	*3 MV and two 200 kV implanters*	
Argonne	*2 MV – 300 kV*	*In-situ TEM*
Tennessee /ORNL Ion Beam Materials Lab	*3 MeV*	
JANNUS Saclay	*3 MV–2.5 MV–2.25 MV*	*Triple-beam*
JANNUS Orsay	*2 MV–150 kV*	*In-situ TEM*
FZ Dresden	*3 MV–500 kV*	
FSU Jena	*3 MV–400 kV*	
Surrey Ion beam centre	*200 kV–200 kV*	
JAERI Takasaki	*3 MV–3 MV–400 kV*	*Triple beam*
HIT Tokyo	*1.7 MV–1 MV*	
IAE Kyoto	*1.7 MV–1 MV–1 MV*	*Triple-beam*
DNE Nagoya	*2 MV–200 kV*	
MSD Kalpakkam	*1.5 MV–150 kV*	
NRC Kurchatov Institute	*60 MeV*	*α-particle cyclotron*
Kharkov	*Typical conditions: Cr^{2+} or Fe^{2+} (400 keV–2 MeV); H^{2+} (10–50 keV) and He^{2+} (10–20 keV) [152]*	*Triple-beam*

Figure 8.25 gives an example of ballistic damage and helium implantation profiles that can be achieved in iron at JANNUS Saclay in a dual beam configuration. Fusion-relevant He/dpa values as well as a large range of other irradiation conditions can be achieved, allowing for parametric studies. This type of ion beam irradiation is well suited for microstructure studies but not for standard mechanical testing due to the very limited depth of the irradiation region (typically only ~1 micrometre layer near the sample surface). The typical displacement damage rates in ion accelerators are several orders of magnitude higher than in fission or fusion environments: ~10^{-3} dpa·s^{-1} to be compared to ~10^{-6} dpa·s^{-1} for the DEMO first wall.

Overall, the advantages of ion beam accelerator irradiations include: the possibility to achieve ultra-high dose levels (above 100 dpa) in short time periods (~1 day), a generally very good temperature control and in-situ access during irradiation, and little to no induced radioactivity. Some multi-beam facilities are also capable of in-situ TEM examination of the effects of variable He/dpa and H/dpa ratios. Key disadvantages include: difficulties to obtain quantitative bulk properties in the limited-depth irradiation volume; potential artefacts associated with implanted ions and the presence of a nearby surface; the effect of long-range Coulomb interactions of the ions with the lattice atoms resulting in a higher fraction of low-angle and low energy collisions, leaving a much higher fraction of surviving defects relative to the calculated dpa value than would occur for fission or D-T fusion neutron conditions [153]; and the consequent need for physical modelling to quantitatively correlate the results with these after effects and (at high damage rates) to fusion-relevant damage rates. Despite these drawbacks, ion-beam irradiations are extensively used in the materials science community and continue to provide key understanding of radiation effects such as swelling, phase stability under irradiation and radiation induced segregation.

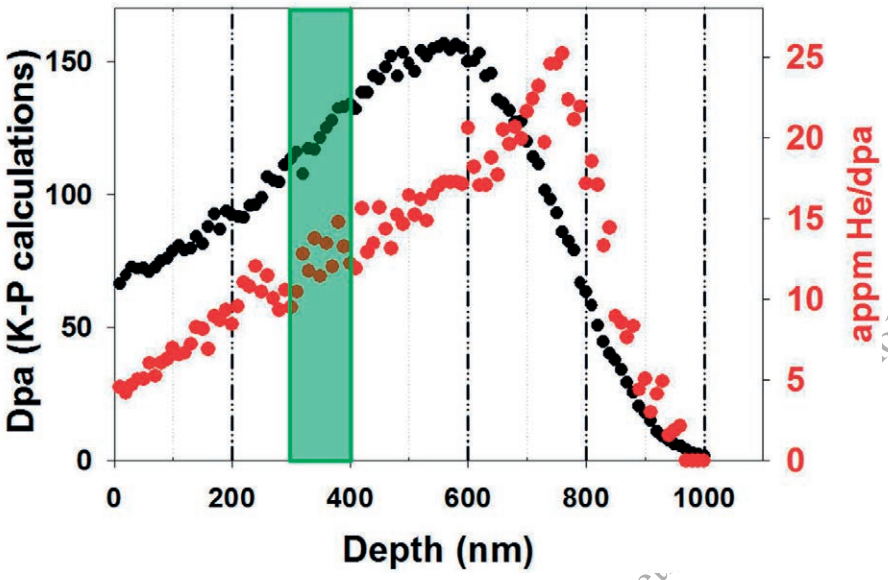

FIG. 8.25. Typical profiles of damage and He obtained in iron via dual-beam irradiation with 2MeV Fe^{2+} ions and 2MeV He^{2+} at JANNUS Saclay. In the region where a thin TEM foil was extracted by focused ion beam (FIB: green slot), the dose, appm-He/dpa and dose rate were 128 dpa, 13 appm-He·dpa^{-1} and 6.8×10-3 dpa·s^{-1}, respectively [154].

8.5.1.3. Cyclotrons and α-particle implantation

Cyclotron facilities (above 10 MeV light ion accelerators) have been extensively used in fusion programmes to study He-embrittlement [155] [156] [157]. Thanks to an energy degrader, α-particles can be uniformly implanted within ~100 μm thick specimens to concentrations of several 1000 appm-He [149] [158], allowing for mechanical testing [159] [160] [161]. These techniques have been extensively used since the 90's at it can be seen for example in the papers produced by D. J. Mazey and H. Schroeder [149] [159]. The conditions, in terms of dpa rate and He implantation, are rather far away from the fusion parameters as the appm-He·dpa^{-1} ratio is rather high (~10^4 versus typical fusion values near 10) and the typical achievable damage levels are relatively low (1–10 dpa), as compared to those expected in a fusion reactor. Nevertheless, cyclotron irradiations have provided important experimental data demonstrating the parameters responsible for He-embrittlement in the high temperature (above 773 K) creep range of materials due to unstable growth of He-bubbles at grain-boundaries, especially for austenitic steels [159], and enhanced hardening and embrittlement at low exposure temperatures (below 623 K) for ferritic-martensitic steels [68] [162] [163] [164].

8.5.2. A dedicated fusion neutron source

The design and construction of a fusion DEMO (demonstration) machine will require the 'fusion-neutron spectrum' radiation damage data on key structural-material mechanical parameters that are needed for the development of engineering design codes and qualification processes. DEMO plasmas will have an initial energy spectrum peaked at 14.1 MeV broadened by the Maxwellian energy spectrum of the plasma particles and further broadened (reduced in energy) by neutron scattering in the structure and coolant surrounding the plasma chamber.

Due to the limitations of the available facilities and multiscale modelling tools to simulate fusion damage and predict radiation effects in actual materials with complex chemical compositions and microstructures, a dedicated high-intensity neutron source — delivering a neutron spectrum as close as possible to the one observed in D-T fusion — is crucial to obtain irradiation data on DEMO relevant materials at the relevant doses and temperatures and build an engineering and scientific data base for the future DEMO projects.

Different proposals are currently under discussion, all of them based on accelerator-type devices. Transmutation rate, dpa-rate, and available irradiation volume (which in turn define the size and number of samples that can be irradiated) are key parameters to be considered in each case.

The parameters for several proposed fusion neutron irradiation sources are summarized in table 8.5. One of the proposals is the international fusion materials irradiation facility (IFMIF) conceived upon Li(D,xn) nuclear reactions. Other proposals are based on 'reduced versions' of IFMIF such as the DEMO oriented neutron source (DONES) and the elementary neutron source (ENS). These concepts use the scheme and technologies developed during the engineering validation and engineering design activities (EVEDA phase) of IFMIF.

TABLE 8.5. *Irradiation capabilities of IFMIF-full, DONES and ENS [165] [103]*

	IFMIF-full	**DONES**		**ENS**
Beam Current [mA]	2×125 (Li target)	1×125 (Li target)		1×125 (Li target)
Beam energy [MeV]	40	40		26.5
Total neutron production per second	10^{18}	5×10^{17}		1.5×10^{17}
Beam footprint [cm^2]	20×5	20×5	10×5	10×3
Typical damage rate per full power year and associated volume	40 dpa in < 60 cm^3 + 20 dpa in < 400cm^3 + 2 dpa in < 1500 cm^3	20 dpa in < 60 cm^3 + 10 dpa in < 400cm^3 + 2 dpa in < 1100 cm^3	20 dpa in < 100 cm^3 + 10 dpa in < 400cm^3 + 2 dpa in < 900 cm^3	15 dpa in > 20 cm^3 + 2 dpa in> 600 cm^3
Capability of Facility	Engineering and scientific database for DEMO and power plant	Engineering and scientific database for DEMO		Scientific reference data for He, H and dpa rate effects like D-T fusion

Small samples test techniques (SSTT) for determining mechanical properties such as tensile, creep, fatigue, fatigue crack growth or fracture toughness, have been established in international collaborations [166] under the umbrella of the international atomic energy agency. Despite their small size, they provide bulk properties like standard specimens, except for fracture toughness and crack growth (such properties being dependent on the thickness of specimens due to geometric constraint considerations). The dimensions for the miniaturized fracture toughness and fatigue crack growth specimens will be close to the thicknesses of the first wall and blanket structures, therefore the corresponding data obtained with these miniaturized specimens will be representative of the first wall and blanket structure conditions of DEMO. Further work in this field towards the standardisation of small specimens to measure all relevant mechanical properties is urgently needed.

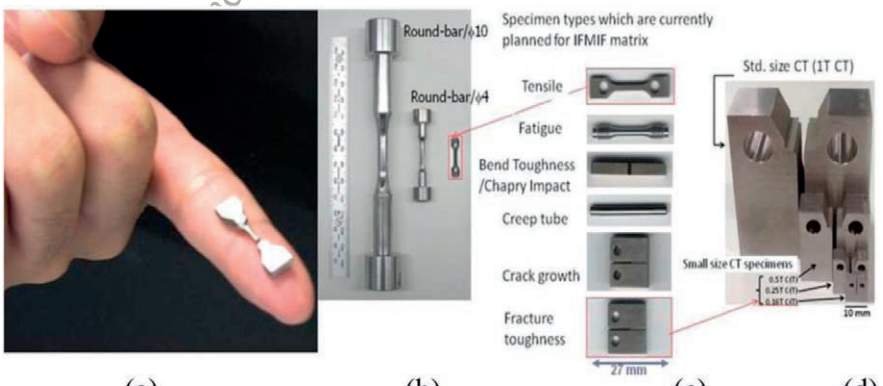

FIG. 8.26. Small samples test technique (SSTT). (a) SSTT tensile specimen compared to a human finger. (b) and (c) SSTT tensile specimens, fatigue, and creep tube compared to standard tensile specimens machined out of a rod with diameter 10 or 4 mm. (c) and (d) SSTT fracture toughness specimens compared with standard compact tension specimens [73]. Copyright 2013 IAEA.

It is worth to mention the potential use of gas-dynamic trap as a neutron source for materials testing. Work done in Novosibirsk (Russia) proposed the use of a gas-dynamic trap (GDT) as a neutron source: the collisional GDT solenoid with high-field mirror coils is well suited for plasma wall interaction studies. The resultant power flux through electron heat conduction would be in the range of several 100 MWm^{-2}, with electron and ion energies in the range of 100–200 eV. Studies with hydrogen, deuterium and tritium could be carried out [167], expanding the available tools for testing fusion candidate materials.

The MYRRHA project (https://myrrha.be/) will include the installation of the Fusion Material Irradiation station already in the first phase of the implementation (by 2026). The Irradiation platform (MINERVA) will be operation already in the period 2026-2033 prior the Phase III (reactor deployment) will take place. The investigation of fusion materials in MINERVA will be fully complementary to the research programme planned in BR2 (Belgian Research Reactor 2) by means of the High Temperature High Flux device which is already operational today. Those programmes will assist in the planning and technical implementation of experiments to be done in the foreseen Fusion dedicated irradiation Facilities such as DONES and IFMIF.

8.6. MODELLING OF RADIATION DAMAGE

8.6.1. Goals of modelling and the multi-scale modelling paradigm

Since the beginning of the new century physically-based material modelling has established its path as one of the basic research activities needed to boost the development and characterization of fusion materials. The term 'physically-based' implies the utilization of mathematical models constructed upon physical laws (e.g. in case of modelling of structural steels and tungsten-based materials the basis is the solid-state theory of metals). Over the last decade, material modelling took a firm hold in the field of fusion materials research mainly due to the lack of experimental testing facilities for 14 MeV neutrons, the possibility to perform irradiation tests in a wide temperature diapason (up to 1473 K are needed to test tungsten) and D-T conditions expected in a thermonuclear fusion environment. Extrapolation of the data obtained from fission neutron or ion irradiation campaigns is another important mission of material modelling, which will have to provide physical grounds for the optimization of the test matrix for the IFMIF/DONES experiments. The material modelling approach contains a hierarchy of tools that operate at physically different time and space scales, known as the multi-scale paradigm. A set of computational tools is being selected depending on the phenomena at stake. Those tools will then be integrated into a single project where self-consistent input-output will be used to deliver the result. With respect to fusion-relevant materials, the material modelling community has reached great advances in the description of iron-based ferritic steels (e.g. RAFM steels), for which the multi-scale paradigm is shown in figure 8.27.

Microstructural evolution of materials (cf. figure 8.27) is driven by the generation, migration and agglomeration of radiation-induced defects, as well as their interaction with the alloying atoms constituting the material and pristine microstructural features such as dislocations and grain boundaries. Because of the radiation-induced modification of the microstructure, the plastic deformation is altered overall, resulting in higher yield stress and lower ductility – i.e. embrittlement (see e.g. [168] [169] [170]). Correspondingly, the mission of material's modelling is to break-down the whole problem into sub-tasks, solve those separately and integrate into an end-user tool.

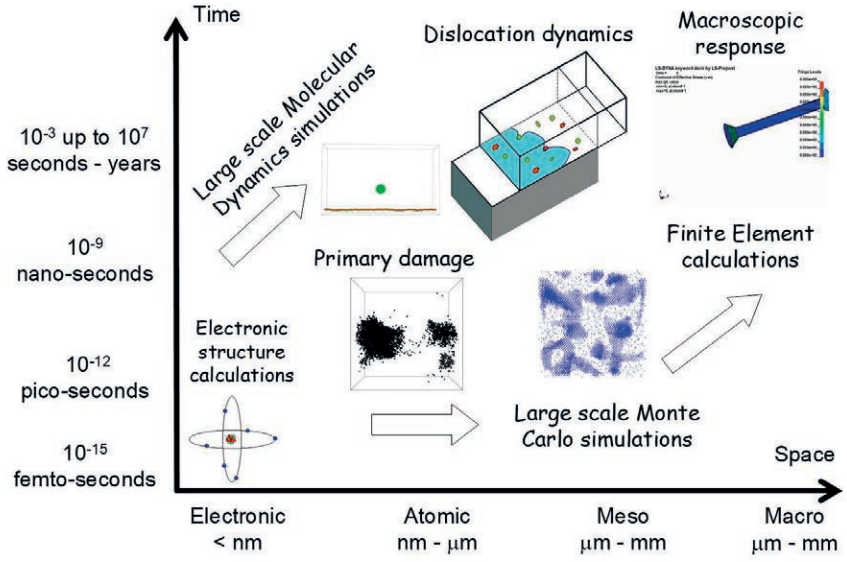

FIG. 8.27. Multi-scale modelling paradigm to assess the modification of mechanical properties of materials under prolonged thermal annealing and neutron irradiation. Microstructural evolution of materials is driven by the generation, migration and agglomeration of the radiation-induced defects. Radiation induced microstructure, consisting of dislocation loops, voids (or bubbles) and precipitates, alters the plastic flow in the material resulting in a higher yield stress and lower ductility – i.e. embrittlement.

8.6.2. Fundamental studies at the atomic-scale

First principle calculations accounting for the electronic structure are at the main tool to explore the atomic-scale. The role of electronic structure calculations (also known as ab initio) is to elucidate the elementary properties of point defects and their interaction, as well as the cohesive and elastic properties of perfect crystals (pure metals as well as alloys). Density functional theory (DFT) calculations are the most common type of ab initio calculations applied in the material science community.

The DFT approach is an excellent tool to characterize the structure of point defects and their small clusters (meaning by 'small' those defects with strain fields extending no further than several lattice periods from the defect core). The most natural application of DFT techniques is to characterize bulk matrix properties, solutes, vacancies, interstitial impurities and other small-size defects. For instance, the description of the vacancy-solute interaction may help to rationalize important phenomena such as radiation enhanced or induced segregation and precipitation (see illustration in figure 8.28). DFT treats magnetic effects – an important issue in dealing with iron-based ferritic steels. For instance, it is by now well established that a self-interstitial atom (SIA) defect adopts the <110>–dumbbell configuration in ferromagnetic bcc iron, while an interstitial defect has a linear one-dimensional <111>–crowdion structure in all the non-magnetic bcc transition metals, including vanadium and tungsten [171]. These two types of SIA defects are essentially characterized by different diffusivity and solute mass transport efficiency. A <110> SIA defect in Fe migrates via a sequence of rotation-translation jumps [172], each time overcoming certain potential barrier (migration energy). The formation of a stable mixed dumbbell can reduce or increase that barrier, depending on the type of solute. The alloying and doping of Fe by different solute elements results in non-trivial effects on the mobility and stability of point defects and their cluster [173], which grow upon prolonged irradiation.

The treatment of large-scale defects such as voids, dislocation loops, grain boundaries etc. (e.g. those visible by transmission electron microscopy), requires less rigorous but computationally faster atomistic calculations where the atomic interaction is parameterized via interatomic potential functions. There is no unique or fully satisfactory scheme to derive an interatomic potential, especially when it comes to complex alloys. Interatomic potentials are derived using various simplifications and assumptions; e.g. model tight-binding Hamiltonians [174]. These Hamiltonians often neglect terms representing electron-electron interaction, which in fact are included in DFT using exchange-correlation functionals. For example, the bcc crystal structure of iron is stabilized by exchange-correlation effects, which give rise to ferromagnetism. Consequently, DFT calculations and available experimental data serve to produce the fitting database and additional information (not included in the fitting scheme) needed to validate the potentials.

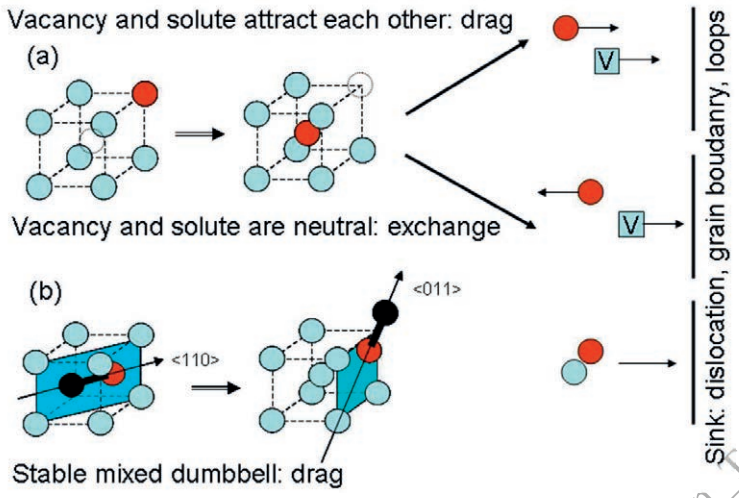

FIG. 8.28. Basic mechanisms of mass transport via radiation-induced point defects in body centred cubic lattice: (a) Vacancy-induced solute diffusion; (b) interstitial-induced solute diffusion. If vacancy-solute or interstitial-solute pair exhibits attractive interaction it may provoke long-range transport of solutes (so-called 'drag') towards sinks, at which the defects disappear. Typical sinks in metallic materials are dislocations, grain boundaries, dislocation loops and voids.

8.6.3. Primary damage and microstructure evolution

One of the most often used applications of the interatomic potentials is the simulation of primary damage states by means of the molecular dynamics method. The displacement cascades are produced by a primary knock-on atom (PKA) with a kinetic energy exceeding several hundreds of electron volts (eV). The PKA itself is produced because of the scattering of energetic neutrons. Given a constant production of 14 MeV neutrons in fusion reactions, the PKA energy for materials of the in-vessel components will be of the order of 200 to 500 keV. In the case of high-energy cascades (i.e. with PKA energy exceeding several keV) three major stages can be distinguished, as shown in figure 8.29 [175]. The first one is the so-called 'ballistic' phase lasting for tenths of picoseconds, during which the PKA energy is distributed among the other atoms thus creating a disorder zone surrounded by outwards-displaced crystal – cascade core. The local temperature of the material in the cascade core exceeds the melting point, however the recovery starts very soon, as the heat is transferred to the surrounding matrix. During the recovery, most of the displaced atoms return to their original lattice sites, but a few percent of displaced atoms are unable to do so. At the end of the recovery (or cooling stage), the core region lacks several atoms, which are displaced and occupy interstitial positions in the periphery. This is how stable Frenkel pairs (i.e. vacancies and self-interstitial atoms) are formed within several pico-seconds. While low-energy cascades produce single or several Frenkel pairs, the high energy cascades generate up to hundreds of Frenkel pairs. In this situation, about two-thirds of the defects are found in clusters. Vacancies generally form spherical voids (near the centre of the cascade core), while self-interstitial atoms arrange in platelets – nucleus of dislocation loops (located in the periphery of cascades) [176]. The central mission of molecular dynamics simulations is to provide both the number of generated Frenkel pairs and the size/spatial distribution of clusterized defects – which is called the 'primary damage state'.

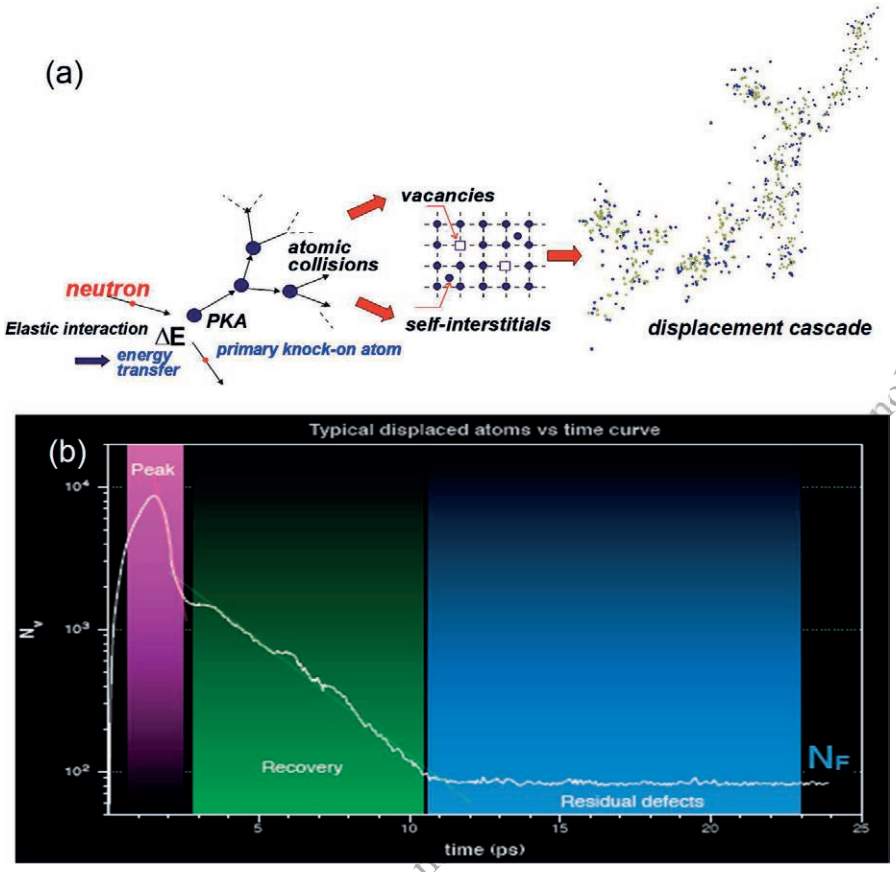

FIG. 8.29. Primary damage: (a) initiation of the primary knock-on atom and cascade event; (b) evolution of the number of the lattice defects as a function of time.

Once the primary damage state is defined and kinetic properties of point defects are established, microstructural models can be applied to predict the accumulation (e.g. formation and growth) of long-term radiation defects (within operational time). Two complementary computational techniques are generally applied for this purpose: (i) kinetic Monte Carlo (KMC) and (ii) mean field rate theory (MFRT). While KMC treats objects, MFRT considers reaction rates for the formation, migration, interaction and annihilation of radiation-induced defects at sinks. The advantage of KMC is the explicit treatment of cascade-generated defects, ability to consider mixed migration modes (1-D, 2-D and 3-D), introduce discrete sinks (dislocation and grain boundaries). However, this come at the price of low computational efficiency in parallel computing and natural limitations on the size and time scale. Typically, KMC is limited to a range up to 1μm. MFRT does not have such limitation but suffers from the ill-defined treatment of 1D-3D and 1D-1D reaction kinetics, which is of essential importance in the description of the evolution of dislocation loops – which is the primary radiation defects at low temperature (523 to 623 K).

8.6.4. Plasticity and mechanical properties

Prolonged neutron irradiation affects the microstructure which generally exhibits dislocation loops; voids and precipitates affects the movement of dislocations. The latter are the major units offering plastic slip which relaxes the material under externally applied load. Correspondingly, the irradiation hardening and embrittlement is determined by the interaction of dislocations with the radiation defects. The appropriate assessment of such interactions requires the application of atomistic techniques since elasticity theory breaks down at the nanometre scale (see e.g. [177]) corresponding to typical radiation induced defects. Dislocation-defect interaction can therefore be studied by means of molecular dynamics simulations, which can treat several millions of atoms thus imposing realistic dislocation density and defect spacing. The flexibility of molecular dynamics simulations allows for the imposition of a variety of conditions (temperature, dislocation velocity, dislocation character, etc.) and thus to extract the full information

about individual dislocation-defects interaction. This information is then transferred to the upper-scale model called discrete dislocation dynamics (DDD), where dislocation segments are represented as objects such that long-range dislocation-dislocation interaction can be treated via elasticity theory, while short-range dislocation-defect interaction is realized on the rules derived from molecular dynamics simulations (see e.g. [178]).

8.6.5. Integrated modelling

Finally, continuum-based kinetic models (e.g. delivering the local microstructure evolution) coupled with the constitutive laws for the mechanical behaviour (describing the evolution of plastic deformations as a function of radiation-induced defects and applied external loading conditions) can be used to address the response at mesoscopic and even macroscopic scales. Finite element or finite difference are typical methods to obtain fast and efficient solutions for given boundary conditions and underlying physical phenomena (e.g. process of neutron irradiation) to predict the integral evolution of the system and model, for instance: uni-axial load of a tensile test specimen. This method closes the hierarchy of scales and tools presented in figure 8.27, as an example of multi-scale modelling approach for the prediction of the change in mechanical properties upon prolonged thermal ageing and neutron irradiation.

The main perspectives of physically-based multi-scale models depend essentially on the complexity of the material (e.g. a tungsten-based system is somewhat less complex than commercial ferritic-martensitic steels) and the range of technological conditions envisaged for the application (e.g. materials for structural application are expected to suffer less-severe damage as compared to the plasma-facing materials). In the case of materials for fusion applications, there exist several principal perspectives:

- Guidance of the development, design and characterization of new materials with quantitative prediction of their structure and properties. Here, physically-based models can suggest alternative chemical elements for alloying or heat-mechanical treatment conditions to improve specific properties of the materials without degrading the other properties

- Discovery and characterization of new physical mechanisms responsible for the degradation of material properties upon operation in a nuclear installation. The atomistically-defined processes in complex materials (e.g. ferritic-martensitic steels) are somewhat less studied and should therefore be addressed in the near future. A good example could be radiation-induced creep, which is one of the main limiting factors defining the upper-bound temperature for structural application in high temperature irradiation environments (naturally, the high temperature operation allows for a better efficiency).

- Complementary assessment of the experimental programme for the qualification of the candidate perspective materials. As mentioned below in Section 8.6.2, the qualification of the radiation resistant materials will require an expensive and well scheduled experimental programme involving 14 MeV neutron sources. Given a limited capacity in terms of volume of the future 14 MeV neutron sources (i.e. IFMIF or DONES), the miniaturization of the samples and testing is the only way to proceed. Therefore, it is of great importance to provide a complementary theoretical assessment to minimize the irradiation programme and prove the adequacy of the miniaturized tests.

8.7. CONCLUSIONS

The main objectives of R&D on materials for fusion reactors are to develop a full scientific and engineering characterisation, and a theoretical understanding of:

1. **neutron resistant structural materials** able to withstand high 14MeV neutron fluxes while maintaining their structural and thermo-mechanical properties (even in a welded condition) over a sufficiently wide window of operation and for sufficiently long lifetime exposures (fluence) to DEMO reactor and fusion power plant conditions;

2. **high-heat flux and plasma facing materials** able to withstand the combined effects of 14 MeV neutron fluxes and high-intensity plasma ion and neutral bombardment while maintaining their mechanical and thermo-mechanical properties and erosion resistance over a sufficiently wide window of operation and for sufficiently high combined fluence for DEMO reactor and fusion power plants conditions;

to produce and qualify suitable structural and high-heat flux materials that also exhibit reduced activation to avoid permanent waste repositories; to develop industrial production and fabrication methods for the structural, high-heat

flux and plasma facing materials, which could lead to cost savings; and to aim, on the long run, for materials capable of withstanding extra high temperatures to help achieve high thermodynamic efficiency for a fusion power plant, and if possible already for a DEMO machine.

Moving towards fusion electricity production demands materials science. There exist three high-priority fundamental challenges for fusion materials [73] [179]:

- Viable divertor and first wall solution for beyond-ITER fusion devices.
- Suitable structural materials for DEMO (fusion irradiation facility needed).
- Viable tritium partial pressure range in fusion coolants (considering tritium permeation and trapping in piping and structures).

Major fusion materials achievements have been accomplished in the past three decades, including:

Improvements of the knowledge base about radiation effects:

- Multiscale modelling and experiments have shown that the displacement damage component but not transmutation effects of radiation damage produced in a fusion power reactor is well simulated by irradiation in a fission reactor neutron spectrum, which validates the use of fission reactors for initial testing and screening.
- The critical role of helium production on the microstructural stability and lifetime of irradiated materials has been highlighted.
- Neutron irradiations of candidate materials (up to high doses) and complex elements, such as beryllium pebble beds, have been launched and are being completed.

Improvements in the development of structural materials:

- Fundamental fabrication and joining procedures for the three main classes of candidate structural materials have been extensively developed .
- RAFM steels have been developed, which possess unirradiated and irradiated properties comparable or superior to those of conventional steels.
- Vanadium-base alloys with controllable levels of interstitial impurities have been successfully fabricated, welded, and mechanically tested.
- SiC/SiC_f composites with improved mechanical behaviour and radiation resistance have been studied and produced based on advanced fibres and fibre-matrix interfaces although considerable work is needed to demonstrate the viability of these materials for fusion structures
- Recent international activities on ODS RAFM and ODS RAF steels led to promising results, although considerable work is needed to demonstrate the viability of these materials for fusion structures.
- The development of tungsten-base structural materials for high-heat flux high-temperature removal units. However, the programme is still in the phase where the understanding of these materials and their behaviour under irradiation is very limited, making tungsten (W) a prime candidate to be used in future fusion power plant. At the same time, the started material evaluation for the application in DEMO clearly shows the inability of any existing plasma-facing materials to withstand the combination of plasma, radiation and neutron power loads. This harsh reality requires the development of new advanced plasma-facing materials.

Identification of provisional temperature operating windows:

Provisional operating-temperature windows have been established for the three main classes of structural materials. The temperature window for structural materials is mainly limited by their mechanical resistance under irradiation. There are large uncertainties in the allowable operating temperature window for several candidate materials due, in particular, to a lack of mechanical test results on irradiated materials under fusion conditions where transmutation reactions, and not only displacement damage is present..

Recognition of the need of an intense fusion neutron source:

The world fusion programme needs dedicate fusion neutron sources adapted where the fusion spectrum can be mimicked as close as possible in order to address all types of damage and reactions that take places when a 14 MeV neutron interact with materials. The licensing of a fusion reactor will not be possible without the full understanding of the degradation of materials exposed to fusion nuclear reactions. Although several high-performance reduced activation structural materials have been developed over more than 25 years [73], the fusion neutron source constitute one of the key time-limiting steps for the development of fusion energy.

Specific challenges have been identified; including to the effects of helium and hydrogen on many facets of the irradiation response

- Fission-fusion correlations may now be focused on the role of fusion-relevant helium and hydrogen generation on the microstructural evolution.
- The use of available irradiation facilities (fission reactors, accelerator-based facilities) must be pursued to validate modelling results and perform a screening of the materials and specimens to be irradiated in IFMIF/DONES.

and important system-dependent issues such as:

- Insulators to limit MHD power losses in liquid metal systems.
- Design methods for ceramic composite structures.
- Feasibility of using ferromagnetic steels in magnetic confinement concepts.

Supported by the Broader Approach (see below) discussions within the framework of ITER negotiations, the major elements of formally developed global fusion strategy scenarios have become very similar for the different parties. In the case of ITER, fully qualified and assembled TBMs available at the beginning of the operation of phase I (in 2025) will require detailed engineering designs as well as the fabrication and testing of TBM components. The ensuing activities include fabrication, assembly and acceptance tests of final TBMs. In the case of DEMO, while the displacement damage level in ITER TBMs will not exceed ~3 dpa during the entire lifetime, 20 to 30 dpa are to be expected in DEMO blankets within a single year. Therefore, for DEMO design and licensing, all necessary materials should be qualified up to 70 to 80 dpa in a fusion-relevant neutron environment like IFMIF/DONES.

The *Broader Approach* agreement, concluded between the European atomic energy community (Euratom) and Japan, consists of activities which aim to complement the *ITER* project and to accelerate the realisation of fusion energy through R&D and advanced technologies for future demonstration fusion power reactors. An underlying R&D mission of international fusion materials programmes is to advance the materials science base for the development of innovative materials and fabrication methods, which will establish the technological viability of fusion energy and enable improved performance, enhanced safety, and reduced fusion systems' costs so as to allow fusion to reach its full potential. Indeed, the development of such innovative materials for the harsh fusion environment requires a firm understanding of the underlying physical phenomena controlling their performance. Such science-based approach should shorten the time to develop fusion materials and can also be harnessed to develop a range of improved high-temperature materials for non-fusion applications. A comprehensive theory and modelling programme that is well integrated with experimental studies using existing materials science facilities (corrosion loops, fission test reactors, accelerator-based facilities, etc.) is very important to accelerate the development of fusion materials.

Furthermore, the recent rapid progress in computational materials science (in conjunction with experimental validation tests in existing facilities) should help solving several of the scientific questions that are critical for the successful development of fusion materials. Indeed, an enhanced theory and modelling programme does not replace the need for a dedicated neutron source such as IFMIF/DONES to fully develop and qualify materials for a DEMO-type fusion reactor. Experimental validation of the behaviour of materials under reactor relevant conditions is necessary to confirm model predictions and to gain approval from licensing and capital investment authorities. As noted in various international fusion energy development roadmaps, the construction of a fusion materials neutron irradiation facility is needed in parallel with ITER for fusion energy to become a major worldwide energy source.

In general, the microstructural modifications made to enhance the radiation resistance of fusion materials also improve the overall unirradiated properties. This can lead to the development of improved materials for near-term commercial applications. For example, a high-density of finely-dispersed precipitates that are resistant to coarsening

or dissolution is a key feature in the development of high-performance structural materials for both irradiation stability and thermal creep strength. Similarly, the improved stoichiometric SiC fibres and tailored interphases that are essential to producing radiation resistant SiC/SiC_f composites also provide improved elastic modulus matching and load transfer balancing between the fibres and matrix, which leads to high mechanical performance in non-irradiation conditions.

The selection and development of adequate materials for fusion power reactors will not solve all design problems. The design is complex by nature, and further innovations will be needed to overcome material limitations. Fabrication and processing are major keys to increase the degrees of freedom for design and the present selection of materials may have to be revised. Close discussions between material scientists and the designers of the various first wall, breeding blanket and divertor concepts are strongly required on the path to the construction of attractive fusion power reactors.

8.8. REFERENCES

[1] BALUC, N. et al., Status of R&D activities on materials for fusion power reactors, Nuclear Fusion **47** (2007) S696-S717, and private communications.
[2] STORK, D. Z. S., Introduction to the special issue on the technical status of materials for a fusion reactor, Nuclear Fusion **57** (2017).
[3] ZINKLE, S., Advanced materials for fusion technology, Fusion Engineering and Design **74** (2005) 31–40.
[4] BLOOM, E., et al., Critial questions in material science and engineering for successful development of fusion power, Journal of Nuclear Materials **367** (2007) 1–10.
[5] PEACOCK, A., et al., EU contributions to the ITER materials properties data assessment, Fusion Engineering and Design **75** (2005) 703–707.
[6] BARABASH, V., et al., Materials challenges for ITER – Current status and future activities, Journal of Nuclear Materials **367** (2007) 21–32.
[7] BALUC, N., et al., Status of reduced activation ferritic/martensitic steel development, Journal of Nuclear Materials **367** (2007) 33–41.
[8] KIMURA, A., et al., Recent progress in US–Japan collaborative research on ferritic steels R&D, Journal of Nuclear Materials **367** (2007) 60–67.
[9] MÖSLANG, A., Towards reduced activation structural materials data for fusion DEMO reactors, Nuclear Fusion **45** (2005) 649–655.
[10] ZINKLE, S., Development of next generation tempered and ODS reduced activation ferritic/martensitic steels for fusion energy applications, Nuclear Fusion **57** (2017) 092005.
[11] TANIGAWA, H., et al., Development of benchmark reduced activation ferritic/martensitic steels for fusion energy applications, Nuclear Fusion **57** (2017) 092004.
[12] RIETH, M. D. B., Limitations of W and W-1%La2O3 for use as structural materials, Journal of Nuclear Materials **342** (2005) 20–25.
[13] ZINKLE, S. G. N., Operating temperature windows for fusion reactor structural materials, Fusion Engineering and Design **51** (2000) 55–71.
[14] HODGSON, E., Materials challenges for diagnostics beyond ITER, Fusion Science and Technology **62** (2012) 89–96.
[15] ROVNER, L. H., HOPKINS, G. R., Ceramic Materials for Fusion, Nucl. Technol. **29** (1976) 274–302.
[16] VAYAKIS, G., et al., Generic diagnostic issues for a burning plasma experiment, Fusion Sci. and Techn. **53** (2008) 699–750.
[17] VOITSENYA, V., et al., Experimental simulation of the behaviour of diagnostic first mirrors fabricated of different metals for ITER conditions, Open Physics Journal **3** (2016) 19–53.
[18] DONNÉ, A., et al., Progress in the ITER physics basis, chapter 7: Diagnostics, Nuclear Fusion **47** 6 (2007) S337–S384.
[19] MOROÑO, A. H. E. R., Radioluminescence problems for diagnostic windows, Journal of Nuclear Materials **224** (1995) 216–221.
[20] MOROÑO, A. H. E. R., Radiation induced optical absorption and radioluminescence in electron irradiated SiO2, Journal of Nuclear Materials **258** (1998) 1889–1892.
[21] KONOVALOV, V., et al., On the problem of material for the in-vessel mirrors of plasma diagnostics in a fusion reactor, Fusion Engineering and Design **56** 57, (2001) 923–927.
[22] HODGSON, E. R., SHIKAMA, T., "Radiation Effects on the Physical Properties of Dielectric Insulators for Fusion Reactors", Comprehensive Nuclear Materials 4, Elsevier, Amsterdam (2012) 701–724.
[23] DECRETON, M., Viewing systems in the fusion reactor vessel – radiation hardened glasses up to 300 MGy, in 18th Symposium On Fusion Technology, Karlsruhe, 1995.
[24] IN'KOV, V. I., et al., Time variation of the optical absorption of quartz KU-1 induced by gamma irradiation, Journal of Nuclar Materials **256** (1998) 254–257.
[25] FUKS, L. D. C., Optical properties of irradiated synthetic sapphire and yttria-stabilized zirconia spectroscopic windows, Journal of Nuclear Materials **280** (2000) 360–364.
[26] GARCÍA–MATOS, M. et al., KU1 quartz glass for remote handling and LIDAR diagnostic optical transmission systems, Journal of Nuclear Materials **283** 287 (2000) 890–893.

[27] NISHITANI, T., et al., Neutron irradiation tests on diagnostic components at JAERI, Fusion Engineering and Design **56** 57 (2001) 905–909.
[28] LIPA, M., et al., Development and testing of diagnostic windows for Tore Supra/CIEL and ITER, Fusion Engineering and Design **61** 62 (2002) 801–806.
[29] SUGIE, T., et al., In situ transmissivity measurements of KU-1 quartz in the UV range under 14MeV neutron irradiation, Journal of Nuclear Materials **307** 311 (2002) 1264–1267.
[30] VUKOLOV, K. L. B., Results of irradiation tests of KU-1 and KS-4V silica glasses as ITER candidate window materials, Fusion Engineering and Design **66** 68 (2003) 861–864.
[31] MOROÑO, A., et al, KU1 and KS-4V quartz glass lenses for remote handling and diagnostic optical transmission systems, Journal of Nuclear Materials **329** 333 (2004) 1438–1441.
[32] ISLAMOV, K., et al., Radiation–optical characteristics of quartz glass and sapphire, Journal of Nuclear Materials **362** (2007) 222–226.
[33] VUKOLOV, K., Radiation effects in window materials for ITER diagnostics, Fusion Engineering and Design **84** (2009) 1961–1963.
[34] LEON, M., et al., Neutron irradiation effects on optical absorption of KU1 and KS-4V quartz glasses and Infrasil 301, Fusion Engineering and Design **84** (2009) 1174–1178.
[35] ORLOVSKIY, I., et al., Neutron irradiation of modern KU-1 and KS-4V fused silica, Journal of Nuclear Materials **442** (2013) S508–S510.
[36] ISLAMOV, K., et al., Efficiency of generation of optical centers in KS-4V and KU-1 quartz glasses at neutron and gamma irradiation, Journal of Nuclear Materials **443** (2013) 393–397.
[37] FAHRBACH, H. E. A., Radiation-induced transmission loss in optical materials at infrared wavelengths, Radiation effects and defects in solids **65** (1982) 127–130.
[38] COLBY, E., et al., Gamma Radiation Studies on Optical Materials, IEEE Transactions on Nuclear Science, 2002.
[39] WHAN, R., Investigations of oxygen-defect interactions between 25 and 700 K in irradiated Ge, Physical Review A **140** (1965) 690.
[40] BECKER, J. C. J., Infrared properties of 40–60 MeV electron irradiated Ge, Journal of Applied Physics **37** (1965).
[41] SHI, Y., et al., Optical studies of infrared active electronic defects in neutron irradiated silicon after annealing at 450 °C, Phys. Status Solidi A **144** (1994) 139–148.
[42] LEVALOIS, M. M. P., Damage induced in semiconductors by swift heavy ion irradiation, Nuclear Instrumentation and Methods in Physics Research B **156** (1999) 64–71.
[43] KONAK, T., et al., Effects of γ-irradiation on optical, electrical, and laser characteristics of pure and transition metal doped II-VI semiconductors, in SPIE 7912, 2011.
[44] DANTAS, N. et al., Optical absorption (OA) bands in fluorites by heavy gamma irradiation **116** (1996) 269–273.
[45] IZERROUKEN, M. et al., Color centers in neutron-irradiated YAG, CaF2, and LiF single crystals, Journal of Luminescence **127** (2007) 696–702.
[46] NEPOMNYASHCHIKH, I., et al., Defect formation and VUV luminescence in BaF2, Radiation effects and defects in solids **157** (2002) 715–719.
[47] JIANG, C., Neutron irradiation of Czochralski and temperature gradient technique grown YAG crystals, Physica B: Condensed Matter 73 (2006) 42–45.
[48] SALASCA, S., et al., Development of equatorial visible/infrared wide angle viewing system and radial neutron camera for ITER, Fusion Engineering and Design **84** (2009) 1689–1696.
[49] HEIDINGER, R. et al., Neutron Irradiation Studies on Window Materials for EC Wave Systems, Fusion Engineering and Design **56** 57 (2001) 471.
[50] KAWANO, Y. et al., Infrared laser polarimetry for electron density measurement in tokamak plasmas, Review of Scientific Instruments **72** (2001) 1068–1072.
[51] MOROÑO, A. et al., Radiation effects on the optical and electrical properties of CVD diamond, Fusion Engineering and Design **82** (2007) 2563–2566.
[52] MALO, M. et al., Radioluminescence characterization of hot pressed, reaction bonded, and CVD SiC, in Confrence Series: Materials Science and Engineering, 2010.
[53] SAKAMOTO, K., Progress of high power 170 GHz gyrotron in JAEA, Nuclear Fusion **49** (2009) 095019.
[54] MOROÑO, A. M. M. H. E., Radiation testing of diagnostic window bondings for enhanced H isotope diffusion, Fusion Engineering and Design **86** (2011) 2466–2469.
[55] YAMAMOTO, S., et al., Impact of irradiation effects on design solutions for ITER diagnostics, Journal of Nuclear Materials **283** 287 (2000) 60–69.
[56] DECRETON, M., et al., Performance of functional materials and components in a fusion reactor: the issue of radiation effects in ceramics and glass materials for diagnostics, Journal of Nuclear Materials **329** 333 (2004) 125–132.
[57] RAMSEY, A., D–T radiation effects on TFTR diagnostics, Review of Scientific Instruments **66** (1995) 871–876.
[58] MAAS, A., et al., Diagnostic experience during deuterium–tritium experiments in JET, techniques and measurements, Fusion Engineering and Design **47** (1999) 247–265.
[59] BRICHARD, B., et al., Radiation assessment of hydrogen-loaded aluminium-coated pure silica core fibres for ITER plasma diagnostic applications, Fusion Engineering and Design **82** (2007) 2451–2455.

[60] FERNANDEZ–FERNANDEZ, A., et al., Real-time fibre optic radiation dosimeters for nuclear environment monitoring around thermonuclear reactors, Fusion Engineering and Design **83** (2008) 50–59.
[61] HODGSON, E., General radiation problems for insulating materials in future fusion devices, Journal of Nuclear Materials **258** 263 (199) 226–233.
[62] PELLS, G. P., et al., "Radiation effects in electrically insulating ceramics, Culham/EEC Fusion Technology Task MAT-13", AERE R 13222 (1988).
[63] SHIKAMA, T. Z. S., Electrical in-situ and post-irradiation properties of ceramics relevant to fusion irradiation conditions, Journal of Nuclar Materials **307** 311 (2002) 1073–1079.
[64] LINKE, J., "Towards Fusion Energy-Plasma Physics, Diagnostics, Spin-Offs", 5th International Workshop and Summer School, Kudowa Zdroj, 2005.
[65] TABARÉS, F., Plasma Physics and Controlled Fusion 58 (2016) 14014.
[66] IBARRA, A., et al., A staged approach from IFMIF/EVEDA toward IFMIF, Fusion Science and Technology **66** (2014) 252–259.
[67] LLEWELLYN-SMITH, C. Fusion Engineering and Design **74** (2005) 3–8.
[68] VLADIMIROV, M. A., Comparison of material irradiation conditions for fusion, spallation, stripping and fission neutron sources, Journal of Nuclar Materials **329** (2004) 233–237.
[69] MÖSLANG, A., "The IFMIF test facilities design", 7th International Symposium on Fusion Nuclear Technology, Tokyo, 2005.
[70] ZAKHAROV, L., et al., Ignited spherical tokamaks and plasma regimes with Li walls, Fusion Engineering and Design **72** (2004) 149–168.
[71] DOLAN, T. J., Magnetic Fusion Technology, Springer (2013) 364–365.
[72] DOLAN, T., Lithium deuteride/lithium tritide pellet injection, Fusion Science and Technology **61** (2012) 240–247.
[73] KNASTER, J., et al., IFMIF: overview of the validation activities, Nuclear Fusion **53** 11 (2013) 116001.
[74] KNASTER, J., et al., The accomplishment of the engineering design activities of IFMIF/EVEDA, Nuclear Fusion **55** (2015).
[75] WARD, D., Plasma Physics and Controlled Fusion **52** (2010) 124033.
[76] KALLENBACH, A., et al., Plasma Physics and controlled Fusion **55** (2013) 124041.
[77] RIETH, M., et. al., Journal of Nuclear Materials **432** (2013) 482.
[78] COENEN, J., et al., Materials for DEMO and reactor applications—boundary conditions and new concepts, Physica Scripta T167 (2016).
[79] WEGENER, T., et al., Nuclear Materials and Energy 9 (2016) 394–398.
[80] KOCH, F., et al., Self-passivating W-based alloys as plasma facing material for nuclear fusion, Physica Scripta T128 (2007) 100–105.
[81] KOCH, F., et al., Journal of Nuclear Materials **386** 388 (2009) 572–574.
[82] KOCH, F., et al., Physica Scripta T145, (2011) 014019.
[83] TELU, S., et al., Metallurgical and Materials Transactions A 46 (2015) 5909–5919.
[84] PRZYBYLSKI, K., et al., Grain boundary segregation of yttrium in chromia scales, Journal of The Electrochemical Society **135** 2 (1988) 509517.
[85] STROOSNIJDER, M., et al., The influence of yttrium ion implantation on the oxidation behaviour of powder metallurgically produced chromium, Surface and Coating Technology **83** (1996) 205.
[86] BIRKS, N. M., et al. Introduction to the High-Temperature Oxidation of Metals, Cambridge University Press, 2006.
[87] MEVREL, R., et al., Cyclic oxidation of high-temperature alloys, Materials Science and Technology **3** (1987) 531–535.
[88] BÜRGEL, R.,et al., Handbuch Hochtemperatur-Werkstofftechnik, PRAXIS, 2011.
[89] LANG, E., The role of active elements in the oxidation behavior of high temperature metals and alloys, Journal of Materials Research (1989) 39.
[90] PILLING, N. B., R., Journal of the Institute of Metals **29** (1923) 529-591.
[91] BARIN, I. P. G., Thermomechanical data of pure substances, 3 ed., New York, 1995.
[92] IGITKHANOV, Y., et al., KIT Scientific report 7637, Karsruhe.
[93] WEGENER, T., et al., Fusion Engineering and Design **124** (2017) 183.
[94] LOPEZ–RUIZ, P., et al., Physica Scripta T145 (2011) 014018.
[95] CALVO, A., et al., Self-passivating W-Cr-Y alloys: characterization and testing, Fusion Engineering and Design **124** (2017) 1118–1121.
[96] CALVO, A., et al., Nuclear Materials and Energy **9** (2016) 422.
[97] GUILLON, O. et al., Advanced Engineering Materials 7 16 (2014) 830.
[98] LITNOVSKY, A., et al., Physica Scripta **T170** (2017) 014012.
[99] ITER, Material Specification for the Supply of Tungsten Plates for the ITER Divertor IDM ITER_D_2EDZJ4, Cadarache.
[100] KRETER A., et al., Linear Plasma Device PSI-2 for Plasma-Material Interaction Studies, Fusion Science and Technology **68** 1 (2015) 8–14.
[101] PHILIPPS, V., Tungsten as material for plasma-facing components in fusion devices, Journal of Nuclear Materials **415** (2011) 2–9.
[102] YOU J.–M., et al., European DEMO divertor target: Operational requirements and materialdesign interface, Nuclear Materials and Energy **9** (2016) 171–176.

[103] STORK, D., et al., Developing structural, high-heat flux and plasma facing materials for a near-term DEMO fusion power plant: The EU assessment, Journal of Nuclear Materials **455** (2014) 277–291.
[104] RIETH, M., et al., A brief summary of the progress on the EFDA tungsten materials program, Journal of Nuclear Materials **442** (2013) 173–180.
[105] REISER, J. R. M., Optimization and limitations of known DEMO divertor concepts, Fusion Engineering and Design **87** (2012) 718–721.
[106] STORK, D., et al., Assessment of the EU R&D programme on DEMO structural and high-heat flux materials, final report of the materials assessment group, Technical Report (12)52/7.2 (2012).
[107] BACHMANN, C., et al., Initial DEMO tokamak design configuration studies, Fusion Engineering and Design. **98-99** (2015) 1423–1426.
[108] RIESCH, J., et al., Development of tungsten fibre-reinforced tungsten composites towards their use in DEMO—potassium doped tungsten wire, Physica Scripta (2016).
[109] LAUNEY, M. R. R., On the fracture toughness of advanced materials, Advanced Materials **21** (2009) 2103–2110.
[110] CZEL, G. W. M., Demonstration of pseudo-ductility in high performance glass/epoxy composites by hybridisation with thin-ply carbon prepreg, Composites Part A: Applied Science and Manufacturing **52** (2013) 23–30.
[111] SHIMODA, K., et al., Influence of pyrolytic carbon interface thickness on microstructure and mechanical properties of SiC/sic composites by NITE process, Composites Science and Technology **68** (2008) 98–105.
[112] CALVO, A., et al., Manufacturing and testing of self-passivating tungsten alloys of different composition, Nuclear Materials and Energy **9** (2016).
[113] WEGENER, T., et al., New smart self-passivating tungsten alloys for future fusion reactors, PFMC (2015).
[114] WEGENER, T., et al., Development of yttrium-containing self-passivating tungsten alloys for future fusion power plant, Nuclear Materials and Energy **9** (2016).
[115] WEGENER, T., et al., Development and analyses of self-passivating tungsten alloys for DEMO operational and accidental conditions, Fusion Engineering Design **124** (2017).
[116] RIESCH, J., et al., In situ synchrotron tomography estimation of toughening effect by semiductile fibre reinforcement in a tungsten-fibre-reinforced tungsten composite system, Acta Materialia **61** 19 (2013) 7060–7071.
[117] RIESCH, J., et al., Enhanced toughness and stable crack propagation in a novel tungsten fibre-reinforced tungsten composite produced by chemical vapour infiltration, Physica Scripta T159 (2014) 014031.
[118] JASPER, B., et al., Behavior of tungsten fiber-reinforced tungsten based on single fiber push-out study, Nuclear Materials and Energy (May 2016).
[119] COENEN, J.W., et al., Advanced materials for a damage resilient divertor concept for DEMO: Powder-metallurgical tungsten-fibre reinforced tungsten, Fusion Engineering Design **124** (2017) 964-968.
[120] RIESCH, J., et al., Chemically deposited tungsten fibre-reinforced tungsten the way to a mock-up for divertor applications, Nuclear Materials and Energy **9** (2016) 75–83.
[121] RIESCH, J., et al., Properties of drawn W wire used as high-performance fibre in tungsten fibre-reinforced tungsten composite, IOP Conference Series: Materials Science and Engineering **139** (2016) 012043.
[122] BOLT, H., et al., Plasma facing and high heat flux materials needs for ITER and beyond, Journal of Nuclear Materials (2002) 43–52.
[123] HU, X., et al., Irradiation hardening of pure tungsten exposed to neutron irradiation, Journal of Nuclear Materials (2016).
[124] HUBERT, M., et al., The absence of plasma in "spark plasma sintering", Journal of Applied Physics **104** 3 (2008) 033305.
[125] ALMANSTOETTER, J., A modified Drucker–Prager Cap model for finite element simulation of doped tungsten powder compaction. International, Journal of Refractory Metals and Hard Materials **50** (2015) 290–297.
[126] WU, Y., et al., Preparation of yttrium oxide coating by MOCVD as tritium permeation barrier, Fusion Engineering and Design **90** 0 (2015) 105–109.
[127] CAUSEY, R., et al., "Tritium barriers and tritium diffusion in fusion reactors.", Comprehensive Nuclear Materials, Oxford, Elsevier, (2012) 511–549.
[128] ZHANG, K. H. Y., Sealing of pores in sol-gel-derived tritium permeation barrier coating by electrochemical technique, Journal of Nuclear Materials **417** 13 (2011) 1229–1232.
[129] CHIKADA, T., et al., Deuterium permeation behavior of erbium oxide coating on austenitic, ferritic, and ferritic/martensitic steels, Fusion Engineering and Design **84** 26 (2009) 590–592.
[130] CHIKADA, T., et al., Microstructure control and deuterium permeability of erbium oxide coating on ferritic/martensitic steels by metal-organic decomposition, Fusion Engineering and Design **79** (2010) 1537–1541.
[131] LEVCHUK, D., et al., Gas-driven deuterium permeation through Al2O3 coated samples, Physica Scripta T108 (2004) 119.
[132] HOLLENBERG, G., et al., Tritium/hydrogen barrier development, Fusion Engineering and Design **28** 0 (1995) 190–208.
[133] DU, J., et al., A feasibility study of tungsten-fiber-reinforced tungsten composites with engineered interfaces (2011) PhD thesis.
[134] DU, J., et al., Thermal stability of the engineered interfaces in Wf/W composites, Journal of Materials Science **47** 11 (2012) 4706–4715.
[135] BONIFACIO, C., et al., Evidence of surface cleaning during electric field assisted sintering, Scripta Materialia **69** 11 (2013) 769–772.

[136] BONIFACIO, C., et al., Time-dependent dielectric breakdown of surface oxides during electric-field-assisted sintering, Acta Materialia **63** (2014) 140–149.
[137] GROZA, J. Z. A., Sintering activation by external electrical field, Materials Science and Engineering: A 287 (2000) 171–177.
[138] COENEN, J., et al., Plasma-wall interaction of advanced materials, Nuclear Materials and Energy 12 August (2017) 307–312.
[139] LI, M. Y. J.–H., Cracking behavior of tungsten armor under ELMlike thermal shockloads II: A revised prediction for crack appearance map, Nuclear Materials and Energy **9** (2016) 598–603.
[140] NEU, R., et al., Advanced tungsten materials for plasma-facing components of DEMO and fusion power plants, Fusion Engineering and Design. **109–111** (2016) 1046–1052.
[141] YOU J.–M., "Progress in the initial design activities for the European DEMO divertor", 29th Symposium on Fusion Technology, Prague (2016).
[142] von Mueller, A., "Melt infiltrated W-Cu composites as advanced heat sink materials for plasma facing components", 29th Symposium on Fusion Technology, Prague (2016).
[143] ENGELS, J., et al., "Yttrium oxide coatings as tritium permeation barriers", 29th Symposium on Fusion Technology, Prague (2016).
[144] YOU J.–M., et al., Thermal and mechanical properties of infiltrated W/CuCrZr composite materials for functionally graded heat sink application, Journal of Nuclear Materials **438** (2013) 1–6.
[145] VLADIMIROV, pp. B. S., Comptes rendus physiques **9** (2008) 303.
[146] DAI, Y., et al., Journal of Nuclear Materials **318** (2003) 167.
[147] ZINKLE, S. M. A., Fusion Enginering and Design **88** (2013) 472.
[148] TANIGAWA, H., et al., Status and key issues of reduced activation ferritic/martensitic steels as the structural material for a DEMO blanket, Journal of Nuclear Materials **417** (2011) 9–15.
[149] MAZEY, D., Fundamental aspects of high-energy ion-beam simulation tech-niques and their relevance to fusion materials studies, Journal of Nuclear Materials **174** (1990) 196–209.
[150] TROCELLIER, P., et al., Nuclear Instrumentation and Methods in Physics B **266** (2008) 3178–3181.
[151] HINKS, J., A review of transmission electron microscopes with in situ ion irradiation, Nuclear Instrumentation and Methods in Physics B **267** (2009) 3652–3662.
[152] BORODIN, O. V., et al., Journal of Nuclear Materials **442** (2013) S817.
[153] STOLLER, R. E., "Primary radiation damage formation", Comprehensive Nuclear Materials, Elsevier, Amsterdam (2012) 293–332.
[154] GONZÁLEZ DE VICENTE, S. M., et al., Nuclear Fusion **57** (2017) 092011.
[155] YABUUCHI, K., et al., Journal of Nuclear Materials **455** 1–3 (2014) 690–694.
[156] ICFRM-16, "Proceedings of the 16th International Conference on Fusion Reactor Materials".
[157] SCHOLZ, H., et al., "Journal of Nuclear Materials" **258–263** 2 (1998) 1572–1576.
[158] ULLMAIER, H., The influence of helium on the bulk properties of fusion reactor structural materials, Nuclear Fusion **24** (1984) 1039–1083.
[159] SCHROEDER, H. U. H., Journal of Nuclear Materials **118** (1991) 179.
[160] JUNG, pp., et al., Journal of Nuclear Materials **318** (2013) 241.
[161] HENRY, J., et al., Journal of Nuclear Materials **318** (2003) 249.
[162] HENRY, J., et al., Tensile and impact properties of 9Cr tempered martensitic steels and ODS-FeCr alloys irradiated in a fast reactor at 325 °C up to 78 dpa, Journal of Nuclear Materials **417** (2011) 99–103.
[163] MOTA, F., et al., Fusion Engineering and Design **86** (2011) 2425–2428.
[164] GILBERT, M., et al., Journal of Nuclar Materials **467** (2015) 121–134.
[165] STORK, D., et al., Fusion Engineering and Design **89** (2014) 1586.
[166] LUCAS, G., et al., The role of small specimen test technology in fusion materials development, Journal of Nuclear Materials. **367–370** (2007) 1549–1556.
[167] IVANOV, A. P. V., Gas-dynamic trap: an overview of the concept and experimental results, Plasma Physics and Controlled Fusion **55** (2013) 6.
[168] SAMARAS, M., Materials Today **12** (2009) 46.
[169] DUDAREV, S., et al., Journal of Nuclear Materials **386–388** (2009) 1.
[170] ZINKLE, S. B. J., Materials Today **12** (2009) 12.
[171] NGUYEN–MANH, D., DUDAREV, S., Materials Science and Engineering **423** (2006) 75.
[172] WILLAIME, F., et al., Nuclear Instruments and Methods in Physics Research B **228** (2005) 92.
[173] TERENTYEV, D., et al., Journal of Nuclear Materials **409** (2011) 167.
[174] DERLET, pp., et al., Physical Review B **76** (2007) 054107.
[175] CALDER, A., et al., Philosophical Magazine & Philosophical Magazine Letters **88** (2008) 43.
[176] TERENTYEV, D., et al., Journal of Nuclear Materials **351** (2006) 65.
[177] HULL, D. B. D., Introduction to dislocations, Oxford, Oxfordshire: Butterworth–Heinemann (2001).
[178] BACON, D., et al., "Dislocation Obstacle Interactions at the Atomic Level", Dislocation in Solids.
[179] ZINKLE, S. J., et al., Multimodal options for materials research to advance the basis for fusion energy in the ITER era, Nuclear Fusion **53** 2013.

[180] ZINKLE, S. H. E., Radiation-induced changes in the physical properties of ceramic materials, Journal of Nuclear Materials **191** (1992) 58–66.
[181] THUMM, M., et al., Status report on CVD-diamond window development for high power ECRH, Fusion Engineering and Design **53** (2001) 517–524.
[182] TAKAHASHI, K., et al., Development of EC H&CD launcher components for fusion device, Fusion Engineering and Design **66** (2003) 473–479.
[183] MAISONNER, D., et al., "A Conceptual Study of Commercial Fusion Power Plants", Final Report (2005) EFDA-RP-RE-5.0.
[184] ITER, "Material Specification for the Supply of Tungsten Plates for the ITER Divertor IDM ITER_D_2EDZJ4;", Cadarache.

Chapter 9

VACUUM PUMPING AND FUELLING

Christian Day*
Karlsruhe Institute of Technology, Institute of Technical Physics
Germany

Seen from a vacuum engineer´s point of view, a fusion device is a very large, very complex vacuum system. ITER will be the most complex vacuum system of the world given the sheer volume of the experiment, the need for double containment barriers for all tritium carrying systems and the variety of operational states. As an example, the complete ITER vacuum system contains 400 vacuum pumps and more than 6 km of vacuum pipework. On the other side, the topic of vacuum pumping provides good examples of fusion-triggered innovative spin-offs for the industry (e.g. new vacuum pump technologies) and opportunities in science (e.g. the rigorous use of advanced vacuum gas dynamic methods in vacuum system design).

The fuelling of a confined plasma is a central operational task and turns out to be much more complicated than one would think. This comes from the fact that the steady state gas throughput of a fusion device is primarily given by control and stability issues rather than the consumption of fuel in the fusion reaction (this actually represents a negligibly small part). On top come the non-fuel type plasma enhancement gases that have to be introduced, e.g. for radiative protection of the divertor high heat flux surfaces. This explains the treatment of vacuum pumping and fuelling in a common chapter. In steady state condition all gas that is injected has to be pumped out. The machine throughput thus directly specifies both the fuelling systems and the size of the vacuum pumps. This chapter is, however, not limited to the provision of fuel but addresses all needs and aspects of injecting matter into the plasma chamber. This topic is not fully understood and represents a field where comprehensive research is ongoing.

The chapter is organized as follows. Section 9.1 offers a general introduction to the fundamental aspects of vacuum science and technology. The state of the art of vacuum gas dynamics is subsequently discussed. The general concepts behind vacuum pressure measurement are presented in Section 9.2, followed by an explanation of the solutions selected for ITER. Section 9.3 introduces various types of vacuum pumps. For each type of pump, a general technological description and a discussion on its suitability for nuclear fusion applications are provided. This section also presents a detailed description of the ITER primary and roughing pumps. In Section 9.4, the vacuum requirements of ITER are compared to those of a fusion power plant (FPP) and potential solutions are discussed. In Section 9.5, the functions of the fuelling systems are explained, including a short excursion to plasma physics for a better understanding. Finally, state of the art technology choices for existing devices and FPP are outlined in Section 9.6. The discussion concludes with a short introduction to the complete inner fuel cycle of a power plant leading to the chapter on tritium handling.

9.1. BASIC CONCEPTS AND TERMINOLOGY

Vacuum is defined in the international norms and standards as '(…) the condition of a gas whose pressure is less than 300 mbar, which is the lowest of the atmosphere at any place of the surface of the earth (…)' (DIN 28400, ISO 3529). The main task of a vacuum engineer is to produce and maintain a specified vacuum condition in a specified place and to properly choose equipment and instruments that serve to produce, apply, and diagnose these most varied vacua. The present section introduces the fundamental concepts and ideas needed to describe a vacuum task and come up with a sound and self-consistent vacuum system design.

9.1.1. Pressure regimes

The quantity named pressure p is defined as the ratio of the force F exerted perpendicularly to a surface element A:

$$p := \frac{F}{A} \tag{9.1}$$

* Parts of this chapter have been taken from Christian Day: Vacuum Technology. Ullmann´s Encyclopedia. 2014. Copyright Wiley-VCH GmbH. Reproduced with permission.

TABLE 9.1. Pressure regimes.

VACUUM RANGE	PRESSURE RANGE
Rough vacuum	10^5 Pa to 10^2 Pa
Fine vacuum	10^2 Pa to 10^{-1} Pa
High vacuum (HV)	10^{-1} Pa to 10^{-5} Pa
Ultrahigh vacuum (UHV)	10^{-5} Pa to10^{-10} Pa
Extreme vacuum (XHV)	$< 10^{-10}$ Pa

Consequently, the international system (SI) unit is the pascal[1] (1 Pa = 1 N/m^2). Other commonly used pressure units are the bar (1 bar = 10^5 Pa) and Torr = 1 mm Hg (1 Torr ≈ 133.322 Pa)[76]. Vacuum technology encompasses a pressure range of ~15 orders of magnitude, from ambient pressure (10^5 Pa) down to 10^{-10} Pa in the extreme vacuum region. Pumps, materials, measurement instruments and joining techniques have to be selected accordingly. It is therefore customary to classify the whole vacuum pressure range as shown in Table 9.1.

9.1.2. Equation of state

At sufficiently low pressures, the ideal gas equation describes the relationship between the state variables, namely pressure, amount of gas and temperature:

$$pV = \upsilon RT = NkT \quad \text{or} \quad p = nkT \tag{9.2}$$

where υ is the number of mols[77], R the universal gas constant (8.314 J·mol^{-1}·K^{-1}), k the Boltzmann constant (1.3805 × 10^{-23} J/K), N the number of particles, and n the number density of particles. The left hand side equation is written in two different ways. The first describing the macroscopic point of view and the second the molecular point of view. The mass and the molar systems are related via the following equations:

$$R = N_\mathrm{A} \times k \quad , \tag{9.3a}$$

$$M = N_\mathrm{A} \times m \quad , \tag{9.3b}$$

whereby M denotes the molar mass and m the mass of a single particle. Standard conditions are defined as p_{st} = 1 atm = 101325 Pa and T_{st} = 273.15 K.

9.1.3. Kinetic theory

The atomistic foundation of the kinetic theory of gases offers the framework to derive the macrosocopic properties of a gas (such as its transport properties viscosity, thermal conductivity and diffusion coefficient) from the microscopic behaviour of individual gas particles. This theory is based on the conception that a gas consists of a very large number of particles that move thermally, colliding with the walls and one another.

To obtain macroscopic information from an ensemble of travelling particles, their velocity distribution has to be known. It is usually given by the Maxwell–Boltzmann velocity distribution, which can be derived from statistical mechanics. It is based on an assymetric distribution function, shown in Fig. 9.1, normalized to the most probable velocity c_{mp}, which denotes the peak value. The most important quantity is the mean thermal velocity $\bar{c}$, which is obtained by calculating the weighted average.

$$c_{mp} = \sqrt{\frac{2kT}{m}} = \sqrt{\frac{2RT}{M}} \tag{9.4}$$

[76] Unit names were chosen in remembrance of Blaise Pascal (1623–1662) and Evangelista Torricelli (1608–1647) who demonstrated with the famous mercury manometer in the 1640s that vacuum exists in nature, a fact which was denied by many ancient philosophers (horror vacui).

[77] One mol has N_A = 6.022 × 10^{23} particles (the Avogadro constant).

$$\bar{c} = \sqrt{\frac{8kT}{\pi\, m}} = \sqrt{\frac{8RT}{\pi\, M}} \qquad (9.5)$$

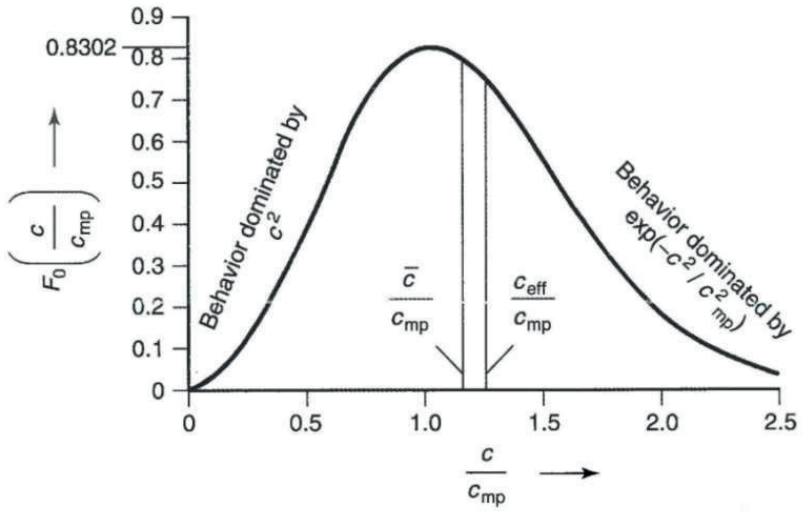

FIG. 9.1. Distribution function of the absolute (scalar) values c of the particle velocity vector normalized to its peak value.

By mathematical manipulation of the distribution function, one obtains the following expression for the surface related incidence rate j, which is defined as the number of collisions with a surface per unit area and time:

$$j := \frac{\dot{N}}{A} = \frac{n\,\bar{c}}{4} \quad , \qquad (9.6)$$

and for the buildup time t_{mon} of a monolayer of gas on a surface, which is an important parameter regarding cleanliness and outgassing effects:

$$t_{mon} := \frac{n'}{j} = \frac{n'}{p \cdot N_A}\sqrt{2\pi MRT} \quad , \qquad (9.7)$$

revealing an inverse relation to pressure and a square root dependence on the molecular mass of the gas. For a closest packing of atoms at a surface (assuming a typical particle radius of 1.6×10^{-10} m), the maximum surface related number density n′ can be calculated as approximately 10^{15} cm^{-2}.

9.1.3.1. Example

Derive the ultimate pressure of a cryocondensation surface at T_c, surrounded by a thermal shield at T_{sh}.
Before stationary operation is established, the pumped flux j_{pump} results as the difference between the condensed flux j_c and the evaporated flux j_{ev}:

$$j_{\text{pump}} = j_c - j_{ev} = j_c \times \left(1 - \frac{j_{ev}}{j_c}\right)$$

At the low temperatures of interest, one can use Eqs (9.5) and (9.6) to write the fluxes and finds the dependence:

$$j \sim \frac{p}{\sqrt{T}}$$

Under ultimate pressure conditions, the pumping speed and hence the pumped flux is zero (thermodynamic equilibrium). Thus, the bracket in the equation above can be set to zero. For the evaporating gas, the temperature of the cold surface T_c and the saturation pressure $p_{sat}(T_c)$ is to be used; for the condensing gas, the higher temperature of the surrounding shield T_{sh} and the gas pressure in the vessel should be used.
This yields the following expression for the ultimate pressure:

$$1 = \frac{p_{sat}/\sqrt{T_c}}{p_{ult}/\sqrt{T_{sh}}} \rightarrow p_{ult} = p_{sat} \cdot \sqrt{\frac{T_{sh}}{T_c}} > p_{sat}$$

It should be noted that the ultimately achievable pressure is always higher (i.e. worse) than the equilibrium saturation pressure. For a typical case where the cryosurface at 4.5 K is surrounded by a thermal shield at 80 K, the square root takes the value 4.5.

Furthermore, the interaction of gas particles with one another is determined in the kinetic theory of gases by the gas kinetic effective molecular diameter d_m and the resulting collision cross section $\sigma = \pi d_m^2$. From there, the mean free path λ, which denotes the average distance a particle travels between two collisions, can be computed. It is important to note that the mean free path is inversely proportional to the pressure whereas the collision rate (like density, via the ideal gas law) is proportional to the pressure:

$$\lambda = \frac{1}{\sqrt{2}\pi d_m^2 n} \quad . \tag{9.8}$$

9.1.3.2. Example

At a temperature of 20 °C, the gas kinetic effective molecular diameter of hydrogen is $d_m = 0.27$ nm. So, the product of mean free path and pressure results to:

$$\lambda \times p = \frac{kT}{\sqrt{2}\pi d_m^2} = \frac{1.38 \times \frac{10^{-23}\,\mathrm{J}}{\mathrm{K}} \times 293.15\,\mathrm{K}}{\sqrt{2}\,\pi \times (0.37 \times 10^{-9}\,\mathrm{m})^2} = 0.0125\,\mathrm{Pa \cdot m}$$

Under atmospheric pressure, the mean free path results to 0.12 µm, whereas at 1 Pa (a typical divertor pressure of fusion devices), the mean free path is 12 mm (of the order of a typical pipe diameter), and at 10^{-5} Pa (the ultimate pressure of a fusion device) it reaches 1.2 km, much more than the size of any vacuum system.

It should be noted that, for a given gas, this product is only a function of temperature.

9.1.4. Flow regime and Knudsen number

A specific challenge in vacuum technology comes from the fact that pressure (hence the mean free path) can change by 15 orders of magnitude, whereas the size of a conventional vacuum system merely covers two orders (between meter to centimeter). This means that particles with a mean free path above the size of the system do not collide as they are first reflected as they hit the surrounding walls. Therefore, the ratio of the mean free path to the characteristic geometrical dimension of the system d (e.g. the diameter of a circular pipe) is an important dimensionless number; it is called the Knudsen[78] number:

$$Kn = \frac{\lambda}{d}\,. \tag{9.9}$$

The Knudsen number indicates the type of flow and the order of the transport coefficients of the gas. The flow of a gas through a vacuum system is characterized by the interactions between the gas molecules themselves and, e.g.

[78] Martin Knudsen (1871–1949), a Danish physicist, presented the important criterion of mean free path related to tube dimension in two pioneering papers in Annalen der Physik **28** (1909).

during pump-down, between the molecules and the surrounding walls. Depending on the Knudsen number, there are three types of flow patterns, as illustrated in Fig. 9.2:

1. A high Knudsen number (Kn > 10) indicates low pressure[79] with no significant particle–particle collisions. The flow results from particle–wall interactions only, where the direction of a particle post collision is usually assumed to be independent of the incoming direction (the so-called diffuse reflection) so that the geometry of the surrounding tube becomes predominant. This flow regime is called free molecular flow.
2. In the medium Knudsen number range, both patterns contribute to the flow. This flow regime is called transitional flow.
3. A low Knudsen number (Kn < 0.01) indicates high pressure with many collisions between the particles which are then the dominant effect. The gas behaves like a continuum. This flow regime is called viscous or continuum flow, normally at sub-critical Reynolds numbers, i.e. laminar flow conditions.

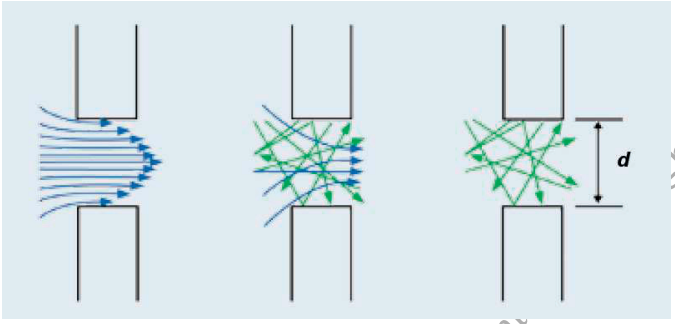

FIG. 9.2. Illustration of the three possible flow patterns: continuum flow (left), transitional flow (middle) and free molecular flow (right). Reproduced with permission from Pfeiffer Vacuum.

In the different flow regimes, different principles are exploited by the vacuum pumps and pressure measurements. The Knudsen number varies in line with the regimes listed in Table 9.1 such that the interactions within the gas characterize the regimes of rough and fine vacuum, whereas the wall reflections determine the high und ultrahigh vacuum gas flows. Section 9.2.2 elaborates further on the mathematical approaches how to calculate vacuum gas flows.

9.1.5. Vacuum pump characteristics

In vacuum engineering, it is customary to give the mass flow rate as a volumetric flow rate in pressure–volume units called throughput. The typical unit of throughput is $Pa \cdot m^3 \cdot s^{-1}$ or $mbar \cdot l \cdot s^{-1}$ and is equivalent to one Watt, although vacuum technology does not usually speak of Watts.

$$Q = \frac{\mathrm{d}(pV)}{\mathrm{dt}} = p \times \dot{V} \quad . \tag{9.10}$$

This can easily be converted to a mass flow rate by using the ideal gas equation, Eq. (9.2) if the pumped gas is known, using the standard temperature $T_{st} = 273.15$ K. The volume flow at the pump inlet is called the pumping speed S. It is related to the throughput of the pump via the pressure at the pump inlet:

$$S = \dot{V}_{in} = \frac{Q}{p_{in}} \quad . \tag{9.11}$$

The pumping speed is the most important information on a vacuum pump, in particular the dependence on inlet pressure. Two typical examples of such a curve are shown in Fig. 9.3. Whenever possible, pump manufacturers will build different sizes of the same pump to cover a range of pumping speeds.

[79] This statement holds for vacuum applications. It is noted that many flows in nano and microapplications (characterized by very small channel dimensions) may involve free molecular flow patterns, even at pressures above ambient. In example 9.1, Kn is 12.5 at 10 bar in a 1 nm diameter channel, which shows that this state is associated with free molecular flow conditions in spite of the high pressure.

As can be seen in Fig. 9.3, the pumping speed is constant over a limited pressure range. This is expressed by the ultimate pressure of the pump, which denotes the lowest achievable pressure (at zero throughput, i.e. measured at blind flanged inlet), together with the discharge pressure (which may be lower than the ambient pressure, then requiring a second pump in series). The ratio of outlet to inlet pressure is called the compression:

$$\kappa = \frac{p_{\text{out}}}{p_{\text{in}}} \quad . \tag{9.12}$$

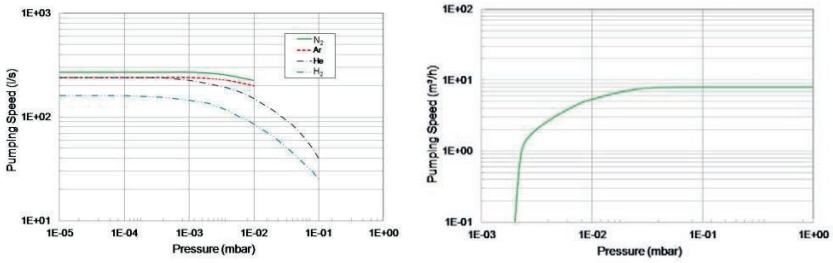

FIG. 9.3. Typical pumping speed curves for a high vacuum pump (left) and a mechanical pump (right).

In the regime of free molecular flow, the wall collision rate j can be seen as the value of maximum particle pumping rate through an opening. Eqs (9.2) and (9.6) may be combined to give a simple expression for the ideal pumping speed S_{id}, which is the pumping rate required to remove all particles impinging on the inlet surface A:

$$S_{\text{id}} = A\frac{\bar{c}}{4} = A\sqrt{\frac{RT}{2\pi}} \quad . \tag{9.13}$$

In reality, there is no ideal vacuum pump. A certain fraction of the particles passing the inlet cross section are reflected back out, hence not removed. To express this fact, the pump is assigned a certain capture probability c which may be understood as the pumping efficiency.

$$S_{\text{real}} = c \times S_{\text{id}} = c \times A\sqrt{\frac{RT}{2\pi M}} \quad . \tag{9.14}$$

9.1.5.1. Example

You have to compare two different high vacuum pumps with identical inlet flange cross-section based on their pumping speed. Pump A is known to have a pumping speed of 200 l/s for hydrogen, for pump B you are measuring 180 l/s for helium (for safety precautions measurements with hydrogen are not allowed in your lab). Based on Eq. (9.13), the influence of the gas being pumped goes with the square root of the molecular mass. Hence, the expected ratio of the ideal pumping speeds in the case above (with $M_{\text{H2}} = 2$ g/mol and $M_{\text{He}} = 4$ g/mol) is

$$\frac{S_{\text{id,H2}}}{S_{\text{id,He}}} = \sqrt{\frac{M_{\text{He}}}{M_{\text{H2}}}} = \sqrt{2} = 1.4,$$

whereas the given ratio is

$$\frac{S^{A}_{\text{real,H2}}}{S^{B}_{\text{real,He}}} = \frac{200}{180} = 1.1,$$

With Eq. (9.14), it becomes obvious that this can be attributed to the different capture coefficients of the two pumps:

$$\frac{c_{\text{B}}}{c_{\text{A}}} = \frac{S^{\text{A}}_{\text{real,He}}}{S^{\text{B}}_{\text{real,H2}}} \cdot \sqrt{\frac{M_{\text{He}}}{M_{\text{H2}}}} = 1.27,$$

This shows that pump B has a higher capture coefficient in spite of the lower pumping speed and is therefore to be preferred. Note: These estimations assume that the capture coefficient is independent of the gas species, which is not necessarily the case. However, as the involved species have similar masses, the associated error should be small.

9.1.6. Conductance

Let us consider the simplest vacuum system comprising a vessel, which is being evacuated by a pump connected to the vessel via a flanged pipe. The pumping speed at the vessel will be restricted as a result of the connecting pipework. It was also Knudsen who introduced the concept of conductance for a pipe element, where p_u denotes the pressure on the upstream side of the duct and p_d the pressure on the downstream side of the duct:

$$C = \frac{Q}{p_u - p_d} \quad , \tag{9.15}$$

Conductances (at known gas species and temperature) depend on the geometry of the components and the flow regime. This vacuum conductance concept is analogous to that of electrical conductance, where pressure difference is the analogue of voltage difference and Q is the analogue of current. From this analogy, the net conductance C_n of a set of pipe elements in series is found from:

$$\frac{1}{C_n} \cong \sum_i \frac{1}{C_i} \quad . \tag{9.16}$$

In a similar way, the effective pumping speed $S_{eff,}$ seen from a vessel to which a pump of speed S is connected via a pipe of conductance C results as:

$$\frac{1}{S_{eff}} \cong \frac{1}{S} + \frac{1}{C} \quad . \tag{9.17}$$

This concept often used in practical vacuum technology, but one should be aware that it accurately holds only under isothermal, steady-state and Maxwellian velocity distribution condition (hence the approximately equal sign).

In the molecular flow regime, maximum conductance is attained when all particles that enter the inlet of the pipe are transported through, i.e. zero backreflection. In this case, geometry wise, the conductance is only depending on the inlet cross-section and becomes equal to the term which was already derived for the ideal pumping speed:

$$C_{mol,max} = A\sqrt{\frac{RT}{2\pi M}} \quad . \tag{9.18}$$

In reality, backreflection increases with pipe length while the resulting conductance gets smaller, see Fig. 9.4. This is expressed by the transmission probability w of a particle entering the pipe, and adopts the same conceptuation as is behind the capture probability concept of a pump:

$$C = w \times C_{max} \quad . \tag{9.19}$$

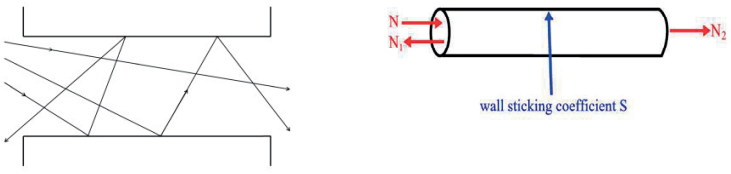

FIG. 9.4. Concept of transmission probability.

To calculate conductances for given flow is one of the major everyday tasks of a vacuum engineer. Section 9.2 will present the most common approaches.

9.1.7. Pump-down equation

The pressure evolution of a vacuum system during pump-down can be derived easily from the non-steady-state mass balance between the incoming and the outcoming throughput:

$$Q_{\text{in}} = Q_{\text{out}} + \frac{\mathrm{d}(pV)}{\mathrm{d}t} \quad . \tag{9.20}$$

Now, using Eq. (9.11) for the outgoing throughput and assuming a constant vessel volume, a simple differential equation in p is found:

$$V\frac{\mathrm{d}p}{\mathrm{d}t} = Q_{\text{in}} - p \times S_{\text{eff}} \quad , \tag{9.21}$$

which has the following solution when being integrated from ($p = p_{\text{start}}$, $t = 0$) for time and pressure independent S and Q_{in}:

$$p\langle t\rangle = \left(p_{\text{start}} - \frac{Q_{\text{in}}}{S_{\text{eff}}}\right) \cdot \exp\left\{-\frac{S_{\text{eff}}}{V} \times t\right\} + \frac{Q_{\text{in}}}{S_{\text{eff}}} \quad . \tag{9.22}$$

The pressure evolution according to this equation is plotted in Fig. 9.5.

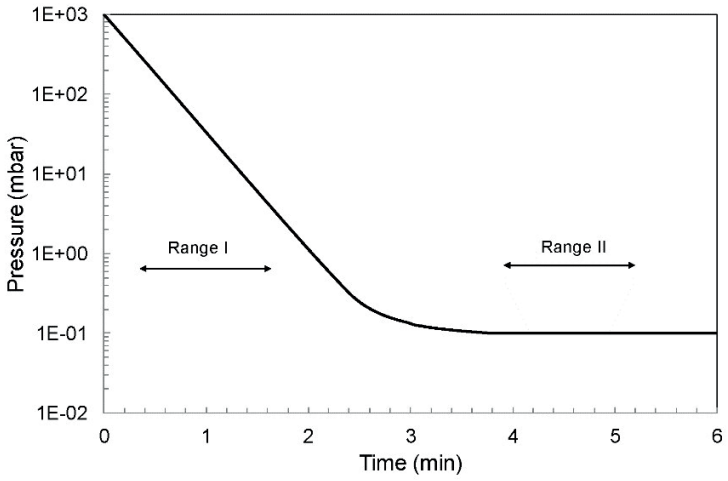

FIG. 9.5. Pump-down curve.

The curve in Fig. 9.5 has two boundary cases. For small times (range I), the exponential pressure decrease term is dominant. For longer times, the ultimate pressure p_{ult} is achieved, given by the last term in Eq. (9.22):

$$p_{\text{ult}} = \frac{Q_{\text{in}}}{S_{\text{eff}}} \quad . \tag{9.23}$$

It can be seen that the ultimate pressure in a vacuum system is given by the effective pumping speed (which includes the influence of the connecting pipework) and the incoming throughput. The incoming throughput may come from the vacuum process in an 'open' vacuum system which asks for maintenance of that ultimate pressure (e.g. in the divertor pumping system of a fusion device) or may be a small parasitic gas flow in a 'closed' vacuum system. In the latter case, and an ideal world, the incoming throughput would be zero. However, in reality, there will always be a leakage flow via the gaskets involved or an outgassing gas flow from the inner surface of the vessel walls (e.g. from hydrogen dissolved in stainless steel). In particular at targeted low ultimate pressures, the parasitic gas flow becomes the dominant effect. To minimize these parasitic gas flows is a pre-requisite to achieve UHV.

The flow of a gas through a vacuum system is characterized by the interactions between the gas molecules themselves and between the molecules and the surrounding walls. On this basis, three basic flow regimes can be defined, as discussed in Section 9.1.4. above.

Continuum flows are described by the Navier–Stokes equations. Nowadays, such flows are calculated by computational fluid dynamics (CFD) codes subject to no-slip or slip boundary conditions. As the Knudsen number increases, rarefaction effects become more important.

The Navier–Stokes equations break down as we enter the transition regime, where the Boltzmann equation can be applied along with some necessary kinetic models that simplify the collision term. The computational effort required to solve kinetic equations is significantly higher than that needed for the Navier–Stokes equations. The computational approaches in this field are either deterministic — e.g. variational methods, discrete velocity methods, integro–moment methods — or stochastic – e.g. direct simulation Monte Carlo method (DSMC).

In the free molecular regime, the collisionless Boltzmann equation can be implemented and the molecular flow is usually treated with high accuracy using test particle Monte Carlo codes. It is important to note that the Boltzmann equation with its kinetic equations are valid in the whole range of Knudsen numbers deducing accurate results not only in the transition but also in the viscous and free molecular regimes. This point is essential as, for example, the gas flow through the ITER or FPP divertor vacuum system starts from the viscous regime in the divertor entrance, covers the transitional regime for the flow through the divertor slots and channels as well as the pumping port and ends in the free molecular flow regime inside the primary vacuum pumps. For a sound numerical modeling of these systems, the whole range of rarefaction is to be covered. Different approaches are addressed in the next section.

9.2.1. Boltzmann equation

The fundamental kinetic equation, which describes the flow of a monoatomic gas, under the sole assumption of molecular chaos and binary collisions, is the Boltzmann equation:

$$[\partial_t + \xi \times \partial_x + \boldsymbol{F} \times \partial_\xi]\mathrm{f}(x,\xi,t) = \mathrm{Q(f)} \qquad (9.24)$$

The basic unknown is the distribution function $\mathrm{f} = \mathrm{f}(x, \xi, t)$ and it is defined such that the quantity $\mathrm{f}(x, \xi, t)\, dx\, d\xi$ is the number of particles in the phase volume $dx\, d\xi$ near the point (x, ξ) at time t. The left hand side represents the streaming motion of the molecules along the trajectories associated with the force $\boldsymbol{F}$. The right hand side represents the effect of intermolecular collisions taking molecules in and out of the streaming trajectory. All macroscopic quantities of the gas flow can be calculated by moments of the distribution function $\mathrm{f}(t, x, \xi)$, e.g.

- The number density $n(t,x) = \int_{-\infty}^{\infty} f(t,x,\xi)d\xi$
- The pressure $P(t,x) = \frac{m}{3}\int_{-\infty}^{\infty}(\xi - u)^2 f(t,x,\xi)d\xi$

In most cases, the streaming term is linear. The collision term is linear when the particles of interest diffuse through a host medium, e.g. neutrons through matter in Chapter 7, light through an atmosphere, low density gas through a high density background gas. The collision term is nonlinear when the particles of interest diffuse and interact among themselves, e.g. molecular gas dynamics and plasma dynamics.

The Boltzmann equation can be solved once an appropriate model kinetic expression for the collision term Q(f) is introduced. The most commonly used is the BGK expression[80]:

$$\mathrm{Q_{BKG}} = \nu[\mathrm{f}^M(n,T,\boldsymbol{u}) - \mathrm{f}(t,x,\xi)] \qquad (9.25)$$

9.2.2. Numerical simulation approaches

Even if a kinetic model is used for simplification, the solution of the Boltzmann equation remains mathematically and computationally challenging due to its complexity and multidimensionality. In general, there are two main approaches: the deterministic and the stochastic. The alternative pragmatic way is to focus on solutions for the viscous

[80] Named after the physicists Bhatnagar, Gross and Krook [1].

and free molecular range and and approximate the description in between by interpolation. This approach is less accurate and more empirical but provides quick solutions, so that it fulfills the requirements of a design–development–support code. It should be noted that, in the last decade, nuclear fusion research has strongly stimulated the development of effective methods to provide accurate solutions to vacuum flow problems; the design of the ITER and DEMO vacuum systems and the high vacuum pumps are very good examples.

In the deterministic approach (discrete velocity method, DVM), a direct discretization of the implemented kinetic equation is taken in time, space and molecular velocity. The discretized equations are then solved in an iteratively in two steps. In the first step, assuming the macroscopic quantities, the kinetic equations are solved for unknown distributions. In a second step, updated estimates of the macroscopic quantities are computed. The deterministic approach can be very efficient in solving vacuum gas flows in relatively simple geometries like orifices and pipes, but it is generally not feasible for complex geometries.

The stochastic approach is based on a particle method proposed by Graham Bird in 1963 for rarefied gas dynamics and widely known as the direct simulation Monte Carlo method (DSMC). In this method, the solution of the kinetic equation is circumvented by simulating groups of computational molecules that statistically mimic the behavior of real molecules. The primary approximation of DSMC is to uncouple the molecular motion and intermolecular collisions over small time intervals. The particle motion is modeled deterministically, while collisions are treated statistically. The DSMC algorithm consists of five main steps. First, molecules are uniformly distributed inside the computational domain according to Maxwellian distributions obeying the initial conditions. Secondly, molecules are allowed to move and collide with the walls. In the third step, the molecular collision part is simulated in a stochastic manner. In the fourth step, indexation of the particles takes place. This is followed by a fifth step which includes a sampling procedure to deduce the macroscopic quantities of the flow. This sequence is repeated at each time step, which needs to be smaller than the collision time.

For the special case of collisionless (free molecular) flows the test particle Monte Carlo (TPMC) is used. In the TPMC method the trajectories of randomly selected particles are tracked down through their motion in the computational domain, see Fig. 9.6. Particles can be tracked in parallel since their movements are considered independent. It is a very good approach to directly calculate transmission probabilities by counting the number of particles exiting the pipe and relating it to the total number of simulated particles, c.f. Fig. 9.4. The TPMC method is suitable to complex geometries, even by direct inclusion of a computer aided designed (CAD) interface.

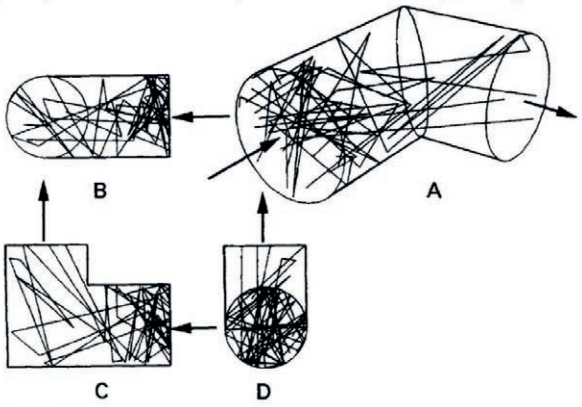

FIG. 9.6. Illustration of the trajectories in a TPMC simulation of an elbow piece.

In all methods discussed so far, the gas–surface interaction has to be modeled and an assumption of the intermolecular potential has to be made. For the gas–surface interaction, there are simple approaches, like purely diffuse, purely specular or Maxwell diffuse specular reflection (a linear combination). In recent years, due to the progress in computational power, molecular dynamics (MD) methods have been applied successfully to describe rarefied gas flows, especially in micro and nanochannels. For intermolecular collisions, various potentials have been employed, such as the hard sphere, variable and perturbed hard sphere or Lennard–Jones potentials. Obviously, the choice of the intermolecular potential becomes less important with increasing Knudsen number.

Due to the fact that both deterministic and stochastic methods to solve the collisional Boltzmann equation only became applicable in the last 15 years — as the required computational power became available — there have been many attempts to come up with empirical formulae to cover the transitional flow, thereby correctly describing the asymptotic cases of free molecular and continuum flow. This empirical approach provides quick solutions and can be handled by users who are not familiar with the details of rarefied gas dynamics. However, in order to have a good

predictive quality, the database for the empirical correlation functions has to be sufficiently large and multidimensional. This comes from the fact that the flowrate has to be described as a smooth function of the Knudsen number and include proper scalings to describe at the same time the influence of variable channel length, the influence of variable pressure ratios (from p_{out} / p_{in} = 1 to 0) and the influence of variable channel cross-section (usually considering a hydraulic diameter and additional correction functions). Furthermore, the correlations for the free molecular flow have to provide a correct description of the so-called beaming effect, which describes the fact that average velocity vectors become more and more parallel to the axis of the tube as the molecules move along a tube from the entrance to the exit. Fig. 9.7 summarizes the various approaches to vacuum flow calculations.

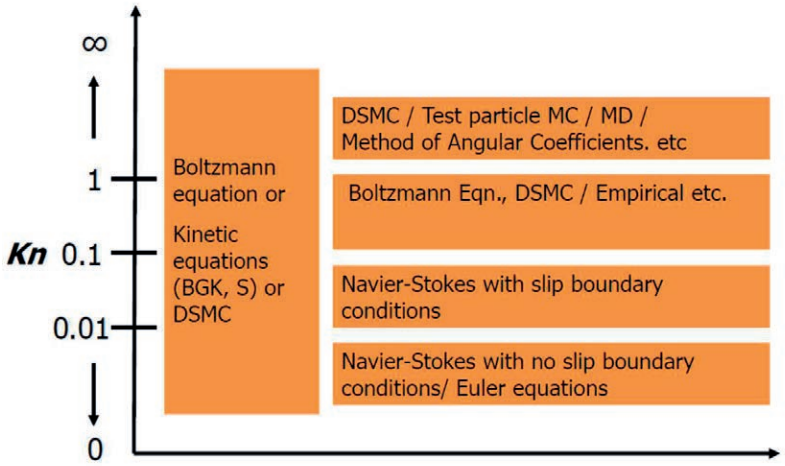

FIG. 9.7. Overview of common calculation approaches in the different flow regimes.

Each of the approaches and corresponding codes have their own advantages and disadvantages and there is no single preferred method. However, Fig. 9.8 establishes four categories expressing the relative importance of each method for nuclear fusion applications. Computation time is essential but expected to become less and less limiting in view of the continuous progress in parallel computing. Of more fundamental importance is therefore accuracy. Physics based approaches (TPMC, DSMC, DVM) can only be as accurate as the input parameters e.g. gas–surface interaction model parameters, intermolecular potential parameters, geometry parameters. Accuracy is often compromised in empirical codes from the simplifications introduced in the simulation model.

Usability addresses the simplicity of handling the codes and the commodities the software provides to its user. Here, a graphical user interface is essential, which is usually non-existing for in-house codes.

Finally, the capability of a code to address complex real vacuum systems real divertor geometries is the most important characteristic. In this aspect, DSMC is still superior to DVM, at the expense of high demands on computational power. Empirical methods satisfy all four requirements (set in Fig. 9.8) and therefore have become the reference within the fusion community; as an example, the design of the ITER divertor pumping system using the ITERVAC code [2].

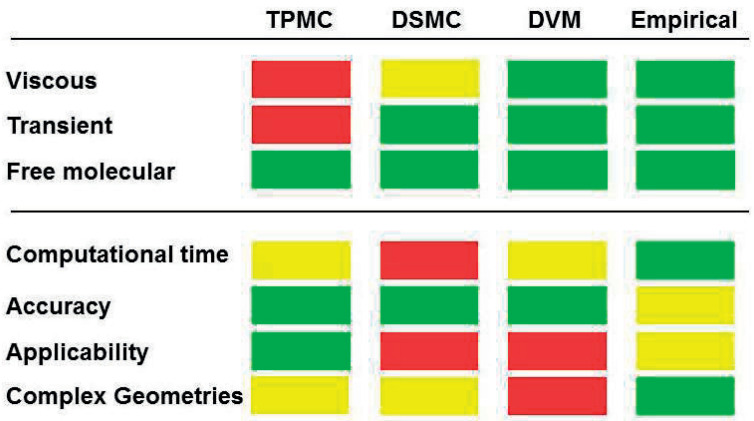

FIG. 9.8. Intercomparison of the different approaches employed in numerical codes; red denotes "impossible", yellow "possible but requiring effort" and green "well suited".

9.2.3. Pipe flows

In this subsection, a quantitative discussion is offered on the most important case of flow: the flow through a pipe. Its most fundamental configuration is the conductance due to a pressure driven flow in steady state isothermal conditions. The simplest case is the circular channel flow under fully developed conditions, i.e. the inlet and outlet regions are neglected. The following considerations are thus only valid if these contribution to the overall flow are small, i.e. if the length of the pipe, L, is large compared to its diameter d. This assumption typically holds for $L/d >$ 60. The case is illustrated in Fig. 9.9.

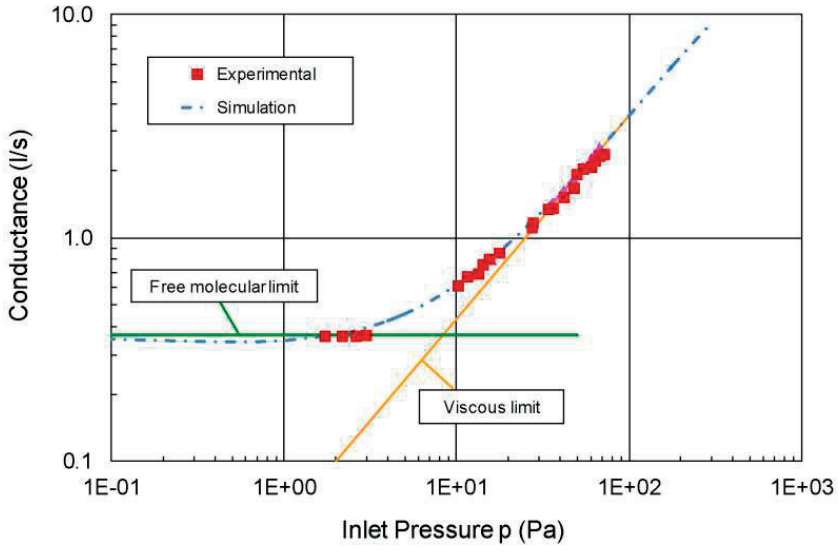

FIG. 9.9. Conductance of a circular pipe (DN16), where L/d = 60, for nitrogen at 295 K. Measurements (in red) are compared with simulations (in green) and the corresponding asymptotic limits of the free molecular and viscous flow regimes.

The free molecular flow conductance is

$$C_{mol} = \sqrt{\frac{RT}{2\pi M}} \times A \times \frac{4d}{3L} = \frac{d^3}{3L}\sqrt{\frac{\pi RT}{2M}} \quad , \tag{9.26}$$

which together with Eqs (9.18) and (9.19) directly gives the transmission probability

$$w_{mol} = \frac{4d}{3L} \quad . \tag{9.27}$$

The viscous laminar flow conductance is given by the well known Hagen–Poiseuille equation, where $\bar{p}$ denotes the average pressure and η the viscosity of the fluid:

$$C_{lam} = \frac{\bar{p} \times \pi}{128 \times \eta} \times \frac{d^4}{L} \quad , \tag{9.28}$$

Note that the free molecular flow conductance is independent of pressure and shows entirely different dependencies on the pipe diameter. Similar curves are available in textbooks for non-circular channel cross-sections in the free molecular regime. Alternatively, the concept of the hydraulic diameter can be applied to find at least a good estimation. This uses the equation of the circular pipe and replaces the pipe diameter by the hydraulic diameter d_h which is defined by the following expression where A is the cross-section and P denotes the wetted perimeter:

$$d_\mathrm{h} = \frac{4A}{P} \, , \tag{9.29}$$

As the L/d ratio of the pipe becomes smaller, inlet and outlet effects have to be considered. In such case, the simulation is more difficult as the regions located upstream and downstream the pipe are included. Typical curves are shown in Fig. 9.10. It is obvious that conventional CFD codes produce very poor results in the rarefied gas regime. In the boundary case of an infinitely thin pipe, i.e. a circular orifice, the transmission probability becomes unity, in agreement with Eq. (9.19).

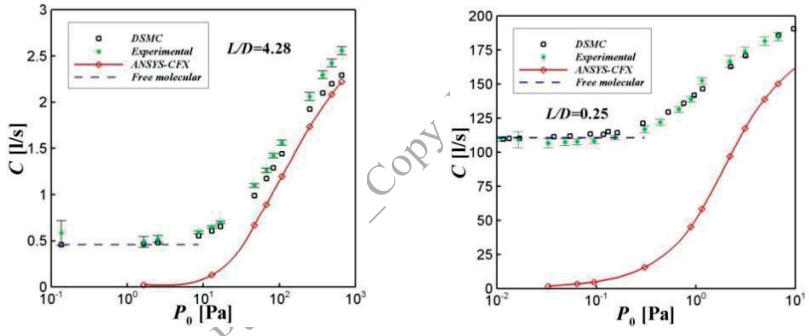

FIG. 9.10. Conductance of a circular pipe, with finite L/d, for nitrogen at 295 K. Measurements (in green) are compared with DSMC and CFD simulations and the corresponding limit of the free molecular flow (courtesy of Stylianos Varoutis, Karlsruhe Institute of Technology).

A variety of flow configurations can be found in literature and textbooks, often limited to the free molecular regime. If the conductance of a complex flow configuration is required and there is no option for a good experiment, the most pragmatic way is still to calculate the asymptotic case and use an interpolation for the Kn number range in between. One good approach, often used in empirical codes, makes use of a four parameter fitting:

$$C = \frac{c_1}{Kn} + c_2 + \frac{c_3 \cdot Kn}{c_4 + Kn} \quad , \tag{9.30a}$$

which meets a constant molecular limit

$$\lim_{Kn \to \infty} C = c_2 + c_3 \quad , \tag{9.30b}$$

and a pressure dependent viscous limit

$$\lim_{Kn \to 0} C = \frac{c_1}{Kn} \quad . \qquad (9.30c)$$

9.2.4. Modelling neutral flow in the divertor

The divertor pumping system can be treated as the classical case in which a certain incoming gas flow passes through a duct system of limited conductance and is finally pumped out. Of course, the quality and correctness with which the input information on pressure and flowrate can be provided directly determines the quality of the vacuum pumping design. In such a model, the pump can be represented by a certain capture probability. By varying the latter, one can assess the resulting pressures at which the given flowrate can be processed. The advantage of that approach is that, in a first step, one finds the requested capture probability to meet the requirements and, in a second independent step, one can design a pump in the given space which provides the requested capture probability. The methods described above can be employed to calculate the conductance of a duct with a non-uniform cross-section.

Another major challenge in modelling the divertor pumping system is the correct description of the neutral gas boundary with the plasma inside the divertor and the correct representation of the competing pumping of the plasma itself, which acts like a black hole initiating significant recycling flows. ITER for example is featuring 54 divertor cassettes with 10 different designs (regular divertor cassettes and diagnostic divertor cassettes). Each divertor has many openings in the radial and the toroidal directions through which gas can flow back to the plasma or towards the pumping system depending on the effective pressure ratio and pumping speed at the inlets and outlets of individual channels. In view of this huge 3D geometric complexity, the neutral gas modelling of the divertor can only be handled by a network code, Fig. 9.11., which uses empiric formulae Eq. (9.30) for each flow channel based on the hydraulic diameter. In a recent exercise, more than 1400 channels were used to describe the full divertor system of ITER [3].

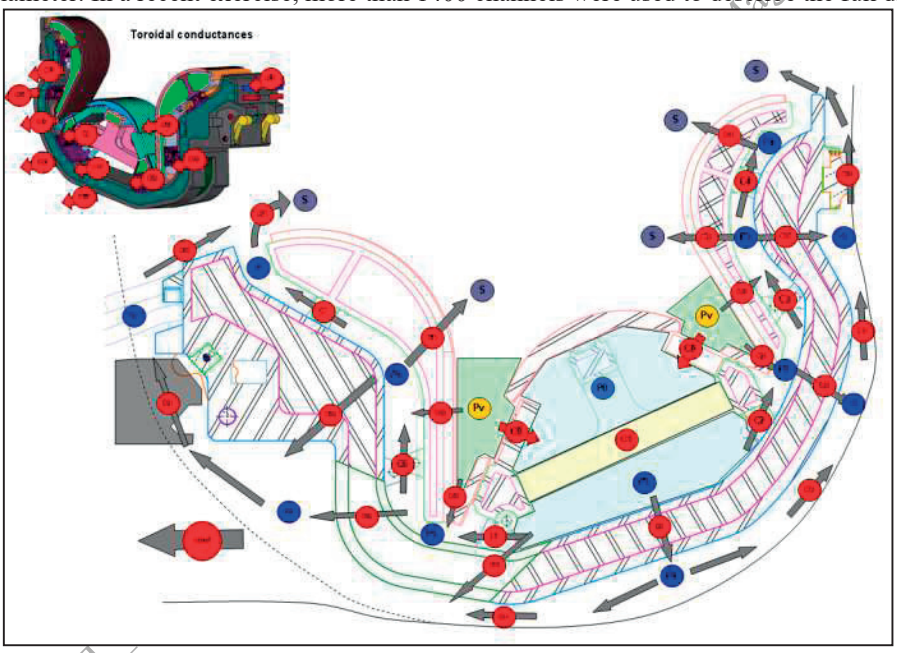

FIG. 9.11. Global flow chart of a typical ITER divertor cassette.

Over the last few years much effort has been invested in modeling the complex geometry of a tokamak divertor. The main challenge in this particular region of a fusion reactor comes from the presence of both ionized and neutral particles requiring different numerical approaches to be applied for a thorough physical description. To approach this, the plasma modelling community is currently using edge codes (e.g. B2-EIRENE or SOLPS), which focus on the description of the plasma and considers exhaust gas pumping by making the assumption of different absorption probabilities (gas sinks) at specific divertor positions, whereas the engineering community used ITERVAC, a network code that starts from the neutral divertor dome pressure. Recently, major achievements in the self consistent description of the subdivertor region have been made with DIVGAS, a novel 3-D DSMC solver for the neutral flow [4]. The correct prediction of the divertor flows is of paramount importance in view of DEMO which will be driven

at higher densities and under detached divertor plasma conditions, which are characterized by reduced power and plasma flux on divertor targets.

9.3. VACUUM PRESSURE MEASUREMENT

The large range of particle densities in vacuum technology results in the fact that a single technology is not sufficient for vacuum pressure measurement. Rough and medium vacuum is the domain of pressure measurements based on mechanical phenomena, which work regardless of the gas species. In the medium and high vacuum regimes, pressure measurement may rely on the principles of heat and momentum transfer; both quantities have a strong pressure dependence in this region. Gas ionization effects are the measure of pressure in the HV and UHV regimes. However, these instruments have a strong gas species dependency. The instruments, which are calibrated for air or nitrogen have to be re-calibrated for other gases. Important points to consider in applying instruments for total pressure measurements are the measurement range, sensitivity and accuracy (uncertainty), conceptuations which are defined in international standards. According to ISO (GUM [5]), the quality of a measurement is given by its trueness (proximity of measurement results to the true value), which describes the systematic error or bias of a method, and its precision (repeatability or reproducibility of the measurement), and determines the standard deviation or confidence interval of multiple measurements.

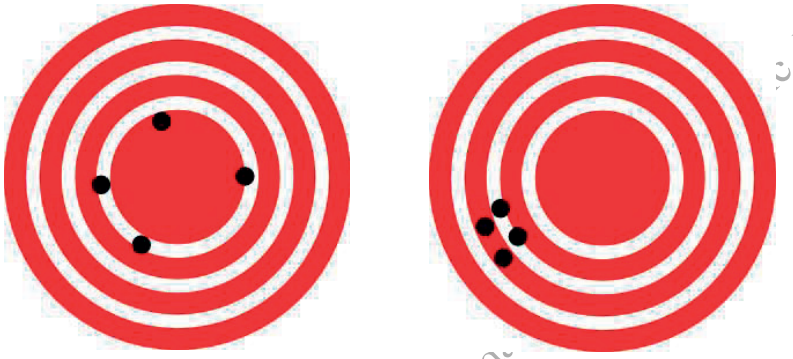

FIG. 9.12. Both cases show a low accuracy. Left has good trueness but poor precision, while right has poor trueness but good precision.

The following subsection only briefly goes through each measurement principle. Standard textbooks are recommended for further details. At the end of this section, special issues of vacuum measurement in fusion devices are discussed.

9.3.1. Total pressures

9.3.1.1. Mechanical instruments

Mechanical vacuum gauges directly measure the force on a membrane or on the surface of a liquid or solid body, Eq. (9.1). These gauges are thus inherently independent of the gas type. The most direct example is the U tube gauge and the Bourdon tube vacuum gauge where the pressure dependent motion of a hollow spring is transmitted by a mechanical linkage to move the indicator pointer. This measurement principle has a practical limitation as the associated forces at lower pressures become too small to read. The most important instruments of this type are based on diaphragms (Inconel, ceramics) whose deformation under pressure is translated into an electrical measurement signal, see Fig. 9.13. Those instruments can be manufactured with very high accuracy. The working principle of the mechanical–electrical transducer may be based on resistance changes in strain gauges, the piezoelectric effect, or the measure of electrical capacitance changes. The latter principle can resolve deformation lengths in the nm scale which allows for pressure measurements from ambient pressure down to 10^{-3} Pa with an excellent uncertainty of 0.05% of the measured value. Due to the electronics on board, the maximum magnetic field for a conventional gauge is 5 mT; special configurations have external electronics with maximum cable lengths of a few meters.

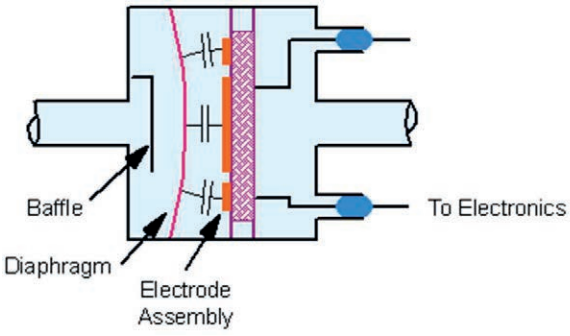

FIG. 9.13. Scheme of the capacitance diaphragm gauge.

9.3.1.2. Transport coefficient instruments

Measurements of lower pressures make use of the fact that transport coefficients, such as viscosity and thermal conductivity, are weakly dependent on pressure in the viscous regime (which defines the upper limit of application) but strongly depend on pressure in the transitional flow regime. The pressure measuring instrument that is based on viscosity is called a spinning rotor gauge. It basically consists of a freely suspended sphere set into rotation in a magnetic field. The instrument measures the pressure dependent decrease in the frequency of rotation due to retarding friction. The measurement range for such friction vacuum gauges extends from 1 to 10^{-4} Pa. The electromagnetic drive rotating the sphere produces a null effect, which determines the lower limit of the pressure range. This laboratory gauge has an excellent uncertainty of 1.5% of the measured value and is known to have a very good long term stability.

Another important instrument, the Pirani gauge, utilizes thermal conductivity to measure vacuum. In principle, the rate of withdrawal of energy from an electrically heated wire serves as the gauge of pressure. In practice, one measures the hot wire temperature thermoelectrically or by means of the resistance. Bridge circuits compensate for temperature deviations from a set value. The compensation serves as the measured variable and is related to pressure. Conductive heat transfer from the lead wires and radiation exchange, which eventually outweigh the gaseous heat transfer to be measured, result in the lower pressure limit that can be measured. Therefore, thermal conductivity vacuum gauges have a measurement range of 10^{4} to 10^{-2} Pa, with an uncertainty of the order of 20% of the indicated value. Thermal conductivity vacuum gauges are simple, reliable and inexpensive, thus appropriate for industrial use when extremely accurate measurements are not required.

9.3.1.3. Ionization instruments

The ionization vacuum gauges infer the pressure by measuring the stream of gas ions produced by electron collision ionization. As the ionization cross-section varies for different gases, these instruments are unavoidably gas species dependent. Either of two methods is used to produce the electrons needed for gas ionization: an independent gas discharge (cold cathode ionization vacuum gauge, Penning gauge) or the glow emission of a heated wire (hot cathode ionization vacuum gauge, Bayard–Alpert gauge), see Fig. 9.14.

The Penning cold cathode gauge consists of two cathode sheets with a ring shaped anode lying in between. A magnetic field of the order of 0.1 to 0.2 T produced by permanent magnets in the direction of the electrode arrangement amplifies the high voltage gas discharge by prolonging the electron paths. The discharge current is pressure dependent over a broad range. Measuring tubes are available for the range of 10^{-1} to 10^{-8} Pa. The measured values may be inaccurate by an approximate factor of two. A more accurate version of the gauge, which enables measurements down to 10^{-9} Pa, is the inverted magnetron configuration. In this implementation, the anode is an axial wire surrounded by a coaxial cylinder and the magnetic field is in the axial direction. In recent years, the combination gauge, which includes a Pirani gauge and a cold cathode sensor in one housing became very popular as it provides access to the full pressure range using a single instrument.

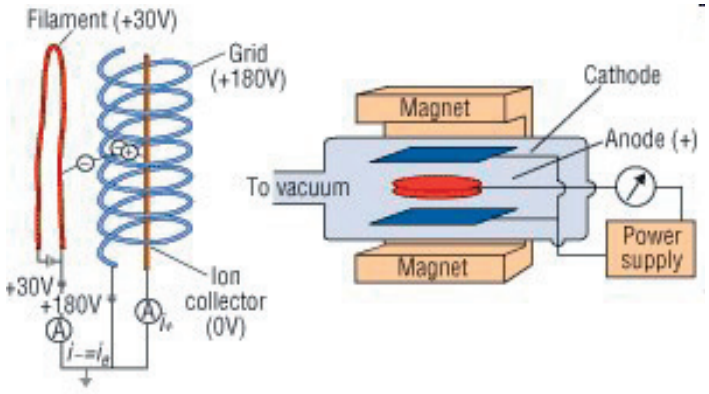

FIG. 9.14. Ion gauge configurations. Hot cathode (left) vs cold cathode (right).

The hot cathode vacuum gauge consists of a glowing cathode that emits electrons, which are accelerated to an anode grid. The positive ions produced by inelastic electron collisions give rise to a current to an ion collector located outside of the grid. The ion current is directly proportional to the pressure and to the electron current with a proportionality constant specific of the type of gas. The operational range of the Bayard–Alpert gauge is 10^{-2} to 10^{-8} Pa. At low pressures, an ion current liberated by the photoeffect dominates (the so-called Roentgen limit). Modulation of the ion current or extraction of the ionization zone are possibilities to further extend the useful range of measurements down to 10^{-10} Pa (extractor gauge, Watanabe gauge). The potential measurement uncertainty of hot cathode vacuum gauges is about 10% of the indicated value. Due to the chemistry going on at the hot wire, those gauges are sensitive to sudden venting and gas corrosion.

9.3.2. Partial pressures

The most important instrument to measure the composition of a gas mixture under vacuum is the mass spectrometer or residual gas analyser (RGA), see Fig. 9.15. The gases are ionized by collisions with electrons from a glowing cathode. A focused beam of ions is then directed into the analyzer section. In most cases, the principle of the electrical quadrupole field is used to separate the ions. This separation system consists of four, equally spaced rod-type electrodes. Between the respective opposite pairs of rod electrodes, a direct voltage is applied to which a high frequency alternating voltage is superimposed. Ions shot axially into the electrode system experience transverse oscillations in the alternating voltage field. Thus, only ions with a certain mass–charge ratio can leave the filter system without touching the electrode surfaces and being neutralized. The ions are detected directly as an ion current by a Faraday collector or converted into secondary electrons and amplified in a secondary electron multiplier. The detector limit for partial pressure measurements lies at 10^{-8} Pa for Faraday collectors and below 10^{-12} Pa using a secondary electron multiplier.

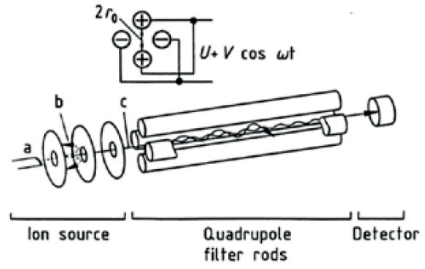

FIG. 9.15. Principle of the quadrupole residual gas analyser (a: cathode, b: electrons, c: ions).

Normally, RGAs are tuned to have unit resolution, this means that they provide one peak per atomic mass unit. This is often insufficient in fusion applications, e.g. to separate helium from deuterium ($\Delta m \approx 0.0256$ amu) and, if possible, from HT ($\Delta m \approx 0.0024$ amu), see Table 9.2.

There are three main ways to advance the performance quadrupole mass spectrometers in the low amu range. One way is to reduce the mass scale by maintaining the number of scan steps so that one has a higher number of mass steps for one amu. Limited by electronics, this can be driven in special devices until a resolution of $\Delta m/m \sim 1/200$ which is enough to have baseline separation of He and D_2. For even higher resolution, the quadrupole can be driven in higher stability regions with improved resolution by giving the ions a higher fundamental frequency. This asks for the application of higher AC and DC potentials. In a third approach, one could change the ionization potential, which is normally fixed at a voltage which produces a good ion yield (e.g. 70 eV). It is a well known fact that the ionization process of neutral particles commences at a minimum (threshold) energy of the impacting electrons. By stepwise ramp up of the ionization potential, one has an additional way of separating different species known as threshold ionization mass spectrometry (TIMS). This allows, for example, a very clear separation of deuterium (with a threshold ionization energy of 15.4 eV) and helium (with a corresponding value of 24.5 eV).

Mass spectra show the ionic current as a function of the mass from the heights of the individual peaks. However, errors come in mainly through the varying probability of ionization of the gases in question and the fragmentation patterns formed during this process. Ionization factors for ions and ionic fragments of gases can be taken from tables or spectra data bases so that ion currents can be converted into partial pressures. However, this demands a very large effort if high accuracy is required. Modern quadrupole mass spectrometers possess either electronically stored mass spectra of frequently occurring gases or determine the partial pressures using fixed, built in evaluation programs. Mass spectrometers can be applied directly only to measure pressures smaller than or equal to 10^{-2} Pa. To measure in the higher pressure regions as well, one has to add commercially available differential pump systems that rarify the gas sample of interest by orifice expansion of small aliquots to provide the necessary pressure drops.

TABLE 9.2. Masses of helium and hydrogen ions.

SPECIES	MASS (amu)
H_2^+	2.01565
$^3He^+$	3.016029319
HD^+	3.021926779
$4He^+$	4.002602
HT^+	4.02387427
D_2^+	4.028203558
T_2^+	6.03209854

9.3.2.1. Example

This example comments on certain mass scans, which provide quick information on the system's status.

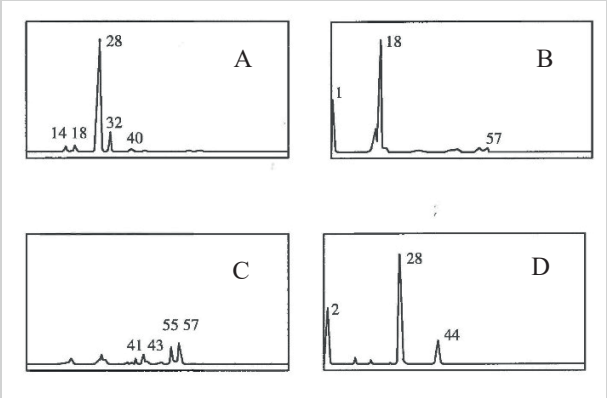

A: This scan indicates an air leak. It shows the peaks at mass 28 (nitrogen) to be 5 times the one at mass 32 (oxygen), as it is the case for air.
B: This scan indicates a dominant peak at mass 18 (water), which is typical of an unbaked vacuum system, the walls of which are covered by a monolayer of adsorbed water.
C: This scan indicates a system that is contaminated with oil, with typical sequences of masses differing by 14 (which comes from CH2 fractions).
D: This scan indicates a well baked system. There is no clear water peak anymore, and hydrogen is of similar order as CO (mass 28) and CO_2 (mass 44).

9.3.3. Aspects of vacuum pressure measurement in nuclear fusion

There are at least three different purposes for pressure and composition measurements in a fusion device. The first is for machine protection and insurance of adequate and safe operation; e.g. tritium accountancy and supporting inventory measurements. With regards to the torus chamber, this mainly asks to measure the (total and partial) neutral pressure profile below the divertor (or limiter) and in the pumping ducts of the chamber during operations, and to confirm the purity of the injected gas streams, which can be done outside the plasma chamber. The second is for control purposes; e.g. monitoring composition for analysis of seeding gas distribution, measuring the fuel ratio and helium fraction in the divertor. The third is for scientific purposes; e.g. fuel–ion ratio measurements of the plasma itself using collective Thomson scattering. Note that all instruments will see tritium, which excludes the use of elastomer materials in contact with the tritiated gas (see also Section 9.4.1.

The lowest pressures to be measured in the plasma chamber are of the order of 10^{-5} Pa (ultimate total pressure requirement). During plasma operation, the neutral pressure below the divertor (or limiter) is of the order of 1 Pa. In principle, this pressure range is fully measurable with a combination of diaphragm and ionization gauges. ITER will have instrumentation boxes connected to the torus covering the full range of vacuum, featuring capacitance gauges, cold cathode gauges, and RGAs providing general vacuum monitoring. In addition, the torus vacuum pumps (located ~10 m away from the chamber) will be equipped with their own instrumentation. In principle, the reading of any of these externally located gauges can be translated into the in situ pressure information if a sufficiently accurate conductance calculation is made. However, in case of a direct measurement, close to or inside the main chamber, additional requirements apply:

1) The measurement should be quick and online, making it very difficult to use a classical RGA, which requires differential pumping above 10^{-2} Pa.
2) A measurement close to the plasma chamber is made in the magnetic field (depending on its magnitude and orientation). The characteristics of a RGA change significantly with an external field, which requires magnetic shielding that can ensure a residual field of the order of 5 mT.
3) The instruments require regular calibration. Intervention time limitations require in situ calibration systems, which complicate system integration.
4) Finally, for a D–T device, there is the question of tritium compatibility (see Section 9.4.1) and ionizing radiation (gammas, neutrons). For example, ceramic insulators and cables can lose their properties in the intense radiation field. During an ITER D–T pulse, the minimum gamma radiation in the divertor region is estimated at ~100 Gy/h, mainly from the water cooling pipes (gamma radiation coming from transmutation of O^{16} into N^{16}). This means accumulated doses in the order of MGy in the lifetime of the machine. Commercial electronics can take up a few tens of Grays in their entire lifetime before deteriorating, which is so low that even radiation shielding becomes impractical. Hence, ongoing efforts are attempting to take the electronics out of the sensor and relocate them at a sufficient distance. The maximum distance is given by the noise picked up by the cable along the signal path which falsifies the measurement, and, thus, instruments with low level signals are especially critical.

For in situ measurements, ITER will use a special multisensor partial plus total pressure instrument cart on two port locations and a special ionization gauge for total pressure measurements, mainly in the divertor. The ion gauge was originally developed for ASDEX (Fig. 9.16) and used in other devices thereafter (in depth experience has been gained at DIII-D). It is currently being modified to meet the ITER requirements [6]:

- Up to 8 T magnetic fringe field for gauges on the inner leg of the divertor cassette, and fields of 0.1 to 0.3 T in the port cells (depending on location).
- A peak neutron fluence of 4×10^{13} n·cm^{-2}·s^{-1}, and total fluence over the ITER lifetime of 1×10^{21} n/cm^2 in the divertor cassettes.
- An upper pressure limit of 20 Pa,
- An accuracy of 20%.

Contrary to the conventional circular configuration of an ion gauge, the ASDEX gauge uses planar electrodes and makes use of the existing tokamak magnetic field (experience up to 6 T), which is an advantage under regular operation. However, the reading depends on the field strength. Furthermore, the gauge features an extra control electrode to modulate the ionization in order to overcome noise. The gauge has been exposed to ITER relevant conditions in an irradiation test reactor and the result was positive. The gauge is known to be very fast (~10 ms) and has so far been tested for a pressure range of 10 to 10^{-1} Pa. It is foreseen to equip four of the 54 ITER divertor cassettes with six gauges each: four underneath the central dome, one under the inner target plate and one under the outer target plate, see Fig. 9.17), in order to have one sensor in each of the pumping ducts and a few sensors placed to monitor the main chamber. For calibration, which will be done in zero field conditions, the external capacitance manometers from the instrumentation boxes will be used. It is also known that the sensitivity of the gauge is not constant and varies with the ion current.

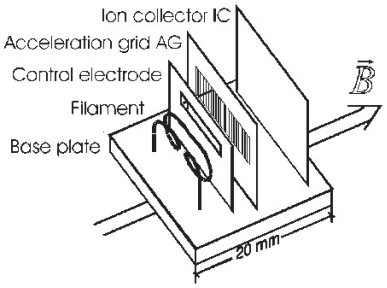

FIG. 9.16. Schematic setup of the ASDEX total pressure gauge. Reprinted from [6] with permission from Elsevier.

To measure the gas composition, ITER will use two identical instrument installations (one on an equatorial port and one on a divertor level port) called diagnostic RGAs, which provide three independent partial pressure measurements and feature additional total pressure measurements as a backup for the ASDEX gauge measurements

and a cross-check for the (integrated) partial pressure instruments. The device may contain (i) a quadrupole mass spectrometer, (ii) an ion trap mass spectrometer, (iii) an optical Penning gauge and (iv) a cold cathode ion gauge (inverted magnetron). A Piriani gauge could also be included. The two spectrometers have a maximum pressure of 10^{-3} Pa and come upstream from the optical penning gauge, which operates between 10^{-1} and 1 Pa. To make good measurements even at very low chamber pressures, the device contains a small (shielded) internal turbomolecular pump to compress the gas.

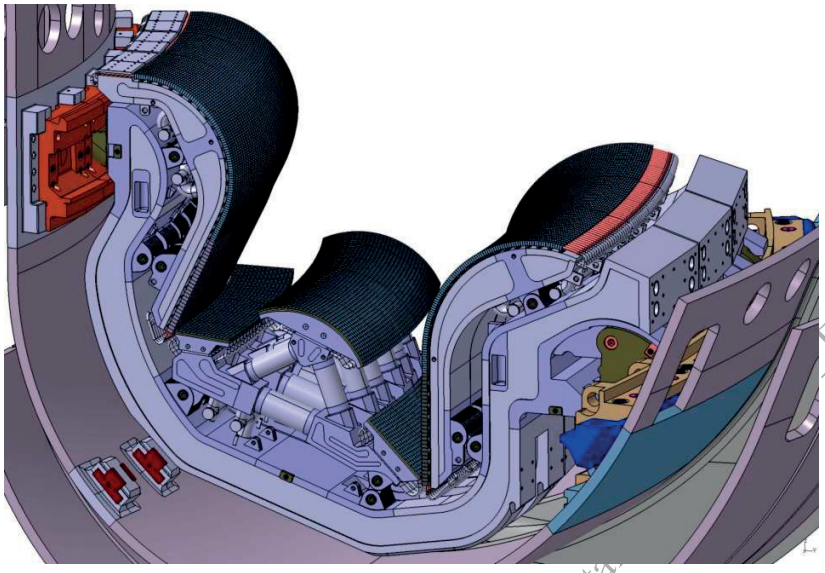

FIG. 9.17. Detailed configuration of the ITER divertor cassette. © ITER Organization, http://www.iter.org/

The ITER requirements for a diagnostic RGA are:

- Depending on location, fringe fields of 0.1 to 0.3 T in the port cells require magnetic shielding and possibly electromagnetic interference shielding[81].
- A radiation dose of 100 kGy in the equatorial port cells (integrated ITER lifetime) and 300 kGy in the divertor port cells.
- Discrimination of the He and D_2 fractions.
- Minimum integration and delay times to measure (almost) in real time.

In response to above, the whole device is housed in magnetic shielding, which reduces the inner field to 5 mT. This is good to avoid potential drifts of the ion gauge readings, which appear if the external field is larger than the internal field of the permanent magnets of the gauge, and essential for the mass spectrometers since the external magnetic fields change the spiral path of the ion trajectories inside the spectrometer's electric fields. The partial pressure instruments as well as the upstream cold cathode gauge will be used in radiation hardened version, i.e. with long cables and intermediate amplification, separating the RF box for the ion trap or quadrupole, and providing a special filament for the cold cathode. The separation of helium and deuterium is not possible in a conventional RGA tuned to have a unit resolution. An optical Penning gauge and an ion trap are candidates for this purpose. Those two special instruments are explained in the following.

The autoresonant ion trap is a mass spectrometer that uses purely electrostatic fields to store ionized gases within a cylindrical ion trap [7]. Ions are generated directly inside the trap by electron ionization of gas molecules. An anharmonic trapping potential well confines the ion trajectories of all masses to stable oscillatory motions along the axis of the trap but is also used for mass separation. Mass selective ejection is achieved by applying a RF potential which couples to the ions and gets them to oscillate with the exact same frequency (autoresonancy). By ramping the RF frequency, one will cause all ions with the same mass–charge ratio to leave the ion trap, so that the resulting current

[81] For radiofrequency.

can be measured in the same way as for a conventional quadrupole. One of the major advantanges is the very fast scan time (below 100 ms), the small size (~15 cm in length) simplifying shielding, and a high achievable resolution, which may allow for He-D_2 separation in full mass scans. This sensor has recently been commercialized.

The optical Penning gauge uses a conventional Penning discharge to excite the neutral gas under scrutiny, so that its species can be monitored by visible light emission spectroscopy. The light is collected in an optical fibre and the signal is led to a low radiation environment. Good experience has been collected for this device for He-D_2 measurements in DIII-D which demonstrated resolution of ~0.5 mol% He [8]. Modifications are under way to qualify this device for the full set of hydrogenic species; promising results were obtained at JET with D–T. Its advantage over other partial pressure measurements is that it works without differential pumping up to the upper range of a Penning gauge (10^{-1} to 1 Pa). The optical Penning gauge is limited to species with optical emission lines; meaning it is good to measure helium and hydrogen isotopes but not suitable for hydrocarbons. Depending on the species, the resolution may be higher than for an RGA, but the pressure limit is about 10^{-4} Pa.

The whole system will be connected to the chamber via an orifice to make sure that the maximum pressure seen from the diagnostic is 1 Pa under any operational conditions. This requires good knowledge of the associated conductances at varying flow conditions, see Section 9.1.6. The connecting pipe will also add a lag on the response time.

The strongest limitation for partial pressure measurements comes from the magnetic fields and resulting shielding requirements. In view of future devices, an essential trick to emancipate from the annoying effects of magnetic fields is to go for a system in which the internal magnetic field is significantly higher than the external magnetic field. This is the case for magnetic sector field mass spectrometers and Penning traps with stored ions at high field. The former are very bulky instruments and therefore not considered to be feasible for a fusion device. The latter is a promising method if based on the determination of the cyclotron frequency of stored ions[82] excited by a RF field. Two ion cyclotron frequency detection techniques are already well established: The time of flight method probes the true cyclotron frequency by exciting the stored ions and ejecting them out of the trap into the detector; the time of flight between the ions' departure from the trap and their arrival at the detector is a measure of the frequency. The second is the Fourier transformed ion cyclotron resonance (FT-ICR) method, using magnetic fields between 7 and 9 T provided by superconducting magnets. Here, the ions stay trapped and their frequency is determined by induced image currents in the trap electrodes when the ion is passing by the surfaces. This signal is then read out and provides the required information on the charge–mass ratio when a Fourier transformation is applied for deconvolution for a properly calibrated setup. For FT-ICR, repeated measurements are possible on the same trap content, which makes this method more advantageous than the time of flight.

In view of DEMO, tritium inventory measurements, accountancy and monitoring become key questions in operation and licensing. In this regard, a Laser–Raman spectrometer was rencently developed for online identification of hydrogen isotopologues [9]. As the information is registered by optical diagnostics, a sampling cell of only a few cubic centimeters was designed for full tritium compatibility. The signal is transferred via fiber optics. It features a sensitivity of a few 0.1% but is (until now) only working in rough vacuum. The development of a reliable real time strategy for tritium measurements enabling a viable accountancy concept is one of the key challenges to be addressed by DEMO R&D programmes.

9.4. VACUUM PUMPS

To master the large range of densities which can appear in vacuum, technology requires the application of many different principles. Therefore, there exist many types of vacuum pumps yet none of them is able to cover the full pressure range. In view of the flow regimes, there are mechanical (positive displacement) pumps for pumping in viscous flow conditions, whereas kinetic and entrapment vacuum pumps work in ultrahigh vacuum conditions. The former is independent of the working gas, whereas the performance of the latter is strongly dependant on the species. Moreover, the latter are not able to compress the taken gas up to ambient pressure so that they have to be combined with a mechanical forepump. The family tree of vacuum pumps is illustrated in Fig 9.18. The pump types which have been highlighted in the figure will be discussed in the following sections emphasizing their suitability to a D–T fusion environment.

[82] Linked to the mass via the magnetic field.

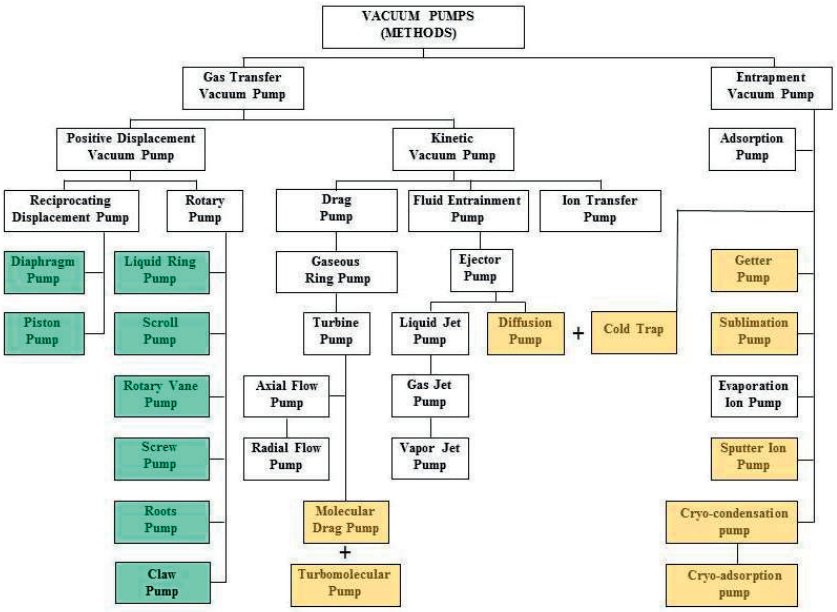

FIG. 9.18. The family tree of vacuum pumps.

The cavity in the positive displacement pumps, whose volume varies periodically, forces the gas through the pump from an inlet to the outlet. The pumping speed of a positive displacement pump is independent of pressure: it is the product of the displacement volume and the frequency of filling the displacement volume, which is given by the rotating frequency of the shaft. Yet, due to sealing losses (leaks) and the partial pressure of the pump´s working fluid (oil), a pressure dependence arises at low pressures and the pumping speed falls very quickly to unusably low values (cf the right hand side of Fig. 9.3.). The most prominent representatives of the displacement pumps are the rotary vane pump, the roots pump, the liquid ring pump and the diaphragm pump.

For kinetic vacuum pumps, the fundament of the pumping effect is momentum transfer. The fluid entrainment vacuum pump uses the gas–gas interchange effect; the drag vacuum pump uses the gas–wall interchange effect. At low pressures, the pumping speed is limited by backflow of the working fluid or of the pumped gases. At high pressures, the pumping mechanism breaks down. The most prominent representatives of the kinetic pumps are the turbomolecular pump (c.f. the left hand side of Fig. 9.3.) and the diffusion pump.

Positive displacement and kinetic pumps move gases continuously through the pumps by compression from the inlet to the outlet opening. Entrapment vacuum pumps however accumulate the pumped gas in some form within the body of the pump itself, and do not exhaust any gas during pump operation. Such pumps use chemical gas bonding at active metals (getter pumps), eventually supported by the use of electrical fields (sputter ion pumps), or thermally remove the gas from the gaseous phase by cryocondensation or cryoadsorption at low temperatures (cryopumps). The following sections will present the variety of pump types and technologies in more detail, give typical examples and address their suitability for applications under D–T fusion conditions.

9.4.1. D–T fusion requirements and tritium compatibility

There are many vacuum applications in the exterior parts of a tokamak and its infrastructure which can be based on conventional vacuum pumps (such as the insulation vacuum pumps of the cryogenic piping) as they do not have to meet fusion specific requirements. For the few vacuum pumps that are close to the plasma chamber of non-D–T devices, the magnetic field requirements come on top. However, for D–T devices, as discussed in Section 9.3.3 above, in addition to the magnetic field, the vacuum pumps in direct connection and close to the machine core see strong neutron fluxes and the associated doses. Additionally, all pumps in contact with radioactive tritium or tritiated gases (even if being away from the machine core) should be designed accordingly. The requirements for ITER and DEMO are as follows:

1) Magnetic field strengths: ITER has a fringe field of 8 T at the position of the inner divertor, and up to 0.3 T in the divertor port cell, where the torus pumps are located. It is expected that the magnetic fields at DEMO will be of similar magnitude.

2) Secondary gamma radiation via fusion neutrons and neutrons of transmutation reactions: The integrated neutron wall load of DEMO will be around two orders of magnitude higher than that of ITER (7 vs 0.07 MWyear/m^2).
3) Hydrogenic explosion hazards: In case of an air leak, hydrogen can form an explosive mixture with the oxygen in the air. Explosion safety is an important concern especially for rough pumping, as the pressures in these pumps are above the minimum explosion pressure of ~370 mbar. The well known methods of explosion safety should be applied.
4) Tritium interaction and decay effects.

The aspect of tritium interaction is not straightforward and very important for the correct choice of a pump. This does not come directly from the energy of the ß particles (the decay electron energy is relatively small, with a maximum value of 18.6 keV, associated to a penetration depth in air of ~6 mm and in metal of ~1 mm, see Chapter 10) but from tritium–material interaction and safety and tritium control issues. Many materials in contact with tritium show deterioration problems. Also, at all times, the operator of a tritium plant has to trace where each amount of tritium is stored (this principle is denoted tritium accountancy).

A design which considers these aspects and avoids contamination problems is called tritium compatible. This means that tritium compatibility is not a strictly defined requirement but is specified administratively. To pump hydrogenic species in mechanical pumps with a high compression a ballast gas is usually added to the process gas for cooling purposes and to avoid explosive conditions. Depending on the pump type — as detailed in the following sections — a purge gas is often added to the shaft sealing system to avoid penetration of the hydrogen into the lubricant chamber. In case of fusion devices, the addition of a ballast gas is very disadvantageous as it contributes significantly to the gas load to the tritium handling plant and thus directly to the size and cost of the peripheral systems. Sound engineering practice for tritium components encompasses the following requirements:

1) Extreme leak tightness to the environment (~10^{-9} Pa·m³·s^{-1}) and material choices such that any permeation can be neglected (especially at the high operational temperatures).
2) No elastomer material on the wetted surfaces and no elastomer seals as this material becomes brittle due to helium production by the ß decay of tritium which gets incorporated via isotope exchange. Metal seals involve higher forces which result in a complete mechanical re-design to make commercial pumps tritium compatible.
3) For pumps with a rotating device, perfect separation between the process gas in the pumping and the lubricant (oil) in the gear compartments without any cross-penetration; this asks for a rotary shaft feedthrough seal tightness of 10^{-10} Pa·m³·s^{-1}. This has never been met in any industrial sealing application.

In the past tritium devices, it was sometimes decided to use non-compatible pumps and give them to waste afterwards, because the modifications to turn them compatible were either seen as being too challenging, too limiting in performance as compared to the regular pumps, or adding too much risk.

9.4.2. Industrial explosion safety

Fusion machines have to be built for hydrogen use. In the case of a leak of the plasma chamber and its connected devices, there is the possibility of air ingress. The oxygen of the air and the hydrogen fill in the plasma chamber can form an explosive gas mixture (hydrogen molar concentrations in air between 4 and 77%, at ambient pressure and room temperature). To address this risk, industrial explosion safety measures have to be considered. They normally comprise three aspects:

1) Primary explosion protection or prevention by avoidance of an explosive atmosphere (primary explosion protection) by regular checks for leak tightness and the installation of hydrogen sensors in the environment of the hydrogen containing systems.
2) Secondary explosion protection or prevention by avoidance of an ignition by eliminating any (active) sources of sparks and ignition in the facility.
3) Constructive explosion prevention or prevention by avoidance of the effect of an explosion by design against the calculated maximum explosion end pressure (~10 bar). This involves a very high effort in vacuum systems, as the vacuum components are normally not designed for this contingency, and hence have to be individually qualified.

9.5. POSITIVE DISPLACEMENT VACUUM PUMPS

The reciprocating piston and membrane pumps are oscillating positive displacement pumps which are used in rough vacuum and as forepumps to high vacuum pumps. They push gas through the pump by back and forth movement

of the pistons or membranes. In rotary positive displacement pumps, rotating internal parts periodically produce the displacement volume.

It is envisaged to use these pumps as roughing pumps, hence the compatibility requirements with magnetic field and neutron irradiation can be relaxed as the pumps, due to their potentially high tritium inventory resulting from the relatively high operation pressures, are located inside glove boxes in the tritium plant, a separate building, some distance away from to the tokamak. However, the tritium compatibility requirements strictly hold and are critical as the displacement involves a moving element (rotary or linear) which needs a sealing and separates the pump part which is in contact with the process gas from the pump part which is generating the displacement motion.

There are also clean industrial vacuum processes, such as deposition and coating, or processes that involve corrosive gases, which ask for oil-free pumps to avoid contamination loads and oil backstreaming into the process chamber. Therefore, some positive displacement pump types are already commercially available in 'dry' versions.

9.5.1. Reciprocating positive displacement pumps

The conventional piston pump technology is well proven. It involves a gear box with a mechanical drive, which leads to an oil sump that is separated from the vacuum chamber by a circular gap between piston and cylinder. This solution is not suitable for pumping tritiated gases, because the hydrogen isotopes can diffuse through the gap and tritium would dissolve in the oil and eliminate its lubricating properties.

The dry piston or diaphragm pump version ensures that the transferred gas is not exposed to any sealing fluids or lubricants. Either an oscillating piston (via shaft and connecting rod) enclosed by a bellow or a tightly welded diaphragm (with connecting rod) takes up the gas during one half cycle and exhausts it during the second half cycle via a valve. The basic design of these pumps leads to a dead space. Therefore, the ultimate pressures are moderate, i.e. in the 1 to 100 Pa range at best, and the compression ratio is limited by the stroke and the dead volume. Due to the limited movement of the employed membrane, the compression ratios of diaphragm pumps are even worse than for a piston pump. In general, dry pumps have reduced reliability so that more frequent preventive maintenance actions are needed.

Depending on the materials used, dry pump designs are not necessarily tritium compatible. For example, most of the diaphragm pumps include plastic membranes. Nevertheless, there are some commercial tritium compatible pump versions available for small throughputs. Examples are piston pump designs, which feature a ceramic cylinder driven by a complex wobble drive with several bearings and bellows (see Fig. 9.19) or piston pumps with dynamic metal bellows. Nevertheless, the experience with these pumps that has been compiled in tritium labs is not conclusive. A modified piston pump is currently being further developed as candidate for the last stage of the ITER roughing pump train. The special diaphragm pump designs (metal bellows pumps) with a welded metal diaphragm and controlled double bellows interspace are ideally tritium compatible, see Fig. 9.19. These pumps are available in sizes up to some 10 l/min pumping speed and work around atmospheric pressure.

Pumps with small pumping speed are not suitable to be used as roughing pumps in the main ITER vacuum systems, as the throughputs to be handled are too large. However, if they have the possibility to compress above ambient, which is the case for the metal bellows pumps, they may do a very good job as transfer pumps in the tritium plant of a fusion device. It is important to note that these pumps are usually required to deliver constant throughput, which they can only provide down to pressures significantly above their ultimate pressure (cf the pumping speed vs pressure characteristic in Fig. 9.3). In consequence, their operational range is much reduced. Theoretically, one would wish to have a mechanical pump with constant throughput rather than constant pumping speed.

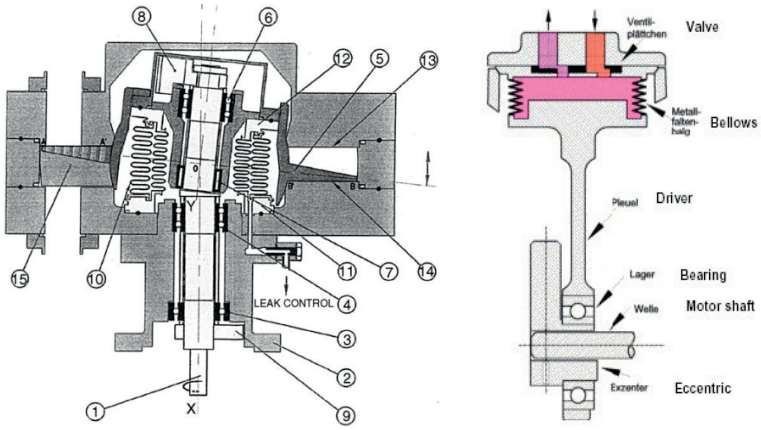

FIG. 9.19. Tritium compatible reciprocating positive displacement pumps: a piston pump (left) and a diaphragm pump (right).

Perspective in fusion

The dry piston pump is prone to wear, thus shows limited lifetime. To improve this, the gaps of the lubricated versions have to be increased, which results in reduced pumping speeds and increased ultimate pressure (due to a larger backflow). The compression for light gases is therefore minimal, so that multistage setups are often considered, which introduce maintenance problems. In view of these fundamental mechanical challenges, piston pumps are not seen to have a promising future in fusion devices. The diaphragm pumps, although fulfilling all tritium compatibility requirements, can not (by their working principle) achieve the ultimate pressures and high pumping speeds required for the main vacuum systems of a power plant. However, they are suitable as tritium transfer pumps between vessels at pressures around atmosphere.

9.5.2. Rotary positive displacement pumps

Classical designs of rotating positive displacement pumps, such as the rotary vane or the scroll pump, are characterized by an intimate contact of the process gas with the sealing oil. In the 1980s, driven by semiconductor industry, dry versions were developed. The basic idea to make these pumps dry is to separate the process gas volume from the oil volume via a rotary feedthrough for the shaft. Of course, only dry versions can potentially be made tritium compatible and become an option for fusion applications. The suitability of such a pump is directly given by the correct functioning and reliability of the rotary feedthrough sealing and the acceptable leak rate of tritium from the process gas into oil and vice versa.

9.5.2.1. Single shaft

The most common pump type is the rotary vane pump available up to a size of some hundreds m^3/h and end pressures of 10^{-1} Pa as a multistage machine. A rotor (2, numbers referring to Fig. 9.20) is placed eccentrically in a cavity (1). When rotating, the vanes (3) are sliding in the vane chamber (4) and separate the inlet chamber from the compression chamber and the outlet chamber. For a good pumping performance, the vanes should be tightened against the cavity. In conventional (wet) pumps, this is done by oil which also has the function of a lubricant and that of a coolant, to handle the compression heat. The oil tends to be taken out of the pump and therefore needs to be separated from the gas flow by an oil mist separator. There are also dry designs, but with very poor ultimate pressure and high maintenance requirements.

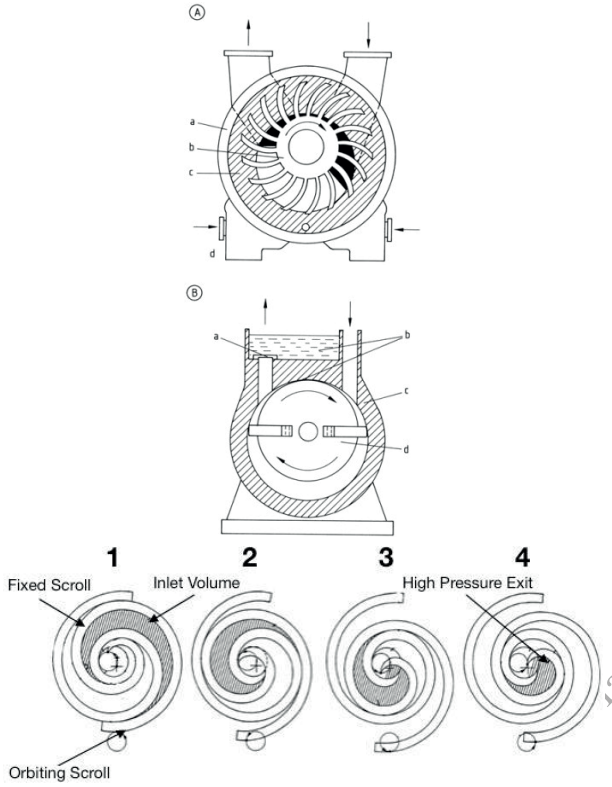

FIG. 9.20. Schematics of single shaft rotary positive displacement pumps. A) Liquid ring pump: a) Stator; b) Rotor; c) Liquid ring; d) Liquid inlet; B) Rotary vane pump: a) Outlet valve; b) Oil; c) Stator; d) Rotor, C) Scroll pump with the four phases of operation.

Much more suitable for our purposes are *scroll pumps* which are also available as tritium compatible pumps with nuclear admission [10]. A scroll pump uses two interleaving scrolls (schematically shown in Fig. 9.20) to transport the gas. Normally, one of the scrolls is fixed, while the other orbits excentrically via a crankshaft without rotating inside the previous one. Thereby, the gas is taken at the periphery of the scrolls and progressively pushed with compression towards the centre from where it is finally evacuated through a discharge port. In the tritium compatible all-metal design, the pumping area is totally isolated from the lubricated parts of the pump mechanism and the external atmosphere. The sealing via a nutating bellow eliminates the need for a rotary shaft seal. The smaller scroll pumps (~15 m³/h), which can compress against atmosphere, are very often used in tritium processing even though they have high maintenance requirements (replacement of the sealing every two years). The large scroll pumps (with pumping speeds of ~1000 m³/h, as would be needed for DEMO) are typically used in series with other scrolls followed by a metal bellow or piston pump as backing pump, because the compression for hydrogen is poor. In the last decade, the scroll pump has become very popular in general vacuum applications as backing pump of turbomolecular drag pumps (Section 9.6.1), and many manufacturers have included them in their programme. But it should be noted that these pumps are of small pumping speed and have a 'cheap' feedthrough design with polymer bearings, which produce contamination.

The third type of single shaft positive displacement pumps are the liquid ring pumps where a liquid ring takes over the function of a piston that compresses the gas and removes compression heat. A wheel (rotor with buckets) is excentrically placed in a cavity. If the cavity is filled to some parts with a working liquid (normally water or oil) and the wheel is turned, a liquid ring is formed (as shown in Fig. 9.20). The liquid ring creates a sickle shaped displacement volume, which is partitioned by the buckets into separate cells. Thus, the process chamber is formed anew in every cycle, starting with zero volume each time. For a liquid ring pump, the contact between the process gas and the working liquid is part of the working principle. The gas volume between the wheel blades is compressed while pushing it from the inlet (upper part) to the outlet (lower part). Due to the intense contact between gas and liquid, the working liquid completely absorbs the compression heat so that the temperature of the pumped gas hardly rises and the compression can be considered quasi-isothermal. The liquid ring pumps are the most often used pump type in the chemical industry

due to their excellent reliability and high speeds. They need a phase separator on the outlet side to separate the working liquid from the exhaust gas. Normally, the ultimate pressure is limited by the vapor pressure of the working liquid which is about 3 kPa for water. However, liquid ring pumps can use any liquid compatible with the process as the sealant liquid, provided it has the appropriate vapor pressure properties. If a liquid of much lower vapor pressure (like liquid metals which would make the pump perfectly tritium compatible) is used, an end pressure of less than 10 Pa could theoretically be reached.

Perspective in fusion

The all-metal scroll pump has for a long time been the reference tritium compatibe rough pump option despite the limited performance data (very poor compression ratio, large size resulting in needs for enormous glove box volumes when operated with tritium)[83]. Also, the nutating bellow has an issue with fatigue and may ask for excessive remote maintenance service. Whereas the liquid ring pump technology, with its high pumping speeds and flexibility given by the use of liquid metals for low ultimate pressures, appears to be very promising. A solution with mercury is currently under development for DEMO and first proof-of-principle results of this technology are very promising [11].

9.5.2.2. Twin shaft

In twin shaft arrangements, the gas portion to be compressed is enclosed between two moving elements. Roots pumps consist of a pair of two matching figure eight shaped lobes. These revolve counter to one another, turning with little clearance between them (Fig. 9.21.). The gas is trapped in pockets and carried from the intake to the outlet side, so that only a small gap remains between the two pistons and towards the pump housing. The compression takes place at the outlet of the pump, not inside, because the volume of the pockets does not change while the gas is carried through the pump. Due to the non-contact operation, the shafts can rotate at high speed, and thus high pumping speed (several 1000 m³/h) can be achieved in small pumps. At high pressures, however, high gas backflow develops through the gas, leading to poor compression. Roots pumps are therefore typical pumps for the intermediate pressure regime (100 to 1 Pa) between a classical backing pump (rotary vane or piston) and a high vacuum pump. If compression to atmosphere is requested, multistage designs are possible. Although most commercial roots pumps nowadays are already dry pumps (no oil in intimate contact with the process gas), they need a gear box with oil. For high gas flows and high pressure ratios, roots pumps tend to have a cooling problem with the fast rotating heavy lobes. This means that a complex cooling concept with gas recycling is applied, which leads to many different components and pump stages. A roots pump can be driven by an electric motor enclosed within the pump housing, avoiding an opening for the shaft and the seal that goes with it. It can thus be made completely tight.

A screw pump is a positive displacement pump that uses two fast rotating screws (see Fig. 9.21) to transport the gas along the screw axis through the pump. Between the two screws, a cavity is formed whose volume decreases along the screw axis which leads to a compression of the gas. Cooling liquid is necessary to carry off the compression heat produced during operation. Large sized pumps (~250 m³/h) employ an effective gas cooling management to limit exhaust temperatures. The two main gas cooling methods are foreign gas feeding into the working chamber (gas ballast) and recirculation of a proportion of the cooled exhaust gas into the working chamber. Obviously, both approaches lead to a loss of performance. Screw pumps can compress to atmosphere and reach an ultimate pressure of 10^{-1} Pa.

[83] The all-metal scroll pump is known as NORMETEX pump, from the single manufacturer NORMETEX in France. Since this company went out of business in 2011, no other commercial supplier could successfully take over yet. This is becoming more and more of a problem, as in the meantime, most pumps at stock are in use.

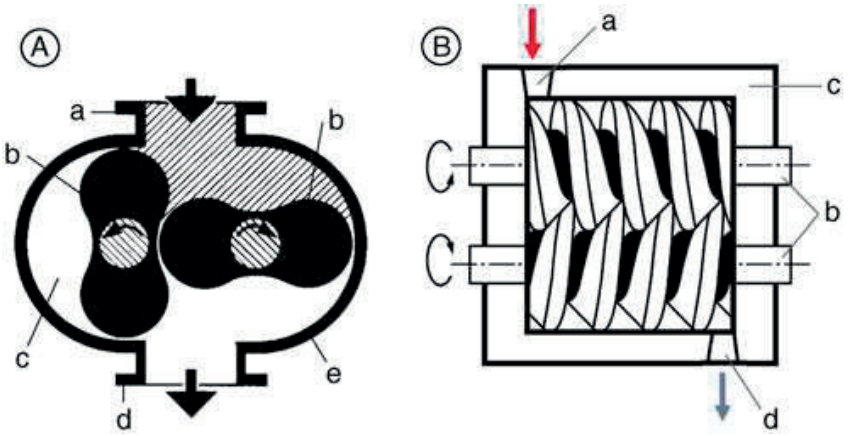

FIG. 9.21. Schematics of twin shaft rotary positive displacement pumps. A) Roots pump: a) Intake flange; b) Rotors; c) Chamber; d) Exhaust flange; e) Casing; B) Screw pump: a) Inlet; b) Screw rotors; c) Housing, reproduced with permission of Leybold; d) Outlet, reproduced with permission of Pfeiffer Vacuum.

Perspective in fusion

The rotary shaft seal is the central problem to make twin shaft positive displacement pumps tritium compatible. Several attempts have been made in the past to develop a tritium compatible seal (labyrinth seals, glide ring seals, static and dynamic floating ring seals, ferrofluidic seals or use of purge gas) for a number of twin shaft pump types (claw, scroll, roots) but without convincing success [12].

9.6. KINETIC VACUUM PUMPS

Kinetic vacuum pumps are pumps that transfer momentum to the pumped gas in such a way that the gas is continuously moving from the inlet to the outlet of the pump. This feature distinguishes it from the positive displacement vacuum pumps where the gas moves in separate portions cyclically isolated from the inlet, and from the entrapment vacuum pumps where the gas exits the pump only from time to time. This chapter is restricted to the two kinetic pump types which are relevant for fusion applications. As primary pumps, they must be checked for compatibility with the machine requirements, as defined in Section 9.4.1 (magnetic field, ionizing radiation and tritium compatibility)

9.6.1. Turbomolecular pumps

Turbomolecular pumps are the standard pumps in clean and high vacuum applications. The pumping effect is based on the momentum exchange between a fast rotating rotor and the gas particles as shown in Fig. 9.22. To get a high pumping speed, the rotor speed has to reach values in the order of the thermal velocity of the gas molecules. As shown in Eq. (9.5), the thermal velocity of the gas molecules depends on the molecular mass and is higher for light species. This means that the pumping speed for turbomolecular pumps decreases for light gases like hydrogen or helium. The achievable compression per stage is of the order of 30 (hydrogen) to 1000 (air). Turbopumps consist of a set of stators and rotors that are rotating at very high speed in a casing. Depending on the number of stages, the resulting overall compression of a turbopump differs by many orders of magnitude between light and heavy gases. As all primary pumps, turbomolecular pumps have a mechanical forepump. For this purpose, most turbopumps on the market today include an integrated drag stage to compress to a higher pressure at the outlet (hPa range), thus enabling a simpler design of the forepump. A modern turbopump has an ultimate pressure in the range of 10^{-8} Pa.

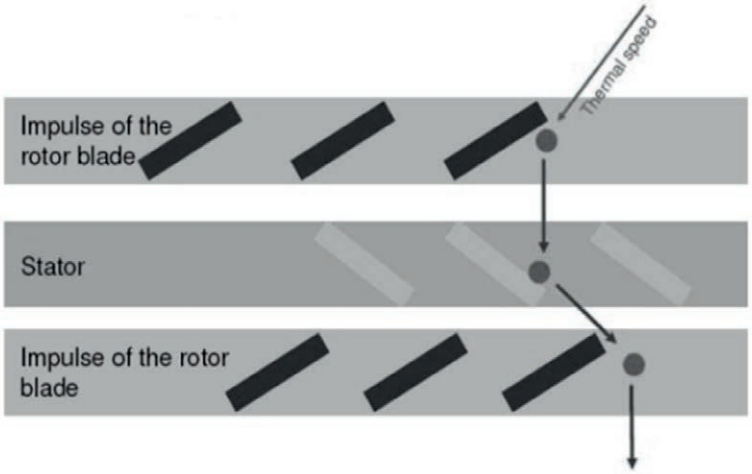

FIG. 9.22. Pumping principle of turbomolecular pumps by momentum exchange between particles and rotor.

Since turbomolecular pumps have become the standard solution for ultrahigh vacuum pumping, they have at various phases in the last 10 years been developed for suitability with a D–T fusion environment. Turbopumps are commercially available with only moderate pumping speeds. The maximum size of these pumps is given by an inlet cross-section with 250–300 mm diameter, ending up with pumping speeds of 2 to 3 m^3/s. This limit comes from safety considerations assuming that in case of a rotor failure all the kinetic energy of the fast rotating rotor (with frequencies of the order of 50000 rotations per minute and more) would have to be taken up from the housing and, in particular, the connection flange between vessel and pump. Very often, the rotor is magnetically levitated to keep the pump clean (no oil, grease or other lubricant) and to extend the service intervals (up to 40000 hours). Turbopumps are sensitive to dust (because of the high rotor speeds), vibrations and sudden vacuum breaks (magnetic bearing with small gaps between rotor and stator), changing magnetic fields (mainly problems of controlling the magnetic bearings and thermal problems due to eddy currents in the rotor) and high gas loads (rotor heat can only be removed by thermal radiation what leads to high rotor temperatures). To reduce the eddy heating effect of the rotor which already becomes inacceptable at field strengths of the order of some mT, ceramic rotors[84] have been developed in the 90s but the achieved performance was not convincing. ITER is currently developing a small turbopump with an integrated magnetic shielding. However, the shielding would become inacceptably bulky if applied to the large pumps needed for the main vacuum systems. A two cubic meters per second turbopump that had been specially developed for fusion applications (with a sealed bearing set and other material changes to make it tritium compatible) has been used at JET, but the tritium compatibility is still questionable and various on-machine failures have been experienced. Other non-conclusive experiences with turbomolecular pumps have also been made at other places such as Ontario Hydro (Canada) and the Tritium Laboratory Karlsruhe (Germany). To overcome the pumping speed limitations, there was an effort within the WEST programme to develop a cold turbomolecular pump, but also this has been abandoned.

Perspective in fusion

The experience in (small) non-D–T fusion machines with turbopumps is good, but the limited size and pumping speeds as well as the eddy current heating of the rotor in magnetic fields and maintenance requirements are a show stopper for applications at a power plant level. The aspect of tritium compatibility is critical.

9.6.2. Vapour diffusion pumps

Vapour diffusion pumps are one of the oldest high vacuum pumps, developed at the beginning of the last century. Like the turbopumps, momentum is transferred to the pumped particles. The function of the turbomolecular pump rotor is taken over by a high speed gas jet of working fluid, as illustrated in Fig. 9.23. Mercury was initially used for this purpose, but nowadays synthetic oils are standard. The vapour is ejected through circular nozzles with supersonic speed against the cooled wall. There, the working fluid condenses and flows back into its reservoir. Each stage

[84] This effort was initiated from the Japanese Fusion Programme.

develops a compression ratio between 100 and 1000. With several stages an ultimate pressure better than 10^{-7} Pa can be reached.

Advantages of the vapour diffusion pumps are that they do not have movable parts and can be used under high magnetic fields when built out of stainless-steel grades with low magnetic permeability. The only electrical component is a heater plate that can be changed without venting the vacuum system. This makes the diffusion pump very reliable. Vapour diffusion pumps are available in sizes with pumping speeds up to 50 m^3/s, which is already of the order which may be needed for one individual primary pump at a fusion power plant. As a disadvantage, to reduce the backflow of the working fluid into the process chamber, a cryogenically cooled (liquid nitrogen temperature) baffle is needed, which increases the complexity of the system. Even today, the diffusion pump is still the primary choice for a high vacuum pump that works reliably under rough applications where other pumps cannot be used (e.g. metallurgy).

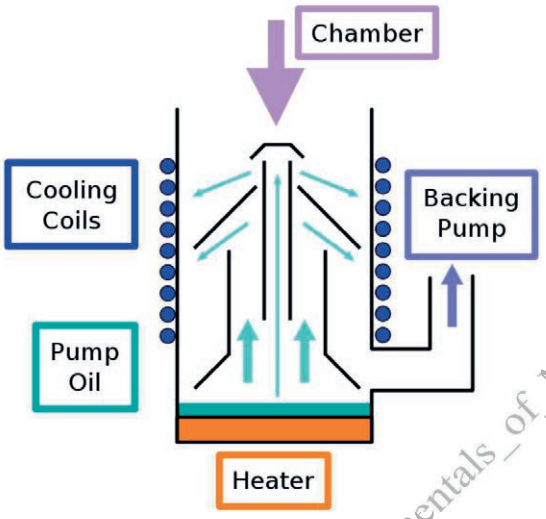

FIG. 9.23. Schematic view of an oil diffusion pump

Perspective in fusion

The diffusion pump technology is well known. If one would employ a tritium compatible working liquid, the diffusion pump principle would be very promising in fusion applications. Mercury diffusion pumps had already been successfully used for tritium processing in the mid 20th century. The fact that, historically, the first diffusion pumps have been developed with mercury (which is tritium compatible) did suggest considering this option more seriously. Indeed, a comprehensive R&D programme is currently ongoing in EU to qualify mercury diffusion pumps for DEMO [13].

9.7. ENTRAPMENT VACUUM PUMPS

An entrapment or capture vacuum pump removes gas molecules from the vacuum chamber and captures them on its internal surfaces. These pumps come in flange designs (as the other vacuum pumps) but can also be placed in-situ of the vacuum chamber, which allows provision of pumping speed without any conductance loss. The performance of entrapment pumps does depend on the amount of gas pumped: At some point in time, the existing capability to pump decreases rapidly, as all bonds are occupied. When this capacity limit has been reached, the pump should be regenerated and cannot be used for active pumping.

Entrapment pumps can produce the highest vacua and are therefore typically related to very high pumping speeds, which are easily scaled, being roughly proportional to the internal surface area. However, one should note that fusion asks for high pumping speeds (denoted as S) due to the high gas flows (denoted as Q) to be processed, and not due to very low pressures, see Eq. (9.11). Having said that, all primary pump technologies that only provide the requested pumping speed and capacity at very low pressures are unsuitable. An example of that is the sputter ion pump, which is the reference pump technology used to maintain the UHV conditions in accelerator systems. The sputter ion pump uses an electric gas discharge to produce ions that sputter cathode material to form thin films which then act as absorbing surfaces.

9.7.1. Getter pumps

The only classical low pressure entrapment pump that is fusion relevant is the non-evaporable getter (NEG) pump. NEG pumps sorb gases by a chemical reaction, for which they use very reactive alloys (such as zirconium or titanium). Active gases, like O_2, N_2, H_2O, CO, CO_2 impinging on the cartridge surface are dissociated and permanently trapped in the form of stable chemical compounds. Hydrogenic species are very effectively pumped by the NEG: the hydrogen atoms for instance diffuse inside the getter bulk and dissolve as a solid solution. Noble gases and CH_4 are not pumped. NEG pumps are therefore efficient and clean sinks for molecules with pumping speed and sorption capacity that can be optimized by selecting the type of getter material, its configuration and the operating temperature. To sorb gases, NEG pumps need first to be activated. The activation process is carried out under vacuum (or noble gas atmosphere) heating the getter at a certain temperature (typically at 400 to 500°C) for a given time (~1 hour). This treatment allows surface oxides and carbides covering the surface to decompose and diffuse inside the getter material bulk structure, leaving a clean and reactive metal surface to sorb gas.

Perspective in fusion

In the past, NEG pumps have always been optimized for XHV conditions and the pump capacity was by orders of magnitude too small to be used in a high throughput process such as fusion. Recently, novel and very promising high capacity materials came on the market which are currently intensively characterized for applications in fusion [14]. There are also applications to use NEG materials for safe tritium storage (as tritride).

9.7.2. Cryopumps

A pump type, which can cope with all requirements in nuclear fusion is the cryogenic pump, which has seen much R&D as part of the worldwide fusion programmes. Cryopumps are installed in all major fusion devices (JET, AUG, DIII-D, JT60, etc.). Mostly, cryopumps can be designed in a tritium compatible way, hence they are suitable for D–T devices (ITER, DEMO), which makes them so important. This present section introduces the principles of cryogenic pumping. In the following, Section 9.7.3, the cryopumps for ITER and the way they are operated are described in full detail.

The cryopumping effect is produced by intimate interaction between the gas particles to be pumped and a cold surface provided inside the cryopump. In all commercially available cryopumps, the low temperatures are generated by closed-loop cryogen-free mechanical refrigerators, which, however, are not an option for fusion, mainly due to their low cooling power. Consequently, the cryogenic pumps in fusion devices are normally directly supplied with cryogen (typically at 4 to 5 K) from the cryoplant which is employed for cooling of the superconducting magnets. The cryopump designs are customized for individual application such that all cryopumps are unique.

There are two most important principles per which a cryopump can work. In the case of cryocondensation, the surfaces are cooled to a temperature which allows the corresponding saturation pressure to remain equal to or below the desired vacuum pressure in the chamber. The achievable pressure is determined by the saturation pressure at the temperature chosen for the cold surfaces. This principle is the most elementary of all forms of capture pumping. For many pumped gases, the pressure range of cryopumps is below the triple point pressure. Thus, the relevant saturation curve becomes identical to the sublimation curve, i.e. during pumping, the gas particles undergo direct phase transition from the gaseous to the solid phase without any liquid phase. Fig. 9.24 shows the sublimation equilibrium curves of some relevant gases. A temperature of ~100 K would be sufficient to condense water and all hydrocarbons. To condense the air components, a temperature of 20 K is needed. The 4 K level is required to condense the hydrogen isotopes and neon.

However, at the normally available 4 K level, helium cannot be condensed. Likewise, it is not possible to pump protium in UHV. A cryopump therefore involves another physical mechanism to remove such particles from the gas phase, namely by physical adsorption on a cryogenically cooled porous material (cryosorption). The equilibrium pressure of adsorbed gas particles is significantly lower than the corresponding saturation pressure for cryocondensation.

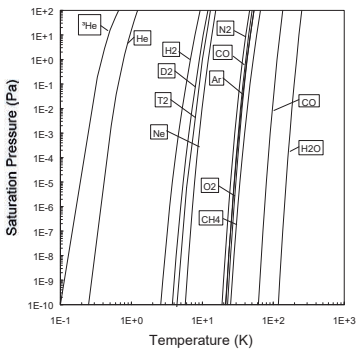

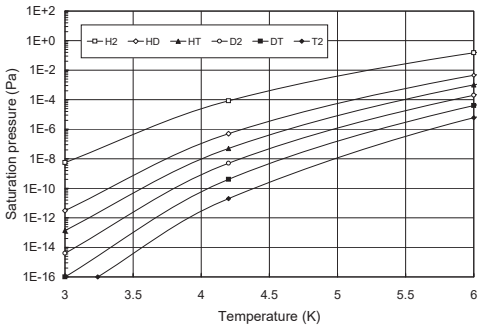

FIG. 9.24. Saturation curves of common gases.

The cryosorption process is quite complex and very much determined by the actual nature of the surface, not only by its temperature as for the case of cryocondensation. The best experience has been made with charcoal as cryosorbent, but any porous material shows this effect (zeolites, sintered metals, layers of precondensed gas frost). The characteristic of cryosorption is given by the respective sorption isotherm. It is possible without any problem to bind helium or hydrogens in the 5 K temperature range and to achieve equilibrium pressures in the 10^{-7} Pa region, see Fig. 9.25.

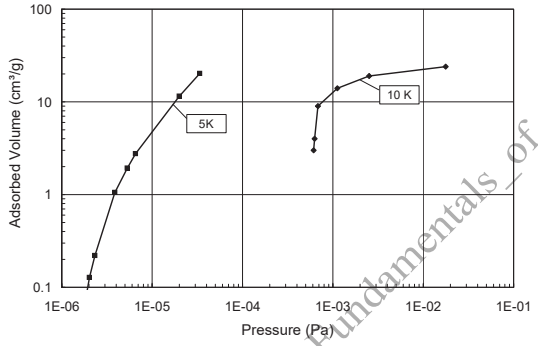

FIG. 9.25. Sorption equilibria for helium at a microporous activated charcoal.

The sorption sticking coefficient i.e. the number of molecules which are sorbed on a surface per unit time divided by the number of molecules impinging on that surface may be considerably below unity depending on the material–gas pair. Due to the physical principle, cryosorption pumping is limited to some monolayers of gas coverage on the surface. The effect of the surface then becomes negligible and the resulting pressure starts to increase rapidly to the saturation pressure.

9.7.2.1. Example

Derive the ultimate pressure of a cryocondensation surface at T_c, surrounded by a thermal shield at T_{sh}.
Before stationary operation is established, the pumped flux j_{pump} results as the difference between the condensed flux j_c and the evaporated flux j_{ev}:

$$j_{\text{pump}} = j_c - j_{ev} = j_c \times \left(1 - \frac{j_{ev}}{j_c}\right)$$

At the low temperatures of interest, one can use Eqs (9.5) and (9.6) to write the fluxes and finds the dependence:

$$j \sim \frac{p}{\sqrt{T}}$$

Under ultimate pressure conditions, the pumping speed and hence the pumped flux is zero (thermodynamic equilibrium). Thus, the bracket in the equation above can be set to zero. For the evaporating gas, the temperature of the cold surface T_c and the saturation pressure at that temperature $p_{sat}(T_c)$ is used; for the condensing gas, the higher temperature of the surrounding shield T_{sh} and the gas pressure in the vessel should be used.
This yields the following expression for the ultimate pressure:

$$1 = \frac{p_{sat}/\sqrt{T_c}}{p_{ult}/\sqrt{T_{sh}}} \rightarrow p_{ult} = p_{sat} \cdot \sqrt{\frac{T_{sh}}{T_c}} > p_{sat}$$

It is noted that the ultimately achievable pressure is always higher (i.e. worse) than the equilibrium saturation pressure. For a typical case where the cryosurface at 4.5 K is surrounded by a thermal shield at 80 K, the square root takes the value 4.5.

9.7.3. ITER cryopumps

The torus exhaust primary (high vacuum) pumping solution for ITER is based on several identical, bespoke, batch regenerating cryosorption pumps which each comprise 28 charcoal coated and cryogenically cooled (4.5 K) hydroformed cryopanels (each 1000 mm long, 200 mm wide, 11.2 m^2 charcoal coated surface in total) arranged in a circular casing and shielded by a radiation and precooling shield at a higher temperature level (80 K), as shown in Fig. 9.26. The ITER cryosorption pumps provide a condensation pump effect at the 80 K thermal shield for heavier species and water as well as a mixed condensation and sorption effect at the 4.5 K cryopanels for the remaining gases. If no helium has to be pumped, the cryopanels can alternatively be operated at correspondingly higher temperature of the order of 10 to 15 K, which is sufficient to sorb hydrogens.

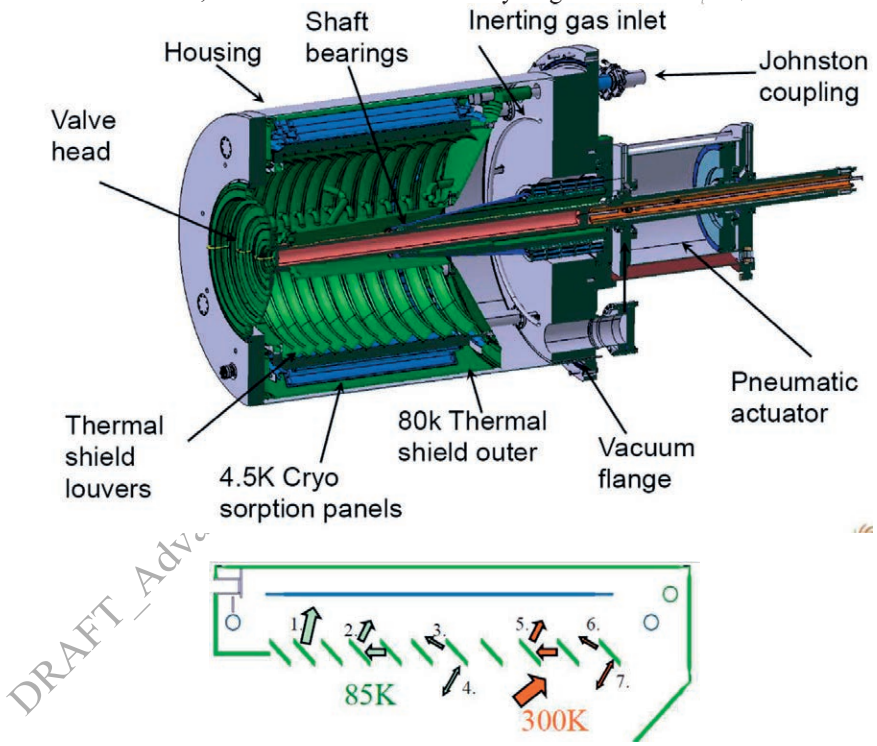

FIG. 9.26. ITER style cryosorption torus pump: schematic cut (top) and detail of the lower shield (bottom).

To be able to keep cryotemperatures at the sorbent surfaces, these have to be appropriately shielded against thermal radiation coming from walls at ambient temperature. As shown in Fig. 9.26, the shielding fully encloses the cryopanels towards the housing, but is of course open towards the direction where the pumped particles come from.

These features are detailed in the bottom part of Fig. 9.26. The thermal shields reconcile two contradictory requirements: On one side, they have to be rather closed in order to minimize thermal radiation on the panels, on the other side, they have to be rather open, in order to minimize particle conductance losses.

As shown in the figure, this pump is equipped with an inlet valve that can be closed to reduce the pumping speed and throttle the gas throughput. Fig. 9.27 shows the measured performance of a 1:2 downscaled model pump to illustrate the expected behavior. The ITER pumps are required to handle a large throughput which results in very atypically high pressures (1 to 100 Pa), which requires a high cooling power. Due to this high cryogenic demand, only directly cryogen driven pumps (large flows of supercritical helium) can be used. The high pressures result in the pump being operated in transitional flow conditions. This also explains that the pumping speed curves are increasing with rising throughput (whereas cryopumps in UHV provide a constant pumping speed). The design of the ITER torus pumping system makes use of the pumping speed increase to reduce the overall number of pumps.

The arrangement of the ITER torus cryopump internal structures was developed on a rigorous (TPMC and DSMC) Monte Carlo analysis, which optimized the capture coefficient as a function of the sorption sticking coefficient. Fig. 9.28 illustrates a typical example of such work. At the ITER type charcoal for ITER relevant cryotemperatures, typical values of the initial (i.e. zero load) sticking coefficients are of ~0.2 for He, ~0.6 for H_2, ~0.9 for D_2 and unity (indicating condensation) for T_2.

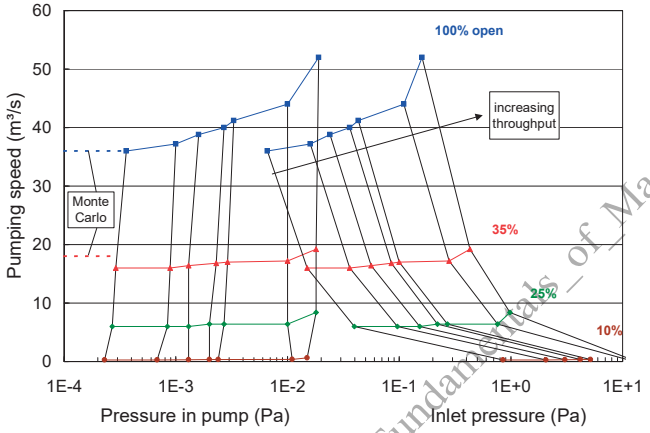

FIG. 9.27. Initial pumping speed of an ITER like model pump (1:2 scale) at different valve positions for a typical fusion exhaust gas as a function of pressure and varied throughput.

The pumping speed curve of a cryosorbed gas first remains constant then decreasing sharply with pumping time until the surface is fully loaded with gas (which means all the porous charcoal surface is covered with gas molecules), upon which the pump has to be regenerated. For the ITER sorbent configuration, this limit is of the order of 0.5 $Pa{\cdot}m^3{\cdot}cm^{-2}$ coated surface for helium and protium and significantly larger for other gases. Within regeneration, the pumping surfaces are heated up to a higher temperature — depending on the gas that was pumped and is being released — and cooled down again. In ITER, for normal operation, the cryopanels are cooled down to 4.5 K by supercritical helium during the pumping cycle, followed by a regeneration cycle at 100 K. As shown in Fig. 9.29 for regeneration in the closed (unpumped) volume of the pump, this temperature is needed to desorb all hydrogenic species and helium and will release the major part of the pumped amount. The reference pumping or regenerating cycle takes 600 seconds. This operating characteristic (cooling and heating cycles) results in a highly pulsed demand of cooling power, which is a very challenging operation mode for the cryoplant. To release impurities (eventually tritiated), the pump should be regenerated to ambient temperature from time to time. In addition, the pump design allows to have a high temperature regeneration step (up to 450 K), which is not included in the regular regeneration programme, but may be needed in case of a safety event that contaminates the pump with water or higher hydrocarbons.

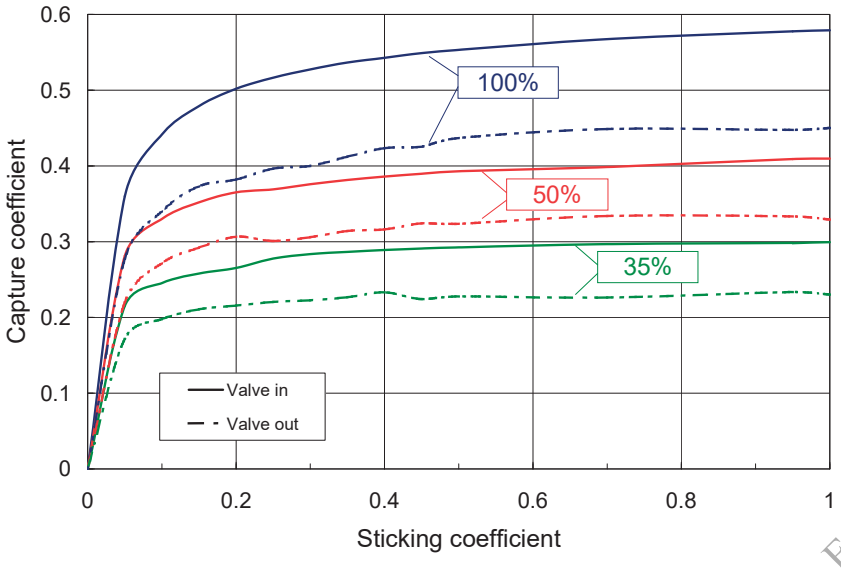

FIG. 9.28. Predictive Monte Carlo calculations of the pump performance for two conceptual pump designs (valve moving inwards vs. outwards) at varied valve opening position.

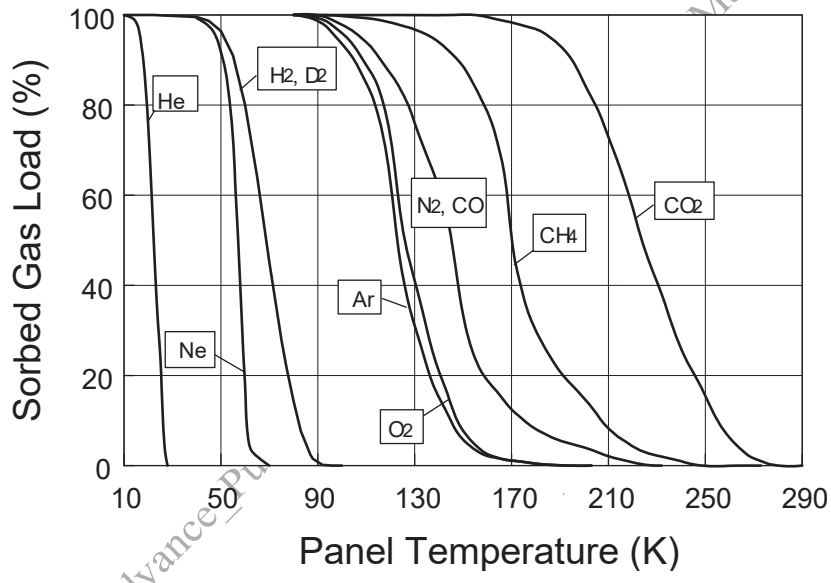

FIG. 9.29. Regeneration curves for the ITER type croyosorbent.

Another cryopump type used at ITER is for pumping the heating neutral beam injection (NBI) vessel. The gases for the operation of the ITER NBIs are protium and deuterium. Under normal operation conditions, these cryopumps do not see tritium. They are split into two rectangular pumps for each injector (each 8 m long and 2.8 m high) placed to the right and the left wall of the beam line vessel, as illustrated in Fig. 9.30. The NBI cryopumps are also based on sorption pumping at charcoal coated cryopanels (about 50 m² of coated surface). Since no helium has to be pumped, a higher temperature of up to 10 K can be acccepted for the cryopanel cooling circuit.

The cryopanel design is based on the use of passively cooled fins on centrally cooled tubes. The complete pump provides an approximate pumping speed of 5 000 m³/s for protium, which is enormous and will be a world record alongside the NBI cryosorption pumps of JET. The conceptual design of the pumping surfaces together with the thermal radiation shields for each pumping stage is depicted in the right hand side of Fig. 9.30. This design is much more complex than the one of the torus cryopump as higher capture coefficients are needed. The primary function of

the NBI pumping system is to provide a sufficiently low pressure density profile against the high gas flows encountered, especially in the gas neutralizer. The pump development has been strictly based on Monte Carlo calculations.

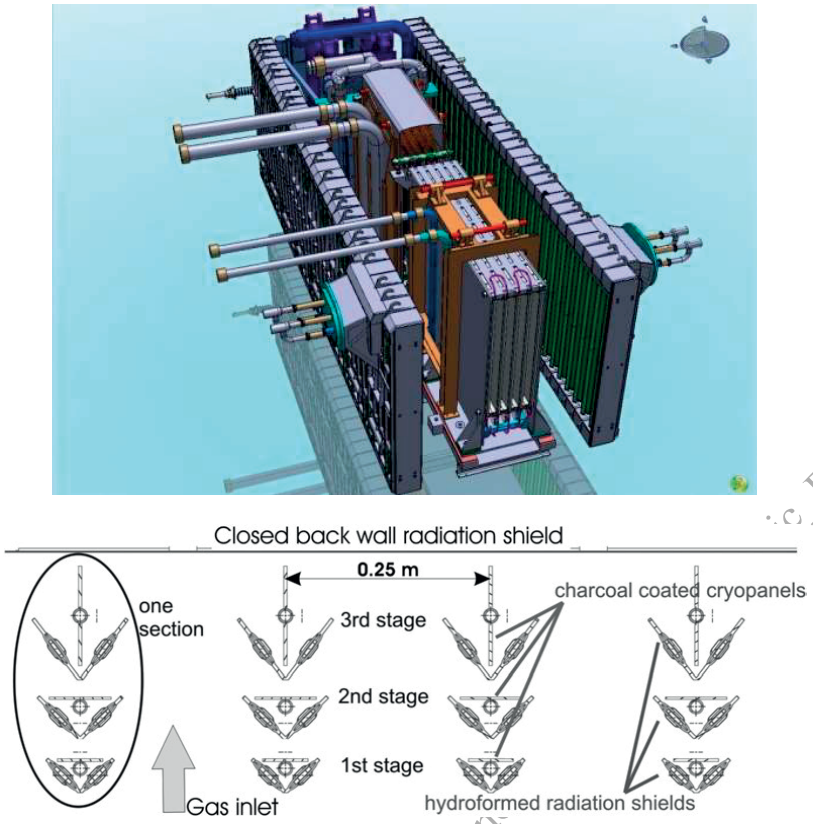

FIG. 9.30. Neutral beam injector of ITER, showing the beamline components in the middle and the pump arrangement on the side walls (top); and details of the conceptual cryopanel arrangement (bottom).

ITER is also using bespoke cryopumps as forepumps. The original ITER reference roughing pump train had two stages, both based on mechanical pumps (scroll or roots and piston) that were planned to be modified to make them tritium compatible for D–T operation. However, the development of a tritium compatible rotary feedthrough was considered too risky and abandoned. In consequence, ITER will now most likely have two types of forepump trains: one for non-tritiated gases based on modified standard mechanical pumps and another for tritiated gases, in which the first stage of the mechanical pumps is replaced by a cryogenic pump at a much smaller volume than the primary cryogenic pump (NBI and torus) so that the regenerated gas will be provided at a higher pressure, compatible with the ultimate pressure limit of a tritium compatible mechanical pump placed further downstream. Design work for this cryogenic forepump is still ongoing (in the USA). Several of these pumps will operate in parallel and are staged to maintain continuous pumping and intrapulse regeneration during plasma operation. The pumps are cooled to operating temperatures of 3.8 K whereas the helium passes through and is pumped by conventional vacuum pumps. The regenerated gas stream will be taken up from dry mechanical pumps and further compressed towards the gas processing unit in the tritium plant. The achievable regeneration pressure will be crucial for the feasibility of this concept for hydrogen. All currently discussed final stage candidates to take up the regeneration gas (scroll pumps, dry piston pumps, roots pumps) have only relatively high ultimate pressures for the light hydrogenic gases, see the detailed discussions of these pump types in Section 9.5.2.

9.7.4. Other cryopump designs in fusion

Cryopumps include a variety of different designs that have some relevance for fusion applications. Most current fusion devices include cryocondensation pumps (pumped divertor cryopumps) operated with liquid helium under subatmospheric conditions to be able to pump hydrogen sufficiently well (as there is no need to pump helium). But

the fact that they are not able to pump the fusion ash excludes them for D–T fusion. A solution to overcome this limitation is to provide a layer of condensed heavy gas acting as sorbent, which has a frost structure so that the particles to be pumped can be incorporated and sorbed. Good experience has been made with argon frost in DIII-D, JET and ASDEX [15]. The advantage of this approach is that the regeneration temperature is much lower than for a solid sorbent. The drawback is that, during regeneration, the frost will evaporate as well and add considerably to the released gas load (usually a factor 4 to 5 over the actual hydrogen gas load to be pumped), so that the frost gas easily becomes the design driver of the peripheral systems (gas supply, piping space, tritium plant and cryoplant). This is the main reason why the ITER project has decided to go for charcoal sorption pumping. However, the capacity is also limited for frost and pumping speed stability is an issue, as the frost layer is very sensitive to throughput fluctuations.

There are a couple of other cryopump concepts that have been developed for fusion but none of them has, until now, been utilized in a fusion experiment. The ITER cryosorption pumps are sorbing all gases concurrently. Another cryopump variant, often denoted compound or cascaded cryopump provides a distributed pumping by having cryosurfaces at different temperatures so that they can be released during regeneration one after the other, if a mechanical mechanism is installed that allows the sampling of the regenerated gases [16]. By this foreseparation, impurities and helium could be separated in a relatively sharp way from the fusion plasma, which would allow a significant reduction in size of the tritium plant. To some extent, this is also possible for a co-pumping cryosorption pump since the desorption curves of the different gas species are quite different. As a solution to allow a cryopump to work continuously, a so-called snail pump was being developed [17]. In this pump, a mechanical or thermal scraper is used to scrape off the adsorbed or frozen gas, which makes this pump relatively bulky. In an updated design, the snail pump included a diffusor stage which provides a separation effect for helium and a compression by enrichment. A test version of this pump has been built and tested in 2005, but the programme was later discontinued.

Perspective in fusion

The cryogenic vacuum pump meets all fusion requirements and seems to be the best solution for a device like ITER, which has the high throughputs levels of a power plant but remains a short-pulse machine (the gas amount accumulated during one pulse stays below the capacity limit). However, the intrinsic limitations of that technology become obvious if simply scaled up to a DEMO class device, namely (i) the required rich cryogenic infrastructure, (ii) the high regeneration frequencies over long pulse times, which consume a big energy budget, and (iii) the buildup of tritium inventories in the cryopumps which may be above the regulatory limit of a power plant.

9.8. FUSION VACUUM SYSTEM DESIGN

This section outlines the system design process, which is illustrated in Fig. 9.31. A good vacuum system design is much more than just choosing the vacuum pump (as discussed above in 9.8.3, all ITER primary pumps are cryosorption pumps). A good design does also address the influence of port geometry (fully exploiting the toolbox, as discussed in Section 9.2.2), and does satisfy all the vacuum vessel pumping and tritium safety requirements. The first subsection will focus on the system requirements and use the ITER divertor pumping system as an example. The second subsection will then provide an outlook to a fusion power plant.

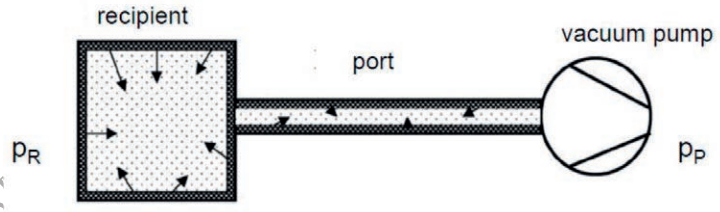

FIG. 9.31. Schematic for the design of a vacuum system.

9.8.1. Vacuum requirements of ITER

A modern nuclear fusion device consists of a vacuum chamber in which the plasma is contained, housed in a cryostat which comprises the superconducting coils. These two systems represent the two major large vacuum systems of the machine core. On top, there come several additional vacuum systems as part of the diagnostic systems; here, the neutral beam injector is known to require a powerful vacuum system.

The cryostat serves to provide an insulation vacuum system. This requires maintaining pressures of the order of 10^{-2} Pa, to exclude any gas conduction between the outer shell and the cryogenic components (thermal shields of the coils), and to reduce the heat load to thermal radiation. This case is a classical pump-down problem (cf Fig. 9.5). Once the required end pressure is achieved, the only gas source is parasitic gas, outgassing from the surface and the components inside the cryostat.

Much more challenging is the torus exhaust pumping system. It should provide two different tasks, namely to pump the exhaust gas during plasma operation and to provide the requested starting condition in the dwell phase between the plasma shots. The former scenario involves the handling of a large gas flow at relatively moderate divertor neutral pressures. The latter asks for lower pressures to be reached in a limited amount of time. Hence, both scenarios lead to high pumping speeds ($S = Q/p$), due to high Q for plasma pumping and low p in the dwell pumping. Hence, the physics of the flow is different in the two cases. The baseline requirements are listed in Table 9.3. In the initial (superseded) version of the ITER requirements, the full throughput was requested down to the lowest pressure. In the course of the detailed design work, it turned out that for the limited number of pumps foreseen, the maximum throughput can only be processed at the high pressure end.

TABLE 9.3. Baseline ITER input requirements for the divertor pumping system.

Parameters	**Unit**	**Value**
Ultimate base pressure for hydrogen isotopes	Pa	$< 10^{-5}$
Ultimate base pressure for impurity gases	Pa	$< 10^{-7}$
Typical divertor pressure during D–T plasma operations for inductive, hybrid and non-inductive plasma discharges[85]	Pa	1–10
Typical divertor pressure during plasma operations for H-phase H-mode plasmas[8]	Pa	0.25–10
Fuelling rate during long pulse D–T plasma operations[8]	$Pa \cdot m^3 \cdot s^{-1}$	120–200
Base pressure between pulses	Pa	$< 5 \times 10^{-4}$

As the pumping speeds may depend on gas species, the information on exhaust gas composition is essential; it is listed in Table 9.4 for the case of ITER. The section on fuelling below will illustrate that the definition of the gas throughput is not very well understood. If it is known to the vacuum designer, he should incorporate safety margins.

TABLE 9.4. Maximum average total gas throughput for ITER.

Gas source	***Pulse Flat top duration (s)***	***Plasma exhaust throughput ($Pa \cdot m^3 \cdot s^{-1}$)***	***Gas species / Comment***
Fuelling	400	200	Fuelling of D–T, H–D, H–H or D–D
Fuelling	1000	160	
Fuelling	3000	120	
Fuelling	200	120	Fuelling of He/H
He Ash		10	He production from burning plasma
Divertor radiative gas (Combined N_2, Ar, Ne)		10	During radiative impurity gas injection to divertor

[85] The formulation is as follows: The divertor pumping system will provide adequate and controllable pumping speed to maintain a specified pressure under the dome for steady conditions with a variable fuelling rate. For He plasma operation (including the simultaneous use of hydrogenic pellet injection) the divertor neutral pressure is expected to be between 0.25 and 10 Pa: a) for an under-dome pressure in the range 4 to 10 Pa: a throughput up to 120 $Pa \cdot m^3 \cdot s^{-1}$. b) for an under-dome pressure < 4 Pa: a throughput < 120 $Pa \cdot m^3 \cdot s^{-1}$ and a minimum pumping speed of 30 m^3/s. For D–T plasma operation the divertor neutral pressure is expected to be in the range 1 to10 Pa: a) for an under-dome pressure in the range 3 to 10 Pa: a throughput up to 200 $Pa \cdot m^3 \cdot s^{-1}$·b) for an under-dome pressure < 3 Pa: a throughput < 200 $Pa \cdot m^3 \cdot s^{-1}$ and a minimum pumping speed of 50 m^3/s.

9.8.1.1. Design for plasma operation conditions

By a combination of throughput, composition and pressure, Tables 9.3 and 9.4 define the effective pumping speed at the divertor. The actual pumping speed of the pumps is not given. Hence, for starting a system design, one should assume a port geometry and calculate the unknown pumping speed of the individual pumps. The now frozen port geometry at ITER is shown in Fig. 9.32, there will be six of these ports in the lower level of ITER, each one being equipped with one of the customized circular ITER cryopumps (Fig. 9.26). Based on this configuration, a conductance calculation can be made, utilizing the appropriate tools for the Knudsen number ranges that are valid under the given flow conditions and port sizes; this was already discussed in Section 9.2.2. As a result, the pumping speed of each cryopump was calculated to be ~80 m³/s for D–T operations.

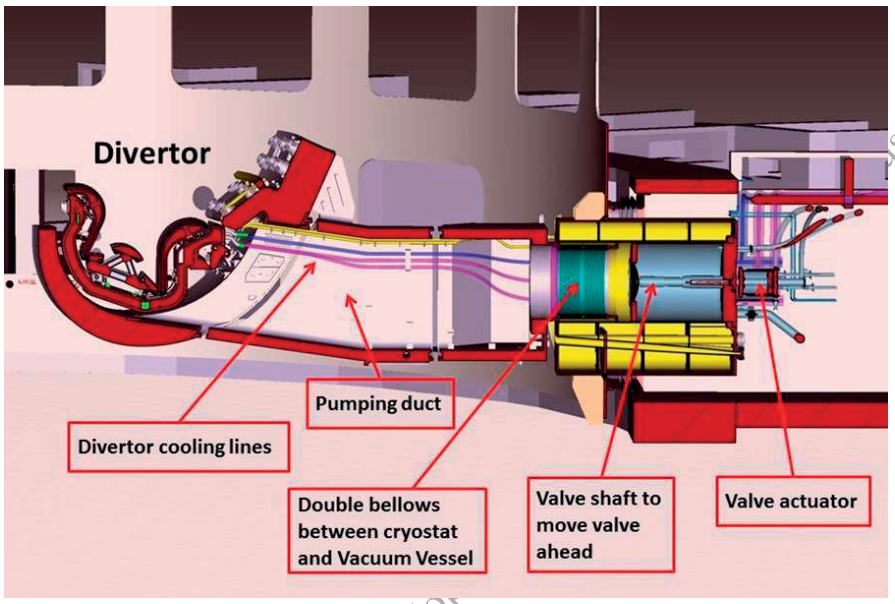

FIG. 9.32. ITER divertor pumping port geometry. © ITER Organization, http://www.iter.org/

In view of the pumping time of cryogenic pumps, one should define the associated pumped amounts and define a regeneration plan. The maximum amount to be accumulated in one pump is given by the smallest number defined by any one of the following constraints:

1) the capacity limitation of the sorbent, in case the gas is being cryosorbed (He, H_2). This assessment needs a good knowledge of the thermodynamic properties of the charcoal and is known for the ITER configuration.
2) the maximum allowed hydrogenic inventory to exclude any oxy–hydrogen explosion hazard in case of an air leak into the cryopump. This is another complex requirement, which is based on the philosophy that the maximum allowed hydrogenic amount in the closed cryopump may not exceed a given maximum explosion pressure to which the system is designed to. As volumetric concentrations are involved, this requirement is interlinked with the pump size as well.
3) the maximum allowed tritium inventory (in the sum of all tritiated species): This is given by administrative limits and operational aspects.

It was found that with the given number of pumps and space, capacity is not sufficient for the 1000 s and the 3000 s pulses; not even always sufficient for the 400 s pulses. To be able to always provide a constant pumping speed, a staggered operation scheme was conceptuated, which involves intrapulse regeneration, as outlined in Fig. 9.33. It shows that each of the 6 pumps has a maximum pumping time of 1200 s, followed by a regeneration phase of 600 s. The regeneration includes 4 steps: (i) closing of the integral inlet valve and pushing cold cryogen out of the cryopanel circuit (enthalpy recovery phase), (ii) warmup by flowing warm gas (100 K) through the cryopanel circuit and release

of the pumped gas, (iii) evacuation of the released gas, (iv) cooldown to nominal temperature by flowing 4.5 K cold gas through the cryopanel circuit and opening of the inlet valve to restart pumping.

Pump No					3000 seconds																			
	77	78	79	80	1	2	3	4	5	6	7	8	9	10	11	12	13	14	15	16	17	18	19	20	21
1	HR	WU	EV	CD	P	P	P	P	P	P	P	P	HR	WU	EV	CD	P	P	P	P	P	P	P	P	HR
2	DP	DP	DP	DP	HR	WU	EV	CD	P	P	P	P	P	P	P	P	HR	WU	EV	CD	P	P	P	P	DP
3	DP	DP	DP	DP	P	P	P	P	HR	WU	EV	CD	P	P	P	P	P	P	P	P	HR	WU	EV	CD	DP
4	DP	DP	HR	WU	EV	CD	P	P	P	P	P	P	P	P	HR	WU	EV	CD	P	P	P	P	P	P	DP
5	DP	DP	DP	DP	P	P	HR	WU	EV	CD	P	P	P	P	P	P	P	P	HR	WU	EV	CD	P	P	DP
6	EV	CD	DP	DP	P	P	P	P	P	P	HR	WU	EV	CD	P	P	P	P	P	P	P	P	HR	WU	EV
					150s																				

FIG. 9.33. Staggered cryopump operation scheme for the 3000 seconds scenario. The operational steps are indicated as enthalpy recovery (HR), warmup (WU), evacuation (EV), cooldown (CD), and pumping (P).

9.8.1.2. Design for pump-down conditions

The dwell pump-down between consecutive plasma shots follows Eq. (9.21) for which, on top of the required base pressure between pulses, one has to specify the chamber volume (~1400 m³ for ITER) and the outgassing gas load as a function of time and pressure. The latter is very difficult to predict, as it depends not only on the wall material and the total outgassing surface, but also on the history of the surface, i.e. the effect of plasma–wall interaction from the previous plasma shots. For ITER, it was decided not to use the dwell as design driver for the torus exhaust cryopumps. It is expected that the dwell pump-down time will be of the order of 30 min.

9.8.2. Vacuum requirements of DEMO

The design of the first fusion power plant (~2 GW fusion power) outputting electricity to the grid is ongoing within the European fusion programme and aiming to produce a pre-conceptual design by 2020. Similar activities are ongoing worldwide in national DEMO programmes in all the ITER member states. It is therefore not possible to have definitive requirements at the moment.

Obviously, the fuelling rate and overall gas throughput will be higher than at ITER (we will learn in Section 9.9 that it is not trivial to predict this value), whereas the pressures (divertor and base pressures) may well be of similar magnitude. In consequence and based on the same arguments as for ITER, cryogenic pumps would be the most suitable solution. However, the main fundamental difference of a power plant compared to ITER is the pulse length of the plasma shot, which is of the order of many hours, and the tritium inventory of the whole device, which should be minimized for licensing reasons, for reasons of limited availability of tritium, and in order to allow for a sound startup (first fill of the facilities with tritium before breeding can take over). In addition, come typical power plant system requirements, namely economic attractiveness, reliability and maintainability, which were not really considered for ITER. In view of all three aspects, cryogenic pumping has some disadvantages: the operational cost is high due to the cryogenic operation with supercritical helium[86] and many intrapulse regenerations, the high number of cyclic operations implies fatigue on the torus pump and the inlet valve bellows as movable component with limited lifetime, and the batch wise character of cryopump operation builds up a high internal tritium inventory. Vacuum solutions based on non-cryogenic and continuous pumps without movable parts are therefore to be favoured. One currently pursuied option is to use a vapor diffusion pump with mercury (as working fluid) as primary pump, and a liquid ring pump (with the same working fluid) as roughing pump; both pumps work without cryogen and compress the gas in a continuous way. To further reduce inventories, the idea is to utilize superpermeable membranes which would separate continuously a clean hydrogenic gas stream, which could be directly fed to the fuelling systems without passing through the tritium plant [19].

[86] The future of helium as a natural resource is also seen as critical on the long term. In view of the limited availability, it is strongly anticipated that the prices will rise significantly [18].

9.9. FUELLING AND MATTER INJECTION

The systems normally denoted with the phrase ´fuelling systems´ comprise all systems by which any matter (not only fuel!) is provided to the torus chamber, we therefore want to use the more general phrase ´matter injection systems´. As will be shown in the following, this includes much more than just injecting the fuel for the fusion reaction and involves a couple of technically very challenging tasks. The injected material can be in the form of a gas, or in the form of cryogenically frozen solid, the so-called pellets. The functions that are to be fulfilled by each of the two methods are summarized in the following:

1) Gas injection: Injection of fuel gases for plasma density control and fuel replenishment for helium removal; injection of plasma enhancement gases (impurity gases for radiative cooling enhancement and for recovery of lost confinement in a metal wall environment); divertor detachment control; controlled discharge termination; injection of minority species to improve coupling of radio frequency heating waves with the plasma; provision of an emergency fusion power shutdown as a safety function; supply of gases for wall conditioning; disruption mitigation by massive gas injection.
2) Pellet Injection: Injection of hydrogen isotope ice pellets into the plasma core for plasma density control; injection of impurity ice pellets into the plasma for studies of impurity transport and possible radiative cooling enhancement at the edge; provision of pellet injection into the edge plasma for control of edge localized modes (ELM); disruption mitigation by shattered pellet injection.

To explain why different approaches are taken for different functions, the following section will have an exemplary look at the ITER case and comment on the baseline number of 200 Pa·m³·s^{-1} which was already shown in Table 9.4 for the 400 s D–T reference shot. The various fuelling functions presented in the above list will then be described in more detail. Similar considerations do also hold for DEMO, but the DEMO reference plasma scenario in quantitative terms is still evolving.

9.9.1. ITER machine throughput

A simple calculation of fuel burnup at ITER yields 0.7 Pa·m³·s^{-1}, which is a negligible contribution. The fusion reaction is

$$D + T \rightarrow {}^4He\ (3.5\ MeV) + n\ (14.1\ MeV)$$

The following expression then results from Eqs (9.2) and (9.10), where the factor 2 considers that 2 particles are involved per reaction:

$$Q = p\dot{V} = \dot{N}kT = \frac{2 \cdot P}{E}kT$$

This yields for P = 100 MW of fusion alpha power (E = 3.5 MeV) (this corresponds to the ITER reference case with 500 MW of total fusion power) an atomic throughput of $N = 3.6 \times 10^{20}$ s^{-1} or a molecular gas throughput of 0.68 Pa·m³·s^{-1} (related to T_{st} = 273.15 K).

9.9.1.1. Neutral beam fuelling:

Altogether, the three ITER NBIs will inject 51 MW with deuterium ions accelerated to 1 MeV. This corresponds to an injected molecular gas throughput of 0.6 Pa·m³·s^{-1}, which is also a negligible contribution.

In order to understand the need for significantly larger throughputs one has to have a closer look at the plasma itself. From the simplest point of view, the plasma can be subdivided in the core and the edge. The density profile in the core can be linear or peaked, but there is always a strong density gradient in the pedestal. This means that any injected material is transported through the scrape off layer (SOL) to the core against that gradient. From transport code calculations, it was found that there is a maximum achievable edge density limit that cannot be surpassed by gas fuelling. In other words: All additional gas flows directly through the SOL to the divertor and increases the flowrate to the pumping system but does not help to fuel the plasma core. These estimations yield a maximum feasible gas fuelling flowrate of ~10 Pa·m³·s^{-1}. The main fuelling is therefore done by pellet injection, which allows to deposit fuel particles deeper into the core. Pellet injection denotes the technology to launch balls (few mm diameter size) of cryogenically frozen species at high frequency (tens of Hertz) and at high velocities (several hundreds of meters per second) into the plasma.

9.9.1.2. Pellet core fuelling for density control

Transport calculations show that that the maximum core density (in order to have maximum volumetric fusion energy production, which is essential to increase the efficiency of a power plant) is given by the the Greenwald density limit [20], which is 1.2×10^{20} m^{-3} for ITER (this value roughly corresponds to one millionth of an atmosphere), which asks for a core fuelling rate of up to 85 $Pa \cdot m^3 \cdot s^{-1}$ (depending on transport in the pedestal and on penetration depth/pellet particle confinement time). Although pellets can survive the edge barrier and reach the core, they also experience significant losses on the way, so that the throughput to be injected as pellets has to be somewhat higher than the number above. The accurate calculation of ablation and deposition profiles is very complex, but an additional SOL flowrate of ~100 $Pa \cdot m^3 \cdot s^{-1}$ is expected to ensure the wanted core fuelling rate. i.e. the pellet injector processes ~180 $Pa \cdot m^3 \cdot s^{-1}$.

9.9.1.3. Fuelling for helium removal

Regarding the core fuelling requirement for a burning D–T plasma, one should check if the acceptable He impurity level stays below 5% (this is a given limit which is imposed to keep the efficiency of the fusion reaction at acceptably high level). This means that the core fueling rate would have to be minimum 20 times the produced He rate (0.7 $Pa \cdot m^3 \cdot s^{-1}$). On top, the so-called helium enrichment factor has to be considered, which describes that the He concentration in the core is always higher than the one in the divertor. This factor depends on the plasma scenario. A factor of 3 between core and divertor plasma is usually assumed such that this constraint is fulfilled for any core fuelling rate above $0.7 \times 20 \times 3 = 42$ $Pa \cdot m^3 \cdot s^{-1}$, which is ensured by the above stated pellet core-fuelling rate. Therefore, this does not add an additional requirement.

9.9.1.4. Edge localized mode fuel pellet pacing

Results from all major devices (AUG, DIII-D, MAST, JET) clearly show that pellet pacing of edge localized modes (ELM) is a viable method. For ITER, the ELM pacing portion is estimated to be ~75 $Pa \cdot m^3 \cdot s^{-1}$. ELM control can also be achieved by magnetic perturbation and the necessary coils have recently been introduced in ITER. This would be a preferable approach as the pellet injector parameters for ELM control and core fuelling are rather different and difficult to combine in a single pellet injector design (see below).

9.9.1.5. Divertor radiative seeding

This does not add fuel but high or medium Z impurities to reduce the power transported into the SOL, thus limiting the peak divertor power load. Calculations show that the impurity seeding rate needed to reduce the divertor wall load to values below 5 MW/m^2 is (I ntegrally) below 0.05% for Xe and 2% of Ne, hence negligible. The value of 5 MW/m^2 is the current accepted value under the neutron loads foreseen in DEMO and considerably less than that accepted for ITER.

9.9.1.6. Gas puffing

This contribution reflects recent findings in metal wall tokamaks, which shows that additional gas has to be puffed to achieve a plasma stability similar to that of a carbon wall. This new result is not yet fully understood and the results are not all consistent, but an additional gas portion of the order of 10% of the injected pellet throughput could be needed. This gas is not fuel, but e.g. nitrogen (an alternative gas is sought, as nitrogen is anticipated to form ammonia which potentially leads to corrosion problems, and because hard nitride coatings would form on top of the tungsten wall and tend to detach).

It is obvious that the 'correct' ITER throughput is not accurately fixed but will be found within the ITER research programme itself. Other contributions, which are planned to be studied in the ITER programme, include e.g. additional gas puffing to ensure a good coupling for ion cyclotron resonant heating (ICRH). From the considerations above, it also seems to be the case that the ITER throughput is potentially larger than indicated in Table 9.4 and probably contains a larger additional portion of non-fuel species. Finally, it should be noted that, in practice, there is an intense exchange of particles with the walls of a fusion device.

9.9.2. Control aspects of matter injection

This section focuses on a more detailed look on plasma and divertor control aspects of fuelling. To maintain the optimum (electron) density in a fusion machine is one of the key requirements. In this effort, one should consider that, if the plasma gets too dense, collisions between nuclei and electrons begin to release large amounts of bremsstrahlung

which is detrimental to plasma burn. Controlling the plasma density profile will therefore allow the operation of a tokamak closer to its limits, hence generate more energy relative to the volume. For density profile and particle control, the matter injection and pumping systems act as the main actuators, whereas heating and current drive systems are most important for plasma current control.

9.9.2.1. Divertor control

Plasma particles are confined to the largest degree within the volume composed of closed magnetic field lines. Around this volume exists a few centimeters wide region, so-called scrape off layer (SOL), see Fig. 9.34. In this region, the magnetic field lines are open, and direct the plasma exhaust into a defined region where the particles are allowed to collide with the wall and much colder neutral gas, the divertor. It also helps to ensure a high core density. Firstly, since the materials facing the exhaust plasma are not in direct contact with the main (confined) plasma, there are lower levels of impurities in the core, and as a result, much higher core temperatures can be achieved increasing the probability of fusion reactions. Secondly, the divertor allows for high confinement modes (H-modes). In the H-mode, a barrier against cross-field transport is created that significantly reduces the diffusion of particles into the open field lines thereby increasing the density and temperature of the core plasma.

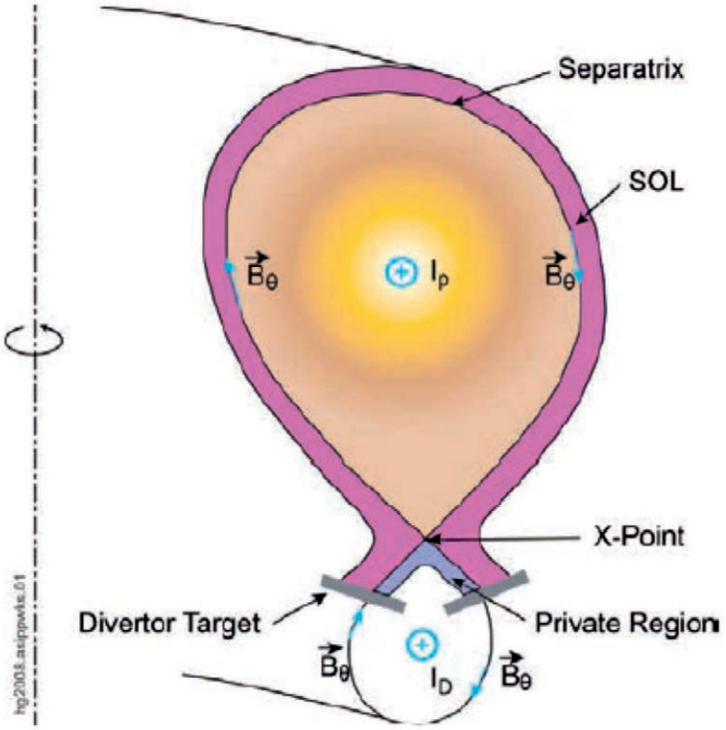

FIG. 9.34. Sketch of a simple, single null poloidal divertor configuration.

With further increase of the plasma density, the amount of charged particles that reach the divertor plates falls to negligible levels. As the density is increased, more impurities are released by plasma facing components raising the radiation levels. For tokamaks, where the walls of the divertor are made of materials that do not radiate efficiently enough, impurities can be puffed into the divertor to obtain the required level of radiation, and thus cooling of the divertor volume. This method is known as radiative seeding.

As the temperature in the divertor decreases over a large volume, electrons and ions can recombine to form neutrals volumetrically. This process is amplified by the presence of those neutrals that, recycled at solid surfaces, now act as a "break" for the plasma that flows towards the divertor targets through friction. They increase the time that the charged particles have to recombine, making this process more likely to happen. When this occurs in large quantities, the measured particle flux at the target plates drops by more than an order of magnitude. Neutral atoms transport the residual power and, as they are not bound by magnetic field lines, they can deposit power and particles over broad areas reducing the peak values to acceptable levels for materials to sustain the bombardment. This regime

is known as the plasma (or divertor) detachment since, ideally, the plasma becomes completely detached (separated) from any solid surface. Plasma detachment (sometimes only partially, at the inner target) allows higher operating temperatures upstream and is very advantageous for handling the exhaust power and fusion ash, sparing the divertor targets from unacceptable localized power loads and removing the helium exhaust [21].

9.9.2.2. Operation control

The H-mode is characterized by the formation of very steep plasma pressure profiles at the edge of the plasma that lead to bursts of edge plasma energy (expelled by the plasma) called edge localized modes. It normally arises from an onset of many small turbulent eddies at the edge due to the pressure gradient having exceeded a critical value for stability. The instability is not necessarily triggered by the pressure itself, but, for instance, by the so called "bootstrap current", an electric current driven by the pressure gradient. Following that, the edge plasma is lost to the SOL where it flows along the magnetic field lines towards the divertor producing a distinctive peak in radiation and potentially causing accelerated erosion of the divertor materials. During the instability, the edge pressure gradient is reduced until the plasma becomes stable again. Depending on the ELM type and the details of a plasma device, each ELM removes several percents of the plasma energy and particles. Fusion plasmas may have ELMs at very high frequency (tens of Hertz).

To decrease divertor erosion and, at the same time, maintain a good control of the pressure profile, several methods of ELM suppression are considered at present. One of them is based on controlled triggering of ELMs by injecting small frozen deuterium pellets into the plasma edge at a typical high frequency (e.g. 40 Hz). It was found in experiments that this can increase the ELM frequency considerably, thereby reducing the average energy per single ELM and thus minimizing the erosion risk. However, the potential damage to components by ELMs is considered a serious issue for a fusion power plant, so that the DEMO programme is also looking in ELM-free plasma scenarios, such as the I-mode or the QH-mode.

Within the course of a safety event, one may see the need to initiate a defined termination of the plasma. This is the purpose of the fusion power shutdown system (FPSS) [22]. Such a situation may be triggered e.g. in a loss-of-coolant accident in the divertor cooling system, to avoid melting of the plasma facing components. The FPSS is based on the same massive gas injection concept employed to kill the plasma in disruption mitigation and reflects estimations on energy balance. The quantity and species combination as well as the question "how fast the gas needs to be injected into the vacuum vessel?" are currently under investigation for ITER and will make use of extrapolations from the disruption mitigation system, as outlined below.

9.9.2.3. Disruption mitigation and runaways

In H-mode operation, ELMs (although they need to be controlled properly) are instrumental to maintain a stable density of the confined plasma. In other words, without ELMs the H-mode plasma density would increase above the overall stability limit, leading to sudden loss of the plasma confinement in a major instability called plasma disruption. Such a disruption may be fatal for a machine, if not reliably mitigated.

The techniques discussed above to improve magnetohydrodynamic (MHD) stability are also the principal means of avoiding disruptions. However, if these techniques cannot prevent an instability, the effects of a disruption can be mitigated by various techniques that are based on controlled removal of plasma energy to avoid local energy peaking on the wall. Currently discussed mitigation techniques are the injection of a large gas puff or an impurity pellet that is shattered inside the plasma chamber to be most effective [23]. The rapidly injected amount of matter results in the energy contained in the plasma being distributed rather evenly on the inner wall instead of being concentrated on a small surfacecreating massive melting.

The high-energy, so-called runaway, electrons generated in the case of a disruption give rise to a serious concern. The large electric fields induced during the current quench phase of a disruption may produce a large number of electrons with energies as high as several hundreds of MeV. Due to the decrease of the Coulomb collision frequency with increasing energy, these high-energy electrons are continuously accelerated by the electric field, i.e., they 'run away'. The final runaway energy can become sufficiently large as to cause serious damage to the confining structures. Moreover, it has been predicted that, in future tokamak reactors, the production of runaway electrons during disruptions will be noticeably increased because of the so-called avalanche mechanism, consisting in the production of runaway electrons by close Coulomb collisions of already existing runaway electrons with bulk electrons. Therefore, a great interest exists in developing experimental methods to control the number and the energy of runaway electrons produced during disruptions.

9.9.3. Gas injection technology

The nominal gas injection system is basically a pipework manifold which connects the gas storage vessels in the background of the machine with the plasma chamber, equipped with mass flow controllers or solenoid valves. The challenges are in the operational control routines to ensure the requested response times (63% of the set-point in less than 1 s) and to find devices that withstand the radiation and magnetic field conditions and still provide excellent repeatability and stability in the whole throughput range. To allow a fast reaction, the controllers are located close to the injection point. The transient flow calculations can easily be done in a wide range of the Knudsen number by one of the methods presented in Section 9.3.2 For FPSS or disruption mitigation, special fast-opening high-throughput valves have been developed.

9.9.4. Pellet injection technology

Pellet launcher technology comprises three different sub-systems:

1) The pellet source: normally a cryogenic machinery which provides frozen hydrogen and creates the pellets by cutting in an extruder.
2) The accelerator: mechanism which speeds up the pellets to the desired velocity.
3) The transfer system: pellets can be injected directly from the injector location by free flight from a hole in the outboard first wall (low field side, LFS) or be guided by a tubing system so that the injection position can also be from the inboard side (high field side, HFS) of the magnetic cage.

The performance of the pellet injector is given by the frequency of the pellets, the average size of a pellet, the velocity at the injection point, and the location of the injected point. For the extruder, batch-wise operated cryosystem should be distinguished from continuous screw-type extruder machines (as used for ITER). For the accelerator, there are two competing concepts: one is based on a pneumatic gas gun (blower gun, one-stage or two-stage), the other on a mechanical centrifuge. The advantage of the mechanical solution is that no carrier gas is needed, which would ask for an additional circuit and adds a gas load on the tritium plant. Mature acceleration techniques exist to launch pellets at speeds of 1000 to 1500 m/s with high (~50 Hz) rate (gas gun or centrifuge), and up to 3000 m/s with low (1 Hz) rate (double stage gas gun). The ITER project has chosen to work with the gas gun accelerator concept for its higher reliability as no fast rotating mechanics is involved. It should be noted that due to the E×B drift — which acts as the main mechanism for the transport of the pellet and plasmoid ablation — the inboard injection is more efficient than the injection from the outboard plane. Hence, in view of a power plant, one does not expect to do without a transfer system. Up to now, the pellet transfer system is acting as a bottleneck to get high acceleration speeds at the injection point (for example it is the main reason that the ITER nominal speed is limited to only 300 m/s). In addition, on their way through the guiding tubes, the pellets suffer from a considerable mass loss due to friction and evaporation.

ITER will have two pellet injectors (one for deuterium, one for tritium) for core fuelling via a HFS guiding system allowing a pellet speed of 300 m/s, and a LFS injector for other tasks (pellet ELM pacing or disruption mitigation) operating at 500 m/s. Core fuelling efficiency is increased with deeper pellet penetration, which can mainly be achieved with higher pellet speed. Higher pellet speed reduces the pellet fraction with low fuelling efficiency and hence also the burden on exhaust system. The R&D focus in view of a fusion power plant will therefore be laid on this aspect, see Fig. 9.35 [24]. There are also alternative deep fuelling concepts which may allow for very high speeds, but are not very well developed so far, such as (i) supersonic molecular beam injection, a very high speed gas injection, (ii) rocket fuel driven pellet acceleration which promises to achieve a few kilometres per second, and (iii) compact toroid injection with electromagnetic acceleration, theoretically able to achieve several hundreds of kilometres per second.

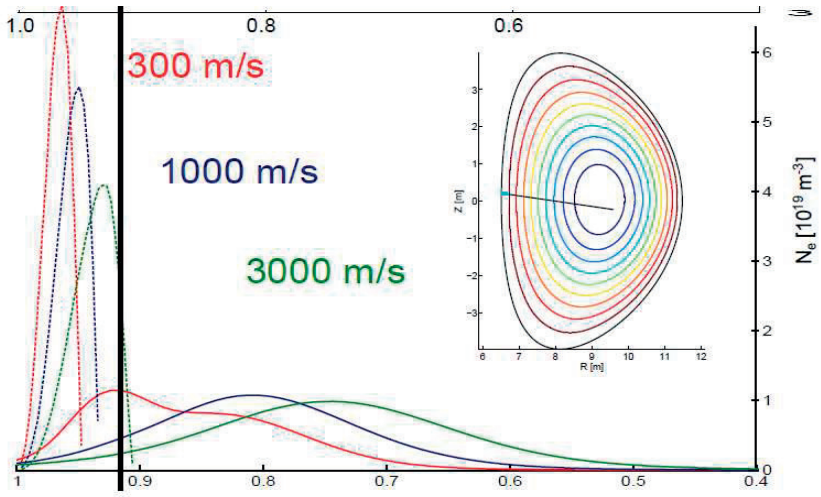

FIG. 9.35. Pellet penetration along the normalized minor radius. The dotted curves denote ablation, the bold curves deposition (DEMO modelling). Reprinted from [24] with permission from Elsevier.

9.10. FUSION FUEL CYCLE

Medium-size tokamaks (for example ASDEX Upgrade) are usually operated at short plasma pulses with helium, protium or deuterium; they can often utilize commercially available components and do not necessarily require a clean-up and re-use of the exhaust gas, and hence do not have a closed fuel cycle (see Fig. 9.36, top). However, if tritium is foreseen, a tritium plant is needed, which takes, in a safe and accountable manner, the fusion exhaust gas from the vacuum pumping systems, cleans it, separates the hydrogenic gas mixture into the pure hydrogen isotopes and supplies the fuelling systems that feed the torus with fuel gas at the right composition (see Fig 9.39, bottom). The tritium plant — described in full detail in Chapter 10 — closes the fuel cycle. The use of tritium and tritiated gases asks for specific and dedicated designs, which are not commercially available. The difference between ITER and DEMO in terms of the fuel cycle is given by the fact that ITER is still actively consuming tritium from external sources, whereas DEMO will demonstrate tritium self-sufficiency by in-situ tritium breeding. The tritium breeding function expands the fuel cycle architecture further by adding an additional outer part. The blankets are a highly multi-functional component and are treated elsewhere in this textbook.

The core challenge of the self-sufficient fuel cycle of a power plant is given by a potentially very high tritium inventory which may conflict with legal limits (radioactivity) and safety requirements (oxy-hydrogen explosion hazards), or result in excessive cycle times, associated with a large plant size. It was quickly found that a simple scale-up of the fuel cycle from ITER to DEMO would result in excessive tritium inventories (of the order of several 10 kg) which represent a showstopper.

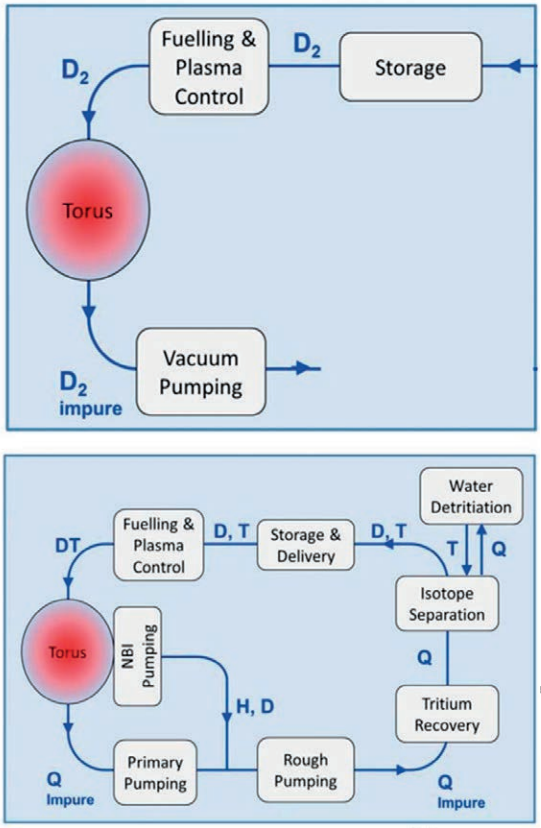

FIG. 9.36. Existing fuel cycle generations. Physics devices without D–T operation (top), ITER with D–T operation (bottom); Q = H/D/T.

Hence, a self-standing system engineering approach has been chosen to develop the DEMO fuel cycle [25]. The main driver in this development was inventory reduction. As a result, a completely novel fuel cycle architecture was derived, see Fig. 9.37. It features an innermost direct internal recycle (DIR) loop as a shortcut between the divertor pumping and the pellet injectors, a second loop, inside the tritium plant and without complete separation of the hydrogen isotopes, and the classical outer loop with full separation of the different hydrogen isotopologues. The KALPUREX (Karlsruhe liquid-metal based pumping process for fusion reactor exhaust gases) concept was developed for the new DEMO fuel cycle [19]. The KALPUREX process is the reference key solution (i) to minimize radioactive inventories in the fuel cycle below the legal limit, (ii) to reduce the tritium start-up inventory to the absolute minimum, (iii) to enable sufficiently high densities so as to harvest the fusion energy gain, and (iv) to limit the use of cryogenic power for operation consequently improving the balance of plant and hence the attractiveness of nuclear fusion as an energy source. It replaces the batch-wise operated cryopumps used in ITER by continuously working liquid-ring and vapor diffusion pumps, utilizing mercury as perfectly tritium-compatible operating fluid, and features a continuous isotope separation technology in the second loop.

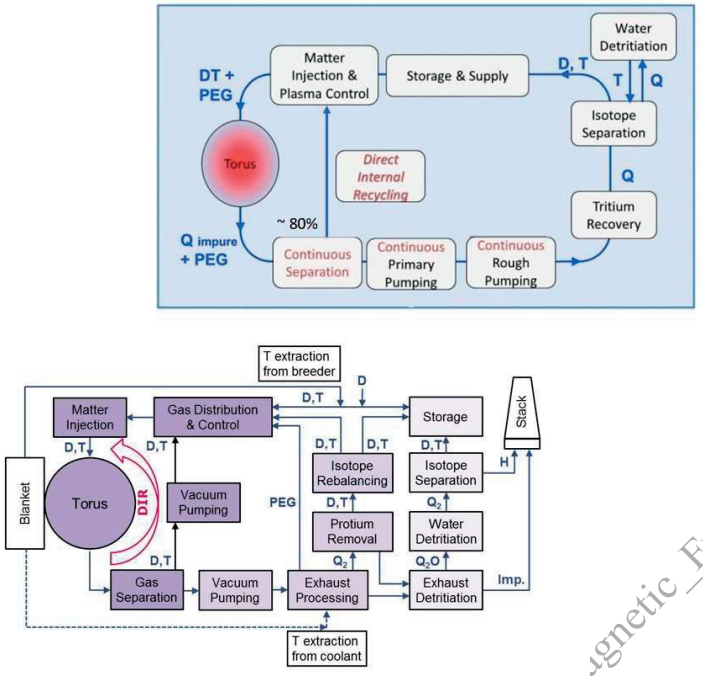

FIG. 9.37. Proposed 3-loop scheme for the DEMO fuel cycle.

9.11. CONCLUSION

The vacuum pumping and fuelling systems play a major role in any fusion device. For a D–T fusion device, such as ITER or DEMO, only very special, mostly customized solutions can fulfill the specific requirements. In both areas, the solutions that are being developed for ITER are not necessarily a good choice for simple scale-up to a fusion power plant, so that additional efforts are needed in the next years to develop efficient systems for power plant use. Due to the direct link to the plasma, both systems are actuators in the control of the fusion plasma. Technologically, the pumping and matter injection systems are embedded in the fusion fuel cycle. The basic considerations of the fusion fuel cycle will be delineated in the next chapter.

9.12. REFERENCES

[9.1] BHATNAGAR, P. L., et al., A model for collision processes in gases, Phys. Rev. **94** (1954), 511–525.
[9.2] HAUER, V., DAY, C., Conductance modelling of ITER vacuum systems, Fus. Eng. Des. **84** (2009) 903–907.
[9.3] HAUER, V., DAY, C., ITER divertor gas flow modelling, Fus. Eng. Des. **98** (2015) 1775–1778.
[9.4] VAROUTIS, S., et al., Simulation of neutral gas flow in the JET sub-divertor, Fus. Eng. Des. **121** (2017) 13–21.
[9.5] BUREAU INTERNATIONAL DES POIDS ET MESURES, Evaluation of measurement data – Guide to the expression of uncertainty in measurement (2008), https://www.bipm.org/utils/common/documents/jcgm/JCGM_100_2008_E.pdf.
[9.6] ARKHIPOV, A., et al., Status of the development of diagnostic pressure gauges for the operation in ITER, Fus. Eng. Des. **123** (2017) 1049–1053.
[9.7] GRANVILLE-PHILLIPS, Instruction Manual for all Series 835 Vacuum Quality Monitors (2015), www.johnmorrisgroup.com/Content/Attachments/122829/ GP-835VQM835000-MAN.pdf.
[9.8] KLEPPER, C. C., et al., Extending helium partial pressure measurement technology to JET DTE2 and ITER, Rev. Sci. Instrum. **87** (2016) 11D442.
[9.9] FISCHER, S., et al., Monitoring of tritium purity during long-term circulation, Fusion Sci. Technol. **60** (2011) 925–930.
[9.10] PERINIC, D., et al., Tests of dry mechanical forepumps for use in the ITER vacuum pumping system, Plasma Physics and Fusion Technology **26** (1995) FZKA-5578.

[9.11] GIEGERICH, T., et al., Mercury ring pump proof-of-principle testing in the THESEUS facility, Fus. Eng. Des. **124** (2017) 809–813.
[9.12] ANTIPENKOV, A., et al., Tritium pumps for ITER roughing system, Fus. Sci. Technol. **48** (2005) 47–50.
[9.13] GIEGERICH, T., DAY, C., Conceptuation of a continuously working vacuum pump train for fuson power plants, Fus. Eng. Des. **88** (2013) 2206–2209.
[9.14] SIRAGUSA, M., et al., Conceptual design of scalable vacuum pump to validate sintered getter technology for future NBI application, Fus. Eng. Des **146** (2019).
[9.15] MENON, M. M., et al., Pumping characteristics of a cryopump with Ar sorbent in He and in a D2/He mixture, J. Vac. Sci. Technol. A **13** (1995) 551–555.
[9.16] MACK, A., PERINIC, D., Conceptual study of the cryocascade for pumping, separation and recycling of ITER torus exhaust, Fus. Eng. Des. **28** (1995) 319–323.
[9.17] FOSTER, C. A., High-throughput continuous cryopump, J. Vac. Sci. Technol. A **5** (1987) 2558–2562.
[9.18] NUTTALL, W. J., et al., The future of helium as a natural resource, Routledge, London (2012).
[9.19] GIEGERICH, T., DAY, C., The KALPUREX-process – A new vacuum pumping process for exhaustgases in fusion power plants, Fus. Eng. Des. **89** (2014) 1476–1481.
[9.20] GREENWALD, M., Density limits in toroidal plasmas, Plasma Phys. Control Fusion **44** (2002) R27–R80.
[9.21] BOEDO, J., et al., A review of direct experimental measurements of detachment, Plasma Phys. Control Fusion **60** (2018) 044008.
[9.22] YANG, Y., et al., Concept design of fusion power shutdown system for ITER, Fus. Eng. Des. **88** (2013) 824–826.
[9.23] MEITNER, S., et al., Design and Ccommissioning of a three-barrel shattered pellet injector for DIII-D disruption mitigation studies, Fus. Sci. Technol. **72** (2017) 318–323.
[9.24] LANG, P.T. et al., Considerations on the DEMO pellet fuelling system, Fus. Eng. Des. **96-97** (2015) 123-128.
[9.25] DAY, C., et al., Consequences of the technology survey and gap analysis on the EUDEMO R&D programme in tritium, matter injection and vacuum, Fus. Eng. Des. **109** (2016) 299–308.

9.13. BIBLIOGRAPHY

CHAMBERS, A., Modern Vacuum Physics, Chapman & Hall, Boca Raton (2005).
JOUSTEN, K., et al., Handbook of Vacuum Technology 2nd edn, Wiley-VCH, Berlin (2016).
O´HANLON, J. F., A User´s Guide to Vacuum Technology 3rd edn, Wiley, Hoboken (2003).
SHEN, C., Rarefied Gas Dynamics, Springer, Berlin (2005).

Chapter 10

TRITIUM HANDLING AND TRITIUM PLANT

B. Bornschein
Tritium Laboratory Karlsruhe, Institute of Technical Physics, Karlsruhe Institute of Technology
Germany

Future fusion reactors are based on the fusion of deuterium and tritium nuclei, which yields (due to momentum conservation) 14.1 MeV neutrons and 3.5 MeV alpha particles. A reactor with a fusion power of 1 GW would need to fuse about 1000 MW / (17.6 MeV × 1.6×10^{-19} C/e) = 3.55×10^{20} tritium nuclei per second, which is equivalent to 1.77 mg of tritium per second or ~153 g of tritium per day (see problem #1 in Section 10.1). Summing up the amount of tritium needed per year, thereby considering that tritium is a radioactive material, one immediately realizes that operating a fusion reactor is not only a huge technological and scientific challenge but also an important issue regarding safety. Consequently, the art of tritium handling follows special rules, which will be discussed later in Section 10.3. In a fusion reactor, tritium and deuterium are continuously injected into the plasma chamber. Since only a small fraction of the tritium (~1%) is burned in the fusion reaction, the residual tritium needs to be pumped out of the plasma chamber for fuel cleanup and reuse, together with helium ash and further impurities. To achieve this goal, a closed tritium cycle has been developed over the last decades. The basic elements of the so-called inner fuel cycle are discussed in Section 10.2. As cars consume petrol (or diesel), drivers have to refill their tanks at the petrol stations. The motor fuel is mainly produced by the petroleum industry utilizing the mineral oil fields of the Earth. Tritium is burnt in the plasma chamber, therefore also needs to be 'refilled'. A natural source of tritium is the atmosphere, in which it is produced by the interaction of high-energy cosmic radiation with oxygen and nitrogen. However, because of its short half-life (12.3 years, see Section 10.1), the existing and usable tritium on Earth is almost exclusively anthropogenic (made or caused by humans). Technically, for the non-continuous ITER operation (duty cycle only at percent level, low tritium consumption), tritium will be supplied externally from CANDU reactors in which it appears as by-product in the heavy water moderator at a rate of 140 to 200 g per year and giga watt electrical power. On the other hand, future fusion reactors such as DEMO — with 2.7 GW of fusion power and a more or less continuous operation — will need more than 100 kg tritium per year so that tritium will have to be produced directly inside the fusion machine within the so-called breeder blanket. Since the blanket as a whole is introduced in Chapter 6, Section 10.2 discusses a few tritium related issues, especially those which are directly linked to the fuel cycle. Tritium handling always requires that one answers the question: How much tritium is where in which chemical form? To answer this question, dedicated analytical methods need to be developed and employed, and adequate methods for tritium accountancy need to be adopted. An introduction to tritium analytics is given in Section 10.4, thereby focussing on workhorses (e.g. ionizations chambers and calorimeters) and advanced techniques (e.g. Raman spectroscopy). The last section of this chapter deals with the so-called tritium plant. This plant is part of the closed tritium fuel cycle and comprises the fuel cycle processing systems as well as the systems for tritium confinement and detritiation. In short, the plant has to process tritiated gases received from the tokamak and other sources to produce the deuterium and tritium gas streams for fuelling. It also has to detritiate various waste streams (including tritiated water) before they are discharged to the environment. At last, the reader will have a look into the tritium plant of ITER to get an idea of its concept. The chapter is closed with a short summary and a list of reading comprehension questions, which the reader should be able to answer. In addition, the reader will find solutions to the problems given in the text. The reference list at the end of the chapter is kept short and focused on review papers, considering that the present text is part of a textbook and not a scientific review. In addition, a short bibliography is provided for further readings. Examples with quantitative calculations and a limited amount of mathematics are included in separate boxes, and the reader is invited to reproduce the results on their own. After working through this chapter, the reader should know:

- Why is tritium needed in fusion?
- What are the basic properties of tritium and what are the consequences of handling of large amounts of tritium?
- Which rules need to be applied to design and operate systems with tritium?
- Why is a closed tritium fuel cycle needed for fusion reactors and what is the basic structure of such a cycle?
- What is a tritium plant? Which are the systems planned for ITER?
- Which are the standard analytical techniques to measure tritium in gaseous form or water?

10.1. TRITIUM PROPERTIES AND THEIR CONSEQUENCES

10.1.1. Basic properties of tritium

Tritium (symbol T or H-3 or ^{3}H) is a radioactive isotope of hydrogen. The tritium nucleus is sometimes called triton and contains 1 proton and 2 neutrons (ref. Fig. 10.1). It decays into helium-3 according to the following equation

$$T \rightarrow {}^3He + e^- + \bar{\nu} \ , \qquad (10.1)$$

where e^- is the electron and $\bar{\nu}$ is the electron antineutrino. The kinetic energy from the β decay is shared between the three particles, thereby obeying the momentum and energy conservation. Fig. 10.2 shows the energy spectrum of the β electron. The maximum energy of the electrons is 18.59 keV and the average is 5.685 keV. Since the electron is easy to detect, a lot of the analytical methods for tritium detection and accountancy is based on the measurement of the β electron; see Section 10.4. The electron antineutrino is nearly undetectable because of its very low cross section for interaction with matter and, therefore, of no further interest to fusion and safety related questions[87].

Additional properties and numbers about tritium are given in the following, the reader is invited to get more information e.g. from the webpages of NIST, the national institute of standards and technology [10.1], or from the publication of the particle data group [10.2]. The half-life of tritium is 4500 ± 8 days [10.3], i.e. after 12.323 years only have half of the tritium is left. The maximum kinetic energy of the β electrons (18.59 keV) is the second smallest in nature, only rhenium-187 exhibits a lower one. Due to this low kinetic energy, the β electrons can penetrate about 6 mm of air and less than 1 μm of metal. They are also incapable of passing through the dead outermost layer of the human skin. This has some consequences regarding both the radiological impact, which is discussed in the next subsection, and the way tritium is handled, which is described in Section 10.3.

The hydrogen isotopes form the diatomic molecules H_2, D_2, T_2, HT, HD and DT, the so-called 'hydrogen isotopologues'. To identify them separately is one of the big challenges of tritium analytics and is discussed in Section 10.4. It is common in the tritium business to use the letter Q if the nuclei could be either H, D or T. Q_2 therefore stands for any of the above mentioned hydrogen isotopologues and CQ4 is methane, which can be found in 15 different combinations of H, D and T, e.g. CT_4 or CD_2T_2.

The molar mass of tritium is 3.016 g/mol (deuterium has 2.014 g/mol and hydrogen 1.008 g/mol). The low molecular mass of tritium makes it extremely transportable and, as a hydrogen isotopologue, it can even permeate through metallic confinement barriers. From a chemical point of view, tritium (hydrogen) is very reactive, by either donating or accepting an electron to form a chemical bond. The consequences for safe handling are discussed in Section 10.3.

For rough estimates of activities and gas amounts it is useful to know that 1 g of tritium has an activity of ~10 kCi (exactly: 9616 Ci). The curie (Ci) is the old unit for the activity, with 1 Ci = 3.7 × 10^{10} Bq = 3.7 × 10^{10} decays per second. Due to the huge numbers[88] in the tritium–fusion business, it is common to use grams or curies as a unit for tritium amounts[89]. At standard temperature and pressure (STP, 1013 mbar, 0°C) 1 g of tritium has a volume of 3.73 ℓ.

10.1.2. Implications of tritium exposure

The β electrons from tritium decays can ionize atoms due to their kinetic energy. Because living cells and, more importantly, the DNA in those cells can be damaged by this ionization, it can result in an increased chance of cancer or — if the radiation is high enough — can be lethal within hours or days. The question is: what is the meaning of 'high radiation' and in what amount is tritium dangerous? To answer this question, a measure for the impact of electrons hitting human cells is needed. The conventional physical quantity that measures the risk of cancer due to ionizing radiation being delivered non-uniformly to parts of the human body is the so-called effective dose. The effective dose considers both the type of radiation (e.g. alpha, beta, gamma radiation) and the nature of each irradiated organ. The unit for the effective dose is the same as for the absorbed dose; it is called the sievert (Sv) and given in joules per kilogram.

[87] This remark about neutrinos holds for tritium handling and its use in the tritium fuel cycle. In the field of astroparticle physics the tritium beta-decay is used to determine the mass of the electron antineutrino by a precise measurement of the electron spectrum.
[88] In terms of becquerels, numbers in the range of 10^{15} to 10^{17} (or higher) are often reached.
[89] Nevertheless, the reader should keep in mind that the official SI-unit for radioactivity is the becquerel (Bq), describing the number of decays per second.

To get a feeling for numbers, a few examples of effective doses are given:[90]

- One flight from Frankfurt to San Francisco due to cosmic radiation: 0.045 to 0.110 mSv.
- Annual effective dose due cosmic radiation in Germany (average per person): 0.3 mSv/a.
- Annual effective dose due to inhalation of radon in buildings in Germany (average per person): 0.9 mSv/a.
- Medical uses of radiation, average annual effective dose per person in Germany: 1.9 mSv.
- Effective dose for one single computer tomography (CT scan) of the thorax: 4.2 to 6.7 mSv.
- Maximum dose per year for a person of the general public due to discharge of radioactive substances into air or water from a facility (e.g. nuclear power plant) to the environment: 0.3 mSv.
- Maximum dose per year for a worker in Germany in a controlled area: 20 mSv.

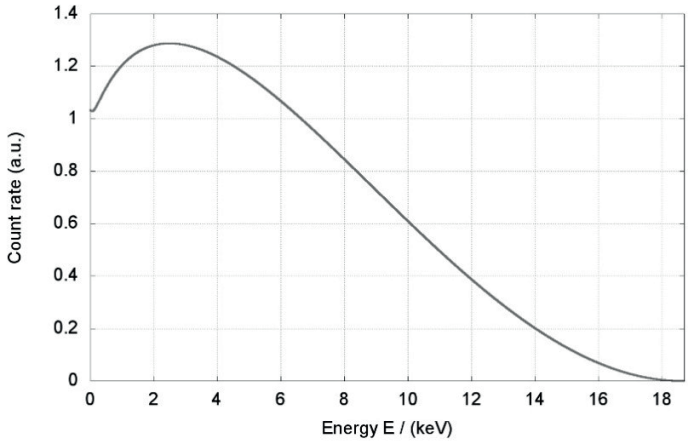

FIG. 10.2. Beta spectrum from tritium decay. Displayed is the number of beta-electrons per unit time as a function of their kinetic energy.

According to the recommendations of the International Commission on Radiological Protection (ICRP) the maximum annual effective dose for workers in a controlled area is 20 mSv [10.4].[91] In the case of tritium, an external dose hazard is very unlikely since the β particles released during beta decay cannot penetrate the outer dermal layers. Biological hazards for workers and members of the public are only linked to the exposure to tritium which may occur by different pathways such as inhalation, ingestion and adsorption through the skin. The effective dose due to an

Problem #1:

Show quantitatively that the following relations are valid:

- 1 g tritium is equivalent to 3.73 ℓ (STP)
- 1 g tritium has 324 mW decay heat
- 1 g tritium is equivalent to 9616 Ci

Hints: Use the above given average energy for the beta-electrons and the given molar masses. You should know the Avogadro constant and the law for the radioactive decay. Also take into account that the decay constant λ is equal to $\ln(2)/t_H$ with t_H = half-life in seconds.

[90] Numbers are from the webpage of the Federal Office for Radiation Protection of Germany (Bundesamt für Strahlenschutz, www.bfs.de, Willy-Brandt-Straße 5, 38226 Salzgitter, Germany). The last 2 numbers are taken from the German Strahlenschutzverordnung, 2012 (German Radiation Protection Ordinance).

[91] A controlled area, according to ICRP, is a defined area in which specific protection measures and safety provisions are, or could be, required for controlling normal exposures or preventing the spread of contamination during normal working conditions and preventing or limiting the extent of potential exposures.

internal exposure to tritium depends on the amount of tritium incorporated, its physical and chemical form, and the age of the person. The effective dose D is calculated according to

$$D = k_{\mathrm{D}} \times A \qquad (10.2)$$

where A is the incorporated activity and kD the so-called dose coefficient. Some example values are given in Table 10.1. In worker dose assessments, tritium is generally considered to be in the form of water (HTO). This conservative assumption considers that tritiated water as HTO or T_2O is about 4 orders of magnitude more radiotoxic than gaseous tritium (HT or T_2). This clearly can clearly be seen in the example shown in Table 10.1, where the amount of inhaled tritium necessary to obtain an effective dose of 20 mSv and 8 Sv are given. Note that an amount of less than 5 µl of T_2O is already a lethal dose. The exposure to tritium of site personnel and releases of tritium to the environment needs therefore be minimized according to the ALARA principle (as low as reasonably achievable).

10.1.3. Consequences on tritium handling

The consequences of the facts given Section 10.1.2 on tritium handling are logically based on three main objectives:

- Don't get tritium in your body!
- Don't spread tritium into the environment!
- Don't let tritium containing gas explode!

To cope with these requirements, one has to:

a) confine the tritium,
b) restrict the access to tritium,
c) identify reliable personnel and educate them,
d) establish sufficient tritium analytics and
e) establish an organizational structure to operate the laboratory and perform the experiments therein in a safe way.

Problem #2:

According to Table 10.1 the dose coefficient for inhalation of tritiated water damp (for adults over than 17 years old) is 1.8×10^{-11} Sv/Bq.

How large is the effective dose for a worker in case of an inhalation of 10 Ci or 3.7×10^{11}Bq water damp and what is the corresponding amount of water (T_2O)?

Hint: Use the relation $A = \lambda N$ (ref. problem #1).

Section 10.3 describes tritium confinement and explosion prevention, using the example of Tritium Laboratory Karlsruhe (TLK) [10.6]. In addition, some administrative rules for safe tritium handling are listed.

10.2. THE CONCEPT OF A CLOSED TRITIUM CYCLE

Tritium is a hydrogen isotope and it has a low molecular mass. Because of this tritium can easily be solved in metals and is even able to permeate through metallic walls. From a chemical point of view hydrogen is very reactive, either donating or accepting an electron to form a chemical bond. Consequently, a person using tritium has to face the following complications:

- Isotope exchange e.g. with in-metal dissolved hydrogen: The experiment is started with pure T_2 and ends up with T_2, HT — or even DT or HD if deuterium was handled before — while the concentration of the T_2 content decreases in time (as depicted in Fig. 10.3). Since water is omnipresent, also HTO will show up. In principle, one will find tritium in all molecules containing hydrogen.

- Chemical reactions: Tritium is usually processed in stainless-steel containers. Therefore, tritiated methane (CQ_4, Q = H, D, T) is formed with the carbon from the stainless-steel walls. This is the most common reaction but not the only one. Another example is the creation of water.

To summarize: One cannot avoid getting tritiated species besides T_2. In addition, one will find the 'usual' contamination, e.g. nitrogen and oxygen (as no containment is infinitely leaktight) and the decay product helium-3.

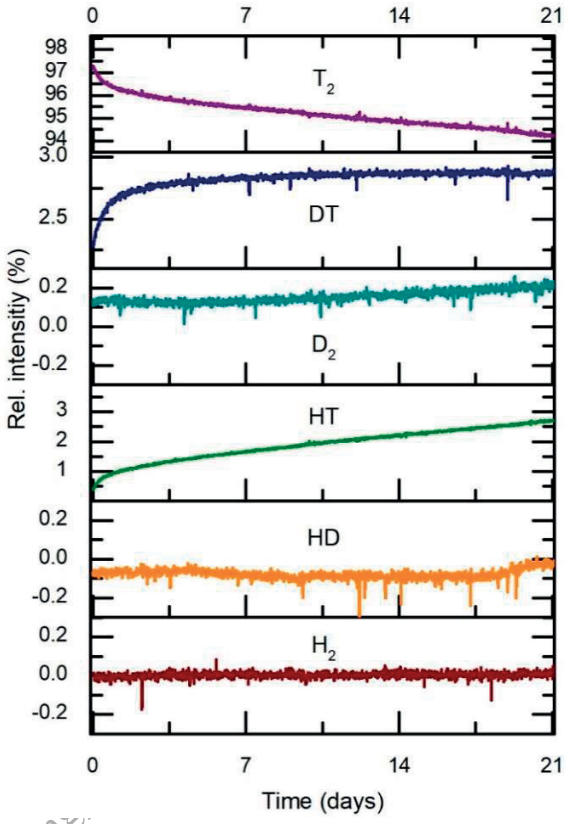

FIG. 10.3. Example of compositional changes of a hydrogen isotopologue mixture with an initially high tritium content. Shown are the Raman intensities (Q1-branches), measured inline with a dedicated Raman spectroscopy setup (Section 10.4). The gas was processed for 21 days in a closed loop within a stainless-steel environment (ca. 2 l) during which the concentrations of the tritiated species varied strongly. The relative intensity of the T_2 Q1-branch decreased to ~94%, while the relative intensities of the DT and HT peaks continuously increased to ~3%. The expected reduction of T_2 concentration in the sample, due to β-decay, is below 0.5% and thus insufficient to explain the observed change in composition. The observed compositional changes are caused by hydrogen isotope exchange reactions. Courtesy M. Schlösser, KIT.

There exist only two different solutions to cope with that issue: The polluted tritium gas or liquid is declared as waste and given to a radioactive waste repository and afterwards fresh pure tritium is bought. It is self-evident that this cannot by the solution for large amounts of tritium. In fact, nowadays, this solution is usually only chosen by laboratories with comparatively small tritium inventories in the Ci range and under. Or, second option, the tritium is processed in a closed cycle to recover pure T_2. Such a closed tritium cycle is mandatory if amounts of tritium larger than a gram need to be handled[92]. A well designed closed tritium cycle minimizes the losses to the environment to less than 10^{-4} of the inventory per year and should be able to decontaminate tritium contaminated devices, such as pumps and tubes, to comparatively low levels before disposing of them.

In the current discussion regarding the maximum tritium release of DEMO, numbers in the order of 1 g per year are considered. Considering that the tritium inventory of such a machine will be of several kilograms and the tritium throughput ~30 kg per day, this requirement is quite challenging and can only be achieved with the help of a closed tritium cycle. In the following subsections, the basic concept of a closed tritium cycle and the concept of the closed

[92] Up to kilogram amounts in fusion power plants.

fuel cycle of a fusion reactor are explained. Afterwards, the existing closed tritium cycle of the Tritium Laboratory Karlsruhe (TLK) is presented.

10.2.1. Basic concept of a closed tritium cycle

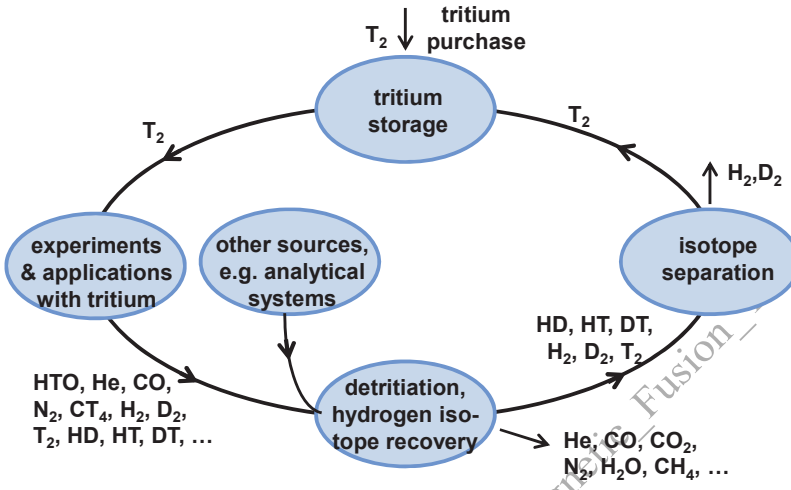

FIG. 10.4. Basic concept of a closed tritium cycle.

Fig. 10.4 depicts the basic concept of a closed tritium cycle. It basically consists of the following four sections: A tritium storage system, an experimental setup or a system for applications with tritium, a system for detritiation and hydrogen isotope recovery, and an isotope separation system. These four stations are shortly discussed in the following, focussing on their function not on their realization. More technical information can be found in Section 10.2.3, where the closed tritium cycle of TLK is explained. For the following discussion tritium is assumed to be in the gaseous state, which is by far the most common scenario.

10.2.1.1. Tritium storage

Tritium that is not being used needs to be stored in a safe way. Possible storage systems are buffer vessels or metal beds, e.g. uranium beds. Buffer vessels are typically used for short term storage in process loops. The advantage of using a buffer vessel is the comparably low prize of a metallic vessel and the fact that the tritiated species exist in gaseous form, tritium storage is the fact that a leak in the vessel immediately results in a tritium release. For this reason, the sizes of buffer vessels are relatively small; typical sizes are a few litres to 100 litres, and the gas pressure is usually kept below 100 kPa. For long term storage of tritium, especially that of larger amounts (say 50 to 100 g), tritium is stored as metal hydride, which is seen as the most compact and safe method: $\mathrm{Me} + x\ 0.5\ \mathrm{T_2} \leftrightarrow \mathrm{MeT_x} +$ energy. The metal hydride is formed by releasing energy. The method can be used to store any hydrogen isotopologue and is (in case of H_2) a well-known technique in the industry. Tritium can be released from the storage by heating the metal hydride. In the field of fusion, zircon–cobalt (ZrCo) and uranium (U) are the materials of choice and those used at TLK. Detailed information on this topic can be found in Section 10.2.3.

10.2.1.2. Experiment or application with tritium

Tritium is transported from the storage system to the section where the tritium is "used" via double walled tubes (see also the discussion in Section 10.3). This can be the torus chamber of a fusion reactor or the setup of an experiment with tritium. After using the tritium, one ends up with a lot of different tritiated and non-tritiated gases, as shown in Fig. 10.4.

10.2.1.3. Detritiation and hydrogen recovery

This section collects the polluted tritiated gases from the experimental section and other sections, e.g. the analytical systems. This section has to perform two tasks in parallel: First, it has to separate the six hydrogen isotopologues (T_2, DT, D_2, HT, HD and H_2) from other gaseous species and second, it has to detritiate the other species.

The standard tool for separation is a Pd–Ag membrane, which is only permeable for the six hydrogen isotopologues. The corresponding device is usually called a permeator. The detritiation of the residual gases can be done by means of catalytic reactions. Depending on the catalyst and the process parameters, one can initiate cracking processes such as, for example $CQ_4 \leftrightarrow 2Q_2 + C$ with Q = H, D, T or hydrogen isotope exchange processes such as $HTO + H_2 \leftrightarrow H_2O + HT$. The detritiated gases are afterwards sent to the stack and the separated hydrogen isotopologue mixture to the isotope separation system.

10.2.1.4. Hydrogen isotope separation

There are different concepts for the isotope separation. The basic idea is to use a physical property which is different for each hydrogen isotopologue. The most well-known technique is a gas chromatograph, whose principle is based on the different adsorption properties of the gaseous species. Every gas chromatograph used to detect hydrogen isotopologues is also an isotope separation system! Two actual concepts for isotope separation are the displacement gas chromatography and the cryogenic distillation. The former, used at TLK, is explained in Section 10.2.3, the latter is based on the different boiling points of the six hydrogen isotopologues (between 20 and 26 K) and will be employed for the isotope separation system of ITER. Fig. 10.5 shows the concept of a cryogenic distillation column.

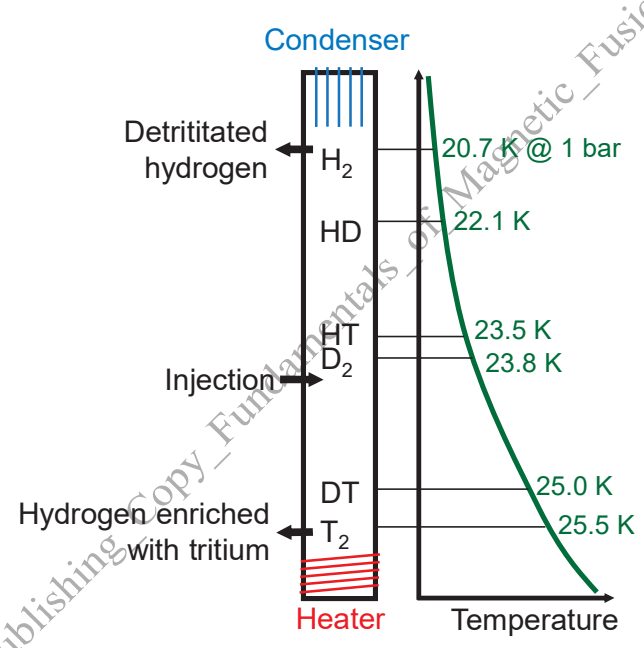

FIG. 10.5. Concept of cryogenic distillation. The position of the hydrogen isotopologues only gives a rough hint of where the maximum concentration of each species is.

10.2.2. Concept of closed fuel cycle of a fusion reactor

Fig. 10.6 depicts the concept of a closed D–T fuel cycle for a fusion reactor. The main difference from the basic concept of a closed tritium cycle (discussed in Section 10.2.1.) lies in the necessary existence of a blanket section.

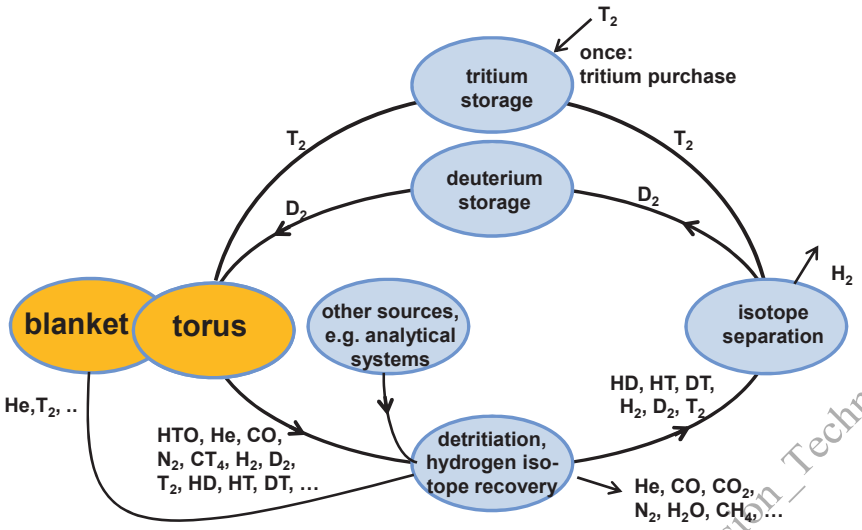

FIG. 10.6. Concept of a closed D-T fuel cycle for a fusion reactor.

Future fusion reactors like DEMO, with 2.7 GW of fusion power, will need more than 100 kg tritium per year so that tritium will have to be produced directly inside the machine within the so-called breeder blanket. The blanket has to provide several functions that are essential to the fusion reactor operation such as heat generation and recovery, tritium breeding, neutron multiplying and magnet shielding. The main reaction for the breeding process is $^{6}Li + n \rightarrow T + {}^{4}He + 4.8$ MeV. From the tritium point of view, a blanket is a kind of box filled with lithium and some kind of neutron multiplier (e.g. Pb, Be), cooled and purged to extract the bred tritium. Basically, two classes of blankets exist: the solid blankets and the liquid ones (see Fig. 10.7). For solid breeders, different types of lithiated ceramics are foreseen, e.g. LiO_2, Li_2TiO_3, Li_2ZrO_3 and Li_4SiO_4. The main liquid breeders are the alloy $Li_{17}Pb$ (Lead with 17% Li, melting point 235°C) and pure lithium (melting point 177°C). The way in which the bred tritium is extracted from the breeder material depends on the blanket concept. Therefore, each blanket concept requires a blanket specific tritium extraction system (TES). Detailed information about blankets is given in Chapter 6 and the tritium management of breeder blankets is discussed in [10.6]. ITER will verify different breeder blanket concepts by employing test blanket modules of different types, coming from different countries. Regarding the closed fuel cycle of a fusion reactor one should only keep in mind that, so far, two important blanket issues have yet to be solved, namely:

- Tritium extraction from the breeder blanket.
- Tritium permeation into the cooling system and the environment.

10.2.3. The Closed tritium cycle of the Tritium Laboratory Karlsruhe

The Tritium Laboratory Karlsruhe (TLK) was founded at the beginning of the nineties to provide the technical means for experiments with relevant quantities of tritium (i.e. grams) and to develop tritium technologies for the fuel cycle of future fusion reactors. It was commissioned with tritium in 1994 and has since then been operated with tritium non-stop [10.8]. Presently the TLK has 31 g of tritium on site and a license for 40 g. A total glovebox volume of 125 m^3 is currently available on an area of 841 m^2 for experimental facilities and 615 m^2 for infrastructure facilities (Fig. 10.8). At present, the TLK staff amounts to 50 people, including guest scientists, students and doctoral researchers.

Problem #3:

Estimate the amount of tritium needed per day for 1 GW of fusion power. Perform a simplified calculation only taking into account the energy generated by the fusion reaction

Hint: The fusion of deuterium and tritium nuclei yields 14.1 MeV neutrons and 3.5 MeV alpha particles per reaction.

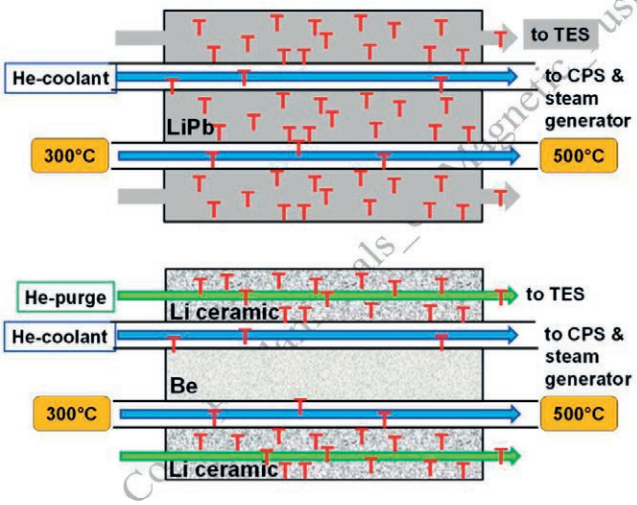

FIG. 10.7. The two cases of He-cooled blanket concepts: liquid breeder (top) and solid breeder (bottom). Tritium is generated via the reaction $^6Li + n \rightarrow T + {}^4He + 4.8$ MeV, in which the neutron arises from the fusion reaction. Lead (Pb) and beryllium (Be) are used as neutron multipliers. Tritium from the liquid breeder blanket is extracted together with the liquid and later separated in the tritium extraction system (TES). To remove the tritium from the solid breeder blanket, a purge gas is employed (e.g. helium). CPS is the acronym for cooling and purification system.

FIG. 10.8. A view of experimental hall A at TLK (courtesy F. Priester, KIT).

Just like a fusion reactor, the TLK needs a closed tritium cycle to handle the tritium in a safe and efficient way. Because of this, the development of technologies for a fusion fuel cycle has been the subject of continuous work alongside the development of a sufficient, robust and reliable closed tritium cycle for the TLK itself. The TLK is now a unique facility, capable of performing tritium experiments in a wide range of size, tritium inventory and duration. A modular setup with more than 10 gloveboxes enables it to simultaneously setup, run and decommission different experiments. Because of this variability, because of its closed tritium cycle and its many auxiliary systems, TLK offers extensive possibilities for research activities on the fusion fuel cycle and basic research topics. Fig. 10.9 depicts the closed tritium cycle at TLK, as it has been operated for the past few years.

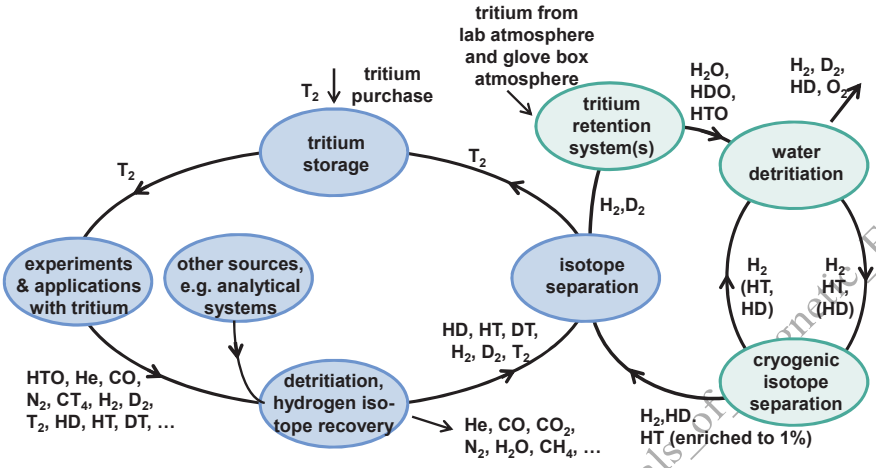

FIG. 10.9. The closed tritium cycle at the Tritium Laboratory Karlsruhe.

In the following, a closer look into some sections of the closed tritium cycle is given, namely the tritium storage section, the detritiation and hydrogen isotope recovery section, the hydrogen isotope separation system and the combination of a water detritiation system with a cryogenic hydrogen isotope separation system. The purpose and functionality of the tritium retention system are explained in Section 10.3. Tritium handling always requires appropriate tritium analytics. Hence, each section of the closed fuel cycle is equipped with sensors or entire analytical systems. Analytics is discussed in Section 10.4.

10.2.3.1. The tritium storage system of TLK

At TLK, most of the hydrogen isotopologue mixtures (Q_2) are stored in the metal getter beds of the tritium storage system, which is housed in a dedicated 6 m^3 glovebox. The storage system is equipped with 10 storage getter beds connected by a manifold, a buffer vessel and a circulation pump, among others. Each getter bed has a storage capacity of 1.25 mol of Q_2. In case of pure tritium, this corresponds to 7.5 gram. For safety reasons, the allowed storage capacity of each bed has been limited to 0.5 mol. With regard to tritium, one ends up with a maximum of 0.5 g per bed and 30 g in total. Nine out of the ten getter beds are filled with depleted uranium (^{238}U), one is filled with ZrCo. Additional tritium can be stored on portable Amersham uranium getter beds with a nominal capacity of 5 g tritium, which can also be used for transport purposes.

In a uranium bed, tritium is stored as UT_x with $x \leq 1.2$ due to the safety measures explained in the above (the maximum would be UT_3). The partial pressure of tritium above the uranium bed at room temperature is ~2×10^{-3} Pa: hence tritium is safely stored. To release the stored hydrogen isotopes, the respective getter bed is heated up to 495°C. The equilibrium partial pressure of tritium is then above 100 kPa. TLK installed one ZrCo bed because this material was selected as the reference getter for the ITER storage and delivery system. TLK also wanted to have a one-to-one comparison of the getter properties of both materials. In a ZrCo bed, tritium is stored as $ZrCoT_x$ (usually $x \leq 1.7$). The equilibrium partial pressure at room temperature is between 8×10^{-3} Pa ($x = 0.1$) and 1 Pa ($x = 1.7$). To release the tritium, the bed is usually heated above 360°C (equilibrium pressure of ~10^5 Pa).

The question of which material is the most appropriate is not easy to answer; both materials have their pros and cons. A major issue with uranium is its ability for self-ignition, as it decomposes to a powder after some cycles of gettering and releasing hydrogen isotopes. Another disadvantage is the fact that uranium is radioactive and is — as a reactor fuel — subject to non-proliferation. ZrCo powder, on the other hand, is not radioactive and not self-igniting. One disadvantage of ZrCo is its aptitude for disproportionation (simplified equation: 2 ZrCo + $T_2 \leftrightarrow ZrT_2 + ZrCo_2$) which leads to a reduction of its storage capacity. To regenerate, this material has to be heated above 470°C and simultaneously pumped. A complete discussion and a wealth of additional information can be found in reference [10.7].

10.2.3.2. CAPER – The detritiation and hydrogen isotope recovery system of TLK

The reference process for the tokamak exhaust processing (TEP) system of ITER is called CAPER (ITER design status 2001) and comprises three different consecutive steps to recover hydrogen isotopes at the highest[93] purity (required decontamination level 10^8) for direct transfer to the cryogenic isotope separation system of the tritium plant (see Section 10.5). The CAPER process is named after a semitechnical tritium facility operated at the Tritium Laboratory Karlsruhe (TLK) for the experimental verification of the different process steps and the demonstration of the TEP concept as a whole [10.9]. The CAPER facility is now an essential and central system within the closed tritium cycle of TLK: all primary gaseous wastes arising from other experiments at TLK are detritiated and the hydrogen isotopologues are recovered. The operation of the facility can therefore be considered as representative for the TEP system within the tritium plant of ITER. Fig. 10.10 shows the principle of the three step CAPER process. This process employs a palladium–silver permeator as a first step ('impurity separation') to separate the bulk of Q_2 from the impurities. Pd–Ag permeators are ideally suited for that purpose since this material is exclusively permeable for hydrogen isotopologues. The permeate stream is therefore of the highest purity and can be fed into any isotope separation system directly.

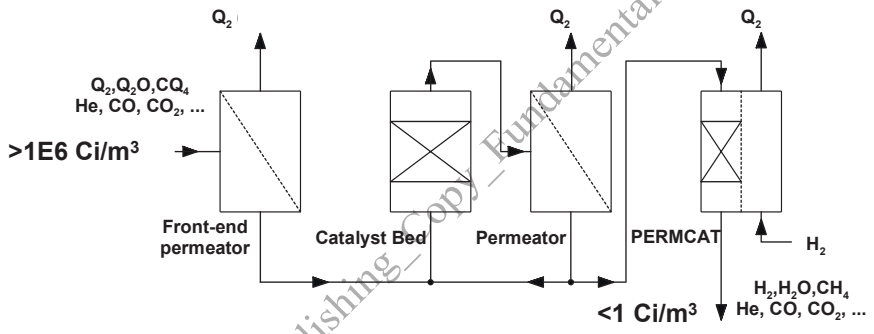

FIG. 10.10. The CAPER process at TLK (Q = H, D, T).

Problem #4:

A maximum of 70 g of tritium has to be stored in an inherently safe way onto an uranium hydride bed (UT3). (a) What is the maximum allowed mass of ^{238}U per bed? (b) Which volume has such a bed (density of U about 19 g/cm^3)?

Hint: The fusion of deuterium and tritium nuclei yields 14.1 MeV neutrons and 3.5 MeV alpha particles per reaction.

The second step (impurity processing) is carried out in a closed loop involving heterogeneously catalyzed cracking or conversion reactions to free tritium from tritiated hydrocarbons or tritiated water combined with permeation of hydrogen isotopologues through a Pd–Ag permeator (23% Ag). While molecular hydrogen isotopologues — e.g. from the carry over (bleed) of the permeator in the first step — will be removed by the permeator

[93] A decontamination factor of 10^8 means that the tritium concentration after treatment is 100 million times lower than before.

in the second step, chemically bounded hydrogen isotopes need to be liberated to allow permeation and removal through Pd–Ag membranes.[94] Heterogeneously catalysed reactions such as hydrocarbon cracking are well suited for that purpose (e.g. $CT_4 \leftrightarrow C + 2T_2$). However, these reactions are typical equilibrium reactions which do not proceed to complete conversion. If these reactions are combined with the removal of molecular hydrogen by means of a permeator, the equilibrium is permanently shifted until the processed gas essentially does not contain hydrogen in molecular or other chemical forms.

The third step (final cleanup) recovers almost all the residual tritium and is based on a so-called permeator catalyst (PERMCAT) reactor. The PERMCAT reactor is a direct combination of a Pd–Ag permeation membrane and a catalyst bed. It has been developed for final cleanup of gases containing up to ~1% of tritium in different chemical forms such as water, hydrocarbons or molecular hydrogen isotopes. The basic principle of a PERMCAT is like a heat exchanger, as illustrated in Fig. 10.10. The gas to be detritiated is fed into the catalyst filled section. In a counter current mode, protium is introduced, permeates through the Pd–Ag membrane (which separates both sections) and decontaminates the impurities by isotopic exchange. The liberated tritium is molecular and can therefore permeate to the section purged with protium (e.g. $CT_4 + 2\ H_2 \leftrightarrow CH_4 + 2\ T_2$). As a result, an exponential tritium concentration profile along the axis is achieved under steady state flow conditions and the impurity outlet of the unit remains essentially uncontaminated. The catalyst in the PERMCAT reactor is employed to support isotope exchange reactions between tritiated species and protium. The tritium decontamination factor is up to 10^5 regarding tritium concentration.

10.2.3.3. The isotope separation system of TLK

Purified gas mixtures of hydrogen isotopologues leaving the experimental facility CAPER are separated into the hydrogen species of protium, deuterium and tritium (H_2, D_2 and T_2) in the isotope separation system (ISS–DGC). The main part of the TLK ISS is a gas chromatographic separation column implementing the so-called displacement gas chromatography (DGC). The column is filled with packing material of α-aluminium oxide powder coated with palladium (20% by weight) The gas mixture is injected into the column filled with the packing material and displaced by protium. Inside the palladium, all hydrogen isotopologues are dissociated and dissolved as atoms. The isotope separation process is based on the strong isotopic effect of the desorption isotherms of protium, deuterium and tritium, the heavier isotope tritium remains preferentially in the gaseous phase. Therefore, tritium (T_2) is reaching the outlet of the column first, followed by deuterium (D_2) and, finally, protium (H_2). Typically, one mol of gas is processed per run and a single run is performed in a day.

10.2.3.4. The water detritiation and cryogenic isotope separation of TLK

Major waste streams in the TLK are the HTO (trititated water) from the more than 20 local tritium retention systems and the central tritium retention system (refer to Section 10.3). To minimize the total amount of tritiated waste at TLK (in other words, to maintain a closed cycle) and to investigate trade-offs between water detritiation and cryogenic hydrogen isotope distillation for ITER (refer to Section 10.5), a combination of a water detritiation system (WDS) and cryogenic distillation system has been setup at TLK: the TRENTA facility described in Fig. 10.11. The tritiated product of the cryogenic ISS (hydrogen enriched with up to 1% of tritium) can be transferred to the ISS–DGC of TLK. The WDS is based on the combined electrolysis catalytic exchange (CECE) process employing a liquid phase catalytic exchange (LPCE) column and a solid polymer membrane electrolyser [10.8].

[94] Remember: only molecular hydrogen isotopologues do permeate through Pd/Ag-membranes, not chemically bound hydrogen as in CT_4.

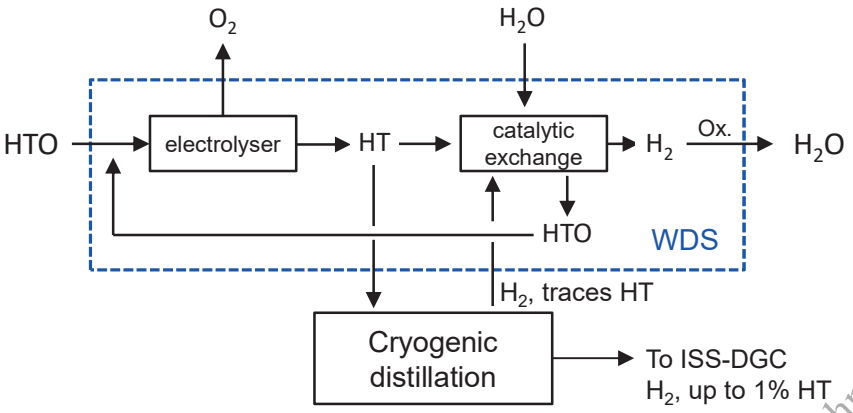

FIG. 10.11. The concept of a combined water detritiation system (WDS) and cryogenic distillation system of TLK. The ISS-DGC is the main isotope separation system of TLK, based on displacement gas chromatography.

10.3. TRITIUM HANDLING RULES USING THE EXAMPLE OF TLK

In Section 10.1.3, is was concluded that tritium needs to be confined in restricted areas. In addition, one needs to establish an organizational structure, which enables the user to operate the laboratory and the experiments therein in a safe way. In the following, a closer look at the basics of tritium handling is taken, thereby using the example of TLK. However, note that the below given rules are valid in all cases, i.e. for ITER, JET and any future fusion reactor.

10.3.1. Confinement concept

Confinement is the most important safety objective in the field of tritium handling. The basic goals of any confinement system are:

- To avoid the spreading of radioactive materials in normal operation.
- To limit the radiological consequences for the operators, the public and the environment in off-normal conditions within acceptable levels.

The confinement of tritium is achieved by a coherent set of physical barriers, by auxiliary techniques intended to confine radioactive substances, or both. Here, the word ‘containment’ is used for physical barriers and the word ‘confinement’ is more general, i.e. it also includes active measures (e.g. filtering and atmosphere processing). The confinement concept of TLK has two major features, namely: a two barrier design and an atmosphere and gaseous waste treatment, the two are shown in Fig. 10.12., an example of a glovebox in Fig. 10.13. The first barrier is the primary system comprising all tritium containing components and pipework of the experiment or facility and the second barrier is the glovebox which, as secondary containment, encloses the primary system. The glovebox is operated under a slight negative pressure of 400 to 700 Pa (with respect to lab atmosphere) and its maximum allowed leak rate is 0.1 vol% per hour (at 10 Pa differential pressure). The maximum allowed leak rate for the primary system is 10^{-8} mbar·l·s^{-1}. Each glovebox is equipped with a local tritium retention system (TRS). The atmosphere in the glovebox is continuously circulated through its TRS. The TRS contains a catalyst bed which converts any hydrogen isotopologue to water. The subsequent molecular sieve bed removes the water from the gas flow.

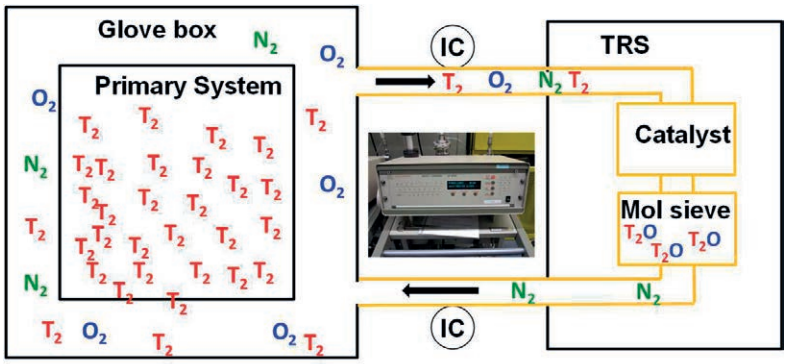

FIG. 10.12. Tritium confinement concept: Tritium is handled in a so-called primary system, surrounded by a glovebox as secondary containment. Each glovebox is equipped with a local tritium retention system (TRS) and ionization chambers (IC). The glovebox atmosphere is continuously circulated through its TRS and tritium is removed. The efficiency of the tritium removal process is determined by comparing the readings of both ionization chambers.

FIG. 10.13. Tritium confinement: Tritium is handled in primary systems (mainly made out of metal) which are installed in so-called secondary containments (mainly glovebox systems). Courtesy F. Priester, KIT.

The efficiency of the tritium removal process is determined by comparison of the readings of two ionization chambers positioned at the inlet and the outlet of the TRS. Typical values for tritium concentration in the TRS atmosphere are 2 MBq.m^{-3} (TRS inlet) and 0.2 MBq (TRS outlet). The atmosphere inside the glovebox is typically nitrogen[95] with a small oxygen content of 0.5 to 1% to enable the platinum catalysed oxidation of tritium into water. During regeneration of the molecular sieve beds, tritiated water is collected and stored for later detritiation in the water detritiation system (WDS). Primary exhaust gases (i.e. from primary systems) are passed through the central tritium retention system (ZTS). The ZTS has two stages for the decontamination of off gases. The first stage is a closed loop for the precleaning of the collected primary gases. After reaching a predefined activity level, the gas is released to the environment via stage two, which works as 'once through then out'. The monitored area of TLK is kept at a negative pressure by the ventilation system. The air of the laboratory is also discharged via the stack up to 10 times per hour. The atmosphere in the stack is monitored for tritium with online instruments (ionization chamber and proportional counter) and an integrating sampling device to measure the HT and HTO content of the released gas. The discharges are usually under 1% of the permitted levels.

10.3.2. Administrative rules

This section will give a very short introduction to the administrative rules which have to be followed if one wants to handle tritium. The focus is set on the principles not on single, site or country specific rules. Since tritium is a

[95] Glovebox atmospheres with oxygen concentrations below 4% are preferred to prevent explosion processes.

radioactive substance, the handling of tritium requires a license, i.e. a permission to handle it. The license of TLK is granted by the German radiation protection ordinance ('Strahlenschutzverordnung'). Every country has similar regulations. A license is the basis for safe operations. It summarizes all administrative rules, including:

- A list of allowed radioactive isotopes and their maximum activity.
- A specification of the location of handling and storage (building number and room number).
- The requirements for the administrative and technical radiation protection (e.g. lab access, definition of radiation protection areas, ventilation of building, fire protection).
- The requirements for the operative radiation protection (e.g. number and types of radiation monitors).

In addition, the radiation protection ordinance itself contains certain rules and requirements, e.g. conducting annual radiation protection briefings for the personnel. The most important requirement regarding tritium handling is that the license owner has to establish site specific radiation protection directives covering the complete onsite handling. Important issues concern accountancy and bookkeeping procedures, contamination and incorporation control procedures, operation instructions, working procedures and technical documentation are:

- Accountancy and bookkeeping procedures: Licence owner must know how much tritium they have at which places. This holds for laboratories as well as for facilities like JET and ITER. The usual way is to define so-called material balance areas (MBA): all incoming and outgoing tritium has to be accounted for (in Bq). In case of the TLK there is only one MBA, i.e. TLK has to account for the newly purchased tritium (incoming flow) and the waste streams (outgoing flow). In addition, one needs to account for the radioactive decay. In case of a fusion reactor with a blanket, the whole story becomes more complicated since there is an additional 'incoming' flow of tritium (i.e. the tritium bred inside the blanket) and an additional 'outgoing' flow (i.e. the tritium burnt in the plasma chamber). Accountancy requirement generates a need for tritium analytics.
- Contamination and incorporation control procedures: Since the tritium decay electrons have a maximum energy of 18.6 keV and an average energy of ~5.6 keV, a relevant dose can only be obtained by incorporation (see Section 10.1.2). Regular tritium-in-urine analyses is a common way to monitor tritium incorporation in the personnel. Tritium contamination of surfaces can be checked by performing wipe tests and subsequent measurements of the tritium activity be means of a liquid scintillation counter.
- Operation instructions: Operation instructions are documents providing a complete overview of a specific facility for both normal and off-normal operation. These instructions contain a set of rules and include, among others, the definition of process conditions for normal and off-normal process states and the definition of safety thresholds and safe states.
- Working procedures: Working procedures are step-by-step descriptions for a single workflow in a specific facility. They define the exact workflow to be followed by the operators during normal operation and regular intervention procedures.
- Technical documentation: The technical documentation is a proof that all technical and administrative requirements postulated in the safety framework are applied to a specific facility. A complete documentation consists of the quality documentation, the operator documentation and the safety description and should be archived. The TLK experience from the last decades has shown that the quality documentation is a real challenge, especially if components or systems are manufactured by industrial partners. Technical documentation covers, among other, material certificates, X ray films from the welds, construction drawings and a list of components.

10.3.3. Tritium handling – a few practical rules

This subsection contains some basic rules which need to be followed in addition to the above. The reason for some of the below given rules is the fact that tritium contaminated systems and parts cannot be repaired in a simple way or sent back to the manufacturer. Quality assurance is therefore very important.

- Design the tritium system according to the RAMI principle! RAMI stands for reliability, availability, maintainability, and inspectability and is a key requirement in the field of tritium technology.

- Use all-metal components for the primary systems! All-metal systems with metallic seals are stable, bakeable and an appropriate subject of quality assurance[96], with only a few exceptions, e.g. if a window for laser spectroscopy is needed. Copper, silver and stainless-steels (e.g. standard VCR or Conflat CF sealings) are appropriate sealing materials (see as example Fig. 10.14.).

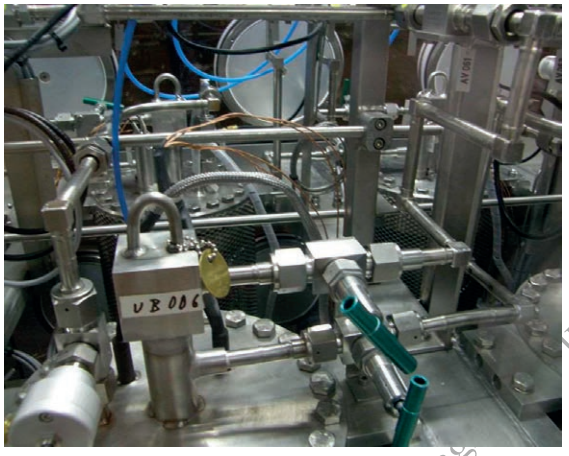

FIG. 10.14. A glimpse into a glovebox. The primary system consists of all-metal systems. Exceptions should be made only if it is absolutely necessary!

- Reduce the number of sealings as much as possible! Each sealing is a possible leak. Always prefer welded connections.

- Design weld seams that can be Xrayed! Since weld seams should be Xrayed for quality assurance, access to the seams should be provided. For the same reason, edge welded bellows should be avoided.

- Avoid organic materials in contact with tritium! Organic materials exposed to tritium unavoidably degrade (radiolysis). Thereby the lifetime of organic materials depends on their tritium exposure (concentration and time). If it is absolute necessary to use organic materials, e.g. for valve seats, polyimide ('vespel') can be used (TLK experience).

- Avoid the usage of fluorine containing materials! Degradation of materials like PTFE (Teflon) leads to the formation of HF, which is a highly corrosive gas. In addition, fluorine is poisonous to many catalysts.

- Stop or minimize the permeation through hot structural materials! Process components with T > 150°C need a 'vacuum jacket', kept at room temperature, which surrounds the hot component. Permeated tritium can be recovered by pumping down the jacket.

- Avoid the formation of tritiated water! Since tritiated water (HTO) has a 10000 times higher dose factor than tritium gas, the unwanted generation of tritiated water should be avoided in all processes. If this is not possible, one should at least make sure that the HTO is in the vapour phase and not condensed (small drops in the pipe work). Bear in mind that a few microliters of incorporated HTO are enough to constitute a lethal dose.

[96] Quality assurance is done according to technical rules and standards and includes requirements with respect to, e.g. to material certificates, welding procedures and technical design of buffer vessels. The AD2000 is such a technical guideline and contains rules for stainless steel. Materials covered by such guidelines should be chosen to allow for quality assurance according to recognized rules.

10.4. TRITIUM ANALYTICS

Tritium technology requires adequate analytical techniques and accountancy methods. One needs to measure the activity and, in some cases, the individual chemical form[97]. Regarding tritium accountancy, the most important number is the tritium activity (in Bq). Here, the question of trueness and precision is of utmost importance. For process monitoring, the knowledge of the species as well as the information about the amount is usually wanted. In addition, the measurement time is a critical issue. To give a complete review of tritium analytics techniques, including their pros and cons, would exceed the space available to this chapter. Therefore, only a short introduction to the field is given, thereby focussing on the basic concepts.

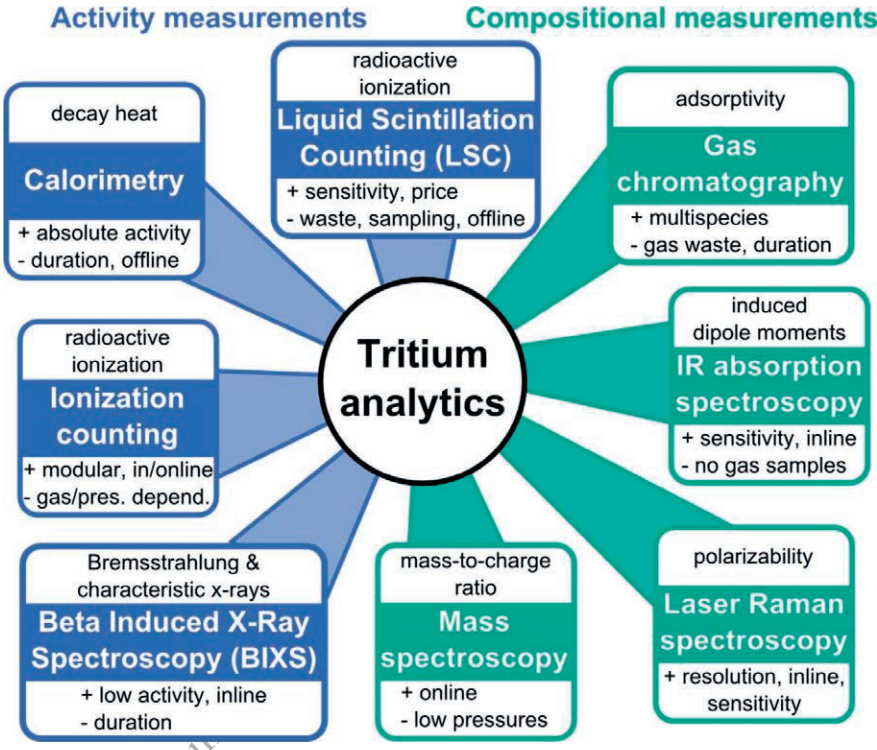

FIG. 10.15. Analytical methods for tritium detection. The measured physical property (top) and pros and cons (bottom) are given in each case. Courtesy M. Schlösser, KIT.

10.4.1. Overview of the analytical methods for tritium detection

Tritium is detected by its mass, charge, decay spectrum, excited states, etc. There are 'inline' and 'real time' methods as well as 'offline' techniques, varying in time from seconds to days. In general, analytical techniques have to cover:

- Large ranges in tritium levels (more than 10 orders of magnitude) typically encountered in different processes and systems of tritium handling facilities.
- Different chemical forms for tritium, e.g. H_2, HD, HT, D_2, DT and T_2, and molecules such as water and hydrocarbons.
- Different states of matter (gaseous, liquid and solid).

[97] The molecules HT, DT and CH_3T, for example, contain one tritium atom and are not distinguishable by activity measurement. However, for scientific or process purposes, this distinction is sometimes necessary.

An overview of tritium analytics techniques is given in Fig. 10.15. These techniques can be divided in two groups: activity measurement methods and compositional measurement methods. Activity measurements usually require highly accurate calibrated systems. They are necessary for licensing and accountancy purposes, whereas information about (gas) composition is usually wanted for process control. In the following, some these methods are briefly discussed.

10.5.1.1. Calorimetry

Inside a tritium laboratory, calorimetry is an important analytical method as it is the only absolute method for tritium determination. Because it is based on the measurement of the heat generated by the radioactive decay (324 mW/g tritium, see Section 10.1.1), the result is independent from the chemical and physical form of the sample. Another advantage is that the calibration does not require a certified tritium source. Ideally, the only uncertainty should come from the decay heat of tritium, which is ~0.3%. TLK is therefore using calorimetry for tritium accountancy. Among the analysed samples are gaseous mixtures from tritium processing experiments, liquid tritiated water and solid materials such as samples of wall materials from experimental fusion reactors, cloths from decontamination operations and contaminated parts from TLK experiments. At TLK, four calorimeters with volumes between 0.5 and 20 l are in operation. Those calorimeters were specially designed and built to allow the measurement of samples containing from 3.09×10^{-6} to 30.86 g of tritium, which corresponds to an activity of 10^9 to 10^{16} Bq. The biggest disadvantage of using calorimetry is the time needed for the measurement, which can last for days if the sample's activity is under 10^{10} Bq.

10.5.1.2. Liquid scintillation counting (LSC)

Liquid scintillation counting is a standard method measuring the radiation from beta-emitting radioactive isotopes and one of the work horses of tritium laboratories. The method requires samples to be taken and mixed with a 'cocktail' containing a solvent and scintillator material. As such, it does not permit inline and real time measurements. This technique is used (by default) to analyse urine samples, wipe tests and tritiated water. Liquid scintillator counters can be bought off the shelf. For accurate measurements however, a calibration with calibrated samples is necessary.

10.5.1.3. Ionization counting

The ionization chamber measures the charge from the number of ion pairs created by the tritium decay electrons within the tritiated gas. Ionization chambers are widely used for tritium monitoring and for radioprotection. The chamber size and the electronics' sensitivity dictate the device's measurement range[98] that can typically cover up to 6 orders of magnitude. For process monitoring, typically small (< 5 cm^3) homemade ionization chambers are used at TLK (see Fig. 10.16), allowing the measurement of gaseous mixtures ranging from pure tritium down to vppm levels.

FIG. 10.16. Components of a small cross ionization chamber (active volume ~5 cm^3) for inline and real time measurements of the tritiated process gases used at TLK (courtesy F. Priester, KIT).

[98] The larger the volume and the gas pressure the larger the detected current.

The main issues are the relatively high sensitivity to the chemical composition of the measured gas and the memory effect that can dramatically affect the quantitative measurements in the lower ranges. The memory effects can be reduced using electrode grids to minimize the electrode surface area or using special coatings that avoid tritium adsorption. Modern ionization chambers claiming 1% accuracy are commercially available. However, they have to be operated under optimal conditions[99], with the possibility of frequent clean-up by gas purge and calibration using certified mixtures.

10.5.1.4. Beta induced X ray spectroscopy (BIXS)

Beta induced X ray spectroscopy (BIXS) is based on the measurement of the X rays produced by the deceleration of tritium decay electrons in a solid or liquid medium (bremsstrahlung effect). In a typical setup, the gas sample is contained in a stainless-steel chamber equipped with a beryllium window, which is gold coated on the chamber side. The X rays produced in the gold layer are detected as they penetrate the beryllium window. Scintillator materials coupled to a photomultiplier tube (PMT) are widely used to detect X rays, but the latest BIXS setup developed at TLK comprises a silicon drift detector (SDD) [10.10]. The SDD produces much lower noise and has an excellent energy resolution (about 160 eV). Such BIXS setups can be used online and in real time to monitor the tritium activity in a sample that contains a Q_2 mixtures at inlet pressures between 10^5 Pa and 10^{-1} Pa. Fig. 10.17 depicts a typical BIXS spectrum measured at TLK.

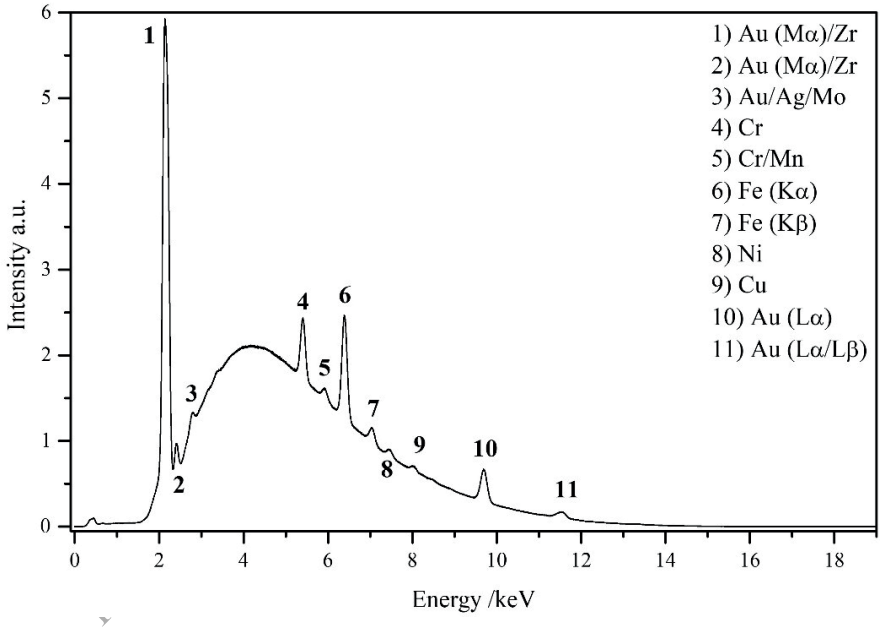

FIG. 10.17. Typical BIXS spectrum measured with a SDD. Shown are the characteristic radiation peaks (e.g. Cr, K_α) and the continuous radiation (courtesy F. Priester, KIT).

The total count rate of the continuous spectrum is proportional to the tritium specific activity. The current detection limit of the TLK setup for gaseous samples is about 5×10^{11} Bq.m^{-3} for 100 seconds measurements with a statistical uncertainty lower than 1%. Its good resolution and easy operation make BIXS an attractive technique for tritium monitoring. Therefore, other applications, such as measurements with tritiated water and the use of BIXS for tritium accountancy in the breeder, are the subject of ongoing R&D.

10.5.1.5. Laser Raman spectroscopy (LARA)

Laser Raman spectroscopy (LARA) is an optical inline method which allows a near real time analysis of gas mixtures. A laser beam is sent through the sample and the inelastic scattered light is analysed. Each Q_2 isotopologue can be identified by the position of its individual rotational–vibrational (Q1)-branch in the spectrum of the scattered light. The quantitative analysis also considers line intensities. Besides Q_2, other molecules relevant for tritium applications can be detected, like CQ_4 or Q_2O.

[99] Constant pressure, within a modest variation of the gas composition.

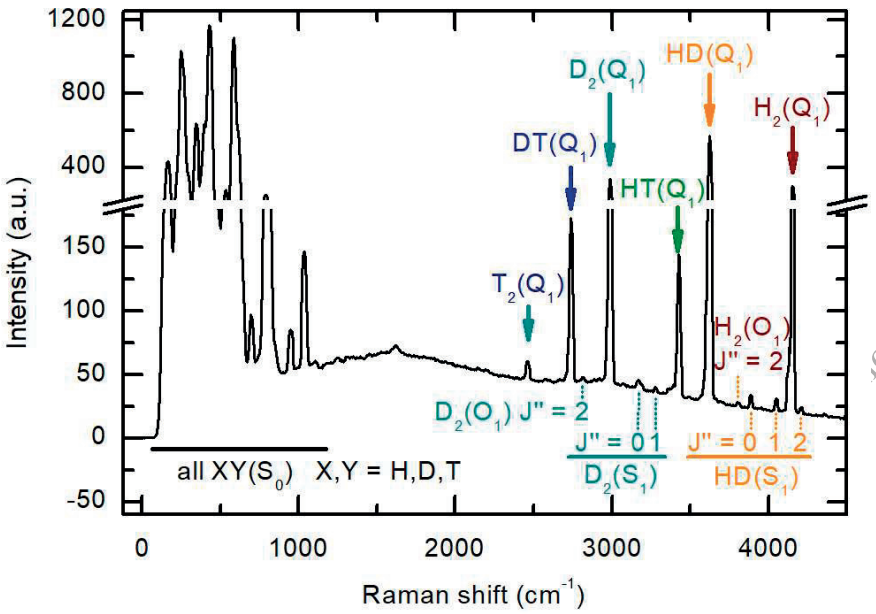

FIG. 10.18. Raman spectrum of a Q_2 spectrum measured at TLK. Especially marked are the so-called Q1 lines (first vibrational transitions). All Q_2 isotopologues are detected simultaneously (courtesy M. Schlösser, KIT).

Fig. 10.18 depicts a typical LARA spectrum of a Q_2 mixture. LARA avoids taking samples and allows automated non-stop inline operation. It is used at TLK to monitor the isotopic composition of Q_2 mixtures in different applications. At TLK, the level of detection (3σ) for a gas sample is ~1 Pa in 100 s, enough for process monitoring and control. A possible application to fusion fuel cycle systems concerns process monitoring in the subsystems, e.g. in the ISS or in the tritium extraction systems of the blankets. Note that a Raman system needs calibration, e.g. with a well-known gas sample; a more detailed discussion is given in the next paragraph.

10.5.1.6. Gas chromatography

Gas chromatography (GC) is probably the most used analytical technique to characterize gaseous mixtures containing tritium. It is based on the different absorptivity of the different gas species and allows a full chemical and isotopic determination. Commercial separation columns and special detectors are available on the market for almost any gas analytical application. Special gas chromatographs, requiring particularly low-temperature columns, have been developed to separate the hydrogen isotopologues. The sensitivity is optimal for tritiated species when using small ionization chambers as detectors. Since the gas chromatography measurement is not an absolute method and the system can slightly change over time, frequent calibrations are necessary to ensure accurate results. For the calibration of the ionization chambers, certified tritium mixtures are required. However, certified mixtures covering a large range of tritium concentration with good precision are not commercially available and have to be produced on-site. A measurement trueness of 5% is reachable. A disadvantage of the gas chromatography method is the measurement time, which can be in the order of 40 minutes for T_2. For this reason, micro gas chromatographs are under investigation at different laboratories.

10.4.2. Short introduction to the concept of precision and trueness

It is important not to confuse the terms precision, trueness and accuracy. Fig. 10.19 depicts a cartoon which helps to visualize the situation. According to the Joint Committee for Guides in Metrology (JCGM), which prepares the international vocabulary of metrology [10.19], the following definitions are valid:

- Measurement precision: Closeness of agreement between indications or measured quantity values obtained by replicate measurements on the same or similar objects under specified conditions.
- Measurement trueness: Closeness of agreement between the average of an infinite number of replicate measured quantity values and a reference value.

- Measurement accuracy: Closeness of agreement between a measured quantity's value and a true quantity's value of a measurand.

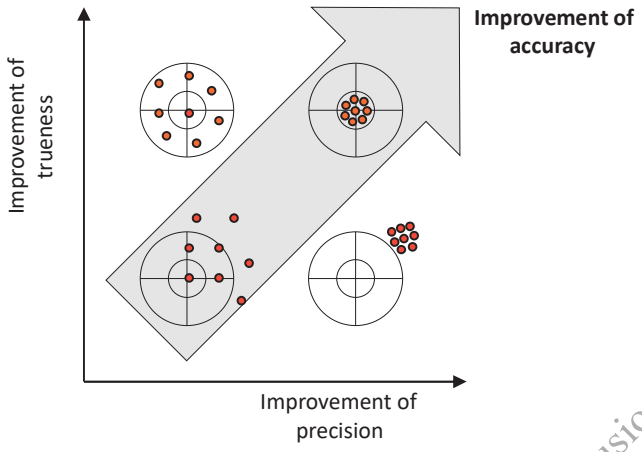

FIG. 10.19. Visualization of the terms trueness, precision and accuracy with the help of a target. The red dots stand for the hits.

Summarizing in words: the terms trueness and precision are used to describe the accuracy of a measurement. Therefore, accuracy refers to trueness and precision.

10.5. THE TRITIUM PLANT OF A FUSION REACTOR

According to the ITER design requirements and guidelines level 1 (2001), the tritium plant has to perform the following main tasks [10.12]:

- Receiving of tritium shipments and loading into the fuel cycle.
- Storage of tritium and deuterium.
- Measurement and determination of tritium inventories.
- Preparation and delivery of deuterium and deuterium–tritium, including the separation of hydrogen isotopologues from all other exhaust gases, separation into specific isotopic species for refuelling, and the detritiation of impurities for controlled release into the environment.
- Detritiation of atmospheres for normal and emergency operations as well as for maintenance.
- Detritiation of water to allow its release to the environment.
- Extraction and processing of tritium from test blanket modules.

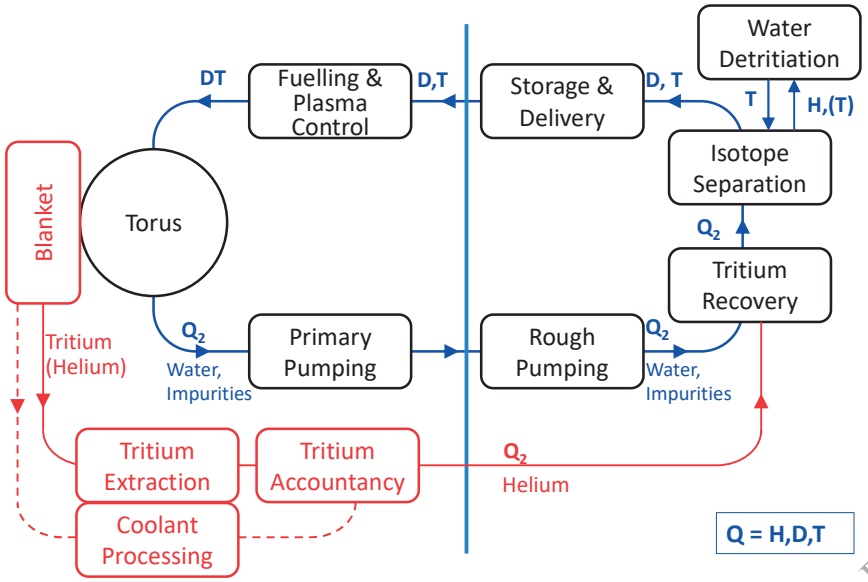

FIG. 10.20. The fuel cycle of ITER. Everything on the right side of the line belongs to the tritium plant, plus additional systems, which are not shown here (e.g. the tritium confinement and detritiation systems).

Fig. 10.20 shows the fuel cycle of ITER with the tokamak fuel cycle systems of the tritium plant (besides the analytical system), which are identical to the systems the closed tritium cycle discussed in Section 10.3. Not shown in Fig. 10.20 are the tritium confinement and detritiation systems (among others the glovebox atmosphere detritiation system and the vent detritiation systems) and other systems such as the control systems. All systems are located in the tritium plant building except the detritiation systems for the hot cell facility, which is located in the hot cell building. The functionality of the infrastructure systems of TLK's closed tritium cycle is basically the same as that of a tritium plant.

10.6. QUESTIONS TO CHECK YOUR COMPREHENSION

1) What are the important properties of tritium?
2) What is the relation between activity of a nuclide and its number of atoms?
3) Why is it only necessary to consider the internal exposition to tritium?
4) What is the meaning of ALARA?
5) Why do is a closed tritium cycle mandatory?
6) Explain the basic function of the detritiation and hydrogen isotope recovery stage.
7) Describe two different mechanisms for hydrogen isotope separation.
8) How can tritium be stored in a safe way?
9) Describe the difference between the concept of a closed tritium cycle in an experimental research facility and the concept of a closed tritium fuel cycle in a fusion reactor.
10) Itemize rules for tritium handling.
11) Explain the difference between analytics for measuring the tritium activity and analytics for measuring the composition of a gas sample. Which type is the standard method for tritium accountancy?
12) Explain the term 'trueness' and the term 'precision'.
13) Describe the main tasks of the tritium plant of ITER.

10.7. SOLUTIONS OF THE PROBLEMS GIVEN IN THE TEXT

In the following solutions, a few tricks and roundings are used to demonstrate the results without a calculator. The reader is invited to calculate the exact values.

10.7.1. Solution of problem 1

a) 1 g T ⇔ 3,73 ℓ at 1013 mbar and 0°C

1 mol $T_2 \cong 6$ g $\cong$ 22,4 ℓ (ideal gas) ⇒ 1 g $T_2 \cong$ 22,4 ℓ / 6 ≈ 3,7 ℓ

b) 1 g T ⇔ 10 kCi

Number of T_2 molecules in 1 g: Start with $N/\mathrm{N_A} = m/M$, where N is the number of T_2 molecules and $\mathrm{N_A}$ is the Avogadro constant, 6.02214129(27) × 10^{23} per mol.

$$\Rightarrow N(T_2) \approx 1\text{g} / (6\ \text{g/mol}) \times 6 \times 10^{23}\ \text{mol}^{-1} \approx 10^{23}\ \text{molecules}$$

Now use the basic equation for radioactive decay:

$$A = \lambda N(T) = \ln 2 / t_{\mathrm{H}} \times N(T)$$
$$\approx 0.7/(12.2 \times \pi \times 10^7) \cdot 2 \cdot 10^{23}\ \text{Bq} \approx 3.5 \times 10^{14}\ \text{Bq}$$

The factor 2 considers that one now needs the numbers of atoms not the number of molecules, while π times 10^7 is roughly the number of seconds in a year (with less than 0.5% deviation!). With $1\ \text{Ci} = 3.7 \times 10^{10}$ Bq one finally obtains:

$$A = 3.5 \times 10^{14}\ \text{Bq} / (3.7 \times 10^{10}\ \text{Bq/Ci}) \approx 10\ \text{kCi}$$

c) 1 g T ⇔ 324 mW

From the above, one can calculate the electrical power by multiplying the number of β electrons per second by the average energy per β electron (for each decay one gets one β electron):

$$P \approx 3.5 \times 10^{14}\ \text{electrons/s} \times 5.7\ \text{keV/electron}$$

With $1\ \text{keV} = 10^3 \times 1.6 \times 10^{-19}$ C·V, one finally obtains:

$$P \approx 0.320\ \text{C·V·s}^{-1} = 320\ \text{mW}$$

10.7.2. **Solution of problem 2**

a) Effective dose D_{eff} for 10 Ci of inhaled tritium

$D_{eff} = 3.7 \times 10^{11}$ Bq $\times$ 1.8×10^{-11} Sv/Bq = 6.67 Sv

b) Necessary amount of water (T_2O)

Calculate the necessary amount of water (T_2O) as in problem #1:

Number of T atoms: $N = A \times T_H / \ln 2 = 2.08 \times 10^{20}$

Using the formula $N / N_A = m / M$ and set $M(T_2O) = 22$ g/mol and keeping in mind that one has 2 atoms of tritium per T_2O molecule:

$$m = M \times N / N_A = 22 \text{ g/mol} \times \tfrac{1}{2} \times 2.08 \times 10^{20} / (6.02 \times 10^{23} \text{ mol}^{-1})$$
$$m = 3.8 \times 10^{-3} \text{ g}$$

Taking the water density to be ~1 g/cm^3 (which is of course an under estimation, since tritiated water is a little bit denser), one ends up with a volume of 3.8 μℓ!

10.7.3. Solution of problem 3

Estimate the necessary amount of T_2 for 1 GW of fusion power

One can perform a simplified calculation only considering the energy generated via the fusion reactions, which totals

14.1 MeV + 3.5 MeV = 17.6 MeV of produced kinetic energy.

Assume that all the neutron and α particle's kinetic energy is transformed into fusion power.

a) First calculate the released energy per fusion reaction in Joules:

$$17.6\ \text{MeV} = 17.6 \times 10^{6} \times 1.6 \times 10^{-19}\ \text{C/V} = 2.816 \times 10^{-12}\ \text{J}$$

b) Now calculate the number of reactions (N) to get 1 GW = 10^9 J/s of fusion power.

$$N = 10^{9}\ \text{J/s} / (2.816 \times 10^{-12}\ \text{J}) = 3.55 \times 10^{20}\ \text{s}^{-1}$$

Thus 3.55×10^{20} tritium atoms per second are needed, which corresponds to $3.55 \times 10^{20} / (6.02 \times 10^{23})$ mol/s = 5.90×10^{-4} mol/s of tritium atoms. Given the molar mass M(T) ≈ 3 g/mol the necessary amount per day is

$$5.90 \times 10^{-4}\ \text{mol/s} \times 3\ \text{g/mol} = 1.77\ \text{mg/s} = 153\ \text{g/day}.$$

10.7.4. Solution of problem 4

a) Maximum allowed mass of the ^{238}U bed for 70 g of tritium as UT_3

Molar mass of T_2 is ~6 g/mol

⇒ One has to store 70 g / (6 g/mol) = 11.7 mol T_2

Maximum stored capacity of UT_3 is

⇒ 3 mol T with 1 mol U or 1.5 mol T_2 with 1 mol U

Therefore, 11.7 / 1.5 mol U ≈ 12 / (1.5 mol U) ≈ 24/3 mol U ≈ 8 mol U is needed, which is equivalent to 8 × 238 g ^{238}U ≈ 1.9 kg ^{238}U

b) Necessary volume

The density of ^{238}U is ~19 g/cm^3

⇒ The necessary volume is 1900 g / (19 g/cm) = 100 cm^3.

One can store huge amounts of tritium in a relatively small volume of uranium (non-pressurized vessel)!

REFERENCES

[10.1] NATIONAL INSTITUTE OF STANDARDS AND TECHNOLOGY, Information about tritium (2018), https://www.nist.gov/fusion-search?s=tritium&commit=Search

[10.2] PATRIGNANI, C., et al., Review of Particle Physics. Chinese Physics C, **40** (2016) 100001.

[10.3] LUCAS, L.L., UNTERWEGER, M. P., Comprehensive review and critical evaluation of the half-life of tritium, Journal of Research of the National Institute of Standards and Technology, **105** (2000) 541.

[10.4] INTERNATIONAL COMMISSION ON RADIOLOGICAL PROTECTION (ICRP), The 2007 recommendations of the ICRP, Elsevier ICRP Publication **103** (2007).

[10.5] FEDERAL OFFICE FOR RADIATION PROTECTION OF GERMANY, Dose coefficients to calculate radiation exposure, Bundesanzeiger August 28 **160a-b** (2001).

[10.6] BORNSCHEIN, B., Between fusion and cosmology – the future of the Tritium Laboratory Karlsruhe. Fusion Science and Technology, **60** (2011) 1088-1091.

[10.7] BESSERER, U., doctoral thesis Philipps Universität Marburg (2002), http://archiv.ub.uni-marburg.de/diss/z2003/0108/pdf/Tritiumspeicherung_in_ZrCo.pdf.

[10.8] DÖRR, L., et al., A decade of tritium technology development and operation at the Tritium Laboratory Karlsruhe, Fusion Science and Technology **54** (2008) 143.

[10.9] BORNSCHEIN, B., et al., Successful experimental verification of the tokamak exhaust processing concept of ITER with the CAPER facility, Fusion Science and Technology, **48** (2005) 11.

[10.10] RÖLLIG, M., et al., GEANT4 Monte Carlo simulations for sensitivity investigations of an experimental facility for the measurement of tritium surface contaminations by BIXS, Fusion Engineering and Design **109-111** (2016) 684-687.

[10.11] JOINT COMMITTEE FOR GUIDES IN METROLOGY, 'International vocabulary of metrology – basic and general concepts and associated terms (VIM)', JCGM **200** (2012).

[10.12] ITER IO, Design requirements and guidelines level 1 (2001), http://www.fusion.qst.go.jp/ITER/FDR/DRG1.pdf.

BIBLIOGRAPHY

BORNSCHEIN, B., et al., Tritium management and safety issues in ITER and DEMO breeding blankets, Fusion Engineering and Design 88 (2013) 466-471.

DEPARTMENT OF ENERGY, Tritium handling and safe storage, DOE-STD-1129-2015, (2015). https://www.standards.doe.gov/standards-documents/1100/1129-AStd-2015.

FIEGE, A., et al., Tritium, KfK-Report 5055 (1992), http://bibliothek.fzk.de/zb/kfk-berichte/KFK5055.pdf.

STACY, W. M., Fusion, Wiley-VCH (2010).

Chapter 11

REMOTE MAINTENANCE

Samuel Jiménez
RACE, UK Atomic Energy Authority
Culham, United Kingdom

Victor Agudo
RACE, UK Atomic Energy Authority
Culham, United Kingdom

Keelan Keogh
RACE, UK Atomic Energy Authority
Culham, United Kingdom

Jorge Rafael González-Teodoro
Princeton Plasma Physics Laboratory
Princeton, USA

Rob Buckingham
RACE, UK Atomic Energy Authority
Culham, United Kingdom

11.1 INTRODUCTION

11.1.1 The need for maintenance

There are two parts to the engineering design of any power plant. The first is to make the plant work, focusing on the function of the individual elements, their interaction and integrated performance. The second is to ensure the plant can continue to work throughout its commercially productive life in an economically viable manner. The latter involves designing the plant to be operated and maintained quickly, efficiently and safely.

In any power plant, a vast range of components require regular maintenance of many different types. For example, consumables are replenished, moving parts which wear need changing, sensor must be re-calibrated periodically, structural materials are replaced as they degrade, safety systems must be inspected to guarantee correct operation, etc. As these actions are essential to the continued operation of the system, maintenance is mission-critical for any power plant.

Although the maintenance of valuable assets is a fundamental aspect of modern engineering practice, fusion technology introduces many new and unique maintenance challenges. For instance, a fusion power plant converts the kinetic energy of the 14.1 MeV neutrons produced in the deuterium–tritium fusion into more useful forms. Currently, this means allowing the neutrons to hit and heat up adjacent materials. However, at these energy levels neutrons displace atoms within crystal lattices and cause nuclear reactions, both of which change the material properties. A key consequence is the weakening of structural materials, which severely limits their useful life. No known material can withstand this barrage for long, and so in-vessel systems, and particularly plasma facing components, need to be repaired or exchanged multiple times throughout the operational life of the power plant, much more frequently than would otherwise be necessary [11.1]. It follows that effective and reliable maintenance systems are essential to achieve fusion power.

11.1.2 Maintenance and fusion power economics

For fusion power to be economically viable, it is essential that its cost per kWh is at least similar to other alternative power generation technologies. The more energy a power plant produces over its lifetime, the more competitive its pricing becomes to consumers, as the initial design and capital costs are fixed. However, when a power plant is being maintained it cannot operate. This reduces its availability, i.e. the percentage of time that the plant is producing useful energy. It follows that for fusion power to be economically viable plants must have high availability. This is achieved by having a reliable plant with an efficient maintenance system, ensuring minimum downtime.

Power plants have operational costs associated with producing energy, and costs incurred when performing the maintenance. Many strategic factors can affect these costs, such as whether worn items are repaired or replaced with

new ones; how much waste is produced and how it must be disposed of; or how many maintenance tools are simultaneously deployed. The economic balance of these factors is a key design consideration, and a viable reactor requires a compromise between optimal operating parameters and the maintenance systems that enable higher availability.

Regulators and investors need to be confident that fusion power plants can operate safely and reliably. The maintenance systems form a key element of this, as they help prevent damaging failures from occurring, and allow early detection and impact mitigation of potential faults. As plants will operate for many decades, the maintenance strategy also plays an important role in the management of component obsolescence and plant upgrades, contributing to overall reliability.

11.1.3 The need for remote maintenance

The use of tritium and the activation of materials due to the extreme neutron flux lead to a radioactive environment inside the machine. In fusion power plants the levels of radiation will be orders of magnitude above safe working levels for hands-on maintenance. These levels are usually specified by regulators in terms of allowable dose rates (for individual workers) and integrated dose rates (the combined total which can be applied to the work force). Activities within nuclear regulated environments are underpinned by the principle that associated risks must be kept As Low As Reasonably Achievable (ALARA), with due consideration of economic, technical and social considerations.

However, radiation is not the only risk to operators of fusion devices. Some of the substances used, such as the beryllium in the first wall tiles, can be toxic to humans and in fact this is usually the primary concern in existing fusion reactors such as JET. Cryogenic systems are used in vacuum pumps and superconducting magnets and carry the risks of asphyxiation due to accidental release of cryogenic gases, or producing cold burns. High electrical currents are commonplace. Activated materials will produce heat, leading to high surface and ambient temperatures within the vessel, enough to preclude safe human access. Fusion devices tend to be very densely packed, with confined spaces in which mobility is severely reduced and rescue of workers in the event of an accident is much more difficult. Like in other industrial sites, handling of very large payloads, working at height, trip hazards, and operation of high-power machinery are all common, and these are often the most likely causes of industrial accidents. Many of these risks are not confined to in-vessel areas alone, and although they can be easily managed in isolation it is the combination of multiple risk factors which poses the greatest challenge in fusion power plants.

Beyond these risks, humans can sometimes introduce problems to the operation of the machine. For example, organic matter such as hair or hand grease left inside the vacuum chamber make achieving high vacuums more challenging, as it releases gas under vacuum conditions (outgassing). Equally, humans have been known to inadvertently damage delicate equipment when moving inside reactors.

With these considerations, the application of ALARA leads to the use of technologies which allow human operators to perform their work without being unnecessarily exposed to risks. Thus, conventional maintenance becomes remote maintenance (RM), constituting a mission-critical element of fusion power plants.

11.1.4 The need for integrated remote maintenance

Current studies of fusion power plants indicate that arriving at a design that will both work and also operate effectively throughout the plant's lifetime is a significant engineering challenge, in part because both objectives often carry conflicting requirements. Lessons learnt from the design of the JET [11.2] [11.3] and ITER [11.4] systems show that the maintenance of a power plant must be considered from the very outset of the design process, as adding RM systems retrospectively is not cost effective and introduces risks. Hence, the maintenance must be an intrinsic aspect of the plant design, and dictate requirements for the plant operational and economic performance.

The unavoidable consequences of the fusion process itself drive the need for many elements of the power plant to be designed with remote maintainability as an essential requirement. This has a profound impact on all aspects of the design of the power plant and the components within, as shown by the studies being conducted for post-ITER reactors such as EU DEMO [11.5] or Japan DEMO [11.6]. Remote maintenance in fusion power plants is hence not only mission-critical, but also device-defining.

11.1.5 Terminology

It is important to distinguish between remote "maintenance" and remote "handling", which are often (incorrectly) used interchangeably. The former constitutes the wide range of operations which an RM system performs, which can include inspection, calibration, welding, repair, etc. The latter refers only to the subset of operations involved in manipulating an object, for example when using a teleoperated manipulator.

In this chapter, the terms "component" refers to the plant hardware and subsystems, on which the RM system acts. In contrast, "equipment" denotes the physical machines which are part of the RM system, such as manipulators, tools, etc.

The term "fusion device" will be used in this chapter to describe experimental fusion reactors, which encompasses all currently existing machines. In contrast, "fusion power plant" refers to a commercially viable power generation plant, which is the ultimate goal of the fusion research community. This distinction is important from an RM perspective, as the maintenance requirements of an experiment are very different to those of a power plant, and some considerations discussed in this chapter may not be applicable to small scale fusion devices. Some important assumed differences are summarized in TABLE 11.4.

TABLE 11.4. Selection of assumed differences between experimental fusion devices and future fusion power plants, and their expected effect on RM systems.

Power plant vs. fusion device	Effect on RM system
Requires higher availability	Shorter maintenance durations Demands higher reliability
Will have harsher environment	More restricted human access More systems require remote operations
Will have higher radiation	Higher component maintenance frequencies Radiation damage to RM equipment is likely
Will be larger	Larger components with higher payloads Larger spaces to cover with RM equipment
No major modifications during lifetime	Better defined long term maintenance needs Standardization and modularity are more effective

11.1.6 Scope of the chapter

This chapter introduces the concept of remote maintenance and discusses the profound impact that a transition from hands-on to remote maintenance has on the design of fusion devices. It seeks to address some fundamental questions in the context of a fusion power plant:

- What are the necessary interventions for RM?
- What remotely operated equipment is required for these interventions?
- What is the role of people in RM?
- How do these elements come together to create a RM system?
- How do RM systems impact the design of the plant?

In combination, answers to these questions lead towards general principles underpinning design for RM. Many of these have been established through the design and operation of the Remote Handling System of the Joint European Torus (JET). This is a first of a kind, end-to-end remotely operated system which has been used, maintained and upgraded to conduct a very wide range of RM tasks within the JET reactor over more than 20 years. However, looking to the future it becomes clear that a step change is required to move from current experimental machines to commercially viable power plants. This chapter therefore also considers what changes are needed to bring about the RM systems of the future.

11.2 ELEMENTS OF A RM SYSTEM

11.2.1 Maintenance Management Plan

One of the most important lessons learnt from the JET system is that the RM equipment is only a small part of the overall RM system, and that success depends on the more intangible strategic, organizational, and integration planning [11.3]. To arrive at a safe and efficient RM system which is highly integrated within the fusion plant, a clearly defined global approach is required. This is captured in the Maintenance Management Plan (MMP), a high level document which puts forward the information and methods of work which allow the maintenance system to achieve its goal of maximizing plant availability while ensuring safety. The MMP is the first element of the RM system, and must be developed from the outset of the plant design process. The MMP should define [11.7] [11.8]:

- The overarching maintenance philosophy and strategy for the plant.
- The stakeholders responsible for the delivery of the maintenance strategy, including the interfaces between them and the scope of their responsibilities.
- The design process for capturing maintenance requirements (including statutory requirements for safety related equipment), and the working practices necessary to control and embody them within the design, throughout the full plant lifecycle.
- The methods of defining and controlling the maintenance classification of reactor components, and managing their contribution to the maintenance burden as the plant design develops.
- Appropriate standards and best practices for the design of RM-compatible components, RM equipment, and RM operations.

11.2.2 RM equipment

A RM system requires a wide range of equipment to provide a sufficiently versatile suite of capabilities to serve the plant. A typical RM system will use a combination of deployers, handling end effectors, and other end effectors (including tools and interfaces).

In general, “deployers” enable access to the reactor areas by providing movement, payload carrying, load reaction and supply of services to other RM systems. The term “end effector” refers to the device at the end of the deployer which interacts with the components and provides a functional capability. End effectors which provide handling capability are a key feature of RM systems, and of these “manipulators” typically refers to the subgroup of devices that enable dexterous, human-like manipulation capabilities. “Tools” can be considered a category of end effector which are usually, but not necessarily, simple passive objects handled by a manipulator, such as screwdrivers, blades, etc. An “Interface” can be considered a tool whose specific role is to provide a known, shared boundary that allows controlled manipulation of a component by a handling end effector.

For a given application, not all types of equipment may be required, and the functions associated with each may sometimes be combined. Thus, the distinctions between the different categories of RM equipment can become blurred in complex systems. FIG. 11.26 shows a schematic of a typical RM system configuration.

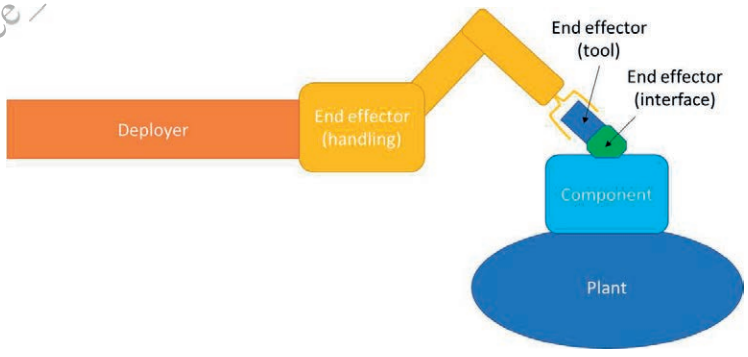

FIG. 11.26. Schematic of a typical RM equipment configuration.

11.2.2.1 Deployers

The deployer design is paramount for the success of the RM system as a whole, as it will define the reachable space within the vessel, the maximum payload of any equipment or component to be handled, and may provide services required by other RM equipment.

The design and configuration of deployers largely depends on the access levels available and the capabilities required for the foreseen maintenance. For example, JET uses two snake-like deployers capable of moving toroidally around the entire vacuum vessel, called booms (FIG. 11.27). Their primary role is as highly versatile transporters with considerable payload rating, up to 650 kg for the octant 5 boom at its full 12.5 m extension. The booms are highly reconfigurable, allowing the number of links to be changed or different end interfaces to be equipped, as shown schematically in FIG. 11.28. This allows the JET RM system to adapt to different tasks by deploying a wide range of equipment. As the structure is cantilevered, the high payloads require high bending stiffness in the vertical direction. Although motion outside of the equatorial plane is limited, the booms are relatively large compared to the vessel so in combination with the end effectors allow full access to all internal surfaces in JET.

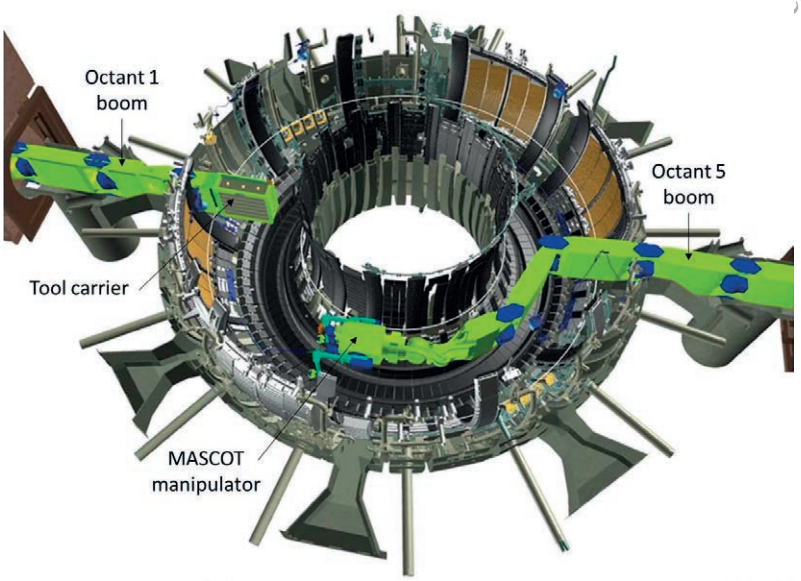

FIG. 11.27. Representation of the RM booms being deployed in JET.

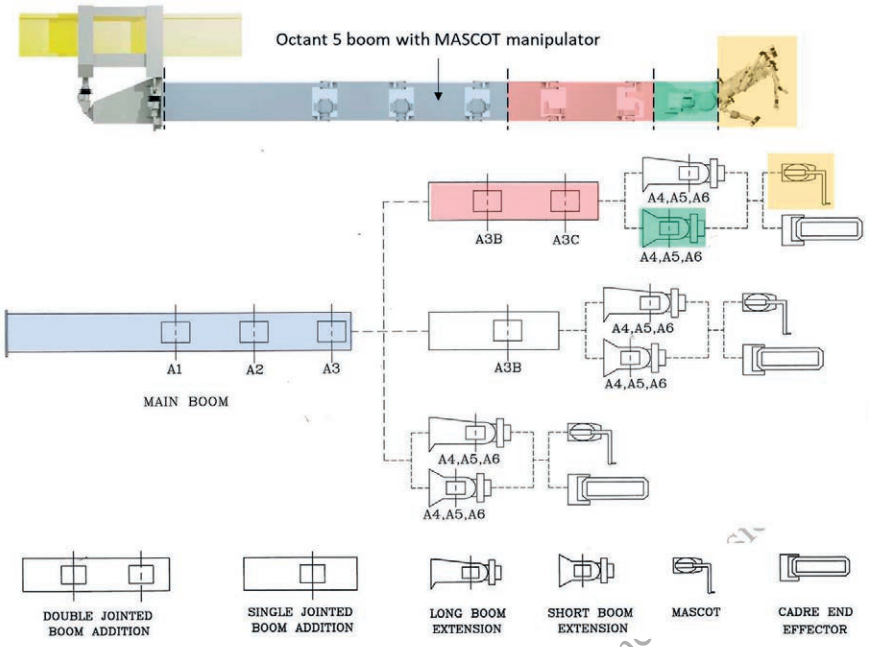

FIG. 11.28. Schematic of the different configurations available for JET's octant 5 boom, showing multiple types of attachment.

For a given JET in-vessel maintenance task, the booms will be equipped with the systems and tools required for the operation. A preprogramed motion path will be automatically executed, under human supervision, to drive the booms to a pre-defined position where the task is to be performed. The trajectory is carefully designed by operators using a digital simulated environment, prior to the operation. This allows complex trajectories to be executed safely and reliably, keeping a clearance of around 50 mm between the RM equipment and the reactor walls and in-vessel components. A final approximation is required to position the RM equipment closer to the component to be maintained. This usually requires manual control by the operator, as it carries a higher level of risk.

Another example of a deployer is the Articulated Inspection Arm (AIA) developed for ITER, which was first used in Tore-Supra and was upgraded for use in the EAST and WEST reactors [11.9]. It is shown in FIG. 11.29. AIA's goal is to enable full visual inspection of the in-vessel plasma facing components without breaching the vacuum. This avoids having to re-establish the vacuum after inspection, which is a very time-consuming operation. Hence, its design focus is on vacuum compatibility instead of payload carrying capacity. AIA must be stored inside the vacuum boundary, survive the in-vessel environment during reactor operation, operate under vacuum conditions and not contaminate the plasma chamber. As it is intended for inspection, it requires very flexible 3-D motion inside the vessel, to ensure all surfaces can be inspected from multiple angles. This is achieved through 5 parallelogram units, linked in series through yaw joints. It achieves a payload of 10 kg at the full 9.5m extension.

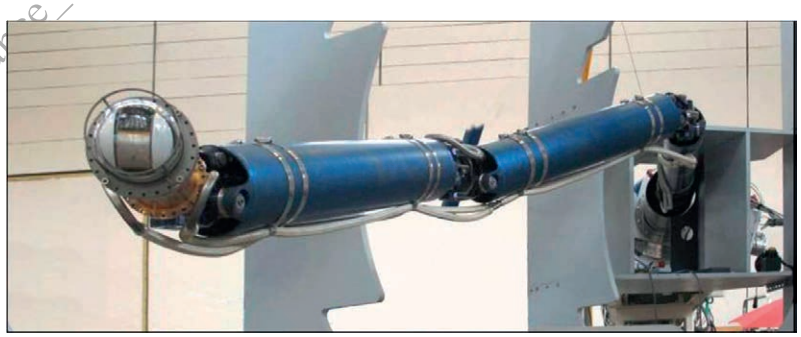

FIG. 11.29. The Articulated Inspection Arm inside the Tore-Supra mock-up [11.9].

As the size of fusion devices grows, so too do the size of the components within and the distances over which the deployers have to provide access to them. This demands more complex deployment systems with full 3-D

positioning and higher payload ratings. For example, to handle the 4-tonne blanket modules, ITER's In-Vessel Transporter (FIG. 11.30) uses a deployable rail system, which requires support from 4 vessel ports [11.10].

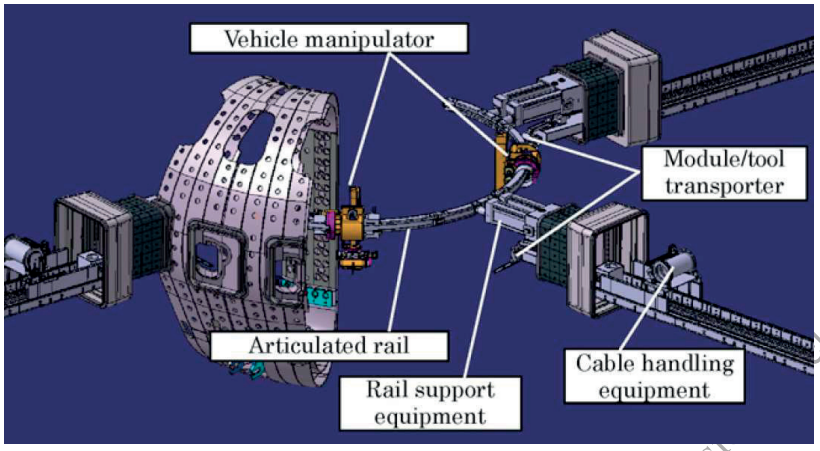

FIG. 11.30. ITER blanket remote handling system with In-Vessel Transporter [11.10].

Current deployers like the JET booms are usually moved slowly, to reduce vibration and dynamic effects. This improves precision and increases their lifetime. However, in future power plants, the high cost of maintenance downtime may demand considerably faster movement speeds, and so deployers will have to cope with much more dynamic motion regimes.

Another key challenge for fusion power plants is that the radiation levels expected inside the vessel during maintenance will be much higher than in current devices. This could mean that complex in-vessel deployers relying on electronic active control may not be feasible, due to concerns over their survivability.

11.2.2.2 Handling end effectors

Handling systems are usually attached to a deployment system and provide the required handling capabilities to perform maintenance tasks. These end effectors enable the RM system to interact with the reactor components by gripping, holding, lifting, fine and coarse positioning, pulling, pushing, etc.

Manipulators such as the JET MASCOT [11.11] are extremely versatile, intended to provide dexterous manipulation capability. They can be viewed as replacing a pair of human hands within the harsh environment. The JET MASCOT is a double arm, force feedback, master-mimic servo manipulator, as shown in FIG. 11.31. Actions performed by the operator on the master side are replicated by the deployed mimic telemanipulator. The haptic feedback system mirrors the loads seen from one side of the system on the other, allowing MASCOT's operator to feel the loads experienced on the mimic side, and vice versa. Operators are capable of feeling steps as small as the thickness of duct tape when running the gripper over a surface. The sensory perception and environmental awareness provided by this feature, in combination with the viewing systems, are critical to achieving reliable and accurate manipulation capabilities, and minimizing damage done in-vessel.

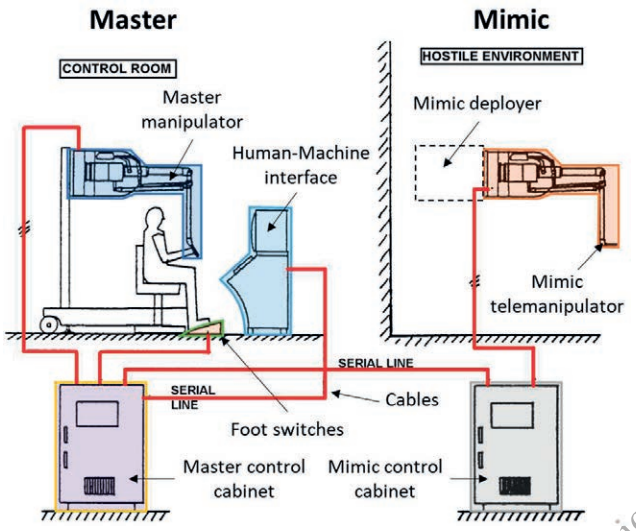

FIG. 11.31: MASCOT system overview diagram.

The JET telemanipulator deployed in the harsh environment side is shown in FIG. 11.32. It is equipped with a pair of grippers, multiple cameras and lights for general and detailed vision, and a range of supporting tool interfaces such as electrical connection points or a dedicated holder for a bolt runner (a tool used for fastening/unfastening bolts).

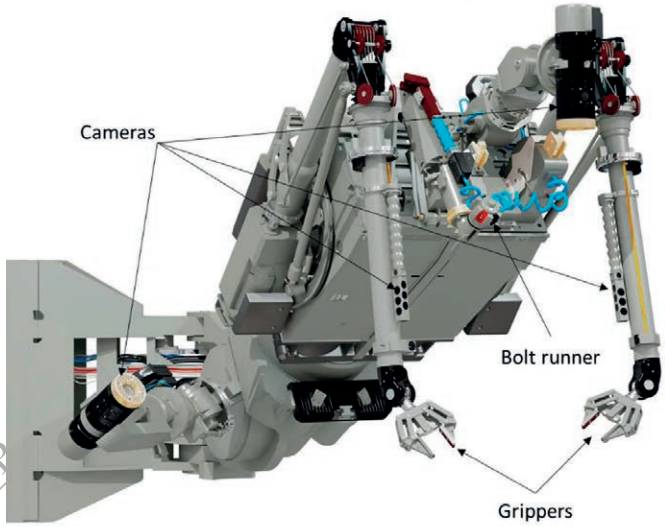

FIG. 11.32. MASCOT telemanipulator deployed in-vessel, with general features labelled.

MASCOT weighs 250 kg and has an allowable payload of ~10 kg per arm. However, this is limited to 5 kg per arm during operations to provide redundancy, so that if an arm were to fail the other can still hold the full payload. This also acts as a safety factor which reduces the wear of the system and improves reliability. MASCOT can also be configured with a supporting winch assembly with a lifting capability of up to 100 kg.

More bespoke handling systems are sometimes required to achieve improved performance for certain functions. For instance, a maintenance task may demand large payload handling, higher positional accuracy than possible with haptic systems, or a specific interface not suitable for other handling systems.

An example of a bespoke handling system is the end effector shown in FIG. 11.33 and FIG. 11.34, deployed on one of the JET booms. Its payload of 280 kg allows it to install large in-vessel items such as TAE antennas and poloidal limiters, which MASCOT cannot handle. As a trade-off for its load carry capabilities, it has a single degree of freedom.

This means that if the fixation between the component being installed and the reactor requires actuation (e.g. bolting an item to the wall before releasing it), this end effector must be complemented by a secondary manipulator. If this is not a viable solution due to space constraints or deployer limitations, the fixation design must be passive (e.g. hanging a painting on a hook). In this case, an integrated load cell is required at the component interface to provide a real time assessment of the load state. This confirms the load has been correctly transferred to the fixation prior to releasing the component.

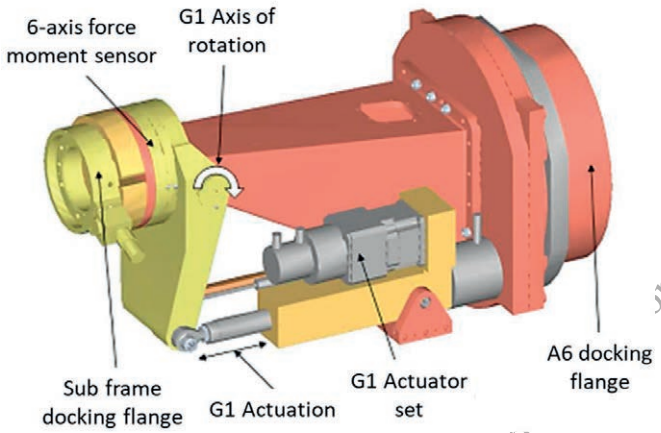

FIG. 11.33. JET poloidal limiter handling end effector.

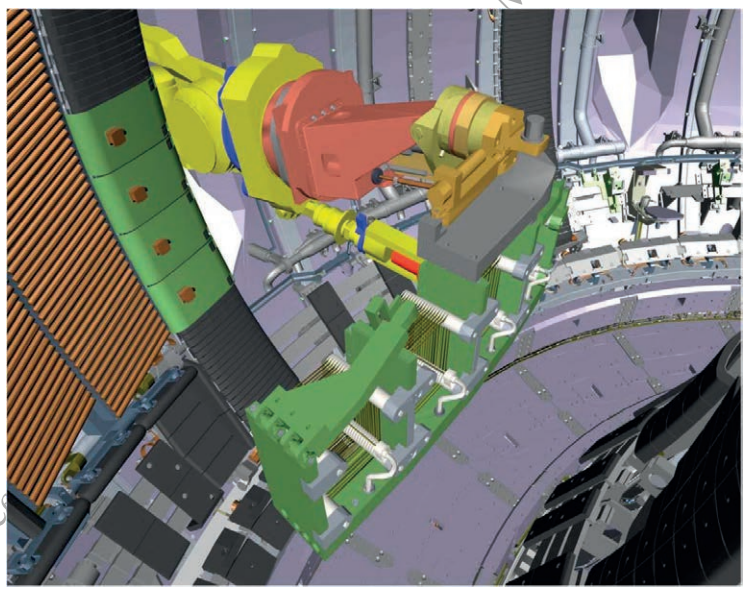

FIG. 11.34. Representation of a JET handling end effector installing a TAE antenna in-vessel.

11.2.2.3 Other end effectors and tools

Handling by itself offers limited RM capability. Like their human counterparts, manipulators require a suitable collection of other tools to make best use of their versatility and meet the range of maintenance tasks required. Therefore, non-handling end effectors are those which equip the RM system with capabilities beyond manipulation, such as bolting, cutting, welding, inspection, interfacing to a component, etc.

Some of these tools will be more widely used than others, and are designed for a common task which is to be performed multiple times at different locations in the reactor. An example of this is the bolt runner shown in FIG. 11.35, the most commonly used tool in JET. It can be configured with different interfaces for different types of threaded fasteners and provides a compatible gripping interface for MASCOT to handle it, with three color-coded

gripping positions. Two of these allow the tool to be used as a ratcheted spanner for fastening or unfastening, depending on the grip colour. This functionality eliminates the need for having to disengage and engage the tool from the fastener on every turn of the bolt, which significantly speeds up operations. The third gripping position is fixed to the bolt interface, allowing the runner to be used as a conventional spanner or Allen key.

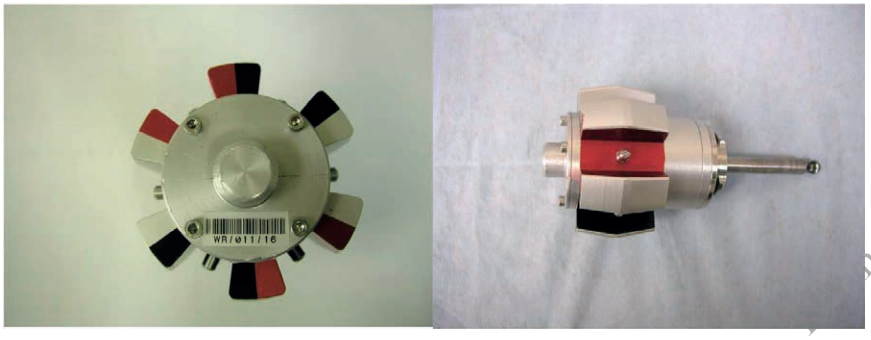

FIG. 11.35: JET RM bolt runner tool.

A key element in achieving an efficient RM system is to ensure an appropriate tool is used for each task. This means that a costly, optimized design may not always be the correct approach. For instance, the very simple tools shown in FIG. 11.36 have provided effective, fast, and low-cost solutions to maintenance challenges in JET. The tools were originally off-the-shelf items for hands-on use, which were modified for MASCOT deployment with the addition of a simple gripping interface.

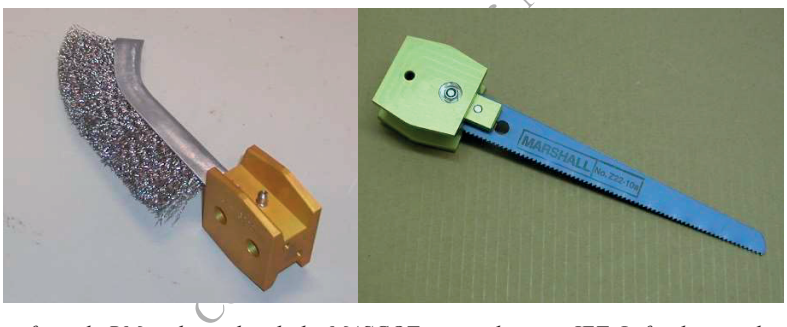

FIG. 11.36. Examples of simple RM tools used with the MASCOT manipulator in JET. Left: cleaning brush. Right: saw blade.

Other tools that have been commonly used in JET are shown in FIG. 11.37:

A. Protective cover to prevent accidental damage of in-vessel components.
B. Bandsaw for removing welded support brackets.
C. Cyclonic vacuum cleaner to collect dust and metallic particles.
D. Photogrammetry targets to conduct in-vessel surveys.
E. Tile-carrying interface with spirit levels to aid in visual alignment.
F. MASCOT-held camera on a flexible support to provide vision around obstacles.
G. Torque wrench for controlled bolt tightening.

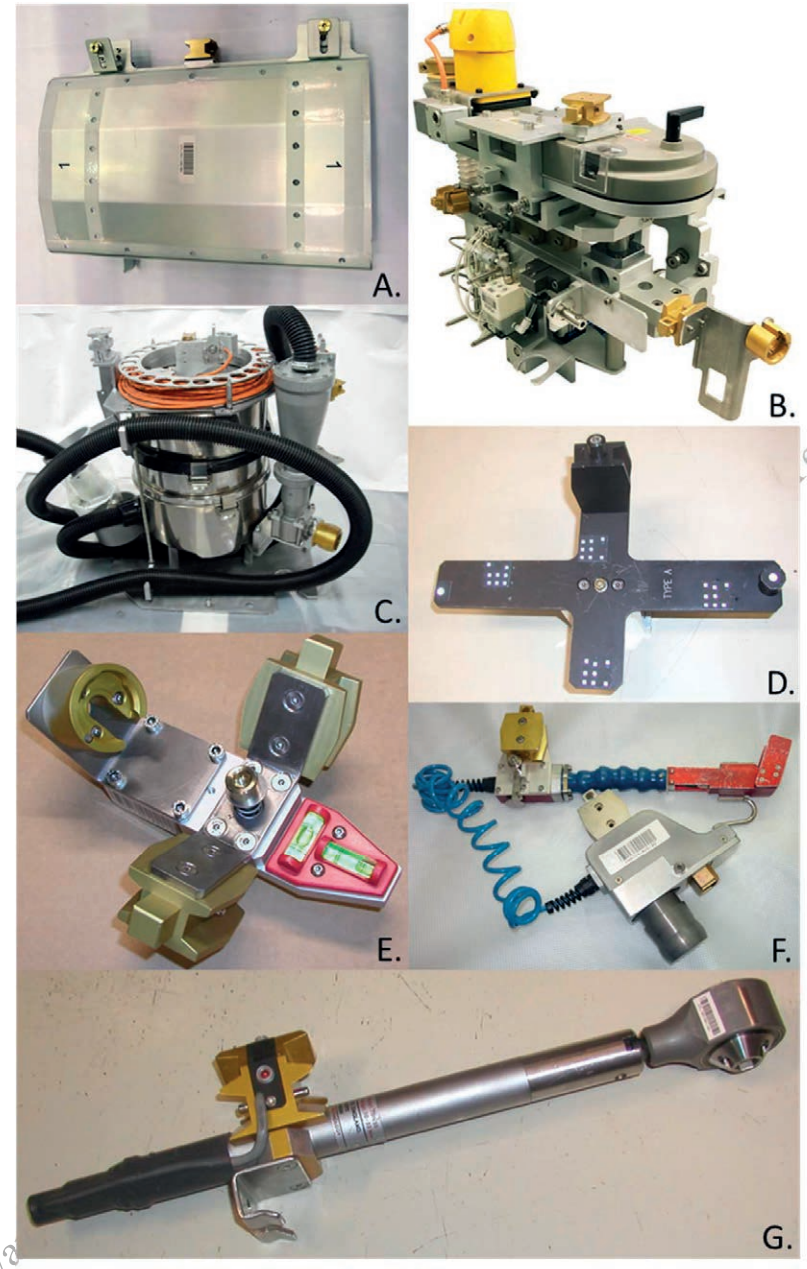

FIG. 11.37. Photographs of commonly used JET RM tools and end effectors.

11.2.2.4 Services

Services are the external material, power or information supplied to a system which it requires to perform its intended function. In a RM context these typically include: electrical, pneumatic or hydraulic power; data; cooling fluids; laser; various gases; vacuum; etc.

The most common services required by RM tools are usually integrated within the deployment system to avoid complex umbilical cable management. For instance, the JET boom can supply MASCOT and other end effectors with data (for measurement and control) and power (electrical, pneumatic and hydraulic). Connection of the services is achieved using standardized interfaces and specifications to speed up the deployment of equipment, improve its reliability, and simplify the design of new equipment.

End effectors will usually rely on the services integrated within the deployer they are attached to, but not all deployers will be able to carry all services. For instance, some activities in JET require MASCOT to operate a welding tool. However, the services required by MASCOT mean that the boom it is deployed from does not have spare service capacity to also supply the welding tool. Hence, the tool is supplied by services from the second boom. Supply of services can therefore have a considerable impact on the configuration of the RM system and the design of operations. To avoid service supplies restricting the capabilities of the RM system, it is key that they are identified, planned and integrated into the components and plant at the outset of the reactor design.

For RM activities, services may be required for static supporting systems which are not mounted on deployers, such as environmental lighting and viewing systems. In JET, these are installed for the duration of the maintenance campaign, and implemented by a rigid feedthrough, illustrated in FIG. 11.38. This feedthrough is clamped at both ends, between the divertor area in-vessel and just outside the port opening in the ex-vessel area, and occupies a small volume along the bottom of the port. Apart from services to the lights and cameras, it provides the option of supplying other services for tooling or other operations.

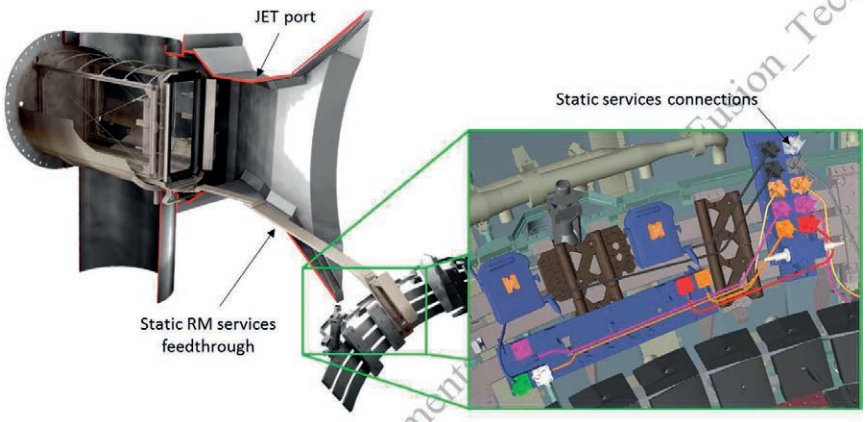

FIG. 11.38. Cross-section of JET showing the static RM services feedthrough and a detailed view of the connections in-vessel.

11.2.3 Human operators

Humans play a fundamental role in maintenance of fusion devices. This can be through direct intervention, where they carry out hands-on maintenance, or through remote operations, where operators control specialist RM equipment from a safe location.

11.2.3.1 Human intervention

Human intervention includes any activity that a human can physically be present for. This is the standard approach in almost all industrial settings and is common for maintenance on many fusion devices.

In most cases, operators must use Personal Protective Equipment (PPE) to conduct human interventions, usually in the form of an under-layer garment with cotton gloves, covered by overalls and nitrile gloves. This is all covered by a pressurized suit and additional thick gloves, as shown in FIG. 11.39, which provides a third layer of protection. The pressurized suit can be cleaned and inspected after use while other items of clothing are single-use, creating large amounts of controlled waste.

FIG. 11.39. Full PPE suit used for JET manual maintenance operations.

Operators may need to wear as many as six layers of gloves (two cotton, two nitrile and two protective). This severely limits dexterity for handling small components, which is problematic when maintaining electronics and small electrical items. PPE can also cause issues with communications, concerns over air supplies, and hinder an operator's movement, causing frustration and a general reduction in their effectiveness. PPE can also reduce the available pool of skills amongst operators, as the people trained to wear the PPE may not be the same people trained to perform certain specialist operations such as welding or electrical work.

Nonetheless, human intervention requires less specialized tooling than remote operations and can be faster to implement because less equipment setup time is required. Humans are very versatile and can execute a wide range of tasks, which allows adapting effectively to unforeseen scenarios. This is particularly useful for experimental reactors, which may undergo changes very regularly in response to scientific findings. Humans also provide high dexterity and manipulation capabilities for smaller objects and can be readily equipped with off-the-shelf tools produced for other industrial uses.

As downsides however, human workers can only handle small payloads if unassisted, and need a considerable supporting safety infrastructure when conducting hazardous tasks. As risks to workers should be ALARA, human intervention is not always possible on devices with high radiation levels or hazardous materials such as beryllium. It is sometimes also undesirable due to the considerable risk of humans contaminating the vessel, making it more difficult to reach high vacuum.

11.2.3.2 Remote operations

Remote operations include any inspection, characterization, or maintenance performed by humans through remote means. This provides the key advantage of enabling maintenance tasks in areas where human access is precluded under the ALARA principle. Aside from this, remote systems can be more resilient than human counterparts, and provide capabilities that would not otherwise be possible, such as higher payload capacities. Hence, there are benefits to using remote operations beyond human safety considerations, although their implementation requires a significant initial design effort to produce an effective and well-integrated system.

On JET, remote operations are conducted from the Remote Handling control room, using the MASCOT telemanipulation system. The team use 18 monitors in the control room, shown in FIG. 11.40, which display the visual feeds from 14 cameras positioned inside the vessel, as well as various sensor readings and the Virtual Reality (VR) model. The VR model uses real-time position feedback from the actuators in the system to show a representation of the RM equipment moving with respect to the fixed reactor structure. The VR representation cannot display the full physical behaviour of bodies (such as the sag of the boom), so has a positional accuracy of ±50 mm. Nonetheless, it provides vital environmental awareness for the operators, who use the camera information to compensate for any discrepancies.

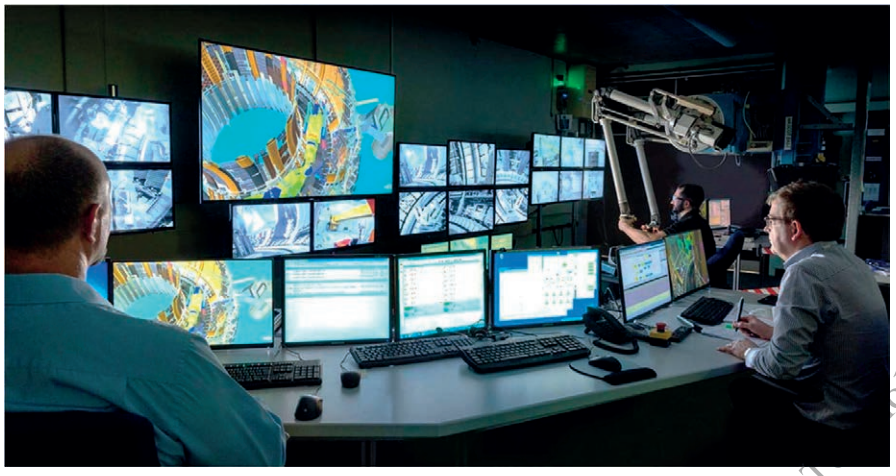

FIG. 11.40. The JET Remote Handling control room during a maintenance campaign, showing the VR model in the large central screen, and the MASCOT operator (centre).

To control the equipment, the operators use a range of human–machine interfaces. These include the master manipulator control arms and foot pedals with which an operator controls the MASCOT arms, as represented schematically in FIG. 11.31. When manual control of the boom is required, the operator controls a joystick which provides simple commands such as "move forward". A virtual rail translates this instruction into the control signals required at each joint to ensure the boom moves safely along the prescribed toroidal path. Boom movements are constantly monitored for possible collisions from the control room, where operators can press emergency stop switches to interrupt the operation and assess the situation if needed. Conventional PC keyboards and mice are also be used to input information and commands into the various control systems. For instance, one of the operators uses a Graphical User Interface to lock and unlock the MASCOT grippers, which ensures that they cannot be accidentally released, and the payload dropped.

11.2.3.3 Resourcing considerations

Operating a RM system with high reliability requires a considerable amount of human resource. For instance, a five person team is usually required to operate MASCOT, operating in two shifts over 16 hours. The roles are defined as:

- MASCOT Operator – Controls the MASCOT manipulator.
- Octant 5 Boom operator – Drives the octant 5 boom.
- Octant 1 Boom operator – Drives the octant 1 boom.
- Deputy Responsible Officer – Supervises and assists MASCOT operation, cameras, services, and general procedures.
- Responsible Officer – In charge of all operations, operates the operations software platform (see Section 11.2.5.4).

Beyond those directly involved in controlling the equipment there is also an on-site service desk consisting of:

- Equipment Manager – Oversees equipment being prepared for deployment, populates operations databases with equipment data.
- Facilities Operations manager – Oversees suited personnel in the RM facilities adjacent to the reactor and the equipment within.
- VR Engineer – Creates visual data for use in the VR model.
- On-call engineers – Several mechanical and electrical specialists are on duty on a rota system to tackle unexpected issues or faults with RM equipment.

These are all highly trained staff who have specialist knowledge of the RM systems they operate, and how these integrate with the wider plant. This experience is built through the extensive training and rehearsal work carried out prior to a RM operation being executed. Maintaining a close collaboration between those operating the equipment and those involved in its design, testing and development also helps build familiarity with the technology. Outside of campaigns, staff maintain and repair equipment, plan and validate operations, update procedures, and review past shutdowns to identify areas of improvement.

It follows that having the necessary level of staffing for undertaking efficient reactor maintenance requires a significant investment in skills and knowledge, which can take years to build up. This factor must not be neglected when planning the maintenance strategy of a new plant. Hence, consideration should be given to the initial recruitment, ongoing training and long term retention strategies for staff involved in reactor maintenance.

11.2.3.4 Balancing human intervention and remote operations

Within the plant maintenance strategy, a key consideration is how and where to use direct human intervention for maintenance tasks. Above all, this decision must be guided by the principle of ALARA, on which basis human access into many parts of the reactor will be strictly forbidden due to radiological and toxicity risks. As discussed in Section 11.1.3, there is also a wide range of other industrial risks which must be considered before an area is deemed sufficiently safe for human access.

As fusion plants develop, the risks to humans performing maintenance will increase, so more and more operations will need to become remote. In principle, having zero manual intervention would provide the lowest possible risk to humans. However, achieving fully remote operation for all possible maintenance task is very challenging with current technology levels. In JET for example, fully remote in-vessel maintenance is regularly used, but human intervention is still required for most of the supporting maintenance operations (see Section 11.2.5.2). Hence, a mix of remote and hands-on maintenance is typically required, but the right balance between the two is a complex design question.

Once human safety targets are met, the guiding aim should be to choose a mix which provides a sufficient level of plant availability at the lowest through-life cost. However, estimating costs accurately can be very challenging when dealing with immature technologies like fusion. In this regard, having clearly defined plant requirements is essential, as these provide the base on which the overall maintenance strategy will be developed. Different maintenance models can be tested against requirements to assess their suitability and determine which solutions perform better against key metrics.

11.2.4 RM plant infrastructure

An effective RM system needs to be highly integrated within the plant it serves. This has direct implications on the plant building and infrastructure requirements, primarily due to the need for RM facilities and the transportation of materials between these and the reactor areas.

11.2.4.1 RM facilities

Many maintenance operations cannot be conducted within the reactor due to their complexity, the need for specialist equipment, or the limited access inside the reactor. For instance, components which are returned to the vessel after maintenance will need to go through a recommissioning process, which may include tests such as visual inspection, mechanical checks, coolant circuit integrity, electrical compliance or optical tests [11.12]. In addition, although waste management falls beyond the scope of RM activities it is often necessary to undertake remote inspection, classification, cleaning, or packaging of items which must safely exit the plant to be discarded as radwaste elements. For these reasons, reactor plants need to be equipped with RM facilities designed to accommodate and process contaminated and/or radioactive material.

The size of these facilities, and the type and amount of equipment within them depends on the capabilities and processing delivery rate required. These are determined as part of the wider plant maintenance strategy and defined in the Maintenance Management Plan (see Section 11.2.1). Driving factors include:

- Frequency of component maintenance
- Size and quantity of components to be processed
- Types of contamination and radiological hazards of concern
- Types of maintenance required
- Speed of maintenance and decontamination operations needed
- Time allowable for the reactor shutdown
- Maximum radwaste that can be temporarily stored in the RM facilities before being sent to permanent radwaste processing, including tritium inventory

As a comparative example, the Beryllium Handling Facility (BeHF) at the JET reactor receives components and RM equipment for maintenance and decontamination. Historically, the principal hazard concern in JET has been beryllium contamination so hands-on maintenance can be conducted throughout the BeHF, although it has strict access control and PPE is required to carry out maintenance operations. FIG. 11.41 provides a simplified schematic of the

BeHF, showing the classification of working areas by level of risk to operators, contamination control access barriers, docking locations for transportation containers (see Section 11.2.4.2), as well as approximate dimensions.

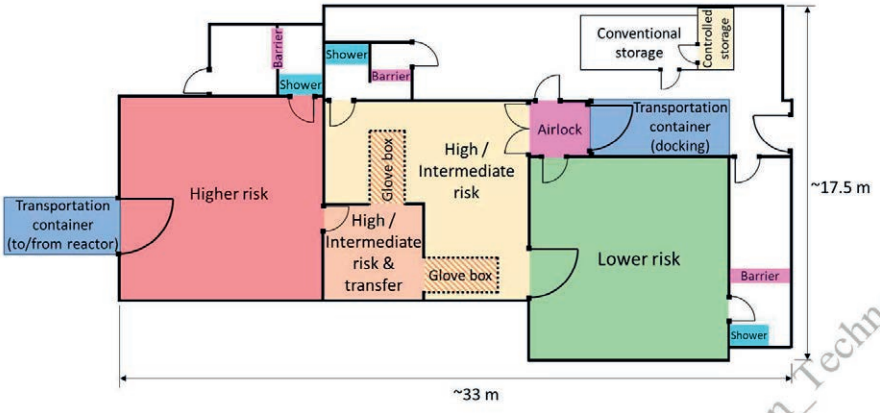

FIG. 11.41. Schematic of the JET Beryllium Handling Facility layout.

In contrast, an additional hazard concern for ITER is the high levels of activated and tritiated dust, which will deposit on RM equipment. Because of this, the ITER RM facility requires a radiologically shielded "hot cell" area, in which remote decontamination can be performed, to reduce radiation levels sufficiently to allow safe hands-on operations [11.13].

Within the RM facilities, the same considerations for remote operations apply as in other parts of the reactor. Equipment such as manipulators, viewing systems, or a wide variety of tools will be required to execute the full range of tasks. If large components must be processed, high payload deployment systems like cranes are necessary. As the components being processed pose serious hazards, access to RM facilities is limited, which makes recovery of failed systems a complex operation. Reliability of the RM equipment in the facility is therefore paramount, as a reduction of its throughput capability can directly impact the maintenance campaign duration.

11.2.4.2 Transportation

Maintenance activities will necessarily require the movement of components, equipment, supplies and consumables, typically between operational areas such as the vacuum vessel and the RM facilities. The risks associated with radioactive and contaminated items become much more significant when they are moved between locations, as this may imply crossing confinement barriers. Hence, transportation has a critical interface with plant safety, even though the latter is not a direct responsibility of the RM system. For radioactive items, the priority must be to shield personnel and sensitive plant systems from the harmful effects of radiation. For contaminated items, the focus is on limiting the spread of contaminants to ensure they remain within designated areas.

The typical safety strategy is to have two independent hazardous material confinement systems, referred to as Primary and Secondary barriers, which are operational at all times. The first is designed to prevent releases of radioactive materials into working areas which are accessible to radiation workers. The second barrier prevents releases of contamination to areas accessible by non-classified radiological workers, the general public and the environment. Before an access point is opened to permit the flow of material, measures must be put in place to ensure the two barriers are not broken. For example, temporary barriers may be installed, or the access point may be fitted with an airlock. The transportation systems must be compatible with the plant safety strategy, and this in turn must permit a suitable material flow rate which prevents bottlenecks and enables a high plant availability.

Transport corridors along which the material will flow are an integral part of the plant building, which cannot be retrofitted. They must be large enough to allow the largest reactor components and the associated handling equipment to pass through. Additional space will be required for turning circles and handling manoeuvres, as components may need to be positioned into a suitable transport orientation. Further space must also be reserved to allow deployment of recovery systems, as a blocked transport corridor may halt plant operations. For this reason, transport corridors should also have redundant access paths, so that any point on the transport route is accessible from two different directions.

In JET, material is transported into and out of the reactor in a secure shipping container, moved by a large gantry crane. The container docks to RM facilities using a specialist double-lidded contamination control door, ensuring that contaminants cannot spread outside of controlled areas. The container is shown docked to the BeHF in FIG. 11.41.

In ITER, the delivery between the operations zones to the hot cell is through a Transfer Cask System [11.14]. In the hot cell, the equipment is placed behind radiation shield walls and cannot be directly accessed by personnel due to the radiation levels. During transport, radiological shielding is provided by the transport corridors, and the transfer cask system (FIG. 11.42) ensures confinement of radioactive dust and contaminants inside the cask. The system is composed of a cask envelope confining the load to be transported, a double-lidded door for docking, in-cask handling equipment, a pallet that holds and aligns the cask, and an air cushion transfer system that allows the cask to remotely move and navigate through the plant.

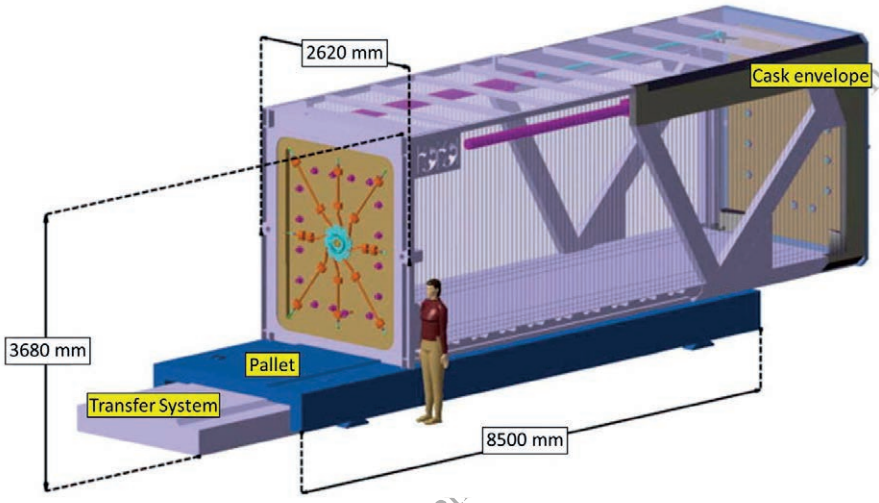

FIG. 11.42. Model of an ITER Transfer Cask, showing a human model for scale [11.14].

The plant infrastructure required to safely move and process hazardous items (nuclear-rated cranes, ground transport, telemanipulation stations, hot cell facilities, etc.) is usually large, costly, and requires extensive integration into the plant layout and design. It can therefore often be the limiting factor for the amount of hazardous material that can flow through the RM system [11.4]. Hence, logistics and transport planning are a key element of RM for achieving maximum plant availability, and must be considered at the earliest possible design stage of the plant to ensure a safe and efficient system.

11.2.5 Operations logistics

Given the difficulties of operating in harsh environments with limited human access, any mistakes made during the execution of maintenance activities could require complex corrective actions and delay the maintenance campaign. It is therefore imperative that any maintenance actions are carefully planned and coordinated to maximize the likelihood of success. This includes considering which tasks should be conducted at what time, what supporting activities will be required by the main maintenance tasks, what is required to ensure an adequate readiness status of the RM equipment, and how all this information is to be used and recorded.

11.2.5.1 Task planning and scheduling

Which tasks are to be performed during a maintenance campaign is determined by the needs of the plant systems throughout their lifecycle. Generally, a programme of preventative maintenance will be carried out to refurbish or replace components before they degrade to the point of failure. However, this must also consider wider plant logistics beyond the components in question. For example, it may be necessary to replace a component considerably before its natural end of life because access to it depends on removing another component with a different maintenance frequency. In addition, reactive maintenance may be required in response to unexpected damage caused by events such as plasma disruptions. In fusion devices, additional tasks will often be performed to carry out modifications and upgrades to the reactor.

Some tasks can happen in parallel (e.g. multiple bolts can be undone from a vacuum flange simultaneously), but others must happen in series if there is a dependency between them (e.g. a vacuum flange cannot be opened until all bolts are removed). For scheduling maintenance operations, the concept of critical path is used. This is the sequence of tasks which determines the minimum time required to complete an activity. The longer the critical path of the maintenance campaign, the longer the shutdown will last. Any delay to a task on the critical path also delays the overall activity by at least the same amount.

Often, there are multiple possible sequences in which tasks could be scheduled. Critical Path Analysis [11.15] considers the list of all tasks in an activity, their duration, and the dependencies between them to establish which tasks lie on the critical path. It is an essential tool to allow operations planners to schedule tasks efficiently, prioritize resources, manage operational risks, and estimate maintenance minimum durations.

The nature and frequency of maintenance tasks required by a component may vary throughout its lifecycle, depending on the operational duty of the reactor, regulatory requirements, modifications to the systems, etc. Hence, the task planning and scheduling usually changes for every maintenance campaign.

Unexpected component failures can often require unscheduled maintenance, even if they do not lead to an immediate plant shutdown. For instance, in-vessel inspections during a scheduled maintenance campaign may find previously unknown damage to a component, requiring corrective action. Providing a fast solution to unscheduled maintenance may require holding a significant inventory of spare items which are unique or otherwise difficult to source. The better designed and prepared the maintenance operations, equipment and design procedures are, the less impact these unscheduled tasks will have on the critical path.

High levels of preparation and planning are time-consuming and resource-intensive but are a necessary investment for large reactors and future power plants to prevent the otherwise unacceptable costs of long plant shutdowns. For example, the ratio between procedure preparation time and shutdown duration for the Remote Tile Exchange shutdown in JET (1998) was 4:1. The experience gained allowed this to be reduced to around 1:1 for the Enhanced Performance 2 shutdown (2009–2011). Nonetheless, the maintenance preparation still required around 26 person-years for the design of new tooling and equipment, and around 15 person-years for the design of the operational procedures [11.16]. Hence, for a maintenance campaign to be executed safely and effectively, task planning and scheduling must begin months or even years in advance.

11.2.5.2 Supporting operations

In support of direct RM operations, other activities are required to ensure the effectiveness and reliability of the RM system. In general, most RM equipment must be removed from the reactor during plasma operation. This is due to: a) the harsh environmental conditions, b) the imposed plasma compatibility requirements on all in-vessel systems, c) the need to maintain the RM equipment in preparation for the next intervention, and d) the premium placed on free space close to the reactor, which is often needed for operational reactor systems. Hence, once access to the reactor and adjacent areas is allowed, the plant must be prepared for the maintenance campaign. Tasks involved in this preparation depend on the maintenance strategy and the support systems required for the RM equipment, but usually involve deploying a wide range of infrastructure and services which remain in place for large parts of the maintenance campaign. These tasks will typically be on the critical path and so their timing directly impacts the duration of the maintenance campaign and, hence, the plant availability.

A typical sequence of tasks required to begin RM activities in JET is:

- To gain access to the ports needed for RM, some parts of the plant are disconnected and moved out of the way, such as the neutron camera.
- To allow the deployment of the maintenance equipment while respecting safety requirements, temporary enclosed structures are installed at the vessel access points (FIG. 11.43). These enable material and equipment to flow in and out of the reactor while providing a controlled space in which to manage the confinement barrier logistics. Components and equipment are posted and received through sealed containers. The structures have sufficient space to allow assembly, installation and service connection of RM equipment. As these operations are conducted by human operators in pressurized suits, the setup also requires installation of the access control, communication and breathing systems which support them.

- Once the temporary structures and the associated safety systems are commissioned, the RM equipment can be transferred to them. Here, it is installed and commissioned prior to operation, to ensure full functionality after transfer.
- The port accessing the vessel can then be opened and a first assessment of the in-vessel area can be performed to ensure the conditions are as expected to allow the maintenance schedule to be carried out as planned.
- Static services are then deployed, followed by the static systems such as the cameras and lighting that provide vision for the control room operators during the maintenance campaign.
- Protection covers are then installed over components to prevent them being damaged by RM equipment as it moves into and around the vessel.

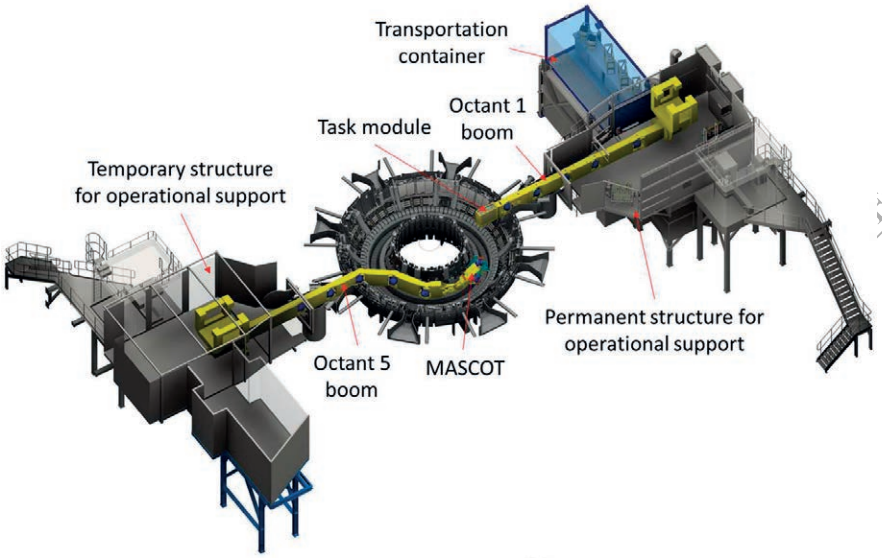

FIG. 11.43. The JET RM system with booms deployed, showing the temporary structures erected to support operations.

Once RM systems are ready for use, the first and last tasks conducted in-vessel are visual surveys, to obtain a reference point of the state of the reactor before and after intervention. During maintenance operations, periodic inspection, servicing, re-commissioning and re-calibration of critical RM equipment is required to keep it working optimally. Although this adds to the overall duration, it is an investment in time which helps prevent much more time-consuming failures.

Finally, it is worth noting that after an operation campaign in reactors where activation of materials is expected, a "cooldown" period is often scheduled. This allows radiation to decay to levels which either allow safe human access or, at least, minimize radiation damage to the electronics in the RM equipment. The duration depends on the neutron flux produced during the operation campaign and the materials in the reactor. In JET the typical cooldown period is around 4 weeks, and this may increase to the range of a few months in future power plants. This represents a significant time overhead which negatively affects plant availability, and so the maintenance strategy must take it into account to try to reduce its impact as far as possible.

11.2.5.3 Inspection and maintenance of RM equipment

After use, the RM equipment itself must be put through an inspection, cleaning and maintenance program. Some items must be recommissioned and placed in a standby state, ready to be deployed again at short notice, should it be required.

These inspection and maintenance tasks will not usually affect the operation of the fusion device directly. However, they must comply with the wider plant waste management and safety strategies, and are driven by the required readiness level expected from the RM system. A typical work plan will involve:

1. Process the equipment to control and minimize the spread of contamination.
2. Carry out a full inspection to monitor the equipment condition.
3. Perform any required repair, refurbishment or reconditioning tasks.
4. Recommission the equipment, demonstrating it still performs as stated in its specifications.
5. Store the equipment in a suitable location, updating inventory records to ensure it can be found and accessed quickly if required.

Once equipment is stored, periodic maintenance will be required to keep it ready for deployment at short notice. For instance, batteries of electronic equipment may need replacing, lifting equipment must undergo statutory inspection and recertification to demonstrate it is fit for purpose, and seals and gaskets must be kept in good working condition.

Decontamination of equipment is a time-consuming and resource-intensive process, usually performed with hands-on human intervention. Therefore, for equipment which is only ever deployed in contaminated areas, there is a trade-off between the cost of cleaning it after use versus the increased complexity of storing it in a contaminated state. The latter is a feasible option for some tools, depending on the level and type of contamination, and the tasks involved in their inspection and recommissioning.

Moderate sized RM equipment will usually be maintained in dedicated RM facilities, as described in Section 11.2.4.1. However, the maintenance of larger systems such as high payload cranes inside hot cells can pose a challenge. These systems are usually integrated directly into the reactor building infrastructure, and their disassembly is usually not an option. If hands-on maintenance is required, additional building infrastructure will be required that allows such equipment to move into a secondary controlled area, separate from the main hot cell, which can be isolated and conditioned for human access. This demands a significant amount of space, so will impact the design of the building.

11.2.5.4 Information and data management

The design of equipment and operations generates a wealth of information which is critical to the success of RM operations. This information must be readily available to the operations team when required, so needs to be up to date and easy to find. Because of this, a single software application is used to provide single-point access to a wide range of types of information. In JET, this system is known as the Operational Management System (OMS).

The OMS provides access to all technical drawings and documentation of the RM equipment and components. This is necessary to determine dimensions, masses, interface points, centres of mass, material composition, etc., which help operators plan handling operations when faced with unexpected scenarios.

Once an operation has been designed, tested and validated, a step-by-step sequence description of the operation is generated. This starts with the tasks required outside of controlled areas, through to the completion of the operation and removal of the RM equipment used. It also includes grip locations, bolt torque values, colour identifiers, and other points of interest. This sequence is used during operation to ensure that all actions are performed in the correct order and is presented as flow chart called an Active Process Map (FIG. 11.44). It is imperative that a quality control process is implemented within the RM strategy to ensure that any changes that are made to a task's operational sequence are correctly recorded and all databases are updated to reflect them. This prevents errors being made during operation which can severely impact the maintenance duration. Controlled procedures also allow tasks to be safely and repeatably performed by different operators, even if executed years after the task was first created, which is not unusual in long term fusion projects.

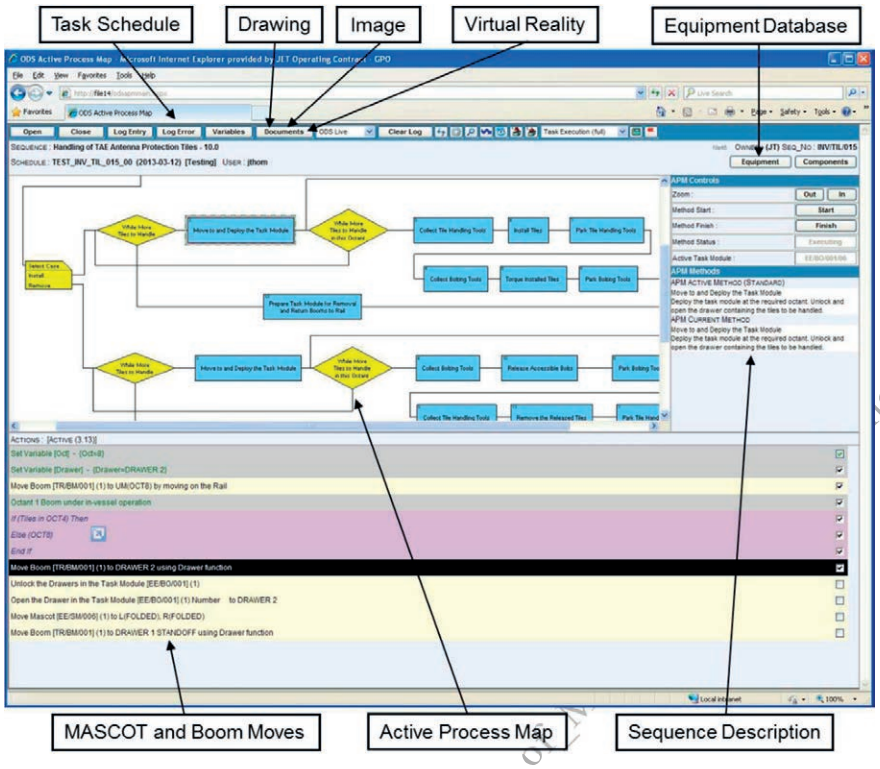

FIG. 11.44. Active Process Map viewer used for JET RM operations.

JET has 1289 different tools in its database. Including duplicates and spares, 3795 individual items are stored and maintained. An equipment and spares management database is required to control such a large inventory, and the OMS provides access to it for planning operations and contingency actions.

Equipment and tools need to be tracked to know which ones are being used and where they are in the plant. Not only does this help prepare and execute tasks but is also key to ensuring that no foreign objects are unintentionally left behind after maintenance, which could cause severe damage once the reactor becomes operational. Operators also need to know which tools are ready to be used, which are undergoing maintenance, which have proven to be less reliable, etc. For this reason, the OMS shows inspection and maintenance logs of all RM equipment and tools, including historic contamination analysis results.

The information accessed through OMS is not just essential during operation, but also for auditing purposes, both internal and external. Internally, keeping detailed logs of the condition of components and equipment, work completed on the reactor, and any deviations from the planned operational sequence is a cornerstone of quality control. This information is essential for ensuring the correct operation of the reactor and diagnosing the source of any faults that may arise. Additionally, like other industrial sites, fusion plants have a duty to comply with relevant regulation. Part of this compliance will include keeping externally auditable records of the operations conducted, so as to demonstrate that any potential risks are being managed responsibly and in accordance with the law.

11.3 REMOTE MAINTENANCE DESIGN PRINCIPLES

The design of a RM system is driven by a need for reliability and error free deployment, as the lack of human access into reactor areas makes mistakes very costly in both time and resources. This reliability is built through careful consideration of the environmental conditions during maintenance, the application of design philosophies intended to reduce the likelihood of errors, and extensive use of physical testing for verification and validation.

The maintenance strategy defined in the Maintenance Management Plant will set the goals and objectives around which the plant design will coalesce. However, an effective implementation of the strategy is only possible if maintainability is embedded into the components and the plant as a whole, and not just the RM systems. This requires close interaction between the component/plant designers and the RM teams. The former must comply with RM requirements, while the RM system must provide sufficient capability to avoid stifling the component or plant performance. Arriving at a RM-compatible design therefore requires a common understanding of the challenges, a

willingness to make design compromises from all parties, and a shared goal of achieving a fully functional plant with high availability.

11.3.1 Environmental conditions during maintenance

The harsh conditions inside fusion reactors not only affect human operators, as described in Section 11.1.3, but also impact the RM equipment and how it can be used. Although conditions in experimental reactors have historically been relatively benign, the requirements of future fusion power plants will lead to conditions which will severely impact the RM systems. Hence, understanding the environmental constraints is essential when designing RM systems.

Components activated by neutron bombardment will emit radiation after plasma operation. This can limit the material selection for RM equipment, as some conventional materials such as PTFE plastic will suffer accelerated degradation. In future reactors, radiation levels during maintenance are expected to be sufficiently high to significantly reduce the lifetime of electronics, which restricts how they can be used within RM equipment.

Activated items will self-heat, which will increase the ambient temperature within fusion power plants. This could introduce difficulties in the heat management of some elements of the RM equipment, such as actuators and sensors. In addition, higher temperatures will cause items to thermally expand, which may introduce a source of uncertainty and error when trying to accurately position items relative to each other inside the vessel.

Some environmental conditions such as radiation and temperature will depend on the operation cycle of the plant, so could vary between maintenance campaigns. Further, as the plant ages defects such as thermal warping and material embrittlement will begin to play a more prominent role, and this may need RM procedures to adjust accordingly.

The consequences of seismic events need to be considered during the design of the plant and RM systems. The seismic scenarios which are relevant to a given plant will depend on its geographic location, and the tolerable consequences will be driven by safety and commercial considerations. For instance, ITER systems must consider a low level seismic event after which the plant must be able to restart and operate without special maintenance or tests, as well as a high level event under which the primary and secondary containment must survive to ensure no radiological release [11.17]. Seismic load cases can be some of the most severe and are particularly challenging for RM systems. This is because applying the seismic accelerations to bodies that are being handled significantly drives up the payload capacity requirements for safe handling. In addition, the dynamic behaviour of the handled bodies during the seismic event need to be studied to assess whether the safety clearances are sufficient to prevent damaging contact between bodies, and this adds considerable complexity to the analysis.

The harsh conditions lead to the use of relatively exotic materials which can sometimes introduce additional constraints for the RM systems. For instance, the reduced activation EUROFER97 steel considered for the European DEMO reactor [11.18] requires time-consuming heat treatment after being welded, unlike more conventional steels. As it is also a ferritic steel, it will display magnetic behaviour after the reactor magnets are switched off. This could lead to components which are affected by magnetic fields as they are being handled, making it harder to accurately move and position them inside the reactor.

Metallic dust can pose a problem for robotic joints, and affect connectors of service supplies. As it can also be a radiation hazard (due to activation) and toxic (particularly beryllium dust) to humans, RM systems deployed inside reactors require decontamination after use. Designs should strive to make decontamination simpler through easy-to-clean geometries, sealed joints, or gaiters.

Cleanliness inside the vacuum vessel must be maintained both to maximize vacuum pump-down rate and to ensure a sufficiently pure environment for plasma operation. This makes the use of many standard technologies much more difficult, for instance lubrication greases, cutting fluids, and conventional hydraulics. The latter is particularly problematic when handling heavy payloads, as the power density of electric powered actuators is significantly lower than that of hydraulic systems. Because of this, some RM equipment in ITER has been developed with water based hydraulic systems, which uses demineralized water to ensure that any leakage will evaporate without leaving residue [11.19].

The radiation and heat levels will also preclude the use of elastomers in demountable vacuum joints. Metallic seals are an established alternative technology but must be plastically deformed to provide a vacuum tight seal. This drives the need for larger and more powerful RM equipment which can apply the significantly higher clamping forces.

Many of the component geometries of fusion reactors are determined by physics requirements, such as the toroidal field coils or in-vessel antennas. These shapes are usually difficult to handle as they are often asymmetric or have delicate protrusions which must be protected during transport. Further, space close to the vacuum vessel will be at a premium, due to the large number of ancillary systems required to operate the reactor. This leads to densely packed reactors with limited access routes, making deployment and movement of RM equipment much more challenging.

11.3.2 Systems engineering

Fusion plants are highly complex machines with many different requirements which are technically challenging to achieve. A particular challenge for RM is the high degree of integration needed with the other reactor subsystems. On the one hand, integrating the maintenance strategy and RM systems must happen at the earliest possible stage to ensure designs develop to be compatible. On the other hand, however, the technical design of RM equipment and operations often requires detailed information about the components and their maintenance requirements, which is not usually available during the early design stages. These conflicting demands can be partly tackled through a systems engineering approach.

Systems engineering is a discipline that focuses on the design of the system as a whole, rather than on its individual parts [11.20] [11.21]. It is extensively used in the design and integration of highly complex systems in all branches of engineering, and includes subfields such as requirements elicitation, architecture definition and risk management. Its underlying principle is "systems thinking", a mindset based on abstracting the underlying properties of a system's constituent elements in such a way that the interactions and dependencies between the elements can be better understood and communicated. Systems engineering techniques are methodical, so can be applied to a wide variety of different problems while ensuring a thorough approach which prevents omissions. Further, the ability to capture and communicate abstract information about components and their interactions is not only important during the design, but becomes invaluable throughout the lifetime of the system, as it evolves and adapts to changing circumstances.

The system engineering approach helps develop a robust and reliable RM system by providing techniques which allow it to be understood and defined as a single cohesive entity, even if its various parts are physically distributed throughout the fusion plant. This way of thinking aids design integration, standardization and modularization, which are all fundamental RM design principles.

In the context of RM design, a key tool derived from systems engineering is functional design, which focuses on analysing the underlying functions of an item or process. These are the core actions which the item or process is intended to perform. For instance, one of the functions of a plastic cup will be "holding a volume of liquid". Importantly, these functions are abstracted beyond the physical details of the object in question, and so the same function of the plastic cup could be shared by a metal barrel or even a swimming pool. Understanding the common elements of disparate systems allows making reasonable comparisons which inform design decisions.

11.3.3 Integration of equipment and operations

When designing RM interventions, two aspects must be considered together: equipment and operations. The former can provide the capability needed to accomplish a task, but only if used as part of a well-designed operation. The success of the maintenance procedure depends on correctly executing the necessary sequence of tasks with the appropriate tool, in the right order, and in the most efficient manner possible. Thus, the equipment design and development is driven by the operations, and vice versa.

11.3.3.1 Design philosophy

In maintenance operation design, the core aim is to minimize the likelihood of errors. Due to the limited human access, correcting even simple mistakes such as installing a component incorrectly, dropping a small item, or forgetting to prepare the right tools can lead to significant delays in the plant's shutdown schedule. Further, a failure of the RM system can lead to significant damage to components. In fusion devices, these are often one-of-a-kind experimental items, whose replacement will be very costly and most likely impose very long delays. Many maintenance tasks will be repeated multiple times over the course of a campaign and must be correct every time, so high operational reliability is essential. For these reasons, the RM design philosophy focuses on, firstly, preventing failures from occurring and, secondly, putting measures in place to mitigate the impact of any failures that do occur.

The risks involved in each operation and the likely impact of a failure can be better assessed as the design matures and experience builds. A common approach to identify operational risks at an early design stage is to rehearse the operations, firstly in digital simulation and then through physical mock-ups. As the design iterates, provision can be made in the design to mitigate identified risks.

RM-compatible bolts (FIG. 11.45) are an example where design features have been derived from operational requirements. The taper on the tip of the bolt helps locate it in the hole, the lead-in allows the shaft to engage before the threads to ease alignment, and the thread is feathered to prevent cross-threading.

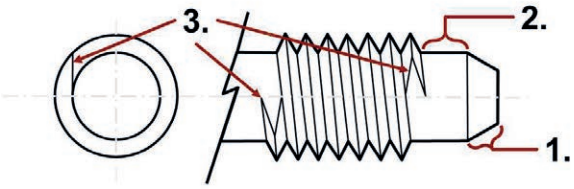

FIG. 11.45. RM-compatible bolt features. 1) tapered end, 2) lead-in, 3) feathered thread.

RM-bolts are often only partly threaded, to allow them to remain captivated, as illustrated in FIG. 11.46. The bolt is inserted into a threaded hole, which has a clearance pocket larger than the thread length. This allows the bolt to be retained when removed from the component, and not be dropped accidentally inside the reactor. It is also spring-loaded, to ensure it clears the threads on the component after unfastening.

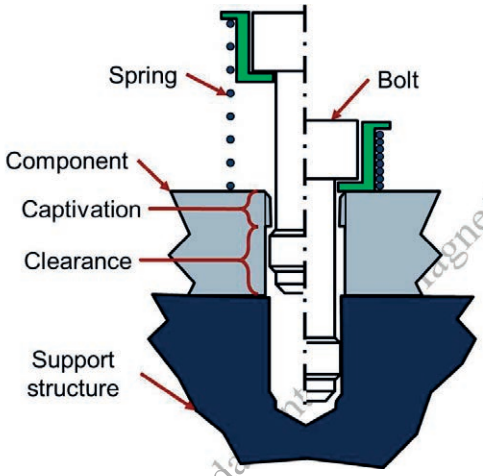

FIG. 11.46. Illustration of the operation of a captivated spring-loaded bolt.

General good engineering practices applied in other industrial settings are also applicable to the design of RM operations. For example, the 5S methodology (Sort, Set in order, Shine, Standardize, Sustain) [11.22] is used for efficiently organizing worksites and improve work control. Documentation and user manuals should provide clear, concise and complete operation instructions, so that operation staff with no prior experience of a task can effectively execute it.

11.3.3.2 Handling and kinematics

As part of their maintenance, components need to be handled to be connected/disconnected, installed/removed and transported. The design of the component significantly impacts how it moves through the plant, what equipment is required for handling it, and how much space must be reserved for maintenance activities. Hence, consideration should be given to the component's through-life handling requirements from the earliest possible design stage. As these determine space allocations and the specification of working areas, it is crucial that they are appropriately recorded through the component's design and included in the building requirements, to ensure the building layout is compatible with the maintenance strategy.

Installation and removal sequences can often involve relatively complex kinematics, particularly in confined spaces. It is important that these operations are designed within the capability of the RM equipment. Manipulators, for instance, will have a finite working envelope (see FIG. 11.47), which will restrict how components can be moved.

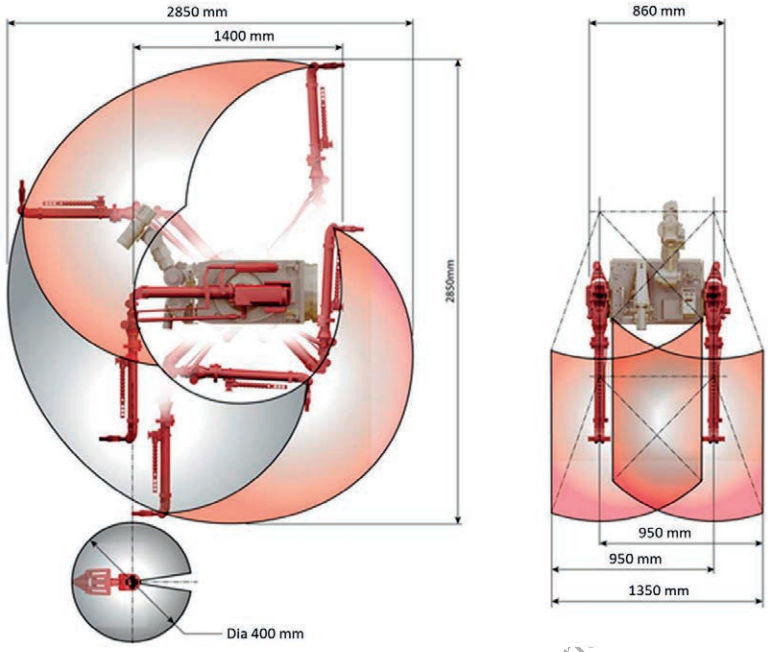

FIG. 11.47. Working envelope of the MASCOT manipulator. Left: side. Right: front.

The handling operation will be controlled with position and motion sensors, usually mounted on-board the RM equipment, such as encoders on the joint motors. However, it is normally good practice to use a secondary sensor network which can confirm a handling operation has been successfully completed. This could include limit switches which are activated when contacted by the handled object, force sensors to detect when payloads have been released, or visual confirmation from operators using specially positioned cameras.

The presence of obstacles can impede the movement of manipulators and severely limit their working envelope. Hence, component kinematics must take into account other hardware items that may be close to the worksite when the operations are being performed. For example, FIG. 11.48 shows a representation of the ITER neutral beam cell before and after including the ancillary support systems. The large number of items turn the area into a relatively confined space, which has a significant impact on access paths and handling strategies of the various components in the cell.

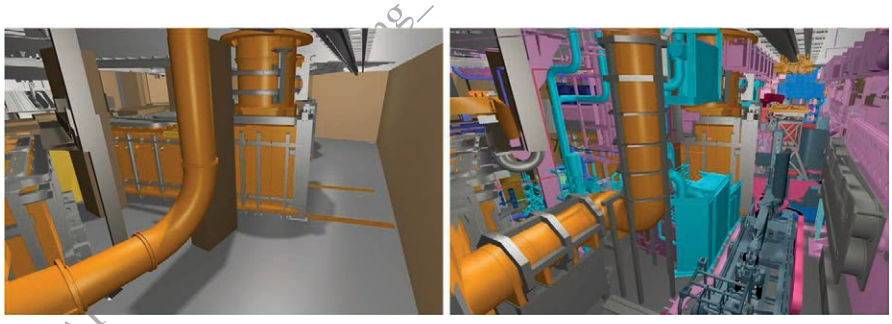

FIG. 11.48. ITER neutral beam cell representation, showing the space taken up by ancillary systems. Left: cell before integration. Right: after integration [11.8].

In confined spaces, it is often necessary to define deployment zone reservations. These are estimations of the space required to carry out a maintenance procedure on a given component. They are based on the expected size of the equipment needed, the assumed operations to be carried out, and the expected plant configuration at the time of operation. Suitable margins will also be included to account for uncertainties. These zones typically define keep-out zones in which no other item can be permanently placed, to ensure that sufficient space is reserved for performing handling operations. FIG. 11.49 shows how these zones are defined and recorded in technical documentation used for remotely maintaining pipes in the ITER neutral beam cell.

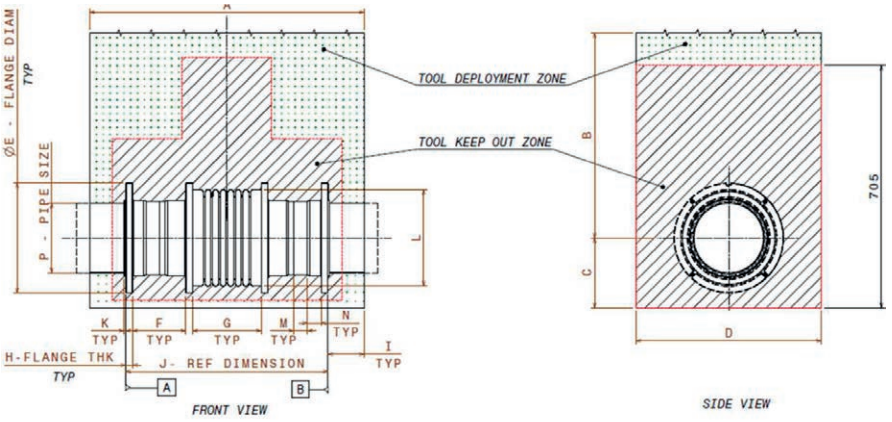

FIG. 11.49. Technical drawing of ITER neutral beam cell pipework showing the defined tool deployment and keep-out zones.

During transportation, the orientation of an item may be different to its usual one when installed. One reason for this is that it may need to be carried through narrow access points, or follow complex kinematic paths to avoid obstacles. Another is that handling and transport orientations of large items should aim to locate the centre of gravity of the item as low as possible, which makes transport more stable and lowers the item's potential energy, reducing the consequences of a drop. The relevance of these different orientations is that they can constitutes different load cases to the operational ones, and must be considered in the component design. The RM system must be able to assume that a component will retain its integrity when being lifted and handled.

To enable handling, components will need features which interface with the RM equipment, such as lifting and gripping points. These must be accessible whenever the component is to be handled, which means that their location must take into account the full component lifecycle and the presence of other components and systems which could obstruct access. Further, these handling interfaces must be located in such a way that the payload requirements of the RM systems do not exceed capacity. For example, lifting points should be over the centre of gravity of the item, to minimize torques on the handling equipment. Cranes can only perform straight vertical lifts, so must have sufficient space to position themselves directly above the component to be lifted, with direct, unimpeded access for lifting cables. In cases where a component's mass exceeds the available payload handling capabilities of the RM system, it may be necessary to breakdown the component design into different parts, which are transported separately and then assembled in-vessel.

If a component is to be put down on the floor, large laydown areas which are clear of any obstruction may need to be reserved in the maintenance areas. The component may also need structural hardpoints that can support the item's self-weight without damage. It is often necessary to lay down the component in a specific orientation for certain maintenance procedures such as visual inspection, which could require a supporting jig to be available in the laydown area, with the matching fixation interfaces present on the component itself. If the maintenance of the component requires disassembling it, even more space will be required to easily lay out the various subcomponents throughout the operation.

11.3.3.3 Alignment

A key step within almost all maintenance tasks is bringing together the reactor structures, the components and the maintenance equipment in a controlled manner. For instance, mounting components onto the vessel, connecting a cable or gripping an item with MASCOT all require controlled and reliable relative positioning, an action referred to as alignment.

The accuracy with which bodies can be aligned is limited by the achievable positional measurement resolution, the level of control afforded by the driving actuators, the practicalities of manufacturing, and the dynamics of the body in motion. Components are not perfect geometric shapes and manufacturing processes can only guarantee their dimensions within a certain error margin, known as geometric tolerance. Vibrations induced in the body as it moves can lead to significant deflections, which is particularly problematic for long, slender objects. Hence, in order to guarantee a minimum level of accuracy, RM operations rely on specialist alignment techniques.

A free body in space has 6 degrees of freedom (DoFs), 3 translational and 3 rotational, as illustrated in FIG. 11.50. The key principle behind remote handling alignment is the sequential removal of DoFs by applying passive

kinematic constraints. This breaks down the full complexity of the operation into simpler and verifiable steps. In this way, the kinematic path of the bodies can be carefully controlled, which is essential in densely packed spaces. This approach also ensures that bodies which are to be held rigidly are not over-constrained, which would lead to build up of stress and uncertain positioning.

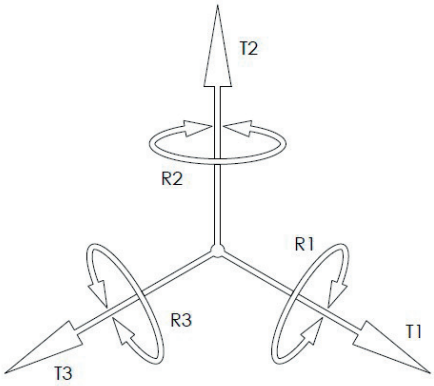

FIG. 11.50. Illustration of the 6 degrees of freedom of a free body in space.

An example of a RM alignment feature is a long ball-ended dowel and a short dowel pin (FIG. 11.51), which has been used to align electrical connectors in JET. TABLE 11.5 describes the alignment process, and how DoFs are eliminated sequentially.

TABLE 11.5. Description of alignment using sequential kinematic constraints.

Step	Description	DoF	Type
1	Component held in free space	6	3 Translation 3 Rotation
2	Component located on dowel ball-end	4	1 Translation 3 Rotation
3	Component located on single long dowel pin	2	1 Translation 1 Rotation
4	Component located on second short dowel pin	1	1 Translation 0 Rotation
5	Component comes into contact with mating face	0	0 Translation 0 Rotation

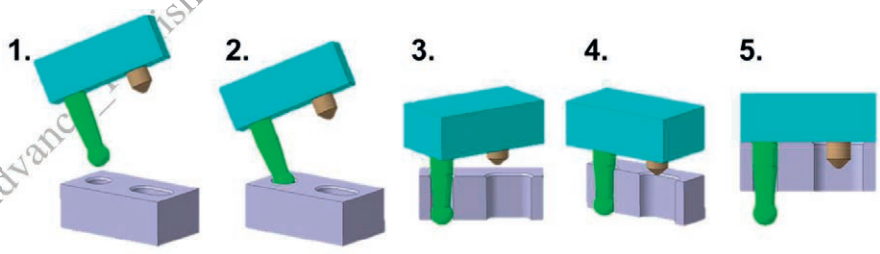

FIG. 11.51. Sequence of alignment using a long ball-ended dowel and a short dowel pin.

Although active alignment using servomechanisms to control the position and motion of a body is a potential solution, best practice in RM is to use passive features such as the dowel interface described above. Passive features are much less likely to fail, provide a known and repeatable kinematic sequence, do not require complex equipment to deploy, and provide easier repair and recovery. Other common passive alignment features include locating end stops (which limit the motion of a body along a particular direction), guide pins (which progressively guide a body into a position to reduce positional uncertainty, FIG. 11.52), and asymmetric interface geometries (which ensures components can only be installed in one position). A well-designed remote-compatible item will often use multiple different features to achieve controlled alignment.

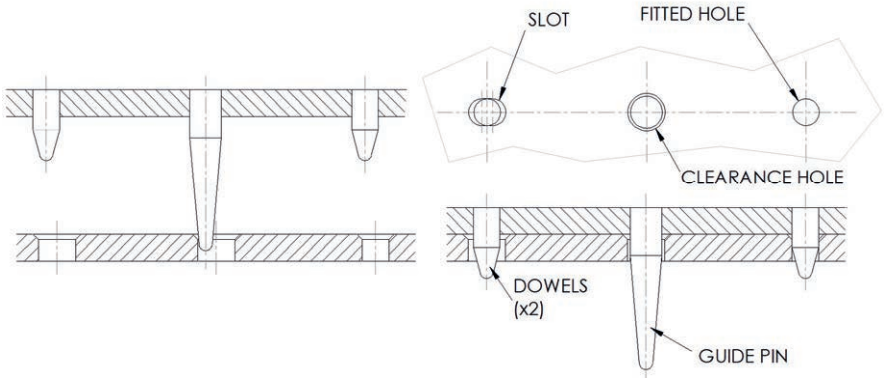

FIG. 11.52. Operating principle of guide pins. Left: before alignment. Right: interfaces correctly mated.

Assembly of two bodies is a common task when installing systems and interfacing the RM equipment with components. The action of inserting one part into another carries the risk of failure by jamming and wedging. The former occurs when an external force causes two components to lock-up during assembly (FIG. 11.53), preventing task completion. It can be recovered from by eliminating the external force. Wedging is a more serious failure in which the forces between the assembled parts are internally balanced, locking them together. Recovering from a wedging condition requires the application of an external force of often considerable magnitude. Good alignment practices are essential to prevent these failure modes.

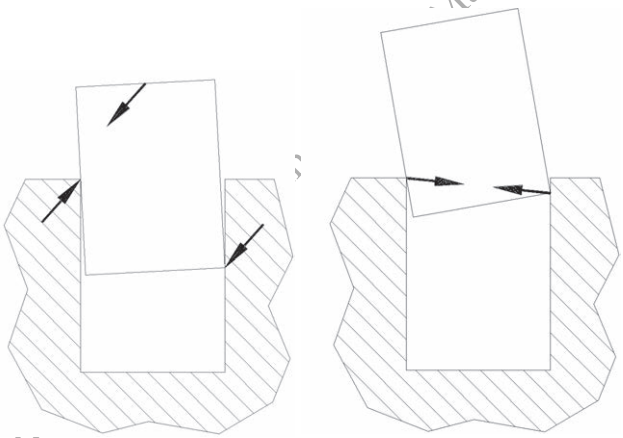

FIG. 11.53. Failure modes of a peg-in-hole insertion task. Left: jamming. Right: wedging.

11.3.3.4 Component lifecycle considerations

To design RM-compatible systems, it is essential to consider their full lifecycle in the plant and not just the installed, fully operational state. This includes assembly, commissioning, testing, storage, maintenance, calibration, transportation, deployment, operation, cleaning, rescue, recovery, inspection, re-commissioning and decommission.

The material selection affects the mass of the item, and hence the handling payload requirements. Consideration should also be given to how a material evolves under the harsh conditions over the lifetime of the plant (embrittlement, fatigue, reduced weldability, etc.), as this can demand changing handling needs over time.

Some manufacturing processes are relatively simple to apply at the manufacturing stage, such as coatings, heat treatments, etc. However, if these need to be reapplied at some point later in a component's life, they may demand unfeasible capabilities from RM facilities. This also applies when considering the repair options for a component. For example, if a particularly stringent surface finish is required for a component, any damage to it may not be repairable in-situ.

Calibration of reactor components such as diagnostics may need controlled conditions which imitate operational scenarios. The component design process should consider how and where the calibration procedures will be carried

out. If it must be inside the reactor, this could require the RM system to have to handle and operate specialist calibration equipment, such as portable neutron sources, or provide very specific service supplies. If the component needs to be recalibrated frequently or the process is very time-consuming, it could affect the maintenance campaign duration.

Aside from planned maintenance, components may need to be inspected to check for unexpected damage or faults. Consideration needs to be given to how this process is conducted. For example, if a visual inspection of a critical part of an in-vessel component is needed then line-of-sight for a camera must be provided. This may be easy in isolation, but access could become restricted by other nearby components or limitations of the RM system.

For components which exit contaminated areas for maintenance, a cleaning process may be required. Complex geometries will be much harder to clean to safe levels, so their decontamination will be more time-consuming.

The component design will heavily influence how rescue and recovery operations can be conducted. A component's fracture mechanics, ductile or brittle, can dictate how the component would behave if it was accidentally damaged. A component which shatters if dropped may be more difficult to fully recover or clean up than one with a more ductile behaviour. For failure modes which are considered more likely, features can be included which aid handling under rescue conditions, such as redundant gripping points or modular mechanical interfaces which can be easily replaced if damaged.

As fusion reactors may be designed over several decades, and will be operational for several more, obsolescence of components and RM equipment is a critical consideration. An obsolete component is one for which a replacement can no longer be readily obtained, for instance because it is no longer manufactured, is forbidden as a result of regulation changes, or relies on expertise which has been lost. If a component becomes obsolete and needs replacing, the system will have to be redesigned with a different component which performs a similar function. This typically involves very extensive rework to many other systems, as changes cascade through the plant, so can lead to long and complex maintenance campaigns or prohibitive replacement costs. Preventing obsolescence is therefore key to the commercial viability of a fusion plant. To tackle these issues, systems designed for ITER are required to have spare part availability for the operating life of the plant, a minimum of 20 years.

At end of life, components will need to be processed to exit the plant for disposal. Building-in easy separation of the parts of a component with different hazardous waste classifications enables a more effective post-life processing. For instance, if the more highly contaminated first wall elements of an in-vessel component can be easily detached, it may be possible to process the rest of the body with simpler contamination control measures. This allows waste streams to be optimized to suit the throughput needs, rather than require all components to be processed to the standard imposed by their most contaminated parts.

11.3.4 Standardization

A key strategy to achieving an efficient and reliable maintenance system is the use of standardization, through which components, equipment and capabilities are designed to maximize commonality, following an agreed set of rules. By reducing customization, the number of different maintenance procedures and tools which need to be developed and tested is dramatically reduced. On the one hand, this reduces the initial development costs of the plant significantly, contributing to the economic viability of fusion power. On the other hand, standard components allow optimized operations with improved reliability, which reduces maintenance shutdown durations.

11.3.4.1 Standardization of RM equipment

The idea underpinning standardization in RM is that common tasks or functions should have common solutions. For instance, lifting of items is a very frequent task. As most components will have different shapes, masses, and centre of gravity, using a common interface where possible reduces the variability of the operation. This means a common handling system can be used for various scenarios instead of each component needing a unique approach, which would increase cost and complexity.

Identifying common functions is an important aspect of standardization. For instance, many JET RM tools require them to be gripped by MASCOT, so they will all require an element whose function is to "interface with MASCOT manipulator for handling". This function can be separated from the design of each individual tool, and instead built into a dedicated object which is then attached to each tool. An example of this in the JET RM system is the specially designed grip block interface, which has been developed to work with the MASCOT grippers. These items are shown in FIG. 11.54, which describes their principal features.

Any new tool that shares this functional need can be equipped with the grip block to produce a compatible gripping interface without any further design work. This allows MASCOT to simply and securely hold any item that is within its payload limits, like the tools shown in FIG. 11.55. The color-coded grips also help MASCOT operators

know which MASCOT arm (left or right) should be used on which grip (gold or silver), to avoid picking up items incorrectly.

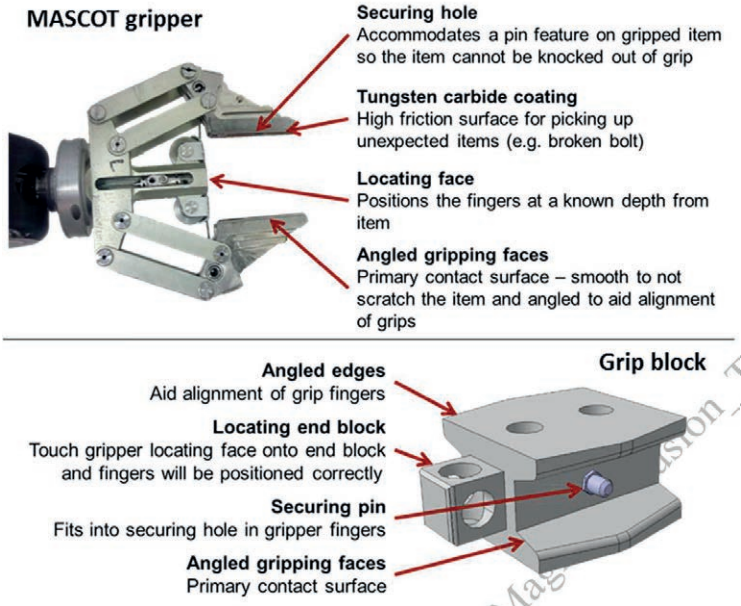

FIG. 11.54. JET RM standard gripping interfaces. Top: MASCOT grippers. Bottom: standard grip block.

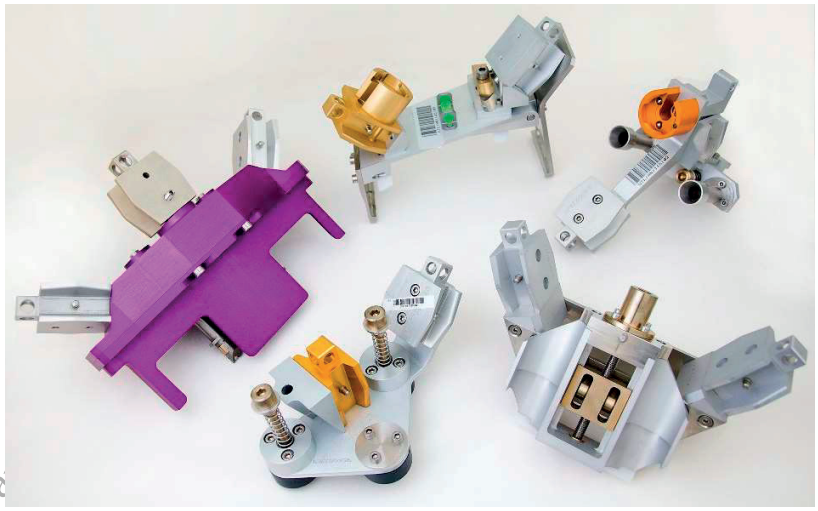

FIG. 11.55. Photographs of a range of JET RM handling interfaces, all of which have the MASCOT grip block attached.

The grip block is a bulky design feature, so cannot normally be incorporated in reactor components. To overcome this, a smaller interface is created on the component that allows a generic handling tool (FIG. 11.56) to be attached over the component's centre of gravity. The same tool can be used with several different components. On the MASCOT side, the handling tool has two standard grip blocks to allow two-handed manipulation, and a holder to carry the bolt runner.

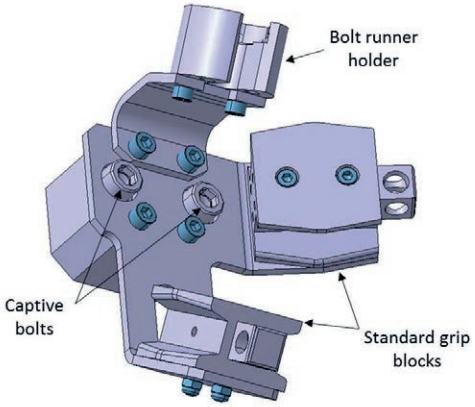

FIG. 11.56. Representation of a generic handling tool which interfaces between a component and the standard MASCOT grip blocks.

When designing operations, it is best practice to firstly attempt to design the task around existing equipment and capabilities. If this is not possible, any new RM equipment should be developed in parallel with the operation and/or component it serves. Standardization is built in by considering potential future applications of such a capability. This approach avoids producing highly specialized equipment and ensures maximum compatibility with current systems. Factors to consider include: the range of different interfaces commonly used with that type of tool, how it will be deployed, what services are available, other plant configurations the tool may be needed for, safety procedures, waste management needs, etc.

11.3.4.2 Standardization of components

For the standardization of RM tools to be fully effective, it is important that reactor components also apply compatible standardization as far as possible. By using common solutions to common problems throughout the plant, maintenance tasks can be simplified and optimized.

As a minimum, components should be designed in accordance with industrial standards. Apart from reducing procurement time and costs, this ensures a first level of commonality between components in the plant. For example, pipe diameters should be primarily driven by the size range available in standard catalogues, and not by the optimal value required for a given application.

Beyond this, however, components should adapt to the fixed RM toolset as far as possible, narrowing down design options to those that are known to be compatible with the RM systems. To this end, the Maintenance Management Plan (Section 11.2.1) must provide component designers with the common standards, best practice guides and user manuals which have been considered applicable to the plant design. Of course, fusion reactors typically consist of many novel, one-of-a-kind components, so although bespoke solutions should be avoided, they may sometimes be necessary. In this instance, it is imperative that the custom solutions be designed in close collaboration with the RM teams, to ensure the item can be maintained efficiently, and that the necessary capabilities are built into the RM system.

Standardization is particularly important when defining interfaces between the component and any other part of the plant, as this is where the work of different design teams will meet. Examples of interfaces include service supply, RM systems, control rooms, or documentation systems. By standardizing items such as electrical connectors, the assumptions regarding how the component will interact with the rest of the plant will be the same for all design teams, which prevents costly mistakes and inefficiencies. In addition, the lessons learnt during the mock-up testing and prototyping can be applied to multiple instances of the same design.

11.3.4.3 Plant-wide standardization

Standardization can be effected throughout the reactor plant, not just in the physical components but also in the working practices and information management. A particularly important example of this for harsh environments is the maintenance classifications scheme. This is a formal categorization framework which allows components or maintenance activities to be classified in accordance with some common characteristic. By grouping together tasks with similar needs, approaches can be standardized throughout the plant, harmonizing designs and procedures.

For the ITER reactor, for example, components are categorized into maintenance classifications depending on the frequency of their remote handling (RH) requirements [11.23]:

- RH Class 1: Components requiring regular scheduled maintenance by remote means.
- RH Class 2: Components that do not require scheduled maintenance by remote means, but are likely to require unscheduled remote maintenance.
- RH Class 3: Components that are not expected to be maintained during the life of ITER, but would need to be replaced remotely should they fail.
- Non-RH classified: Components whose maintenance does not require remote means, or whose failure can be tolerated.

One benefit of the classification system is that component designers can be made aware of the RM requirements which their design needs to comply with at the earliest possible design stage. This reduces the likelihood of errors or omissions during the design, reducing costs and saving time. In addition, the classification scheme allows components with similar maintenance needs to be identified early, which then enables common solutions to be found that are suitable for all items in a given class.

However, it is important to note that designs are fluid, particularly in the early stages. Hence, a component may be reclassified as the design matures, perhaps because other systems which raise the classification level are placed in the same reactor area, or because more accurate predictions of the environmental conditions become available. Reclassification could also happen during the lifetime of the plant, as conditions change throughout the reactor in response to evolving operating regimes, accident scenarios, etc. Thus, it is best practice to embed RM maintainability principles into all reactor components, which ensures the system as a whole is more resilient to changes.

11.3.5 Modularity

The concept of modularity is that complex systems can be designed as an assembly of independent functional units, which come together to form the final product. One benefit of modularity is that it allows functions to be easily replaced in the case of failure. When used in conjunction with standardized interfaces, it also allows components and equipment to be interoperable, and work with other systems within the plant without requiring extensive setup and customization.

11.3.5.1 Modular RM equipment

Modularity is key to providing RM systems with a wide range of capabilities while limiting the amount of equipment required to achieve them. Being able to easily attach different end effectors to deployers to perform different tasks is one example. JET's booms are a modular design which can be easily reconfigured by exchanging its interoperable parts, as illustrated in FIG. 11.28.

Further, modularity is also important for RM equipment in the context of maintenance, recovery and decontamination. Consider as an example the scenario of a failed motor assembly in a manipulator's arm. A modular motor assembly would be designed as a separate unit to the overall manipulator with external access to the fixations.

In a "Maintenance" scenario where the motor is changed as part of regular upkeep of the equipment, it can be removed and replaced quickly and easily, reducing the burden on the workers.

In a "Recovery" scenario the motor could have failed while being used in-vessel. It can be easily removed by a second recovery system, and then replaced in-situ. Even if the latter is not possible, the modular design gives access to the exposed arm drive, so that a tool could engage it to retract the arm, allowing the manipulator to safely disengage and exit the area.

In a "Decontamination" scenario, the RM equipment is disassembled and decontaminated. The motor assembly can be a modular sealed unit, preventing ingress of contaminants in the mechanism while allowing easy cleaning of its outer surface.

11.3.5.2 Modular reactor components

As with the RM system, building modularity into reactor components contributes to the speed and efficiency of the plant maintenance. If components and their subsystems can be grouped together into modules, it allows them to be removed and replaced easily with fewer operations, reducing the overall downtime of the machine. This enables the parallelization of the handling of the various components, reducing the assembly dependencies between them that extend the critical path.

An example of component modularization in JET is the design of the Neutral Beam Injectors (NBI). Their central support column holds together many of the different subassemblies, which allows them all to be extracted with a single

vertical lift (shown in FIG. 11.57). This makes it much easier to disassemble the NBI and transport its constituent elements into the assembly hall for maintenance.

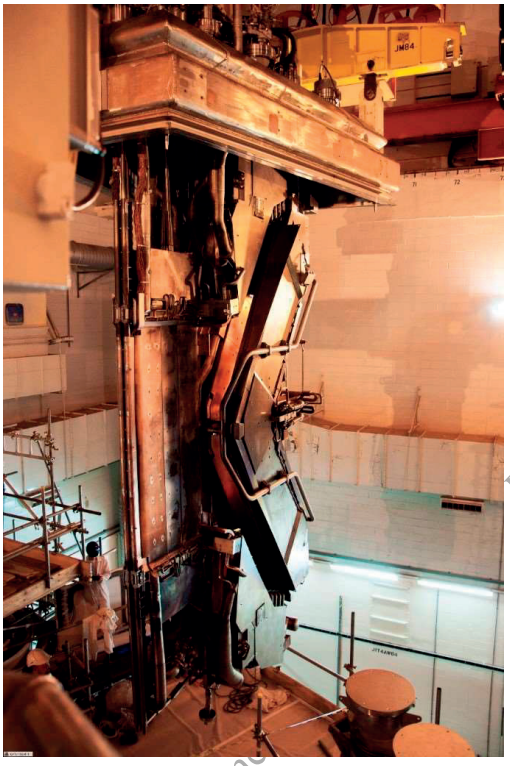

FIG. 11.57. Lifting of the JET NBI central support column.

This principle is also applied to the heating and diagnostics systems in ITER, which are installed in the reactor via modular Port Plugs (FIG. 11.58). By grouping together several of these systems into modules they can be installed and extracted together, reducing the number of operations required. Further, the modularity also allows the interface between the heating/diagnostic components and the RM system to be standardized, such that a single handling approach can be used for all port plugs [11.24], reducing the amount and variety of RM equipment needed.

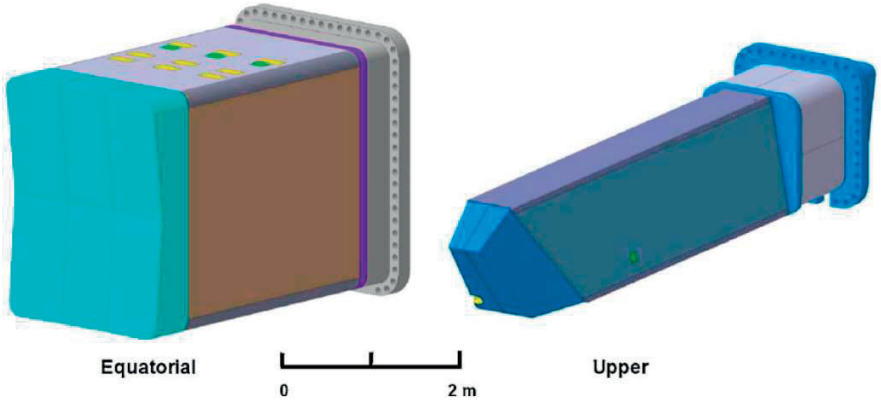

FIG. 11.58. ITER Port Plugs, which act as a modular and RM-compatible housing for a range of different heating and diagnostic systems [11.25].

When making components modular, a common systems engineering approach is to conduct failure risk analysis and group together similar functions considered to be more likely to fail. The module is provided with a simple

interface connecting it to the rest of the system, which allows it to be exchanged quickly if needed. In fusion environments, it is common practice to apply this to electrical components, as they can fail suddenly and prevent the RM systems from operating. Diagnosing the exact location and cause of the fault would be very time-consuming, so instead all the electronics can be quickly replaced as a single module.

11.3.6 Testing for verification and validation

To reduce the likelihood of errors during maintenance operations, it is imperative to demonstrate that the equipment and procedures designed are fit for purpose, a process referred to as Verification and Validation (V&V). The use of digital and physical mock-ups is central to this, and particularly relevant when opportunities for testing in the actual environment are limited.

As a testing platform, mock-ups aid the design process by allowing the underlying assumptions and requirements to be validated or disproved. The sooner this testing can be performed, the smaller the impact of necessary modifications will be on the cost and timeline of the design process. Digital simulations are used extensively during the concept and development phase, as they typically require lower investment and can be faster to deploy. However, they are no replacement for physical mock-ups when first-of-a-kind equipment is to be de-risked, due to the limitations and uncertainties associated with modelling the real world. The experience gained through hands-on testing also allows the operation team to develop best practices and share them with designers to improve equipment and operations.

Building up the familiarity of human operators with the equipment, the procedures and other team members is essential to achieving a reliable RM system, and requires extensive training in representative physical mock-ups. Unforeseen situations are not unusual when conducting remote operations so the ability to respond calmly to new scenarios is a key attribute of the operating team, which is developed by having rehearsed worst-case scenarios such as recovery from failure. Maintaining this operational capability requires ongoing operator training and continuous improvement of equipment and control software to respond to evolving requirements. Hence, physical mock-ups are required not only during the design phase but also throughout the life of the reactor, providing an efficient response to changing operational demands.

Equally as important as the hazardous environment itself is the external space through which the RM equipment gains access to it. Hence, function-defining interface features of the real world should be replicated in the mock-up. Ideally, full size mock-ups should be used wherever possible. However, designing and building large testing facilities can incur significant cost, so mock-ups should have clear objectives and delivery plans to mitigate identified risks as part of an appropriate V& V process. Full-scale testing may be preceded by smaller, simplified mock-ups to address particular concerns earlier in the design phase.

First interventions into hazardous environments will typically require approval from various stakeholders, including regulators, investors, site and asset managers, operators, designers, etc. A key function of mock-ups is therefore to generate objective evidence of whether a given solution is suitable or not, helping build stakeholder confidence. Stakeholders should be able to engage with the V&V process throughout to influence what evidence is gathered and how, and thus reach a collective agreement to begin operations. Because of this, ownership and location of physical mock-ups is critical to ensuring timely access and interaction of stakeholders over the full project life. For instance, transfer of knowledge from design teams to operations teams is critical during factory commissioning and process development.

The RM operations in the JET reactor are supported by the In-Vessel Training Facility (IVTF), see FIG. 11.59. This is a full-scale mock-up of several JET vacuum vessel octants. It has been extensively used for two decades for functional testing, process development and operator training.

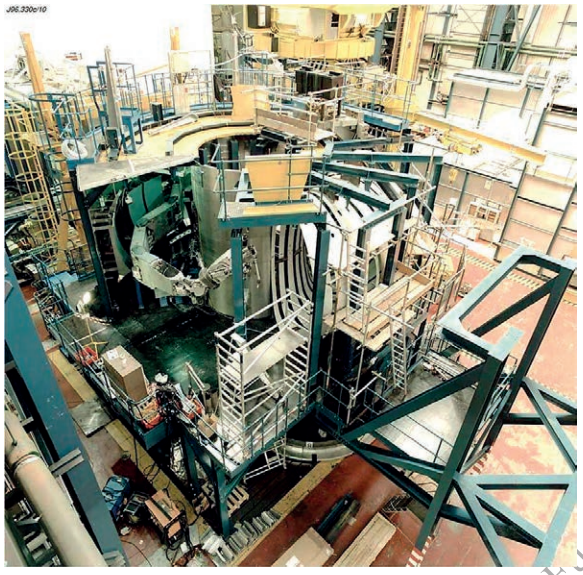

FIG. 11.59. JET In-Vessel Training Facility, showing MASCOT being deployed.

The need for full-scale mock-up maintenance test facilities has also been recognized for the ITER reactor. Consequently, the hot cell is equipped with a dedicated test stand used to validate technology and procedures, commission equipment before deployment, and train operators [11.4].

11.3.7 Rescue and Recovery

Failure of RM equipment can lead to a halt of productive maintenance activities and a delay on the critical path, which reduces overall plant availability. Because of this, when a fault occurs, all efforts must be directed at the recovery of operational capability. It is therefore essential that RM systems are highly reliable, and failures can be mitigated quickly if they occur.

After a fault occurs, its root cause must first be identified to allow an effective correction plan to be developed. Some potential failures can be foreseen through the design process, but studying all possible failure scenarios is usually not a viable solution due to the large effort this requires. Hence, key failures are typically identified with a systems engineering risk-based approach such as a RAMI assessment (Reliability, Availability, Maintainability, Inspectability). This is composed of a functional analysis, a FMECA (Failure Mode, Effects & Criticality analysis) and a reliability block diagram analysis, which are all tools to systematically consider the likelihood and impact of different failure modes within the system. Only those failure modes which are identified as posing a high risk to the system are addressed, with measures put in place to either reduce their likelihood of occurrence or minimize their impact if they materialize. Strategies for mitigating failures in RM focus on three main areas: redundancy, recovery, and rescue.

Redundancy of a system ensures that critical subsystems are duplicated to ensure a given function can be performed by the secondary equipment if the primary fails. Examples include adding spare wiring to provide an alternative power/data flow route or installing a secondary motor which can drive the equipment if the first fails. The redundant equipment does not necessarily need to allow the RM system to continue operation as normal, just provide sufficient capability to allow recovery.

Recovery is the ability of the RM system to return any failed subcomponent to a maintenance area for repair, using only its existing capabilities. Features and functions that enable recovery will have typically been included in the design of the RM system as a result of the RAMI assessment, to tackle high risk failures. For example, motors may have been over-specified to have reserve capacity to overcome failed brakes, or a manipulator may be equipped with a specialist tool to cut a winch cable to release the load during a lifting operation. On JET, any in-vessel bolt over M10 is designed with a 2 mm pilot hole (FIG. 11.60), making it easier to drill it out of the vessel if it seizes due to vacuum-induced cold welding [11.26], the bolt head is damaged, it is cross-threaded during installation, or any other potential failure occurs. Without this feature, drilling through the high-strength steel would require specialist tools and be more time-consuming. The recovery operation may also damage the hole threads, which will be a permanent feature of the vessel, so removable threaded inserts are used which can be remotely replaced as required.

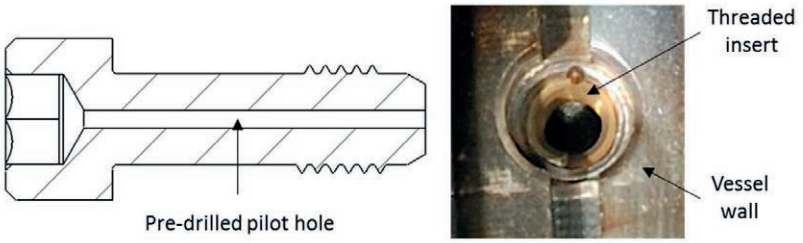

FIG. 11.60. Design features to aid recovery. Left: schematic of a pre-drilled bolt. Right: photograph of a threaded insert in JET.

Rescue is the removal of failed equipment from the restricted area using additional equipment, necessary when the RM system cannot recover from a fault with its existing capabilities. Rescue operations are typically very complex, time-consuming, and disruptive to other systems in the reactor. A rescue operation may, for instance, require the deployment of a crane to lift failed equipment out of the vessel or the development of new tools to provide a specific capability. As a minimum, all RM systems must be rescuable by some means, although, ideally, they should be recoverable too, as this minimizes the disruption caused by unexpected failures.

To reduce the impact of a failure, RM equipment should be designed to fail safe, such that the failure state is known and controlled. This is common in lifting interfaces, for instance, which remain closed by default and require an active effort to open and release the load. This ensures that in a loss of power scenario, the load remains attached to the interface. While fail-safe design does not reduce the likelihood of failure, it does ensure that the outcome of a failure is more easily managed, reducing its impact.

Operationally, steps can also be taken to minimize the likelihood of failures. Whenever two interfaces align and engage, there is a risk of damage, breaking, or failed engagement. Hence, operations can be designed to minimize the number of times engagement needs to happen. For example, some tasks can be designed in a way which minimizes the number of tool changes required. This reduces the number of times that the manipulator has to release and re-grip tools, reducing the likelihood of an accidental drop.

Specialist equipment intended for use in rescue scenarios can be designed and built as part of the overall RM system design, before any failure occurs. However, it can be very difficult to specify the requirements of such systems, as, by their nature, they are usually designed to tackle hypothetical rescue scenarios for which much of the information is unavailable. They will therefore usually be designed to be highly versatile, such that they are able to adapt to the widest possible range of potential rescue situations. This brings with it a significant cost. Thus, the decision to design and build rescue equipment pre-emptively must balance the investment cost against the increased loss of plant availability of a hypothetical failure scenario where no solution was readily available. Rescue equipment may be built but never used, so a suitable compromise in some cases is to design the equipment but not build it unless required.

An example of specialist rescue equipment is the JET Telescoping Articulated Remote Mast (TARM). TARM , FIG. 11.61, was designed to maintain and recover all equipment inside the JET torus hall on the machine exterior [11.27]. TARM was mounted on the 150-tonne crane with a MASCOT manipulator on the end of its telescopic arm. MASCOT would provide capabilities similar to a human operator when recovering failed components, while the crane could perform high payload lifts. However, TARM was never used in this fashion as the JET machine never reached the level of radioactivity that prevented people from preforming ex-vessel recovery.

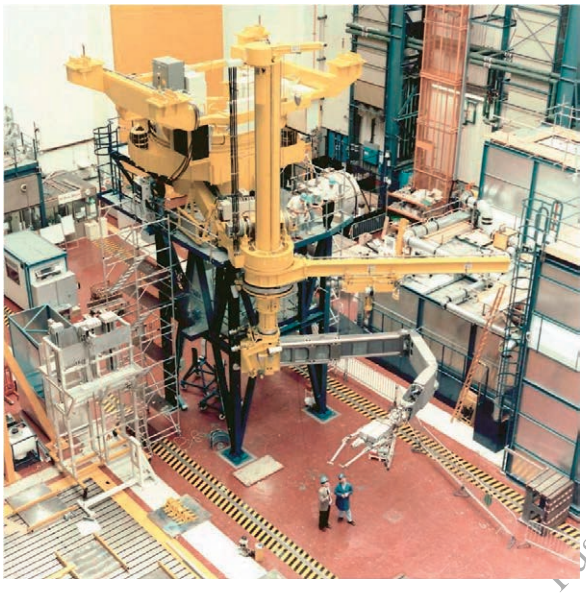

FIG. 11.61. Photograph of JET's Telescopic Articulated Remote Mast (TARM), equipped with a MASCOT manipulator.

11.3.8 Summary of RM design principles

From the experience of RM operations at JET and the design of other fusion-related machines [11.23] discussed in this chapter, the following general summary of RM design principles can be derived:

RM operations

- Environment and plant configuration must be considered in operation design.
- Manipulators will need an envelope up to twice the size of the component.
- Unfastening torque required can be higher than the fastening torque.
- Operations should rely on secondary confirmation of critical interfaces and motions (e.g. motor position with encoder and back up with potentiometer or visual check with cameras).
- Detection of faults is useless if no action can be taken.
- Common tasks should have common solutions.
- All first-time activities should be tested in a representative mock up prior to use in-situ.

Component and equipment design

- Component designs should consider size, shape, weight, rigidity, and possible entanglement with other components.
- Component design must consider the capabilities of the RM equipment which will handle it.
- Design must include consideration for handling and kinematics sequences, with particular attention to the inclusion of realistic clearances.
- Use passive alignment features which sequentially remove degrees of freedom through kinematic constraints.
- Ensure parts have a high level of asymmetry so they cannot be installed incorrectly.
- Designs should allow assembly without obstruction, with direct line of sight.
- Reduce number and variety of parts.
- Design subassemblies to be as modular as possible.
- Components should be inserted from a single direction.
- Lifting/handling interfaces should bridge over the centre of gravity of components.
- Items should be clearly, uniquely and permanently labelled.
- Requirements for services must be highlighted and included from concept, with note that each connection has an addition of time to RM activities.
- Remote maintainability should be considered in the design of all components, as plant environment and configuration may change over time.

Plant-wide strategies

- Standardization of RM design should be applied throughout the plant.
- Extensive use of modularization permits interoperability and eases repair.
- Transport routes for components and the connected manipulator must be planned in concept, to ensure adequate access and clearance.
- Minimize the number of connections between components.
- Use of quick disconnect fasteners instead of bolted joints if possible.
- Service connections should be as simple as possible.
- Services should be grouped reduce the number of connections required.

11.4 FUTURE DEVELOPMENTS

As summarized at the beginning of this chapter in TABLE 11.4, the realization of future fusion power plants poses significant technical challenges from the perspective of RM. Addressing these requires the development of new technologies which provide RM systems with the capability and reliability needed to deliver the plant availability levels that are required for commercially viable fusion power. In this section, five potentially transformative technologies are briefly discussed.

11.4.1 Radiation-hard RM equipment

Future fusion power plants will need to produce higher power levels, increasing radiation in the reactor during both operation and maintenance. On the one hand, this will accelerate component degradation, increasing requirements for inspection and maintenance imposed by regulatory and commercial drivers. On the other, higher levels of gamma radiation emitted by activated components may have a detrimental impact on the performance of RM equipment. The areas of most concern are the electronic components deployed on the RM equipment such as motor drivers and sensors, as these can be damaged by exposure to high levels of radiation and typically have sudden and catastrophic failure modes.

As a minimum, the RM equipment must survive the intervention period with an appropriate safety margin, so this duration determines the amount of radiation-hardness that must be built into the equipment. However, estimating the maximum intervention period is nontrivial, as, forexample, failures in other systems could require the maintenance operations to be halted for an extended period. Further, the type of radiation, absolute levels and cumulative dose are all important factors. For instance, a rapid intervention may be a sensible strategy if cumulative dose is the key cause of damage. The amount of hardening that RM equipment requires may also be driven by regulatory concerns, for instance if a hypothetical failure was considered to impact the plant's safety case. It is also a commercial decision, since moving away from standard technology will generally increase costs and decrease reliability. In some instances, unhardened but low-cost equipment which can be quickly replaced may be preferable to very radiation-hard but costly systems. Hence, the extent to which RM equipment must be made radiation-hard requires careful consideration within the context of the fusion plant as a whole, but will always be underpinned by achieving a solution which maximizes plant availability.

Radiation hardness of electronics remains an active area of research as few options currently provide effective solutions: adding shielding to RM equipment will significantly increase weight and bulk, separating electronics from the exposed equipment requires complex umbilical cable management, and radiation-hard electronics technology suitable for fusion radiation levels is currently immature. A breakthrough in this technology would enable more capable RM systems to be deployed with confidence into the harshest areas of fusion power plants.

11.4.2 Precision placement of heavy components

As structures become larger it is often the case that geometric tolerances can be increased. However, in fusion reactors any neutrons that stream through gaps in the first wall components have the potential to cause damage to critical structures such as the vacuum vessel. This demands that first wall structures and components with a shielding function are positioned very close together, forming labyrinth structures, to reduce the size of any gaps. This poses a problem if the structures need to be moved, as minimum clearances are necessary to ensure safe manipulation of large payloads.

In a fusion power plant these components may be many meters in length, relatively flexible, irregularly shaped and weigh several tones. They may also have to be manipulated along complex paths through narrow vessel ports, avoiding collision with any other components around them. This also implies there could be limited space available

for the handling equipment, meaning that the structure may be slender and could deflect during operation by amounts that are of similar magnitude to the precision requirements of the task. In the worst case, therefore, this operation could consist of a flexible tool, manipulating a large, heavy, flexible component with very high precision demands through a confined space.

This challenge has prompted a significant research effort into exploring the feasibility of such a proposition within the EU DEMO reactor development programme [11.28]. Part of this effort has involved the refurbishment of TARM (Section 11.3.7) as a test bed to explore methods of controlling large, heavy, flexible loads with slender manipulators. The test platform (FIG. 11.62) comprises a 12 m telescopic vertical mast and a 12 m horizontal boom which includes a telescopic axis and numerous planar axes. The total system has 38 DoF when equipped with a MASCOT manipulator, with each of these introducing manufacturing tolerances, backlash and material deflection under variable static and dynamic loading conditions.

FIG. 11.62. TARM-based test platform for development of large-scale remote handling technologies, at the UK Atomic Energy Authority.

The usual method of controlling a robot is to apply appropriate control algorithms to drive joint motion. However, any disturbances that are not measured will cause a significant error in the forward kinematic calculation of the end effector position and velocity. In the high radiation environment, any on-board sensors which might compensate these errors may be unreliable, as they could degrade quickly. Therefore, TARM has been equipped with a second set of off-board sensors that use vision and LiDAR to identify the absolute position of different elements of the manipulator, using fiducial markers and other algorithmic methods. Off-board sensor networks like this could allow the high-fidelity position measurements required to achieve the required levels of precision, while enabling the measurement electronics to be shielded behind windows, using mirrors to view the environment.

11.4.3 Faster fluid service connections

Making and breaking service connections is a fundamental element of RM activities when physically connected components need to be exchanged. Each time the components are moved for maintenance, these connections need to be broken and remade, which takes time and requires care to ensure the connectors are not damaged. Plasma facing components may have multiple functions, including cooling circuits and tritium breeding, which will likely require fluid connections within the vacuum boundary. Plant wide, there may be thousands of separate connections, so in combination this operation has been identified as being one of the most time-consuming RM activities, accounting for as much as 60% of the total maintenance downtime if current joining technologies are used [11.29]. New technologies are therefore necessary to address this issue, if plant availability is to be increased.

As the fluid flows will be pressurized, the pipes and connections will act as a pressure boundary between the fluid and the high vacuum in the vessel, which must survive the harsh environment without failure. Because of this, welding the pipes is currently the standard approach, but this can be very time-consuming and require specialist equipment and procedures which are difficult to deploy remotely. To overcome these difficulties, research is being carried out into novel in-bore laser welding technology, such as the prototype shown in FIG. 11.63. Laser welding is faster than other methods, and the optical systems and power transport fibres can be packaged into a sufficiently

compact form to allow deployment inside the pipes. This is essential for joining pipes in densely-packed reactors, as external orbital welding techniques require a significant amount of clear space around the pipes.

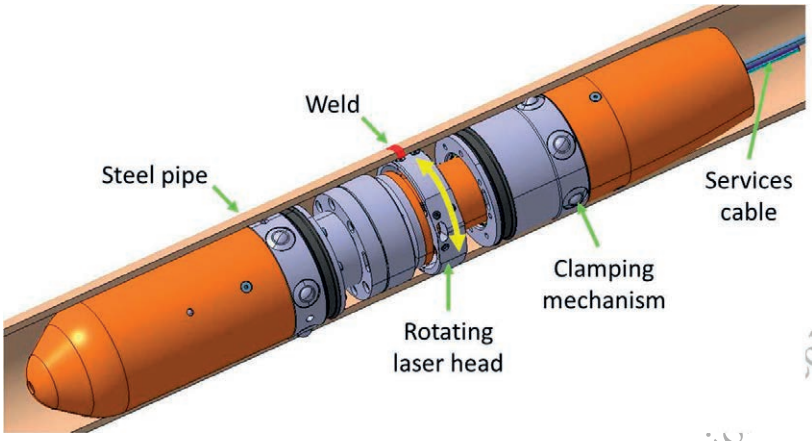

FIG. 11.63. EU DEMO in-bore laser welding tool prototype deployed inside a pipe.

Alternatives to welding technology are also being explored, particularly mechanical connectors. Although these are routinely used in other industrial settings, the harsh environment could mean that ensuring the connection integrity under all conditions may not be possible. Hence, the feasibility of their use must be demonstrated. If viable, however mechanical connections could provide a much faster joining technology which would further improve plant availability.

Pressure boundaries in industrial facilities must comply with industrial safety standards. This implies that critical service connections will require a degree of inspection after being made to guarantee their quality. Further, regular inspections will have to be carried out at relevant intervals to ensure that connections have not degraded, and the reactor is still safe to operate. Remotely inspecting thousands of connections is a significant undertaking for the RM systems, which will require technological developments to ensure it can be conducted without significantly impacting maintenance campaign durations.

11.4.4 Automation

The need for higher availability in fusion power plants drives proportionately shorter maintenance cycles in which tasks must be completed reliably in less time. To achieve this, it is likely that multiple RM systems will have to be deployed in parallel, performing many operations simultaneously and moving at higher speed to cover large distances quickly. These demands begin to exceed the level of control that humans can exert over remote systems, and so automation emerges as a key technology to drive up plant availability.

Automation has been used in industrial manufacturing for decades and can achieve much faster production rates than equivalent human-based processes. Like with conventional teleoperated RM, fusion power plants offer the possibility of building-in automated maintenance from the very beginning of their design, which greatly increases the system's potential and capabilities.

However, some standard tasks remain difficult for machines to execute reliably without human assistance, such as handling and managing cabling. In addition, much of current automation relies on relatively simple pre-programmed operations in a well-known, well-controlled environment. The fusion environment means that degradation of components and RM systems will introduce uncertainty into many RM operations, especially in the harsher in-vessel reactor areas. Importantly, when failures of robotic systems occur in a conventional factory setting, any repair work will usually be carried out by human operators, but this will not be possible in many of the fusion reactor areas. Thus, automating RM in fusion reactors is a significant technical challenge.

Above all, the deployment of automation should serve to increase plant availability. However, any gains derived from automating the processes could be undone by a system which is prone to accidents or is very slow at recovering from them. Thus, aside from enabling faster maintenance, it is essential that an automated RM system is reliable, robust, can recognize faults, and does not exacerbate them when they occur. Having human operators take over control of the systems in fault scenarios could provide a good compromise between the speed of automated systems and the problem-solving skills of humans.

The emergence of artificial intelligence (AI) may enable automated systems to manage higher levels of uncertainty in real time without direct human input. For example, advanced machine vision would allow RM systems to identify tools in a work area automatically. However, AI also brings with it many open questions regarding its safe deployment. For instance, verification and validation of AI algorithms is needed to provide guarantees that the decisions the machine makes are always within certain behavioural bounds, but this is currently an active field of research. Standards and regulations for AI are also still in their infancy, and these need to be extensively developed before AI can be safely adopted in high-consequence industries such as nuclear power generation.

11.4.5 Plant-wide predictive maintenance

Preventative maintenance methods seek to avoid the occurrence of component failures. This is achieved by replacing components as part of planned interventions which are scheduled at intervals shorter than the component's expected lifetime. In this way, components will not fail (under normal circumstances), and so the associated consequences are avoided. However, this approach also means that a proportion of the component's useful life is wasted. In the context of fusion RM, this translates into components being replaced more frequently than necessary, which increases maintenance downtime over the life of the plant.

An improvement over this approach is predictive maintenance, which relies on gathering and analysing system data to better predict the health state of components. In this way, the timing of component replacement can be optimized to maximize the useful life without reaching failure point. The health estimation process, referred to as condition monitoring, can take advantage of existing data sources, such as equipment motor currents, or use sensors specifically installed to capture useful data. The latter can provide more directly relevant data measurements but implies a cost to the plant in terms of increased complexity, additional sensors, increased service supply requirements, and more sensor maintenance. These costs need to be balanced against the potential benefits of a more optimal use of the total life of components.

Given the harsh environment, sensor deployment may be severely restricted in some areas. Sensors located in more benign areas will typically be further from critical reactor areas, so provide poorer estimates of the system's health. However, data from large amounts of these sensors can be combined to extract useful health information, leveraging techniques such as signal processing, sensor fusion, the pattern-finding capabilities of artificial intelligence, and novel methods of storing and analysing vast amounts of data. An alternative but complimentary method relies on reconstructing synthetic sensor signals from real measurements. In this case, a computational simulation of the reactor or its components is used to generate simulated signals at locations where sensors could not be placed, taking as input measurements from instrumented parts of the machine. This approach has been developed in JET [11.30] and is being studied for ITER.

When applied to the RM equipment, condition monitoring is a core element of reliable automation. Over a short time horizon, health measurement provides fast detection of faults in the system, which allows fast remedial actions. Further, the health monitoring can be used to predict long term trends in a machine's state. This means that degradation and potential faults can be better predicted, and the system's behaviour can then be optimized to ensure higher reliability. For example, condition monitoring may help predict the time to failure of a gear box on a manipulator that was starting to wear. Rather than halt mid-way through operations, the RM system could reduce the manipulator's speed to complete a final series of tasks more conservatively, before exiting the area to be serviced. This approach implies a slightly longer task duration, but would be less disruptive to the overall plant logistics.

11.5 Acknowledgements

Parts of this work have been carried out within the framework of the Contract for the Operation of the JET Facilities and have received funding from the European Union's Horizon 2020 research and innovation programme. The views and opinions expressed herein do not necessarily reflect those of the European Commission.

11.6 References

[11.1] BUCKINGHAM, R., LOVING, A., Remote-handling challenges in fusion research and beyond, Nature Physics **12** 5 (2016) 391.

[11.2] RAIMONDI, T., The JET experience with remote handling equipment and future prospects, Fusion Engineering and Design **11** 1-2 (1989) 197-208.

[11.3] ROLFE, A., A perspective on fusion relevant remote handling techniques, Fusion Engineering and Design **82** 15-24 (2007) 1917-1923.
[11.4] TESINI, A., PALMER, J., The ITER remote maintenance system, Fusion Engineering and Design **83** 7-9 (2008) 810-816.
[11.5] WOLFF, D., et al., The impact on remote maintenance of varying the aspect ratio and number of TF coils for DEMO, Fusion Engineering and Design **124** (2017) 553-557.
[11.6] UTOH, H., et al., Comparative evaluation of remote maintenance schemes for fusion DEMO reactor, Fusion Engineering and Design **98-99** (2015) 1648-1654.
[11.7] TESINI, A., ROLFE, A. C., The ITER Remote Maintenance Management system, Fusion Engineering and Design **84** 2-6 (2009) 236-241.
[11.8] CROFTS, O., LOVING, A. B., GOWLAND, R., KEECH, G., "Early definition of the Maintenance Management Plan is essential to achieve a feasible EU DEMO", Proc. 27th IAEA Fusion Energy Conf., 2018, Gandhinagar, India, (2018).
[11.9] VILLEDIEU, E., et al., An Articulated Inspection Arm for fusion purposes, Fusion Engineering and Design **109-111** Part B (2016) 1480-1486.
[11.10] NAKAHIRA, M., et al., Design progress of the ITER blanket remote handling equipment, Fusion Engineering and Design **84** 7-11 (2009) 1394-1398.
[11.11] GALBIATI, L., RAIMONDI, T., GARETTI, P., COSTI, G., "Control and operational aspects of the Mascot 4 force feedback servomanipulator of JET", Proc. 14th IEEE/NPSS Symposium Fusion Engineering, 1991, San Diego, CA, USA, (1991).
[11.12] WALKER, C., et al., ITER diagnostics: Maintenance and commissioning, Fusion Engineering and Design **74** 1-4 (2005) 685-690.
[11.13] FRICONNEAU, J.-P., et al., ITER hot Cell—Remote handling system maintenance overview, Fusion Engineering and Design **124** (2017) 673-676.
[11.14] GONZÁLEZ GUTIÉRREZ, C., et al., ITER Transfer Cask System: Status of design, issues and future developments, Fusion Engineering and Design **85** 10-12 (2010) 2295-2299.
[11.15] LOCKYER, K. G., An introduction to critical path analysis, Pitman, London, (1969) 219 pp.
[11.16] LOVING, A., et al., Development and application of high volume remote handling systems in support of JET and ITER, Fusion Engineering and Design **87** 5-6 (2012) 880-884.
[11.17] SANNAZZARO, G., et al., "Structural load specification for ITER tokamak components", Proc. 23rd IEEE/NPSS Symp. on Fusion Engineering, 2009, San Diego, CA, USA, (2009) 1-4.
[11.18] YOU, J., et al., Conceptual design studies for the European DEMO divertor: Rationale and first results, Fusion Engineering and Design **109-111** Part B (2016) 1598-1603.
[11.19] KEKÄLÄINEN, T., MATTILA, J., VIRVALO, T., Development and design optimization of water hydraulic manipulator for ITER, Fusion Engineering and Design **84** 2-6 (2009) 1010-1014.
[11.20] WALDEN, D. D., et al., Systems Engineering Handbook: A Guide for System Life Cycle Processes and Activities, John Wiley & Sons, (2015).
[11.21] INTERNATIONAL ORGANIZATION FOR STANDARDISATION, ISO 15288:2015, System and software engineering - System life cycle processes, Geneva (2015).
[11.22] LIKER, J. K., Toyota Way: 14 Management Principles from the World's Greatest Manufacturer, New York: McGraw-Hill (2013).
[11.23] DAVID, O., et al., Overview of the preliminary remote handling handbook for IFMIF, Fusion Engineering and Design **84** 2-6 (2009) 660-664.
[11.24] JOSSEAUME, F. et al., Development and qualification of the ITER port plug handling process, Fusion Engineering and Design **136** Part B (2018) 902-907.
[11.25] PITCHER, C., et al., Nuclear engineering of diagnostic port plugs on ITER, Fusion Engineering and Design **87** 5-6 (2012) 667-674.
[11.26] MERSTALLINGER, A., SALES, M., SEMERAD, E., DUNN, B. D., Assessment of Cold Welding between separable contact surfaces due to impact and fretting under vacuum, European Space Agency, Noordwijk, The Netherlands (2009).
[11.27] RAIMONDI, T., The JET Remote Maintenance System, IAEA Technical Document IAEA-TECDOC-495, Vienna (1989).
[11.28] KEEP, J., et al., Remote handling of DEMO breeder blanket segments: Blanket transporter conceptual studies, Fusion Engineering and Design **124** (2017) 420-425.
[11.29] KEOGH, K., et al., Laser cutting and welding tools for use in-bore on EU-DEMO service pipes, Fusion Engineering and Design **136** Part A (2018) 461-466.
[11.30] IGLESIAS, D., et al., Digital twin applications for the JET divertor, Fusion Engineering and Design **125** (2017) 71-76.

Chapter 12

STELLARATORS

Dirk A. Hartmann
Max-Planck-Institute for Plasma Physics, Greifswald
Germany

12.1. INTRODUCTION

12.1.1. Fundamentals

Magnetic plasma confinement in toroidal devices requires toroidally and helically twisted magnetic field lines to avoid the generation of strong electric fields that are caused by particle drifts in magnetic field gradients. In addition, the field lines — when followed over many toroidal turns — need to stay on surfaces, the so-called flux surfaces. FIG.12.3 shows a toroidal section of four nested flux surfaces with one highlighted magnetic field line.

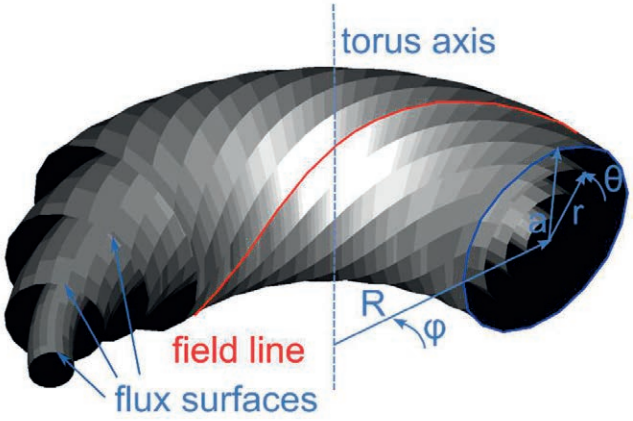

FIG.12.3 Nested flux surfaces densely covered by helical field lines.

Lyman Spitzer realized that there are three ways to achieve such a twist of field lines [1, 2] in a toroidal magnetic field:

1. Driving a toroidal current,
2. Elongating the flux surfaces and having them rotate in the poloidal direction when moving in the toroidal direction
3. Making the magnetic axis, i.e. the field line that is enclosed by all flux surfaces, non-planar.

Tokamaks and reversed field pinches achieve plasma confinement with the fist method, i.e. they drive a toroidal current in a toroidal magnetic field. Helical confinement devices use any of the latter or a combination of several of these methods. For example, the design of the Large Helical Device, LHD (Secs 12.2.4, 12.4.8), uses an elongation of the flux surfaces, the design of Wendelstein 7-X (Secs 12.2.6, 12.4.10) and TJ-II (Secs 12.2.5, 12.4.6) uses a combination of methods 2 and 3, the design of the National Compact Stellarator Experiment, NCSX, used all three (12.4.4). All helical devices share the property that the net toroidal current is much smaller than in tokamaks of comparable size.

Stellarators — used as a short term for all helical devices — offer some distinct advantages over tokamaks and thus offer an alternative confinement scheme for a future fusion power plant. The main features of a stellarator fusion power plant are [3]:

- They use externally created magnetic fields. These are sufficient for plasma start up and operation with the need for driving an additional toroidal plasma current. This reduces the internal power flow, eliminates the

need for current drive components and for internal energy storage and eliminates the potential for plasma confinement disruptions.
- They can operate at higher plasma densities since, up to now, no plasma density limit has been observed in stellarator experiments. Operation at higher density reduces the growth rate of fast-ion instabilities and facilitates divertor operation.

However, there are challanges associated with this approach:

- There is no first principle rule from which to derive that any set of coils generating helical field lines generates nested flux surfaces. One has to use field line tracing codes to calculate the flux surfaces.
- The flux surfaces are inherently three-dimensional and not toroidally symmetric. Thus, there is no additional conserved generalized canonical momentum as there is in tokamaks that restricts particle movement and thus guarantees confinement.
- The neoclassical confinement of plasmas in stellarators at the low collisionality of a fusion reactor, depends sensitively on the properties of the magnetic field. For that reason, the magnetic field of classical stellarators, see Sec. 12.2.3, is not suitable for a fusion power plant. Rather it is required to tailor the magnetic field in order to improve the neoclassical confinement.

The goal of stellarator research is to prove that its concept is suitable for a fusion power plant. This requires to determine the magnetic field structure that can confine plasmas at sufficiently high density, n, and temperature, T, for a sufficiently long energy confinement time, τ_E, to meet the Lawson criterion.

In TABLE 12.1 the highest plasma parameters achieved in tokamaks and stellarators are summarized. The maximum central ion and electron temperatures and the fusion triple product of helical systems are smaller than those of tokamaks. It is therefore not obvious why this concept is still being pursued. According to present understanding, however, the differences are largely due to the relative small size of present-day devices, and not to an inherent shortcoming of the stellarator concept. Furthermore, the dependencies and proportionality factors of the energy confinement time scaling of stellarators and tokamaks are similar [4].

Plasma quantity		***Tokamaks***	***Helical Systems***
Ion temperature [5] [6]	[keV]	30	10
Electron temperature [6]	[keV]	15	10
Electron density [7], [8]	[10^{20}m^{-3}]	10	4
Energy confinement time [9]	[s]	1	0.20
Continuous plasma duration [10]	[s]	120	3268
Volume averaged plasma beta [10]	[%]	12.3	5
Fusion triple product $n_D\tau_E T_i$ [11, 12] [7]	[m^{-3} s keV]	$15.3\cdot10^{20}$	$0.08\cdot10^{20}$
Fusion power [13]	[MW]	16.1	-

TABLE 12.1 Maximum plasma parameters achieved in tokamaks and stellarators.

12.1.2. History

The pursuit of harnessing thermonuclear power has been ongoing since the 1950ies. The first attempts at magnetic toroidal confinement were made with the model C stellarator under Lyman Spitzer [1]. Most of the research was classified then. This changed with the International Atomic Energy Agency (IAEA) conference in 1968 where the experimental results of the Russian tokamak T-3 were presented and demonstrated the achievement of energy confinment times about thirty times higher than in stellarator experiments. This led to strong interest in tokamaks and waning interest in stellarators. In the aftermath, the model C stellarator was modified into the ST tokamak. For some time after this event stellarator research continued at four laboratories in the U.S.A., United Kingdom, Japan and Germany only.

Meanwhile, the challenges of the stellarator concept appear to be understood. They are poor neoclassical confinement at collisionalities of plasmas of fusion reactors. The key to overcome them is an optimization to the confining magnetic field. This has already been adopted in a number of more recent helical devices: the Large Helical Device (LHD) in Japan (R = 3.9 m, in operation since 1998, [14]) and Wendelstein 7-X in Germany (R = 5.5 m, in operation since 2015, [15], [16]). The size of these experiments still does match up with the large tokamaks. Both experiments already employ superconducting coils and are equipped with continuous plasma heating sources to study the technological aspects related to fusion power plants. A number of smaller helical experiments have been also been

built or designed to improve neoclassical confinement of helical devices, e.g. the quasi-Helically Symmetric eXperiment, HSX, (R = 1.2 m, in operation since 2000, [17]) and the National Compact Stellarator eXperiment, NCSX, (R = 1.2 m, not completed, [18].

12.1.3. Key aspects of a fusion power plant

The design of a physically, technologically and economically viable power plant is subject to several key physics and technology related conditions. The following physics aspects need to be addresse [3]

- The energy confinement time of tokamaks and helical devices improves with magnetic induction. For energetic reasons a fusion reactor has to employ superconducting coils. Present day superconductors, for example NbSn, can only operate up to a magnetic induction of about 12T. This then limits the maximum magnetic field in the centre of the plasma to about 5 T. This might be a good compromise since the forces on the coils and support structures increase quadratically with increasing the magnetic field strength.
- The fusion output power should be approximately 3000 MW. For an on-axis magnetic field of 5 T, this requires a volume-averaged plasma beta of about 5%. In this range, plasma operations should be reliable, stable and well controlled.
- The energy loss due to radiation and convection should be small enough for ignition and a self-sustained plasma burn. The plasma density and energy confinement time then need to satisfy the Lawson criterion $n\tau_{\mathrm{E}} > 2 \cdot 10^{20}\mathrm{m}^{-3}\mathrm{s}$.
- The α-particles should be sufficiently well confined to sustain the plasma ignition temperature and to limit the wall loading. This requires a minimum confinement time of about 0.1 s.
- The maximum plasma temperatures should be in the range of 15 keV to keep the Bremsstrahlung sufficiently low. This then implies plasma densities in the range of $(1{-}3) \times 10^{20}\mathrm{m}^{-3}$ and a need for plasma fuelling that is effective in the plasma centre.
- In tokamaks, plasma stability affects plasma density. Experiments indicate plasma density limits due to impurity radiation, plasma transport and plasma heating. One therefore has to develop tools to control the impurity content of the plasma and the plasma stability.
- The output power of a fusion power plant should be controllable. Full control is also necessary for the start-up and ramp-down phases.

In addition, the following technological aspects need to be addresse [3]

- The coil system required to generate the desired magnetic field topology should be mechanically feasible, including the boundary conditions imposed by the required accuracy, maximum tolerable deformation under load and maximum magnetic field at the location of the superconductor.
- The choice of the blanket system has a strong impact on the economic aspects of the power plant, including radiation safety, tritium production and the amount and composition of the nuclear waste.
- The fuel cycle should be reliable, maximizing tritium breeding and minimizing the losses to allow self-sufficient operation.
- Reliable and safe operation must be possible to guarantee investment, environmental and human protection.
- The availability of the plant should be sufficient to achieve the desired financial return on investment at a tolerable ecological impact.

In this chapter, the physical and technological aspects of a stellarator fusion power plant will be addressed in detail. For this purpose, possible coil configurations and topologies are presented in Sec. 12.2. In Sec. 12.3, the physical aspects of stellarators are addressed including how the magnetic field can be optimized to improve the desired plasma properties. In Sec. 12.4 several stellarator experiments are presented together with some of their major scientific findings. In Sec. 12.5, technological aspects of stellarators are addressed and various concepts of stellarator-based fusion power plants are presented.

12.2. Coil Configurations

12.2.1. Vacuum field properties

A set of toroidal field coils generates the magnetic field of a stellarator. Since there is generally no externally induced net toroidal current, the poloidal component of the magnetic field can be obtained from the integral $\int B_\theta(r) r \mathrm{d}\theta = 0$. The magnetic field lines have to be twisted and they need to trace out nested magnetic flux

surfaces. There is no general analytic proof that a stellarator field has nested flux surfaces. However, one can numerically trace the field lines and investigate whether such surfaces exist. If they do exist, one can show that they cannot be toroidally symmetric. Thus whereas for an ideal tokamak field, $B = B(r, \theta)$, for the stellarator field $B = B(r, \theta, \varphi)$. At first glance this seems to be a disadvantage since it entails that the generalized momentum, p_φ, is not a separable quantity, i.e. it is not conserved as it is in a tokamak. However, this freedom can also be used to one's advantage by tailoring the magnetic field to the specific needs of a fusion power plant. This is done in most of the recently designed stellarator experiments.

The magnetic field of a stellarator provides confinement of the plasma without need of an additional externally driven toroidal current. Historically, stellarators are classified by the topology of the coils they use. To create the needed helical field components, helical field coils — coils that are toroidally and poloidally closed around a torus — are particularly effective, however, other coil arrangements are also possible. One can prove that the properties of stellarator magnetic field are completely described by the shape of the outmost magnetic surface [19] [20]. This can be extended by providing the current distribution on another surface that envelops the first surface. Grouping the current distribution into individual current filaments leads to deviations of the generated magnetic field from the intended one. However, the deviations but can be kept sufficiently small by a proper discretization scheme. To compare different devices and describe fundamental properties of the vacuum magnetic field, a few quantities are particularly important: the poloidal cross-section of the flux surfaces —including magnetic islands and mod $\boldsymbol{B}$ contours — the profile of the rotational transform and the magnetic well.

The magnetic field of stellarators is never toroidally symmetric, however, it can still contain some other symmetry. This symmetry is then also retained by the plasma equilibria. Fourier decompositions of the magnetic field in both the vacuum case and the plasma equilibrium case have proven to be potent tools to understand plasma behaviour. This Fourier decomposition is defined as follows using the Boozer magnetic flux coordinates [21]:

$$\frac{B(r,\varphi,\theta)}{B_0(r)} = 1 + \sum_{n=1}^{\infty} b_{0,n}(r)\cos(nN\varphi) + \sum_{m=1}^{\infty}\sum_{n=-\infty}^{\infty} b_{m,n}(r)\cos(m\theta - nN\varphi) \quad (12.1)$$

The cross-section of the magnetic field flux surfaces in one poloidal plane can be obtained by tracing field lines and plotting their intersection with this plane, similar to Poincaré plots in real space. The shape of the surface of a magnetic flux tube is identified as the line traced out by the intersection points of one field line with this plane when followed for many revolutions around the torus. Using different starting positions one can obtain different flux surfaces. These results can be compared with measurements of an electron beam generated by an electron gun inside of the evacuated magnetic field region. The beam electrons follow the magnetic field line at the location of the emitter and circle around the torus several times until they are observed by an intersecting scintillating grid [22] or by a moving scintillating rod in one poloidal plan [23] By moving the beam emitter to different starting points, one obtains the location of different flux surfaces. FIG.12.4 shows the measured and calculated flux surfaces in W7-X [24].

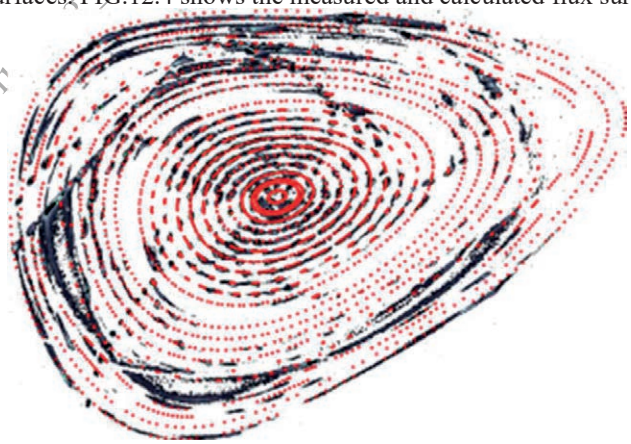

FIG.12.4 Measured (black) and calculated (red) flux surfaces of W7-X (courtesy of Matthias Otte, IPP).

In a poloidal cross-section of traced-out magnetic field with different starting positions, one can typically identify three different regions: (1) An inner region with nested flux surfaces up to one final flux surface, the so called last closed flux surface (LCFS). If one chooses starting point for tracing magnetic field lines outside of this surfaces it does no longer ergodically cover another surface but rather diverts stochastically. This defines region (3). In toroidal

devices, detailed examination of the structure of the flux surfaces reveals a 3D structure in form a chain of islands in the poloidal cross-section. A chain of five islands can be seen in FIG.12.4 at about 75% of the radius of the last closed flux surface. These islands are particularly pronounces near flux surfaces where field lines after few poloidal and toroidal revolutions come back to their starting position. They are called flux surfaces of low rational order. The observed islands are called natural islands since they are an inherent property of the toroidal magnetic field (2). Since additional islands are created by inaccuracies in the assembly of the device or as a result of the influence of the Earth magnetic field, they are a powerful tool to determine the accuracy of the coil assembly. Between the islands and the nested flux surfaces, one can identify X- and O-points as in the field of a diverted tokamak. Taking advantage of those, one can adapt the successful divertor concept to stellarator [25] Even though the flux surfaces have a complicated 3-D structure, fast equilibrium processes along the field lines assure that they are also surfaces of constant plasma pressure. They can be ordered by assigning each surface an effective radius, r_{eff}, of a torus with cylindrical cross-section and the same mean major radius R, to each surface containing the same volume.

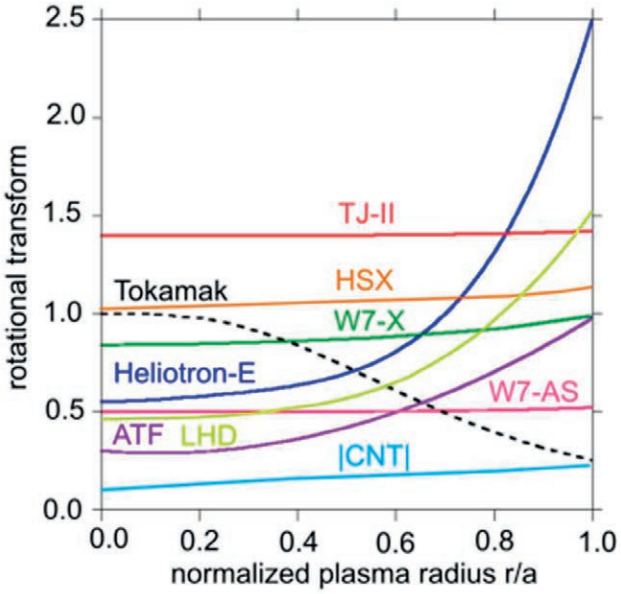

FIG.12.5 Radial profiles of the rotational transform of different helical devices as compared to the tokamak profile [2].

The average twist of the magnetic field lines on a given flux surface is described by the rotational transform, ι, given by

$$\iota(r_{\text{eff}}) = \frac{R \cdot \langle B_\theta \rangle}{r_{\text{eff}} \cdot \langle B_\varphi \rangle} = \frac{2\pi}{q(r_{\text{eff}})} \qquad (12.2)$$

The rotational transform is proportional to the inverse of the safety factor, q. Geometrically, this is the number of toroidal rotations that are necessary for one poloidal rotation. Historically, tokamak design and operation use the safety factor q while stellarators use the rotational transform. FIG.12.5 shows the radial profiles of the rotational transform for different stellarators. The rotational transform of a typical tokamak plasma is also shown. In a tokamak, the toroidal plasma current, thus the contribution to the poloidal magnetic field and the rotation, decreases with the distance from the centre. In a stellarator field, the poloidal field increases with the distance from the centre faster than the toroidal field.

Magnetic shear, $S = \mathrm{d}\iota/\mathrm{d}r$, describes the radial variation of the rotational transform. It is obvious from FIG.12.5 that the magnetic shear has an opposite sign in stellarators and tokamaks. It is interesting to note that tokamak discharges with "reversed shear" — which often improve plasma confinement properties — have the same local shear sign as stellarators. Negative shear is beneficial for plasma confinement since it stabilizes neoclassical tearing modes. If the ι profile is flat, the pitch angle of the magnetic field of neighbouring flux surfaces changes only slightly. Wendelstein 7-AS, Wendelstein 7-X and TJ-II are examples.

LHD, Heliotron-E and other torsatrons has strong magnetic shear. Devices with strong shear inevitably include low order rational flux surfaces among their set of nested flux surfaces. Local instabilities can develop and locally destroy these flux surfaces thus deteriorating confinement. The toroidal structure of the confining magnetic and

possibly magnetic field errors cause islands that also deteriorate plasma confinement. Since the width of the islands W becomes smaller with increasing shear, $W \approx \sqrt{b_{\mathrm{per}}/S}$, [26], Strong shear is favourable for plasma confinement. On the other hand, in devices with nearly vanishing shear, it is possible to avoid low order rational surfaces all together by properly choosing the rotational transform at the edge.

Plasmas tend to expand such as to occupy the largest possible volume dV. If the plasma is collisionless, the flux dΦ through a given magnetic flux tube is conserved and the plasma behaves to maximize $U = \mathrm{d}V/\mathrm{d}\Phi$ [27]. Stable plasma operation thus requires U to be maximum at the centre of the plasma and to decrease towards the edge. This is called the magnetic well configuration. In toroidal confinement, this requirement can only be satisfied on average.

12.2.2. Particle orbits

It is instructive to "unfold" a flux surface and plot the contours of the magnetic field versus the toroidal angle, φ, and the poloidal angle θ, see FIG.12.3. On the outside horizontal midplane, $\theta = 0$. FIG.12.6 shows the mod $\boldsymbol{B}$ plots of an ideal tokamak and that of the stellarator W7-AS. The solid line marks one representative field line as it wraps around the torus. An ideal tokamak has infinitely many toroidal field coils; a finite number of coils will cause additional small ripples. It is toroidally symmetric and the highest field is on the inboard side, $\theta = 180°$, while the lowest is on the outboard side, $\theta = 0°$. In a stellarator, this toroidal symmetry is broken by the helical field coils leading to an additional fine structure of magnetic hills and valleys. The additional variation of the magnetic field along a field line is called magnetic ripple.

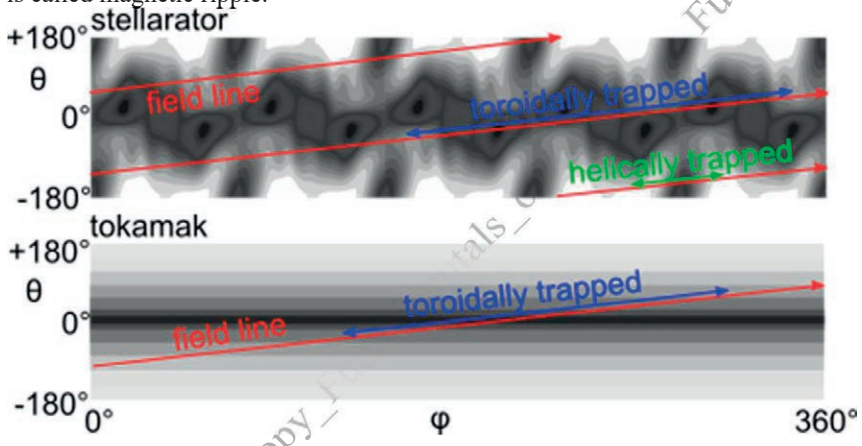

FIG.12.6 Mod B plots of W7-AS and an ideal tokamak. Lighter shading indicates higher magnetic fields.

The undulating magnetic field leads to different classes of particle motion. In a tokamak, there exist passing particles that approximately follow the magnetic field lines and toroidally trapped particles, shown in blue, that bounce back and forth between the magnetic field peaks near the centre of the torus, as indicated in FIG.12.6. In a stellarator, there are also toroidally trapped particles, but, in addition, there a further class of particles, shown in green, that are trapped in the local magnetic mirrors of the helical field.

The curvature and $\nabla \boldsymbol{B}$-drifts cause deviation of the particle orbits from the flux surface, in particular for trapped particles. FIG.12.7 shows the trajectories of examples of the three classes of particles projected into a poloidal plane of magnetic coordinates for W7-AS. The circles indicate the magnetic flux surfaces where the high field side is on the left. Passing particles have orbits that stay close to the magnetic flux surface. Toroidally trapped particles have the banana-shaped orbits similar to those in tokamaks. Helically trapped particles are trapped in a small poloidal range and often have a superposed radial outwards drift. If the plasma temperature is high, the collision frequency is correspondingly low and those particles can quickly be lost. They are the reason for the unfavourable high-temperature confinement regime of stellarators known as the $1/\nu$-regime. However, if there is a radial electric field, the additional $\boldsymbol{E} \times \boldsymbol{B}$-force leads to an additional poloidal drift that can compensate for the radial outward drift thus reduce the confinement degradation in the $1/\nu$-regime.

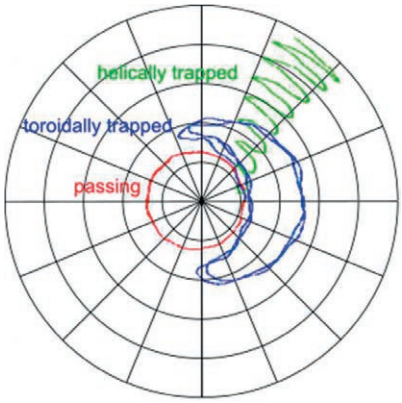

FIG.12.7 Poloidal cross-section in Boozer coordinates indicating the particle orbit classes of W7-AS.

There are numerous ways to externally produce a helical field. Those can be divided into two groups: In the first group, an assembly of field coils of simple geometric forms, e.g. planar or helical coils, generate the magnetic field. These devices require at least one coil to encircle the torus toroidally (except the stellarator in Figure-8). In the second group, a set of three-dimensionally shaped coils that encircle the torus only poloidally generate the magnetic field. This simplifies the optimization of the magnetic field properties.

12.2.3. The classical stellarator

In the classical stellarator, as in the tokamak, planar coils arranged along the torus to generate a toroidal magnetic field. In addition, 2 l coils (l = 1, 2, 3, …) of helical windings with pairwise opposite direction of the current are arranged on the torus. FIG.12.8 shows the toroidal and helical field coils of an l = 2 stellarator and the cross-section of the nested flux surfaces. Several experiments were built using this configuration since it allows varying the helical and toroidal field component independently and facilitates the study of the transition of tokamak operation to stellarator operation. Examples of classical stellarators are Wendelstein 7-A [28] and Proto-CLEO [29].

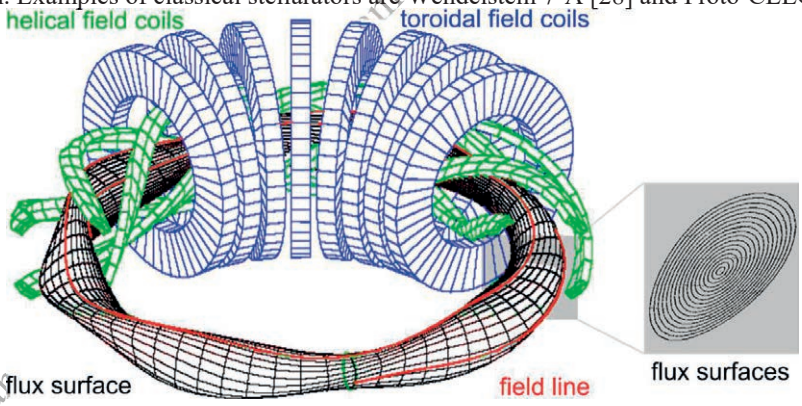

FIG.12.8 Toroidal and helical field coils of an l = 2 stellarator (W7-A) and cross-section of the nested flux surfaces.

Since the helical coils are embedded in the field of the toroidal coils, large radial forces arise changing direction from one helical coil to the next. In addition, there is very little space for the support structure, which would pose serious challenges for the extrapolation to a power plant.

12.2.4. Heliotron – torsatron

The heliotron – torsatron family addresses the force problem identified in the classical stellarator. In these devices, the all helical coils carry the current in the same direction and the toroidal field coils are eliminated. The helical coils thus generate both the toroidal and the helical field components. However, since this arrangement also generates a vertical field (which can be avoided in certain specific cases) that partially destroys the flux surfaces, additional poloidal coils are needed to compensate, see FIG.12.9. In this arrangement, the flexibility of the classical stellarator is lost, but can be restored by installing an additional set of toroidal field coils, for example. Torsatrons

have the advantage that, for certain helical windings, the radial force averaged over one field period is zero. Large forces are then exerted on the poloidal coils which however, can be located at some larger distance from the plasma where there is more space for the required support structures. ATF, Heliotron-1, CHS and LHD are examples of such helical devices.

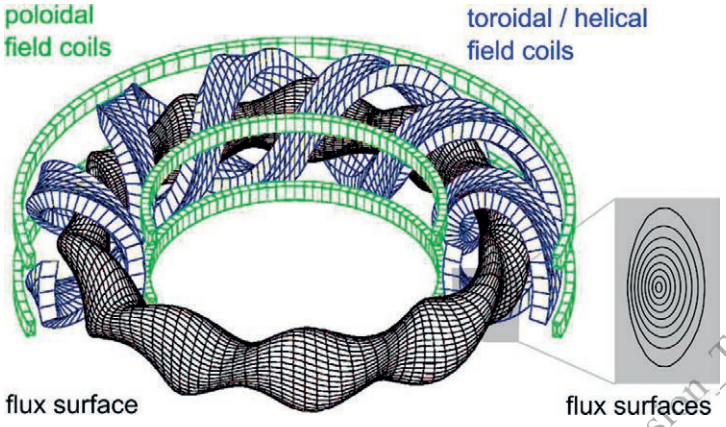

FIG.12.9 Schematic view of the helical and poloidal coils of a torsatron – heliotron (l = 2, m = 12 torsatron ATF, on the left). The cross section (on the right) of the flux surfaces is taken from [30].

12.2.5. Heliac

In a heliac, see FIG.12.10, circular coils are arranged in such a manner that helical field lines and nested flux surfaces are generated. One achieves this by arranging the centre of the circular coils around a helical path around the central coil a. Additional circular coils are needed to compensate for the generated vertical field. This arrangement generates helical flux surfaces that wrap themselves around the central coil. It offers large flexibility to study the influence of the rotational transform and the magnetic well on plasma stability. However, it is also prone to high magnetic field ripples, which have a detrimental effect on transport at low collisionality.

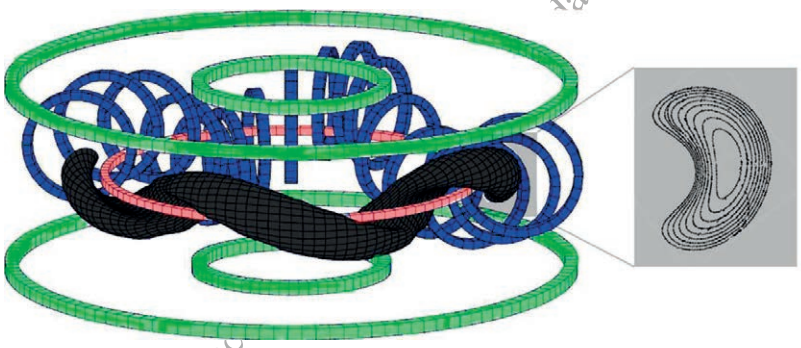

FIG.12.10 Schematic of the coil arrangement of a heliac (TJ-II) and an example of the flux surfaces next to the central conductor [31].

The stellarator with the least number of coils, namely four, the Columbia Non-neutral Torus (CNT), belongs to the heliac class. FIG.12.11 shows a schematic view of the interlinked and external planar coils.

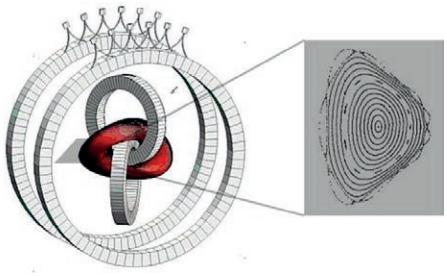

FIG.12.11 Schematic view of the heliac CNT and poloidal cross section of the flux surfaces at two different toroidal locations, taken fro [32]

12.2.6. Modular stellarators

In modular stellarators, specially designed three-dimensional coils are used that are only closed in the poloidal direction. There, one starts out with a magnetic field of desired properties and uses the fact that the magnetic field on an enclosing surface uniquely determines the inner magnetic field. This magnetic field can be generated by a current distribution on another enclosing shell [20]. The current distribution might be continuous but one can approximate it with a set of discrete paths of constant current. These discrete paths define the coils. After calculating the magnetic field generated by the coils and comparing it with the desired field, one can modify the shape of the coils in an iterative process until the desired magnetic field is achieved with sufficient accuracy.

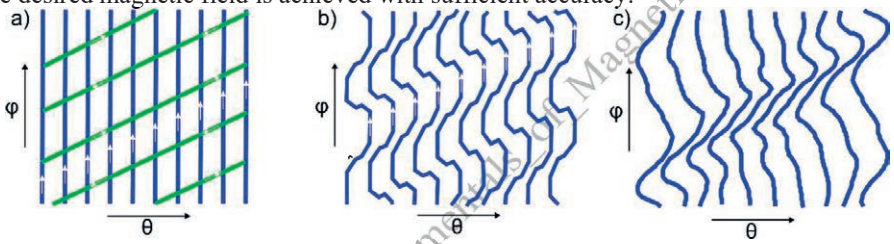

FIG.12 a) 1/5 of the current sheet of an unfolded torus of an n=5, l=2 stellarator, b) a set of modular field coils that approximately generate the same magnetic field, and c) the modular coils of W7-X as an example for optimized coils.

FIG.12 a) shows the currents in the toroidal and helical coils of 1/5 of a standard $l = 2$, $n = 5$-stellarator projected into the φ, θ-plane. If the currents in the toroidal and helical coils are equal, one can generate nearly the same current pattern by the set of coils shown in FIG.12 b). All coils are closed in the poloidal direction and are therefore called modular coils. It is simpler to modify such coils in order to achieve an optimized magnetic field. As an example, FIG.12 c) shows the modular coils of W7-X; some resemblance to an $l = 2$, $n = 5$-stellarator is still obvious.

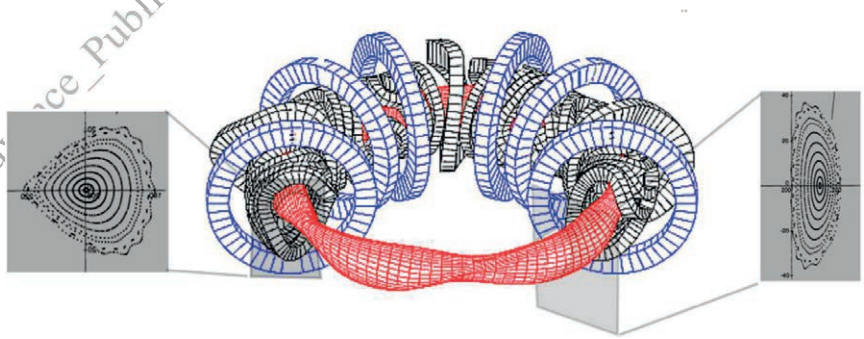

FIG.12.13 Schematic of the modular stellarator W7-AS and shape of the flux surfaces at two toroidal location [26] The additional toroidal coils are not essential, yet useful to increase the experimental variability.

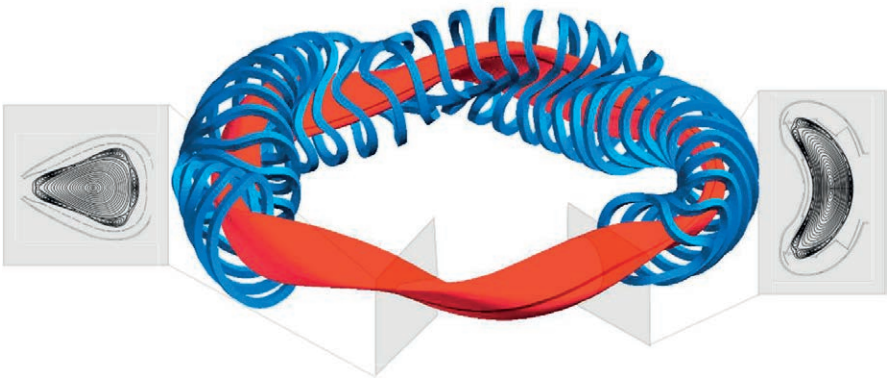

FIG.12.14 Schematik of the modular stellarator W7-X and shape of the flux surfaces at two toroidal locations.

Wendelstein 7-AS [33] was the first stellarator to use such a modular coil system. FIG.12.13 shows the set of coils. The blue toroidal coils have been added for experimental flexibility to superpose an additional toroidal field to the field of the modular field coils. The magnetic field is based on that of an $l = 2$, $n = 5$ stellarator. The $n = 5$ structure was retained such that the magnetic field has a five-fold symmetry, i.e. the magnetic field is invariant under rotation around the z-axis by 360°/5 = 72°. The magnetic field resembles five magnetic mirrors aligned along the edges of a pentagon. Regions of high magnetic curvature, thus poor confinement, are located at the mirror ends where the magnetic field is higher and where there are thus fewer particles. The freedom gained by giving up the requirement of simple geometrically-shaped coils was used to optimize the magnetic field. Other helical devices with modular coils include HSX (see Sec. 12.4.3), featuring a quasi-helical magnetic field, W7-X (see Sec. 12.4.10), optimized for a reduced Shafranov shift, and the planned QPS experiment in the U.S.A. [34] characterized by a quasi-poloidal field.

12.3. STELLARATOR PHYSICS

12.3.1. The Pfirsch–Schlüter current

The orbit of individual charged particles in a stellarator vacuum magnetic field depends only on their starting location and velocity. If many particles are involved that fulfil the conditions of a plasma, internal plasma currents arise that affect the particle orbits. These currents are the diamagnetic current, the Pfirsch–Schlüter current and the bootstrap current. Sometimes also further currents are induced in the plasma by induction as in a tokamak, by absorption of asymmetrically launched electro-magnetic waves or neutral beam injection.

The stellarator plasma equilibrium is governed by the force-balance equation: $\boldsymbol{j} \times \boldsymbol{B} = \nabla p$. This equilibrium has magnetic flux surfaces that are differ slightly from the vacuum flux surfaces but equally fulfil the requirement $\boldsymbol{B} \cdot \nabla\Psi = 0$, where Ψ is a function that is constant on a flux surface. The diamagnetic component of the current, $\boldsymbol{j}_\perp$, balances the pressure gradient. However, since this current is not divergence–free, an additional component along the field lines, the Pfirsch–Schlüter current, $\boldsymbol{j}_{\mathrm{ps}}$, is necessary such that $\nabla \cdot \boldsymbol{j} = \nabla \cdot \left(\boldsymbol{j}_{\mathrm{ps}} + \boldsymbol{j}_\perp\right) = 0$. These two components of the current are indicated in FIG.12.15.

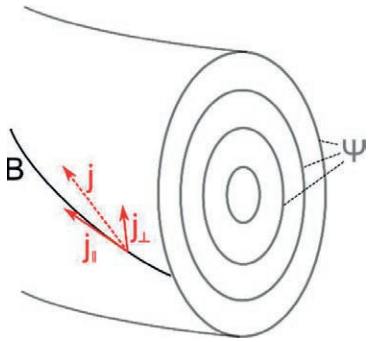

FIG.12.15 Schematic of the Pfirsch–Schlüter and diamagnetic current components.

The Pfirsch–Schlüter current generates a vertical magnetic field. Since this current increases with plasma density and temperature, thus with plasma beta, this vertical field displaces the flux surfaces horizontally. The displacement is called Shafranov shift Δ_{sh}. In a classical stellarator, the Shafranov shift is approximately given by $\Delta_{sh} \approx 4\pi^2 \beta R/\iota^2$ [19]. FIG.12.16 shows the internal plasma currents in a tokamak and in the Stellarator W7-X. In W7-X the magnetic field has been optimized such that the internal currents loops are nearly in poloidal planes. Therefore, the vertical magnetic field component is reduced and thus the Shafranov shift.

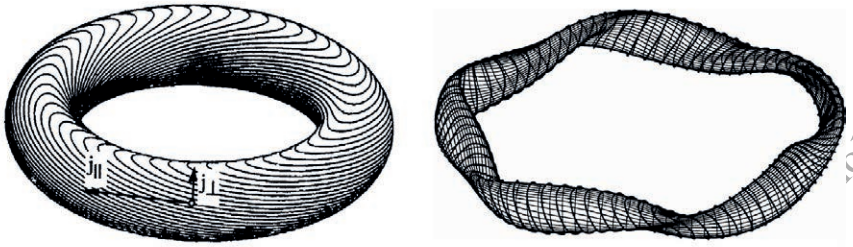

FIG.12.16 Current filaments on the flux surfaces of a tokamak (left) and those of W7-X (right), taken from [35].

Due to plasma equilibrium requirements, the maximum achievable value of beta is approximately reached when the Shafranov shift equals the plasma minor radius, a, thus $\beta_{max} = 4\pi^2 \iota^2/A$ where A is the aspect ratio, $A = R/a$. This limit, however, can be increased by changing ι or A accordingly, or by changing the ratio of $\langle j_\parallel \rangle / \langle j_\perp \rangle$, which is one of the goals of stellarator optimizatio [36 [37] [35]. In the design of stellarator W7-AS, the current ratio was reduced by about a factor of 2 compared to the l = 2-stellarator W7-A.

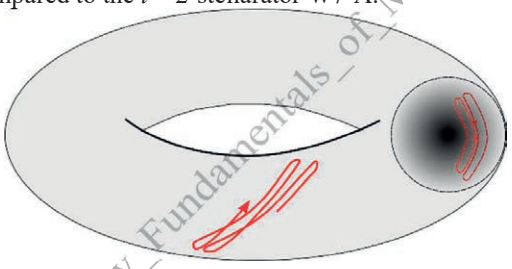

FIG.12.17 Perspective and poloidal projection of toroidally trapped particles. A density gradient causes a toroidal flux of particles.

12.3.2. The bootstrap current

Stellarator plasmas generate a toroidal current as a result of the radial plasma density gradient and friction between trapped and not trapped particles as is also observed in Tokamaks. FIG.12.17 a) sketches the orbit of a toroidally trapped particle. Superposed to the banana-orbit motion is a precession in the toroidal direction. In FIG.12.17 b), the orbit is shown in its poloidal projection. If there is a density gradient, then there is a local toroidal flux of particles. Since they are trapped, no direct toroidal net current is associated with them. However, frictional drag with passing particles leads to a toroidal net current: the bootstrap current.

In stellarator plasmas there are helically and toroidally trapped particles. A bootstrap current is associated with both trapping mechanisms, however, the direction of their drift is opposite to each other due to the change in sign of $\boldsymbol{B} \times \nabla \boldsymbol{B}$. This is illustrated in FIG.12.18. There sections of the mod B contours are schematically shown where particles are toroidally or helically trapped.

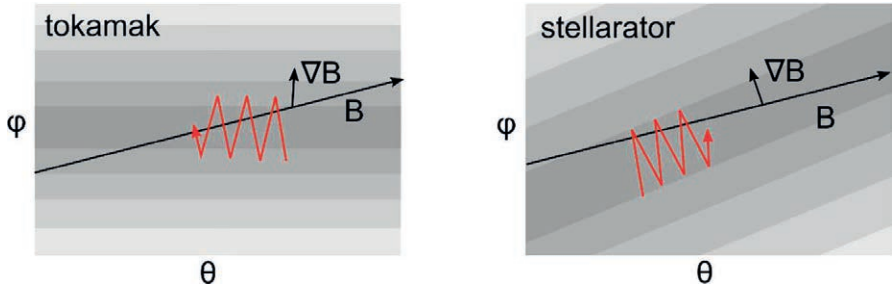

FIG.12.18 Drift motion of a toroidally trapped particle in a tokamak and a helically trapped particle in a stellarator.

The bootstrap current due to helically trapped particles reduces the externally applied rotational transform whereas the bootstrap current associated with toroidally trapped particles increases the rotational transform. Since it is in general undesirable to have the rotational transform being modified by the plasma pressure (except for compact stellarators, see Section 12.4.4) one can minimize the bootstrap current by an optimization procedure, which consists in balancing the toroidal and helical component of the magnetic field against each other. Any residual bootstrap current can easily be measured in a stellarator plasma since it is not necessary to single out the (large) inductive plasma current as in a tokamak plasma. This was done on the ATF stellarator whose magnetic field structure could be changed such that the number of helically and toroidally trapped particles was affected [38]and thus the sign of the bootstrap current. On this device, the bootstrap current was measured with a Rogowski coil.

Perfect cancellation of the bootstrap current for all values of plasma beta and vacuum magnetic configurations is not possible. It is therefore important to have means to compensate the residual bootstrap current by an externally driven toroidal plasma current inductively as it is done in a tokamak. But even if the total current is compensated there is usually a non-vanishing toroidal current profile since the ohmic current density profile peaks in the plasma centre where the electron temperature is highest and the plasma resistivity is lowest, whereas the bootstrap current peaks off-axis where the density gradient is highest. This can lead to different rotational transform ι profiles for identical rotation transform $\iota(a)$ at the plasma edge. It is also possible to drive a current non-inductively by launching electromagnetic waves in one preferential toroidal direction. With electron cyclotron heating (ECH), the direction of the wave propagation can be steered with a mirror. Finally, a current can also be driven by neutral beam injection heating tangentially to the toroidal direction. W7-X is optimized for a minimal bootstrap current. The first experiments have indicated bootstrap currents up to about 10 kA that could have been compensated with ECH current drive.

12.3.3. Neoclassical diffusion

Neoclassical transport theory ([39], [21])is the calculation of the transport coefficients of density, energy and momentum based on the particle drift orbits over which the particles experience Coulomb collisions. The transport is calculated using a diffusion equation with a diffusion coefficient χ given by $\chi = \langle \Delta r^2 \rangle / \tau_{\mathrm{coll}}$, where Δr is the radial movement of particles between two collisions and τ_{coll} is the time between two collisions. The transport calculation assume all particles to have the same energy. The collision frequency is decisive since it has an impact on the role of trapped particle orbits. If the time between collisions is much shorter than the time that it takes a trapped particle to complete a bounce motion, the radial transport is similar for trapped and not trapped particles. This is the case at low temperatures compared to a reactor plasma. Under these conditions, the neoclassical transport theory predicts similar transport coefficients for stellarators and tokamaks, thus the transport coefficients of stellarators show a Pfirsch-Schlüter regime and a plateau. If, however, the time between collisions is much longer than the time that it takes a trapped particle to complete a bounce motion, then the large radial excursions associated with the bounce motion significantly influence the overall radial transport. This is particularly the case for helically trapped particles that often are not confined. The stellarator transport coefficients then show an increase inversely proportional to the collision frequency. This is called the $1/\nu$ -regime. In tokamaks, however, there are no helically trapped particles, if one neglects trapped particles in the magnetic ripple attributed to the torodial field coils, and the toroidally trapped particles are confined. Thus, the transport coefficients do not show this prohibitive behaviour but rather decrease with collision frequency.

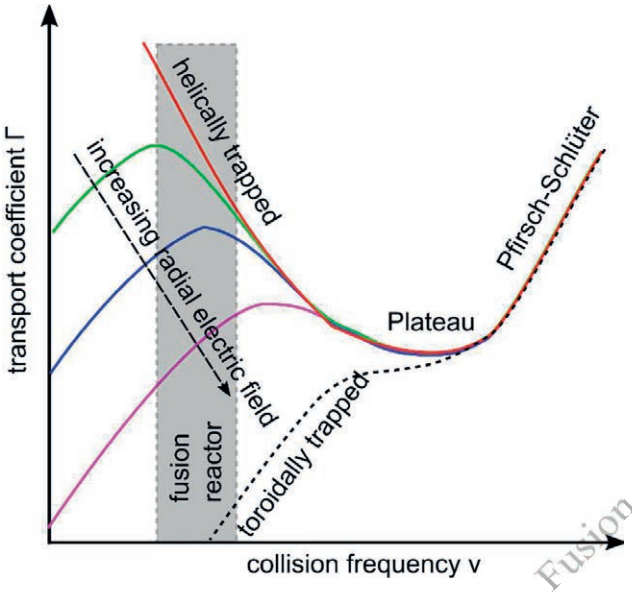

FIG.12.19 Particle transport coefficient vs. normalized collision frequency.

The collisionality of a fusion reactor falls into the $1/\nu$-regime of a stellarator. On this basis a stellarator reactor does not work. However, a radial electric field improves the neoclassical confinement considerably. This radial electric field leads to an $\boldsymbol{E} \times \boldsymbol{B}$ poloidal rotatio [40]of the helically trapped particles and thus reduces their neoclassical transport coefficients. FIG.12.19 shows this schematically. With a radial electric field the neoclassical transport coefficients show a $\sqrt{\nu}$-dependence rather than a $1/\nu$ dependence. In tokamaks, there is no dependence of the neoclassical transport coefficients on the radial electric field since trapped and not trapped particles are confined.

The neoclassical transport coefficients of ions and electrons are different at the same temperature. This would lead to different radial fluxes and thus to an excess charge of the plasma and an associated radial electric field which in turn affects the neoclassical transport. The particle fluxes adjust themselves self-consistently according to the requirement of ambipolarity of the particle fluxes such that the outward particle fluxes of electrons Γ_e and ions Γ_i are equal. Since the transport coefficients depend on E_r multiple solutions (roots) are possible. Solutions with negative electric fields are found for plasmas where ion and electron temperature are similar. They are called "ion root". Plasmas with peaked electron temperatures and lower and flat ion temperature profiles exhibit positive electric fields; these solutions are called electron root. Because of the small values of the transport coefficient in the centre, these discharges showed record electron temperature [41 [42]

Near the plasma centre, experimental and neo-classical values of the transport coefficients and the electric fields approximately agree with each other. Near the plasma edge, the experimental values of the diffusion coefficients are much larger than neo-classical values. The enhancement of the measured transport over the neo-classical transport is called anomalous transport and it is particularly pronounced for electrons.

The particle flux $\boldsymbol{\Gamma}$ and the energy flux $\boldsymbol{Q}$ are calculated from a known velocity distribution function of the particles according to the following expressions where $\boldsymbol{v_s} = \boldsymbol{v} - \boldsymbol{u}$ is the particle velocity in the moving frame.

$$\boldsymbol{\Gamma} = n\boldsymbol{u} = \int \boldsymbol{v} f(\boldsymbol{r}, \boldsymbol{v}) \mathrm{d}\boldsymbol{v}, \tag{12.3}$$

$$\boldsymbol{Q} = \int \frac{1}{2} m v_s^2 \boldsymbol{\Gamma} \boldsymbol{v_s} f(\boldsymbol{r}, \boldsymbol{v}) \mathrm{d}\boldsymbol{v}, \tag{12.4}$$

One should note that both quantities are zero in the case of a symmetric velocity distribution function, e.g. in the case of a Maxwellian distribution function. In most cases, it is justified to linearize the state equation of the distribution function around a Maxwellian. Using the linearized drift kinetic equation, one can finally arrive at a transport matrix that relates the particle flux, the energy flux and the toroidal current to particle and temperature gradients. In one dimension this transport matrix is given by the following expression, where the last row gives the toroidal current, j_φ, that is also dependent on the pressure gradient via the already encountered bootstrap current:

$$\begin{pmatrix} \Gamma \\ \frac{2Q}{m} \\ j_\varphi \end{pmatrix} = -n \begin{pmatrix} D & D_{12} & D_{13} \\ D_{12} & \chi & D_{23} \\ D_{13} & D_{23} & \sigma_\parallel \end{pmatrix} \begin{pmatrix} \frac{\nabla n}{n} - \frac{3}{2}\frac{\nabla T}{T} - \frac{qE_r}{T} \\ \frac{\nabla T}{T} \\ -\frac{E_\varphi}{TB} \end{pmatrix} \tag{12.5}$$

12.3.4. Confinement optimization

At prospective power plant temperatures and densities, the diffusion coefficients for energy and particle confinement are in the $1/\nu$ regime. To operate in this regime, a fusion power plant based on a classical stellarator would become uneconomically large. In this regime, the value of the diffusion coefficients tends to increase since the radial drift of poloidally localized trapped particles does not average out (in contrast to banana trapped particles). A branch of stellarator research addresses this topic and searches for magnetic configurations with overall improved particle confinement.

Ideal magnetic configurations where all particles are confined to the vicinity of their flux surfaces are called omnigenous and it can be shown that such ideal magnetic configurations cannot be achieved for a stellarator. However, it is possible to tailor configurations that approach this ideal. These configurations are called quasi-omnigenous. Within the framework of neoclassical theory, quasi-omnigeneity states that the bounce-averaged drift of the parallel, i.e. second, adiabatic invariant $J = \int mv_\parallel dl$ perpendicular to the flux surface vanishes for all trapped particles. If the resulting drift of the trapped particles is only in the poloidal direction the configuration is called quasi-isodynamic. The magnetic field of W7-AS is optimized to improve the confinement of trapped particles in the low collisionality regime and to reduce the pressure driven currents in the plasma, in order to increase the equilibrium pressure limit that is otherwise the result of an increasing Shafranov shift. This is done following the ideas of Polumbo [43] (see Section 12.3.4) who realized that the drift is zero if the magnitude of **B** is constant orthogonal to the magnetic field lines on a flux surface. He called an equilibrium of such properties "isodynamic". Since those cannot be perfectly achieved in a toroidal device, the result of magnetic field optimization approximating such equilibria is called "quasi-isodynamic". Wendelstein 7-X is an experiment that can be operated with a quasi-isodynamic configuration. This has the additional advantage that the bootstrap current in quasi-isodynamic configurations is reduced thus divertor operation does not depend critically on the plasma beta.

A subset of the quasi-omnigenous configurations exhibit magnetic field symmetry in the Boozer coordinates. Using these coordinates, the drift-kinetic equation becomes isomorph to the tokamak equations if the magnetic field is poloidally, helically or toroidally symmetric. Similar to omnigeneity, these symmetries cannot be achieved exactly but to a tolerable approximation. HSX is an experiment with a quasi-helical symmetry. NCSX was designed and fabricated to become a stellarator with a quasi-toroidal symmetry, before it was mothballed. The Quasi-Poloidal stellarator Experiment, QPS, was designed to become the first stellarator with quasi-poloidal symmetry [44].

For stellarator plasmas in the $1/\nu$ regime, the particle diffusion coefficient can be expressed as $\varepsilon_{\text{eff}}^{3/2} \cdot T^{7/2}$, where ε_{eff}, describes the effects of trapping for the given magnetic configuration in an average sense. ε_{eff} is called the effective ripple and equals ε_h for an ideal helical stellarator. It is instructive to compare ε_{eff} for various devices. As shown in FIG.12.20., devices that employ a certain degree of symmetry or optimization in their magnetic configuration show a pronounced reduction of the effective ripple in comparison to the classical heliac TJ-II.

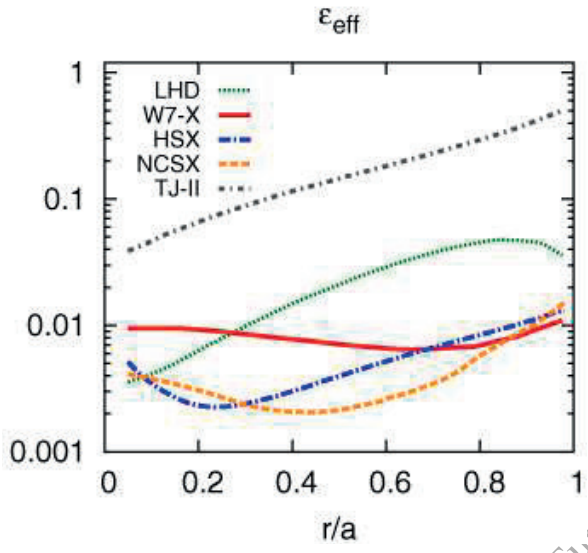

FIG.12.20 Radial dependence of the effective ripple for various stellarators, taken from [2].

Experiments have shown that the observed diffusivities in the centre of stellarator plasmas are well described by neoclassical transport theory. Near the plasma edge the observed values are much higher than predicted. Based on neoclassical transport predictions in the plasma centre and assumptions for the anomalous transport near the plasma edge one can predict the achievable plasma properties. For instance, this was done in [45] where the increase of the plasma beta with heating power was predicted for W7-X, LHD and a modified TJ-II, scaled to the same aspect ratio.

12.3.5. Energy confinement

An important factor in the design of a fusion power plant is the energy confinement time, τ_E. This is the ratio of plasma energy to the total heating power in steady-state conditions. Over the years progress has been made in understanding the role of neo-classical transport and the properties and mechanisms of anomalous transport, however, it is still impossible to reliably predict the energy confinement time of any device based on first-principle-reckoning. In a different approach, a statistical best fit of the measured energy confinement time of different stellarator experiments to a product of important engineering quantities (where the quantities may appear as rational powers) is developed. This procedure has a long tradition in tokamak research and was used to determine the principal dimensions and parameters of ITER. It can provide insight into the importance of certain macroscopic quantities but due to the lack of underlying physical understanding the reliability of extrapolations made from such a scaling is unknown.

The principal engineering quantities used in the energy confinement time scaling of stellarators is based on tokamak scalings and encompasses the average minor radius, a, the average major radius, R, the absorbed plasma heating power, P, the mean plasma density, $\bar{n}$, the average magnetic field on axis, B, and the rotational transform at two thirds of the plasma radius, $\iota_{2/3}$. Experimental data is chosen prudently to exclude any biasing and non-reproducible events, it is collected in the International Stellarator Confinement Database. The regression parameters of the above quantities are determined according to a best-fit procedure. This was first done in 1996 [46]. Since then, more data has become available from TJ-II, LHD, HSX, W7-AS and other devices. The data collected up to 2004 formed the basis of an extended set used to revise the scaling, which confirmed the basis dependencies of the above quantities [4]. The measured energy confinement time versus the value derived from the best fit regression of various devices and different configurations of the same device are clearly grouped, indicating that some important factors are still missing among the quantities of the regression. This can be seen in FIG.12.21 where some experiments consistently fall below the ideal fit while others stay above. To improve the fit and therefore the predictive power of the regression, an additional form factor for experiments with different magnetic configurations was included in the regression finally leading to [4]:

$$\tau_E^{ISS04,\infty} = f(\text{config}) \cdot 0.137 a^{2.40} R^{0.64} P^{-0.57} n_e^{0.55} B^{0.90} \iota_{2/3}^{0.09} \qquad (12.6)$$

The values of the form factor vary between 0.3 (TJ-II) and 1 (W7-AS low iota discharges). Notice that due to this configuration factor $f(\text{config})$ the power dependence in the rotational transform is almost eliminated.

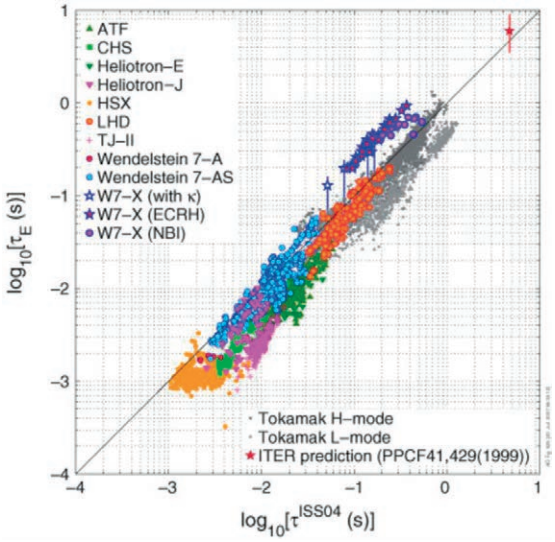

FIG.12.21 Measured energy confinement time of existing experiments (and calculations for Wendelstein 7-X) versus the best fit values of the regression, taken from [4].

Tokamak data in L-mode and H-mode discharges are also shown in FIG.12.21. The highest values achieved belong to JET. In tokamaks, the energy confinement time of H-mode plasmas is typically a factor of 2 higher than corresponding L-Mode Plasmas. The parametric dependence of tokamaks and stellarators is similar albeit tokamaks do not show a positive dependence on density while stellarators do not show a dependence on the mass of plasma particles. Extrapolation based on this scaling is used to determine the required size of a power plant. The resultant dimensions of $R = 20$ m and $a = 2$ m are considered feasible.

Configurational effects based on the natural magnetic islands are not included in the scaling. Magnetic islands are particularly pronounced at low order rational magnetic surfaces. They are usually no addressed in neoclassical theory. Such islands can provide increased radial transport and lead to a deterioration of plasma confinement. Strong shear in a plasma inhibits the formation of islands. However, strong shear also entails that the ι-profile crosses several of the low-order rational surfaces. Higher order rational surfaces are not important since the large number of necessary toroidal and poloidal rotations renders other transport effects more important. The fractions made up of low integers are not equally densely spaced, rather regions around the simplest fractions, like 1/2, are void of higher fractions. Low shear stellarators show the highest confinement times in these regions [40], [47]. In contrast, high-shear stellarators do not show such dependence [48].

12.3.6. Alpha-particle confinement

In a fusion power plant, good alpha-particle confinement is necessary to sustain the fusion reactions after ignition. Alpha-particles are the product of the deuterium-tritium reaction; the most promising fusion reaction in both tokamak and stellarator-based power plants. They have an initial energy of 3.5 MeV, an isotropic velocity distribution and are predominantly generated in the region of highest plasma beta. They have to well confined to collisionally heat the bulk plasma during their slowing-down process.

For heliac power plants, alpha-particle confinement has been examined in [49] and [50]. The magnetic field configurations are optimized such that, at the desired plasma beta of 5%, the contours of constant J are nearly circles in the plane of the magnetic field coordinates, indicating that J is constant on magnetic flux tubes and good confinement is achieved. In such plasmas 90% of the alpha-particles are confined for longer than the energy slowing-down time. Further improvement is possible by increasing the number of coils per field period to reduce ripple losses.

The confinement of energetic ions was also studied for the heliotron device LHD [51]. Particle confinement was improved for inward shifted magnetic configurations [52]. The confinement of most alpha-particles is longer than the energy slowing-down time. Barely-trapped particles contribute the most to particle losses, since their deflection time is much longer than their energy slowing-down time.

12.3.7. Long-pulse plasma operation

Stellarators are inherently capable of steady-state operation since the externally generated magnetic field provides plasma confinement. Thus, the development of devices capable of long-pulse operation is conceptually simpler since it is not required to continuously and externally drive a large toroidal plasma current. If fine-tuning the magnetic configuration by an externally driven toroidal current becomes necessary in helical devices, the current values are expected to be two orders of magnitude smaller than in tokamaks of comparable size.

Long pulse plasma operation is challenging also for stellarator devices and only LHD and W7-X are presently capable of such operation at reactor relevant conditions. At low power level, low magnetic field and low plasma density, ATF has already performed a one-hour discharge with electron cyclotron heating [53]. Long pulse plasma operation at reactor parameters in experimental devices requires superconducting magnets, heating and diagnostic systems capable of long-pulse operation and active cooling of most of the components inside of the plasma vessel. The cooling of the in-vessel components can become particularly challenging since the convective plasma losses can reach power densities up to 10 MW/m^2, while plasma thermal radiation power densities are in the range of 100 kW/m^2.

LHD has extended the achieved range of heating energy and plasma duration over the years [54], [6], [55]. The heating energy is the time integral over the externally applied combined plasma heating power. By now plasma duration of up to one hour has been achieved. FIG.12.22 shows an example taken from [55]. Plasma heating was provided by electron cyclotron (ECH) and ion cyclotron heating (ICH). The line averaged density was feed-back controlled. Over time more helium gas was released from the vessel wall than plasma operation required. Which eventually terminated the plasma operation.

W7-X is still in the process of completing the in-vessel components to achieve steady-state capabilities [7]. A first example for a long pulse plasma with ECH is shown in FIG.12.22. The duration was limited by the increase of the divertor temperature, since this component was not yet water-cooled.

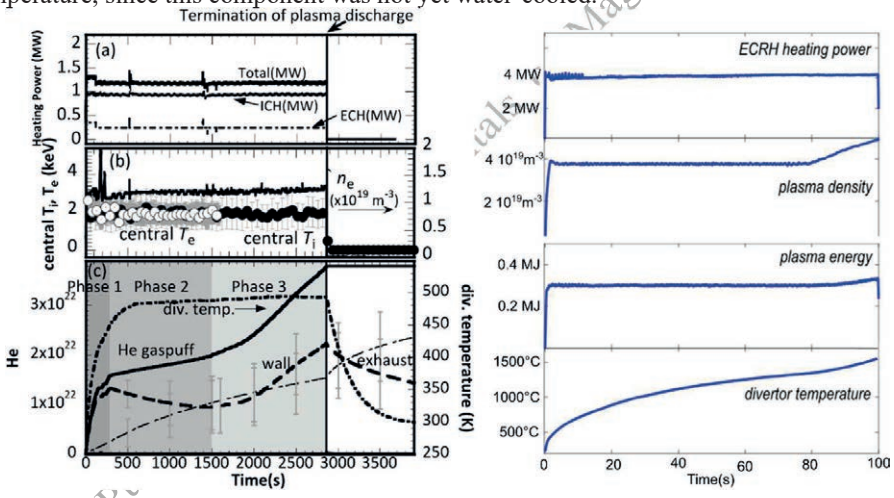

FIG.12.22 Long-pulse discharges of LHD [55] and W7-X.

12.3.8. Impurity control

Plasma impurities are all plasma ions other than the hydrogen isotopes. Plasma impurities are detrimental for energy confinement since they account for an additional radial energy transport mechanism. The impurities usually stem from the components installed in the plasma vessel and are released by sputtering. Stellarators and tokamaks need to prevent the impurities from entering the plasma. In tokamaks, additional magnetic coils generate a magnetic X point near the outer flux surfaces. The magnetic surface that passes through the X point becomes the last closed flux surface (LCFS). Outside of the LCFS the magnetic field lines fan out until they intersect specially designed hit target plates, the divertor plates, at acute angles such that the power flux associated with the convective particle flux density along the field lines is sufficiently low so that the active cooling of these plates can cope with it. This arrangement channels the convective losses into limited poloidal sections where they are intercepted by the target plates. Near such structures vacuum pumping capabilities are installed to pump the neutralized impurities out of the plasma vessel.

The divertor concept can also be implemented in stellarators, since the required magnetic field X point structure naturally exists. With the help of additional coils, the location of these X points or the structure of the magnetic field

lines outside of these X points can be modified. Up to now, three different schemes have been used: a helical divertor in the heliotron/torsatron LHD [56, 57], a local island divertor in LHD [58] and CHS [59], and an island divertor in W7-AS [60], [61] and W7-X [62], [7].

The helical divertor in heliotrons/torsatrons uses the natural set of X points. For example, an $l = 2$ heliotron has two X points in each poloidal plane on opposite sides at the boundary of the confinement region. These X points rotate in the poloidal direction with toroidal angle. The helical divertor structure thus follows the location of these X points. On LHD, such a divertor structure has been installed using graphite tiles. It remarkably reduced the iron impurity influx and led to improved plasma performance [56, 57], FIG.12.23 left shows the plasma confinement region, the X-points and the sample magnetic field lines projected into a poloidal plane. FIG.12.23 right shows a photograph of the installed divertor plates. The location of the divertor plates follows the toroidal movement of the X-point with increasing toroidal angle. Neural gas pumping with dedicated vacuum pumps is provided in the volume behind the divertor structure.

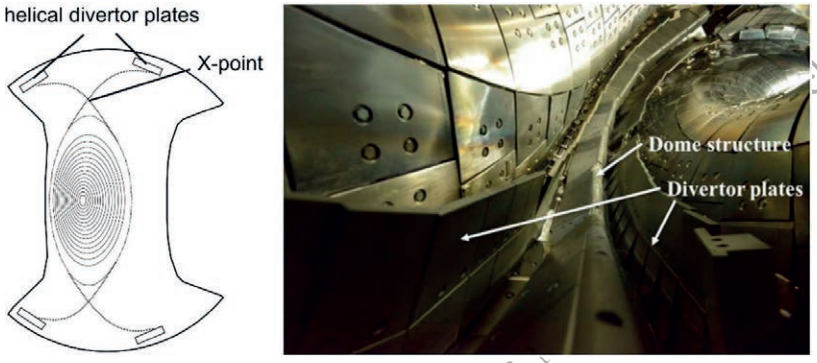

FIG.12.23 Structure of the magnetic field, location of the divertor plates (adopted from [63]) and section view of the divertor plates in a helical divertor configuration.

The inherently three-dimensional nature of helical devices complicates the design of divertors. A divertor-like device with only limited toroidal extend is the local island divertor. Such a device was first installed on CHS and LHD to study its neutral gas pumping capabilities and influence on plasma performance before the helical divertor was equipped with a gas closure. An $m = 1$, $n = 1$ island generated by an external set of magnetic field perturbation coils around an X-point was used for that purpose, see FIG.12.24 left. The field lines of this magnetic island are then intersected by this local island divertor where also local neutral gas pumping is possible, see FIG.12.24 right.

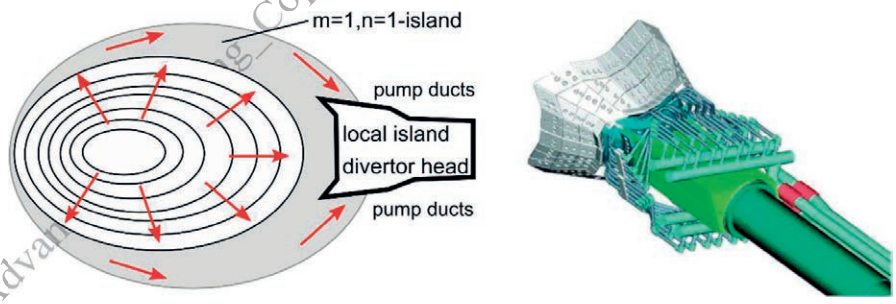

FIG.12.24 Local island divertor functional concept and design, taken from [64].

The natural chain of islands of helical devices with low shear also provide a viable possibility for the design of a divertor. In the Wendelstein line of stellarator experiments, these islands have a wide radial extent and are particularly large near low order rational rotational transform values. In W7-AS an island divertor was installed using the $\iota = 1/2$ islands. It proved sufficient to install the divertor in ten individual toroidal sections. This divertor consisted of 5×2 modules located at isomorphic positions in the vessel. In W7-X also an island divertor is installed that also consists of 5×2 modules. Each divertor module is designed such that it can operate for rotational transforms between 0.8 and 1.2. FIG.12.25 shows the magnetic topology in the bean-shaped cross-section of W7-X and one of the installed divertor modules. Each module consists of ten sets of CFC target plates separated by a small gas pumping region that intersects the islands and baffles used to shield the back side of the divertor module from the plasma and allow additional gas pumping.

The first results obtained with W7-AS divertor were encouragin [33] The configuration facilitated plasma operation at high densities (line-averaged density larger than 3×10^{20} m^{-3}) under steady-state conditions. The plasma edge temperature near the target plates could be reduced to values of ~10 eV. At this temperature, the plasma ions start to recombine and high radiation loss occurs due to partially ionised carbon (partial detachment). This isotropic radiation reduces the heat load on the target plates, therefore the sputtering of target material. The radiation profile of the plasma was thus dominated by the radiation from the plasma edge. In addition, it was found that the confinement time of artificially injected impurities (aluminium) decreased in these high-density scenarios, which is also encouraging for power plant operation. Finally, the density in these discharges was sufficiently high to centrally heat the plasma with electron cyclotron resonance heating, invoking the mode conversion of the ordinary plasma wave into an electron Bernstein wav [41] which can overcome the usual plasma density cut-off for wave propagation.

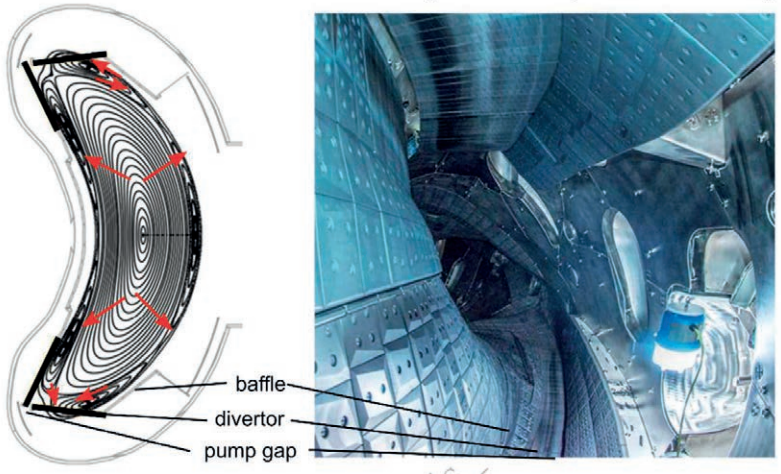

FIG.12.25 Poloidal cross-section of the flux surfaces with the 11/5 islands and a picture of a module of the W7-AS island divertor.

12.3.9. High beta plasmas

Up to now, the maximum achieved plasma beta in stellarator experiments is limited by the available heating power and the degradation of the energy confinement time with increased heating power [65, 66]. With increased plasma density at constant plasma heating power a plasma radiation collapse is observed where the impurity radiation reaches levels comparable to the plasma heating power. A limitation to the maximum plasma density that is attributed to instabilities or disruptions is usually not observed. At LHD, volume averaged beta values of ~5% have been obtained. Both for W7-AS and LHD, the achieved plasma betas were well above the predicted MHD instability thresholds for global modes in W7-AS and Mercier modes in LHD. Since MHD related effects do not seem to play a dominant role in determining the maximum achievable plasma beta, the pressure equilibrium limit is more decisive for plasma confinement than in a tokamak.

A possible explanation for the beta limit of stellarators can be found in the deterioration, at high plasma pressure, of the outermost flux surfaces resulting in the effective reduction of the confinement zone [67, 68]. FIG.12.26 shows calculated Poincare plots of the field lines in LHD for a high beta discharge. In the outer part of the plasma nested flux surfaces cannot be discerned, thus the effective radius of the plasma is reduced. Also W7-AS has provided evidence that in the high beta regimes the beta-limit is in fact an equilibrium limitation [67]. For W7-X, the same effect is predicted whereby the plasma volume shrinks from 31.7 m^3 to 9.3 m^3 when the plasma pressure increases from 1 to 5 %.

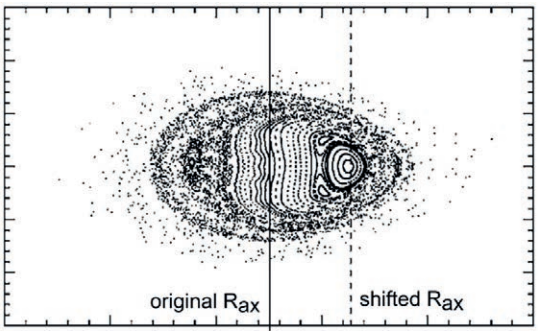

FIG.12.26 Poincaré plots of the magnetic field lines in LHD for high beta plasmas, taken from [68].

12.3.10. Stability

So far, no disruptions have been observed in stellarators unless large ohmic, bootstrap or externally driven currents are present. For example, in more than 120 000 plasma discharges, LHD has never experienced a single disruption [2]. Kink modes, sawteeth and resistive or neoclassical tearing modes are thus absent in a stellarator plasma if the net toroidal current is sufficiently small [2]. In helical devices, in general, tearing modes do not exist since the global magnetic shear has the opposite sign than in tokamaks. The flattening of the pressure profile associated with the development of an island thus results in a reduction of the bootstrap current and thus the island shrinks.

A large number of MHD instabilities can nevertheless be observed and identified in stellarators. An overview on the MHD instabilities in W7-AS is given in [69]. Highly energetic particles are potentially dangerous for the wall, however, clear deleterious effects have not yet been observed.

12.3.11. High density operation

Limits in the achievable density limit similar to the Greenwald density limit [33] have not been observed in helical devices. Rather, experimental data from LHD and W7-AS shows that stable operation is possible well above the Greenwald density limit, see FIG.12.27. Sudo [70] has proposed a semi-empirical scaling law for the maximum achievable density in helical devices, which is the density at which the plasma has a maximum temperature of less than ~50 eV. However, the density is ultimately limited by the bremsstrahlung, when it exceeds the fusion power. For a pure plasma, the ratio of the power radiated via bremsstrahlung to the power of alpha-particle heating is a function of temperature only and is equal to one at a temperature of 4.3 keV.

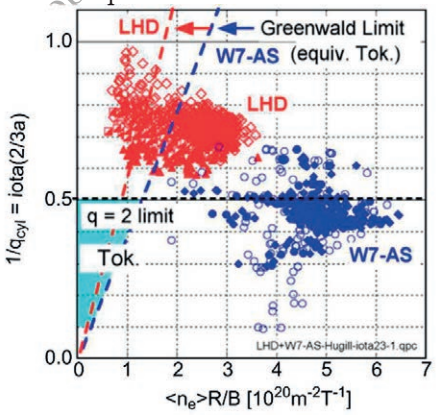

FIG.12.27 Experimental data of LHD and W7-AS demonstrating operational conditions well above the Greenwald limit of an equivalent tokamak [65].

12.4. STELLARATOR EXPERIMENTAL DEVICES

12.4.1. Overview

TABLE 12.2 gives an overview of the aspect ratios and main parameters of a selection of helical devices, further described in the following.

Type		H-1NF	HSX	Heliotron J	LHD	NCSX	T-J-II	W7-AS	W7-X
Mag. Field	T	1.0	1.37	1.5	3.0	1	1.2	2.5	2.5
Major axis	m	1.0	1.2	1.2	3.7	1.5	1.5	2.0	5.5
Minor axis	m	0.2	0.11	0.2	0.64	0.3	0.18	0.18	0.55
Periods		3	4	4	10	3	5	5	5
Rot. Transf.		0.6 – 2	1.06	0.3-0.8	0.45	0.5	0.6 - 1.5	0.3-0.8	0.8-1.2
Volume	m3	0.8	0.44	0.95	30	2.6	0.96	1	32.8
Location		AUS	USA	Japan	Japan	USA	Spain	Germany	Germany
Operation years		1994-2017	started 1996	started 1999	started 1998	-	started 1997	1988-2002	started 2015
ECRH	MW		0.1	0.5	3.7	0	0.7	2.5	8
NBI	MW		-	1.5	23	0	2.4	3.2	6.8 (H)
ICRH	MW		-	2.5	2.9	0	0	1	1.3
Design plasma duration	sec	1	0.2	0.5	3600	0		1.5	1800
Divertor		none	none	none	helical	none	none	island	island

TABLE 12.2 Overview of the main parameters and aspects of a selection of helical device. The values are taken from [21] [10] [71], [72], [73], [74].

12.4.2. CNT

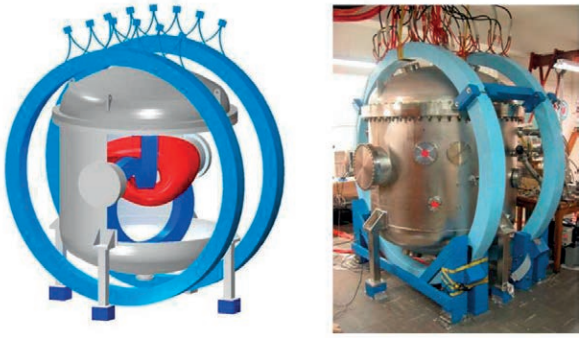

FIG.12.28 Cut-away view of Columbia Non-neutral Torus (CNT) [75] and the actual device.

The Columbia Non-neutral Torus (CNT) is an experiment in operation since 2006 at Columbia University, New York, U.S.A. It is designed to use the unique properties of the stellarator for fascinating physics experiments: the confinement and study of pure electron plasma, the confinement and study of plasmas of arbitrary neutrality and the confinement of electron positron plasmas [32, 75, 76]. CNT is a heliac with the simplest set of coils and a particularly low aspect ratio.

CNT consists of only four circular and planar coils: two poloidal field coils and two interlocking coils. The interlocking coils are arranged in a vacuum chamber while the poloidal coils are located outside of it. The angle between the interlocking coils can be set to three different values, see FIG.12.28. Changing the angle between the interlocking coils and changing the current ratio between the poloidal coils and the interlocking coils change the magnetic configuration. One magnetic configuration is almost completely devoid of internal islands and has a 9/2 island chain outside of the last closed flux surface. A conducting shell made of chicken wire is placed inside of the vacuum vessel that still allows access to and observation of the plasma.

12.4.3. HSX

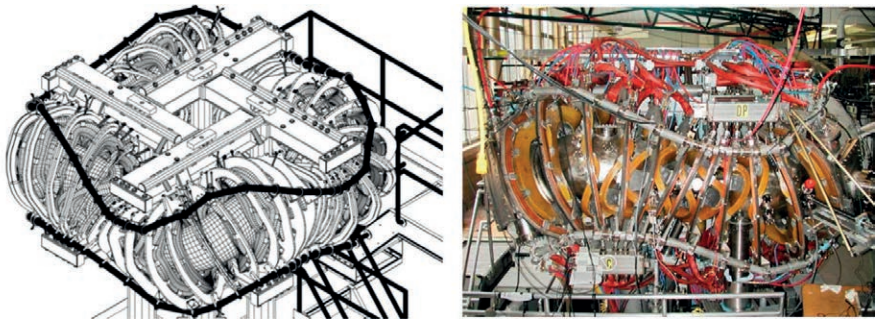

FIG.12.29 Isometric view of the HSX stellarator device showing the key features of the device beginning with the plasma boundary, the vacuum chamber, the main and auxiliary magnet coils along with the support structure, [77] and the actual device.

The Helically Symmetric eXperiment (HSX) is a stellarator experiment in operation since 1998 at the University of Wisconsin-Madison, U.S.A. [17, 78] [79]. It uses a modular set of coils to generate a magnetic field that has a quasi-helical symmetry. The goals of this experiment are to demonstrate the feasibility of a device for studying single particle confinement in magnetic fields of broken symmetry, to study and compare the energy confinement with that of tokamaks and other stellarators, and to study the reduction of the Pfirsch–Schlüter current [69, 76].

HSX consists of 48 nonplanar, modular coils arranged in four field periods, see FIG.12.29. They produce a quasi–helically symmetric field with mode numbers (n, m) = (4, 1). Additional coils are available to modify the magnetic field configuration into a mirror-type configuration, typical of conventional stellarators. The coils are normal conducting and situated outside the vacuum vessel. Generation and heating of the plasma is done with ECRH at 28 GHz.

The improvement of energy confinement in the quasi–helically symmetric configuration (QHS) has been convincingly demonstrated [80]. The electron temperature and electron density profiles were measured for the two magnetic configurations: quasi-helically symmetric and mirror, i.e. classical stellarator. Since the anomalous transport is superposed to the neoclassical transport and might depend on temperature, plasma discharges were performed where the temperature profiles are made similar by varying the input power, see FIG.12.30. This required 67 kW of heating power in the mirror case and only 26 kW of heating power in the QHS case.

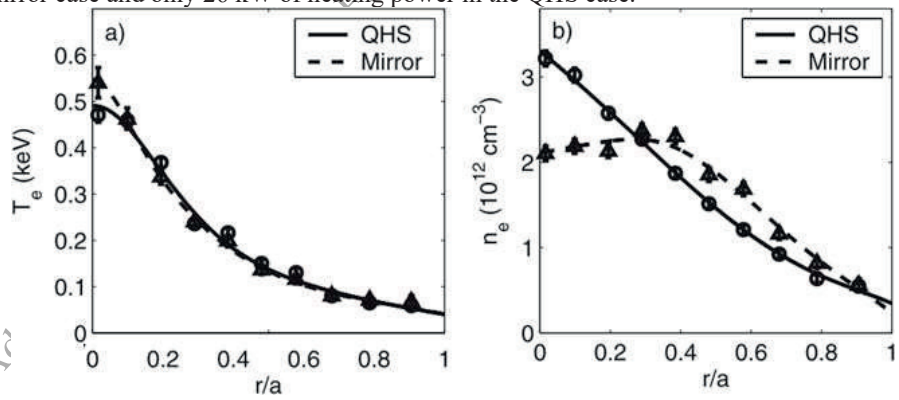

FIG.12.30 Temperature and density profiles for two different magnetic configurations and plasma heating, adapted from [80].

12.4.4. NCSX

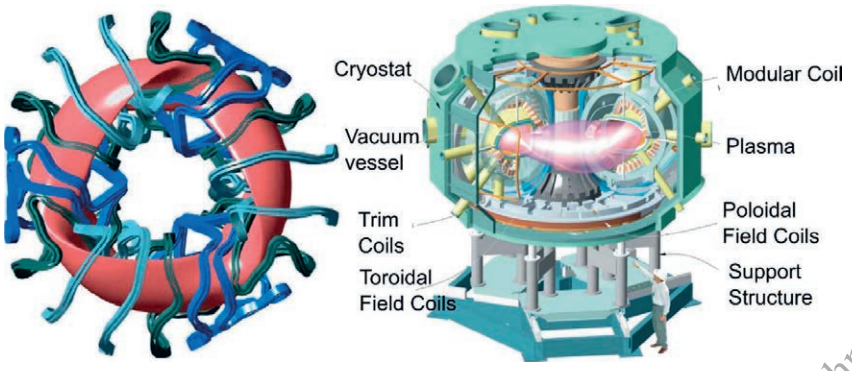

FIG.12.31 CAD-representation of the coils and plasmas of NCSX (left), taken from [18].Schematic of the completed device (right) [81].

The National Compact Stellarator eXperiment (NCSX) was a planned experiment of the Princeton Plasma Physics Laboratory (PPPL) at Princeton University, New Jersey, U.S.A. (see FIG.12.31). It was designed as a quasi-axisymmetric, low aspect–ratio, high–beta stellarator [18, 82]. The magnetic field was to be generated by 18 modular coils arranged in three modules and a set of six poloidal field coils [82], see FIG.12.31. The resulting effective ripple was calculated to be well below 0.01 %, except near the plasma boundary. The design and manufacturing drawings of the major technical components had been completed and the fabrication and installation of the coils was ongoing when its funding was stopped and all related activities were shut-down. It is to be hoped that the activities will be resumed since the device follows a different line of stellarator optimization, thus offers a rich area for experimental investigation. The ARIES power plant line (see Section 12.5.4) is based on this principle, which requires proof-of-principle verification.

Quasi-axisymmetric stellarators combine features of stellarators and tokamaks that have been found to be beneficial to confinement and extrapolation to a power plant. These include a low circulated power in steady-state operation, disruption resilience, high beta limit and good confinement of plasma and fast particles, similar to a tokamak [18]. The high bootstrap current in a quasi-axisymmetric plasma leads to shapes of the external coils that need to contribute correspondingly less to the rotational transform. NCSX was designed to generate such a quasi-axisymmetric magnetic field. At high plasma beta, about 25 % of the rotational transform was to be generated by the bootstrap current at an aspect ratio of 4 and an elongation of 1.8. The purpose of NCSX was to study the physics of the beta limit in these configurations, the effects of quasi-symmetry on neoclassical and anomalous transport, the role of the three-dimensionality on disruptions and the residual flow damping.

12.4.5. H-1

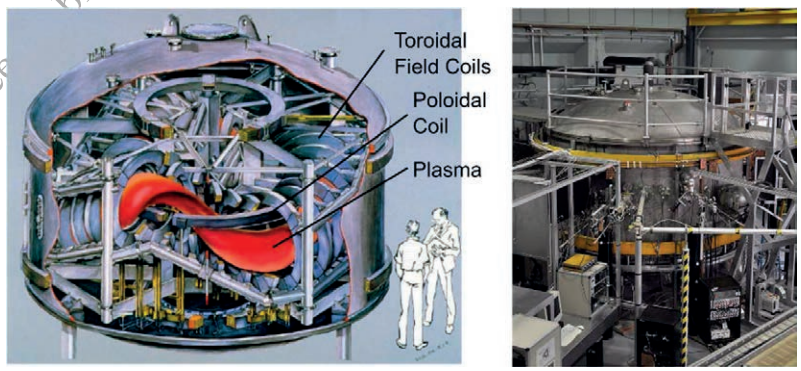

FIG.12.32 Representation of an H-1 plasma showing the locations of the Mirnov arrays, the RF antenna, the interferometer and 18 out of 36 toroidal field coils, taken from [83] (left). Actual device (right).

The H-1 and its later upgrade H-1NF is a heliac in operation at the Australian National University in Canberra since 1994 [84, 85, 86, 87, 72]. The magnetic field in H-1 is generated by a set of 18 circular planar coils arranged in

3 modules and interlinked with a poloidal field coil and an additional helical field coil, see FIG.12.32 [85]. All coils are located inside of a vacuum tank. The large flexibility of the device's magnetic configuration allowed for the study of its effect on Alfvén wave instabilities and magnetic islands [88], [72]. In addition, several 2-D diagnostics were developed on this device.

12.4.6. TJ-II

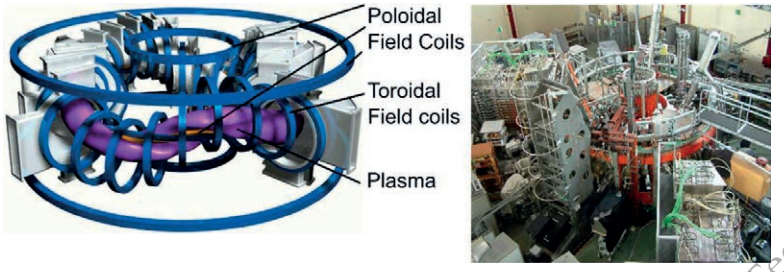

FIG.12.33 CAD design and the real TJ-II device at CIEMAT, Madrid (courtesy of Laboratorio Nacional de Fusion, Spain).

TJ-II is a low magnetic shear stellarator of the heliac type operated since 1999 by the national fusion laboratory CIEMAT, Madrid, Spain [73, 31, 89], see FIG.12.33. The purpose of the device is to study plasma confinement for a wide variety of magnetic topologies with respect to plasma volume, shape and rotational transform at low shear. The large configurational flexibility enables detailed investigations of the assumptions and predictions of neoclassical theory [90].

The confining magnetic field in TJ-II is generated by a set of circular planar toroidal field coils that are interlinked with one planar and two helical field coils, see FIG.12.33. There is a considerably large space between toroidal field coils to allow a good access to the plasma, which is particularly useful for the development of diagnostics.

The importance of the magnetic well is studied in TJ-II by changing the magnetic configuration from a magnetic well near the plasma edge to a magnetic hill. In response, the relative plasma density fluctuation level is observed to double at the edge of the plasma [73]. Whether this increased level of plasma density fluctuations is caused by pressure driven instabilities and whether this leads to a degraded plasma confinement is under investigation.

In discharges heated by neutral beam injection (NBI), spontaneous confinement mode transitions are observed, reminiscent of L-H mode transitions in tokamaks [89], e.g. reduction of the H_α-signal, a sheared poloidal electric field, and increases in plasma density and plasma energy.

12.4.7. Heliotron J

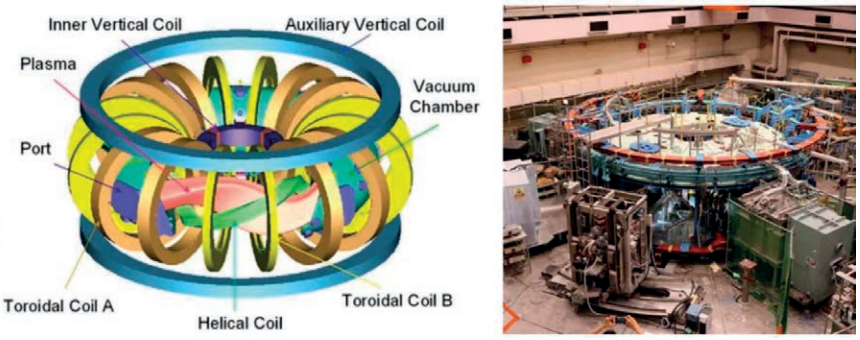

FIG.12.34 Schematic of the coils of Heliotron-J and a picture of the device, taken from [91].

Heliotron J is a medium size experimental device with a helical magnetic axis [74] in operation at the University of Kyoto, Japan, see FIG.12.34, since 1999. The coil system consists of an $l = 1$, $m = 4$ continuous helical field coil, 8 toroidal field coils and three pairs of vertical field coils. The helical coil was wound on the outside of a precisely machined vacuum vessel to achieve the desired coil accuracy. The aspect ratio of the device is 7. The magnetic topology is flexible to accommodate either a helical divertor or an island divertor. In the straight confinement sections, between the edges of the approximately square-shaped magnetic axis, local iso-dynamicity can be achieved for certain magnetic configurations. L-H mode transitions in electron cyclotron resonance heated discharges have been observed

[92]. As in other helical devices, a density threshold has to be exceeded for the H-mode to appear and observation is only possible within a rather small configurational window.

12.4.8. LHD

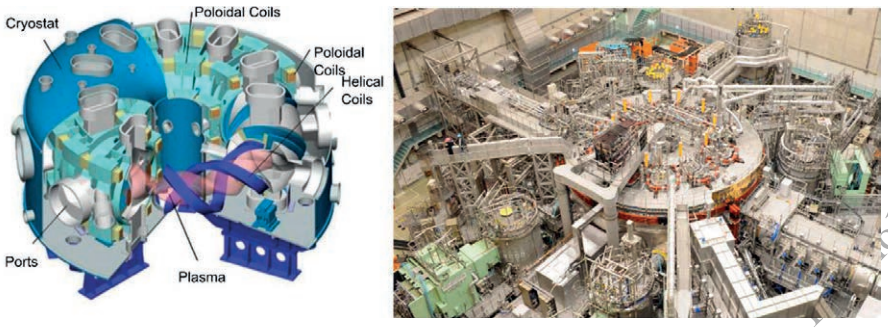

FIG.12.35 Schematic view of the large helical device (LHD), taken from [93] Photograph of LHD inside the experimental hall, taken from [94]

The Large Helical Device (LHD) is a stellarator of the heliotron/torsatron kind, with $l = 2$ and $m = 10$ [14], in operation since 1998 in Toki, Japan. The major goal of LHD is to develop physics and technologies needed for a steady-state fusion power plant where the confining magnetic fields are generated external to the plasm [95] The basics physics objectives are [14]:

- To produce high $n\tau T$ currentless plasmas and study transport issues to obtain a reliable data basis data basis to be extrapolated to power plant grade plasmas.
- To achieve high β plasmas ($\langle\beta\rangle > 5\%$) and study the corresponding physics.
- To install a divertor and obtain basic data for steady-state operation.
- To study the behaviour of high energy α-particles in power plant plasmas.
- To promote complementary studies for tokamak plasmas towards an increased understanding of magnetically confined toroidal plasmas.

To achieve these goals, the device was equipped with the following technical elements:

- superconducting coils that generate the confining magnetic field, thus facilitate steady-state operation,
- on axis magnetic field, major radius, minor radius, rotational transform expected to yield high $n\tau T$ currentless plasmas.
- sufficient plasma heating, including ECH for plasma startup, NBI for high performance discharges and ICH for steady-state discharges.
- rotational transform at the edge of the plasma chosen to allow the use of the m = 1, n = 1 island as a natural island divertor.
- NBI, ICH and lost ion diagnostics to study α-particle confinement.

The magnetic configuration chosen for LHD was chosen to be of the heliotron type for its long and successful tradition at various research institutes and universities throughout Japan. This choice of configuration and the required flexibility were the result of a trade-off between MHD stability and neoclassical confinemen [96] With experimental hindsight on the parameters achieved so far, the neoclassical confinement plays a more important role on the maximum achievable plasma parameters than MHD events. In this sense, the chosen standard configuration of $R = 3.75$ m is not the optimum configuration. Inward shifted configurations with a reduction of effective diffusion coefficients are beneficial for plasma confinement [21 [96] However, they reduce the effective plasma radius thus render the plasma volume smaller.

Two superconducting helical coils and three poloidal field coils generate the confining magnetic field. The winding pack of the superconducting coils consists of three packs that can be operated independently. Together with the poloidal field coils, the magnetic configurations can be modified affecting the radial position, iota, shear and magnetic well. With twenty additional normal conducting coils located symmetrically on the top and bottom of the device one can influence the $m = 1$, $n = 1$ islands used for the local island divertor. A schematic view and a photograph of device are shown in FIG.12.35.

The design of the super conducting coil system, the associated power supplies and the cryogenic supply system are the result of an extensive R&D program successfully completed to find technical solutions to the physics and technology requirements, some of which are listed in the following [97]

- An overall accuracy of the magnetic field in the plasma region $B_{\text{error}}/B_0 < 10^{-4}$, thus a mechanical accuracy of the winding pack of the helical and poloidal coils better than 1.5 mm and 2 mm, respectively.
- An on axis magnetic field (R = 3.75 T) of 3T and up to 4 T with a later upgrade of the cryo plant.

These requirements led to the choice of NbTi for the superconductor. To meet the force and accuracy requirements, the helical coils were wound on site directly to a stainless-steel housing with 100 mm thick wall whose lid was finally electron beam welded to create a vacuum-tight stiff structure. The force requirement implied that the superconductor and the insulating layers had to be assembled with high accuracy so that the magnetic forces on the coil windings can be taken up by the casing and do not result in a quench inducing movement of the superconductor. For stability reasons, the highest grade aluminium makes up for a large fraction of the superconducting wire. During the first experimental campaigns, the nominal 3 T operation was not achieved since the voltage measurements on the coils indicated an impending quench. Later on, with additional diagnostics installed, it was concluded that local heat was being generated due to a slow current diffusion into the aluminium, increasing the coil temperature. U the cryo plant to supply liquid helium at 3.6 [98]solved this problem. The poloidal coils are cooled with helium flowing in a cable-in-conduit since these coils did not require as many windings resulting in a shorter total length of the superconducting cable.

The design, fabrication, assembly and commissioning of the device was achieved in as little as 8 years between the inauguration of the National Institute of Fusion Science, NIFS, and the first plasma on March the 31st, 1998. At that time, all three heating systems were already available. The complete commissioning of the device starting from the evacuation of the plasma vessel and the cryostat up to the first plasma took only 2 months. Measurements of the flux surfaces confirmed [14] that the required accuracy of the shape and alignment of the helical and poloidal coils had been achieved. FIG.12.35 shows the device in the experimental hall.

Since the beginning of operation, the heating systems and the set of diagnostics has been constantly enlarged and upgraded. Five beam lines for hydrogen or deuterium beam injection are in operation with a total maximum power of 35 MW [99]. Acceleration voltages of up 190 keV can be achieved based on negative ion technology. The ECH system consists of three gyrotrons at 77 GHz and two gyrotrons at 154 GHz for a total launch power of 5.5 MW. The ICRH system consisted of up two 5 antennas with 3 MW launched power [6]. After initial operation with hydrogen and helium, LHD has begun deuterium operation in 2017. In separate experiments using high power ECH or NBI record electron of 20 keV [100] and ion temperatures of 10 keV [101] have been obtained. The transport characteristics and the measured radial electric field agrees indicate that the plasma is well described by the electron root of neoclassical theory. The maximum energy confinement times and the observed neutron radiation in deuterium plasmas confirm the improved confinement of fast particles for magnetically inward shifted plasmas.

12.4.9. W7-AS

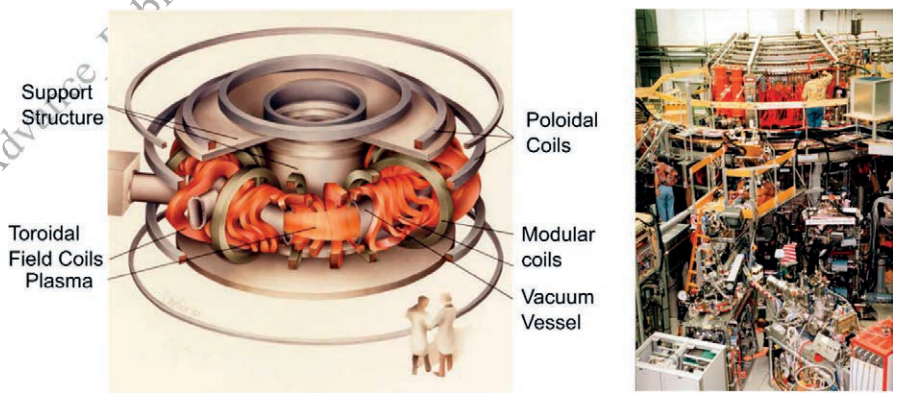

FIG.12.36 Artist view of the device with partially removed vacuum vessel and coils [102] (left). View of the experiment (right).

Wendelstein 7-AS (W7-AS) was an advanced stellarator (AS) of the modular type designed and operated by the Max-Planck institute for plasma physics, Garching, Germany from 1988 until 2002 (see FIG.12.36). It was the first

stellarator to use modular field coils to generate a magnetic field of optimized properties ([33] and references therein) and stands in the line of the Wendelstein stellarator experiments, whose experimental results eventually led to the development of W7-X.

The magnetic field of W7-AS is optimized to improve the confinement of trapped particles in the low collisionality regime and to reduce the pressure driven currents in the plasma (see Section 12.3.4) and thus a reduction of the Shafranov shift. For the first time, modular coils were designed to create the optimized magnetic field.

W7-AS fulfilled its mission over the lifetime of the experiment. An overview of the experimental results is given in [33]. Some of the highlights are:

- The experimentally measured dependence of the Shafranov shift on plasma pressure and rotational transform agreed with the predictions. In particular, the Shafranov shift was ~50% smaller than in an $l = 2$ stellarator of equal size.
- Stable plasmas with a maximum average magnetic field pressure $\beta = 3.4\%$ were obtained.
- In the plateau regime, the neoclassical transport was reduced as predicted, confirming the reliability of the calculations and optimization.
- The measured bootstrap current agreed with the predictions.
- A modular island divertor was tested for the first time in a helical device.
- High density operation up to $\bar{n}_e = 4 \times 10^{20} m^3$ was achieved under steady-state conditions after the island divertor had been installed. Since the properties of these discharges were reminiscent of H-modes, yet at considerably higher density, they were termed high-density H mode discharges (HDH). Those showed improved energy and low impurity confinement and could be maintained under steady-state conditions for the maximum pulse duration of the device.
- The energy confinement showed a noticeable dependence on the rotational transform; the maxima are 1.5 to 2 times larger than predicted by the ISS95 stellarator scaling [46]. With the help of 3D-modelling (EMC3-EIRENE), it was possible to understand these findings as a result of increased cross-field transport due to the small pitch of the field lines in the islands, thus a reduction of the parallel ion heat flux [60].

12.4.10. W7-X

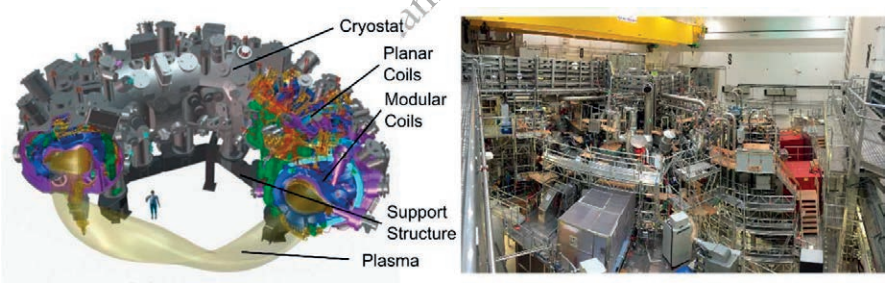

FIG.12.37 Schematic cut-open view of the basic elements in Wendelstein 7-X. View of the experimental hall.

Wendelstein 7-X (W7-X), see FIG.12.37, is an iso-dynamically optimized, modular stellarator at the Max-Planck Institute for Plasma Physics in Greifswald, Germany [103, 104]. The first plasma was achieved in 2016 after nearly twenty years of design, fabrication, assembly and commissioning. The main design parameters of W7-X are: major average radius of 5.5 m, minor average radius of 0.5 m, magnetic field of up to 3 T on axis.

The scientific goals of W7-X focus on issues that are of direct relevance for a fusion power plant [105]

- quasi-steady state operation, i.e. plasma pulse duration of 1800 secs ate 10 MW plasma heating power
- plasma temperatures exceeding 5 keV
- densities on the order of $10^{20}\mathrm{m}^{-3}$
- plasma equilibrium with an average beta of 5%
- control of plasma density and impurities

The device is being operated with hydrogen, deuterium and helium, but will not be operated with a deuterium-tritium mixture. Therefore, all plasma experiments rely on external plasma heating. The present goal is to have 10 MW continuous plasma heating with ECH for up to 30 minutes available and up to 20 MW of pulsed NBI heating and up to 1.5 MW of ICH.

The standard magnetic configuration simultaneously meets the following criteria:

- Nested magnetic surfaces exist with a corresponding iota profile that avoid low order resonances and limits the effect of internal islands on transport.
- The bootstrap current is largely reduced compared to a classical stellarator in order to avoid a beta dependent iota profile that could lead to internal low order resonance islands.
- The Pfirsch-Schlüter current and the bootstrap current are reduced in order to reduce the Shafranov shift and allow the installation of an island divertor.
- Magnetohydrodynamic stability up to plasma beta of five percent.
- Reduced neoclassical transport in the $1/\nu$ regime.

The magnetic field configuration is quasi-isodynamic [21] and has a five-fold symmetry. It is generated by a set of 50 modular superconducting coils of five different types, see FIG.12.13. In addition, 20 superconducting planar coils of two types are added for additional experimental flexibility. The winding packs of the coils consist of NbTi strands in an aluminium cable with in-conduit helium cooling. Power supplies individually provide the electrical currents to sets of coils of the same type. All coils are supported by a stainless-steel coil housing and are mounted onto a ring-shape support structure. The superconducting magnets, support structures and supply lines are located in a toroidal, vacuum-tight, double shell cryostat, whose inner wall is the plasma vessel.

The assembly of the device was done module by module. To that purpose, modules consisting of all coils of a 72 degree segment, sections of the central support ring, the plasma vessel, cryo lines, superconducting electrical bus lines, sensors were completed on separate assembly sites. Upon completion, these modules were lowered into the prepared and positioned lower half shell of the outer vessel in the torus hall. Then the upper shell of the outer vessel was welded on top. Since the overall required accuracy of the location of the current paths of the coils amounts to a few millimetres, diligent care and multiple intermediate measurements were taken throughout all assembly steps.

The inside of the plasma vessel is clad with water cooled liner elements that are designed to cope with expected thermal and convective plasma losses. A toroidally extended island divertor for heat loads up to 10 $MW \cdot m^{-2}$ is installed at ten symmetric locations in the plasma vessel. Its plasma facing elements consist of CFC (carbon fibre reinforced carbon) material that is brazed on an actively water-cooled support structure. The area behind to the divertor can be actively pumped with cryopumps to reduce the effects of recycling and impurity generation on the plasma. Areas with heat loads less than 500 $kW \cdot m^{-2}$ are covered with graphite tiles that are clamped onto a water-cooled support structure. Areas with heat loads less than 100 $kW \cdot m^{-2}$ are covered with water-cooled stainless-steel sheets.

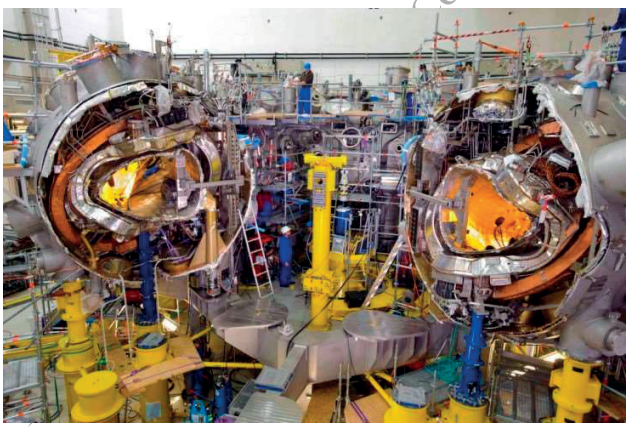

FIG.12.38 View of the basic W7-X device in the experimental hall in 2012 after 4 out of 5 modules had been installed.

Multiple peripheral components, e.g. diagnostics, heating systems, peripheral supply lines, support structures, are placed in the experimental hall in addition to the device itself. Due to the limited space and the need for simultaneous development, the design and layout of these components followed the principles of concurrent engineering. To that purpose, a reference computer aided design (CAD) model set describing the current state and

design maturity of the various components is updated daily and configuration management tools are applied throughout. By 2019 the reference model set encompasses about 80000 models and about 800000 representations.

The experimental strategy of the device is based on the understanding that procedures for generating a plasma and optimizing its properties are unknown at the start of operation and have to be deductively developed over time by conducting thoughtful experiments. Since these experiments require less heating power and the plasma durations initially is shorter than 30 minutes, they are conducted with less than the full set of hardware leaving room for later modifications and protecting costly hardware from mishaps during early plasma explorations. Thus for the first operational phase, OP1.1, only parts of the water-cooled vessel liner were installed, in particular the ten divertor units were replaced by five inboard limiters. The inboard limiters consisted on five graphite-tiled components that were installed at symmetric locations in all five modules. This facilitated plasma discharges with a total injected energy of 2 MJ. For the operational phase OP1.2, the inboard limiters were replaced by ten divertor modules without water cooling. Only some of the other liner components were connected to water cooling circuits. This facilitated heating energies of close to 200 MJ and plasma durations of 100 seconds. For the operational phase OP2.1 close to the full specification of the device is achieved: the divertor and many, but not all plasma facing components are water cooled such that plasma heating energies of 1 GJ and plasma durations of several minutes can be achieved.

The commissioning of W7-X with the hardware installed for OP1.0 started in summer 2014 and required putting about 50 different sub-systems into operation. Each system was commissioned before its control was integrated into the W7-X control system. The commissioning was completed with measurements of the magnetic flux surfaces that fully agreed with the predictions [24].

The first phases of operation focussed on operational experience and addressing the scientific goals. Up to 7 MW of ECRH and up to 3.4 MW of NBI were coupled into hydrogen and helium plasmas. Hydrogen pellet injection and boronisation techniques were also put into operation and facilitated the highest triple product achieved up to now in helical confinement devices of $6.5 \cdot 10^{19}$ keV m^{-3} s [7].

12.5. STELLARATOR POWER PLANT

12.5.1. Introduction

The ultimate purpose of stellarator research is to investigate and find solutions for the pertinent questions that are relevant to designing, building and operating a reliable, safe and economically viable fusion power plant. Planned fusion and stellarator experiments will address the remaining issues. The principal physics issues are [106], [107]:

- Reducing neoclassical transport to reach ignition and self-sustained burn conditions by optimizing the externally generated magnetic field. During operation, additional current drive by ECCD or NBI to adjust or compensate the internal plasma currents may be required.
- Confining alpha-particles sufficiently well to sustain plasma burning by optimizing the externally generated magnetic field. Excitation of Alfvén modes has to be avoided.
- Finding burning plasma operation modes with low plasma dilution by helium ashes and impurity influxes. According to present understanding, the influx of impurities can be reduced by insulating the plasma from the wall lining of the vessel with the help of a natural or induced magnetic island divertor. This might require plasma operation at sufficiently high densities to reduce or even reverse impurities' inward drift. Central fuelling via pellet injectio [108]or NBI may also be required.

In addition to physics-related issues, the design of a stellarator power plant needs to fulfil more general requirements related to the properties of available materials and their impact on investment costs, maintenance periods, safety aspects and decommissioning costs. The main features of a stellarator fusion power plant should thus be [107] (see also section 12.1.3):

- Confinement by externally generated steady-state magnetic fields and self-consistently generated internal currents.
- Steady-state operation at high Q.
- No requirement of an energy storage system and low circulating power.
- No need to replace the external coils, vacuum vessel and cryostat vessel over the lifetime of the device.
- Sufficiently high tritium breeding ratio in the blanket.
- Sufficiently short downtime of the device for replacement of first wall and blankets.
- No major plasma disruptions that could lead to excessive energy loads on the first wall, the divertor or additional high forces on the supports.

In the following, some technical aspects that deserve special attention in the early conceptual design phases of stellarator power plants are being addressed. Three major design studies are presented following the experimental lines of NCSX, LHD and Wendelstein 7-X, respectively. The main parameters of these devices are given in TABLE 12.3.

		ARIES-CS	FFHR 2m1	HELIAS 22/5
Magnetic field	T	5.7	6.2	5.0
Major axis	m	7.75	14	22
Minor axis	m	1.7	1.73	1.8
Number of field periods	-	3	10	5
Max. Field at coil	T	15.1	13.3	11
Toroidal plasma current	MA	4	0	0
Fusion power	GW	2.4	1.9	3
Avg. neutron wall load	MWm^{-2}	2.6	1.5	1
Avg. beta	%	6.4	3	5.5

TABLE 12.3 Overview of the parameters of three stellarator power plant studies [109, 110, 111].

12.5.2. Technical Requirements

12.5.2.1. Coil design

There are various kinds of commercially-available superconducting materials suitable to the fabrication of coils, for example NbTi, Nb_3Sn and more recently Nb_3Al [112]. To obtain an on-axis induction of 5 T, the magnetic induction at the conductors is about 10 to 12 T. At 4.2 K, NbTi can be used up to a magnetic induction of 10 T, at 1.8 K it can be used up to 12 T. The critical current of Nb_3Sn is influenced by the imposed stress either from the coil steel jacket during thermal contraction or from additional bending induced during the fabrication of the three dimensional conductor. At 4 K, thermal contraction reduces the critical current by 50%, whereas for Nb_3Al the reduction amounts only to ~20%. The bending stress induced reduction of the critical current can be eliminated by heat treatment of the coils after bending (*wind and react*). Such heat treatment is only feasible for coils of sufficiently small size that do not have to be fabricated at the device for which they are intended. It also requires the development of electrical insulation around the cables that can withstand the temperatures of the curing process. This procedure is thus not applicable to the helical coils of an LHD type power plant. Whereas LHD used cryo-bath cooling for the helical coils, all power plant design studies now expect to use force-cooled cable-in-conduit conductors.

12.5.2.2. Coil fabrication and assembly

Great accuracy is required in fabricating and assembling the coils. Typical values of the tolerable relative error of the overall magnetic field is $2 \cdot 10^{-4}$ when expressed in Fourier components. At higher values, the likelihood of additional magnetic islands appearing inside the plasma, or distortion of the islands outside of the plasma that play a crucial role for the island divertor operation is increased possibly leading to heat load power imbalances and thus intolerable high heat loads on some divertor modules.

12.5.2.3. Divertor design

Tokamak and stellarator fusion experiments have shown that the plasma performance is greatly improved by the use of a divertor. The maximum achievable steady-state heat loads are on the order of 10 $MW{\cdot}m^{-2}$. The divertor has to cope both with the heat load due to the plasma convection, plasma thermal radiation and the neutron flux. CFC materials are not permissible in a fusion power plant due to safety hazards associated with the high tritium retention in carbon. Recent tokamak experiments with tungsten first walls have shown that it is possible to achieve sufficiently low values of erosion and impurity influx to the plasma, so that these results can be extrapolated to the design of fusion

power plants. Any stellarator power plant will benefit from the operational experiences of ITER since many fundamental requirements are identical.

12.5.2.4. First wall and blanket

Various blanket and first wall concepts have been developed [113, 114]. Blankets are designed to fulfil several technical requirements:

- The blanket has to provide sufficient neutron shielding to protect all subsequent structures outside the vacuum vessel from radiation damage. Typically, this amounts to an overall radial thickness of the blankets of about1.3 m. Therefore, they need to provide cooling for a neutron power flux of about 1 MW/m^2 with local peaking factors up to 3 MW/m^2.
- The coolant has to operate at high temperature of 700 to 800 °C to thermodynamically achieve the economically required electricity conversion ratio.
- The structural integrity against operational stresses, against run-away electrons and plasma disruption requires special steels to be developed that are able to withstand the expected number of atomic displacements as result of neutron radiation. For the device to be economically viable the replacement it is expected to take place less often than once in ten years of operation. It is also being investigated whether a moderation of the neutron velocity spectrum via first wall graphite tiles can mitigate the radiation damage and increase the lifetime of the blankets [11]. In general, stellarators impose less stringent requirements on the forces and extraordinary loads since the internal plasma currents are one to two orders of magnitude smaller than in a corresponding tokamak [114].
- The blankets need to breed tritium with a breeding rate of approximately 1.2. This is planned to be accomplished by including Beryllium as a neutron multiplier material.
- Tritium needs to be extracted continuously from the blankets since the available inventory is expected to be insufficient to operate a power plant for extended periods. A fusion power plant with 3 GW of fusion power consumes about 300 kg of tritium in one year. Since the fuel burnup efficiency is about 1%, about 100 kg of deuterium, tritium fuel are required daily.
- All associated activities related to the exchange of blankets during the lifetime of the power plant are done by remote handling (see Chapter 6).

Stellarators and tokamaks impose nearly the same requirements on the blankets. The operational experience of ITER with blankets can therefore be used in choosing and adapting the various existing blanket concepts for a stellarator. The number of geometrically different types of blankets modules will be larger for a stellarator than for a tokamak power plant because of the three dimensional shape of the vacuum vessel. This will have an impact on the investment, running costs and possibly on the maintenance time.

12.5.2.5. Maintenance

It is necessary to access the inside of the vacuum vessel during maintenance periods to warrant the soundness of critical components and replace the damaged ones. Since maintenance intervals require a shutdown of operations, thus no electricity production, they need to be as swift as possible. It is expected that the blankets and first wall need be replaced after about ten years of operation. Two different maintenance concepts exist for this task. If the blanket modules are sufficiently small to be extracted via vacuum vessel ports, then remote handling booms could be installed at several locations to perform all associated tasks. Boom extension lengths of about 10 m with load capacities of several tons are viable. All present, stellarator power plant concepts allow for sufficiently large ports between the coils without deteriorating the plasma confinement by an increased magnetic ripple. In principle, maintenance could be performed while the components in the cryostat are cold. But the duration of the maintenance is determined by the number of simultaneously operable booms in the vacuum vessel. Alternatively, access could be simplified if the complete torus is separated into two sectors, then can be moved apart. Then access is not limited by the port size, but is also challenging since it requires warming up the cryostat, cutting of the vacuum and cryostat vessels and separation of all structures inside the cryostat, detaching all supply media on the outside of the sector that is to be moved. The inverse sequence will be performed after successful exchange of the blankets.

12.5.2.6. Costs

Several cost studies have been performed to investigate the impact of various aspects of the power plant concept on the investment cost and cost of electricity [115, 116]. The major single item of the list of investment costs is the magnet system, which accounts for about 25%.

12.5.3. Helical advanced stellarators (HELIAS)

The helical advanced stellarators (HELIAS) power plant studies are based on the concept of quasi iso-dynamically improved magnetic configurations generated with modular field coils. This design is, for instance, followed by Wendelstein 7-X. Several conceptual studies on the details of the magnetic field structure have been performed [117, 118, 119, 120, 121, 21, 122]. The optimization followed the design criteria of Wendelstein 7-X, including the requirement that the maximum magnetic field at the coils should be sufficiently low to use NbTi. The superconductor material, maximum field, coil sizes, current densities, forces, stored energy per coil, and other parameters are comparable to the characteristics of the ITER toroidal field coil magnet system. Many ITER technologies can thus be directly applied to this type of power plant despite the three dimensional shape of the coils. The number of magnetic field periods was also varied. Using only three periods deteriorated alpha-particle confinement and would have caused a larger fraction of particles to be lost from the plasma region before equilibration. FIG.12.39 shows the modular field coils and a conceptual design of the coil support structure of a HELIAS-type power plant with 5 magnetic field periods.

The scaling of the device follows the ISS-04 (see section 12.3.5) scaling without any additional confinement improvement factor, although it seems likely that W7-X and thus also the HELIAS power plants will show an improvement due to the reduced effective ripple. Many relevant issues remain to be investigated in detai [123]

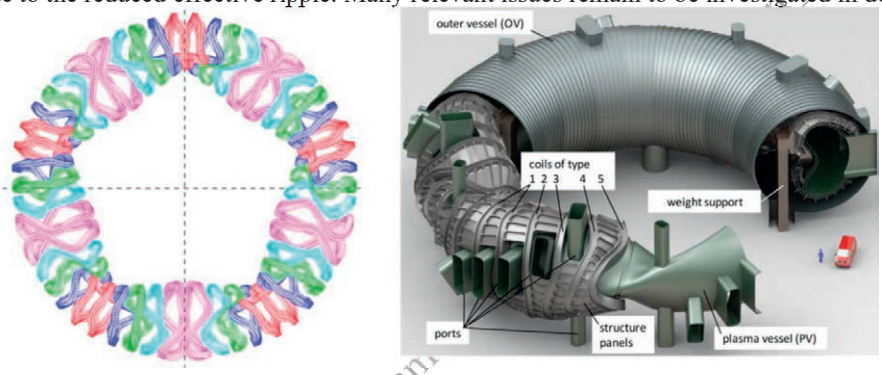

FIG.12.39 Modular field coils and conceptual design of the support structure of a HELIAS-type power plant [111].

12.5.4. ARIES-CS

ARIES [124] was an U.S.A. multi-institutional research activity with the mission to "perform advanced integrated design studies of the long-term fusion energy embodiments to identify key R&D directions and to provide visions for the fusion program". Within this program, aspects of a fusion power plant based on a compact stellarator (CS) along the design line of NCSX (see section 12.4.4) have been developed by the project ARIES-CS [125, 126, 109, 127, 116]. A stellarator power plant study (SPPS) investigated a four-field-period modular HELIAS-like heliac. Since initial studies predicted large investment costs based on the large size and mass of the device, later studies were directed towards compact stellarator devices with a size and mass comparable to relevant tokamak devices.

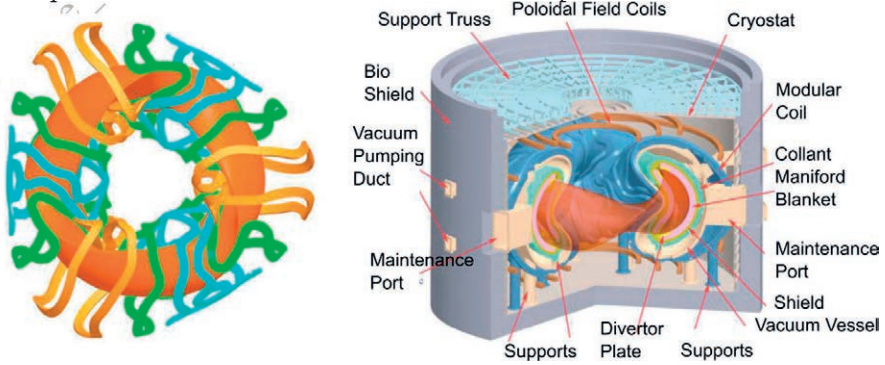

FIG.12.40 Arrangement of the modular coils and the fusion power core of ARIES-CS [109].

ARIES-CS is a quasi-axisymmetric stellarator with three field periods and modular coils of the NCSX type. The arrangement of the modular field coils and the design concept of the device are shown in FIG.12.40. Based on the experimental findings of W7-X and LHD, where MHD activity was not observed to cause detrimental effects on confinement, the magnetic field structure was optimized for small aspect ratio while relaxing the MHD stability requirements. The maximum magnetic field at the coils is approximately 15 T. The rotational transform in the centre of the plasma is 0.4 and increases to 0.5 near the edge in the vacuum case and becomes 0.7 in the plasma case due to the strong bootstrap current. The effective ripple is 0.1 % near the centre of the plasma and 0.6 % near the LCFS. Alpha-particle loss is estimated to be about 5%. The extrapolation to a power plant followed the ISS-95 scaling [46] under the assumption that the device has a confinement time improvement of a factor 2 with respect to the scaling due to the reduction of the effective ripple. An auxiliary heating power of 20 MW is required to achieve ignition. Since the aspect ratio is partly determined by the radial size of the blankets, the tritium breeding capability of the blankets on the high field side, near the inner side of the vacuum vessel was eliminated in favour of a more compact design. The predicted overall breeding ratio of all blankets is still 1.1. A large peaking factor of the neutron wall load of about 2 will be included in the design of the first wall. Assembly and maintenance of the blanket modules is planned to be simultaneously performed in all three modules via ports. The available size of the ports leads to a total of about 200 blanket modules. The high magnetic field at the coils requires Nb_3Sn as base material for the superconducting wire with the mandatory heat treatment. Similar to the NCSX design, the coil support structure is a toroidal ring structure with grooves into which the coils are wound.

12.5.5. Force free helical power plants (FFHR)

Many stellarator power plant studies follow the design principles of LHD [128, 129, 11, 110, 130]. This design is attractive since the coil shape can be adjusted such that the forces on the coils in the magnetic field of the device are minimized. The support structure can thus be simplified, providing additional access to the vacuum vessel. This line of power plant concepts is therefore called the force-free helical power plant (FFHR).

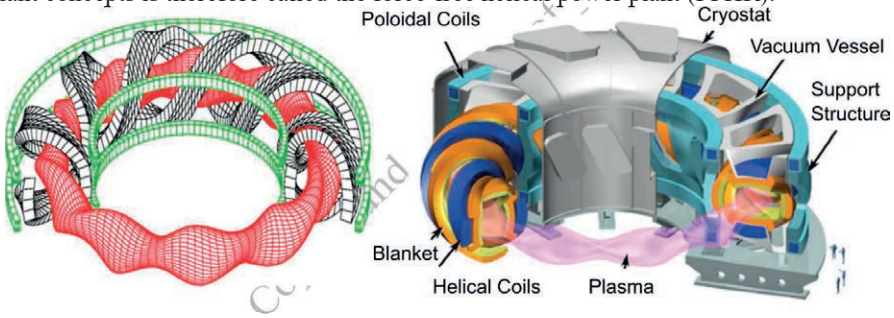

FIG.12.41 Arrangement of the helical and poloidal coils and conceptual design of the FFHR-m1 power plant [130].

The FFHR family of conceptual power plant studies are $l = 10$, $m = 2$ heliotrons with slightly varying parameters; mainly the pitch of the helical coils [130]. The arrangement of the helical field coils and the conceptual design of the core power plant are shown in FIG.12.40. Extensive work on the conceptual design of a fusion power plant is ongoing and places a particular emphasis on superconducting magnets, in-vessel components and power plant system design. Achieving sufficient plasma-vessel clearance and blanket module installation are particularly challenging. In these studies, it is assumed that the energy confinement time is better than the ISS-94 scaling would predict. Typical improvement factors H of 1.4 are assumed, which does not seem too optimistic. Smaller values of H can be assumed if the major radius is increased, or if the plasma size is increased, at the cost of reducing the radial thickness of the blankets.

Detailed design studies of the coil manufacturing are also performed. The maximum value of magnetic induction at the superconductor is about 13 T. Nb_3Al is planned to be used rather than Nb_3Sn since its critical current is less stress dependent. A fabrication process has been developed whereby the superconducting cable in conduit is taken off a spool, pre-bent, heat treated and ultimately aligned in its final location such that the induced stress, associated with the last step, can be tolerated. More ambitious scenarios investigate the on-site electrical connection of pre-bent sectors with high-temperature superconductors.

12.6. OUTLOOK

Any stellarator power plant will benefit from the operational experiences of ITER since the fundamental requirements are identical. To feel confident about the stellarator as a viable fusion power plant concept, several physics challenges need to be overcome or their proposed remedies demonstrated:

- First and foremost, neo-classical transport is to be reduced to acceptable levels. From the particle point of view, this can be done by further optimizing the magnetic field into quasi-symmetric configurations (quasi-helical, quasi-axial, quasi-omnigenous). This can also be achieved by enhancing the radial flux of one particle species to drive a radial electric field. Experiments aiming to test these approaches are being planned, while others have already been built.
- Second, the viability of the island divertor should be experimentally demonstrated. The current profile control with ECCD or tangential neutral beam for bootstrap current compensation should be tested in high density situations. Whether there is an experimental limit imposed by MHD events on the maximum achievable plasma beta are still being investigated. Up to now, no universal features have been identified that account for limitations of the maximum achievable energy. Central particle fuelling could be a problem but might be accomplished with negative neutral beam injection.
- Finally, high alpha-particle confinement at high energies and simultaneously low confinement at thermal energies for helium ash removal remain to be investigated.

12.7. REFERENCES

[1] L. Spitzer, "The stellarator concept," *Phys. Fluids,* vol. 1, p. 253, 1958.

[2] P. Helander, "Stellarator and tokamak plasmas: a comparison," *Stellarator and tokamak plasmas: a comparison,* vol. 54, 2012.

[3] H. Wobig and F. Wagner, Energy technologies, Berlin Heidelberg: Springer, 2005.

[4] A. Dinklage, "Assessment of Global Stellarator Confinement: Status of the International Stellarator Confinement Database," *Fusion Science Technology,* vol. 51, pp. 1-7, 2007.

[5] R. Fonck, "Ion Thermal Confinement in the Enhanced-Confinement Regime of the TFTR Tokamak," *Phys. Rev. Lett.,* no. 63, p. 520, 1989.

[6] Y. Takeiri, "The Large Helical Device: Entering Deuterium Experiment Phase Toward Steady-State Helical Fusion Reactor Based on Achievements in Hydrogen Experimental Phase," *IEEE Transactions on Plasma Science,* vol. 46, pp. 2348-2353, 2018.

[7] R. Wolf and et al., "Performance of Wendelstin 7-X stellarator plasmas during the first divertor operation phase.," *Physics of Plasmas,* p. 082504, 2019.

[8] F. Wagner, "W7-AS: One Step of the Stellarator Wendelstin Line," *Physics of Plasmas,* pp. 072509-1 - 072509-22, 2005.

[9] H. Yamada, "Characterization of energy confinement in net-current free plasmas using the Extended International Stellarator Database," *Nucl. Fusion,* no. 45, p. 1684, 2005.

[10] H. Yamada, "Overview of results from the Large Helical Device," *Nucl. Fusion,* no. 51, p. 1, 2011.

[11] O. Motojima, "Progress of design studies on an LHD-Type steady state reactor," *Fus. Eng. Des.,* vol. 83, p. 983, 2008.

[12] T. Sunn Pedersen, "First results from divertor operation in Wendelstein 7-X," *Plasma Phys. Control. Fusion,* vol. 61, p. 014035, 2019.

[13] J. Jacquinot, "Deuterium-tritium operation in magnetic confinement experiments: results and underlying physics," *Plas. Phys. Contr. Conf.,* vol. 41, p. A13, 1999.

[14] A. Iiyoshi, "Overview of the Large Helical Device project," *Nucl. Fusion,* vol. 39, p. 1245, 1999.

[15] G. Grieger, "The Wendelstein 7-X project," *J. Plasma Fusion Res.,* vol. 1, p. 53, 1998.

[16] H.-S. Bosch, "Experience with the commissioning of the superconducting stellarator Wendelstein 7-X," *Fus. Eng. Design,* 2015 in press.

[17] D. Anderson, "Goals and Status of HSX: a Helically Symmetric Stellarator," *J. Plasma Fusion Res.,* vol. 1, p. 49, 1998.

[18] M. C. Zarnstorff, "Physics of the compact advanced stellarator NCSX," *Plasma Phys. Controll. Fusion,* vol. 43, p. A237, 2001.

[19] H. Wobig, "The theoretical basis of a drift-optimized stellarator reactor," *Plasma Phys. Control. Fusion,* vol. 35, p. 903, 1993.

[20] J. Nührenberg, "Quasi-helically symmetric toroidal stellarators," *Phys. Lett.,* vol. A 129, p. 113, 1988.

[21] C. Beidler, "Benchmarking of the mono-energetic transport coefficients—results from the International Collaboration on Neoclassical Transport in Stellarators (ICNTS)," *Nucl. Fus.,* vol. 51, p. 076001, 2011.

[22] E. Ascasibar, " Magnetic Surface Mapping Experiments in TJ-II Heliac," *J. Plasma Fus. Res.,* vol. 1, p. 183, 1998.

[23] R. Jaenicke, *Nucl. Fusion,* vol. 33, p. 687, 1993.

[24] T. Sunn Pedersen and et al., "Confirmation of the topology of the Wendelstein 7-X magnetic field to better than 1:100,000," *Nature Communications,* vol. 7, p. 13493, 2016.

[25] P. Grigull, *Plas. Phys. Cont. Fus.,* vol. 43, p. A175, 2001.

[26] R. Jaenicke, "Detailed investigations of the vacuum magnetic surfaces of the Wendelstein 7-AS stellarator," *Nucl. Fision,* vol. 33, p. 687, 1993.

[27] M. Wakatani, Stellarator and Heliotron Devices, Oxford: Oxford University Press, 1998.

[28] W.-A. Team, "Recent results on plasma behaviour in the W VII-A Stellarator," *Plas. Phys. Contr. Fusion,* vol. 26, p. 183, 1984.

[29] R. Bolton, "Plasma Containment in Medium and High Shear Stellarators," *Physics of Fluids,* vol. 14, p. 1566, 1971.

[30] J. Shohet, in *Fusion* , vol. I, Cambridge, Academic Press, 1980.

[31] C. Alejaldre, "Confinement studies in the TJ-II stellarator," *Plasma Phys. Control Fusion,* vol. 41, p. B109, 1999.

[32] T. Sunn Pedersen, "The Columbia non-neutral torus," *Fus. Sci. Techn.,* vol. 46, p. 200, 2004.

[33] M. Hirsch, "Major results from the stellarator Wendelstein 7-AS," *Plasma Phys. Contr. Fusion,* vol. 50, p. 053001, 2008.

[34] D. Sponge, "Physics Issues of Compact Drift Optimized Stellarators," *18th IAEA Fusion Energy Conf. Proc.,* 2000.

[35] H. Wobig, "The theoretical basis of a drift-optimized stellarator reactor," *Plas. Phys. Cont. Fus.,* vol. 35, p. 903, 1993.

[36] J. Nührenberg, *Trans. Fus. Techn.,* vol. 27, p. 71, 1995.

[37] G. Grieger, *Phys. Plas.,* vol. B4, p. 2081, 1992.

[38] M. Murakami, *Phys. Rev. Lett.,* vol. 66, p. 707, 1991.

[39] A. Dinklage, Plasma Physics, Berlin: Springer, 2005.

[40] R. Brakel, *Plas. Phys. Cont. Fus.,* vol. 39, p. B273, 1997.

[41] H. Laqua, *Phys. Rev. Lett.,* vol. 78, p. 3467, 1997.

[42] H. Idei, *Phys. Rev. Lett.,* vol. 71, p. 2220, 1993.

[43] D. Palumbo, "Some considerations on closed configurations of magnetohydrostatic equilibrium," *Il Nuove Cimento Series B,* vol. 10, p. 507, 1968.

[44] B. Nelson, "Design of the quasi-poloidal stellarator experiment (QPS)," *Fusion Engineering and Design,* Vols. 66-68, p. 205, 2003.

[45] Y. Turkin, "Neoclassical transport simulations for stellarators," *Physics of Plasmas,* vol. 18, p. 022505, 2011.

[46] U. Stroth, "Energy confinement scaling from the international stellarator data base," *Nucl. Fus.,* vol. 36, p. 106, 1996.

[47] R. Brakel, "Electron energy transport in the presence of rational surfaces in the Wendelstein 7-As stellarator," *Nuclear Fusion,* vol. 42, p. 903, 2002.

[48] H. Yamada, "Effect of Rotational Transform on Thermal Transport in Stellarator–Heliotron Plasmas on LHD," *Journal of Fusion Energy,* vol. 36, p. 197, 2017.

[49] W. Lotz, "Collisionless alpha -particle confinement in stellarators," *Plasma Phys. Control. Fusion,* vol. 34, p. 1037, 1992.

[50] C. D. Beidler, "Stochastic diffusion of energetic ions in optimized stellarators," *Physics of Plasmas,* vol. 8, p. 2731, 2001.

[51] S. Murakami and H. Yamada, "Study of energetic particle confinements in strongly inward shifted configurations of LHD," *J. Plasma Fusion Res. SERIES,* vol. 5, p. 620, 2002.

[52] H. E. Mynick and T. K. Chu, "Class of model stellarator fields with enhanced confinement," *Physical Review Letters,* no. 48, p. 322, 1982.

[53] T. Jernigan, *Phys. Plas.,* vol. 2, p. 2435, 1995.

[54] O. Motojima, "Progress of plasma experiments and superconducting technology in LHD," *Fus. Eng. Des.,* vol. 81, p. 2277, 2006.

[55] Y. Takeiri, "Extension of the operational regime of LHD towards a deuterium experiment," *Nuclear Fusion,* vol. 57, p. 102023, 2017.

[56] S. Mazusaki, "Design and installation of the closed helical divertor in LHD," *Fusion Engineering and Design,* vol. 85, p. 940, 2010.

[57] S. Mazusaki, "Helical divertor and the local island divertor in the Large Helical Device," *Plasma Phys. Control. Fusion,* no. 2002, p. 795, 2002.

[58] T. Morisaki, "Local island divertor experiments on LHD," *Journal of Nuclear Materials,* p. 337, 2005.

[59] S. Masuzaki, "A study of the plasma properties under an LID configuration in the CHS," *J. Plasma Fusion Res. SERIES,* vol. 1, p. 310, 1998.

[60] Y. Feng, "Modelling of the island divertor physics and comparison to W7-AS experimental results," *Journal Nucl. Mat.,* p. 857, 2003.

[61] Y. Feng, "Physics of island divertor plasmas in stellarators," *Contrib. Plasma Phys.,* vol. 46, p. 504, 2006.

[62] H. Renner, "Divertor development for Wendelstein 7-X," *J. Plasma Fusion Res SERIES,* vol. 1, p. 143, 1998.

[63] M. Kobayashi, "Divertor transport study in the large helical device," *Journal of Nuclear Materials,* Vols. 363-365, p. 294, 2007.

[64] T. Morisaki, "Progress of the local island divertor experiment," *Fusion Engineering and Design,* no. 65, p. 475, 2003.

[65] A. Weller, "International Stellarator/Heliotron Database progress on high-beta confinement and operation boundaries," *Nuclear Fusion,* vol. 49, p. 065016, 2009.

[66] S. Sakaikibara, "MHD study of the reactor-relevant high-beta regime in the Large Helical Device," *Plas. Phys. Controll. Fusion,* p. 124011, 2008.

[67] J. Reimann, "Pressure-induced breaking of equilibrium flux surfaces in the W7AS stellarato," *Nuclear Fusion,* no. 47, p. 572, 2007.

[68] T. Morisaki, "Superdense core mode in the Large Helical Device with an internal diffusion barriera," *Physics of Plasmas,* vol. 14, p. 056113, 2007.

[69] A. Weller, "Survey of magnetohydrodynamic instabilities in the advanced stellarator," *Phys. Plas.,* vol. 8, p. 931, 2001.

[70] S. Sudo, "Scalings of energy confinement and density limit in stellarator/heliotron devices," *Nuclear Fusion,* vol. 30, p. 11, 1990.

[71] "HSX-assembled.jpg," [Online]. Available: http://www.hsx.wisc.edu/pictures/construction/HSX-assembled.jpg. [Accessed 1 1 2014].

[72] S. T. A. Kumar, "Core magnetic islands and plasma confinement in the H1-NF heliac," *Phys. Plasmas,* vol. 17, p. 082503, 2010.

[73] C. Alejaldre, "First plasmas in the TJ-II flexible heliac," *Plasma Phys. Control. Fusion,* vol. 41, p. A539, 1999.

[74] T. Obiki, "First plasmas in Heliotron J," *Nuclear Fusion,* vol. 41, p. 833, 2001.

[75] T. Sunn Pedersen, "Experimental demonstration of a compact stellarator magnetic trap using four circular coils," *Physics of Plasmas,* vol. 13, p. 012502, 2006.

[76] T. Sunn Pedersen, "Plans for creation and studies of elctron-position plasmas in a stellarator," *New Journal of Physics,* vol. 14, p. 035010, 2012.

[77] A. F. Almagri, "A Helically Symmetric Stellarator (HSX)," *IEEE Trans. Plas. Sci.,* vol. 27, p. 114, 1999.

[78] F. S. Anderson, "Helically symmetric experiment, (HSX) goals, design and status," in *Fusion Technology: 6. international Toki conference on plasma physics and controlled nuclear fusion*, Toki, Japan, 1994.

[79] J. N. Talmadge, "Drift Orbit and Magnetic Surface Measurements in the Helically," *Proc. of 18th IAEA conference,* 2000.

[80] J. M. Canik, "Experimental Demonstration of Improved Neoclassical Transport with Quasihelical Symmetry," *Physical Review Letters,* vol. 98, p. 085002, 2007.

[81] D. Williamson, "Challenges in Designing the Modular Coils for the National Compact Stellarator Experiment (NCSX)," *21st IEEE/NPS Symposium on Fusion Engineering SOFE 05,* 2005.

[82] N. Pomphery, "NCSX magnetic configuration flexibility," *Fus. Sci. Techn.,* vol. 51, p. 181, 2007.

[83] R. L. Dewar, "Relaxed Plasma Equilibria and Entropy-Related Plasma Self-Organization Principles," *Entropy,* vol. 10, p. 621, 2008.

[84] M. G. Shats, "Experimental investigation of the magnetic structure in the H-1 heliac," *Nuclear Fusion,* vol. 34, p. 1653, 1994.

[85] J. H. Harris, "A flexible heliac configuration," *Nucl. Fusion,* vol. 25, p. 623, 1985.

[86] S. M. Hamberger, "H-1 design and construction," *Fusion Technology,* vol. 17, p. 123, 1990.

[87] B. D. Blackwell, "Results from helical axis stellarators," *Phys. Plasmas,* vol. 8, p. 2238, 2001.

[88] B. D. Blackwell, "The Australian plasma fusion reseach facility: recen t results and upgrade plans," in *IAEA conference proceedings*, 2009.

[89] J. Sánchez, "Overview of TJ-II experiments," *Nucl. Fusion,* vol. 51, p. 094022, 2011.

[90] E. Ascasibar, "Overview of recent TJ-II stellarator results," *Nuclear Fusion,* vol. 59, p. 112019, 2019.

[91] [Online]. Available: http://www.iae.kyoto-u.ac.jp/gaiyou/center2.html. [Accessed 4 5 2014].

[92] F. Sano, "H-mode confinement of Heliotron J," *Nuclear Fusion,* vol. 45, p. 1557, 2005.

[93] 10 2013. [Online]. Available: http://htpp.lhd.nifs.ac.jp/. [Accessed 6 October 2013].

[94] 10 2013. [Online]. Available: http://www.sinet.ad.jp/case/nifs/LHD-11cycle4x3.jpg.

[95] M. Fujiwara, "Overview of LHD experiments," *Nucl. Fusion,* vol. 41, p. 1355, 2001.

[96] S. Murakami, "Neoclassical transport optimization of LHD," *Nucl. Fusion,* vol. 42, p. L19, 2002.

[97] O. Motojima, "Initial physics achievements of large helical device experiments," *Phys. Plasmas,* vol. 6, p. 1843, 1999.

[98] S. Imagawa, "Achievement of high availability in long-term operation and upgrading plan of the LHD superconducting system," *Nucl. Fusion,* vol. 47, p. 353, 2007.

[99] K. Ikeda, "First results of deuterium beam opration on neutral beam injectors in the large helical device.," *AIP Conference Proceedings,* vol. 2011, p. 060002, 2018.

[100] F. Warmer, "Energy confinement of hydrogen and deuterium electron-root plasmas in the large Helical Device," *Nucelar Fusion,* vol. 58, p. 106025, 2018.

[101] H. Takahashi, "Realization of high Ti plasmas and confinement characteristics of ITB plasmas in the LHD deuterium experiments," *Nuclear Fusion,* vol. 58, p. 106028, 2018.

[102] IPP, "Research status:," [Online]. Available: http://www.ipp.mpg.de/ippcms/de/pr/forschung/w7as/stand/. [Accessed 12 1 2014].

[103] R. C. Wolf, "A stellarator reactor based on the optimization criteria of Wendelstein 7-X," *Fus. Eng. des.,* vol. 83, p. 990, 2008.

[104] T. Klinger, "Towards assembly completion and preparation of experimental campaigns of Wendelstein 7-X in the perspective of a path to a fusion stellarator plant," *Fus. Eng. des.,* 2013.

[105] C. Beidler, *Fus. Tech.,* vol. 17, p. 11, 1990.

[106] P.-H. Rebut, "A program toward a fusion reactor," *Phys. Fluids B,* no. 3, p. 2209, 1991.

[107] C. D. Beidler, "Stellarator fusion reactors - an overview," in *Proceedings of Toki Conf. ITC12*, Toki, 2001.

[108] H. Maassberg, *Plas. Phys. Contr. Fus.,* vol. 41, p. 1135, 1999.

[109] F. Najmabadi, "The ARIES-CS compact stellarator power plant," *Fus. Sci. Techn.,* vol. 54, p. 655, 2008.

[110] A. Sagara, "Review of stellarator/heliotron design issues towards MFE Demo," *Fus. Eng. Des.,* vol. 85, p. 1336, 2010.

[111] F. Schauer, "Building Block Support Structure for HELIAS," in *IEEEIN PSS 24th Symposium on Fusion Engineering*, 2011.

[112] F. Schauer, "Extrapolation of the W7-X Magnet System to Reactor Size," *Contrib. Plasma Phys.,* vol. 50, p. 755, 2010.

[113] T. Ihli, "Review of blanket designs for advanced fusion reactors," *Fus. Eng. and Des.,* vol. 83, p. 912, 2008.

[114] J. E. Menard, "Prospects for pilot plants based on the tokamak, spherical tokamak and stellarator," *Nuclear Fusion,* vol. 51, p. 103014, 2011.

[115] T. J. Dolan, "Helical fusion power plant economics studies," *Fus. Sci. Techn.,* vol. 47, p. 60, 2004.

[116] J. F. Lyon, "Systems studies and optimization of the Aries-CS power plant," *Fus. Sci. Tech.,* vol. 54, p. 695, 2008.

[117] C. Beidler, *Proc. 16th Fus. Energy Conf. 1996 Montreal, IAEA, Vienna,* vol. Vol. 3, p. 407, 1997.

[118] T. Amano, in *12th Int. Stellarator Workshop,* , Madison, WI, 1999.

[119] H. Wobig, "Group VIIII Adv. Mar. and Techn.," *Nucl. Energy,* no. Vol. 3B, p. 418, 2005.

[120] F. Schauer, *Cont. Plas. Phys.,* vol. 50, p. 755, 2010.

[121] F. Schauer, *Fus. Eng. Des.,* vol. 86, p. 636, 2011.

[122] G. Grieger, "HELIAS stellarator reactor studies and related European technology studies," *Fus. Eng. Des.,* vol. 25, p. 73, 1994.

[123] C. Beidler, "Helias Reactor Studies," Garching, 1995.

[124] "ARIES Web site," [Online]. Available: http://aries.ucsd.edu/ARIES/. [Accessed 4 1 2014].

[125] F. Najmabadi, "Recent progress in the Aries compact stellarator study," *Fus. Eng. Des.,* vol. 81, p. 2679, 2006.

[126] A. R. Raffray, "Engineering challenges in designing an attractive compact stellarator power plant," *Fus. Eng. Des.,* vol. 82, p. 2696, 2007.

[127] T. K. Mau, "Divertor configuration and heat load studies for the ARIES-CS fusion power plant," *Fus. Sci. Techn.,* vol. 54, p. 771, 2008.

[128] A. Sagara, "Improved strcutre and long-life blanket concepts for heliotron reactors," *Nucl. Fus.,* vol. 45, p. 258, 2005.

[129] A. Sagara, "Conceptual design activites and key issues on LHD-type reactor FFHR," *Fus. Eng. Des.,* vol. 81, p. 2703, 2006.

[130] A. Sagara, "Design activites on helical DEMO reactor FFHR-d1," *Fus. Eng. Des.,* vol. 87, p. 594, 2012.

INTERNATIONAL ATOMIC ENERGY AGENCY
VIENNA